**ТРЕТИЙ
МОСКОВСКИЙ
СИМПОЗИУМ
ПО СОЛНЕЧНОЙ СИСТЕМЕ**

**THE THIRD
MOSCOW
SOLAR SYSTEM
SYMPOSIUM**

**8-12 ОКТЯБРЯ 2012
ИНСТИТУТ
КОСМИЧЕСКИХ
ИССЛЕДОВАНИЙ
РАН
МОСКВА**

**8-12 OCTOBER 2012
SPACE
RESEARCH
INSTITUTE
MOSCOW**

3M-S[3] ABSTRACTS

THE PHYSICS OF LUNAR VOLATILES: HOW WET IS THE MOON?

O. Aharonson

A suite of exciting observations indicate water and other volatiles are present at the surface of the Moon. Water molecules may be found as bound, chemically adsorbed, physically adsorbed, or as free ice. Detailed data from multiple instruments on board the Lunar Reconnaissance Orbiter constrain theoretical models for the distribution and mobility of volatiles.

The evidence for water from infrared spectral lines, LCROSS impact release and neutron fluxes will be reviewed and placed in the context of the governing physics.

NEUTRON SUPPRESSION REGIONS ON THE LUNAR POLES: RECENT DATA FROM LEND LRO

I. Mitrofanov, W. Boynton, G. Chin, L. Evans, J. Garvin, A. Kozyrev, M. Litvak, T. McClanahan, R. Sagdeev, A. Sanin, V. Shevchenko, V. Shvetsov, R. Starr, V. Tret'yakov, J. Trombka

Main scientific results are presented from Lunar Exploration Neutron Detector (LEND) after 2 years of lunar mapping onboard NASA's Lunar Reconnaissance Orbiter. The main findings from LEND measurements are described, which corresponds to the major objectives of LEND investigations. Using the LEND neutron data, it is shown that large Permanently Shadowed Regions (PSRs) at lunar poles are not associated with large enhancement of water in the regolith, as it has been previously expected. There are two exceptional cases among them, Shoemaker and Cabeus, which have the signature of enhanced hydrogen in regolith at the permanent shadow. On the other hand, it is found that there are local Neutron Suppression Regions (NSRs) at lunar poles, which are regularly illuminated by the Sun, but could be possible spots of lunar water-rich permafrost.

DIFFERENT FORMS OF SPACE WEATHERING PROCESSES FOUND ON THE MOON AND VESTA

C. M. Pieters[1], the Dawn Team, and NASA Lunar Science Institute (NLSI) associates
[1]Brown University, Providence, RI USA. Contact: Carle_Pieters@brown.edu

Introduction and background: Space weathering refers to an array of processes that measurably alter the character of surfaces that are exposed to the space environment with time. In the lunar case complex agglutinate-rich regolith is formed and grains accumulate nanophase metallic iron (npFe^0) with time [Keller et al., 1997; Pieters et al., 2000; Hapke et al., 2001; Sasaki et al., 2001; Noble et al. 2007]. Several processes are involved, and those driven by extended exposure to the solar wind and a by rain of high velocity micrometeorite bombardment are believed to be the most dominant. The effect on lunar optical properties is dramatic: diagnostic absorption bands are weakened, the near-infrared continuum becomes steeper toward longer wavelengths, and soils typically become darker than their host rock [e.g., Pieters et al, 2000].

As long suspected, a few asteroids (in particular, some S-type asteroids) also appear to have developed similar, but less pronounced, spectral variations as their regolith evolves from the spectral properties of more pristine materials (in particular, ordinary chondrites) [Clark et al., 2001; 2002; Chapman et al., 2004]. A direct association of an S-type asteroid with ordinary chondrites [Gaffey 1993], was confirmed with compositional measurements of the NEAR spacecraft when it landed on Eros (e.g., McCoy et al., 2001). Most importantly, the samples recently returned from the S-type near-earth asteroid Itokawa by Hayabusa [Hiroi et al., 2006; Nakamura et al., 2011; Noguchi et al, 2011] not only showed that the small asteroid is indeed a LL chondritic body, but half of the soil grains studied in Earth-based laboratories also exhibited nanophase coatings of not only Fe, but also a sulfur bearing phase.

The Vesta Story: On the other hand, data from the Dawn mission suggest different processes are dominant in determining the optical properties of soils on Vesta. Dawn data reveal the cratered surface of Vesta to be covered with an extensive regolith that varies in thickness [Jaumann et al., 2012; Denevi et al., 2012]. Morphologically fresh craters often exhibit a prominent surrounding ray system, most of which are brighter than surroundings, but some ray systems are also darker than surroundings [Li et al., 2012; McCord et al., 2012]. As on other planetary bodies, however, the ray systems disappear for somewhat older craters indicating some form of space weathering is in operation. Dawn spectroscopic data [De Sanctis et al., 2011; 2012; Sirkes et al., 2011; Reddy et al., 2012] show that the form of space weathering that occurs on Vesta is distinctive from that of the Moon and the S-type asteroids [Pieters et al, 2012a,b]. Although a wide range of variations in albedo and band strength are observed at craters across Vesta, no systematic near-infrared continuum variations are observed, relative to surrounding soils indicating that development of nanophase-bearing rims or coatings on regolith grains has not occurred. The space weathering model for Vesta is instead one that depends on regolith formation and small scale mixing processes involving dispersed dark and bright components that affect the strength of absorption bands, but little if any nanophase opaques in a transparent matrix that affect the continuum [Pieters et al., 2012b].

Conclusions: The alteration of surface material by space weathering on airless bodies is very dependent on the particular space environment and the geology and composition of the host. The evolving story for the optical properties of regolith on airless bodies include the following general principles and hypothesized implications:

1. Accumulation of nanophase opaque coatings on regolith grains with time is very important and involves solar wind and/or micrometeorite vaporization.
2. Impact mixing within and between local lithologies is very important and is driven by small-scale events.
3. Gravity and electrostatic forces strongly affect the development (and retention) of space weathering products.

Implication I: Impact darkening that creates and disperses micron-scale opaques is common.
Implication II: Stochastic events provide temporary local heterogeneity, but steady-state processes provide regional uniformity.

Some References:

Clark B.E., Lucey P., Helfenstein P., Bell III J.F., Peterson C., Veverka J., McConnochie T., Robinson M., Bussey B., Murchie S., Izenberg N., and Chapman C., Space weathering on Eros: Constraints from albedo and spectral measurements of Psyche crater. Meteoritics and Planetary Science 36, 1617-1638, (2001)
Clark B.E., Hapke B., Pieters C., Britt D. Asteroid space weathering and regolith evolution. In "Asteroids III", Bottke et al. , Eds, pp. 585–599 (2002)

Chapman, C. R., Space Weathering of Asteroid Surfaces, *Annu. Rev. Earth Planet. Sci.* 32:539–567 (2004).
Denevi, B. W. et al., Global Variations in Regolith Depth on Asteroid Vesta, EPSC abstracts (2012).
De Sanctis, M. C., et al., The VIR Spectrometer, *Space Sci Rev*.,163:329–369, (2011)
De Sanctis, M.C. et al. Spectroscopic characterization of mineralogy and its diversity across Vesta. *Science*, 336, 697-700 (2012)
Gaffey, M. J. et al. Mineralogical Variations within the S-Type Asteroid Class, *Icarus* 106, 573-602, (1993).
Hapke, B. Space weathering from Mercury to the asteroid belt. *J. Geophys. Res*.106, 10039–-10073 (2001).
Hiroi, T. et al., Developing space weathering on the asteroid 25143 Itokawa, *Nature* 443, 56- 58 (2006).
Jaumann, R. et al. Vesta's shape and morphology. *Science*, 336, 687-690 (2012)
Keller L. P. and McKay D. S., The nature and origin of rims on lunar soil grains. *Geochimica et Cosmochimica Acta* 61:2331–2341 (1997).
Li, J-Y. et al., Investigating the Origin of Bright Materials on Vesta: Synthesis, Conclusions, and Implications, , *Lunar Planet. Sci.* 43, abstr. 2381 (2012)
McCord T. B. et al., Dark material on Vesta: Synthesis and Interpretations from Dawn Observations, *Lunar Planet. Sci.* 43, abstract #1352, (2012)
McCoy, T.J et al. The composition of 433 Eros: a mineralogical-chemical synthesis. *Meteorit. Planet. Sci.* 36:1661–1672 (2001).
Nakamura, T. et al., Itokawa Dust Particles: A Direct Link Between S-Type Asteroids and Ordinary Chondrites, *Science*, 333, 1113-1116 (2011).
Noble, S. K., Pieters, C. M. & Keller, L. P. An experimental approach to understanding the optical effects of space weathering, *Icarus*, *192*, 629-642, (2007).
Noble, S. K., Keller, L, P. & Pieters, C. M. Evidence of space weathering in regolith breccias II: Asteroidal regolith breccias, *Meteorit. Planet. Sci*. 45, 2007–2015 (2010)
Noguchi, T. et al., Incipient Space Weathering Observed on the Surface of Itokawa Dust Particles, *Science* 333, 1121-1125 (2011).
Pieters C. M. et al., Space Weathering on Vesta: Processes and Products, *Lunar Planet. Sci.* 43, #1254 (2012a)
Pieters et al., The Distinctive Space Weathering on Vesta, *Nature* in review (2012b)
Pieters, C. M. et al. Space weathering on airless bodies: Resolving a mystery with lunar samples, *Meteorit. & Planet. Sci*., 35, 1101-1107 (2000)
Reddy, V. et al. Color and Albedo Heterogeneity of Vesta from Dawn. *Science*, 336, 700-704 (2012)
Sasaki, S., Nakamura, K., Hamabe, Y., Kurahashi, E. & Hiroi, H. Production of iron nanoparticles by laser irradiation in a simulation of lunar-like space weathering. *Nature* 410, 555-557 (2001).
Sierks, H. et al., The Dawn Framing Camera, *Space Sci Rev*, 163:263–327, (2011)

STUDY OF WATER RESOURCES ON THE MOON; FIRST RESULTS AND WORKING PLANS.

A. T. Basilevsky[1], A. M. Abdrakhimov[1], E. N. Slyuta[1], A. V. Ivanov[1], N. R. Khisina[1], V. A. Dorofeeva[1], J. W. Head[2], C. M. Pieters[2], M. T. Zuber[3],
[1]Vernadsky Institute, RAS, Kosygin Str., 19, Moscow, 119991, Russia; [2]Dept. Geological Sciences, Brown University, Providence 02912, USA; [3]MIT, Cambridge, 02139, MA, USA. **Contact:** *atbas@geokhi.ru and alexander_basilevsky@brown.edu*

Introduction: Until recently it was believed that the Moon is very dry and only the permanently shadowed cold traps at lunar poles were suspected of having water ice (e.g., Watson et al., 1961). New studies have changed our thinking about the presence of water on the Moon: 1) The presence of water ice in polar regions was confirmed in several space mission (e.g., Feldman et al., 1998, 2000; Mitrofanov et al., 2010, 2011; Colaprete et al., 2010). 2) New studies of some lunar samples showed that they contain H_2O/OH in amounts suggesting that some lunar magmas had 100's of ppm water (e.g., Saal et al., 2008; Greenwood et al., 2011). Signatures of the presence of H_2O/OH in lunar magmas were found in some lunar olivines in the form of Cr,Ca-rich symplectic inclusions (Khisina, 2012) and Chandrayaan-1 M3 spectral observations showed the presence of H_2O/OH in the central peak of the lunar crater Bullialdus (Klima et al., 2012). Our research project is devoted to the study of water ice in polar areas and potential resources of water outside the poles.

Water ice in polar areas: The presence of H_2O ice in the polar areas of the Moon is now confirmed but understanding details of its accumulation versus loss and its current distribution demand further studies. The LRO/LEND neutron-spectrometer measurements (low flux of epithermal neutrons is indicative of the presence of hydrogen) revealed an enigmatic picture: Not all of the permanently shadowed areas are characterized by a substantial decrease in the neutron flux, and the decreased flux is frequently observed outside the permanently shadowed areas (Mitrofanov et al., 2010, 2011; Sanin et al., 2012). Figure 1 (left) shows four craters: Shackleton (D = 21 km), Haworth (35 km), Shoemaker (51 km) and Faustini (39 km), whose floors are permanently shadowed, but only one of them (Shoemaker) shows a statistically significant decrease in the flux of epithermal neutrons (e.g., Sanin et al., 2012). We are working on the geologic context of this enigma. In particular we use LOLA data to confirm or disprove the suggestion that downslope movement of regolith on the slopes of permanently shadowed craters could episodically destroy ice accumulations (Basilevsky et al., 2012). Figure 1 (right) shows the LOLA-derived distribution of relatively small (D >250 m) impact craters superposed on the crater Shackleton and its close vicinity (Zuber et al., 2012). It is seen that the density of small craters on the Shackleton inner slopes is significantly lower than on its rim and close environs; this agrees with the previously mentioned suggestion that downslope movement of regolith is the mechanism responsible for the destruction of the near-surface ice accumulation.

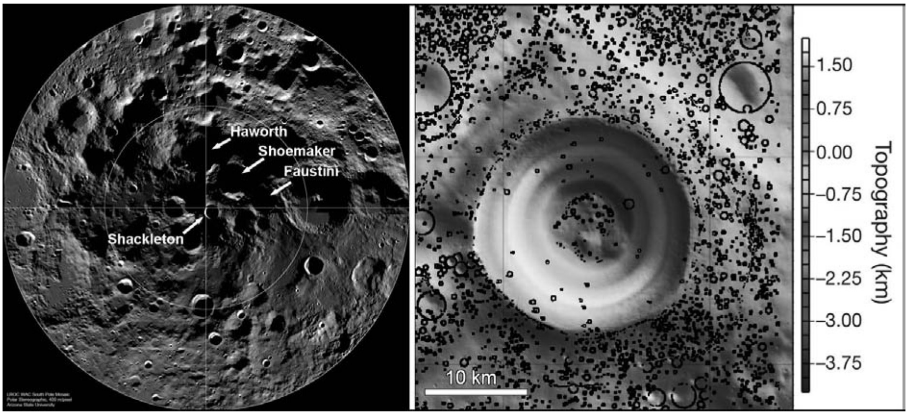

fg. 1. Left is LROC WAC mosaic of the South pole of the Moon (80 to 90°S); Right is the topographic map of Shackleton crater with the superposed small impact craters (black dots and circles), source is Figures 1a,e of Zuber et al., 2012.

The decrease of epithermal neutron flux indicative of the presence of hydrogen in some periodically illuminated areas mentioned above can be explained by recent modeling of the LRO/Diviner radiometer measurements (Elphic et al., 2012). We plan to complete the analysis of LROC-NAC images seeking morphologic signatures of the presence of ice in the areas thermally favorable and not favorable for near-surface ice accumulation.

H_2O/OH in non-polar areas: The presence of H_2O/OH was found in samples of pyroclastic glasses (up to 240 ppm, Weber et al., 2009), melt inclusions in olivine grains in pyroclastic glasses (up to 1400 ppm, Hauri et al., 2011), and in apatite grains (up to 2400 ppm, Boyce et al., 2010). Signatures of the presence of H_2O/OH in lunar magmas were also found in some lunar olivines in the form of Cr,Ca-rich symplectic inclusions (Khisina, 2012). Pyroclastic deposits, whose distribution on the Moon was mapped via remote sensing (Gaddis et al., 2003) are interesting as a potential water resource and we plan to study them geologically, in particular, to estimate thicknesses of their mantles through analysis of the morphology of superposed small impact craters on LROC-NAC images. The relatively high water contents in some lunar magmas imply the possibility of postmagmatic hydrothermal activity and incorporation of water in major magmatic minerals (amphibole?). Spectroscopic signatures of H_2O/OH (Klima et al., 2012) recently found in the central peak of the 61-km crater Bullialdus (Figure 2) may indicate the presence of relatively large areas with hydrothermal/magmatic mineralogy.

Central peaks of large lunar craters are special places in two senses. One is that if they are high and steep-sloped enough that regolith on their surfaces should be very immature. This effect was found on the edges of large and steep-sloped lunar rilles and fossae (e.g., Swann et al., 1972; Florensky et al., 1974) and its applicability to the case of the Bullialdus central peak is demonstrated by the peak blocky surface seen in Figure 2c. The mature regolith should be essentially free of H_2O/OH due to long history of meteorite/micrometeorite regardening even if its source material had initially contained the volatiles. The immature regolith has a much better chance to preserve the initial H_2O/OH content.

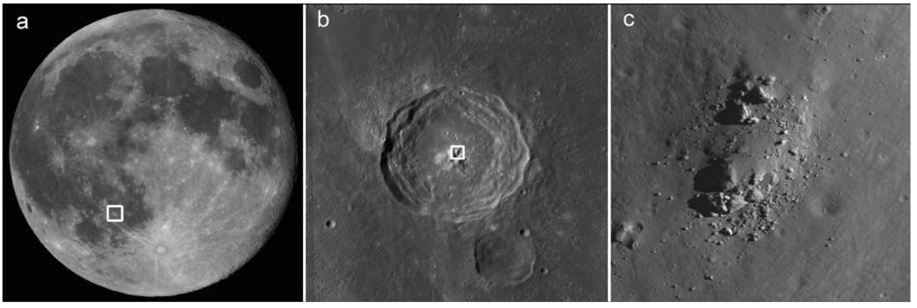

fig. 2; **a** – global view of the near side of the Moon with position of crater Bullialdus shown (white box); **b** –portion of LROC WAC image of crater Bullialdus, white box shows the position of area presented in the framelet **c**; **c** – portion of LROC NAC image M114098458LE, the image area is 500 x 500 m.

The second special feature of central peaks is that they are localities of significant uplift of material from depths beneath the crater floor of about 1/10 of the crater diameter (Melosh, 1989). In the case of Bullialdus crater the material of its central peak probably derived from a depth of ~6 km, certainly beneath the Mare Nubium basaltic fill. This is confirmed by analysis of the Clementine and Chandrayan-1 M3 data which show the presence of anorthositic norite and noritic anothosite within the Bullialdus central peak (Thompkins et al. 1994; Klima et al., 2012). Bullialdus is a post-mare crater of Eratosthenian age (Wilhelms and McCauley, 1971), but the material of its central peak is certainly pre-mare, representing the floor of the Nubium impact basin which is of Nectarian or pre-Nectarian in age. We plan to better understand the geologic context of the Bullialdus H_2O/OH anomaly through its geologic mapping.

Conclusions: The considerations outlined above show that water in polar areas of the Moon and in the products of lunar magmatic/postmagmatic activity deserve thorough study and could be a practical resource in the future exploration of the Moon. The photogeologic analysis of the LROC, LOLA and Mini-RF data appears to be a promising approach to better understand the details of the distribution of water ice in polar areas of the Moon and processes responsible for its accumulation and loss. The significantly lower density of small impact craters on the inner slopes of crater Shackleton seen in the LOLA data compared to that on its rim and close vicinity (Zuber et al., 2012) seems to confirm the suggestion of Basilevsky et al. (2012) that the downslope movement of regolith on the inner slopes of the relatively large permanently shadowed craters is the mechanism responsible for the episodic destruction of the near-surface ice accumulation. Photogeologic analysis of LROC images also appears to be a promising approach to better understand the geologic structure of potential resources of water of magmatic/postmagmatic origin. Missions involving lunar rovers may be a productive way to make progress in the study of polar and non-polar water resources of the Moon.

Acknowledgements: We acknowledge support from the Program 22 of Russian Academy of Sciences and help in preparation of this work by D.D. Badyukov and B.A. Ivanov.

References: [1] Basilevsky et al. SSR, 2012, 49, 89-107. [2] Boyce et al. Nature, 2010, 466, 466–470. [3] Colaprete et al. Science, 2010 330, 463-466. [4] Elphic et al. LPSC-43, 2012, abs. 1895. [5] Feldman et al. Science. 1998. 281. 1496–1500. [6] Feldman et al. JGR-Planets, 2000. 105, 4175-4195. [7] Florensky et al. Soviet Academy Doklady, 1974, 214, No 1, 75-78. [8] Greenwood et al. Nature Geoscience, 2011. 4. 79-82. [9] Hauri et al. LPSC-40, 2009, abs. 2344. [10] Khisina et al. LPSC-43, 2012, abs. 1068. 11] Klima et al. LPSC-43, 2012, abs. 2517. [12] Melosh H.J. Impact cratering – A geologic process, Oxford, NY, 1989, 245 p. [13] Mitrofanov et al. Science, 330. 2010. 483-486. [14] Mitrofanov et al. LPSC-42, 2011, abs. 1787. [15] Saal et al. Nature. 2008. 454. 192-195. [16] Sanin et al. LPSC-43, 2012, abs 2134. [17] Swann et al. Apollo 15 Preliminary Science Report. 1972. 5-1 – 5-112. [18] Tompkins et al. Icarus, 1994, 110, 261-274. [19] Watson et al. JGR 1961. 66, 1598-1600. [20] Wilhelms & McCauley Geologic Map of Near Side of the Moon, USGS Map I703, 1971. [21] Zuber et al. Nature, 2012, 486, 378-382.

LUNAR FLOOR-FRACTURED CRATERS: ASSESSMENT OF FORMATION BY MAGMATIC PROCESSES.

L. M. Jozwiak[1], J. W. Head[1], M.T. Zuber[2], D.E. Smith[2], G.A. Neumann[3],
[1]Department of Geological Sciences, Brown University, Providence, RI 02912, USA; [2]Department of Earth, Atmospheric, and Planetary Sciences, Massachusetts Institute of Technology, Cambridge, MA 02139, USA, [3]Solar System Exploration Division, NASA Goddard Space Flight Center, Greenbelt, MD 20771, USA. Contact: lauren_jozwiak@brown.edu

Introduction: Floor-fractured Craters (FFCs) are a distinct class of lunar crater identified by an anomalously shallow floor, covered in radial/concentric/ or polygonal fractures; additional features of FFCs include patches of mare material, dark-halo pits, moats, and ridges. The morphologic characteristics of these craters were first described by Schultz [1], who also classified FFCs into 8 subcategories based on morphology. Two formation mechanisms (Fig. 1) have been proposed for FFCs: 1) magmatic intrusion [1] and uplift in which an intruding dike encounters the low density brecciated lens beneath a crater and begins to spread laterally and inflate, uplifting and fracturing the floor of the crater (Fig. 1c), 2) viscous relaxation [2] in which the rheologic properties of the crust permit viscous flow in the newly emplaced crater, relaxing long-wavelength topographic features, uplifting and fracturing the floor (Fig. 1b).

Analysis of FFC Morphology, Distribution, and Formation: Using the newly available Lunar Orbiter Laser Altimeter (LOLA) and Lunar Reconnaissance Orbiter Camera (LROC), we make detailed morphometric and morphologic observations of FFCs [3]. We compare FFCs to Copernican-aged craters to highlight the differences between the crater populations. We classify the lunar population of FFCs using the Schultz [1] classification scheme as a starting point, and including a newly recognized class, morphologically distinct from the previously recognized classes. Our global catalogue of FFCs also permits mapping of the spatial distribution of FFCs (Fig. 2), which we use in conjunction with our measurements of the morphologic and morphometric characteristics of FFCs to assess the viability of the proposed formation mechanisms.

Our data and analyses support formation of FFCs by magmatic intrusion, with many FFC morphologies showing an intimate link between crater location, crustal thickness, and intrusion driving pressure. We provide estimates of intrusion dimensions and emplacement driving forces for a variety of FFC morphologic types [4]. We then analyze the process of magmatic intrusion, and the mechanics associated with each part of the intrusion process. We then use the inferred intrusion dimensions to make predictions about the gravity signature of these intrusions, using the hypothesis that laccoliths beneath the crater floor will produce an identifiable gravity anomaly [5]. Our predictions about the presence and size of intrusion related gravity anomalies can be tested with data from the Gravity Recovery and Interior Laboratory (GRAIL) mission [6].

References: [1] P. Schultz (1976) *The Moon* 15, 241; [2] Z. Danes (1965) *Astrogeologic Studies, Annu. Prog. Rep. A,* 81; [3] L. Jozwiak, J. Head, M. Zuber, D. Smith, and G. Neumann (2012) Lunar Floor-Fractured Craters: Classification, Disribution, Origin and Implications for Magmatism and Shallow Crustal Structure, *Journal of Geophysical Research- Planets, in revision.* [4] L. Jozwiak, J. Head, and L. Wilson (2012) Lunar Floor-Fractured Craters: Mechanics of Magmatic Intrusion Formation and Analysis of Crustal Structure, *Geophysical Research Letters, in preparation.* [5] J. Dvorak and R.J. Philips (1978) *Proc. Lunar Planet Sci. Conf. 9th*. 3651-3668. [6] M. Zuber, D. Smith, L. Alkalai, D. Lehman, and M. Watkins (2008) *Lunar Planet Sci. Conf. XXXIX*, Abstract #1074.

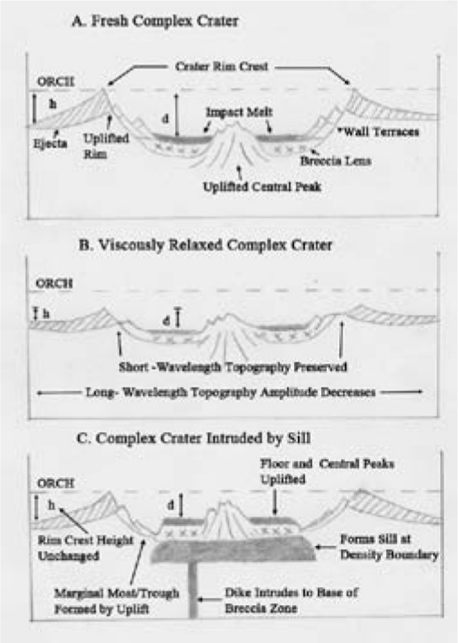

fig. 1. Morphologic effects of Viscous Relaxation (b.) and Magmatic Intrusion (c.) on the topography of a complex crater. Although both processes shallow the floor of the crater (decrease d), note how viscous relaxation relaxes the original rim crest height (ORCH), whereas magmatic intrusion has no effect on the ORCH.

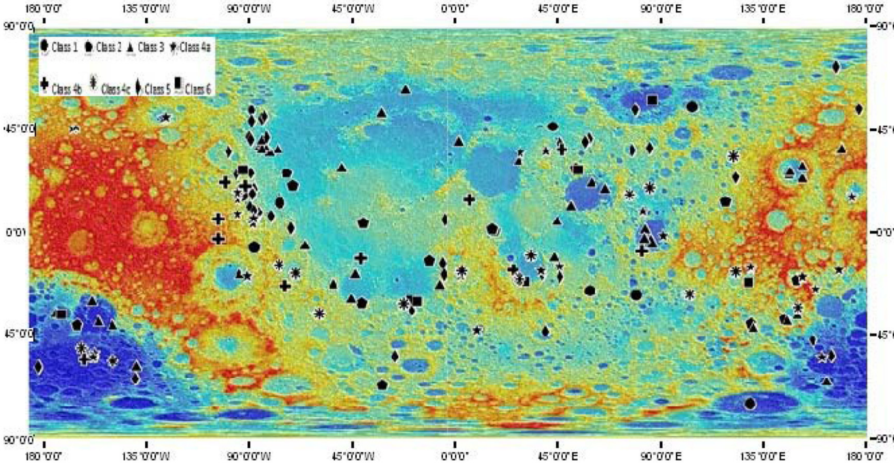

fig. 2. Areal Distribution of Lunar Floor-Fractured Craters[3].

LUNAR ORIENTALE BASIN: CHARACTERIZATION AND INSIGHTS INTO MULTI-RINGED BASIN FORMATION.

J. W. Head,
Department of Geological Sciences, Brown University, Box 1846, Providence, RI 02912, USA. Contact: James_Head@brown.edu

Introduction: The 930 km diameter Orientale basin is the youngest and most well-preserved large multi-ringed impact basin on the Moon [1-10]; it has not been significantly filled with mare basalts [20], as have other lunar impact basins, and thus the nature of the basin interior deposits and ring structures are very well-exposed and provide major insight into the formation and evolution of planetary multi-ringed impact basins [1-10] (Fig. 1). New data from the armada of recent and ongoing lunar spacecraft are providing multiple data sets, new characterization, and new insights into the origin and evolution of the Orientale basin [11-15].

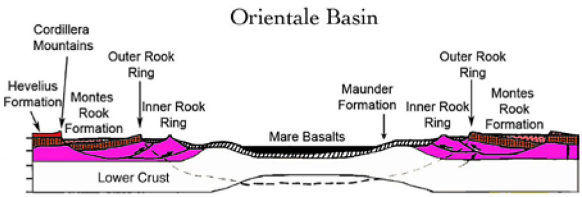

fig. 1. Schematic cross section of the Orientale basin illustrating the relation of the basin rings to basin deposits (interior and exterior) as envisioned in 1993 [4].

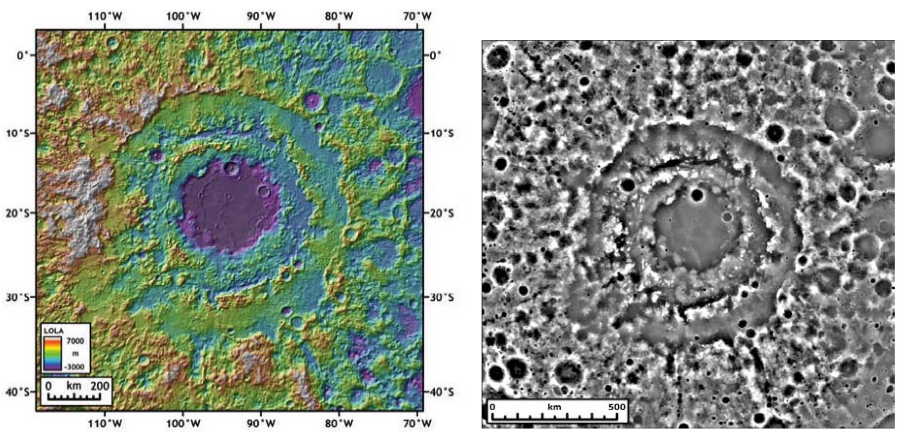

fig. 2. LOLA altimetry map (left) and detrended map (right) of the Orientale basin region.

Lunar Orbiting Laser Altimeter Data: Acquisition of new altimetry data for the Orientale basin from the Lunar Orbiting Laser Altimeter (LOLA) on board the Lunar Reconnaissance Orbiter (Fig. 1,2) has permitted characterization of the pre-basin, basin and ring topography, and we have previously outlined several implications for basin formation and evolution.

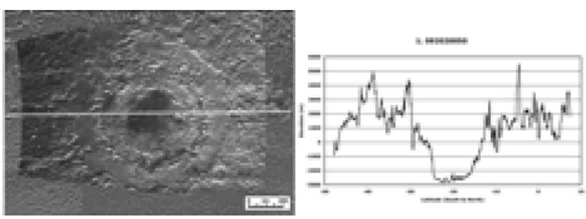

fig. 3. LOLA profile 092020050 through the center of the Orientale basin and into the pre-Orientale Mendel-Rydberg basin to the south (left).

Pre-basin topography: There is a broad W-E decrease in elevation, consistent with regional changes in crustal thickness [15]. Pre-basin topography had a major effect on the formation of Orientale; we have mapped dozens of impact craters underlying both the Orientale ejecta (Hevelius Formation-HF) (Fig. 2; see rough terrain between -5 and +10 degrees in Fig. 3) and the unit between the basin rim (Cordillera ring-CR) and the Outer Rook ring (OR) (known as the Montes Rook Formation-MRF) (Fig.1), ranging up in size to the Mendel-Rydberg basin just to the south of Orientale (Fig. 2;3-left); this crater-basin topography has influenced the topographic development of the basin rim (CR), sometimes causing the basin rim (see peaks in Fig. 3) to lie at a topographically lower level than the inner basin rings (OR and Inner Rook-IR). LOLA data show the pre-Orientale Grimaldi basin (Fig. 2, upper right) and several crater-basin structures in excess of 200 km. Several ghost craters are observed in LOLA data between the Cordillera and the Outer Rook ring [1], but not inside the Outer Rook. A dark ring previously thought to represent a crater partly located inside the IR [16] is now known to be a pyroclastic deposit from an eruption plume [17]. The deposits inside the OR are dominated by the Maunder Formation (MF) (Fig. 1) which consists of smooth plains (on the inner basin depression walls and floor) and rough corrugated deposits (on the IR plateau); this topographic configuration supports the interpretation that the MF consists of different facies of impact melt.

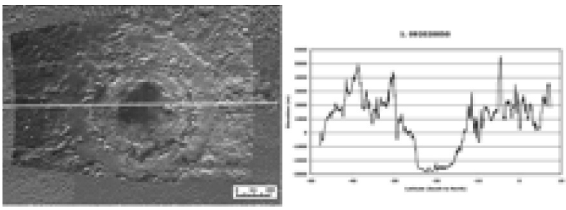

fig. 4. LOLA profile 092012251 through the center of the Orientale basin and the 55 km diameter crater Maunder on the northern part of the inner basin floor (right).

Basin Interior Topography: The total basin interior topography is highly variable and typically ranges ~6-7 km below the surrounding pre-basin surface, with significant variations in different quadrants (Fig. 1-4). The CR consists of linear and cuspate inward-facing scarps; continuity is interrupted by radial crater chains, and amplitude varies due to pre-existing topography (very high in southern quadrant due to M-R basin rim; lower in east quad due to intersecting pre-existing basin and crater interiors). Between the OR and CR, topography dips away from the OR to the base of the CR; lowest depressions are often filled with mare. The OR is generally continuous topographically and consists of a set of asymmetrical massifs with steeper scarps facing inward, prominent near-rim crest topography, and transitioning outward to the outward sloping MRF surface. Compared to the CR, the OR is often much more sinuous in outline, with numerous re-entrants. The IR ring is characterized by a ring of peaks and massifs situated on a broad plateau between the inner depression and the OR, surrounded and sometimes covered by Maunder Formation, interpreted to be impact melt. The plateau itself is very rough (Fig. 2-4) and LOLA data reveal the presence of a narrow 10-25 km wide deep depression between the plateau and the base of the OR ring. This depression is often over a km deep, and is floored by impact melt and mare deposits.

The topography of the western quadrant is highly variable compared to the rest of the basin interior; here the CR and OR rings are much less distinctive, the topography between the CR and MR is higher and radial structure is more prominent, and the IR is subdued except for a very prominent arrow-shaped massif at ~225° (Fig. 2). This asymmetry is paralleled in the HF in that secondary crater chains are much more prominent in the western than eastern quadrant.

Nature of the inner basin depression: The inner basin depression is about 2-4 km deep below the IR plateau (Fig. 2,4); although some of this topography is due to post-basin-formation thermal response to impact energy input and uplifted isotherms [5], a significant part of it may be related to the initial short-term collapse of an inner melt cavity, as outlined in the nested melt cavity model of ringed basin formation [18-19]. The inner depression is floored by tilted mare basalt deposits [20] surrounding a central pre-mare high of several hundred meters elevation and deformed by wrinkle ridges with similar topographic heights (Fig. 4). We have explored the possibility that the very sharp boundary scarp of the inner depression is due to thermal stresses associated with the cooling of the melt sheet; these data suggest that the melt sheet thickness may be in excess of 10 km [21] and together with consideration of the nested melt cavity model [18,19], that the impact event melted significant volumes of mantle material. This material would have undergone differentiation [22]. The depth of the 55 km diameter post-Orientale Maunder crater, located at the edge of the inner depression, is in excess of 3 km (Fig. 4); this depth permits the quantitative assessment of the nature of the deeper sub-Orientale material sampled by the crater. The mineralogy of the Orientale deposits favors the interpretation that the Orientale basin sampling depth was largely confined to the upper crust [13-15]; the mineralogy of the central peaks of the post-Orientale 55 km diameter Maunder crater, located in the basin interior depression inward of the IR (Fig. 4), are somewhat enriched in low-Ca pyroxene, apparently sampling noritic material [20] likely to be part of the differentiated melt sheet [22,23].

Location of the basin rim and excavation cavity: In contrast to some previous interpretations [see summary in 16], the distribution of these features and deposits supports the interpretation that the OR ring (Fig. 1) is the closest approximation to the basin excavation cavity. This is supported by estimates of the thickness and volume of the Hevelius Formation [24] (Fig. 5). The prominence of the pre-Orientale craters right up to the Cordillera ring, the outward-sloping surface of the MRF, the ghost craters between the Cordillera and Outer Rook, all support the model that the Cordillera ring represents failure of the rim crest (Outer Rook ring) at the structural uplift hinge line, and collapse inward to form a megaterrace [1,4,19] (Fig. 6).

Origin of basin rings in multi-ringed basins: These new data for the Orientale basin provide insight into basin ring formation (Fig. 6), supporting a model that includes the formation of a nested melt cavity, the expansion of a peak-ring basin [25, 26] by addition of an outer (Cordillera) ring by inward collapse at the edge of structural uplift along the base of the displaced zone, and the addition of an inner depression formed from an expanding nested melt cavity, and its collapse [18,19], followed by solidification of a melt sea [21-23]. The newly documented annular depression at the base of the OR is interpreted to have formed during the inward collapse of the peak-ring bounded inner melt cavity. Mare volcanism is shown to have occurred later, over an extended period of time, and does not appear to be directly associated with the basin-forming event [20]. Together, these observations provide a comprehensive new model [27, 28] for the formation and evolution of Orientale a large, young, multi-ring basin.

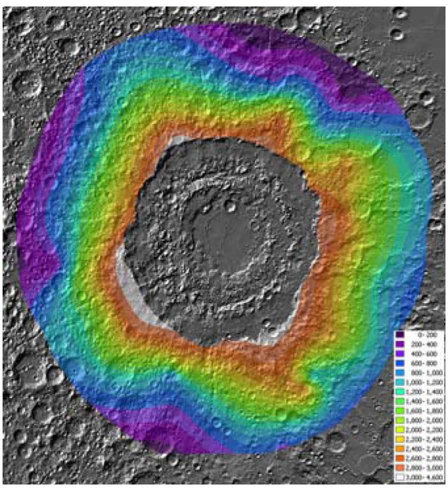

fig. 5. Estimates of the thickness and radial thickness decay of the Hevelius Formation (Orientale radial ejecta facies) from analysis of the burial of pre-Orientale craters [24].

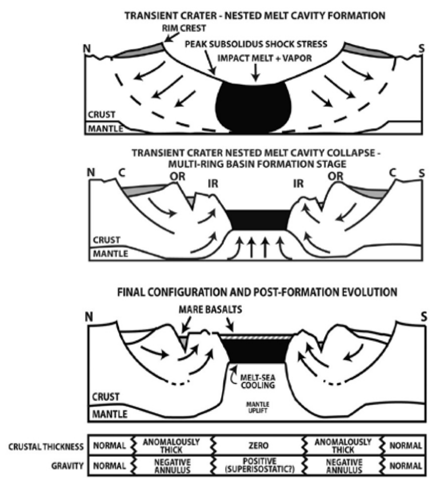

fig. 6. Stages in the formation and early evolution of the Orientale basin and predictions for crustal structure [27, 28].

References: 1. J. Head, Moon 11, 327, 1974; 2. K. Howard et al., RGSP 12, 309, 1974; 3. J. McCauley, PEPI 15, 220, 1977; 4. J. Head et al., JGR 98, 17149, 1993; 5. S. Bratt et al., JGR 90, 3049, 1985; 6. P. Spudis et al., JGR 89, C197, 1984; 7. B. Hawke et al., JGR 108, 5050, 2003; 8. B. Hawke et al., GRL 18, 2141, 1991. 9. C. Pieters et al., JGR 98, 17127, 1993; 10. B. Bussey & P. Spudis, GRL 24, 445, 1997; JGR 105, 4235, 2000; 11. T. Matsunaga et al., GRL 35, L232012008, 2008; 12. M. Ohtake et al., Nature 461, 236, 2009; 13. C. Pieters et al., LPSC 40, 2052, 2157, 2009; 14. S. Kumar et al., LPSC 40, 1584, 2009; 15. M. Wieczorek et al., Rev. Min. Geochem., 60, 221, 2006; 16. P. Spudis, Geology of Multi-Ringed Basins, 263 p., 1993; 17. J. Head et al., JGR, 107, 1413, 2002; 18. M. Cintala and R. Grieve, MAPS, 33, 889, 1998; 19. J. Head, GRL, *37,* L02203, 2010; 20. J. Whitten et al., JGR, *116,* E00G09, 2011; 21. W. Vaughan et al., LPSC 43, 2012; 22. W. Vaughan et al., 3M3, this volume, 2012; 23. W. M. Vaughan, J. W. Head, L. Wilson, P. C. Hess, Geology and petrology of enormous volumes of impact melt on the Moon: A case study of the Orientale basin impact melt sheet, *Icarus*, submitted, 2012; 24. C. Fassett et al., GRL, 38, L17201, 2011; 25. D. M. H. Baker et al., JGR., 117, E00H16, 2012; 26. L. Cheek et al., 2nd Lunar Highlands Conference, 2012; 27. J. Head et al., Orientale Multi-Ring Impact Basin: New Insights into Crustal Structure and Depth of Sampling from Chandrayaan-1 Moon Mineralogy Mapper (M³) Spectroscopy Data, *JGR*, to be submitted, 2012; 28. J. W. Head, M. T. Zuber, D. E. Smith, G. A. Neumann, C. I. Fassett, I. Garrick-Bethell, J. L. Dickson, Orientale Multi-Ring Basin: New Insights into Ring Origin and Transient Cavity Geometry from Lunar Reconnaissance Orbiter (LRO) Lunar Orbiter Laser Altimeter (LOLA) Data, to be submitted to *PSS*, 2012.

STATISTICS OF SUBKILOMETER-SCALE TOPOGRAPHY OF THE MOON: SEARCH FOR A SIGN OF VOLATILES

M. A. Kreslavsky[1], J. W. Head[2],
[1]Earth and Planetary Sciences, University of California – Santa Cruz, Santa Cruz, CA, 95064, USA; [2]Geological Sciences, Brown University, Providence, RI, 02912, USA. Contact: mkreslav@ucsc.edu

Introduction:

The statistical characteristics of subkilometer-scale topography turned out to be a very effective indicator of a range of volatile-related geological processes shaping the surface of Mars. For example, there is a very strong latitudinal trend in the abundance of very steep (>25º) slopes on Mars: steep slopes are virtually absent at high latitudes and abundant in the tropics [1]. In both mid-latitude zones, a very strong north-south asymmetry of steep slopes is observed: pole-facing slopes are almost absent. These trends are caused by episodic effective destruction of steep slopes by flowing liquid water [1]: at high latitudes and at the pole-facing slopes in mid-latitudes the day-average surface temperature exceeded 0ºC during periods of high obliquity of the martian spin axis, while in the tropics and on the equator-facing slopes in mid-latitudes, the day-average surface temperature has never exceeded 0ºC during the last ~3 Ga of martian geological history. Another conspicuous latitudinal trend on Mars is topographic smoothness and increased topographic concavity at the high latitudes [2, 3]; this has been explained as the result of repeated deposition and removal of thin ice-rich mantles that smoothly fill local topographic lows [3]. The detection of these martian trends has been made possible by the high internal precision of range measurements by Mars Orbiting Laser Altimeter (MOLA) onboard Mars Global Surveyor (MGS). Here we report on our attempts to search for volatile signatures in the statistical characteristics of the topography of the Moon with even more precise data from Lunar Orbiter Laser Altimeter (LOLA) onboard the Lunar Reconnaissance Orbiter (LRO) [4,5].

Expectations:

If a large but typical cometary nucleus (~ 10 km diameter) hit the Moon, it would make a ~ 100 km diameter crater and bring the equivalent of an ~1.5 cm thick global layer of volatiles. H_2O would quickly condense on the night side of the planet forming thin deposits, then, at a time scale of a few months it would migrate to generally cold areas (polar regions and pole-facing slopes in mid-latitudes), where it would form much thicker deposits. Then, at much longer time scales, H_2O would progressively migrate to deeper cold traps and/or dissipate to space. Residuals of such deposits in the coldest places on the Moon are thought to be responsible, at least, partly, for the observed enhancement of the H abundance in the uppermost meter of the surface in these places [6-8]. Some of these transient deposits could potentially leave some traces in the surface morphology. Such traces are not easy to see in the images, because the cold traps are often in shadow or illuminated by too low sun. They are not detectable in laser-altimeter-derived topographic maps because of insufficient resolution. However, they might affect topography sufficiently to be potentially detectable by statistical means.

If the comet contained large quantities of more volatile species (e.g., CO_2), they would form a transient atmosphere with a pressure on the order of ~10 Pa, and later condense in the coldest cold traps (after a significant part of H_2O migrated there) and/or dissipate to space. The possible atmospheric pressure (~10 Pa) is much lower than the triple point of H_2O (~600 Pa), and liquid water and related distinctive morphologies are not expected. Formation of some aeolian features might conceivably be possible, but no signs of them have ever been reported. The latter does not mean that limited aeolian transport has never occurred on the Moon. Aeolian morphologies might be absent because, on one hand, a "windy" atmosphere did not last a long time, and thus large-scale aeolian bedforms had no time to form, and on the other hand, the last such cometary impact happened long ago and the small-scale aeolian features were completely obliterated by regolith gardening with small meteoroids.

Observations:

We analyzed a number of statistics of slopes and curvatures at the shortest baselines (~50 – 200 m) achievable with the LOLA data set. At these baselines surface topography is dominated by regolith gardening and the most recent (Copernican and Eratosthenian) geological events; the effect of the early lunar geological processes is minor. All techniques and approaches that proved diagnostic on Mars were applied to the Moon using LOLA data: we visually analyzed global LOLA-derived maps of the topographic roughness, concavity, and slope asymmetry; we also plotted latitudinal variations of slope asymmetry, abundance of steep north- and south-facing slopes, etc. In addition, we considered the roughness and concavity on the north-facing and south-facing 230 m baseline slopes steeper than some limit (5º, 10º, 20º). None of these approaches and techniques shows any detectable lunar latitudinal trends.

The only detected latitudinal effect was seen in the density of large impact craters with steep walls in the highlands: it generally increases by a factor of 1.5 from polar to equatorial regions [9]. This effect, however, is probably not related to volatiles; estimates based on the present-day NEA population [10-12] predict (a somewhat weaker) enhancement of the effective impact rate at low latitudes.

One poorly understood observation are statistically significant regional variations of the density of steep-walled craters in addition to those predicted in [6-8], namely, a significant shortage of such craters in southern farside (partly in the area of the South Pole-Aitken (SPA) basin). The topographic roughness of the highlands also shows significant regional variations, with a relatively smooth southern farside and relatively rough north-eastern farside. Both distributions correlate with topography at regional scales, if we smooth down the distributions of steep-walled craters, highland roughness and topography to spherical harmonics of degrees 1 and 2. If the observed correlation with topography is causal, a possible mechanism could be related to a transient atmosphere in the past. The regional-scale topographic amplitude is ~ 1/2 of the scale height of the possible transient CO_2 atmosphere; that is the pressure in SPA was a factor of 1.6 greater than at high farside highlands. This might cause a difference in atmosphere-induced surface alteration, but only for very short periods of time.

Conclusions:

Analysis of LOLA data with statistical methods did not reveal any signs of a role of volatiles of formation of subkilometer-scale geomorphological features on the Moon. We have not exhausted all potential of LOLA data yet. We continue to assess the data to search for the presence of any signals in the LOLA altimetry data that might be related to the current presence or past history of volatiles on the Moon.

References:
[1] Kreslavsky & Head (2003) GRL 30, 1815, doi: 10.1029/2003GL017795.
[2] Kreslavsky & Head (2000) JGR 105, 26695-26712, doi: 10.1029/2000JE001259.
[3] Kreslavsky & Head (2002) GRL 29, 1719, doi: 10.1029/2002GL015392.
[4] Smith et al. (2010) GRL 37, L18204, doi: 10.1007/s11214-009-9512-y.
[5] Rosenburg et al. (2010) JGR 116, E02001, doi: 10.1029/2010JE003716.
[6] Feldman et al. (2001) JGR 106, 23,231–23,251, doi: 10.1029/2000JE001444.
[7] Lawrence et al. (2006) JGR 111, E08001, doi:10.1029/2005JE002637.
[8] Mitrofanov et al. (2012) JGR 117, E00H27, doi:10.1029/2011JE003956.
[9] Kreslavsky et al. (2012) LPS XLIII, 1193.
[10] Gallant et al. (2009) Icarus 202, 371-382, doi: 10.1016/j.icarus.2009.03.025.
[11] Le Feuvre & Wieczorek (2011) Icarus 214, 1-20, doi: 10.1016/j.icarus.2011.03.010
[12] Ito & Malhorta (2010) Astron. Astrophys. 519, A63, doi: 10.1051/0004-6361/200912901.

PLACING CONSTRAINTS ON THE LUNAR INTERNAL STRUCTURE BY SELENE-2 GEODETIC MEASUREMENTS.

K. Matsumoto[1], F. Kikuchi[1], R. Yamada[1], T. Iwata[2], Y. Kono[1], S. Tsuruta[1], H. Hanada[1], S. Goossens[3], Y. Ishihara[4], S. Kamata[5], S. Sasaki[1],
[1]National Astronomical Observatory of Japan, Japan; [2]Japan Aerospace Exploration Agency, Japan, [3]NASA/Goddard Space Flight Center, U.S.A., [4]National Institute for Environmental Studies, Japan, [5]The University of Tokyo, Japan.
Contact: matumoto@miz.nao.ac.jp

Internal structure and composition of the Moon provide important clue and constraints on theories for how the Moon formed and evolved. The Apollo seismic network has contributed to the internal structure modeling. Efforts have been made to detect the lunar core from the noisy Apollo data (e.g., [1], [2]), but there is scant information about the structure below the deepest moonquakes at about 1000 km depth. On the other hand, there have been geodetic studies to infer the deep structure of the Moon. For example, LLR (Lunar Laser Ranging) data analyses detected a displacement of the lunar pole of rotation, indicating that dissipation is acting on the rotation arising from a fluid core [3]. Bayesian inversion using geodetic data (such as mass, moments of inertia, tidal Love numbers k_2 and h_2, and quality factor Q) also suggests a fluid core and partial melt in the lower mantle region [4]. Further improvements in determining the second-degree gravity coefficients (which will lead to better estimates of moments of inertia) and the Love number k_2 will help us to better constrain the lunar internal structure.

Differential VLBI (Very Long Baseline Interferometry) technique, which was used in the Japanese lunar exploration mission SELENE (Sept. 2007 - June 2009), is expected to contribute to better determining the second-degree potential Love number k_2 and low-degree gravity coefficients. In SELENE, the VLBI radio sources (called VRAD) were on board the two sub-satellites, Rstar and Vstar. The differential VLBI data, when both the radio sources were within the beam-width of the ground antennas, were of particular importance because they are highly accurate with atmospheric and ionospheric disturbances almost cancelled out by the simultaneous observation. Such tracking data, i.e. “same-beam differential VLBI data” were useful for precision orbit determination [5] and also used to develop an improved lunar gravity field model SGM100i [6].

SELENE will be followed by the future lunar mission SELENE-2 which will carry both a lander and an orbiter. We propose to put the VRAD-type radio sources on these spacecraft in order to accurately estimate k_2 and the low-degree gravity coefficients. By using the same-beam VLBI tracking technique, these parameters will be retrieved through precision orbit determination of the orbiter with respect to the lander which serves as a reference. The VLBI mission with the radio sources is currently one of the mission candidates for SELENE-2. We have conducted a preliminary simulation study on the anticipated k_2 accuracy. With the assumed mission duration of about 3 months and the arc length of 14 days, the k_2 accuracy is estimated to be better than 1 %, where the uncertainty is evaluated as 10 times the formal error considering the errors in the non-conservative force modeling and in the lander position.

We carried out a feasibility study using Bayesian inversion on how well we can constrain the lunar internal structure by the geodetic data to be improved by SELENE-2. It will be shown that such geodetic data contribute to narrow the range of the plausible internal structure models, but there are still trade-offs among crust, mantle, and core structures. Preliminary inversion results of using both of geodetic and seismic data will be presented to show that the accuracy of core structure estimation will be improved in consequence of better determination of the mantle structure.

References:

[1] Weber et al. (2011), Science, 331, 309-312, doi:10.1126/science.1199375
[2] Garcia eta l. (2011), PEPI, doi:10.1016/j.pepi.2011.06.015
[3] Williams et al. (2001), JGR, 106, E11, 27,933-27,968
[4] Khan and Mosegaard (2005), GRL, 32, L22203, doi:10.1029/2005GL023985
[5] Goossens et al. (2011), J. Geod.,85, 487-504, doi:10.1007/s00190-011-0446-2
[6] Goossens et al. (2011), J. Geod., 85, 205-228, doi:10.1007/s00190-010-0430-2

FREE OSCILLATIONS FOR MODERN INTERIOR STRUCTURE MODELS OF THE MOON

S. Raevskiy, T. Gudkova,
Schmidt Institute of Physics of the Earth, B.Gruzinskaya 10, Moscow 123995, Russia. Contact: rs1989@rambler.ru

Introduction: Besides the Earth, the Moon is the only cosmic body for which seismic data were obtained. Despite the recent reanalyses of limited Apollo-era seismic data by two research teams [1, 2] with searching of wave phases, reflected from core, there remain questions about seismic velocity variations in the planetary interior and structure of the planetary core. Since the Moon's outer shells are very inhomogeneous, a global, spherically symmetric model of its interior structure is difficult to construct by using only seismic body-wave data. The measurements of the periods of free oscillations, if they are excited, could provide additional constraints for interior structure models. Interpretation of data on free oscillations does not require knowledge of the time or location of the source; thus, data from a single station are sufficient.

Models: The models fit both geodetic (lunar mass, polar moment of inertia, and Love numbers) and seismological (body wave arrivals measured by Apollo network) data.

MW model[1]: Apollo lunar seismograms were reanalyzed using array processing methods to search for the presence of reflected and converted seismic energy from the core. The results suggest the presence of a solid inner (240 km) and fluid outer (330 km, 8 g/cm^3) core, overlain by a partially molten boundary layer (about 150 km thick).

MG model[2]: The Very Preliminary Reference Moon model was constructed and the core radius was estimated by detecting core reflected S wave arrivals from waveform stacking methods. The core radius is 380±40 km and the average core mass density is 5.2±1.0 g/cm^3.

Free Oscillations: Since the planet has finite dimensions and is bounded by a free surface, the study of the free oscillations is based on the theory of vibration of an elastic sphere. The planet reacts to a quake (or an impact) by vibrating as a whole, vibrations being the sum of an infinite number of modes that correspond to a set of frequencies. The free oscillations are divided into two types: torsional oscillations, whose displacement vector is perpendicular to the radius of a sphere - $_nT_l$; and spheroidal oscillations, whose displacement vector has components in both the radial and azimuthal direction – $_nS_l$ The important feature of free oscillations is that they concentrate towards the surface with increasing the degree *l*. Therefore different regions of interiors are sounded by different frequency intervals. The fundamental modes sound to those depth in the interiors where their displacements ≥ 0.3 (above horizontal line) [3]. This line enables one to judge graphically which modes give information about one or another zone of the planet (see Figure 1).

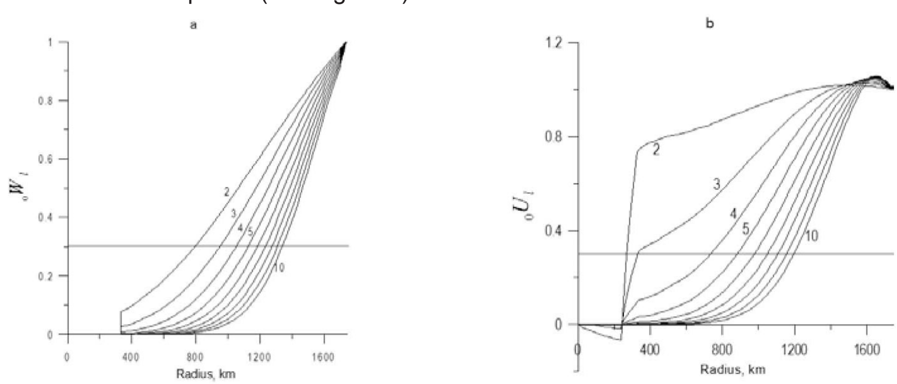

Fig. 1. Functions $_oW_l$ and $_oU_l$, proportional to the displacements of torsional (a) and spheroidal (b) oscillations for fundamental modes for *l*=2 to 10 for the MW interior structure model as a function of radius. The values of $_oW_l$ and $_oU_l$ are normalized to unity at the surface.

The effect of the inner core rigidity on the structure of oscillations is shown in Figures 2 and 3. The model MW has the 'core oscillation' - FC. As the rigidity of the inner core increases, its period (42.96 min at μ=0) decreases up to 6.94 min at μ=4.23x10^{11} dyne/cm^2, and its amplitude covers the mantle. At μ=0.5x10^{11} dyne/cm^2 it looks like a regular oscillation R with a period of about 16 min. Besides the regular oscillation and its overtones O1,O2, ... , there are 'inner core' oscillations, with the energy localised in the core. The curves are not crossed, they change a slope and a type of oscillation.

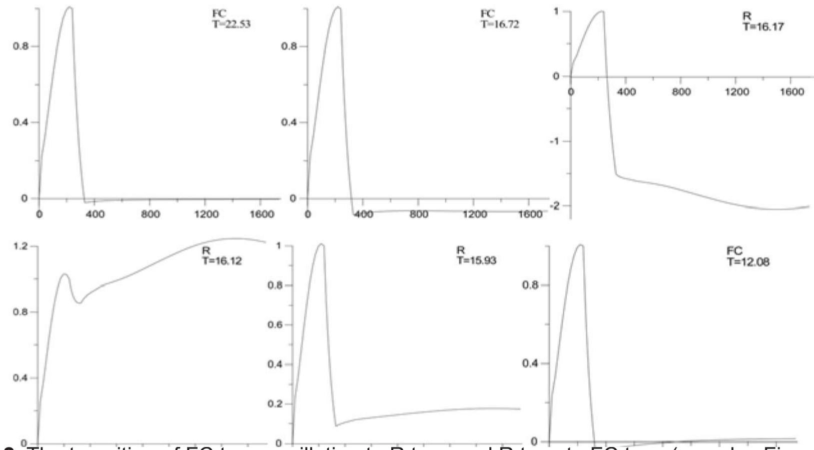

Fig. 2. The transition of FC type oscillation to R type and R type to FC type (see also Figure 3) for the model from [1], spheroidal oscillations*, l*=2

As the lunar core is rather small, the period difference of oscillations for the regular oscillation and the first overtone, for the models with inner core and without it, is very small, about 0.1 and 0.7%, respectively. It increases with the overtone number, and reaches 5-10% for the second and third overtones (Figure 4). The rigidity of the inner core influences mostly the periods of core oscillations, but their amplutudes are very small at the surface.

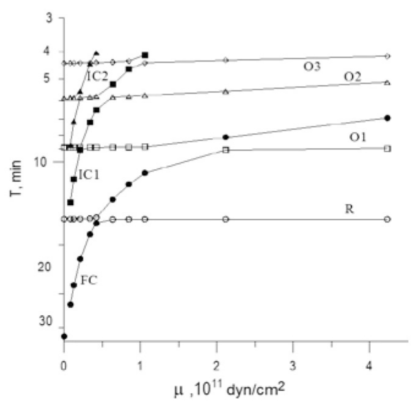

Fig. 3. Spheroidal oscillations, *l*=2. Period T (in min) as a function of shear modulus of the inner core (for the model in [1] μ =4.23x10^{11} dyn/cm^2) . R – relular, FC – basic core and IC – inner core oscillations; O – overtones of regular oscillations.

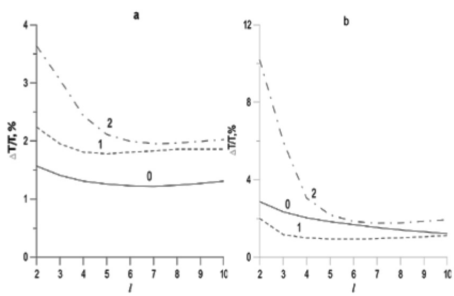

Fig. 4. Relative period difference ΔT/T(%) as a function of the oscillation number for fundamental mode (solid line) and two first overtones (dashed and dot-dashed lines) of torsional (a) and spheroidal oscillations (b) for models from [1] and [2].

Conclusion: Free oscillations, if they are excited, are indeed particularly attractive to probe beneath the surface of the Moon into its deep interiors. The spectrum of torsional modes $_nT_l$ would allow noticeable progress to be made in constructing a global model of the Moon's interior structure (up to about 500 - 700 km depth), as it was shown in [4], that the torsional modes with *l* > 5-7 can be recorded with current instruments. The seismic events on the Moon detected so far are too weak to excite free oscillations that could be recorded [4, 5]. The accuracy of seismometers has been improved [6], and the application of new methods for processing seismic data let us hope to identify harmonics with smaller amplitudes in the future.

Acknowledgements: This work was supported by Grant No. 12-02-00378 from the Russian Fund for Fundamental Research.

References: [1] Weber, R.C., Lin, P., Garnero, E.J., Williams, Q., Lognonné, 2011, Science, 331, 309-395. [2] Garsia, R.F., Gagnepain-Beyneix, J.G., Chevrot, S., Lognonné, 2011, PEPI, 188, 96-113. [3] Zharkov V.N. Physics of the Earth and planetary interiors, 1986. [4] Gudkova, T., Zharkov, V.N. 2001. Astronomy Letters, 10, 658-670. [5] Gudkova T., Lognoné, P., Gagnepain-Beyneix J. 2011, Icarus 211, 1049-1065. [6] Lognoné, P., Johnson, C. 2007, Planetary Seismology, in: Schubert, G., (Ed.), Treatise on Geophysics, V. 10, Els, pp.69-122.

THE EFFECTS OF THE PHYSICAL LIBRATIONS OF THE MOON, CAUSED BY A LIQUID CORE, AND THEIR POSSIBLE DETECTION FROM THE LONG-TERM LASER OBSERVATIONS AND IN THE JAPANESE LUNAR PROJECT ILOM

Yu.V. Barkin[1,2,3], H. Hanada[1], K. Matsumoto[1], H. Noda[1], N. Petrova[3], S. Sasaki[1],
[1]National Astronomical Observatory of Japan, Mizusawa, Japan; [2]Sternberg Astronomical Institute, Moscow, Russia; [3]Visiting professor at Mizusawa Astronomical Observatory of Japan. Contact: barkin@inbox.ru

In a recent paper (Weber et al., 2011) the existing seismic data of era of lunar Appollo missions to the Moon have been revised with the help of modern methods for analyzing of seismic signals on the Moon, taking into account the properties of reflected and converted signals from the core. As a result, received strong arguments in favor of the existence of a solid and a liquid core with a radius of 240 km and 330 km. In this paper, we use the results of this work to determine the dynamic parameters of the core and mantle of the Moon in order to further investigate the influence of the liquid core of the Moon on its physical libration.

The main geodynamic parameters of the Moon system.

The sizes of the liquid core and solid core. According to the work (Weber et al., 2011) on the distribution of the density of the Moon with the depth we have the following average values of the density of liquid and solid core, respectively, $\delta_{l,c}$ = 5.11 g/cm^3 и $\delta_{s,c}$ = 8.04 g/cm^3. For values of the mean radii of the solid and liquid core, we have the following estimates $r_{l,c}$ = 330 ± 20 km, $r_{s,c}$ = 240 ± 10 km. ***The mass of liquid and solid core.*** For the mass of the solid core, liquid core, and all of the compound nucleus for the error in determining the radii of the shells, we obtain the corresponding values are: $m_{s,c}$ = (4.65 ± 0.59)·10^{20} kg, $m_{l,c}$ = (4.73 ± 1.78)·10^{20} kg и m_c = (9.38 ± 2.37)·10^{20} kg. That is, the mass of the core of the model is determined with a relative error in the 25.2%.

The moments of inertia of the liquid and solid core. The polar moment of inertia, the dynamic oblateness of the core, etc. we calculate, based on the corresponding homogeneous models of core in the form of homogeneous spheres or ellipsoids, using additional observational data, such as lunar laser ranging (Williams, Boggs, 2009). Estimates of the model values of the axial moments of inertia of the nucleus, considered as a homogeneous sphere, $C_{s,c}$ and the liquid core as a uniform spherical shell, $C_{l,c}$, respectively, are: $C_{s,c}$ = (1.07 ± 0.23)·10^{38} g·cm^2, $C_{l,c}$ = (2.67 ± 0.81)·10^{38} g·cm^2 and the total moment of the core is equal to $C_c = C_{s,c} + C_{l,c}$ = (3.74 ± 1.04)·10^{38} g·cm^2. The relative error in determining of the moment of inertia of the Moon is 27.8%.

The dynamical parameter of the influence of liquid core on the rotation of the Moon. To study the effects of librations of the Moon, caused by a liquid core, the important role played by the parameter L equal to the ratio of axial polar moments of the core C_c and the Moon C. For this parameter we have obtained the estimation $C_c = C_{s,c} + L = C_c / C$ = (4.28 ± 1.19)·10^{-4}.

Dynamic oblateness of the Moon core. LLR detects fluid-core/solid-mantle boundary (CMB) flattening. Currently the product of CMB oblateness $e_c = (C_c - A_c) / C_c$ and fluid core moment of inertia is determined more strongly than either factor separately. That product is $e_c C_c / C_c$ = (3 ± 1)·10^{-7} (Williams, Boggs, 2009).The detection of CMB flattening is one of the demonstrations that there is a fluid core. For these values we find dynmical oblateness of the core of the Moon e_c = (0.70 ± 0.43)·10^{-3}. The geometric and dynamic compression of the core have approximately the same value. The difference between the equatorial a_c and polar c_c semiaxes of model ellipsoid of the core is $a_c - c_c$ = 231 ± 156 m. Found parameters allowed us to construct a model of the Moon with a liquid core. Identified the principal moments of inertia of the Moon, as well as the axial moments and product of the Poincare ellipsoidal nucleus. The effective use here has obtained a modern model of the gravitational field of the Moon (Matsumoto et al., 2010).

Some dynamical effects of the liquid core on forced physical librations of the Moon and its free librations. At the heart of all of our estimates is the analytical solution of the model problem of the physical librations of the Moon with a liquid core.

The increase in the amplitude of forced librations in longitude due to core influence. We have shown that the amplitude of forced librations of the moon with a liquid core is proportional to the longitude of the parameter $1+L$. By $L = 0$ we have the case of the rigid Moon (without a liquid core). Thus, the liquid core leads to an increase in the amplitudes of the librations (modulo) to the 0.043 ± 0.012 %. In this paper (Rambaux, Williams, 2011), based on long-term series of observations of laser reflectors on the Moon was constructed empirical theory of physical libration of the Moon with an accuracy of about 0"001. The tables specify the periodic variation of the classical angular variables contain the values of the periods, amplitudes (for the sine and cosine trigonometric arguments), as well as secular terms-corrections to amplitudes. The tables contain a wealth of information and estimates as known from theoretical considerations librations (forced and free), and a large number of new pertubations, the nature and origin of which is not yet clear. Since the values of the amplitudes of the librations are derived from observation the figures, they include the effects caused by the liquid core, as do some other little-studied factors. We have given theoretical estimates of the contributions to the core values of the amplitudes of librations of the Moon. As an example, we show that the contribution of the liquid core to the value of the amplitude of the observed annual libration in longitude is 0"039 ± 0"011.

The influence of the liquid core on the values of the periods of free librations. For this model the liquid core of the Moon we have been estimated periods of free libration in longitude, in the inclination and in the pole wooble of the Moon pole and have discovered a new period - the core free nutation in 27.204 days. One of the first estimatuion of this period of the Moon was 27.215 ± 0.003 d (Barkin, Ferrandiz, 2004). However, in mentioned paper contribution to the value of the period, due to a force function of the Moon, is not considered. The influence of the liquid core leads to a decrease in the period of free libration in longitude in 0.226 ± 0.063 d. That is the period of libration in longitude is reduced on 0.0214% comparatively with rigid model of the Moon so that observed value of this period consists 1056.13 d (Rambaux,Williams, 2011). We have shown also that in a first approximation, the liquid core does not affect the free nutation of the angular momentum vector with the observed period in 8822.88 d (Rambaux, Williams, 2011). But it has a significant effect on pole motion of the Moon (comparatively with the rigid model of the Moon). Namely, the period decreased by 25.8 d. This contribution is caused by liquid core and consists about 0.1% from observed period in 27257.27 d (Rambaux,Williams, 2011).

The period of nutation of the core. Finally, the predicted period of nutation of the core (by analogy with the Earth quasi-diurnal), the possibility has already been reflected in empirical theory in some unexplained librations of the Moon in the work (Rambaux, Williams, 2011). This question needs more thorough study, involving new methods and new techniques, including observations on the lunar surface (Japanese project ILOM). Although preliminary, you can specify that with the free core nutation, apparently associated with the observed libration periods of 27.214 d, 27.295 d, 27.312 d. In the first two periods we can estimate the period of free nutation of the core 27.2684 d and 27.2412 d. The librations wth this periods are not observed in present, but its frequency may occur in combination with other known frequencies of the theory of orbital motion of the Moon and the peridium of the free libration in longitude and in the motion of the pole. Prospects for further studies of rotational motion of the Moon and its internal structure, based on high-precision laser observations from the lunar surface in the light of the planned Japanese space missions are discussed.

References:

Weber R.C. et al. (2011) Seismic Detection of the Lunar Core. Science **331**, 309.
Williams J.G., Boggs D.H. (2009) Lunar Core and Mantle. What Does LLR See? Proceedings of the 16th International Workshop on Laser Ranging. Pp.101-120.
Matsumoto K. et al. (2010) An improved lunar gravity field model from SELENE and historical tracking data: Revealing the farside gravity features, J. Geophys. Res., doi:10.1029/2009JE003499.
Barkin Yu. V., Ferrandiz J.M. (2004) New Approach to Development of Moon Rotation Theory // 35th Lunar and Planetary Science Conference, March 15-19, 2004, League City, Texas., abstr. no.1294.

LANDING DYNAMICS ON THE MOON IN “LUNA-GLOB” PROJECT

Yu.G. Sikharulidze[1], B.I. Zhukov[1], A.G. Tuchin[1] (), Yu.K. Zaiko[2], V.P. Fedotov[2], V.N. Likhachov[2], P.E. Rozin[2],
[1]KIAM RAS, [2]Lavochkin Design Center

Annotation

Current Russian lunar program includes two missions with landing of the spacecrafts in the polar regions of the Moon: “Luna-Resurs” (South pole) and “Luna-Glob” (North pole). It is necessary to provide a high landing accuracy in the given place for the scientific investigations. So, the terminal guidance algorithm is developed for the “Luna-Glob” lander.

Total descent trajectory includes tree phases. The first phase starts in de-orbit point (near the pericenter of the prelanding orbit) and terminates by the vertical descent with given velocity and altitude. The second phase is a vertical descent trajectory above the given landing point. The phase is terminates at altitude of a few ten meters and velocity of a few meters per second. The engine with thrust of 4120 N is used during both phases for deceleration and correction of trajectory. The third phase is also vertical and terminates by the soft landing. At last phase the engine with thrust of 1177 N is used for precise deceleration.

Developed terminal guidance algorithm is used at all phases with adaptation to the real deceleration conditions. For this purpose the phantom acceleration measurements (due to engine only) are used. The algorithm is based on the numerical prediction of the remained trajectory in the two-point boundary problem (so called the numerical prediction-corrector NPC).

Allowable initial conditions and boundary conditions between phases are investigated. The total optimization of trajectory from de-orbit point till landing provides the minimal propellant consumption. There are also the mathematical simulation results with estimation of the required propellant and preliminary estimation of the landing accuracy.

GEOLOGY AND PETROLOGY OF ENORMOUS VOLUMES OF IMPACT MELT ON THE MOON: A CASE STUDY OF THE ORIENTALE BASIN IMPACT MELT SEA.

W. M. Vaughan[1], J. W. Head[1], L. Wilson[2], P. C. Hess[1],
[1]Department of Geological Sciences, Brown University, Providence, RI 02912, USA,
[2]Lancaster Environment Center, Lancaster University, Lancaster LA1 4YQ, UK.
Contact: William_Vaughan@brown.edu

Introduction: Lunar basin-forming impacts are predicted to produce enormous volumes (>10^5 km^3) of impact melt by analytic scaling relationships [1-3] and hydrocode models [4,5]. All known basin-forming impacts combined may produce ~10^8 km^3 of impact melt [6], ~1/20th the volume of the lunar crust. Despite their volumetric importance, the geology and petrology of massive deposits of impact melt on the Moon have been little studied, in part because most basin impact melt deposits are old and have been obscured or buried by impact cratering and mare infill. We investigate the geology and model the petrology of fresh massive impact melt deposits in the young Orientale basin.

Distribution, thickness, and volume of massive impact melt deposits in Orientale: Impact melt volume scaling relationships [1,3] adjusted [7] for a proposed impact angle of the Orientale-forming projectile [8] predict that the Orientale-forming impact produced ~1.5 × 10^6 km^3 of impact melt; ~25 vol. % of this melt is excavated [1] in forming the transient cavity, leaving ~1.1 × 10^6 km^3 of melt inside the Orientale basin rim. Our geologic analyses based on recent LOLA topographic data suggest that most of this melt occurs in a ~15.5 km thick impact melt sheet (better described as an impact melt sea) 350 km in diameter with a volume of ~10^6 km^3.

Cumulate stratigraphy of the Orientale melt sea: We anticipate that the Orientale melt sea has undergone large-scale igneous differentiation, since terrestrial impact melt sheets (such as Manicouagan, Sudbury, and Morokweng) less than a tenth of the thickness and a hundredth of the volume of the Orientale melt sea have differentiated [9-12].

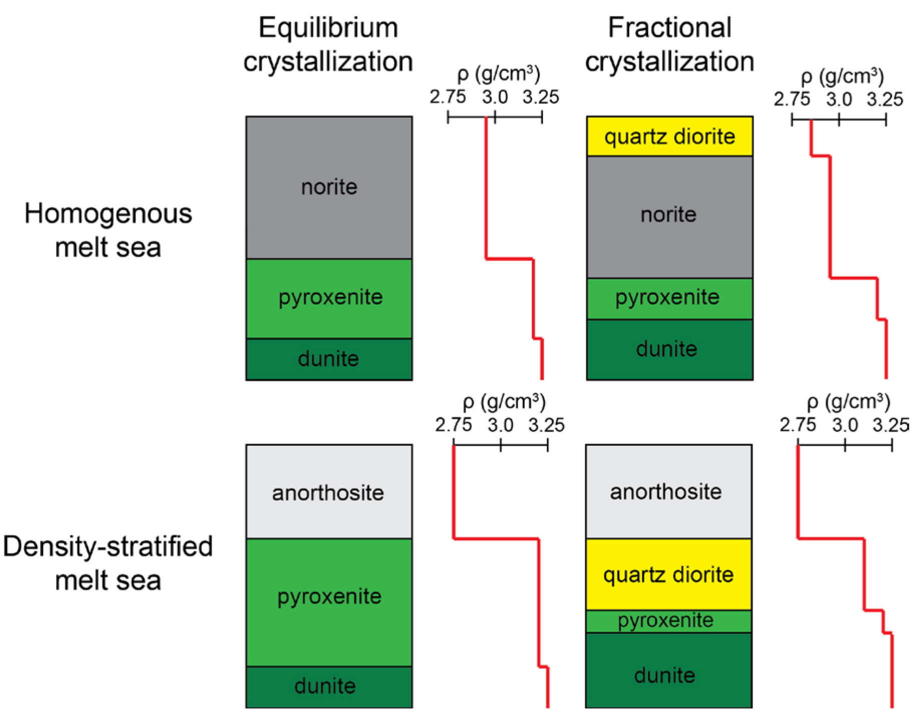

fig. 1. Model Orientale cumulate stratigraphies and density profiles (to scale) produced by equilibrium and fractional crystallization of homogenous and density-stratified [10] melt seas.

We develop a model for the cumulate stratigraphy of the solidified Orientale impact melt sea which 1) determines the composition of the differentiating liquid by mixing lunar crust and upper mantle compositions weighted by their mass fractions in a modeled melt cavity, 2) finds the crystallization sequence of this liquid on the Fo-An-Qz pseudoternary phase diagram, and 3) sinks or floats crystals according to crystal-liquid density contrasts in order to convert this crystallization sequence into a stratigraphic sequence (Figure 1). A modeled cumulate stratigraphy with a ~7.5 km thick layer of norite overlying a ~4.25 km layer of pyroxenite and a basal ~2.25 km thick layer of dunite produced by equilibrium crystallization of a homogenized melt sea (Figure 1, upper left), consistent with vigorous convection in that melt sea, is supported by remotely-sensed norite excavated by the central peak of Maunder crater from ~4 km depth [13].

Cumulate stratigraphy of other lunar melt seas: Melt sea bulk composition is a function of depth of melting, which in turn is a function of basin size. We predict that very large basin-forming impacts, including the South Pole-Aitken (SPA) basin-forming impact, produce melt seas with a cumulate stratigraphy similar to the Orientale melt sea (Figure 2, right). Impact melt differentiation may explain apparently anomalous lithologies [14] excavated in the SPA basin interior [15]. Smaller basin-forming impacts, which mainly melt anorthositic crust, produce melts that become saturated with plagioclase early and give rise to anorthosite-bottomed melt seas with characteristic inverted density profiles (Figure 2, left).

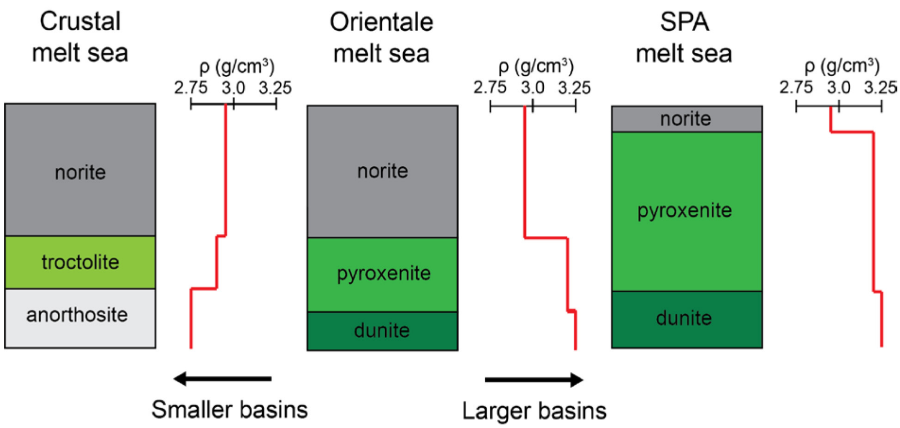

Fig. 2. Model cumulate stratigraphies and density profiles for melt seas in basins of three different sizes: a "crustal" melt sea occuring in a small basin approximately the size of Milne [16]; the Orientale melt sea; and the SPA melt sea. Layers in each melt sea are to scale, although melt seas are not to the same scale.

We note that impact melt differentiates are slow-cooled and, if meteoritic siderophiles fractionate into metal or sulfide layers [9], may not be siderophile-enriched; therefore, impact melt differentiates may pass for pristine [16] highland plutonic rocks in the lunar sample suite. Analyses based on the high-resolution spectroscopic and geophysical data collected by the M³ instrument on India's Chandrayaan-1 mission and the ongoing LRO and GRAIL missions will further our understanding of the geology and petrology of massive impact melt seas, which constitute ~1/20th of the lunar crust.

Readers are referred to [18] for additional information.

References: [1] M. J. Cintala and R. A. F. Grieve (1998) Meteorit. Planet. Sci., 33, 889-912. [2] R. A. F. Grieve and M. J. Cintala (1992) Meteoritics, 27, 562-538. [3] O. Abramov et al. (2012) Icarus, 218, 905-916. [4] G. S. Collins et al. (2002) Icarus, 157, 24-33. [5] B. A. Ivanov (2005) Solar Syst. Res., 39, 381-409. [6] D. A. Kring et al. (2012) LPS, 43, abstract #1615. [7] E. Pierazzo and H. J. Melosh (2000) Ann. Rev. Earth Planet. Sci., 28, 141-167. [8] P. H. Schultz et al. (2012) LPS, 42, abstract #2428. [9] A. M. Thierrault et al. (2002) Econ. Geol., 97, 1521-1540. [10] M. J. Zieg and B. D. Marsh (2005) Geol. Soc. Am. Bull., 117, 1427-1450. [11] C. D. O'Connell-Cooper and J. G. Spray (2011) J. Geophys. Res., 116, B06204. [12] R. J. Hart et al. (2002) Earth Planet. Sci. Lett., 198, 49-62. [13] J. S. Whitten et al. (2011) J. Geophys. Res., 116, E00G09. [14] R. Nakamura et al. (2009) Geophys. Res. Lett., 36, L22202. [15] D. A. Morrison (1998) LPS, 29, abstract #1657. [16] D. M. H. Baker et al. (2012) J. Geophys. Res., 117, E00H16. [17] P. H. Warren (1993) Am. Mineral., 78, 360-376. [18] W. M. Vaughan, J. W. Head, L. Wilson, P. C. Hess (2012), Geology and petrology of enormous volumes of impact melt on the Moon: A case study of the Orientale basin impact melt sheet, Icarus, submitted.

IS A LUNAR SOIL STICKY?

D. P. Skulachev,
Space Research Institute (IKI), 117997, 84/32 Profsoyuznaya Str, Moscow, Russia.
Contact: dskulach@mx.iki.rssi.ru

Introduction:

A lunar soil (regolith) was usually considered as a composition of absolutely dry grains. Recent observations by a neutron detector on the Lunar Prospector spacecraft indicate a presence of some form of hydrogen in the upper layer of regolith. This work based on an assumption that there are thin water ice mantles on regolith grains, so the hydrogen may be found in every mantle molecule.

Lifetime of water in the lunar regolith:

The Moon has no atmosphere so water escapes regolith by evaporating, sublimation and desorption. Water may exist in regolith during a long time only in a form of ice at a cryogenic temperature. Such temperature is measured at high lunar latitudes in regolith at a depth of 0.25-1 m [1].

A desorption rate of water may be described roughly by Polanyi-Winger equation

$$dN/N = (kT / h)\cdot\exp(-E_d/kT) \quad (1)$$

where k and h are Boltzmann and Planck constants,

T – temperature,

E_d – desorption energy (about 0.5 eV for H_2O on silicate surface).

The desorption rate derived from equation (1) is $3\cdot10^{-13}$ per second for T = 100 K. It means that a lifetime of ice is about 100,000 years in these conditions. It should be noted that desorption rate depends on temperature exponentially and at 80 K ice lifetime is about 3 billion years.

The ice mantle thickness:

If we assume a mean range of regolith grains as 100 μ, a 0.5 μ thick ice mantle leads to relative ice mass about 1%. This value is comparable with the data in real observations.

The regolith thermal conductivity:

A simplest thermal model of lunar regolith is an array of small bodies, contacting each other in vacuum. A thermal resistance of contacting grains is determined almost completely by thermal resistance of the contact area.

The contact area may be considered as a disc on a semibounded body. In this case the contact area thermal resistance may be estimated as

$$R_t = 1/(4\cdot\lambda\cdot r) \quad (2)$$

where $\cdot\lambda$ is a thermal conductivity of grain material, and r the contact area radius.

The contact area radius of pure (iceless) grains may be calculated by Gauss equation and is about 0.02-0.05 μ.

A glue ice:

If there are ice mantles on neighboring regolith grains, grains may stick together. For 0,5 μ ice mantle the contact area radius may increase to several microns. In this case a thermal resistance of contacting grains will decrease in orders. Another consequence of the ice mantle presence is that regolith may loose a friability and became some sticky.

Regolith thermal conductivity and a remote sensing:

A thermal conductivity and thermal diffusivity of lunar regolith are rather small. Therefore direct measurements of the regolith thermal properties are difficult: contact sensors may dramatically disturb thermal field structure. In this case most suitable may be remote sensing. For example, multichannel microwave radiometer may measure natural thermal radiation of lunar regolith at different depths. If such measurements will be carried out during lunar day, one may analyze a diurnal temperature variation, estimate regolith thermal conductivity and make a judgment about a presence of ice.

References:

1. FA WenZhe, JIN YaQiu. Analysis of microwave brightness temperature of lunar surface and inversion of regolith layer thickness: Primary results of Chang-E 1 multi-channel radiometer observation. // SCIENCE CHINA. Information Sciences - Vol. 53. - January 2010. - No. 1. - P. 168–181.

STRUCTURE OF THE MOON BY SEISMIC DATA

V.Yu. Burmin,
Schmidt Institute of Physics of the Earth, Russian Academy of Sciences, Moscow, Russia

Introduce

The moon is the only object other than Earth, which successfully applied seismic methods, which give the most complete and objective information in the study of its internal structure. By definition, the velocity distribution of seismic waves in the interior of the Moon published a lot of controversial works published fewer papers devoted to the study of the density distribution in the interior of the moon. Virtually unstudied was the core of the moon, because records of seismic signals from moonquakes detected at distances not greater than 135^o.

Between 1969 and 1972 by the American lunar program “Apollo” was deployed a network of high-sensitivity seismometers in the central part of the visible side of the moon. Seismometers, “Apollo” continued to work for eight years, during which they passed on information about the natural seismic activity of the moon, and the structure of the lunar crust and upper mantle [Goins et al., 1981; Lognonne, 2005]. However, the deep portion of the Moon has remained inaccessible to the Apollo seismic network. As a result of observing not only the physical state and composition, but even the very existence of the lunar core remains in question.

Since the seismic data, “Apollo” was impossible to determine the size and physical condition of the lunar core, this information was obtained from the study of the moment of inertia of the Moon, physical libration (the measurements were performed using a laser reflector), and measurement of electromagnetic induction [Wieczorek et al. , 2006; Kuskov et al 2009]. As a result, it is assumed that the moon has a small (R <400 km), perhaps partially liquid core. Suggestive of its structure - it is solid solutions or melts of iron-nickel to Fe-FeS. Does the moon, like Earth, a liquid outer core and solid inner core - is currently unknown. Knowing the size, composition and physical state of the lunar core is critical for understanding the origin of the Moon, the evolution of the mantle and the nature of magnetism. The latter, together with the study of the remanent magnetization of rocks on the lunar surface is of great importance for our understanding of the origin and evolution of planetary magnetic fields.

The first results of the velocity of seismic wave propagation in the interior of the Moon were published in the papers [Nakamura et al., 1973, 1974]. To study the structure and condition of the subsoil of the moon were used seismic waves from distant meteorite impacts of four and two moonquakes. None of Fig. 1 shows the hodographs of the first arrival of the longitudinal (*P*) and shear (*S*) waves from these events. In Fig. 2 shows the distribution of velocities of *P*-and *S*-wave velocities for the crust, mantle and core of the Moon, obtained in [Nakamura et al., 1974].

In Fig. 3 shows the velocity distribution of *P*-and *S*-waves in the crust and mantle of the Moon to a depth of 800 km, obtained in [Nakamura et al., 1976] for the same travel-time curves (Fig. 1).

Input data

The initial data for determining the velocity in the interior of the moon were taken montages seismograms shown in Fig. 1. Records of seismic events in the assembly of these components obtained from the radial long-period seismic stations of Apollo from falling meteorites and man-made events, resulting in dumping space station modules [Lognonne, et al., 2003].

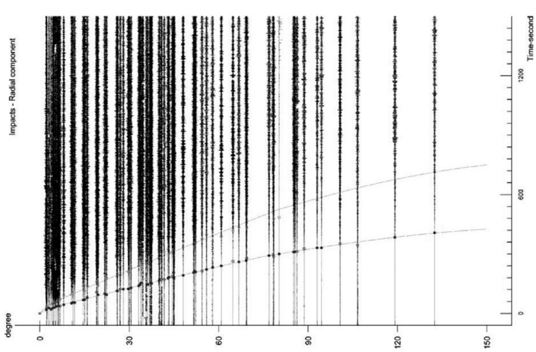

fig. 1

Note that due to the lack of quality in the record-section presented in Fig. 1, the experimental points were taken in accordance with the correlation of the waves carried by the author presented in montages of seismograms [Nakamura, 1983].

In addition, the literature contains different values of the dimensionless moment of inertia of the Moon. In the present work for calculations were taken one of the last values of the dimensionless moment of inertia of the Moon - 0.3931 ± 0,02% [Konopliv et al., 1998]. The mass of the Moon was taken to be ×7.349 1022 kg ± 0,1%.

The results of determining the velocity of seismic waves in the mantle and the core of the moon. Core radius of the Moon [Burmin, 2012a]

The results of determining the velocities of longitudinal and transverse waves are shown in Fig. 2. Thickness of the crust according to various sources varies from 30-45 km [Lognonne, et al., 2003] to 60 km [Nakamura et al., 1974]. We have taken the crust thickness 54 km. The figure 9 shows that in the mantle of the Moon in the depth range 120 - 480 km there is a decrease in the velocity of both longitudinal and transverse waves. In the depth range 480 - 1100 km of seismic wave velocities change little and remain almost constant. At a depth of 480 km there is a jump of velocities of P-and S-waves, which caused a sharp change in the apparent velocity hodograph in the values of 7.2 km / s to 7.8 km / s for longitudinal waves and from 4.2 km / s to 4.5 km / s for transverse waves.

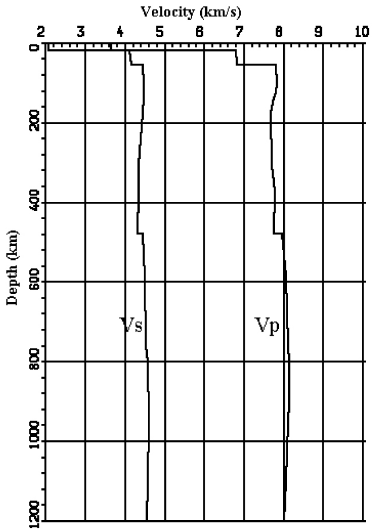

fig. 2

The density and elastic modules of the mantle of the moon are determined from the corresponding equations for a given velocity distribution of *P*-and *S*-waves [Burmin, 2006]. To determine the distribution of velocities of seismic waves at depths greater than 1100 km we have observed data. Therefore, in contrast to the determination of the density in the core of the Earth, which is known for the depth of the mantle-core boundary according to the reflected waves and the distribution of the velocity of longitudinal waves in the core, the moon does not know of any position of the boundary mantle-core, or the velocity distribution in the nucleus. The initial data for determining the radius of the considered four models of the nucleus of the moon in accordance with [Kuskov, Kronrod, 2008].

Summary and Conclusions

In this report, based on data obtained in the 70's Apollo program and a better method of interpreting seismic data held redefinition of the velocity distribution in the mantle of the Moon.

The distribution of density and elastic parameters in the bowels of the Moon derived from Williamson-Adams equation and the corresponding relations for the velocities of *P*-and *S*-waves. As a result, estimates are given for the core radius of the moon for a different chemical composition. Result of the density distribution in the interior of the moon are in good agreement with the distributions obtained earlier in [Kuskov, Kronrod, 1998; Kuskov, Kronrod, Hood, 2002]. Complete coincidence, of course not, but this is due to the fact that in these studies was determined by the density to a depth of about 1200 km and the radius of the lunar core and the density of it were given a fairly wide range. The problem of unique determination of the radius of the lunar core remains open. It could be removed if on lunar seismograms have found records of the reflected waves from the nucleus. Perhaps future lunar seismic experiments will do it.

In conclusion, I want to express my deep gratitude to O.L. Kuskov for your interest in this work and valuable comments made during the discussions.

DEVELOPMENT STATUS OF LUNAR LASER RANGING EXPERIMENT ABOARD JAPANESE LUNAR LANDER SELENE-2

H. Noda[1], H. Kunimori[2], H. Araki[1,3], K. Funazaki[4], T. Fuse[2], H. Hanada[1], S. Kashima[3] , M. Katayama[3], H. Mashiko[4], Y. Matsumoto[5], K. Murata[4], T. Otsubo[6], S. Sasaki[1], H. Taniguchi[4], S. Tazawa[1,7], S. Utsunomiya[8]
[1]National Astronomical Observatory of Japan, 2-12 Hoshigaoka, Mizusawa, Oshu, 023-0861 Iwate, Japan;
[2]National Institute of Information and Communications Technology, Koganei, Tokyo, Japan ; [3]National Astronomical Observatory of Japan, Mitaka, Tokyo, Japan; [4]Iwate University, Morioka, Iwate, Japan; [5] Planet Inc., Tokyo, Japan;[6] Hitotsubashi University, Kunitachi, Tokyo, Japan;[7] National Astronomical Observatory of Japan, Hilo, Hawaii, U.S.A.;[8] Japan Aerospace Exploration Agency, Tsukuba, Ibaraki, Japan; Contact: noda@miz.nao.ac.jp

Introduction: We present the development status of the Lunar Laser Ranging experiment proposed to Japanese SELENE-2 lunar landing mission. The Lunar Laser Ranging measures the distance between laser link stations on the Earth and retroreflectors on the Moon, by detecting the time of flight of photons of high-powered laser emitted from the ground station. Since the Earth-Moon distance contains information of lunar orbit, lunar solid tides, and lunar orientation and rotation, we can estimate the inner structure of the Moon through orientation, rotation and tide.

For better estimation of the lunar physical parameters, the more precise ranging than 1cm accuracy is needed. Murphy et al. [1] showed that the main source of range error comes from the fact that the retroreflectors placed on the lunar surface are array-type retroreflectors which consist of arrays of small corner cube prisms (CCP). Because of the optical libration, the direction of the face of the retroreflector changes up to 10 degrees, and the pulse width of the returned laser is broadened which causes less accurate ranging. To overcome this problem, large single aperture retroreflectors are needed for the future lunar landing missions.

Dihedral Angle Offset and its realization: However, the larger the aperture is, the smaller the return pulse width becomes, so that the emitted laser light cannot be detected at the same ground station (velocity aberration). To cancel the velocity aberration, a large, single aperture retroreflector needs small amount of offset angle between the reflecting planes to spoil the return beam pattern. This angle offset, called Dihedral Angle Offset (DAO) must be optimized to be less than 1 second of arc with 0.1 seconds of arc accuracy to accumulate more photons. This optimization has been done by Otsubo et al. [2, 3]. The realization of such small DAO is challenging with current technology, therefore the development of fabrication method is important.

Selection of the mirror material must be done in terms of mass, hardness, thermal property, optical response and handling. The thermal quality of the material can be evaluated by both the thermal conductivity and the coefficient of thermal expansion. Currently we have several candidates for the mirror material such as glass ceramics, SiC (silicon carbide), and ZPF (zero-expansion stiffness ceramics). The optical response such as the point spread function of a retroreflector which is deformed by thermal expansion and gravity deformation under the lunar environment is calculated to confirm the laser return can be detected at the ground station.

References: [1] Murphy T. et al. (2008) PAPS, 120, 20-37. [2] Otsubo T. et al. (2010) Adv. Space Res., 45, 733-740. [3] Otsubo T. et al. (2011) Earth Planet Space, 63, e13-e16.

EFFUSIVE VOLCANISM ON MERCURY FROM MESSENGER MISSION DATA: NATURE AND SIGNIFICANCE FOR LITHOSPHERIC STRESS STATE AND MANTLE CONVECTION.

James W. Head[1], Sean C. Solomon[2], Caleb I. Fassett[3], Scott L. Murchie[4], Louise M. Prockter[4], Mark S. Robinson[5], David T. Blewett[4], Brett W. Denevi[4], Thomas R. Watters[6], Jennifer L. Whitten[1], Timothy A. Goudge[1], David M. H. Baker[1], Debra M. Hurwitz[7], Paul K. Byrne[8], Christian Klimczak[8],
[1]Department of Geological Sciences, Brown University, Providence, RI 02912, USA. [2]Lamont-Doherty Earth Observatory, Columbia University, Palisades, NY 10964, USA. [3]Department of Astronomy, Mount Holyoke College, South Hadley, MA 01075, USA. [4]The Johns Hopkins University Applied Physics Laboratory, Laurel, MD 20723, USA. [5]School of Earth and Space Exploration, Arizona State University, Tempe, AZ 85251, USA. [6]Center for Earth and Planetary Studies, National Air and Space Museum, Smithsonian Institution, Washington, DC 20560, USA. [7]Lunar and Planetary Institute, Houston TX 77058 USA. [8]Department of Terrestrial Magnetism, Carnegie Institution of Washington, Washington, DC 20015, USA.
Contact: James_Head@brown.edu

Introduction: Analysis of the generation, ascent, and eruption of magma on the Earth and planets provides substantial information about the geological history and thermal evolution of each body. Here we synthesize the array of extrusive features and landforms seen on the terrestrial planets [1,2] and those observed to date on Mercury by the MESSENGER spacecraft [3-8] and explore how they provide insight into eruption styles, lithospheric stress states, and mantle convection on Mercury.

Volcanic Features and Styles on the Terrestrial Planets: Surface elemental compositions of the terrestrial planets are consistent with a range of mantle compositions, but all are likely to produce mafic to ultramafic melts. The main controls on the types of surface volcanic features and accumulations are thus expected to be differences in 1) magma compositions and volatile contents, 2) tectonic regimes, 3) crustal densities, 4) crust and lithosphere thicknesses, and 5) mantle convective style. Preferred locations for magma reservoirs appear to be either at depth within a planetary interior or relatively shallow within a volcanic edifice. Deeper reservoirs can form near the rheological change at the base of the lithosphere, at upwellings due to pressure-release melting, or at vertical discontinuities in density such as at the base of the crust. Evidence for reservoirs in edifices is seen in calderas. Evidence for deeper magma bodies is seen in giant dike swarms. The position of ascending mantle flow is often marked by broad rises formed from thermal uplift, enhanced crustal construction, and individual edifices built by surface eruptions (e.g., Iceland and Hawaii on Earth, Tharsis on Mars, Beta Regio on Venus). On Venus, volcanic complexes and rises are often accompanied by large annular deformational features (coronae) produced by some combination of uplift and accommodation of intrusive and extrusive loads.

Shallow magma reservoirs are commonly formed within volcanic edifices on Earth, Mars, and Venus. Building a volcanic edifice and reservoir requires multiple pulses of magma to rise frequently within a spatially restricted region over an extended period of time. On the Moon, in contrast, low eruption frequencies and great flow lengths ensure that typical large edifices will not form. Shallow reservoirs form within edifices at levels of neutral buoyancy. Repeated, relatively small-volume eruptions from these shallow reservoirs (Fig. 1) progressively build shield volcanoes of a range of sizes and aspect ratios on Earth, Mars, and Venus. These shield volcanoes commonly host collapse calderas at their summits, produced when substantial volumes of magma are erupted on the volcano flanks.

Deeper magma reservoirs have certainly existed on Earth, Venus, and Mars. Giant dike swarms can be recognized by eroded outcrops (Earth and Mars), the radial patterns of volcanic vents that they feed (Venus), and/or the graben formation that they cause (Venus and Mars). These giant dikes are close analogs to the large dikes that fed magma to the surface of the Moon from near the base of its crust. When mantle magma rises to a density step at the crust-mantle boundary, a stress regime characterized by net horizontal extension will favor upward propagation of dikes, whereas horizontal compression will favor initial sill formation.

Evidence for volcanism from surface features on Mercury: On the basis of Mariner 10 [3-5], MESSENGER flyby data [6-7], and initial orbital observations from MESSENGER [8], we see no evidence for large shield volcanoes on Mercury like those on Earth, Mars, and Venus, and we see only small numbers of low shield-like constructs and candidate calderas, some reminiscent of those on the Moon. No evidence has been discerned for extensive centers of volcanism as seen on Mars (e.g., Tharsis, Elysium) or Venus (e.g., Beta and Atla Regiones), or less well-developed ones as seen on the Moon (e.g., Marius and Rumker Hills). Nor has evidence been seen for any Venus-like corona or related annular deformational features displaying associated volcanism. Only one radial graben structure (Pantheon Fossae), centrally located in the Caloris basin, has been documented [7].

Observations of Mercury to date also reveal no evidence for several types of volcanic features (cones, leveed flows, or sinuous rilles). Instead, we see evidence on Mercury for extensive flooding of the surface to form regional smooth plains that appear to be very extensive lava sheet flows, and intercrater plains (found between large, old impact craters) that may also be formed by volcanic eruptions [3]. Volcanic plains filling the interior of the Caloris basin show generally uniform ages and spectral characteristics [10-11] and are up to several kilometers thick [12]. Exterior plains of volcanic origin have similar to slightly younger ages [10-11]. Contiguous plains at northern high latitudes cover ~6% of the surface of Mercury, have surface ages and spectral properties that show no resolvable variation, and reveal no specific source regions or associated edifices [8]. Generally the Caloris-related and northern volcanic plains show no signs of broad, rifted rises, constructional landforms (shield volcanoes), or individual linear, leveed flow fronts. The general characteristics of the plains deposits and features on Mercury strongly suggest that they were emplaced by flood-lava-style eruptions (Fig. 1) [5] rather than collections of narrow, leveed flows typical of small dike-emplacement events and more limited-volume surface eruptions.

This overview of the range of volcanic and associated tectonic landforms seen on Mercury from Mariner 10 and MESSENGER data indicates little deformational or constructional evidence for localized convective upwelling (e.g., radially/concentrically deformed structures, volcanic rises/edifice concentrations, coronae) or the presence of local shallow crustal magma reservoirs (e.g., large shields, abundant floor-fractured craters, calderas, narrow channelized flows, aggregation of small volcanic constructs). Magma delivery to the surface in the presence of convection occurs as both the host rock and melt rise together in convection cells and encounter more brittle rocks; dikes then transport melt to the surface in the vicinity of a rising mantle diapir. Where convection is suppressed or absent, the process is different; a vertically and laterally extensive melt layer can form beneath a conductively cooled lithosphere and as the amount of partial melting increases, the corresponding volume increase causes an increase in pressure in the growing melt layer [13]. Expansion of the melt layer exerts extensional stresses on the overlying lithosphere, inducing vertical fractures that form dikes through which melt escapes. In non-convecting mantles the elastic lithosphere will tend to be thinner and more susceptible to penetrative dike formation than for convecting systems, and flood volcanism will be favored. Analysis of magma transport and delivery from depth predicts eruptive fissure widths of ten to several tens of meters and lengths in the 40-90 km range, consistent with flood volcanism [13].

The typical mode of eruption of magma in the flood lava mode has been explored [6,13] for a range of mafic mantle melts. The great lengths of fissures and large dike widths cause broad sheet flows rather than long, narrow, leveed and channelized lava flows. Lava is released at high volume fluxes from these long, wide fissures to flow downslope in a turbulent manner. A typical flow will be 1.4-1.9 times thicker than comparable flows on Earth, reaching distances of ~300 km in ~20-60 hours. Flow fronts cease to advance not due to cooling but instead due to cessation (or major reduction) of supply at the vent (flows are volume-limited, not cooling-limited). Under these conditions, the vast majority of lava-flow emplacement events will be in the flood lava mode, and lava distribution will vary as a function of global magma generation history and longer-term thermal evolution. Direct eruption from depth will slow and cease as lithospheric horizontal stresses increase. These conclusions hold equally well for both basaltic magma and magma with compositions intermediate between basaltic and komatiitic [14], because the changing stresses exert more influence on the ability of a dike to remain open through the full vertical extent of the lithosphere than on the speed with which magma can flow through the dike.

In summary, magmatism on Mercury appears to be characterized predominantly by: 1) deeper magma sources of large volume, 2) minimal shallow crustal storage of magma, 3) vertically extensive and wide dikes penetrating completely through the lithosphere and crust, and 4) high-volume eruption rates of lava and correspondingly voluminous outpourings producing long/wide lava flows covering extensive areas.

These observations are interpreted to mean that the ability of magma to reach the surface on Mercury has been strongly influenced by 1) the presence or absence of mantle convection and 2) the lithospheric stress state. The comparatively small vertical extent of Mercury's mantle [15] may inhibit convection and favor sublithospheric magma buildup and extensional lithospheric stresses on local to regional scales in the planet's early history. A late-stage tectonic history dominated by horizontally compressive lithospheric stresses could account for the termination of an early period of voluminous volcanic activity. Modeling of the effect of increasing horizontal compressive stress on the ability of dikes to penetrate and remain open through the full thickness of Mercury's lithosphere [5] has shown that lithospheric magma transport was suppressed when compressive stresses exceeded critical values in the range of several tens of MPa, similar in magnitude to the stresses thought to form the global system of lobate scarps and other contractional landforms [16].

References: [1] L. Wilson and J. W. Head, *Nature* 302, 663, 1983; [2] L. Wilson, *Nat. Geosci.* 2, 389, 2009; [3] R. G. Strom et al., *JGR* 80, 2478, 1975; [4] P. D. Spudis and J. E. Guest, *Mercury*, UofA, 118, 1988; [5] L. Wilson and J. W. Head, *GRL* 35, L23205, 2008; [6] J. W. Head et al., *EPSL* 285, 227, 2009; [7] J. W. Head et al., *EPSL* 285, 251, 2009; [8] J. W. Head et al., *Science* 333, 1853, 2011; [9] S. L. Murchie et al., *Science* 321, 73, 2008; [10] R. G. Strom et al., *Science* 321, 79, 2008; [11] C. I. Fassett et al., *EPSL* 285, 297, 2009; [12] C. M. Ernst et al., *Icarus* 209, 210, 2010; [13] L. Wilson and J. W. Head, *LPS* 43, 2012; [14] L. R. Nittler et al., *Science* 333, 1847, 2011; [15] D. E. Smith et al., *Science*, submitted, 2012; [16] T. R. Watters et al., *EPSL* 285, 283, 2009.

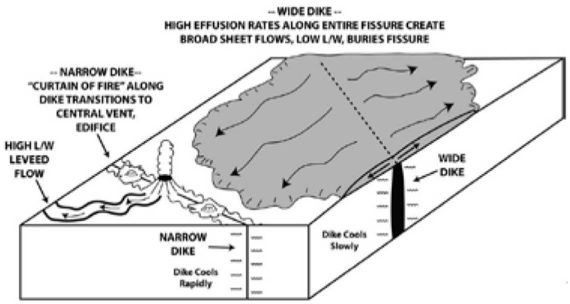

fig. 1.

VERY LOW-fO_2 CRYSTALLIZATION OF MERCURY SURFACE COMPOSITIONS: IMPLICATIONS FOR THE MINERALOGY OF MERCURY.

W. M. Vaughan[1], J. W. Head[1], S. W. Parman[1],
[1]Department of Geological Sciences, Brown University, Providence, RI 02912, USA.
Contact: William_Vaughan@brown.edu

The chemical composition of the surface of Mercury has recently been measured [1,2] with unprecedented precision and spatial resolution by the ongoing MErcury Surface, Space ENvironment, GEochemistry, and Ranging (MESSENGER) mission [3]. Specifically, the X-Ray Spectrometer aboard the MESSENGER spacecraft has measured the abundance ratios (relative to silicon) of all major elements except oxygen [1], and the Gamma Ray Spectrometer has measured the absolute abundance of the minor element potassium [2]. Spatially resolved measurements of Mg, Si, Al, S, and Ca reported by [1] suggest high-Mg and low-Mg endmember compositions. These compositions are reported in Table 1. Notably, the abundance of Fe is low (<4 wt. %) and the abundance of S (sulfur) is very high, up to 4 wt. %, an order of magnitude greater than in terrestrial igneous rocks.

	Mg/Si	Al/Si	S/Si	Ca/Si	Fe/Si	K
high-Mg	0.67	0.18	0.15	0.30	0.06	0.1
low-Mg	0.36	0.26	0.06	0.18	–	0.1

table 1. The chemical composition of the surface of Mercury from [1,2] reported as elemental wt. % ratios or elemental wt. %. The high-Mg and low-Mg compositions correspond to flare nos. 5 and 9 of [1]. K abundance [2] is not spatially resolved.

Potentially, the normative mineralogy of the surface of Mercury can be calculated from the chemical compositions reported in Table 1 (as has been done in [4]). This normative mineralogy suggests research questions, for instance: 1) What minerals are unstable on the surface of Mercury and destroyed to form the pits known as hollows [5]? 2) What minerals should be measured as spectral analogs to calibrate the MERcury Thermal infrared Imaging Spectrometer (MERTIS) [6], part of the ESA BepiColombo mission to Mercury?

However, conventional normative calculations make assumptions about oxidation state and the speciation of major cations that do not apply to Mercury. The mantle of Mercury (and melts of this mantle) may be extremely reduced [1,7] as suggested by the large iron core of Mercury and the high sulfur abundance of the surface. Consequently, Fe as well as the lithophile elements Ca and Mg may be present in exotic sulfides such as oldhamite or niningerite [1] rather than in native iron or silicate minerals.

Accurate normative calculations require new experimental data on the subsolidus phase assemblages of sulfur-rich Mercury surface compositions (previous low-pressure crystallization experiments on Mercury surface compositions [8] are sulfur-free). We crystallize Mercury surface compositions like those in Table 1 at low pressures and very low oxygen fugacities, up to seven $\log_{10}$ units below the iron-wüstite buffer (IW-7). Controlling the oxygen fugacity of these experiments presents unique challenges: these experiments are difficult to perform in gas-mixing furnaces because the sulfur fugacity above the sulfur-rich melt gives rise to sulfur species such as H_2S that attack the gas-mixing system. Consequently, we enforce low oxygen fugacities using exotic solid buffers such as Nb-NbO (IW-7 at 1500°C).

We will present preliminary experimental results and discuss their implications for the mineralogy of Mercury, focusing particularly on the speciation of iron and sulfur on the surface of Mercury.

References: [1] Nittler L. R. et al. (2011) Science, 333, 1847-1850. [2] Peplowski P. N. et al. (2011) Science, 333, 1850-1852. [3] Solomon S. C. et al. (2007) Space Sci. Rev., 131, 3-39. [4] Stockstill-Cahill K. R. et al. (2012) LPS, 43, abstract 2107. [5] Blewett D. T. et al. (2011) Science, 333, 1856-1859. [6] Arnold G. E. et al. (2009) P. Soc. Photo-Opt. Inst., 7453. [7] Zolotov M. Y. (2011) Icarus, 212, 24-41. [8] Charlier B. et al. (2012) LPS, 43, abstract 1400.

TOPOGRAPHY OF MERCURY FROM MESSENGER ORBITAL STEREO MAPPING

Jürgen Oberst[1], Frank Preusker[1], James W. Head[2], Mark S. Robinson[3], Thomas R. Watters[4], and Sean C. Solomon[5].
[1]German Aerospace Center, Institute of Planetary Research, D-12489 Berlin, Germany (Frank.Preusker@dlr.de), [2]Department of Geological Sciences, Brown University, Providence, RI 02912, USA; [3]School of Earth and Space Exploration, Arizona State University, Tempe, AZ 85287, USA; [4]Center for Earth and Planetary Studies, National Air and Space Museum, Smithsonian Institution, Washington, DC 20560, USA; (5) Lamont-Doherty Earth Observatory, Columbia University, Palisades, NY 10964, USA.

Introduction:

In March 2011 the MErcury Surface, Space ENvironment, GEochemistry, and Ranging (MESSENGER) spacecraft was inserted into orbit about Mercury [1]. MESSENGER is equipped with the Mercury Dual Imaging System (MDIS) [2] consisting of a wide-angle camera (WAC) and a narrow-angle camera (NAC) co-aligned on a pivot platform. During its first Mercury solar day (~176 Earth days), the spacecraft acquired several thousand images to create a monochrome base map using mainly the WAC for the northern hemisphere and NAC for the southern hemisphere, respectively, from its highly eccentric near-polar orbit. In September 2011, with the beginning of the second Mercury day, MESSENGER started acquiring a complementary image dataset under high emission angles (by tilting the camera), but similar Sun elevation and azimuth. The combination of both base maps enables us to analyze the images stereoscopically and to generate digital terrain models (DTMs). The DTMs are particularly important for the southern hemisphere, most parts of which are out of range of MESSENGER's Mercury Laser Altimeter (MLA).

Image Data and Methods:

The stereo-photogrammetric processing for Mercury is based on a software system that has been developed over the last decade [3-6]; the methodology includes photogrammetric block adjustment, multi-image matching, surface point triangulation, digital terrain model (DTM) generation, and base map production. We have selected images that have resolutions better than 600 m/pixel (~58,000 images in total) and have compiled the stereo coverage obtained under "optimal" stereo conditions (Table 1).

differences in illumination	0-10°
stereo angle	15-60°
incidence angle	0-70°
emission angle	0-65°
phase angle	5-180°

table 1. Stereo processing conditions

We divided the stereo coverage into 15 tiles that conform to the quadrangle scheme proposed by Greeley and Batson [7]. Here, we have selected one southern hemisphere area (Figure 1, H14 – Cyllene quadrangle) to carry out tests for topographic surface reconstructions. The area is covered by about 1,300 stereo images with a mean resolution of about 230 m/pixel and includes a portion of the 715-km-diameter Rembrandt basin (Figure 2).

Results:

We collected ~15,000 tie points in selected stereo images for navigation data correction with photogrammetric block adjustment. This step improves the three-dimensional (3D) point accuracy from ±700 m (using nominal navigation data) to ±50 m. Next, 1,585 individual matching runs were carried out to yield ~540 million object points. The mean ray intersection error of the ground points was ±55 m. Only triple-overlapping images were used for the matching. Finally, we generated a DTM with a lateral spacing of 250 m/pixel (~170 pixels per degree) and a vertical accuracy of about 30 m; the DTM covers ~ 6 % of Mercury's surface. Updates on our processing will be given at the conference.

Acknowledgements: The MESSENGER project is supported by the NASA Discovery Program under contracts NASW-00002 to the Carnegie Institution of Washington and NAS5-97271 to The Johns Hopkins University Applied Physics Laboratory

References: [1] Solomon S.C. et al.: Mercury after six months of MESSENGER orbital observations, EPSC-DPS Joint Meeting Abstracts and Program, abstract EPSC-DPS2011-430, 2011.. [2] Hawkins S.E., III, et al.: The Mercury Dual Imaging System on the MESSENGER spacecraft, Space Sci. Rev., 131, 247-338, 2007. [3] Gwinner K. et al.: Topography of Mars from global mapping by HRSC high-resolution digital terrain models and orthoimages: Characteristics and performance, Earth Planet. Sci. Lett., 294, 506-519, 2010. [4] Oberst J. et al.: The morphology of Mercury's Caloris basin as seen in MESSENGER stereo topographic models, Icarus, 209, 230–238, 2010. [5] Preusker F. et al.: Stereo topographic models of Mercury after three MESSENGER flybys, Planet. Space Sci., 59, 1910–1917, 2011. [6] Scholten F. et al.: GLD100: The near-global lunar 100 meter raster DTM from LROC WAC stereo image data, J. Geophys. Res., 117, E00H17, 10.1029/2011JE003926, 2012. [7] Greeley, R. and Batson, R.M.: Planetary Mapping, Cambridge University Press, 296 pp., 1990.

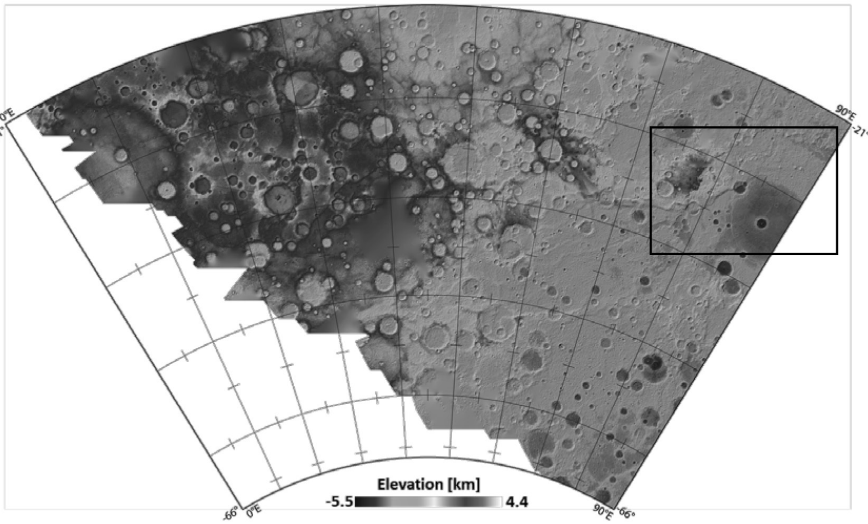

fig. 1. DTM of Cyllene (H14) quadrangle (hill-shaded color-coded height) with a lateral spacing of 250 m in Lambert (conformal) projection centered at 45°E. White areas are gaps in the current stereo coverage. Note the Rembrandt basin area (red rectangle); see Figure 2 for a detailed view.

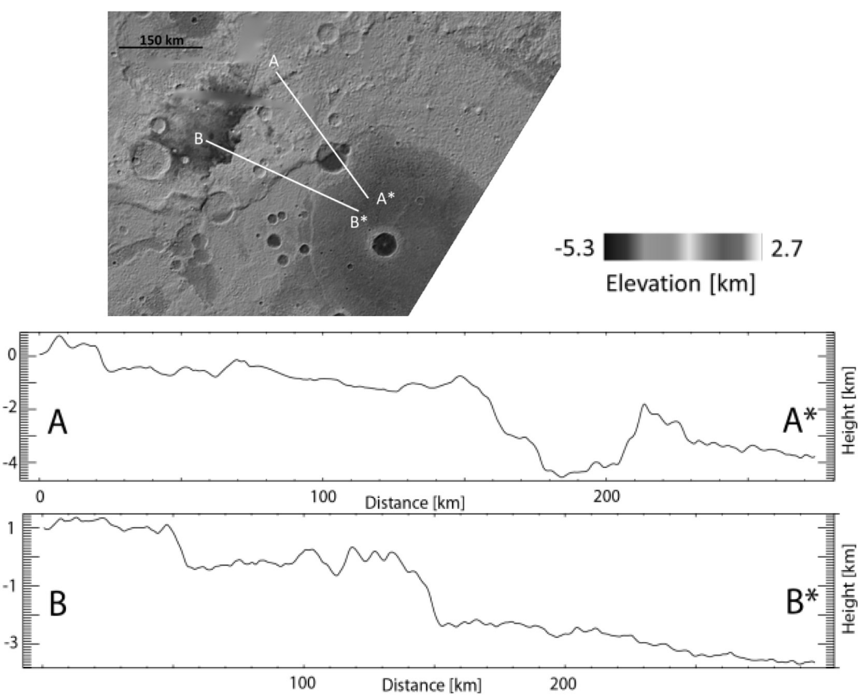

fig. 2. Magnified portion of the DTM and selected topographic profiles of the Rembrandt impact basin area (cf. Figure 1)

MERCURY LIMB TOPOGRAPHY FROM MESSENGER IMAGES.

Stephan Elgner[1], Jürgen Oberst[1], Mark E. Perry[2], Maria T. Zuber[3], Mark S. Robinson[4], Sean C. Solomon[5].
[1]German Aerospace Center (DLR), Institute of Planetary Research, Berlin, Germany, [2]Johns Hopkins University Applied Physics Laboratory, Laurel, USA, [3]Massachussetts Institute of Technology, Department of Earth, Atmospheric, and Planetary Sciences, Cambridge, USA, [4]Arizona State University, School of Earth and Space Exploration, Tempe, USA, [5]Carnegie Institution of Washington, Department of Terrestrial Magnetism, Washington, USA. Contact: stephan.elgner@dlr.de

Introduction:

The MESSENGER spacecraft is determining Mercury's global shape and topography by means of several complementary techniques, including laser altimetry [1], measurements of radio occultation timing [2], stereo image analysis [3-4], and limb imaging [5]. We have analyzed Mercury's topography by using limb imagery obtained by MESSENGER's Mercury Dual Imaging System (MDIS) [6] consisting of a wide-angle camera (WAC) and a narrow-angle camera (NAC) co-aligned on a pivot platform.

Image Data and Methods:

Since orbit insertion in March 2011 [7], MESSENGER has obtained more than 1,600 limb images through August 2012. From these images, we have constructed a near-global network of limb profiles, which include large numbers of crossovers between individual limb tracks. The image coordinates of limb positions were determined by a contrast-based search, and measured line and sample coordinates of limb positions were corrected for image geometric distortions, following methods developed earlier [5]. Whereas limb profiles obtained during MESSENGER's Mercury flybys extended from pole to pole and are easily interpreted in terms of planet radius, limb images from orbit are typically obtained from closer range, show comparatively shorter arcs, and lack global geodetic control. It is therefore more difficult to derive the absolute distance of the limb from the planet's center and consequently the absolute heights of limb profiles. Hence, we use height information at crossovers between limb profiles and carry out a least-squares adjustment to obtain correct heights and tilts of the profiles.

Results:

Our recent analyses of about 640 limb images providing 153,000 limb points and 7,300 intersections yield a near-global representation of Mercury's topography (Fig. 2). We see a substantial decrease in crossover height errors with an overall standard deviation of height differences at crossover points of better than ± 0.8 km. The topography has a full dynamic range of 8.2 km and a standard deviation of ± 0.9 km over the entire limb network. Also, a Mercury mean radius of R = 2441.1 km has been derived. Comparisons between individual limb profiles and digital terrain models (DTMs) derived by stereo photogrammetry [3-4] show good agreement (Fig. 3) for large-scale topography. Height offsets are visible and will be addressed in the future by tying the limb profiles network to MLA data in the northern hemisphere.

Acknowledgements:
The MESSENGER project is supported by the NASA Discovery Program under contracts NASW-00002 to the Carnegie Institution of Washington and NAS5-97271 to The Johns Hopkins University Applied Physics Laboratory.

References:
[1] M. T. Zuber et al.: Topography of the northern hemisphere of Mercury from MESSENGER laser altimetry, Science, 336, 217-220, 2012. [2] M. E. Perry et al.: Measurement of the radius of Mercury by radio occultation during the MESSENGER flybys, Planet. Space Sci., 59, 1925-1931, 2011. [3] J. Oberst et al.: The morphology of Mercury's Caloris basin as seen in MESSENGER stereo topographic models, Icarus, 209, 230-238, 2010. [4] F. Preusker et al.: Stereo topographic models of Mercury after three MESSENGER flybys, Planet. Space Sci., 59, 1910-1917, 2011. [5] J. Oberst et al.: Radius and limb topography of Mercury obtained from images acquired during the MESSENGER flybys, Planet. Space Sci., 59, 1918-1924, 2011. [6] Hawkins S.E., III, et al.: The Mercury Dual. Imaging System on the MESSENGER Spacecraft, Space Science Review, 131, 247-338, 2007. [7] Solomon S.C et al.: Mercury after Six Months of MESSENGER Orbital Observations, 2-7 October 2011, Nantes, France, 2011. [8] F. Preusker et al.: Topography of Mercury from stereo images: first samples from MESSENGER orbital mapping, Lunar Planet. Sci., 43, abstract 1913, 2012.

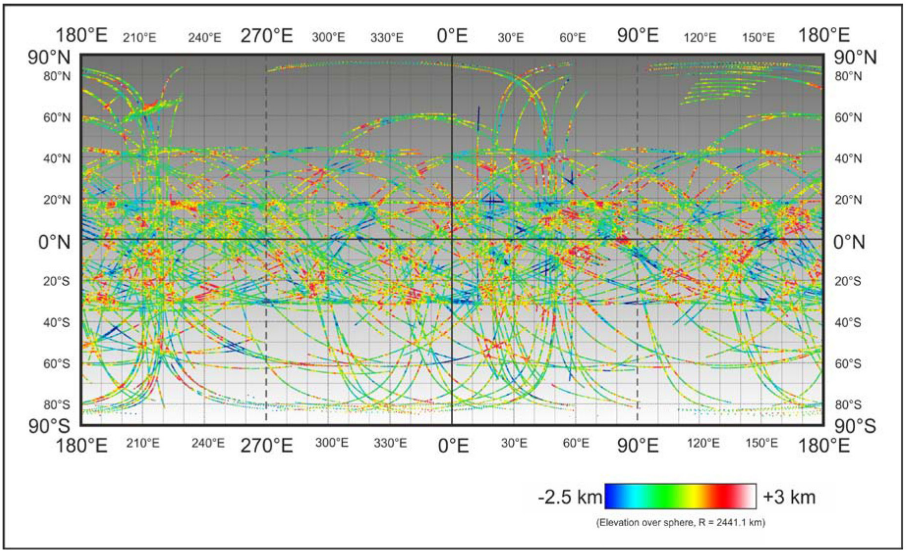

fig. 1. Limb profiles in equidistant projection.

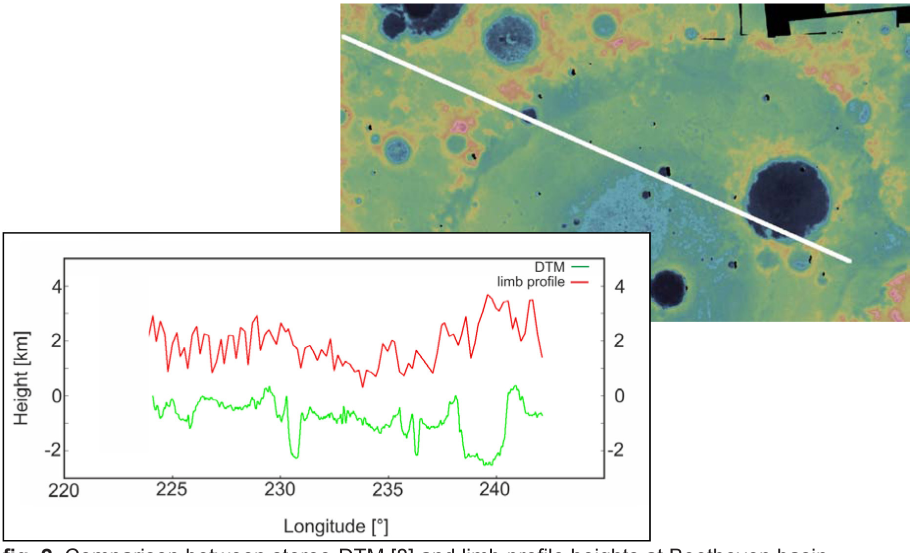

fig. 2. Comparison between stereo-DTM [8] and limb profile heights at Beethoven basin.

MEASUREMENT OF MERCURY'S PHYSICAL LIBRATIONS FROM ORBITAL OBSERVATIONS BY THE MESSENGER SPACECRAFT

Alexander Stark[1], Jürgen Oberst[1], Frank Preusker[1], Klaus Gwinner[1], Stanton J. Peale[2], Jean-Luc Margot[3], Maria T. Zuber[4], and Sean C. Solomon[5],
[1]German Aerospace Center, Institute of Planetary Research, D-12489 Berlin, Germany (Alexander.Stark@dlr.de); [2]Department of Physics, University of California, Santa Barbara, CA 93106, USA; [3]Department of Earth and Space Sciences, University of California, Los Angeles, CA 90095, USA; [4]Department of Earth, Atmospheric and Planetary Sciences, Massachusetts Institute of Technology, Cambridge, MA 02139, USA; [5]Lamont-Doherty Earth Observatory, Columbia University, Palisades, NY 10964, USA.

Introduction:

We present a technique for the in situ measurement of physical librations of a celestial body from orbiting spacecraft. In order to perform this measurement our approach combines laser altimeter and image data obtained by onboard instruments. In our method we are combining the benefits from those individual data sets as well as making use of their complementarity. The knowledge of the physical libration of a planet or a moon is important for accurately constraining the geodetic reference system of the celestial body. These reference systems are used to produce accurate maps and for mission planning. In special cases, e.g., Mercury, it is also possible to determine constraints on the internal structure and, by extension, the thermal evolution of a planet by measuring the amplitude of the librations. In this paper we present an update of the application of our method to physical librations of Mercury. We use image data and laser profiles obtained by the NASA MESSENGER spacecraft now in orbit about Mercury.

The longitudinal librations of Mercury are related to the orbital motion of the planet and have a main period of 87.9693 days [1]. Previous estimates from Earth-based radar observations suggest an amplitude of 38.0±1.8 arc seconds, i.e., more than 450 m at the equator [2]. The MESSENGER spacecraft has been collecting image and laser altimeter data since Mercury orbit insertion in March 2011. The instruments on the spacecraft carry out comprehensive measurements of Mercury's topography, gravity and magnetic fields, surface chemical composition, and other first-order science observations of this extraordinary planet.

Method:

We use a recently developed method for co-registration of laser altimeter profiles and digital terrain models (DTMs) obtained from stereo imaging [3]. Provided that the planetary surface is sufficiently rough, topographic data sets can be co-registered with very high accuracy, much below the size of individual laser spots or terrain model grid elements (Figure 1). Co-registration is performed using least-squares fitting, i.e., by minimizing the standard deviation of the two datasets. In order to measure the libration amplitude we first derived the position of Mercury Laser Altimeter (MLA) profiles [4] on the surface, under the assumption of no libration effects. After co-registration with the stereo DTM we obtained systematic longitudinal shift patterns of the laser profiles in relation to the fixed stereo DTM, probably representing the libration signature (Figure 2). In this step we assume that there is no effect of the librations on the stereo models. The DTMs are typically composed of large blocks (groups) of images, and during the block adjustments the offsets between the different blocks, which can be caused by librations, are minimized [5,6].

In the co-registration process we determine global (DTM) and local (MLA profile) parameters. The global parameters are the longitudinal and latitudinal tilts between the datasets and global lateral offsets, in latitude and longitude, respectively [8,9]. Local parameters, latitudinal and longitudinal shifts, are obtained for each laser profile crossing the area represented by the DTM. The sources for the different offsets are currently being studied and could be related to orbit geometry, image acquisition, laser altimeter pointing, uncertainties in rotational parameters of Mercury, or a combination thereof.

The basis of our study is the set of topographic profiles acquired by the MLA in the primary and extended orbital phase of the MESSENGER mission between 29 March 2011 and 6 May 2012. In addition, we use four stereo photogrammetric DTMs computed from stereo images obtained by the Mercury Dual Imaging System (MDIS) [7]. The DTMs cover parts of the northern hemisphere of Mercury (between 21° N and 66° N) where we find the best compromise between laser altimeter coverage (increasing with higher latitudes) and libration effect [decreasing with cos(λ) in latitude λ].

We used the mathematical model for the libration function $\varphi(t)$ described by Peale [1] and Margot [2]

$$\varphi(t)=\frac{3}{2}\frac{B-A}{C}\sum_k f_k(e)\sin(kM(t)),$$

where $A < B < C$ are the principal moments of inertia, $f_k(e)$ are a power series in the eccentricity, and $M(t)$ is the mean anomaly of Mercury. In our measurement we obtain the amplitude of the librations, which corresponds to the ratio of the principal moments of inertia of the planet.

Results:

The systematic longitudinal shift pattern obtained in the co-registration process is shown in Figure 2. In this plot we combined the shifts of MLA profiles from different observation periods with respect to their librational phase (time). Even though errors in co-registrations are on the order of the libration amplitude, we can clearly see a temporal variation with the characteristic period and phase of the expected librations. In total over 750 longitudinal shifts were obtained (gray dots). In order to provide a reliable estimate for the error of the libration measurement we performed a binning of several tens of longitudinal shifts in bins covering two Earth days (black dots with error bars). The standard deviation of the shifts in each bin provides an estimate of the error in the binned value.

On the basis of the model function we obtained a libration amplitude of 42±5 arc seconds through an error-weighted fit to the binned values (black curve). This amplitude corresponds to the fraction of $(B - A)/C =$ 2.4 ± 0.3) · 10-4 . The recently obtained libration amplitude from Earth-based radar measurement [2] is within the ±5 arc seconds uncertainty of our result. The strong scatter of the shifts and consequently the large error of the measurement are assumed to be caused mainly by three factors: the spatial resolution of the DTM, the number of MLA spots per track, and the topography of Mercury in the specific region of each MLA track.

We are working on improvements to the co-registration method, to be followed by further analysis of the results. With the acquisition of more MLA profiles and DTMs, we expect to reduce the error and to obtain an accurate and independent in-situ measurement of the libration function.

References: [1] S. J. Peale (1988), in Mercury, Univ. Arizona Press, Tucson, pp. 461-493. [2] J. L. Margot et al. (2012), submitted to J.Geophys.Res. [3] P. Gläser et al. (2010), EPSC 2010, abstract EPSC2010-296. [4] M. T. Zuber et al. (2012), *Science,* 336, 217-220. [5] F. Preusker et al. (2011), Planet. Space Sci., 59, 1910–1917. [6] J. Oberst et al. (2010), Icarus, 209, 230–238. [7] F. Preusker et al. (2012), Lunar Planet. Sci., 43, abstract 1913 [8] A. Stark et al. (2012), Lunar Planet. Sci., 43, abstract 1389 [9] A. Stark et al. (2012), EPSC 2012, abstract EPSC2012-254

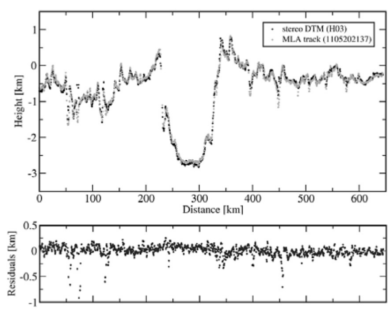

fig. 1. Top: MLA profile (gray dots) and heights derived from a stereo DTM (black dots) after co-registration of the data sets. Bottom: residuals between the two data sets after co-registration (root mean square residual = 98 m).

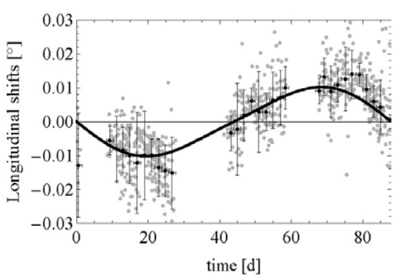

fig. 2. Fit of the libration model function to longitudinal shifts between MLA profiles and stereo topographic models (gray dots). The black dots with error bars represent binned values with a bin size of two Earth days. The black curve shows the best fit of the binned values to the libration model function with amplitude of 42±5 arc seconds.

RETURN TO VENUS OF AKATSUKI.

M. Nakamura[1] and AKTSUKI Project team,
[1]Institute of Space and Astronautical Science, 3-1-1 Yoshinodai, Chuo-ku, Sagamihara, Kanagawa, Japan 252-5210; Contact: nakamura.masato@jaxa.jp

Japanese Venus Climate Orbiter ‘AKATSUKI’ (PLANET-C) was proposed in 2001 with strong support by international Venus science community and approved as an ISAS mission soon after the proposal. AKATSUKI and ESA’s Venus Express complement each other in Venus climate study. Various coordinated observations using the two spacecraft have been planned. Also participating scientists from US have been selected. The mission life we expected was more than 2 Earth years in Venus orbit.

AKATSUKI was successfully launched at 06:58:22JST on May 21, by H-IIA F17. After the separation from H-IIA, the telemetry from AKATSUKI was normally detected by DSN Goldstone station (10:00JST) and the solar cell paddles’ expansion was confirmed. AKATSUKI was put into the 3-axis stabilized mode in the initial operation from Uchinoura station and the critical operation was finished at 20:00JST on the same day.

The malfunction, which happened during the Venus Orbit Insertion (VOI) on 7 Dec, 2010 is as follows. We set all commands on Dec. 5. Attitude control for Venus orbit insertion (VOI) was automatically done on Dec. 6. Orbital maneuver engine (OME) was fired 08:49 JST on Dec. 7. 1min. after firing the spacecraft went into the occultation region and we had no telemetry, but we expected to continuous firing for 12min. Recording on the spacecraft told us later that, unfortunately the firing continued just 152sec. and stopped. The reason of the malfunction of the OME was the blocking of check valve of the gas pressure line to push the fuel to the engine. We failed to make the spacecraft the Venus orbiter, and it is rotating the sun with the orbital period of 203 days.

Most of the fuel still remains, but the OME was found to be broken. We decided to use only RCS for orbit maneuver and 3 minor maneuvers in November 2012 were successfully done so that AKATSUKI will meet Venus in 2015. We are considering several scenarios only using RCS for VOI. It will be hard to keep the equatorial orbit through the VOI in 2015, but if we wait another year and will do the VOI in 2016 there is a chance to have an equatorial orbit. Preferable orbit and the life time of the spacecraft is the trade off.

We have to be very careful about the thermal condition during the extended cruise phase. We expected about 2600W/m^2 solar flux in the Venus orbit, but it is exposed to more than 3600W/m^2 at perihelion (0.6AU from the sun). The temperatures of the instruments exposed to space gradually increased as the spacecraft approaching the perihelion. We try to minimize the number of instruments whose temperatures exceed the allowed upper limits by letting a certain side of the spacecraft face to the sun.

VENUS EXPRESS – NEW RESULTS AND FUTURE PLANS.

H. Svedhem[1], D. Titov[1], C. Wilson[2],
[1]ESA/ESTEC, PB 299, 2200AG Noordwijk, The Netherlands,[2] University of Oxford, Oxford, UK.

Introduction:

Venus Express has now been in a 24 hour polar orbit around our neighbor planet for more than six years. The spacecraft and its scientific instruments are in an excellent condition barring a few items that have reached their end of life. The fuel situation is good and it is expected that the supply will last until at least early 2015 and possibly longer. From the six active instruments on board well above 3 Tbit data has been down-linked to ground.

The 24 hour polar orbit has allowed extended global studies of the southern hemisphere and in particular of the southern polar vortex structure and dynamics, studies of chemical composition and processes throughout the atmosphere, and dedicated observations of the structure and dynamics of the cloud layers. Radio occultation measurements have provided the most comprehensive data set to date of the atmospheric density and temperature, and of the electron density in the ionosphere. Stellar and solar occultations have allowed very high spatial resolution vertical profiles of the abundance of many chemical species. Wind velocities have been measured by cloud tracking at several altitudes and the super-rotating atmosphere has been confirmed and further characterized. The interaction of the upper atmosphere with the solar wind has been studied and escape rates for the major escaping ions (Hydrogen, Oxygen and Helium) have been estimated. These results have led to new ideas about how an intrinsic magnetic field protects a planetary atmosphere. The conventional theory is that an atmosphere without a magnetic field would erode faster than one with a magnetic field but as measurements show that the Earth is losing more matter to space than Venus does, this cannot be true.

Studies of the surface in the near infrared have shown several areas of recent geologic activity. These areas correspond well to the suspected ‘hot spots’ previously identified in the Magellan radar and gravity field maps.

Recently the atmospheric density has been probed in situ by reducing the pericentre altitude such that the drag force on the spacecraft has become significant and thus measureable. In this way the altitude range 165-200 km, which is not possible to address with remote measurements, has been characterized. For the first time a new technique has been applied whereby the solar panels are set in an asymmetric position with respect to each other such that a torque is acting on the spacecraft during the atmospheric pass. Since the spacecraft attitude is maintained automatically be the reaction wheels the rotation rate changes of the wheels provide a very sensitive measure of the atmospheric density.

The Venus Express team has prepared for several new types of observations during the last years, including aerodrag measurements that started in 2009, solar spectral scans that started in 2011 and airglow measurements of on the dayside that will start in 2012. Original observation plans for 2011 included exciting and unique joint measurements with the Akatsuki mission, but due to the unfortunate failure during its orbit insertion plans had to be changed. The atmospheric drag measurements have been performed during eight dedicated campaigns, when, due to solar gravity perturbations of the orbit, the pericentre altitude has reached levels below 200km and as far down as 165km. These measurements have revealed a much less dense atmosphere at the polar latitudes than what existing models predict. In addition the density seems to vary up to a factor three in a semi periodic manner. The mechanism causing this variation is not yet understood but it is possible that waves propagating from the polar vortex far below have some influence.

Continued measurements the coming years will provide new insights to the importance of the solar activity for the different processes already studied at low solar activity. This is particularly important for the study of atmospheric loss. Joint measurement campaigns with complementary ground based observations of various kinds will continue. These are mostly focused at times of Venus maximum elongations due to the limited opportunities for good observations at other times.

CHEMISTRY OF VENUS' ATMOSPHERE

V.A. Krasnopolsky[1, 2],
[1]Catholic University of America, Washington, DC 20064, USA; [2] Moscow Institute of Physics and Technology, Dolgoprudnyy, Russia. Contact:vlad.krasn@verizon.net

Introduction:

Recent finding in the chemical composition of the Venus atmosphere from the Venus Express orbiter and ground-based submillimeter and infrared observations require interpretation in terms of adequate models for chemical composition. Here we will briefly discuss three one-dimensional global-mean models for various altitude ranges and conditions on Venus.

Photochemical Model for 47-112 km

This is an altitude range where basic photochemical processes occur on Venus. Numerical accuracy of our model (Krasnopolsky V.A. 2012, Icarus 218, 230-246) is significantly improved by reduction of the altitude step from 2 km in the previous models to 0.5 km. Effects of the NUV absorber are approximated using the detailed photometric observations at 365 nm from Venera 14. The H_2O profile is not fixed but calculated in the model. The model involves odd nitrogen and OCS chemistries based on the detected NO and OCS abundances. The number of the reactions is significantly reduced by removing of unimportant processes. Column rates for all reactions are given, and balances of production and loss may be analyzed in detail for each species.

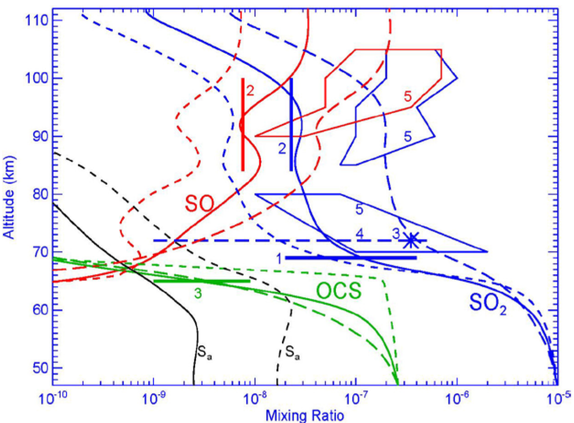

Fig. 1. Basic sulfur species: model results and observations. SO_2, OCS, and SO profiles are shown for the models with the eddy break at h_e = 55, 60, and 65 km (long dash, solid, and short dash curves, respectively). The aerosol sulfur S_a mixing ratio is 4×10^{-11} at 47 km for h_e = 55 km and not shown. Observations: (1) PV, Venera 15, HST and rocket data (Esposito et al. 1997); (2) mean results of the submillimeter measurements (Sandor et al. 2010); the observed SO_2 varies from 0 to 76 ppb and SO from 0 to 31 ppb; (3) IRTF/CSHELL (Krasnopolsky 2010c);
(4) SPICAV_UV, nadir (Marcq et al. 2011); (5) VEX/SOIR and SPICAV-UV occultations (Belyaev et al. 2012).

The calculated vertical profiles of CO, H_2O, HCl, SO_2, SO, OCS (Fig. 1) and of the O_2 dayglow at 1.27 μm generally agree with the existing observational data; some differences are briefly discussed. The OH dayglow is ~30 kR, brighter than the OH nightglow by a factor of 4. The H + O_3 process dominates in the nightglow excitation and O + HO_2 in the dayglow, because of the reduction of ozone by photolysis. A key feature of Venus' photochemistry is the formation of sulfuric acid in a narrow layer near the cloud tops that greatly reduces abundances of SO_2 and H_2O above the clouds. Delivery of SO_2 and H_2O through this bottleneck determines the chemistry and its variations above the clouds. Small variations of eddy diffusion near 60 km result in variations of SO_2, SO, and OCS at and above 70 km within a factor of ~30. Variations of the SO_2/H_2O ratio at the lower boundary have similar but weaker effect: the variations within a factor of ~4 are induced by changes of SO_2/H_2O by ±5%. Therefore the observed variations of the mesospheric composition originate from minor variations of the atmospheric dynamics near the cloud layer and do not require volcanism. NO cycles are responsible for production of a quarter of O_2, SO_2, and Cl_2 in the atmosphere. A net effect of photochemistry in the middle atmosphere is the consumption of CO_2, SO_2, and HCl from and return of CO, H_2SO_4, and SO_2Cl_2 to the lower atmosphere. These processes may be balanced by thermochemistry in the lower atmosphere even without outgassing from the interior, though the latter is not ruled out by our models. Some differences between the model and observations and the previous models are briefly discussed.

Chemical Kinetic Model for the Lower Atmosphere (0-47 km)

A self-consistent chemical kinetic model of the Venus atmosphere at 0−47 km (Krasnopolsky V.A., 2007, Icarus 191, 25-37) involves 82 reactions of 26 species. Chemical processes in the atmosphere below the clouds are initiated by photochemical products from the middle atmosphere (H_2SO_4, CO, S_x), thermochemistry in the lowest 10 km, and photolysis of S_3. The sulfur bonds in OCS and S_x are weaker than the bonds of other elements in the basic atmospheric species on Venus; therefore the chemistry is mostly sulfur-driven. Sulfur chemistry activates some H and Cl atoms and radicals, though their effect on the chemical composition is weak. The lack of kinetic data for many reactions presents a problem that has been solved using some similar reactions and thermodynamic calculations of inverse processes. Column rates of some reactions in the lower atmosphere exceed the highest rates in the middle atmosphere by two orders of magnitude. However, many reactions are balanced by the inverse processes, and their net rates are comparable to those in the middle atmosphere.

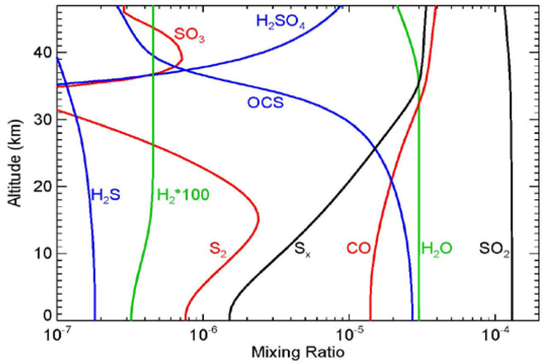

fig. 2. Basic chemical species in the Venus lower atmosphere.

The calculated profile of CO (Fig. 2) is in excellent agreement with the Pioneer Venus and Venera 12 gas chromatographic measurements and slightly above the values from the ground-based and VEX nightside spectroscopy at 2.3 μm. The OCS profile also agrees with the nightside spectroscopy which is the only source of data for this species. The abundance and vertical profile of gaseous H_2SO_4 are similar to those observed by the Mariner 10 and Magellan radio occultations and ground-based microwave telescopes. While the calculated mean S_3 abundance agrees with the Venera 11-14 observations, a steep decrease in S_3 from the surface to 20 km is not expected from the observations. The existing concept of the atmospheric sulfur cycles is incompatible with the observations of the OCS profile. A revised scheme involves the basic photochemical cycle that transforms CO_2 and SO_2 into SO_3 and CO. The net effect of thermochemistry in the lowest 10 km is formation of OCS from CO and S_x. Chemistry at 30−40 km removes the downward flux of SO_3 and the upward flux of OCS and increases the downward fluxes of CO and S_x. The geological cycle of sulfur remains unchanged.

Photochemical Model for Nighttime Atmosphere at 80-130 km

This model (Krasnopolsky V.A., 2010, Icarus 207, 17-27) is aimed to simulate observations of the night airglow on Venus. The model involves 61 reactions of 24 species, including odd hydrogen and chlorine chemistries, with fluxes of O, N, and H at 130 km as input parameters. To fit the OH vibrational distribution observed by VEX, quenching of OH(v>3) in CO_2 only to v≤2 is assumed. According to the model (Fig. 3), the nightside mean O_2 emission of 0.52 MR from the VEX and our observations requires an O flux of 2.9×10^{12} cm^{-2} s^{-1} which is 45% of the dayside production above 80 km. This makes questionable the nightside mean O_2 intensities of ~1 MR from some observations. Bright nightglow patches are not ruled out; however, the mean nightglow is ~0.5 MR as observed by VEX and supported by the model. The NO nightglow of 425 R needs an N flux of 1.2×10^9 cm^{-2} s^{-1}, which is close to that from VTGCM at solar minimum. However, the dayside supply of N at solar maximum is half that required to explain the NO nightglow in the PV observations. The limited data on the OH nightglow variations from the VEX and our observations are in reasonable agreement with the model. The calculated intensities and peak altitudes of the O_2, NO, and OH nightglow agree with the observations. Relationships for the nightglow intensities as functions of the O, N, and H fluxes are derived.

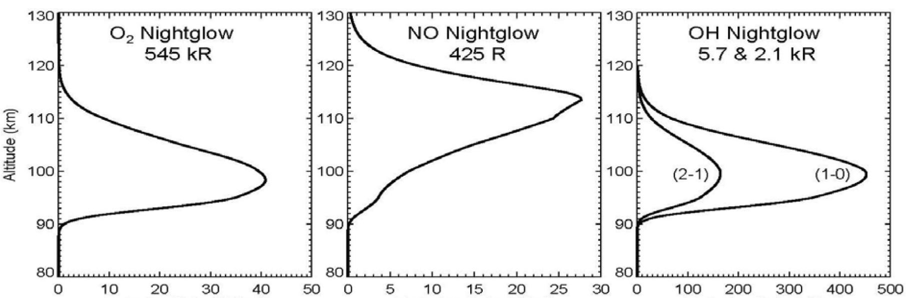

fig. 3. Calculated altitude profiles and intensities of the basic night airglow on Venus.

CLOUD MORPHOLOGY AND DYNAMICS OF THE VENUS ATMOSPHERE FROM THE VENUS EXPRESS OBSERVATIONS.

D.V. Titov[1], N.I. Ignatiev[2], I.V. Khatuntsev[2], A. Piccialli[3,1], Y.J. Lee[3], S.S. Limaye[4], W. J. Markiewicz[3], G. Piccioni[5], M. Paetzold[6], H. Svedhem[1],
[1]ESA/ESTEC, The Netherlands; [2]Space Research Institute (IKI), Moscow, Russia; [3]Max Planck Insttitute for Solar System Research, Katlenburg-Lindau, Germany; [4]University of Wisconsin, USA, [5]Institute for Space Astrophysics and Planetology, Rome, Italy; [6]Rhenish Institute for Environmental Research, Universität zu Köln, Cologne, Germany. Contact: Dmitri.Titov@esa.int.

Since April 2006 Venus Express has been performing a global survey of the remarkably dense, cloudy, and dynamic atmosphere of our near neighbour. More than 300 radio-occultation experiments covering all latitudes and local times had been acquired so far. They reveal highly variable temperature structure in the mesosphere and within the clouds. Temperature sounding suggests that the cloud deck at 50-60 km is convectively unstable, in agreement with the patterns seen in UV images. Joint analysis of several experiments indicated latitudinal trends in the cloud top structure. The cloud top altitude varies from approximately 67 ± 2 km in low latitudes to 63 ± 4 km at the pole marking vast polar depressions. The aerosol scale height decreases from about 4 ± 1.6 km to 1.7 ± 2.4 km. UV imaging monitors strongly variable cloud patterns showing for the first time the middle latitudes and polar regions in unprecedented detail.

Tracking of the cloud features at both UV and thermal infrared wavelengths characterizes the global wind field and its variations. Low and middle latitudes show an almost constant with latitude zonal wind speed of 90 ± 20 m/s at the cloud tops and vertical wind sheer of 2-3 m/s/km. Towards the pole, the wind speed drops quickly and the vertical shear vanishes. The zonal winds show significant variability on a time scale of days and clear periodicities. The meridional poleward wind ranges from 0 m/s to about 15 m/s and there is some indication that it may change its direction at high latitudes. The global zonal circulation converges to giant vortices at the poles. Comparison of the thermal wind field derived from temperature sounding to the cloud tracked winds confirms the approximate validity of cyclostrophic balance, at least in the latitude range from 30S to 70S. The observations are supported by development of General Circulation Models.

LIMB ALTITUDE FROM VENUS MONITORING CAMERA

Sanjay S. Limaye, R.J. Krauss, W.J. Markiewicz

Precision conic fits to the visible limb in the Venus Monitoring Camera (VMC) have been performed to look for dependence of the limb altitude with latitude in all four available wavelengths. The limb altitude is seen to show a decrease towards the pole, similar to what has been inferred from VIRTIS and SPICAV/SOIR observations. Little variation is seen between late afternoon and early morning. Small daily variations in the limb altitude are suggested.

TEMPERATURE STRUCTURE OF VENUS NIGHTSIDE WITH VIRTIS/VENUS EXPRESS

A. Migliorini[1], D. Grassi[1], S. Lebonnois[2], L. Montabone[2,3], G. Piccioni[1], P. Drossart[4], *[1]IAPS-INAF, Via del fosso del Cavaliere, 100, 00133-Rome, Italy; [2]LMD, Jussieu, Box 99, 75252 Paris,France; AOPP, Dept. Of Physics, University of Oxford, Parks Road, Oxford OX14 PU, UK; LESIA, 5, Place J. Janssen, 92195 Meudon, Paris, France. Contact: Alessandra.Migliorini@iaps.inaf.it*

We present the investigation of the thermal structure of the nightside of Venus, using remote sensing data acquired with the VIRTIS (Visible and Infrared Thermal Imaging Spectrometer) instrument on board the European Venus Express mission. With this instrument, we can investigate the thermal region from 4 to 5 μm, through the inversion of the CO_2 band, centered at 4.26 μm. The inversion method is based on the radiative transfer equation, and it requires a first guess of the atmospheric temperature, provided from the VIRA profiles, based on in situ measurements by Venera spacecrafts, the four Pioneer Venus probes and the Pioneer Venus Orbiter. On the other hand, these results can provide important hints for an update of the VIRA model itself.

In the pressure range from 100 to 4 mbar (which corresponds approximately to the altitude range 65-80 km), the northern and southern hemispheres present similarities in the thermal structure. The cold-collar feature is detected around 60-70° on both hemispheres. This region is on average 15 to 20 K colder than the temperature at the pole at 100 mbar (about 65 km), also showing a significant thermal inversion. A peculiar pattern of maxima and minima in temperature is observed at 100 and 12 mbar. However, differences between the dusk and dawn sides are observed in the temperature values, the dawn being the coldest quadrant in the pressure range 100 to 12 mbar.

The application of the Venus global circulation model (Lebonnois et al., 2010b) of the Laboratoire de Météorologie Dynamique (LMD) to the present results allows to interpret the features observed at 100 mbar and 12 mbar as indication of diurnal and/or semidiurnal thermal tides.

VENUS NON-LTE EMISSIONS FROM VENUS EXPRESS

P. Drossart, LESIA,
Observatoire de Paris, 5 place Janssen 92195 Meudon, FRANCE.
Contact : pierre.drossart@obspm.fr

Introduction:

Observation of Venus with Venus Express has provided a new database sounding Venus atmosphere and environment at various levels. In particular, VIRTIS and SPICAV spectroscopic observations in the infrared and visible have renewed our knowledge of the aeronomy of Venus, mapping horizontally and vertically the emissions, confirming and sometimes challenging previous interpretations.

Venus Express observations: The sounding of the upper atmosphere of Venus has been obtained on Venus Express (Svedhem et al., 2007) by SPICAV (Bertaux et al., PSS, 2007) in UV and IR spectroscopy, and VIRTIS (Drossart et al, PSS, 2007) in visible and IR spectroscopy and spectro-imaging. The observations have been obtained since April 2006 after Venus Orbit insertion and during the whole nominal mission of Venus Express. During the extended mission, a failure in the cryo-coolers on VIRTIS have limited the observations to the period 2006-2008 for IR imaging spectroscopy, 2006-2009 for the IR high resolution channel, and only visible channel observations remaining active after.

Venus aeronomy : Observation of several constituents was achieved, some well known like $O_2(1\text{-}\Delta)$ at 1.27 µm or NO at 200 nm, as well as new molecules like OH (Piccioni et al., 2008) first detected by Venus Express/VIRTIS. Its mapping capabilities has allowed VIRTIS to make the first global map of the statistical distribution of O_2 emission on the night side of Venus, confirming a high temporal and spatial variability, with predominance of emission around the antisolar point as predicted from ground-based observations (Connes et al., 1979).

The vertical resolution obtained from solar occultation mode (SPICAV) or limb observations (VIRTIS) give important constraints on the Spatial and temporal variations of the emissions give access to some constraints on the dynamics of the upper atmosphere.

Non-LTE emissions in CO and CO_2 : CO_2 and CO non-LTE emission regularly observed by VIRTIS in the 4.3-4.7 µm range give another sounding of the mesosphere of Venus at altitudes as high as 120 km. The modeling of these emissions, vertically resolved in limb observations gives access to density measurements. Dynamical effets are also observed in imaging mode in CO_2 emissions, related to wave activity, most probably interpreted as gravity waves propagating in the upper atmospheres

Conclusion : In conclusion, the Venus Express observations now available to the science community through ESAC center provide a new vision of the upper atmosphere of Venus, completing previous observations by Pioneer Venus and Venera spacecraft and paving the way for future space exploration of Venus.

THE AIRGLOWS IN THE UPPER ATMOSPHERE OF VENUS OBSERVED BY VIRTIS ON VENUS EXPRESS

G. Piccioni[1], A. Migliorini[1], P. Drossart[2], and the VIRTIS-Venus Express Team
[1]IAPS-INAF, Via del fosso del Cavaliere, 100, 00133-Rome, Italy; [2]LESIA, 5, Place J. Janssen, 92195 Meudon, Paris, France.
Contact: Giuseppe.Piccioni@iaps.inaf.it

After more than 6 years from the Venus orbit insertion, the Visible and InfraRed Thermal Imaging Spectrometer (VIRTIS) on board the ESA Venus Express mission provided an extended data set very valuable to study Venus from the surface up to the thermosphere in long term. The VIRTIS instrument consists of two channels: VIRTIS-M, an imaging spectrometer with moderate spectral resolution in the range from 0.25 to 5 mm and VIRTIS-H, a high spectral resolution spectrometer in the range from 2 to 5 mm co-aligned with the field of view of –M. The spectral sampling of VIRTIS-M is 2 nm from 0.25 to 1 mm and 10 nm from 1 to 5 mm while for VIRTIS-H it is about 2 nm.

In this talk we focus on the airglows phenomena, in particular the nightglows, of which VIRTIS allows a detailed study in both nadir and limb observation geometry.

The most intense nightglow emission is observed at 1.27 μm and it is due to the (0-0) transition from the three bodies recombination of the atomic oxygen. Both limb and nadir views provide the 3-dimensional structure of the emission. The peak altitude of the limb profile is typically found at 96-97 km, with a maximum emission at low latitudes and near the antisolar point. The nadir measurements confirm the same behavior and the global mean map of the oxygen nightglow shows an almost perfect symmetry of the SS to AS circulation, with a maximum of the emission rate of about 1.2 MR in the antisolar region.

The hydroxyl nightglow has been discovered on Venus at 2.8 (1-0 transition) and 1.46 (2-0 transition) μm. It peaks a couple of km lower than the oxygen. The most probable mechanism is the Bates-Nicolet from the combination of H and O3. OH nightglow is thus an important tool to infer the abundance of these two chemical species.

The NO infrared nightglow emission at 1.224 μm has also been observed for the first time at Venus in the VIRTIS spectra. The NO nightglow comes from the energetic recombination of oxygen and nitrogen and typically it peaks at about 110 km altitude.

Other emissions are also observed in the visible range due to the O2 Herzberg II and Chamberlain systems, of which we have measured their vertical profile and intensity distribution.

OXYGEN NIGHTGLOW EMISSION AS TRACER OF VENUS' ATMOSPHERE CIRCULATION NEAR MESOPAUSE

L.Zasova[1,2], I. Khatuntsev[1,2], A.Shakun[1,2], J. Brekhovskikh[1], D. Gorinov[1,2], G.Piccioni[3], P. Drossart[4], *[1]Space Research Institute, IKI RAS, Moscow, Russia, [2]Moscow Institute of Physics and Technology, Dolgoprudny, Russia, [3]Istituto di Astrofisica e Planetologia Spaziali, INAF, Rome, Italy , [4]LESIA, Observatoire de Paris, Meudon, France; contact: zasova@iki.rssi.ru, fax: +7-495-333-12-78*

Introduction:

Maps of the $O2(a^1\Delta_g)$ 1.27 μm night airglow intensity were obtained from nadir measurements with the mapping VEX VIRTIS–M spectrometer, its IR–channel, with spectral range 1 - 5.1 μm and spectral sampling of 10 nm [1]. In VIRTIS spectra the oxygen nightglow at 1.27 μm is recovered by the thermal emission of the lower atmosphere, escaped through the window between CO_2 bands and scattered by non-absorbing sulfuric acid clouds. To obtain the absolute intensity of the airglow the thermal emission was taken into account by comparison with the thermal emission in the1.18 μm window [2]. The VIRTIS-M nadir measurements cover the Southern hemisphere and low latitudes of the Northern one.

Horizontal distribution of the oxygen nightglow in the Venus atmosphere is an effective tracer of circulation in upper atmosphere and lower thermosphere (in the vicinity of the mesopause level). This is a transition region between two major circulation modes. In thermosphere the subsolar-to-antisolar (SS-AS) circulation prevails, while in mesosphere a zonal retrograde superrotation (ZRS) dominates [3]. Besides, the thermal tides are observed in mesosphere with diurnal and semi-diurnal amplitudes of exceeding 5 K at 90-100 km height [4]. Gravity waves are also present there, revealing itself in the vertical distribution of the O_2 emission [5]. The layer of the O_2 emission is centered at 97 ± 3 km, with half width of the emitting layer 8 ± 3 km (VIRTIS-M, limb measurements [2]).

Results and discussion:

Maps of airglow were obtained in the coordinates "local time – latitude" for individual data cubes as well as the global map averaged over 718 orbits. Individual maps of airglow show highly variable character of the O_2 nightglow distribution. Maximum emission in equatorial region may be observed in the local time interval LT= 20 h ÷ 4 h. Several examples of the oxygen emission rate maps are shown in Figure 1.

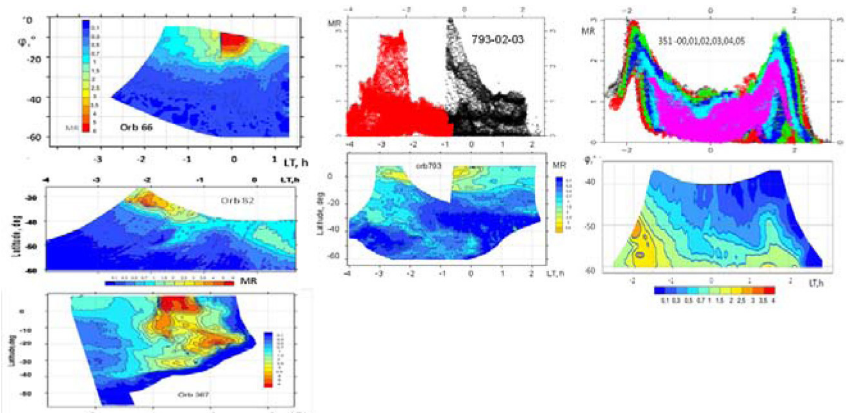

a b c

fig.1. Examples of maps of the O_2 nightglow emission: (**a**) upper panel: orbit 66, maximum emission at midnight indicates the SS-AS flow, which converges in the antisolar point; middle panel: orbit 82, maximum emission is around 22 h (-2h) before midnight; lower panel: orbit 367 – maximum emission is between 1 - 2h in the morning;
(**b**) orbit 793, upper panel: emission rate vs. local time diagram for two data cubes: 02 (LT= -4 ÷ -0.5 h) -black points and 03 (red points); lower panel: map of emission. The measurements are absent between 22(-2) h and 23 (-1) h, however one may see that maximum emission is shifted from midnight to morning site;
(**c**) orbit 351, same as (b), upper panel all – data cubes 00-05 are used (black, red, green, blue, cyan, magenta points respectively). Two symmetric maxima of oxygen emission are seen at 2h before and after midnight (higher intensity peak is before midnight). Lower panel: map of emission.

One may see (Fig 1) that the oxygen emission distribution indicates that the circulation at the nightglow level is much more complex than SS-AS or RZS, or interaction between them. In the case of SS-AS flow the convergence should be observed at antisolar point (as example in Figure 1a, orbit 66). In the case of the interaction of flows, the area of convergence would be shifted from midnight to the morning side. It is really observed in some cases (f.e. orbit 367). Yet in many other cases the maximum of oxygen emission is observed before midnight (orbit 82) or two maxima symmetrically located at both sides of midnight (orbit 351).

In Fig 2 the global map of the oxygen nightglow emission, averaged over 718 orbits, is shown. The most intense emission is observed at low latitudes, around midnight, φ = 20N - 20S, LT=22h - 3h, with no local maximum at the antisolar point. At the middle southern latitudes the asymmetry in local time distribution of the airglow emission rate is observed being higher before midnight at all latitudes.

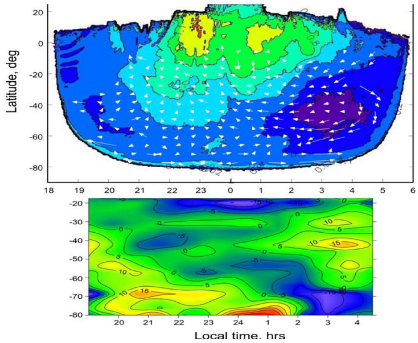

fig. 2. Top: global map of the O_2 emission intensity (MR) overlapped by vectors of horizontal wind speed (arrows). Bottom: the horizontal divergence map expressed in 10^{-6} s^{-1}

Obtained global map differs significantly from those published earlier [5, 6], where it was stated that global circulation at mesopause layer presents SS-AS flow. Actually, as we show, the situation is much more complex. Indeed, SS-AS circulation is important at transition altitudes, however it may be also a superposition of SS-AS, ZRS, tides, gravity waves etc. Input of these components is highly variable in time.

Wind speed map (arrows in Fig. 2, top panel) was calculated for practically the same set of orbits as the global map of the airglow intensity. Highest horizontal wind is found at the morning terminator. If we deal with superposition of SS-AS and ZRS, highest horizontal wind should be observed at evening one [3]); the minimum speed of horizontal wind is observed between 22 – 23 h, as well as the change of direction of horizontal wind, indicating the convergence of the flow.

The horizontal divergence was calculated from the “latitude - local time” wind field. In spherical coordinates the two-dimensional divergence defines by equation:

$$\nabla \bullet \vec{V} = \frac{1}{R\cos\varphi}\frac{\partial u}{\partial\theta} + \frac{1}{R}\frac{\partial v}{\partial\varphi} - \frac{v\tan\varphi}{R}$$

where V = (u, v) is the wind field, φ and θ are latitude and longitude, and R=6150 km is the Venus radius at the O_2 airglow altitude.

Horizontal divergence map reveals the areas of divergence and convergence of the flow: high positive values of divergence correspond to the areas of minimum intensity of the airglow, and vice versa, negative values (meaning a convergence) coincide with the maxima intensity of airglow. Maximal wind speed, observed at the morning side, corresponds to the minimum intensity in the global map.

Wind velocity field and global airglow map were obtained independently, so the observed correlation, mentioned above are real being a result of the existing interconnections between different physical processes in the transition region. The result is statistically meaningful because it is based on analysis of 718 orbit’ data (it was taken only non-noisy data, obtained with exposure > 3 s). To understand the mechanism, which explain the observation is a goal of future work.

Acknowledgements: This work is suppoted partially by the Russian Government grant to MIPT for the ISPAVR laboratory and the Program 22 of Presidium RAS

References: [1] Piccioni, G., P. Drossart , et al. (2009), Eur. Space Agency Spec. Publ., ESA SP-1295, [2] Shakun, A., L.Zasova, G.Piccioni, et al. (2010), Cosmic Research, 48, 3. [3] Schubert, G., S. W. Bougher, A. D. Covey, et al. (2007), Geophys.Monogr. Ser., vol. 176, 121-138. [4] Zasova, L.,I. Khatuntsev, Ignatiev N. et al. (2007), Planet. Space Sci., 55, 1712– 1728, doi:10.1016/j.pss.2007.01.011 [5] Piccioni, G., L. Zasova, A. Migliorini, et al. (2009), J. Geophys. Res., 114, E00B38, doi:10.1029/2008JE003133. [6] Gérard, J. C., A. Saglam, G. Piccioni, etal. (2008), Geophys.Res. Lett., 35, L02207, doi:10.1029/2007GL032021

MODELING OF VIRTIS/VEX $O_2(A^1\Delta_G)$ NIGHTGLOW PROFILES AFFECTED BY GRAVITY WAVES ACTION.

F. Altieri[1], A. Shakun[2,3], L. Zasova[2,3], A. Migliorini[1], G. Piccioni[1], G. Bellucci[1],
[1]IAPS, Istituto di Astrofisica e Planetologia Spaziali, INAF, Rome, Italy; [2]IKI, Space Research Institute, Russian Academy of Sciences, Moscow, Russia, [3]Moscow Institute of Physics and Technology, Dolgoprudnyy, Russia.
Contact: francesca.altieri@iaps.inaf.it

Introduction: On Venus' nightside, $O_2(a^1\Delta_g)$ molecules arise by the three-body reaction O + O +M → $O_2(a^1\Delta_g)$ + M, then they decay at the fundamental state $O_2(X^3\Sigma^-_g)$ by emitting most of the photons at 1.27 μm or through quenching $O_2(a^1\Delta_g)$ +M → $O_2(X^3\Sigma^-_g)$ + M. The 1.27 μm emission falls inside the VIRTIS/VEX

spectral range and it has been studied through both nadir and limb data [1]. Volume emission rate profiles reveal usually a peak at 97~ km, but a double peak frequently appears as well, at 103-105 km [1]. The double peak structures originate by the propagation of GWs, common features of planetary atmospheres that play a crucial role in defining circulation and structure of the mesosphere. By inducing vertical fluctuations on both temperature and density profiles, GWs can also affect the airglow intensities. In this study we propose to apply a well-known theory developed for studying terrestrial airglows [2] to model the Venus GWs responsible for the fluctuations observed in the VIRTIS $O_2(a^1\Delta_g)$ nightglow data.

VIRTIS instrument and Data Set: VIRTIS (Visible and InfraRed Thermal Imaging Spectrometer) is the imaging spectrometer covering the 0.27-5.1 μm range on board the ESA mission Venus Express (VEX). It includes two spectrometers: VIRTIS-M, a mapping spectrometer with medium spectral resolution, and VIRTIS-H, an echelle spectrometer with higher spectral resolution than VIRTIS–M but no imaging capability. VIRTIS-M consists of two channels: a visible channel (0.27-1 μm range) and an infrared channel (1-5.1 μm range). In this study the data of the VIRTIS-M infrared channel (spectral sampling =10 nm, IFOV = 0.250 mrad) that show $O_2(a^1\Delta_g)$ nightglow profiles double-peak shaped are considered.

Modeling: Assuming monochromatic GWs propagating in an isothermal and windless atmosphere, the relative density perturbation introduced in the initial profiles by the wave action can be derived as described in [2]. For the initial (unperturbed) profiles, we considered a Gaussian profile for the $O_2(a^1\Delta_g)$ density distribution, and CO_2 density and temperature profiles as derived from the SPICAV data [3,4]. The atomic oxygen density profile has been modelled following the method in [3]. An exemplum of the fluctuation introduced in the initial O_2(a1Δg) nightglow volume emission rate profile by GWs propagation is shown in the Figure 1 (vertical wavelength = 7 km, and GW amplitude at 100 km = 20%). This confirms the high variability induced by wave propagation in the $O_2(a^1\Delta_g)$ profiles, as observed in the VIRTIS data.

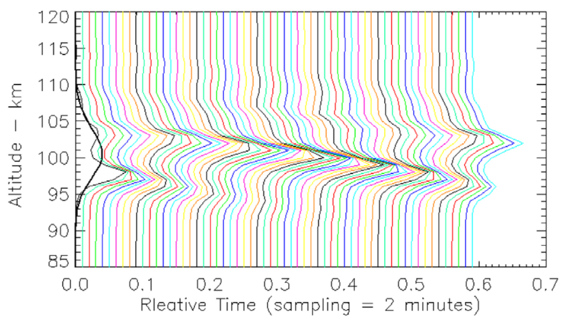

Fig.1. $O_2(a^1\Delta_g)$ volume emission rates perturbed by GWs (thin lines). Black thick line: initial profile

References: [1] Piccioni, G., L. Zasova, A. Migliorini, P. Drossart, A. Shakun, A. Garcıa Munoz, F. P. Mills, and A. Cardesin-Moinelo, Near-IR oxygen nightglow observed by VIRTIS in the Venus upper atmosphere, J. Geophys. Res., 114, E00B38, 2009. [2] Swenson, G. R., C. S. Gardner, Analytical models for the responses of the mesospheric OH* and Na layers to atmospheric gravity waves, J. Geophys. Res., 103, D6, 6271-6294, 1998. [3] Gerard, A. S., G. Piccioni, P. Drossart, F. Montmessin, J-L. Bertaux, Atomic oxygen distribution in the Venus mesosphere from observations of O2 infrared airglow by VIRTIS-Venus Express, Icarus, 199, 264–272l. 2009. [4] Bertaux, J-L., Vandaele, A.C., Korablev, O., Villard, E., Fedorova, A., Fussen, D., Quemerais, E., Belyaev, D., A warm layer in Venus' cryosphere and high altitude measurements of HF, HCl, H2O and HDO, Nature 450, 646 – 649, 2007.

POSSIBLE LIFE FOUND AT A WRONG PLACE

Leonid Ksanfomality,
Space research institute of the RAS. Profsoyuznaya str. 84/32, Moscow 117997, Russia. Contact: ksanf@rssi.ru

The position of the hypothetical habitability zone in extrasolar planetary system is considered by many authors. Approximately 1/4 of exoplanets orbit their stars at very low orbits, which leads to high temperatures of their surface (if any), up to 800 K or more. Some of them should have the physical conditions close to those of Venus. Is there any possibility that the life forms can exist at quite different environment than “normal”, Earth-like physical conditions?

The natural laboratory for studies of this type could be the planet Venus, with its dense, hot (735 K) oxygenless CO2 - atmosphere and high, 9.2 MPa, pressure at the surface. It should be recalled that the only existing data of actual close in observations of Venus' surface are the results of a series of missions of the Soviet VENERA landers which took place the 1970s and 80s, working in the atmosphere and on the surface of Venus. A re-exemination of images of venusian surface obtained from the VENERA landers has been undertaken with a view to detect any possible signs of life under the specific conditions on Venus.

This speculative identification rests on two characteristics of these features: (a) their temporal appearance and behavior (present, than absent in subsequent images, or absent and then present on images of the same area; or changing appearances) and (b) their somewhat suggestive morphology. The re-exemination has identified previously unreported features that may correspond to hypothetical life forms on Venus' surface. Two of them, ‘scorpion” (1) and “hespera” (2) are shown here.

Analysis and comparison of the contents the sequence of panoramas of the venusian surface obtained in the course of the soviet TV-experiments on the VENERA landers (1975-82), allowed the author to detect the appearance or disappearance of some details displayed on panoramas obtained. Following the change in their appearance on the sequence of images allowed a suggestion that such changes may be related to the possible habitability of the planet. Some of the objects found were described in (Ksanfomality, 2012). There are also found and listed in the report images of objects with special morphology resembling the shape of some terrestrial large insects. In the absence of new landing missions to Venus, the same study was carried out on the other remaining panoramas. There is a reason to believe that in many panoramas another special class of objects has been found, which will be shown in the report. The report presents the results obtained and analyzes signs suggesting reality of the registration of these features.

The in-situ surface observations were available from the Soviet VENERA series mission from the 1970s and 80s. No other results of this kind were obtained since.

References: *Ksanfomality L. V.* Venus as a Natural Laboratory for Search of Life in High Temperature Conditions: Events on the Planet Venus on March 1, 1982. // Solar System Research, 2012, Vol. 46, No. 1, pp. 41–53.
Ksanfomality L. V. Possible Detection of Life on the Planet Venus // Doklady Akademii Nauk, 2012, Vol. 446, No. 1, pp. 42–47. **DOI:** 10.1134/S1028335812090

RETRIEVAL OF SURFACE PROPERTIES IN THE NIR NIGHTSIDE WINDOWS OF VENUS

Gabriele Arnold[1], Rainer Haus[2], David Kappel[1],
[1]Institut of Planetary Research, DLR, Rutherfordstr.2, 12489 Berlin, Germany; [2]Institut für Planetologie, WWU, 48129 Münster, Germany

Abstract

Based on a radiative transfer simulation model as well as new multi-window retrieval techniques, deep atmosphere and surface parameters can be retrieved from VIRTIS-M-IR data in the NIR nightside spectral transparency windows of Venus. A detailed error analysis for surface emissivity retrieval demonstrates the necessity for a new multi-spectrum retrieval technique.

Local emissivity anomalies and differences in highland and lowland regions of Venus have been identified. One example (Idunn Mons) is discussed in the present paper.

Introduction

Retrieval of Venus' surface emissivity is a key challenge to study surface composition, weathering processes, and as a consequence crucial aspects of planetary evolution, geology, and climate of Venus. The Visible and Infrared Thermal Imaging Spectrometer (VIRTIS) aboard ESA's spaceprobe Venus Express records spectrally, spatially, and temporally resolved data of the atmosphere and surface in the NIR nightside spectral transparency windows of Venus [1, 2]. The infrared mapping channel VIRTIS-M-IR yields a spectrum of 432 bands covering the range between 1.0 μm and 5.2 μm at 256 spatial pixels for each exposure. Hundreds of successive exposures at a time yield spectrally resolved two-dimensional images of targets on Venus, providing an excellent data base for surface emissivity retrieval [3, 4].

Methodical approaches

In order to extract surface parameters from the measurements, a Radiative Transfer Simulation Model (RTM) including special features of Venus' deep atmosphere like continuum absorption was developed and applied to the data [5]. The RTM simulates observed radiances in dependence on atmospheric and surface parameters on a line-by-line basis. It incorporates absorption, emission, and multiple scattering by gaseous and particulate constituents.

The Multi-Window Retrieval Technique (MWT) makes simultaneous use of information from different atmospheric windows of an individual spectrum. It iteratively optimizes several atmospheric and surface parameters until the simulated spectrum well fits the measurement for all utilized spectral windows. The determined parameters are interpreted as the state of atmosphere and surface that led to the observed spectrum. However, this is mathematically an ill-posed problem, since different state vectors can parameterize the same spectrum equally well. The usual approach to improve the situation is the regularization of the retrieval by incorporating *a priori* mean values and standard deviations of the parameters to be retrieved. This way, the probability to determine unlikely values for the parameters is decreased.

Due to a certain continuity of atmospheric composition, contiguous measurements are not likely to originate from completely un-related single-spectrum state vectors. These spatial and temporal correlations between the state vectors are always present, but usually neglected in retrieval algorithms. The new Multi-Spectrum Retrieval Technique (MST) [3] allows for additional incorporation of physically reasonable spatial-temporal *a priori* information on atmospheric parameters. Since the context of adjacent measurements is taken into account now, the reliability of retrieved single-spectrum state vectors is improved, and the probability to determine unlikely spatial-temporal distributions for the state vectors is decreased. Also, MST allows for the determination of parameters common to a selection of several spectra. Neglecting geologic activity, surface emissivity for a pixel on Venus' surface can be retrieved as parameter that is common to several measurements repeatedly covering that pixel. This considerably enhances the reliability of retrieved emissivity.

Results

The RTM-MWT results show an excellent agreement of simulated and measured spectra in most cases as it is illustrated in Figure 1.

A detailed retrieval error analysis using RTM-MWT reveals that surface emissivity is particularly difficult to determine from VIRTIS-M-IR spectra [6]. For instance, an uncertainty in the abundance of cloud mode 1 particles of 50% can lead to an error of 20% in retrieved emissivity, depending on the utilized spectral ranges for retrieval. Similarly, 1 km uncertainty in bottoms / tops of the cloud mode altitude profiles can lead to 5% emissivity error, 6% uncertainty in H_2SO_4 concentration to 9%, 100 m in surface elevation to 8%, and 1 K in deep atmospheric temperature profile at 0 km to 13% emissivity error (Figure 2). Therefore, MST is utilized for a more reliable retrieval of a surface emissivity map.

One example for MST outputs is visualized in Figure 3. It shows scatterplots of retrieved 1.02 µm surface emissivity in the region of Idunn Mons as a function of surface elevation when emissivity is considered as common parameter or not. The scatter of the results is much higher in the latter case, i.e. the treatment of emissivity as common parameter significantly improves the retrieval reliability. 1570 spectra were used in total, corresponding to 99 surface bins with at least 15 repetitions for each bin.

The shield volcano Idunn Mons represents an isolated emissivity anomaly on Venus' surface. The 1.02 µm emissivity differs between Idunn hills and surrounding lowlands. This can be the result of recent volcanic activity [7] or may result from different material, and/or variable weathering conditions.

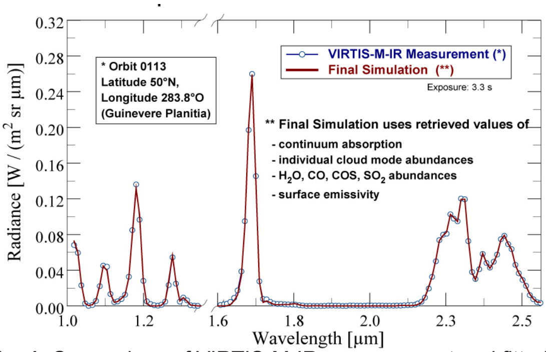

fig. 1. Comparison of VIRTIS-M-IR measurement and fitted simulation.

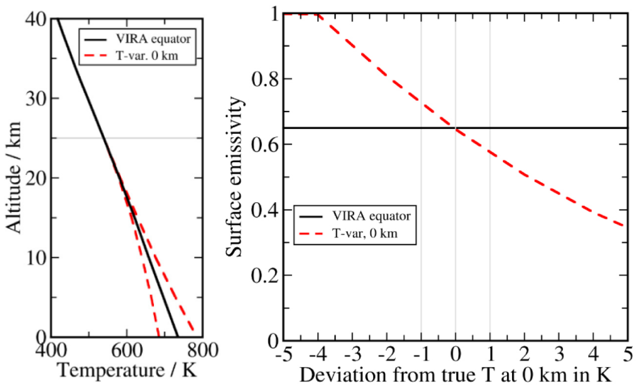

fig. 2. Example for retrieved surface emissivity as a function of deep atmospheric temperature profile. *Left:* Exaggerated perturbations around equatorial VIRA temperature profile. *Right:* Retrieved 1.10 µm emissivity for unperturbed and perturbed temperature profiles. Equatorial VIRA is the true temperature profile, 0.65 is the true emissivity of the analyzed synthetic spectrum.

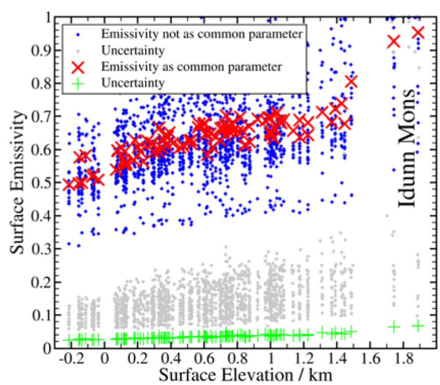

fig. 3. Scatterplots of retrieved 1.02 µm emissivity as a function of surface elevation near Idunn Mons.

References

[1] Drossart P. et al., Planet. Space Sci. 55(12), 1653-1672, 2007.
[2] Piccioni, G. et al., ESA Spec. Publ. SP-1295, 1–27, European Space Agency, Paris, 2007.
[3] Kappel et al., Adv. Space Res. 50, 228-255, 2012.
[4] Arnold G. et al., J. Geophys. Res. 113 (E5), E00B10, 2008.
[5] Haus R. and G. Arnold, Planet. Space. Sci. 58 (12), 1578-1598, 2010.
[6] Kappel, D. et al., COSPAR, B0.8-0008-12, 2012.
[7] Smrekar S. et al., Science 328, 605-608, 2010.

EVOLUTION OF VOLCANISM ON VENUS.

M.A. Ivanov[1], J.W. Head[2],
[1]Vernadsky Inst., Moscow; [2] Brown Univ., USA. Contact: mikhail_ivanov@brown.edu

Introduction: Manifestations of major internal processes, such as volcanism, are directly related to the loss of internal heat of the planets, which governs the geological histories of the planets to a large extent. This is especially true for Venus where erosional/depositional processes are strongly inhibited [1,2] and impact craters are relatively rare [3,4]. The nature of volcanic landforms revealed on Venus permit the tracing of the history of volcanism, which plays a key role in understanding of the geological evolution of the planet. A recently compiled global geological map of Venus [5] portrays the spatial and temporal distribution of specific units interpreted to be of volcanic origin and permits global assessment of the history and styles of volcanic activity and helps to constrain their relationship to the major episodes of the geological evolution of Venus.

Main volcanic units of Venus: Although the surface of Venus displays a variety of volcanic landforms [6-8], three major volcanic material units are most important: shield plains, psh; regional plains, rp; and lobate plains, pl (Fig. 1). Together they comprise ~96% of all volcanically dominated units and cover ~70% of the surface of Venus. *Shield plains* (~26% of the total surface of the major volcanic units, ~17% of the surface of Venus): Abundant small (2-10 km across) shield-like features (volcanic edifices [6,7,9]) characterize shield plains. In many cases the shields occur close to each other and form clusters. Shield plains are only mildly deformed by wrinkle ridges and sparse fractures/graben. *Regional plains* (both the lower and upper subunits, ~61% of the three major volcanic units, ~40% of the surface of Venus) are composed of morphologically smooth, homogeneous plains the sources of which are not discernible. Networks of wrinkle ridges deform the surface of the plains [10]. *Lobate plains* (~13% of the three major volcanic units, ~8% of the surface of Venus): The surface of lobate plains is occasionally disturbed by graben of rift zones. The most characteristic features of lobate plains are numerous bright and dark flow-like features. The flows can be as long as several hundred kilometers and tens of kilometers wide. The plains are usually associated with the large dome-shaped rises (e.g., Beta, Eistla, Atla Regiones, etc.).

Age relationships among the main volcanic units: In almost all regions of Venus where the main volcanic units occur together they display the same sequence (Fig. 2). Shield plains predate regional plains (exceptions are rare and were mapped as a specific unit of shield clusters) and wrinkle ridges deform both units (Fig. 2). Lobate plains superpose the surface of shield and regional plains (Fig. 2), and embay wrinkle ridges. These relationships strongly suggest that at the global scale shield plains represent the oldest volcanic unit, regional plains are at the middle stratigraphic position, and lobate plains are the youngest. Due to the significant burial of shield plains by regional plains, the abundance of shield plains is underestimated.

Topographic distribution of main volcanic units: Shield plains often occur in spatial association with large and small exposures of older tectonized units (e.g., tessera) that form either local or regional highs, whereas the largest occurrences of regional plains tend to be associated with regional lowlands (Fig. 1). As a result, the hypsogram of shield plains is shifted to higher elevations relative to regional plains (Fig. 3). Lobate plains are preferentially associated with regional dome-shaped and rifted rises. Due to this, the hypsogram of lobate plains is strongly shifted to higher elevations (Fig. 3).

Discussion and conclusions: One of the most obvious relationships of the main volcanic units of Venus is that they embay and bury most of strongly tectonized units/structures (black areas in Fig. 1, see also Fig. 2). These relationships are observed everywhere on Venus [5,11-13] and indicate that a tectonically dominated regime near the beginning of the observable geological record underwent a change to a volcanically-dominated regime that characterizes the geological history of Venus since the time of the emplacement of shield plains. The minimal (exposed) area of the older tectonized units comprises ~21% of the total surface. Formation of these units/structures was probably related to specific patterns of mantle convection and the change from the tectonic- to volcanic dominated regimes may indicate diminishing of mantle convective vigor and enhancement of generation of melts. Late tectonic activity, which occurred during emplacement of lobate plains (rift zones, white zones in Fig. 1), has affected only a small fraction of the surface of Venus (~5%).

Distinctly different morphologies characterize the main volcanic units (Fig. 2). Small volcanic constructs of psh are consistent with globally distributed volcanism (multiple eruptions from small, shallow, and broadly distributed sources [e.g., 6,14]). Regional plains form very broad and morphologically homogenous surfaces where the sources are not visible at the resolution of Magellan SAR. These characteristics are consistent with voluminous volcanic activity resulting in lava flooding [6,15-17] of a significant portion of the surface of Venus. The lack of sources, however, suggests that individual volcanic eruptions during formation of regional plains did not last long and were not associated with persistent magma supply (flood volcanism). In contrast to regional plains, numerous and very distinctive lava flows characterize pl. Typically, the flows are associated with very prominent but isolated volcanic centers such as large volcanoes [e.g., 8]. The abundance of lava flows and association with distinctive centers of volcanism strongly suggest that lobate plains formed due to long-lived, persistent, and likely deep-seated magmatic centers.

These characteristics of the main volcanic units have been documented in practically all regions of Venus [e.g., 5,18-21]. Thus, specific types of volcanism that were responsible for formation of the units had a global-scale nature. The consistent age relationships of the main volcanic units (from psh through rp to pl) suggest that different volcanic styles have succeeded each other sequentially at a global scale during the later-stage (post tessera) volcanically dominated regime.

The stratigraphically older shield plains often occur in the vicinity of the elevated tectonized units and embay them. This means that these units and associated several dome-shaped rises and rift zones that characterize less than 10% of the surface of the planet.

The characteristics of the main volcanic units and their topographic highs formed before emplacement of psh. Shield plains extend from the elevated terrains along the regional slopes toward the lowlands (basins) where the plains are embayed and buried by regional plains. In places, however, the stratigraphic windows of shield plains occur near the bottom of the basins. Regional plains are preferentially concentrated within the basins and are less abundant at their elevated edges where shield plains prevail. This correlation of psh and rp with the long-wavelength topography suggests that the regional- to global-scale topographic pattern controlled the spatial distribution of shield plains to a lesser degree but was an important factor in distribution of regional plains. This suggests that the basins predated emplacement of regional plains and served as sites of preferential accumulation of their material. Thus, the most important features of the long-wavelength topography of Venus, such as the high-standing tessera plateaus and the broad basins, were largely established prior to the emplacement of regional plains. Since that time, the major changes in the global-scale topographic pattern were related to evolution of relationships with tectonized terrains and the global-scale topographic pattern suggest that (1) the major features of the surface of Venus (most of tectonic terrains, the most widespread volcanic units, the principal features of the long-wavelength topography) were established early on in the geological history of the planet and (2) the types and intensity of internal activity on Venus were strongly time-dependent.

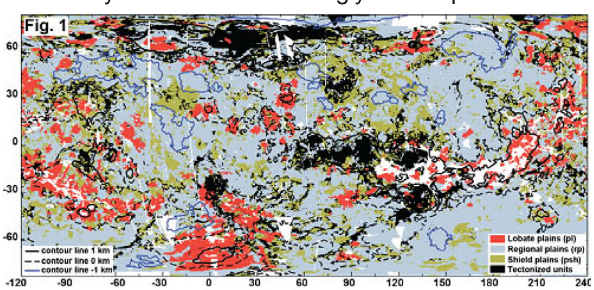

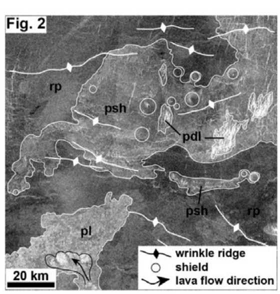

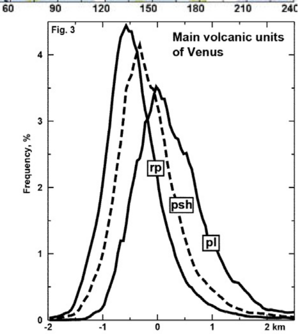

References: l., JGR, 97, 13303, 1992, 3) Herrick et al., in: Venus II, 1015, 1997, 4) Schaber et al., USGS OFR 98-104, 1998, 5) Ivanov and Head, PSS, 59, 1559, 2011, 6) Head et al., JGR, 97, 13153, 1992, 7) Guest et al., JGR, 97, 15949, 1992, 8) Crumple and Aubele, in: Encyclopedia of Volcanoes, 727, 2000, 9) Aubele and Slyuta, EMP, 50/51, 493, 1990, 10) Bilotti and Suppe, Icarus, 139, 137, 1999, 11) Basilevsky and Head, EMP, 66, 285, 1995a, 12) Basilevsky and Head, PSS, 43, 1523, 1995b, 13) Ivanov and Head, JGR, 106, 17515, 2001, 14) Greeley, JGR, 87, 2795, 1982, 15) Senske et al., JGR, 97, 13395, 1992, 16) Renne et al., Science, 269, 1413, 1995, 17) Johnston and Thorkelson, EPSL, 175, 247, 2000, 18) Aubele, LPSC-25, 45, 1994, 19) Aubele, LPSC-26, 59, 1995, 20) Bridges and McGill, USGS Map I-2747, 2002, 21) Ivanov and Head, USGS Map I-2920, 2006.

ANALYSIS OF THE IMAGES OF THE VENUS SURFACE TAKEN BY THE VENUS MONITORING CAMERA, VENUS EXPRESS

E.V. Shalygin[a], A. T. Basilevsky[a,b], W. J. Markiewicz[a], D.V. Titov[c,a], W.J. F. Scholten[d], Th. Roatsch[d], M.A. Kreslavsky[e], L.V. Moroz[f,d], N.I. Ignatiev[b,g], B. Fiethe[h], B. Osterloh[h], H. Michalik[h], N.L. Mironov[b], J.W. Head[i], *[a]Max-Planck-Institut für Sonnensystemforschung, Katlenburg-Lindau, Germany; [b]Vernadsky Institute, 119991 Moscow, Russia; [c]ESA-ESTEC, SRE-SM, Noordwijk H, The Netherlands; [d]Institut für Planetenforschung, DLR, Berlin, Germany; [e]University of California, Santa Cruz, CA, USA; [f]Institut für Planetologie, Westfalische Wilhelms-Universität, Münster, Germany; [g]Space Research Institute, Moscow, Russia; [h]IDA, Technische Universität, Braunschweig, Germany; [i]Brown University, Providence, RI, USA.. Contact: Eugene.Shalygin@gmail.com*

Introduction: Here we report results of several stages of our work on analysis of the night-time near-infrared (NIR) thermal emission images of the Venus surface obtained with the 1-micron channel of the Venus Monitoring Camera (VMC) onboard Venus Express (VEX) (Baines et al., 2006; Markiewicz et al., 2007, 2008). We consider results obtained for three areas of Venus: 1) Chimona-mana tessera massif in the SW part of Beta-Phoebe region; 2) Tuulikki Mons volcano, also in Beta-Phoebe region; and 3) Maat Mons volcano in Atla Regio.

1) Chimona-mana tessera massif: In this part we consider if tessera terrain has a different NIR emissivity and thus possibly different mineralogic composition in comparison to the surrounding basaltic plains. Maps of surface emissivity can be obtained by fitting the VMC observations with model images. The latter were obtained by convolving the surface brightness distribution based on the Magellan surface topography and the vertical temperature lapse in the atmosphere with the atmosphere blurring function (see details in Basilevsky et al., 2012). Our analysis shows that 1-micron emissivity of tessera surface material is 15–35% lower than that of relatively fresh putative basaltic lavas of the plains (Figure 1). This is consistent with hypothesis that the tessera material is not basaltic and maybe felsic. This is also in agreement with the results of analyses of VEX VIRTIS and Galileo NIMS data (Helbert et al., 2008; Mueller et al., 2008; Hashimoto et al., 2008 and Gilmore et al., 2011) and with early suggestions of Nikolaeva et al. (1992). If the felsic nature of Venusian tesserae will be confirmed in further studies this may have important implications for geochemical environments in early history of Venus allowing formation of large amounts of granitic rocks and thus indirectly supporting a hypothesis of water-rich early Venus (e.g. Kasting et al., 1984; Kasting, 1988; Grinspoon and Bullock, 2003). We have also found that the surface materials of plains in this study area are very variegated in their inferred 1-micron emissivity, probably reflecting variability in degree of their chemical weathering.

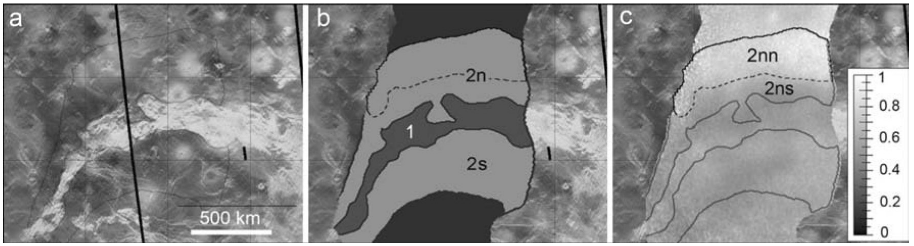

fig. 1. a) SAR image of the study area; b) outlines of VMC image 0470 with simplified geologic map showing basic units under study: 1 – Chimon-mana Tessera, 2 – adjacent plains with units 2n (including subunits 2nn and 2ns) and 2s; c) map of retrieved emissivity.

2) Tuulikki Mons volcano: Studying the VMC 1-micron data from the Tuulikki Mons volcano and the surrounding plains, also in Beta-Phoebe region, we found a possible decrease of the retrieved emissivity at the top of the volcano (Figure 2a,b). This may be due to different, possibly more felsic, composition of volcanic products on the volcano summit. This suggestion is further supported by the observation of a feature resembling a steep-sided dome on the volcano summit (Figure 2c,d) (see details in Basilevsky et al., 2012a,b). Steep-sided domes on Venus are considered to be formed by eruptions of viscous lavas geochemically more evolved than basalts (Pavri et al., 1992) although other suggestions on their nature have also been published (Pavri et al., 1992; Bridges et al., 1995; Fink & Griiffits, 1998). More felsic composition of the Tuulikki summit material could be explained by differentiation within the magma chamber resulting in more evolved composition of the late portions of the lavas. On Earth an intrachamber differentiation from basaltic to more felsic compositions is typical for subduction zones (e.g., Perfit & Davidson, 2000; Rogers & Hawkesworth, 2000) (Figure 2e) and also occurs on ocean islands related to hot-spot magmatism (Iceland, Azores, Hawaii etc.) (Figure 2f). In the latter case felsic volcanics are usually more alkaline and shifted toward trachytic compositions (http://georoc.mpch-mainz.gwdg.de/ georoc).

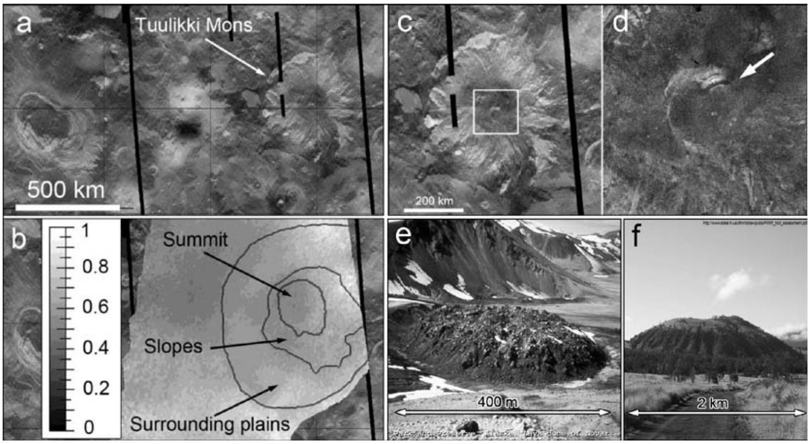

fig. 2. a) Magellan SAR image of the Tuulikki Mons area; b) the map of 1-micron emissivity of the Tuulikki summit, slopes and the surrounding plains with the legend bar of 1-μm emissivity. c) morphology of Tuulikki Mons volcano as seen on Magellan SAR image; d) Magellan image of the summit area (white box in Figure 2c); arrow shows the feature resembling a steep-sided dome; e) Novarupta rhyolite dome, Alaska http://pubs.usgs.gov/dds-40/images/JPG/;arge_screen/fig15.jpg; f) Trachyte dome Puu Waawaa on Hualalai volcano, Big Island, Hawaii http://www.soest.hawaii.edu/GG/HCVhualalai.html.

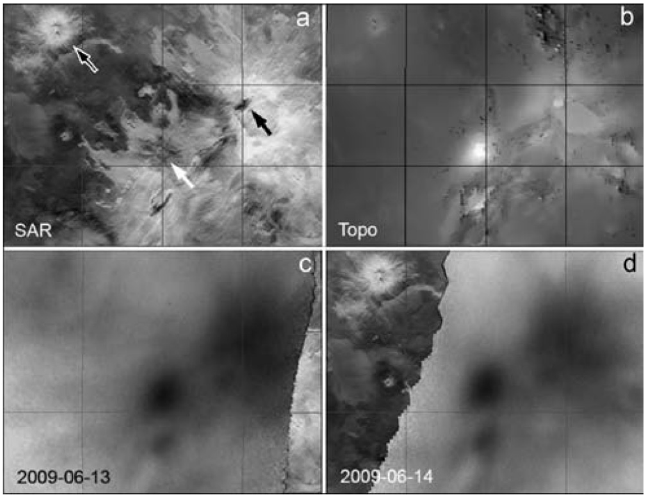

fig. 3. a) Magellan SAR image of the area with three volcanoes: Maat Mons (white arrow), Sapas Mons (black-and-white arrow) and Ozza Mons (black arrow), the coordinate grid is 5 x 5 degrees; b) Image showing topography of the study area (brighter shades denote higher elevations); c) VMC image of the area taken on June 13, 2009 superposed on SAR image; d) VMC image of the area taken on June 14, 2009 superposed on SAR image.

3) Maat Mons volcano and search for ongoing volcanism: Here we consider various aspects of the search of the ongoing volcanic activity from observations taken by the VMC 1-micron channel. Our emphasis is the area of Maat Mons volcano and its vicinities which based on analysis of the Magellan SAR images show evidence of geologically very young volcanism (e.g., Basilevsky, 1993). Analysis of VMC images taken in 12 observation sessions during the time period from 31 Oct 2007 to 15 Jun 2009 did not reveal any suspicious high-emission spots which could be interpreted as signatures of the ongoing volcanic eruptions (Figure 3). We compared these time sequences of observations with the history of eruptions of volcano Mauna Loa, Hawaii, in the 20th century. This comparison shows that if Maat Mons volcano had the eruption history similar to that of Mauna Loa, the probability to observe an eruption in these VMC observation sequences would be about 8%, meaning that the absence of detection does not mean that Maat is not active in the present epoch. These estimates do not consider the effect of absorption and blurring of the thermal radiation coming from Venus surface by the planet atmosphere and clouds, which decrease detectability of thermal signature of fresh lavas. To assess the role of this effect we simulated near-infrared images of the study area with artificially added lava flows having surface temperature 1000 K and different areas. These simulations showed that 1km^2 lava flows should be marginally seen by VMC. Increase of the lava surface area to 2–3 km^2 makes them visible on the plains and increase of the area to 4–5 km^2 makes them visible even in deep rift zones. Elongation of lava fields in general increases these values. However, for typical length to width ratios of about 10 the decrease of contrast is not significant, but becomes significant for extremely long fields with aspect ratio more than 1000 (Figure 4).

fig. 4. a) SAR image of Tuulikki Mons volcano; b) lava flows not covered by the younger ones; c) distribution of the surface area of selected lava flows on Tuulikki Mons, lines mark level of

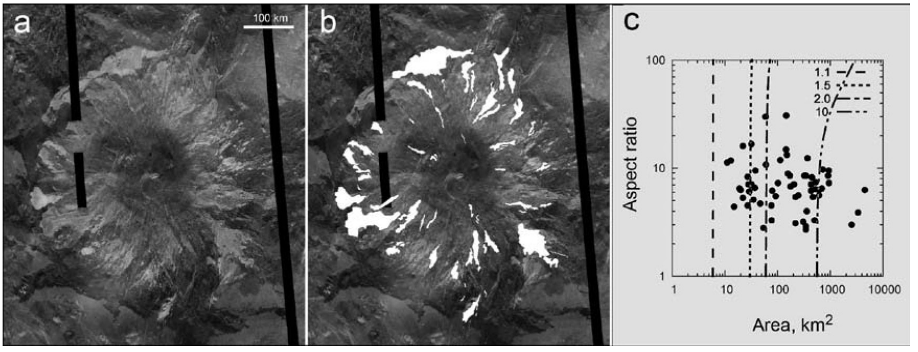

visibility that produce given contrast by lava fields with temperature 1000 K.

Typical individual lava flows on Mauna Loa are a few km. large, however, they often have been formed during weeks to months and the instantaneous size of the hot flow surface was usually much smaller. Thus the detection probability is significantly lower than 8%., but probably is far from negligible. Our consideration suggests that further search of Maat Mons and other areas including young rift zones makes sense and should be continued. More effective search could be done if observations simultaneously cover most part of the night side of Venus for relatively long time of continuous observations (years).

Conclusions: The above considerations shows that analysis of the VMC 1-micron channel data led to several important results. 1) We found that surface emissivity of Chimona-mana tessera is lower than that of neighboring presumably basaltic plains suggesting nonbasaltic, probably more differentiated, composition of tessera material. This agrees with the results taken by the VEX VIRTIS spectrometer and may have serious implications on the geologic history of Venus. 2) The summit part of Tuulikki Mons volcano was found to have the 1-micron emissivity lower than that of slopes of this volcano whose morphology suggests its essentially basaltic nature. The lower 1-micron emissivity of the volcano summit may suggest its nonbasaltic, probably felsic composition, a conclusion supported by the presence of a steep-sided dome. This may suggest that differentiation of basaltic magma in magma chambers of some Venusian volcanoes could produce non-basaltic compositions as it happens in some terrestrial volcanoes. 3) Systematic search for the ongoing volcanic activity in the vicinity of Maat Mons volcano did not lead to finding the shining spots suggesting the present eruptions. But application of the VMC observations of Maat Mons to the case of terrestrial Mauna Loa volcano shows that the probability to observe the ongoing volcanic eruption is less than 8%. This means that the fact that the ongoing volcanic eruptions on Venus had not been observed yet, does not mean that at present time this planet is volcanically not active.

References: [1] Baines et al., Planet. Space Sci. 2006, 54, 1263–1278. [2] Basilevsky, GRL, 1993, 20, 883–886. [3] Basilevsky et al. Icarus, 2012a, 217, 434-450. [4] Basilevsky et al., LPSC-43, 2012b, abs. 1092. [5] Bridges N., GRL, 1995, 22, 2781–2784. [6] Fink & Griffiths, JGR, 1998, 103, 527–545. [7] Georoc database: http://georoc.mpch-mainz.gwdg.de/ georoc/. [8] Gilmore et al., LPSC-42, 2011, abs. 1498. [9] Grinspoon & Bullock, Bull. Am. Astron. Soc., 2003, 35, 1007. [10] Hashimoto et al., JGR, 2008, 113, E00B24. [11] Helbert et al., GRL, 2008, L11201. [12] Kasting et al., Icarus, 1984, 57, 335-355. [13] Kasting, Icarus, 1988, 674, 472-494. [14] Markiewicz et al., Planet. Space Sci. 2007, 55, 1701–1711. [15] Markiewicz et al., In: ESA SP-1295. 2008. [16] Mueller et al., JGR, 2008, 113, E00B17. [17] Nikolaeva et al., Venus Geology, Geochemistry, Geophysics, U. Arizona Press, 1992, 129-139. [18] Pavri et al., JGR, 1992, 97, 13445–13478. [19] Perfit & Davidson, In: Encyclopedia of Volcanes, Acad. Press. 2000, 89-113. [20] Rogers & Hawkesworth, In: Encyclopedia of Volcanes, Acad. Press. 2000, 115-131.

THERMAL EVOLUTION OF AN EARLY MAGMA OCEAN IN INTERACTION WITH THE ATMOSPHERE

T. Lebrun[1], H. Massol[1], E. Chassefière[1], A. Davaille[2], E. Marcq[3], P. Sarda[1], F. Leblanc[3], G. Brandeis[4],
[1]IDES/CNRS/Univ. Paris-Sud, France; [2]FAST/CNRS Univ. Paris-Sud, France; [3]LATMOS/CNRS/Univ. of Versailles St-Quentin, France;
[4]IPGP/Sorbonne Paris Cité/CNRS, France. Contact : Thomas.lebrun@u-psud.fr

Early in terrestrial planet formation the heat of accretion, radiodecay, and latent heat due to core formation may have melted the silicate portions of the planets either wholly or partially. Also it is likely that giant impactors late in accretion created hemispheric or shallow planetary magma oceans. Thermal evolution of the magma ocean is expected to depend on the composition and structure of the atmosphere, through the greenhouse effect of CO_2 and H_2O released from the magma during its crystallization. In order to constrain the various cooling timescales of the system, and the timing of formation of the water ocean and of early tectonic plates, we developed a 1D parameterized convection model of the thermal evolution of a magma ocean that we couple with a 1D radiative-convective model of a primitive atmosphere. The coupling consists of balancing heat and volatiles fluxes at the planetary surface. We conducted a parametric study in order to investigate the influence of different processes on the magma ocean thermal evolution. We studied more particularly the influences of the initial volatile inventories, the initial depth of the magma ocean, the radiogenic heat production rate by short-lived and long-lived elements, the liquidus-solidus equation, the distance from the sun and compared the evolutions of the three telluric planets, Earth, Mars and Venus. Our results show that the presence of a convective-radiative steam atmosphere has a strong influence on the duration of the magma ocean phase and the timing of the appearance of primitive plates and formation of an ocean of water. Without atmosphere, the duration of the magma ocean phase is a few thousand years while with an atmosphere, it is typically 1 Myr. The time required for the formation of a water ocean is about 0.1 Myr for Mars, 1.5 Myr for the Earth and 10 Myr for Venus. This time would be virtually infinite for an Earth size planet located closer than 0.65 AU from the Sun. Because for Mars and Earth, these times are definitely shorter than the accretion time, more specifically the average time between major impacts (able to melt a significant fraction of the mantle), serial water oceans could have developed on Earth and Mars during accretion, making easier the loss of their atmospheres by impact erosion. On the contrary, Venus could have remained in the magma ocean stage for most of its accretion. From our present model, not taking into account the heating by small impactors and not including hydrodynamic escape, an ocean of water could have formed on Venus at the end of the accretion.

THE EFFECT OF VENUS TOPOGRAPHY ON THE DYNAMICS OF POLAR VORTEX: RESULTS FROM NON-HYDROSTATIC GENERAL CIRCULATION MODEL.

A. V. Rodin[1,2], I. V. Mingalev[3], K. G. Orlov[3],
[1]Moscow Institute of Physics and Technology, Dolgoprudny, Russia; [2] Space Research Institute, Moscow, Russia; [3]Polar Geophysical Institute, Apatity, Russia.
Contact: alexander.rodin@phystech.edu

Introduction:

Understanding of the Venus atmosphere dynamics has been substantially improved during last years, first of all due to the extraordinary dataset returned by the Venus Express spacecraft. It has been established that zonal flow, as observed at the cloud top level, reveals maximal rate in two midlatitude jets centered about 60º in each hemisphere. Numerous wave perturbations to the mean zonal flow has been detected, with most prominent harmonic having the period of 4.5 days, and sun-sinchronous component with a structure typical for diurnal thermal tide. Solar occultation profiling of CO_2 density reveals strong perturbations of the thermal profile between 90 and 120 km, consistent with adiabatic heating of the nightside atmosphere by convergent downwelling branch of the SS-AS circulation [1]. One of the most striking features of the Venus atmospheric dynamics is the prominent polar vortex, observed in detail in the South hemisphere by Venus Express instruments. The nature of this persistent, yet highly variable mesoscale structure and its connection with the global circulation is poorly understood.

Due to recent progress in Venus atmospheric modeling[2], general circulation models are now able to reproduce zonal superrotation, although the detailed circulation pattern varies from model to model and depends on initial conditions. However, most of models fail to reproduce SS-AS circulation and polar vortices. We assume that the reason is that at the scales of these features hydrostatic balance breaks, and non-hydrostatic effects play an important role. In particular, the analogy of Venus polar vortex with a hurricane suggests that downward vertical velocity in its “eye” may exceed few meters per second, while trade upward motion, producing “eye wall”, is substantially non-hydrostatic. In order to simulate both global and mesoscale atmospheric motion, we have developed a general circulation model with high spatial resolution, based on a full set of gas dynamics equations. As orographic wave perturbations induced by mountains and other major topographic features are also non-hydrostatic, we included Venus topography in simulations in order to study the potential effect of topographic perturbation to the global and mesoscale circulation.

The model: The dynamics of Venus atmosphere was modeled using a non-hydrostatic code based on the full set of gas dynamics equations. The hybrid semi-Lagrangian numerical scheme involves a Lagrangian half-step in the vertical dimension, interpolation of a deformed grid into a fixed vertical grid, and an Eulerian half-step in the horizontal dimensions. This scheme recently generalized for non-uniform grids, is strictly conservative and has no linear numerical viscosity. The model is run on the grid with 1.4062º resolution in horizontal dimensions and 250 m in the vertical, which required timestep from 0.5 sec to 2 sec. Subgrid turbulence was parameterized using local Richardson number. The model has no radiation block, with thermal forcing being represented in a relaxation approximation. Adopted heating rate is set to be proportional to the deviation of the actual temperature from specified relaxation profile, with timescale dependent on altitude. Relaxation profile corresponds to standard VIRA thermal profile with correction representing contrast between the equator and poles and between night- and dayside of the Venus atmosphere. As equator-to-pole thermal contrast was a tuning parameter in the model, diurnal thermal tide was represented by heating rate component proportional to the cosine of solar zenith angle.

Topography: The model included detailed topography map based on Magellan data. Surface elevation was smoothed with horizontal resolution of the model and interpolated into its vertical grid. One of the main purposes of the current work was the attempt to study the potential contribution of topography to general ans mesoscale circulation of the Venus atmosphere.

Initial conditions: Developed superrotation concentrated at the altitude of main cloud layer (55-65 km) has been chosen as initial condition, with decreasing zonal velocity to the poles and no variations with local time. Wind field relaxes to steady state as quick as within few Venusian sols.

Platform: As the non-hydrostatic model demands substantial computing resources, it has been run on the graphical processors using CUDA technology, which gives approximately 50-fold acceleration compared to single-thread calculations. The model was implemented in Fortran code compiled with the extension providing porting to graphical accelerator, and on a regular PC equipped with NVIDIA GTX-470 video card.

Results: Within approximately one Venusian sol the model relaxes to quasi-steady-state solution. The global atmospheric circulation is characterized by zonal superrotation concentrated within two midlatitude jets centered at ~60º of each hemisphere. Velocity field reveals strong meridional variations, characteristic of diurnal thermal tide; zonal flow expands at warmer dayside and shrinks at colder nightside of the planet, so that the effective axis of superrotation shifts to the morning terminator, forming prominent polar vortices. Above 100-110 km, superrotation in the model fades, being completely replaced by tidal pattern. The presence of of pole-crossing flows in both hemispheres implies contribution of the SS-AS circulation.

Vertical velocity fields in the gas dynamics model is different from what can be expected in hydrostatic approximation. At mid-to-high latitudes, where absolute vorticity gradient changes significantly, periodic perturbations of vertical velocity are developed due to barotropic instability, forming zones that could be interpreted as ‘eyes’ of the polar vortex. Typical values of vertical velocity perturbations at the upper cloud level (65-70 km) in calculations without topography are 10 cm/sec. However, this pattern dramatically changes in calculations taking into account Venus surface relief. In the upper part of the model domain, an ensemble of strong gravity waves develops, with vertical velocities reaching few meters per second. SS-AS circulation resembles a complex superposition of large-scale eddies. Near the poles, wave perturbations due to barotropic instability become stronger and reveal properties of non-hydrostatic orographic waves, especially prominent in the North polar region due to the influence of Ishtar Terra. On the South pole, topographic features at the cloud level are not evident. Instead, a regular wave-2 polar vortex with dominant downwelling motion in the central part and upwelling “wall” around it is formed, consistent with Venus Express observations. In contrast with real Venus polar vortex, simulations predict stable position of this

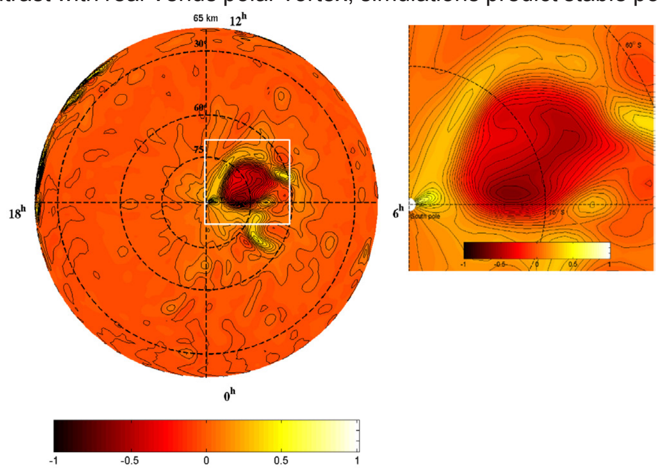

feature at the morning terminator.

fig. 1. Vertical velocity at the altitude 65 km in the South hemisphere according to simulations taking into account topographic effects. Local solar time is indicated on the limb.

We propose that this feature is formed due to self-organization, with topographically induced gravity waves creating a background of perturbations whose energy and momentum are pumped into polar vortex. Formation of the distinct upwelling wall around the vortex and its similarity with typhoon eye supports the idea that the polar atmospheric dynamics on Venus reveal deep analogy with terrestrial hurricanes[3].

The work has been supported by the Ministry of Education and Science of Russian Federation grant #11.G34.31.0074 and RFBR grant #10-02-01260-a.

This work was supported by the grant of the Russian academy of sciences Presidium Program 22: “Fundamental problems of research and exploration of the Solar system”.

References

[1] Bertaux, J.-L., et al..: A warm layer in Venus’ cryosphere and high-altitude measurements of HF, HCl, H_2O and HDO. Nature, Vol. 450, 7170, pp. 646-649, 2007.
[2] Lebonnois, S., et al.: Superrotation of Venus’ atmosphere analyzed with a full general circulation model. J. Geophys. Res., Vol. 115, E6, CiteID E06006, 2010.
[3] Limay, S.: Venus atmospheric circulation: Known and unknow. J. Geophys. Res., Vol. 112, E4, CiteID E04S09, 2007.

THE RESULTS OF THE VMC/VEX PHOTOMETRY AT SMALL PHASE ANGLES: GLORY AND THE PROPERTIES OF THE UPPER CLOUDS OF VENUS

W.J. Markiewicz[1], E.V. Petrova[2], O.S. Shalygina[1], M. Almeida[3], D.V. Titov[4,1], S.S. Limaye[5], N.I. Ignatiev[2], T. Roatsch[6], and K.D. Matz[6],
[1]Max-Planck-Institut für Sonnensystemforschung, Max-Planck-Str 2, 37191 Katlenburg-Lindau, Germany; [2]Space Research Institute, Moscow, Russia; [3]ESA-ESAC, Villanueva de la Cañada, Madrid, Spain; [4]ESA-ESTEC, SRE-SM, Noordwijk ZH, The Netherland; [5]Space Science and Engineering Centre, University of Wisconsin-Madison, Madison, Wisconsin, USA; [6]German Aerospace Research Center (DLR), Institute of Planetary Research Berlin, Germany.
Contact: epetrova@iki.rssi.ru

To study the major problems on the atmosphere of Venus - its super-rotation and origin of the runaway greenhouse effect, we need to know the size distribution, number density and composition of the aerosols that compose the clouds completely enveloping the planet. Moreover, the nature of the UV-absorbing substance that is responsible for the UV contrasts seen at wavelengths of about 0.365 µm is still obscure although many candidates have been proposed [1, 2]. From the measurements of the phase function of clouds near backscattering, the restrictions on the sizes and refractive index of particles in the upper cloud layers can be obtained, since the interference feature that may appear at small phase angles - the so-called glory - is sensitive to these parameters.

We report on the first observations and analysis of a complete glory on top of the Venus clouds captured by the Venus monitoring camera (VMC), when the Sun was almost directly behind the Venus-Express spacecraft. The measurements were made in three narrow band filters with central wavelengths of 0.365, 0.513, and 0.965 mm (see Figure 1). The successful observation of glory itself suggests that the scattering medium at the level, where the radiation comes from, is rather homogeneous, its particles are spherical and their size distribution is narrow. The positions of the glory extrema unambiguously and uniquely determine the dominant particle size of the cloud layer. From the VMC phase curves, the effective radius of the scattering particles was estimated to be from 1.0 to 1.4 mm for different regions of the cloud layer. This corresponds to the so-called mode 2 particles, which are thought to be composed of concentrated sulfuric acid [3, 4].

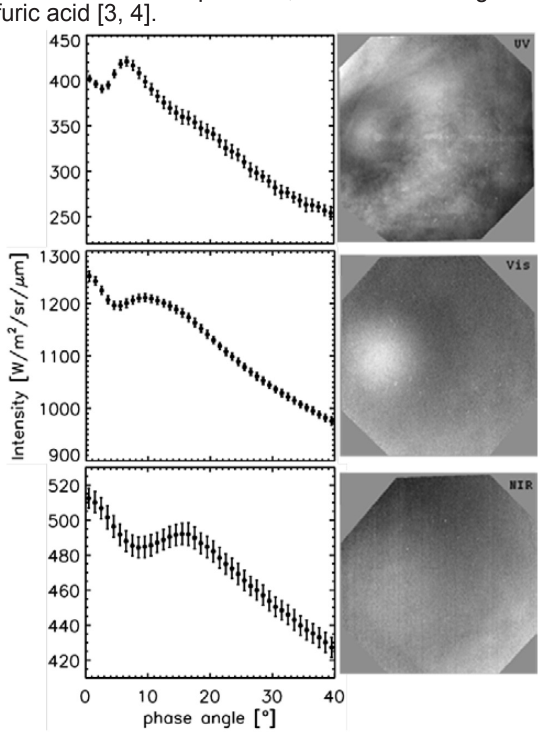

Fig. 1. Venus glory as observed in three of the VMC channels (UV – 0.365 µm, Vis – 0.513 µm and NIR – 0.965 µm, top to bottom). Left panels: Averaged intensity as a function of phase angle (orbit 1809). Right panels: VMC images (orbit 1920).

However, in some cases analyzed to date, mostly corresponding to low latitudes near the local noon, sulfuric acid droplets alone cannot explain several other aspects of the observed glory, such as the ratio of the primary and secondary maxima and the phase slope at phase angles larger than 20°. These disagreements can be obviated by assuming an increased, relative to the standard value [5], real part of the refractive index of the scattering particles. It is worth mentioning that the higher values of the refractive index of mode-2 particles were also obtained from nephelometry on the *Venera* and *Pioneer Venus* probes (e.g., [4]).

We can think of two ways of realizing this increase. One would be to lower the cloud temperature [6, 7], but we estimate this effect to be much too weak. The other is to introduce an admixture of some substance with a high refractive index. This possibility seems quite reasonable, since submicron particles that are ubiquitous in the Venus clouds and hazes can serve as condensation nuclei for sulfuric acid droplets. The nature of the haze particles is not yet clear, and it likely varies with altitude [4]. Among probable candidates ferric chloride and sulfur are worth mentioning. Moreover, both these materials are often suggested to be the unknown UV absorber [1, 2]. Our calculations for layered spheres composed of sulfuric acid with a sulfur coating or a sulfur core (depending on formation of different sulfur allotropes and their wetting by sulfuric acid [1, 8, 9]) shows that a volume fraction of sulfur of 1-3% is sufficient. If ferric chloride (soluble in sulfuric acid) is added into sulfuric acid droplets, its portion should be larger, since its refractive index is lower than that of sulfur. The analysis of the phase function of the clouds cannot distinguish between these possibilities. Nevertheless, it is clear that in some cases the refractive index of the cloud particles must be greater than the standard value for sulfuric acid in order to fit the VMC measurements. The time and spatial variations of this phenomenon is a subject of the further analysis.

References

1. Mills et al., in *Exploring Venus as a Terrestrial Planet*, Esposito, Stofan, Cravens, Eds. (AGU Monogr. Ser, Washigton, DC), **176**, 73-100 (2007).
2.. Krasnopolsky, *Planet. Space Sci*. **54**, 1352-1359 (2006).
3. Hansen, Hovenier, *J. Atmos. Sci*. **31**, 1137-1160 (1974).
4. Ragent et al., *Adv. Sp. Res.* **5**, 11, 85-115 (1985).
5. Palmer, Williams, *App. Opt*. **14** (1), 208-219 (1975).
6. Beyer, Ravishankara, Lovejoy, *J. Geophys. Res.* **101** (D9), 14519-14524 (1996).
7. Biermann, Luo, Peter, *J. Phys. Chem. **A*** **104**, 783-793 (2000).
8. Toon, Pollack, Turco, *Icarus.* **51**, 358-373 (1982).
9. Young, *Icarus*. **56**, 568-577 (1983).

EARLY CLIMATE HISTORY OF MARS: A GEOLOGICAL PERSPECTIVE.

J.W. Head, III,
Brown University, Department of Geological Sciences, Providence RI 02912 USA.
Contact: James_Head@brown.edu

Introduction and Approach: Deciphering climate history has been one of the major goals of the scientific exploration of Mars because of the significance of climate as a proxy for understanding: 1) planetary volatile accretion, 2) outgassing history, 3) the distribution and stability of water and the nature and evolution of the water cycle, 4) the surface weathering environment, 5) the presence, stability, and abundance of liquid water, and 6) the implications for environments conducive to the origin and evolution of life [1]. Recent intensive exploration has contributed significantly to the understanding of current Mars weather, and lengthening observational baselines are beginning to reveal the basic elements of climate. This baseline knowledge is essential to the proper understanding of the longer-term history of climate. Assessing longer-term climate change and its history can be approached from a process-response standpoint through the identification of cause and effect [2] (Fig. 1). Among the most important causes of climate change (input parameters) are external forcing functions linked to spin-axis and orbital variations, elements whose nature and history have recently become much more well-understood in both the time and frequency domain [3]. The influence of these external forcing functions on the climate system (the internal response mechanism) are becoming more well known through increasingly more sophisticated atmospheric general circulation models [4-7], including the behavior of water. Finally, the consequences of the causes (the external forcing functions, spin-axis/orbital parameters, operating on the internal response mechanism, the climate system) produces an effect in the time and frequency domain (the geological record); increasing availability of global data is providing a more comprehensive view of over four billion years of geological history [8]. Specifically, increased knowledge of the structure of current polar deposits [9], the location of geological deposits that chronicle the distribution and history of non-polar ice [10], and the context in which to interpret ice deposits in extremely cold hyper-arid Mars-like conditions [11], have all contributed to an increased understanding of the climate history of Mars.

Amazonian: (present to ~3 Ga; [20-22]) A robust prediction of the spin-axis/orbital parameter-based insolation input to the climate system has been developed for the last 20 Ma [3] and these predictions have been used to begin to decipher the history of the polar cap [12-14], the nature of recent ice ages [15], the timing of active layers at high latitudes [16], and the conditions under which liquid water might form gullies during this time [17]. Prior to the last 20 Ma, deterministic predictions are not currently possible because solutions based on the input parameters become chaotic; nevertheless exploring this parameter space, Laskar et al. produced 15 scenarios showing candidate obliquity histories over the last 250 Ma (Fig. 2), and predicted that mean obliquity would be ~38° [3]. Analysis of these 15 examples shows the huge range of options for Late Amazonian climate history. In contrast to the last 20 Ma, where input parameters to the climate system are well-known, there is no robust prediction for a specific input parameter history to use as a test in interpreting the geological record. Therefore, we have adopted a different approach and use the geological record of non-polar ice deposits [10] (the output of the external forcing function and climate system) and a general knowledge of the behavior of the GCM and climate system under different obliquity baselines, to evaluate the 15 candidate scenarios of the obliquity component of the external forcing function.

Earlier Amazonian: Using a general knowledge of the behavior of the GCM under different obliquity conditions, we chose four mean baselines to form a framework for evaluating the 15 candidate obliquity scenarios for the last 250 Ma (Fig. 2) [18]. We applied the geological observations, in terms of interpreted latitude and time [10], to assess the candidate obliquity scenarios and found that the obliquity scenario that was most consistent with age and obliquity constraints (Fig. 2-8) is characterized by 45° obliquity at the times of both the early and late TMGs, and obliquity at or close to 35° during mid-latitude glaciations. Examination of the geological record of non-polar ice deposits, together with related information strongly suggests that the climate of Mars throughout the Amazonian was much like at is today, but with migration of surface ice in response to variations in spin-axis/orbital parameters, primarily obliquity. A corollary is that the hydrological cycle was horizontally stratified during the Amazonian [19].

The Hesperian Period: (~3-3.6 Ga; [20-22]): The martian outflow channels debouched into the northern lowlands primarily in the Late Hesperian Period [1] and their characteristics suggest to many workers that a large standing body of water, or ocean, was produced as a result. Characteristics of northern lowland deposits in the Early Amazonian Period suggest that by this time that if such an ocean existed it was gone. The evolution of water loaded with sediments emplaced by outflow channel formation has been modeled [23]; results suggest that it would freeze and sublime on very short time scales. The Late Hesperian Vastitas Borealis Formation may be the sublimation residue of the ocean [23]. In the Early Hesperian Period, a significant flux of volcanism occurred in the form of the Hesperian ridged plains, and this may well have represented a major pulse of volatiles into the atmosphere [24-25]. In addition, there is clear evidence of interaction of these volcanic deposits and large volatile-rich deposits in the south polar region [26], causing melting and drainage of liquid water.

Over the last 80% of the history of Mars, permafrost and the cryosphere dominate the surface. Although there is compelling evidence that liquid water formed occasionally on the surface and moved locally, there is no compelling evidence that indicates that the global cryosphere was absent at any time throughout the most recent 80% of the history of Mars. Mars surface conditions appear to have been cold and dry throughout most of its history, very similar to the way they are now. Further evidence of this is the limited amount of aqueous chemical alteration detected from orbit [27] and in martian meteorites [28]. Obliquity extremes, and intrusive volcanic activity related to the two major rises, Tharsis and Elysium, appear to have redistributed some water but liquid water was transient on the surface for the vast majority of Mars' history.

The Noachian Period: (>3.6 Ga; [20-22]): Geological evidence has been cited to support a 'warm, wet' era [29] in the late Noachian Period (e.g., valley networks, degradation rates, etc.). Critical assessment of this evidence and new data lead to several scenarios for the emplacement style, location and fate of water on early Mars during the first 20% of its history, and the important transition to conditions similar to those of today. This traditional view has recently been challenged by several developments [19]: 1) The growing evidence that mineralogic indicators for early phyllosilicates (interpreted to support warm and wet surface conditions [30]) could also be explained by subsurface hydrothermal effects in an early period of high thermal flux [31]; 2) The difficulty of producing and maintaining an atmosphere that could lead to a warm and wet early Mars with pluvial activity [32]; 3) Evidence that south circumpolar ice deposits are consistent with cold lower latitude surface temperatures [33]; 4) The poor integration of the surface hydrologic system (valley networks, open-basin lakes [34-35], suggesting short term activity, rather than long term integrated pluvial systems; 5) Emerging evidence in the Antarctic Dry Valleys that Mars-like fluvial and lacustrine activity can occur under surafce climate conditions with mean annual temperatures (MAT) well below 0°C [11]; 6) The possibility that surface drainage features could be explained by top-down transient atmospheric effects caused by punctuated volcanism during the late Noachian-early Hesperian (LN-EH) [36]. Three alternate scenarios for a "non-warm and wet" early Mars appear to be consistent with the six new developments outlined above [19]. Could Mars have been cold and dry or cold and wet, instead of the pluvial warm and wet early Mars envisioned by many [e.g., 29]? Our current data and analyses suggest that Mars was more likely to have been characterized by a "cold and dry" early history and a horizontally stratified hydrologic system throughout most of its history. In this scenario, the Hesperian represents a *perturbation* on the historically horizontally integrated hydrological system, rather than a *transition* from vertical integration to horizontal stratification. We continue to test these scenarios.

References: 1) M. Carr, *Water on Mars*, 1996; 2) J. Imbrie, *Icarus* 50, 408, 1982; 3) J. Laskar et al, *Icarus* 170, 343, 2004; 4) F. Forget et al., *JGR* 104, 24155, 1999; 5) M. Richardson and J. Wilson, *JGR* 107, 5031, 2002; 6) M. Mischna et al., *JGR* 108, 5062, 2003; 7) R. Haberle et al., *JGR* 106, 23317, 2003; 8) M. Carr, *The Surface of Mars*, Cambridge, 2006; 9) R. Phillips et al., *Science* 320, 1182, 2008; 10) J. Head and D. Marchant, *LPSC 39* 1295, 2008 and this volume; 11) D. Marchant and J. Head, *Icarus* 192, 187, 2007; 12) J. Laskar et al, *Nature* 419, 375, 2004; 13) S. Milkovich and J. Head, *JGR* 110, 2349, 2004; 14) B. Levrard et al, JGR 112, E06012, 2007; 15) J. Head et al., *Nature* 426, 797, 2003; 16) M. Kreslavsky et al., *MAPS* 41, 1659, 2006; 17) F. Costard et al. *Science* 295, 110, 2002; 18) J. Head et al. LPSC 40, 1349, 2009; 19) J. Head, LPSC 43, 2137, 2012; 20) W. Hartmann and G. Neukum, SSR, 96, 165, 2001; 21) G. Neukum et al., SSR, 96, 55, 2001; 22) B. Ivanov, SSR, 96, 87, 2001; 23) M. Kreslavsky and J. Head, JGR, 107, 1831, 2002. 24) T. Watters, JGR, 96, 15599, 1991. 25) J. Head, et al., JGR, 107, 1445, 2002; 26) G. Ghatan and J. Head, JGR, 107, 1519, 2002. [27] P Christensen et al., JGR, 106, 23823, 2001. [28] J. Bridges et al., SSR, 96, 365, 2001; 29) R. Craddock and A. Howard (2002) *JGR 107*, 5111;30) J.-P. Bibring et al. (2006) *Science 312* 400; 31) B. Ehlman et al. (2011) *Nature 479*, 53; 32) R. Wordsworth et al. (2011) *4th Mars Atmosphere Workshop*; 33) J. Fastook et al. (2012) *Icarus*, 219, 25; 34) C. Fassett and J. Head (2008) *Icarus 195,* 61; 35) C. Fassett and J. Head (2008) *Icarus 198,* 37; 36) I. Halevy and J. Head, (2012) *LPS 43*, #1908.

RADAR SOUNDINGS OF THE NORTH POLAR CAP OF MARS

A. Frigeri[1], R. Orosei[1], M. Cartacci[1], A.Cicchetti[1], S. Giuppi[1], R. Noschese[1], G.Mitri[1], G. Picardi[2], J.J. Plaut[3] *[1]Istituto di Astrofisica e Planetologia Spaziali - Istituto Nazionale di Astrofisica, via del Fosso del Cavaliere 100, Rome, Italy; [2]Università ``La Sapienza", Rome, Italy; [3]NASA Jet Propulsion Laboratory, California Institute of Technology, Pasadena, California, USA..*
Contact: alessandro.frigeri@iaps.inaf.it

Introduction: Mars Advanced Radar for Subsurface and Ionospheric Sounding (MARSIS) [1] is an orbital subsurface sounder aboard ESA's Mars Express spacecraft [2]. It transmits a low-frequency radar pulse that is capable of penetrating below the surface, and is reflected by subsurface dielectric discontinuities. MARSIS has been used to probe both the south [3] and the north [4,5] polar caps of Mars, revealing their thickness and structure. We report on the results of a campaign of observations of the north polar ice cap of Mars that took place between May and December 2011 in uniquely favorable conditions and produced data of unprecedented quality. The focus of this work is the so-called Basal Unit, a dark, ice-rich, complexly layered geologic unit lying stratigraphically between the polar layered deposits and the Vastitas Borealis Formation [6,7,8,9], and extending beneath most of Planum Boreum [10,11] and Olympia Planitia [5]. The objective of this work is the to study the full three dimensional structure of the Northern Polar Deposit and in particular of the Basal Unit (BU).

The Basal Unit: It has been recently found [12] that the BU consists of two markedly different units, called the Rupes Tenuis unit and the Planum Boreum Cavi unit. The Rupes Tenuis unit appears to be older, horizontally layered, and lacking erosional contacts. It has been thus interpreted [12] as the result of precipitation and cold-trapping of dust-laden volatiles. The Planum Boreum cavi unit displays cross-bedding, indicating dune accumulation [12]. Bright layers within it are interpreted as being made of ice-cemented dust, while dark layers should consist of weathered basalt fines [12]. It seems likely [12] that, in places, the Planum Boreum Cavi unit rests directly on the Vastitas Borealis, without the Rupes Tenuis unit in between. Because the two units in the BU have formed much earlier than the north polar layered deposits, and at some interval from each other [12], they bear evidence of past climatic conditions that were very different from present, so that they represent an important element to understand better the Martian climate [13].

Radar soundings of the Basal Unit. Subsurface sounding radar investigations [10,11,5] by both MARSIS and SHARAD [14] revealed that the BU has radar properties that are different from both the polar layered deposits and the Vastitas Borealis Formation [10], probably because of a mostly icy composition, but with a larger fraction of impurities than the polar layered deposits above [10]. The upper surface of the BU exhibits significant relief, with features appearing to be erosional cutbacks and reentrants, indicating a complex accumulation history [11,15]. Higher dust content and the resulting stronger attenuation is thought to be the reason why SHARAD radar signal could not penetrate through the BU and detect its bottom face [10,11]. Recent observations on MARSIS signals penetrating the Rupes Tenuis suggest that the dust content of the BU is as high as 40-50% .

Data Processing: From the summer phase of the Polar Campaign of data acquisition we have selected 161 MARSIS observations. The radargrams were processed in order to cancel the effect of the ionosphere and to align the primary echo to a vertical datum. In order to detect possible lateral variations of the dielectric constant in the totality of measurements, in the first phase of our study we have converted the time delay of echoes into depths considering a dielectric constant of 3.15 [16].

Detection of BU Internal Layering: We find weak echoes within the BU that appear to outline a two-layer structure, perhaps corresponding to the Rupes Tenuis unit and the Planum Boreum Cavi unit. This was found through visual inspection, however, because echoes within the BU are too sporadic to be automatically picked, thus further data processing and analysis is needed to confirm the result.

Exploring MARSIS Data in Three Dimensions: As subsurface radar data returns signals from the depth axis, we have assembled MARSIS data in a three dimensional space. Using computer visualization techniques it has been possible to explore the geometric distribution of radar echoes related to the geologic features of the North Polar Cap of Mars.

Volume rendering of data from the polar campaign allow to recognize the main features of the icecap (Figure 1). Through the combined inspection of single radargrams within the volumetric dataset we have detected signals related to the upper and lower contact of the Basal Unit. These signals, tracked in the three dimensional volume, allow to study the morphology of the Basal Unit alone.

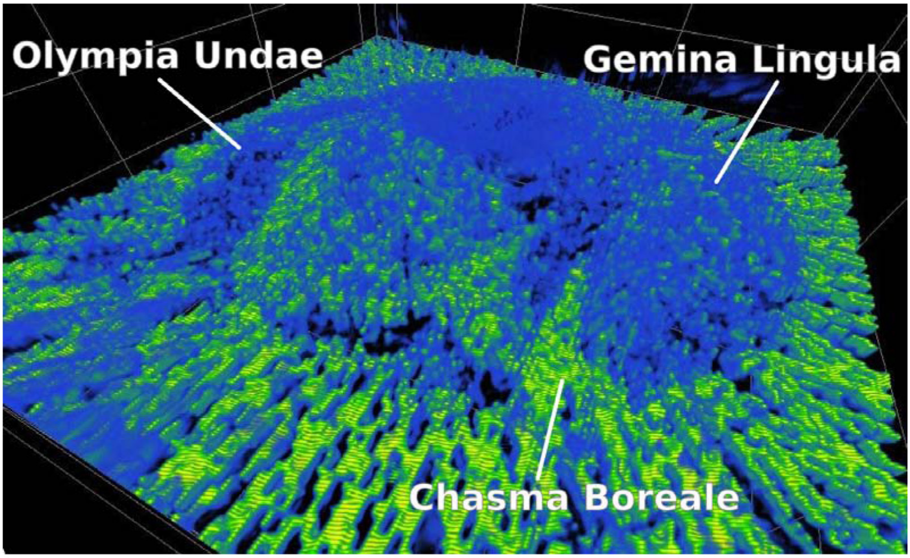

fig. 1. Volume rendering of selected MARSIS data from the summer 2011 data acquisition campaign. The three dimensional visualization allow to recognize the main geologic features of the icecap. Yellow voxels represent strong echo returns (from Planum Boreum and the floor of Chasma Boreale), while blue voxels are representative of echo returns of medium strength.

Conclusions: Signals acquired by MARSIS during the campaign between May and December 2011 in uniquely favorable conditions for observing the North Pole of Mars, produced data of unprecedented quality. New data acquisition and analysis techniques have been successfully applied.

The operative frequencies of MARSIS have revealed themselves to be ideally suited to the study the geology of the icecap at a regional scale, and with penetration depths capable of scan the internals of entire icecap of Mars. Another similar acquisition campaign will give us the opportunity to get more dense results and to address detailed observations on areas that the current campaign has revealed to be particularly interesting.

References: [1] Picardi G. et al. (2004) Planet. & Space Sci., 52, 149. [2] Chicarro A. et al. (2004) in Mars Express: the Scientific Payload, 3. [3] Plaut, J. J. et al. (2007) Science, 316, 92. [4] Picardi G. et al. (2005) Science, 310, 1925. [5] Plaut J. et al. (2012) 43rd Lunar and Planetary Science Conference, Abstract 1659 [6] Byrne S. and Murray B.C. (2002) J. Geophys. Res., 107, 5044. [7] Edgett K. S. et al. (2003) Geomorphology, 52, 289. [8] Fishbaugh K. E. and Head J.W. (2005) Icarus, 174, 444. [9] Herkenhoff K. E. et al. (2007) Science, 317, 1711. [10] Phillips R. J.et al. (2008) Science, 320, 1182. [11] Putzig N. E. et al. (2009) Icarus, 204, 443. [12] Tanaka K. L. et al. (2008) Icarus, 196, 318. [13] Fishbaugh K. E. et al. (2008) Icarus, 196, 305. [14] Seu R. et al. (2007) J. Geophys. Res., 112, 5. [15] Brothers T. C. et al. (2010) LPSC XLI, Abstract #2590. [16] Matzler C. (1998) in B. Schmitt et al. (eds.) ``Solar System Ices'', Kluwer

SURFACE CHRONOLOGY OF PHOBOS - THE AGE OF PHOBOS AND ITS LARGEST CRATER, STICKNEY.

N. Schmedemann[1], G. Michael[1], B. A. Ivanov[2], J. Murray[3] and G. Neukum[1],
[1]*Institute of Geological Sciences, Malteserstrasse 74-100, Building D, 12249 Berlin, Germany;* [2] *Institute of Dynamics of Geospheres, Moscow, Russia;* [3] *Department of Earth Sciences, Open University, Milton Keynes, UK.*
Contact: nico.schmedemann@fu-berlin.de

Introduction:

Since its discovery in 1877 by A. Hall, Phobos has been investigated by many scientists and a fleet of spacecraft. And yet, the origin of this larger of the two Martian moons is not well understood. Unraveling the history of Phobos may also shed some light on the evolution of Mars. There are three theories for Phobos' origin under discussion (Giuranna et al., 2011). I Phobos is a captured asteroid. II Phobos formed in-situ from the same material as Mars. III Phobos formed from ejecta of (a) large impact(s) on Mars. Various investigations of Phobos have revealed that it is in an unstable orbit with a high probability of disintegrating or crashing into Mars within 30 to 50 Ma (Burns, 1978). Spectroscopically Phobos was found to be consistent with C-type asteroids at first, but this was revised later and now seems to be more consistent with D- and T-type asteroids (Giuranna et al., 2011). Morphologically Phobos has an unrelaxed topography, dominated by large craters and it shows various sets of grooves, the origin of which is also uncertain. In order to provide further constraints on the formation and the evolution of Phobos, we derived surface ages of Phobos. For this purpose we developed two crater production functions and two chronologies for two end-member cases of Phobos' evolution. Case A: Phobos was in its current orbit since its formation. Case B: Phobos is a recently captured Main Belt asteroid.

Methodology:

Crater Production Function: In order to derive the crater production functions for both cases we calculated the respective impact velocities. Average impact velocities on Phobos at its current orbit should be on the order of 8.5 km/s (Case A). This value was derived from the squared differences of Mars' escape velocity at the Martian surface and at the orbit of Phobos and the impact velocity on Mars (9.4 km/s; Ivanov, 2008). If Phobos is a recently captured Main Belt asteroid (Case B) the average impact velocity should be on the order of 5 km/s (Bottke et al., 1994). Using these velocities we scaled the lunar crater production function (Neukum and Ivanov, 1994) to the impact conditions of Phobos. This also takes Phobos' small surface gravity into account, which leads to a larger crater on Phobos than on Mars for equivalent projectiles, even with the higher impact velocity at the surface of Mars. We used the scaling laws of Ivanov (2001, corrected - pers. comm. O'Brien, Ivanov, 2011).

The derived crater production functions are very similar to each other. The asteroidal case predicts a slightly flatter crater distribution above 1 km crater size.

Chronology Functions: The Phobos chronologies are based on the lunar chronology (Neukum and Ivanov, 1994). The impact rate for our case A scenario is a modified impact rate for Mars (Ivanov, 2001). The rate for Mars was modified to apply to Phobos in the sense that we accounted for differently-sized crater formation rates for a given impactor flux. The chronology is valid for the cumulative crater frequency of 1 km craters on Mars and Phobos. Since the projectiles forming 1 km craters on Mars are smaller than on Phobos, their frequency is somewhat higher according to the crater production function of Phobos. This ratio was applied to the Martian chronology function, in order to transform it for Phobos.

In the case B scenario we used the average impact probability of Main Belt asteroids to derive a chronology for Phobos. Given the average asteroidal intrinsic impact probability, mean radius of Phobos and the number of Main Belt bodies creating ≥ 1 km crater on Phobos, O'Brien et al. (2006) provide an equation to calculate the current formation rate of such craters, which can be used to adapt the lunar chronology to the case of an asteroidal target.

Software: Crater counting on Phobos was performed utilizing the ESRI ArcGIS mapping software along with the CraterTools plug-in (Kneissl et al., 2011). This tool simplifies crater counting in the sense of map-projection independent measurements. Crater statistics were analyzed utilizing the craterstats software (Michael and Neukum, 2010). Furthermore, we did randomness analyses of the spatial crater distribution (Michael et al., 2012).

Imaging data: For large scale counting we mapped craters on an HRSC basemap

(Wählisch et al., 2010) and for higher resolution we used an HRSC/SRC image (h3769_0004) for a part of Stickney crater.

Results:

In general we agree with the findings of Thomas and Ververka (1980). Based on Viking data they concluded a high average surface age of Phobos in the range of 4 Ga and similar relatively old ages for the grooves and for Stickney, the largest crater on Phobos. Given these high surface ages the crater distribution is expected to be close to an equilibrium distribution (Neukum and Dietzel, 1971). While Thomas and Veverka measured a -2 cumulative slope in agreement with equilibrium, we measured a steeper slope around -3, in agreement with a lunar-like crater production distribution for small craters.

For an average surface west of Stickney we obtained a surface age of 4.3 +0.03/-0.04 Ga (case A; 3.66 +0.03/-0.04 Ga – case B). The same area shows two sets of grooves perpendicular to each other. The cratering data also suggests two resurfacing events probably connected to these grooves. The derived resurfacing ages are 3.81 +0.01/-0.02 Ga (2.96 +0.06/-0.09 Ga) and 4.04 +0.02/-0.02 Ga (3.4 +0.03/-0.03 Ga).

Measurements inside Stickney crater revealed a similar picture. Based on crater counting inside Stickney we determine a formation age of 4.18 +0.07/-0.13Ga (3.54 +0.07/-0.15 Ga). We also found what appear to be two resurfacing events. These events may have resulted from down-slope movements of material at the crater rim slopes or it also could be caused by the formation of grooves also present inside Stickney. According to our measurements these events happened 3.29 +0.09/-0.18 Ga and 3.84 +0.03/-0.04 Ga ago. A refining measurement utilizing the higher resolution HRSC/SRC image unfortunately could not confirm these ages within the given error. However, from the relative stratigraphy of the groove morphologies and the derived ages, there might have been one single event that created a north-south striking set of grooves in two different counting areas around 3.81-3.84 Ga ago.

We also measured global crater frequencies in order to test Phobos' crater distribution for an apex-/antapex asymmetry. We found such an effect with a ratio of about 1.5 +/-0.1. The calculated magnitude of the effect for the current orbit of Phobos was determined to be about a factor of 4.1, which is significantly larger.

References:

Bottke, W.F., Nolan, M.C., Greenberg, R., Kolvoord, R.A., 1994. Velocity Distributions among Colliding Asteroids. Icarus 107, 255-268.
Burns, J.A., 1978. The dynamical evolution and origin of the Martian moons. Vistas in Astronomy 22, Part 2, 193-210.
Giuranna, M., Roush, T.L., Duxbury, T., Hogan, R.C., Carli, C., Geminale, A., Formisano, V., 2011. Compositional interpretation of PFS/MEx and TES/MGS thermal infrared spectra of Phobos. Planetary and Space Science 59, 1308-1325.
Ivanov, B., 2008. Size-Frequency Distribution of Asteroids and Impact Craters: Estimates of Impact Rate
Catastrophic Events Caused by Cosmic Objects, Edited by V.V. Adushkin and I.V. Nemchinov. ISBN 978-1-4020-6451-7. Berlin: Springer, 2008, p.91.
Ivanov, B.A., 2001. Mars/Moon Cratering Rate Ratio Estimates. Space Science Reviews 96, 87-104.
Kneissl, T., van Gasselt, S., Neukum, G., 2011. Map-projection-independent crater size-frequency determination in GIS environments---New software tool for ArcGIS. Planetary and Space Science 59, 1243-1254.
Michael, G.G., Neukum, G., 2010. Planetary surface dating from crater size-frequency distribution measurements: Partial resurfacing events and statistical age uncertainty. Earth Planet Sc Lett 294, 223-229.
Michael, G.G., Platz, T., Kneissl, T., Schmedemann, N., 2012. Planetary surface dating from crater size–frequency distribution measurements: Spatial randomness and clustering. Icarus 218, 169-177.
Neukum, G., Dietzel, H., 1971. On the development of the crater population on the moon with time under meteoroid and solar wind bombardment. Earth Planet Sc Lett 12, 59-66.
Neukum, G., Ivanov, B.A., 1994. Crater Size Distributions and Impact Probabilities on Earth from Lunar, Terrestrial-planet, and Asteroid Cratering Data. Hazards due to comets and asteroids, Space Science Series, Tucson, AZ: Edited by Tom Gehrels, M. S. Matthews. and A. Schumann. Published by University of Arizona Press, 1994., 359.
O'Brien, D.P., Greenberg, R., Richardson, J.E., 2006. Craters on asteroids: Reconciling diverse impact records with a common impacting population. Icarus 183, 79-92.
Thomas, P., Veverka, J., 1980. Crater densities on the satellites of Mars. Icarus 41, 365-380.
Wählisch, M., Willner, K., Oberst, J., Matz, K.D., Scholten, F., Roatsch, T., Hoffmann, H., Semm, S., Neukum, G., 2010. A new topographic image atlas of Phobos. Earth Planet Sc Lett 294, 547-553.
Neukum, G., Dietzel, H., 1971. On the development of the crater population on the moon with time under meteoroid and solar wind bombardment. Earth Planet Sc Lett 12, 59-66.

PHOTOMETRIC ANALYSIS OF MARTIAN MOON PHOBOS WITH THE HRSC ON MARS EXPRESS.

A. Pasewaldt[1], J. Oberst[1,2], K. Willner[2], F. Scholten[1], M. Wählisch[1], K.-D. Matz[1], T. Roatsch[1], H. Hoffmann[1], A. Grechishev[3], and V. Patsyn[3].
[1]German Aerospace Center, Berlin, Germany; [2]Technische Universität Berlin, Berlin, Germany; [3]Moscow State University of Geodesy and Cartography, Moscow, Russia. Contact: andreas.pasewaldt@dlr.de

Introduction:

Between May 2004 and July 2012 the Mars Express spacecraft carried out over 175 Phobos' flybys, during which a large number of HRSC images was taken. From these flybys a subset of 18 orbits with about 90 images was selected in order to perform surface photometry of Phobos. Phobos, the larger and inner of two Martian moons, revolves in a mean distance of 9,376 km from Mars' center in a nearly circular, nearly equatorial orbit. It is tidally locked to its parent planet. Because Phobos is moving far inside of the synchronous orbit, it is subject to tidal acceleration. Its main morphological characteristics are a large number of impact craters and several sets of parallel grooves. More recent works on Phobos' surface composition distinguish a blue (leading side) from a red (trailing side) unit, whose spectra are similar to those of low-albedo carbonaceous T-type respectively D-type asteroids (Rosenblatt 2011). These findings are often related to theories about Phobos' origin and evolution: Is it a captured asteroid or did it form from a circum-Mars debris disk? One aim of our investigation is to put further constraints on the physical properties of the surface of Phobos.

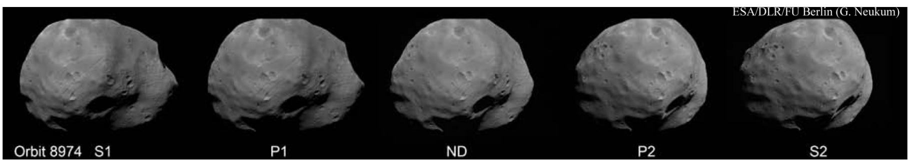

fig. 1. During one flyby (orbit 8974) the five panchromatic channels of the HRSC camera acquire images of Phobos under varying phase angles.

Methods:

Image selection. The selected images cover a large part of Phobos' surface in high-resolution in the panchromatic band's spectral range under various phase angles (*see Fig. 1*).

Bundle adjustment. Control and tie points were collected in the images as input data for a photogrammetric bundle (block) adjustment, in which especially the exterior orientations of the camera – i. e. the positions (X_0, Y_0, Z_0) and pointings (φ, ω, κ) – were improved. Later on, this information was used to perform an orthorectification of the imagery. With the bundle adjustment, all HRSC images were co-registered on the control network of Willner et al. (2010).

Image processing. First, DN values for the blemish pixels were interpolated. Then, all DN values were converted to surface reflectances by applying the respective reflectance scaling factors (radiometric calibration). Finally, the HRSC images were orthorectified by using the improved exterior orientation data and the DTM of Willner et al. (2010). As result we obtained co-registered images that show the albedo of Phobos' surface.

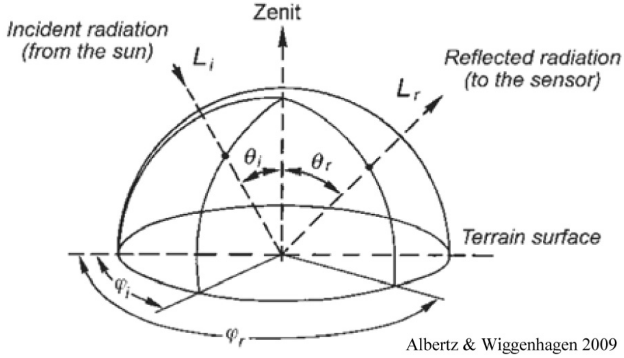

fig. 2. Illumination and observation geometry for a surface area element

Angle Measurements. There are three angles that describe the illumination and observation geometry of an image. These are the incidence, phase, and emission angles (*see Fig. 2*). The phase angle is the angle between the incident and the reflected radiation. Incidence and emission angles are measured with respect to the local surface normal that is computed based on a selected reference body, e. g. the tri-axial ellipsoid.

Outlook:

Further on, our investigation involves drawing of phase curves and estimating the parameters of theoretic photometric functions. As results we want to obtain information on the physical properties of Phobos' surface as well as photometrically corrected topographic and albedo maps.

References:

Albertz, J., and Wiggenhagen, M.: Guide for Photogrammetry and Remote Sensing, Herbert Wichmann Verlag, 2009.

Jaumann, R., et al.: The high-resolution stereo camera (HRSC) experiment on Mars Express: Instrument aspects and experiment conduct from interplanetary cruise through the nominal mission, Planetary and Space Science, Vol. 55, pp. 928-952, 2007.

Rosenblatt, P.: The origin of the Martian moons revisited, Astronomy & Astrophysics Review, Vol. 19, pp. 1-26, 2011.

Simonelli, D. P., Wisz, M., Switala, A., Adinolfi, D., Veverka, J., Thomas, P. C. and Helfenstein, P.: Photometric Properties of Phobos Surface Materials From Viking Images, Icarus, Vol. 131, pp. 52–77, 1998.

Noland, M., and Veverka, J.: The Photometric Functions of Phobos and Deimos, I. Disc-Integrated Photometry, Icarus, Vol. 28, pp. 405-414, 1976.

Willner, K., et al.: Phobos Control Point Network, Rotation, and Shape, Earth and Planetary Science Letters, Vol. 294, pp. 541-546, 2010.

Willner, K., et al.: A new topographic image atlas of Phobos, Earth and Planetary Science Letters, Vol. 294, pp. 547–553, 2010.

FIRST DATA FROM DAN INSTRUMENT ONBOARD MSL CURIOSITY ROVER.

M. L. Litvak[1], I.G. Mitrofanov[1],
[1]Space Research Institute, Moscow, Profsouznaya 84/32, 117997, Russia. Contact: litvak@mx.iki.rssi.ru

Introduction:

In August 5, 2012 NASA's Mars Science Laboratory (MSL) has successfully landed on Mars at the Gale crater. MSL science payload includes Dynamic Albedo of Neutrons (DAN) instrument selected for the monitoring of water abundance along the path of the MSL rover (see 1-2). To estimate average content of water and its depth distribution we plan to use both passive measurements of natural martian neutron flux (due to bombardment of Galactic Cosmic Rays) and methods the neutron-neutron activation analysis (irradiation of the surface by a pulsing neutron source).

The main purpose of this work is a study of Gale crater area with analysis of the first surface measurements (search for subsurface water) accomplished by DAN and comparison DAN data with the orbital neutron measurements from High Energy Neutron Detector (HEND) onboard Mars Odyssey mission.

SEASONAL AND INTER-YEAR VARIATIONS OF THE WATER CONTENT WITHIN THE SURFICIAL LAYER OF THE MARTIAN SOIL REVEALED BASED ON THE TES, THE OMEGA AND THE HEND DATA ANALYSIS

R.O.Kuzmin[1,2], E.V. Zabalueva[1], N. A. Evdokimova[2], M.L. Litvak[2], I.G. Mitrofanov[2], P.R. Christensen[3],
[1]Vernadsky Institute of Geochemistry and Analytical Chemistry RAS, Kosygin str. 19, Moscow 119991, Russia, e-mail: rok@geokhi.ru; [2]Space Research Institute, RAS; [3]School of Earth and Space Exploration, ASU, Tempe, Arizona.

Introduction: The water amount involved in the condensation and sublimation processes associated with formation and degradation of both the seasonal polar caps and the seasonal permafrost on Mars represents one of the key aspects for understanding of the modern water cycle on the planet and especially in the system "atmosphere-permafrost-polar caps". In the work we report the study results of the seasonal and inter-years variations of the water ice content within the surficial soil layer (as well as on the periphery of the seasonal polar caps) revealed based on the TES, the HEND and the OMEGA data analysis.

The TES and the OMEGA observations: To estimate and map the winter- and spring-time water ice amount in the surficial soil layer (corresponding to the daily thermal skin depth of 2-10 cm) outside of the seasonal CO_2 ice caps we used the recently developed method (see details in [1]). To study the inter-years difference of the winter-time water ice amount within the surficial soil layer we conducted the mapping of the thermal inertia parameter for the summer and winter season within the latitude belt ±50º separately for each of three the Martian years of the TES observations. The frequency distribution of the mapped water ground ice content values is shown on the Fig.1, where one can see the notable difference in the winter-time ground ice formation at transition from one year to other. The difference of the water ground ice content between 1-th and 2-th years is not so significant (< 10%) except the range of the values 8-9 vol. %, where the difference has achieved up to 40%. More significant difference has been found for 3-th years: the frequency distribution of the water ground ice content values in the range 2-5 vol. % is less on 13-30% and in the range 6-12 vol. % on 25-40% more than in two first years. Additionally, we conducted mapping of the seasonal changes of the water ground ice amount in the surficial soil layer in the vicinity of the edge of the retreating Northern seasonal polar cap. For this we used all the TES observations, collected during three the Martian years. The mapping was executed through the time interval in the 20°Ls in the period from the Ls =340° to the Ls=70° (Fig.2). It was found that very distinct latitudinal annulus (5°-7° in the width) with sharply increased values of the water ground ice amount arises around the edge of the seasonal cap at each stage of the cap's recession. At a transition from one stage of the spring recession to other the water ground ice annulus decreases in both the diameter and the width. The rate of the annulus displacement in direction to pole is 4°-6° during the ~40 Martian days. At that, the average water ice content within the annulus decreases gradually from an early stage of the spring recession to a later stage. After Ls=70° the ground water ice annulus has been completely vanished. To see how the evolution of the TES water ground iceannuluses is related with the evolution of the seasonal polar cap we conducted the mapping of the surface water ice (WI) annuluses on the cap's edge for the same stages of its spring recession (Fig.2)

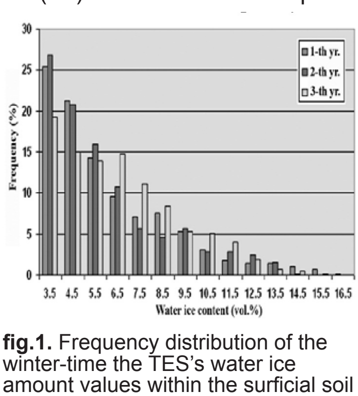

fig.1. Frequency distribution of the winter-time the TES's water ice amount values within the surficial soil layer for each of three the Martian years of the spectrometer observations.

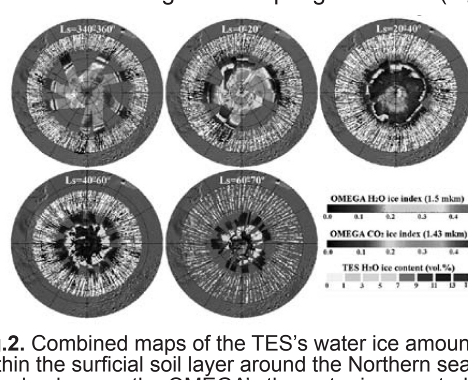

fig.2. Combined maps of the TES's water ice amount within the surficial soil layer around the Northern seasonal polar cap, the OMEGA's the water ice spectral index depth (on 1.5 μm band) on the cap's edge and the CO_2 ice cover spectral index (on 1.435 μm band), compiled for the different stages of a spring retreating of the seasonal polar cap.

based on the water ice spectral index (depth of the band 1.5 μm) from the OMEGA data. The CO2 ice band depth at 1.435 μm was used also for mapping of the seasonal CO2 ice cover. The mapping results show that during the spring movement from the Ls=0º to the Ls=70º the significant widening of the WI annulus is observing while the area of the CO2 ice cover is rapidly decreasing. At the stage of Ls=40º-60º the CO2 ice cover is remaining in the form of the separate patches while the water ice cover occupies mostly all surface of the retreating seasonal cap. At that, the rate of the WI annulus outer edges retreat during the spring duration is equal to 6.2 km per the Martian day. It is interesting that in the separate longitudinal sectors both the TES's water ground ice and the OMEGA's WI annuluses come into contact (see Fig.5). This fact let us to suppose that the water ground ice annuluses are most likely extends up to the edge of the seasonal polar cap at all stages of the seasonal cap retreating.

The HEND observations: In our study we focused on the variations of the fast neutrons flux (FN2) with effective depth of their generation ~20 cm that is equal to the seasonal thermal skin layer of the Martian soil. The measured fast neutrons flux (with energy 2.5-10 Mev) has been normalized to the flux from the Solis Plunum area (most dry place with water content 2 mass %). To convert the normalized fast neutrons flux into the water equivalent content (in mass. %) we did numerical simulations based using the MCNPX Monte Carlo code [2]. Measured normalized flux has been compared with model predictions calculated as a function of water content (see details in [3]. Best correspondence between data and simulations gave us best estimation of water content (the hydrogen water equivalent content) within the surficial soil layer up to the depth ~20 cm.

Zonally averaged meridional profiles of the water equivalent content within the surface soil in the latitude belt 0°-50°N for different seasons are shown on the Fig.3. As it well seen from the plots, the values of the water equivalent content decrease gradually from the winter to the spring's end and approach finally it's the summer-time values. Comparison between the summer-time and the winter-time zonally averaged meridional profiles of the water equivalent content (for each of the three Martian years of the HEND's observations) is presented on the Fig.4a, b. It is notable that the summer-time profiles of the water equivalent content for each of three years are very similar, while the winter-time profiles show very noticeable differences. At that, the water equivalent content difference between the winter-time profiles varies from 3 to 7 mass. %. At that, the difference of the water equivalent content between the winter and the summer seasons has been changed notably from one to other year of the observations (Fig.4c).

Summary: The joint analysis of the TES and the OMEGA data demonstrates the existence of significant seasonal variations of the water ice abundance within the active layer and on the surface of the Northern seasonal polar cap periphery during its recession. Comparing the temporal and the spatial relationship between the HTI and the WI annuli shows the close interdependence between the natures of the two annuli types. The distinctive seasonal and the inter-years variations of both the ground water ice and water equivalent content in the surficial layer of the Martian soil (to the depth from 2-10 cm up to ~20 cm) has been found based on conducted analysis of the multiyear's observations fulfilled by the TES and the HEND instruments. More results will show during the presentation.

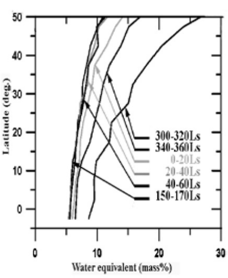

Fig.3. Zonally averaged meridional profiles of the HEND's water equivalent content in the surficial soil layer for the different seasons in the Northern hemisphere of Mars.

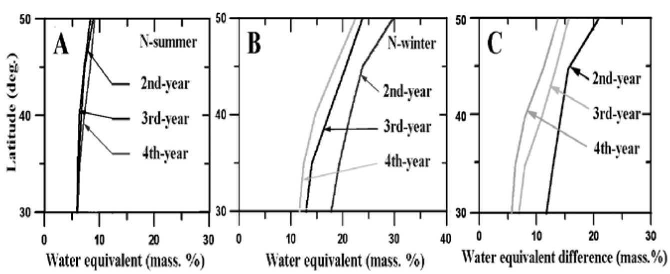

Fig.4. Zonally averaged meridional profiles of the HEND's water equivalent content in the Martian surficial soil derived from different Martian years of the detector's observations in the summer (A) and the winter (B) seasons. C – Difference of the water equivalent content values between the winter and the summer seasons as function of the latitude.

Acknowledgements: This work was partly supported by the Programme-22 of the Russian Academy of Science Presidium.

References: [1] Kuzmin R.O. et al. , (2009), JGR, 114, EO4011; [2] Waters, L.S., MCNPX User's Guide (document LA-UR-99-6058). Los Alamos National Laboratory, 1999; [3] Mitrofanov et al. , (2004), Sol. Sys. Res., 38, 4, 253-257.

CO_2-SO_2 CLATHRATE HYDRATE FORMATION ON EARLY MARS

E. Chassefière[1,2], E. Dartois[3], J.-M. Herri[4], F. Tian[5], F. Schmidt[1,2], O. Mousis[6], A. Lakhlifi[6],
[1]Univ Paris-Sud, Laboratoire IDES, UMR8148, Université Paris-Sud, Bât. 504, Orsay, F-91405, France; [2] CNRS, Orsay, F-91405, France ; [3] IAS, Université Paris-Sud, CNRS, France ; *[4] Centre SPIN , ENS des Mines de Saint-Etienne, France*, *[5] Center for Earth System Sciences, Tsinghua University, Beijing, China* ; *[6] Institut UTINAM, UMR 6213, Université de Franche-Comté & OSU THETA de Franche-Comté, France. Contact : eric.chassefiere@u-psud.fr*.

It is generally agreed that a dense CO_2-dominant atmosphere was necessary in order to keep early Mars warm and wet. However, current models have not been able to produce surface temperature higher than the freezing point of water. Sulfate minerals discovered on Mars are dated no earlier than the Hesperian, despite likely much stronger volcanic activities and more substantial release of sulfur-bearing gases into Martian atmosphere during the Noachian. Here we show that clathrate formation during the Noachian would have kept the atmospheric CO_2 pressure of early Mars below 2 bars and maintained a global average surface temperature ~230K. Because clathrates trap SO_2 more favorably than CO_2, all volcanically outgassed sulfur would have been trapped in Noachian Mars cryosphere, preventing the formation of sulfate minerals during the Noachian and inhibiting carbonates from forming at the surface in acidic water resulting from the local melting of the SO_2-rich cryosphere. The formation of sulfate minerals at the surface of Mars during the Hesperian could be the consequence of a drop of CO_2 pressure below 2 bars at the late Noachian-Hesperian transition, which would have released sulfur gases into the atmosphere from both the Noachian sulfur-rich cryosphere and still active Tharsis volcanism.

ON DETERMINATION OF THE MOMENT INERTIA AND THE RADIUS OF THE MARTIAN CORE

V.N. Zharkov, T. Gudkova,
Schmidt Institute of Physics of the Earth, B.Gruzinskaya 10, Moscow 123995, Russia. Contact: zharkov@ifz.ru

Introduction: For the first time the period of the Chandler Wobble was estimated from observations in [1]. In publications, the model values of Chandler period for a set of interior structure models of Mars are about 200-203 days. The signature at the Chandler frequency is mixed with the nearly 1/3 Mars year mass redistribution term (229 days), and may cause the polar motion signal to shift to longer periods. Accounting this fact Konopliv et al. [1] looked for a Chandler wobble of Mars with a period of 200 to 210 days and pointed out, that it might be possible to resolve the free wobble period from the spectra with about 6 years of Odyssey Doppler data. The value of Love number k_2 was significantly increased in [2].

Chandler period: If a Chandler period T_W and corresponding Love number k_2 were determined from observations, the moment of inertia of liquid Martian core $(A_cB_c)1/2\sim A_c$ could be defined from the formular

$$T_W = T_E\left(1-\frac{(A_cB_c)^{1/2}}{(AB)^{1/2}}\right)/(1-k/k_0)\ ,\ T_E=\tau_M(\alpha\beta)^{-0.5}\ ,\ \alpha=(C-A)/A\ ,\ \beta=(C-A)/B \qquad (1)$$

where T_E is the Eulerian period., τ_M is the period of the rotation of Mars; A, B, and C are the principal moments of inertia of the planet (see [3]). In all calculations of the interior models only elastic models were considered. To obtain a new constraint on an elastic model of the internal structure of the planet (in addition to the mean moment of inertia), an elastic component k_2^s (the value of Love number based on mantle elastic modulus profiles at seismic frequencies) should be extracted from the observed value of k_2(k_2=0.164±0.009 [2]). The corresponding elastic Love number is k_2^s = 0.159±0.009 [2]. Because of the inelasticity of Martian interiors, Love number k increases slowly when the frequency decreases. The period of the solar semidiurnal tidal wave, for which the value k_2 was obtained, is T_{2S}=12h19min=44340 s. We will denote the corresponding frequency as σ_S. Taking into account that the Chandler period is hundreds times larger than T_{2S}, and taking $k=k_2$=0.164 in (1), we obtain the model values of Chandler periods, which can be considered as a lower estimate. For all models the Chandler periods T_w^t (without correction for inelasticity and because of change from σ_t to σ_W) are about 204 days.

Interior structure models: The set of interior structure models with 50- and 100-km thick crust and averaged crustal density varying in the range of 2.7-3.2 g/cm³ were constructed taking into account the chemical model by Dreibus and Wänke [4] and experimental data at high pressure and temperature by Bertka and Fei [5]. The models differ in density contrast at the crust-mantle boundary and the core radius. The observational data constrain the radius of a liquid core to be within 1700-1850 km (see Figure). For 50-km thick crust its density is within 3.0-3.2 g/cm³ (an iron atomic number of mantle silicates $Fe^{2+}/((Fe^{2+}+Mg)$ multiplied by 100: Fe#20), 2.8-3.1 g/cm³ (Fe#22), 2.7-2.8 g/cm³ (Fe#25); for 100-km thick crust we have 3.2 g/cm³ (Fe#20), 3.1-3.2 g/cm³ (Fe#22), 3.0-3.1 g/cm³ (Fe#25). The parameters of the models are given in [6, 7]. For all models the weight ratio Fe/Si is about 1.7. The technique of the modelling is described in detail in [6].

The increased value of k_2 influences the choice of models (see Figure). From this Figure we see that now the model radius of Martian core is near 1800 km. If the radius of Mars is about 1800 km, there is no a perovkite layer, and the models have the ratio Fe/Si close to a chondritic one (see Table2 in [3]). The model value of a Chandler period is also increased, it is about 204 days. Thus, the range of Chandler period is narrowed and it is in the range of 204-209 days.

Conclusion: The increase of Love number k_2 has led to the increase of a model value of Martian core (about 1800 km). The composition of Mars is close to a chondritic one. Taking into account observational data and interior structure modelling, the predicted value of a Chandler period is in the range of 204-209 days.

Acknowledgements: This work was supported by Grant No. 12-02-00378 from the Russian Fund for Fundamental Research.

References: [1] Konopliv, A.S. et al. (2006) Icarus, 182, 23-50. [2] Konopliv, A.S. et al. (2011) Icarus, 211, 401-428. [3] Zharkov, V.N., and Gudkova, T.V. (2009) Planet.Space Sci., 57, 288-295. [4] Dreibus,G., and Wänke, H. (1985) Meteoritics, 20, 367-381. [5] Bertka, C. and Fei, Y. (1997) J. Geophys. Res. 102, 5251-5264. [6] Zharkov, V.N., and Gudkova, T.V. (2005) Solar System Res., 39, 343-373. [7] Zharkov, V.N. et al. (2008) PEPI, 172, 324-334.

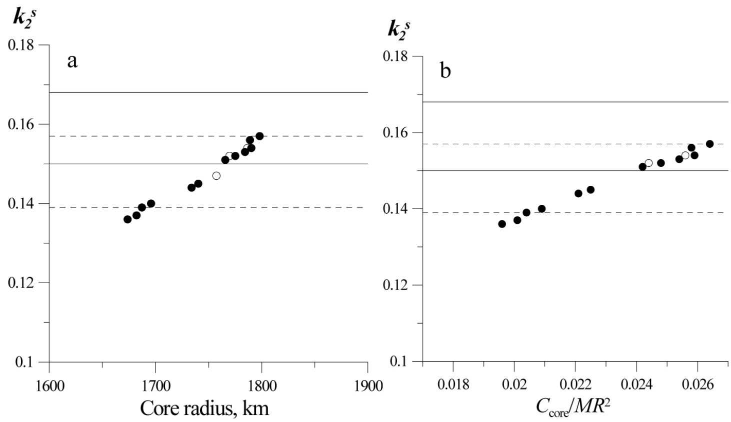

fig. The elastic Love number k_2^s as a function of the core radius (a) and the moment of inertia of the core C_{core}/MR_0^2 for a set of Martian models used for the calculation of Chandler wobble periods (the filled circles (●) are for the 50 km crust and the open circles (○) are for the 100 km crust). The horizontal lines (dashed line – data from [1] and solid line –data from [2]) show the upper and lower bound for k_2^s.

MARS/MOON IMPACT RATE RATIO: 2000/2012 COMPARISON.

B. A. Ivanov,
Institute for Dynamics of Geospheres, Russian Academy of Sciences, Leninsky Prospect 38-1, Moscow, Russia. Contact: baivanov@idg.chph.ras.ru, boris_a_ivanov@mail.ru

Introduction:

For many decades the technique of impact crater chronology is used to estimate geologic age of planetary surfaces [1]. In 2000 the Mars-moon comparison was updated in preparation of the Mars Express mission [2-4]. Since 2000 many new observations and models have been published potentially important for the correction of relatively simple estimates routinely used to compare impact cratering rates on Mars and the Moon. The presentation is aimed to check how new data affects the interplanetary comparison technique.

Population of planetary crossing objects:

The essential part of the bombardment rate comparison is the estimate of a number of asteroid and comets having non-zero probability to collide a planet. In the early pioneer paper [4] orbits of 20 known planetary crossing objects have been used to estimate the cratering rate. In 2000 the Minor Planet Center catalogue of osculating (astorb.dat file) listed about 1000 Mars crossers with H<18. The Öpik formulas, refined by Wetherill for the general case of elliptic orbits for both target and projectile, are applied to all bodies in the "astorb.dat" file resulted in calculation of impact probability and velocity [2] with some correction to observational incompleteness. In July 2012 the "astorb.dat" offers ~6000 small bodies (H<18) with asteroid-like orbits (T_J>3) and ~340 bodies with comet-like orbits (T_J<3) having non-zero Öpik-Wetherill (ÖW) probabilities of the collision with Mars. We use osculating orbits under assumption that the momentary snapshot of orbital parameters is a proxy to the long-term orbital population in a state of slow chaotic orbital evolution. The average impact ÖW probability of a Mars crosser is about $2*10^{-10}$ 1/yr. Hence the body should occupy the same orbit for ~5 Gyr to collide Mars. Celestial mechanics modeling reveals much shorter time scale of planetary crossers orbital evolution, so many "generations" of bodies of a given size at a given orbit will change before one of them create an impact crater. With this philosophy we use osculating orbits to estimate the impact probability. Table 1 compares some numbers resulted from estimates of ÖW probabilities. Values for H<16 are closer to the observational completeness, while values for H<18 illustrate the effect of more numerous (but incomplete – especially for Mars-crossers) observations.

	the Moon (Earth) crossers		Mars-crossers	
	H<18	H<16	H<18	H<16
asteroid-like orbits T_J > 3				
N	458	82	5774	1416
P_{col}, yr^{-1}	0.16×10^{-9}	0.14×10^{-9}	0.23×10^{-9}	0.17×10^{-9}
$<U_{imp}>$	17.0	19.0	9.3	10.0
JFComet-like orbits 2< T_J <3				
N (% of total)	97 (17%)	18 (25%)	336 (5.5%)	83 (5.5%)
P_{col}, yr^{-1}	0.051×10^{-9}	0.045×10^{-9}	0.07×10^{-9}	0.06×10^{-9}
$<U_{imp}>$	23.4	25.5	17.3	16.7

table 1. Probability and average impact (pre-atmospheric) velocity on the Moon and Mars

In total we conclude that in limits of our assumptions (1) the percentage of comet-like orbits (higher impact velocities) on the Moon is about 25% to 20%, while on Mars this number is factor of ~2 less; (2) for the modern Mars orbit (e=0.094) the "bolide ratio" (the ratio of impact number per unit area per unit time) is about R_b=5.5 in comparison with 2000 estimates of R_b=4.9 [3]; (3) the average impact velocity for asteroid-like objects on the moon increases to ~19 km/s in comparison with 16.1 km/s in 2000 estimates.

Scaling laws: The conversion of the projectile size into crater rim diameter is provided with a set of rules known as impact scaling laws. Our preliminary resent results [5] open the new question of scaling laws for real rock media with dry friction. In the standard to date scaling law the effect of the impact velocity increase is described in terms of slowly decreased impact coupling efficiency and of the porosity effect. In [5] we show that thermal softening (decrease of the dry friction with shock heating) results in a scaling rule in terms of D_{rim}/D_{proj} ratio intermediate relative to the common scaling laws for "porous" and "non-porous" media. The idea should be tested more. If confirmed, the result will be a slightly larger scaled crater size on the Moon v.s. Mars, where the average impact velocity is twice smaller (see Table 1). The effect tends to decrease somewhat the estimated Martian cratering rate.

Mars Reconnaissance Orbiter (MRO) observations: MRO experiments (HiRISE and CTX) give an outstanding opportunity to estimate modern impact crater formation rate on Mars comparing images before and after impact. To date around 200 "new" impact cites (impact craters and crater clusters) are found with well bounded formation time [6, 7]. Previously [6] the impact cratering rate was estimated by dividing the number of "new" craters by the area and the time period of observations. An example of this estimate is shown in Fig. 1 for a subset of "new" craters formed in dusty areas during 4 years. With a lot of possible bias mechanisms, the number of craters in the upper diameter bins (22 m < D < 44 m) the observed impact rate is comparable with isochrones, transferred from the lunar crater chronology ([3, 6] and this work). The recent data based on the discovery rate based solely on CTX/CTX image comparison (with crater size improved with HiRISE images) gives factor of 2 to 3 lower cratering rate in the upper diameter bins [8] (Fig. 1). Besides possible reasons for this discrepancy, listed by authors of [8], it demands the rethinking of each step in the technique of inter-planetary comparison.

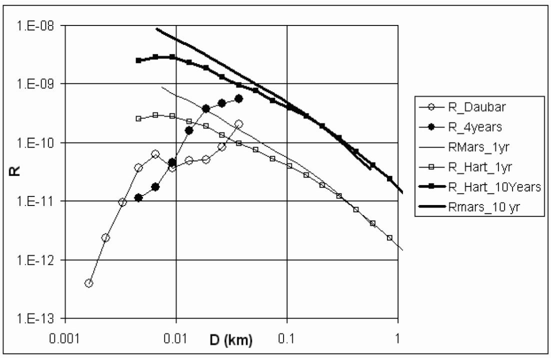

fig. 1. Relative crater surface density (R-plot) on Mars for 1 year and 10 years exposition time estimated in this work (thin and thick curves, no correction for atmospheric shielding), by W. Hartmann [6] (curves with squares, simple atmospheric shielding), and from HiRise/CTX MRO observations: black circles – 4 years subset, open circles- 40 CTX/CTX discovery cases for overlapping imaged area only [8] (effective ~6.5 year of exposition). Error bars are not shown for the figure clarity.

Discussion and Outlook: It is too early to make a solid conclusion about changes occurred in Mars/moon cratering rate comparison since year 2000. Pure updating of planetary-crosser's orbit list of crossers does not change the Mars/moon impact ratio dramatically (despite ~6 fold increase in the number of known objects). Future discussion should include possible difference in crater-forming projectile properties. Small crater clusters found on Mars witness in favor of the presence of 10% to 20% low density (high porosity?) projectiles. The percentage looks larger than orbital predictions for projectiles in comet-like orbits (Table 1). For NEA the comet-like orbits may be typical for 20% to 25% of crater-forming projectiles (Table 1). However comet-connected (by composition and evolution history) small bodies may occupy both asteroid-like and comet-like orbits [10]. Standard Mars/moon comparisons [3, 6] are based on orbital data for large (>1 km) asteroids, while available data about modern impact rate are for small craters (<50 m in diameter on Mars and <8 m in diameter on the Moon [11]). Two additional questions concern (1) the difference in mechanical properties of regolith on the dry Moon and possibly ice-saturated Martian soil, and (2) the efficiency of lunar impacts of low-density objects assumed from Martian strewn fields. Definitely new observational data demands new supportive research and modeling.

References: [1] Hartmann, W. K., R. G. Strom, S. J. Weidenschilling, et al. Chronology of planetary volcanism by comparative studies of planetary craters, in Basaltic Volcanism on the Terrestrial Planets, pp. 1050-1127, Pergamon Press, Elmsford NY, 1981. [2] Neukum, G., B. A. Ivanov, and W. K. Hartmann, Cratering Records in the Inner Solar System in Relation to the Lunar Reference System, in Chronology and Evolution of Mars, vol. 12, edited by R. Kallenbach, J. Griss and W. K. Hartmann, pp. 55-86, Kluwer Academic Press, Dordrech-Boston-London, 2001. [3] Ivanov, B. A., Mars/Moon cratering rate ratio estimates, ibid, pp. 87-104. [4] Hartmann, W. K., and G. Neukum, Cratering chronology and evolution of Mars, ibid, pp. 165–194. [5] Ivanov B. and D. Kamyshenkov, Impact cratering: scaling law and thermal softening, LPSC 43, abstract #1407, 2012. [6] Hartmann, W., Martian cratering 8: Isochron refinement and the chronology of Mars. Icarus 174: 294–320, 2005. [7] Daubar et al., LPSC 41, abstract #1978, 2010. [8] Daubar et al. The current Martian cratering rate, submitted to Icarus, 2012. [9] Ivanov, B., H. Melosh and A. McEwen, New impact craters and meteoroid densities on Mars, in EPSC-DPS Joint Meeting 2011, abs. #786, 2011. [10] DeMeo, F., and R. P. Binzel, Comets in the near-Earth object population, Icarus, 194, 436-449, 2008. [11] Daubar, I. J., A. S. McEwen, S. Byrne, C. M. Dundas, A. L. Keska, G. L. Amaya, M. Kennedy, and M. S. Robinson, New Craters on Mars and the Moon, LPSC 42, abstract # 2232, 2011.

EVIDENCE FOR EFFUSIVE MUD VOLCANISM IN UTOPIA PLANITIA ON MARS.

M.A. Ivanov[1,2], H. Hiesinger[2], G. Erkeling[2], and D. Reiss[2],
[1]Vernadsky Inst., Moscow; [2] Wilhelms-Universität, Münster, Germany.
Contact: mikhail_ivanov@brown.edu

Introduction: Utopia Planitia is one of the largest impact basins on Mars [1,2] that is ~2000 km in diameter but only 1.5-2 km deep. The larger portion of the basin floor is covered by the Hesperian-age Vastitas Borealis Formation (VBF), materials of which may indicate existence of an ocean in the geological past of Mars. SW edge of Utopia Planitia hosts occurrences of the thumbprint terrain (TPT) [3,4], the largest exposure of which is in Isidis Planitia that we recently mapped in detail [5]. One of the goals of our study is the comparison of the geological settings of TPT in both regions that can help to constrain the origin of this terrain. The area of our study is between 20-45°N and 100-120°E and we mapped this region using all available imagery data sets. Here we describe the most important units and structures that form the regional geological context for TPT in Utopia Planitia.

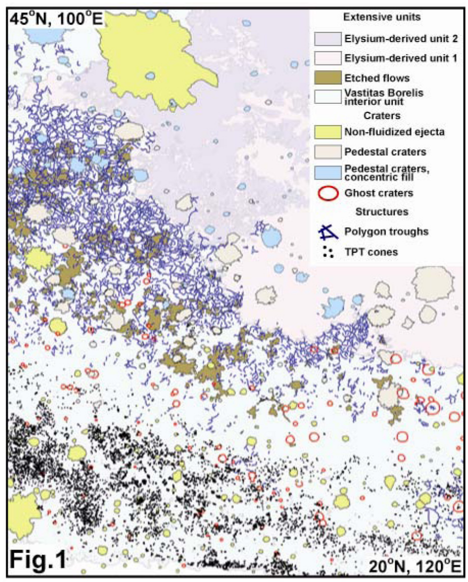

Fig.1

Major units and structures in SW Utopia: Extensive material units: Vastitas Borealis interior unit [6] occupies the largest portion of our study area (Fig. 1). Vast plains that appear morphologically smooth at the resolution of the CTX images make up the surface of the unit. Its southern margin consists of numerous lobes that extend southward and overlap the surrounding terrains. The daytime THEMIS IR data show that the peripheral portions of the unit have uniform and higher brightness temperature but large darker spots are seen closer to the center of Utopia. Materials derived from the Elysium rise are concentrated in the center of the Utopia basin, superpose the surface of the interior unit, and have been formed by volcanic and fluvial activity [6]. The stratigraphically higher deposits in this region are related to flows from Tinjar Vallis and have bright surface with numerous short ridges and very sinuous/digitate boundary. The size-frequency distribution (SFD) of impact craters on the surface of these materials corresponds to the absolute model age of ~1.4 Ga.

Impact craters: Impact craters in Utopia Planitia show a variety of morphologies likely related to the target properties and degree of degradation. The most degraded craters [7] appear as very shallow depressions surrounded by concentric graben [8-10]. In our study area there are 90 of these structures in the diameter range from ~20 to ~35 km that are distributed apparently randomly in the area of the interior unit (Fig. 1).

Morphology of ejecta from prominent craters in Utopia is changed as a function of the distance from the basin center. In the peripheral zone of the basin (Fig. 1) the ejecta of craters in all visible range of diameters have usual morphology but in places show broad lobes suggesting some degree of fluidization during impact [11-13]. Closer to the center of Utopia (at angular distance <~20 degree from the center, Fig. 1), most of the impact structures > ~1 km in diameter are pedestal-like craters, the formation of which seems to require the presence of ice in the target [14-18].

Giant polygons: The polygonal terrain in Utopia Planitia [8,19,6] is formed by intersecting of broad and shallow troughs that cut the surface of the interior unit. Areas of polygonal terrains in Utopia occur circumferentially around the flat central portion of the basin [8]. In our study area the onset of the polygons approximately coincides with the transition from the common to the pedestal craters (Fig. 1).

Structures of TPT: Numerous small cone-like structures with a summit pit characterize TPT in Isidis and Utopia Planitiae [20,21]. The main difference of TPT in Utopia is that the cones in this region usually form broad clusters and are not arranged in long, curvilinear, and nested chains as it often occurs in Isidis Planitia. The absolute majority of the cones in Utopia are concentrated within a broad (200-300 km) zone near the periphery of the basin and almost do not occur in the zone of polygons (Fig. 1).

Flows: Lobe- and flow-like features (tens of km wide, many tens of km long) are seen in the high-resolution images (e.g., CTX, THEMIS-VIS, Fig. 2a) within the zone of polygons. In many cases they correspond to the darker spots seen in the daytime THEMIS IR data. The flows usually emanate from long and narrow fractures and produce the classical pattern of fissure eruptions. In many places they consist of several stacked layers and superpose most of the polygon troughs.

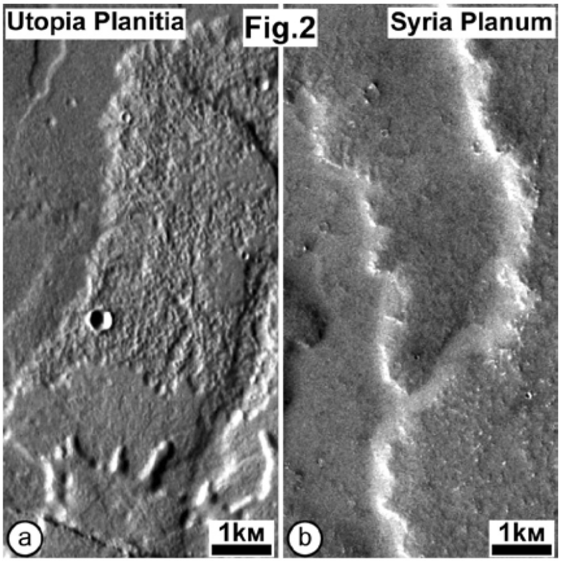

The most important characteristic of the flows is that they are significantly more eroded than the underlying plains (Fig. 2a). The marginal portions of the flows are etched and scalloped and the smoother surface in their central portions displays collapse pits (Fig. 2a). The uppermost layers of the stacked flows sometimes consists of isolated, flat-topped, and pitted mesas with very sinuous boundaries. Such morphologic characteristics of the etched flows in Utopia Planitia strongly distinguish them from the usual lava flows (Fig. 2b).

Discussion: The oldest features detected in the area of our study are the ghost craters. In contrast to all younger features that form broad concentric zones around the center of Utopia Planitia, the ghost craters are apparently randomly distributed within the interior unit (Fig. 1). This suggests that 1) the craters likely represent remnants of the background population that existed before emplacement of the interior unit (VBF) and 2) formation of the unit was not able to erase completely the older craters with diameters ~20 km and larger. The size-frequency distribution of the ghost craters corresponds to the absolute model age of ~3.6 Ga, which likely represents the lower time limit for VBF. The population of larger impact craters (1-20 km) superposed on the surface of the interior unit corresponds to the absolute model age of ~3.5 Ga. Crater counts on the etched flows that superpose the surface of VBF indicate the age of emplacement of the flows to be ~3.2 Ga. This age likely represents the upper time limit for VBF.

The etched flows play an important role in understanding of the nature and mode of emplacement of VBF. The source areas of the flows and their pattern of emplacement strongly indicate that the flows formed due to effusive eruptions. Morphology of the flows, however, is strongly different from that of typical lava flows (Fig. 2). Three important features characterize the flows: (1) selective erosion of the flow materials without evidence of erosion of the adjacent plains, (2) abundant rimless pits that most likely are collapse structures, (3) mesas that are bordered by very sinuous cliffs and probably represent isolated remnants of previous contiguous layer(s).

All these features are consistent with and indicative of the presence of volatiles whose escape upon emplacement of the flows would cause their partial collapse and formation of the observed unusual morphologies. In no case, however, features related to explosive activity were met in association with the etched flows in Utopia Planitia and emplacement of gas-saturated lava flows under very low atmospheric pressure on Mars is extremely unlikely [22]. Thus, we interpret the etched flows as evidence for widespread (Fig. 1) effusive mud volcanism in Utopia Planitia.

The etched flows similar to those in Utopia were not detected on the floor of Isidis Planitia [5] where the characteristic features of TPT (cones) are very abundant [20]. In Utopia Planitia, the TPT cones are concentrated away from the zone where the etched flows occur (Fig. 1). Thus, the possible explanation of formation of the cones by the processes related to mud volcanism [23,24] is poorly consistent with the observations.

The occurrences of the mud flows in SW Utopia probably mark approximate extension of a subsurface reservoir of water/ice-rich materials that may represent remnants of the former and more extensive body of water/ice in the northern lowlands of Mars [25-27]. Eruption of the mud flows require the presence in the reservoir of either liquid materials, or their liquefaction under thermal influence of the Elysium magmatic center, or squeezing of the solid-state ice-rich material under the load of the late Amazonian materials derived from the Elysium rise. The last hypothesis is not consistent with the modal absolute age of emplacement of the mud flows (~3.2 Ga). Although the time of onset of magmatic activity in Elysium is unknown, the areal distribution of the mud flows follows the pattern of concentric distribution typical of other units/structures in the Utopia basin unrelated to volcanism in Elysium. This does not favor the hypothesis of triggering of the mud volcanism in Utopia by the thermal pulses from the Elysium center. Thus, we prefer to link emplacement of the mud flows with the final episodes of evolution of a standing body of water that was responsible to formation of VBF. In this scenario, which is consistent with the age estimates and the general pattern of the spatial distribution of features in Utopia Planitia, the flows may represent the last portions of still liquid material [28] squeezed to the surface from the residual reservoir under the pressure of growing bodies of ice.

References: 1) McGill, G.E., JGR, 94, 2753, 1989; 2) Smith, D.E. et al., Science, 284, 1495, 1999; 3) Grizzaffi, P. and P.H. Schultz, Icarus, 77, 358, 1989; 4) Lockwood, J.F., et al, LPSC-23,795, 1992; 5) Ivanov M.A. et al., Icarus, 2012; 6) Tanaka, K.L. et al., USGS Map 2888, 2005; 7) McGill, G.E., GRL, 13, 705, 1986; 8) McGill, G.E. and L.S. Hills, JGR, 97, 2633, 1992; 9) Buczkowski, D.L. and G.E. McGill, GRL, 29, 2002; 10) Buczkowski, D.L. and M.L. Cooke, JGR, 109, 2004; 11) Head, J. W. and R. Roth, LSI, 50, 1976; 12) Carr, M.H. et al., JGR, 82, 4055, 1977; 13) Mouginis-Mark, P. JGR, 84, 8011, 1979; 14) Mouginis-Mark, P.J., Icarus, 71, 268, 1987; 15) Schultz, P.H., and A.B Lutz, Icarus, 73, 41, 1988; 16) Wrobell, K.,P.et al., MPS 41, 1539, 2006; 17) Kadish, S.J. et al., GRL, 35, 2008; 18) Kadish, S.J. et al., JGR, 114, 2009; 19) Hiesinger, H. and J.W. Head, JGR, 105, 11999, 2000; 20) Hielscher, F.J. et al., LPSC-41 #2394, 2010; 21) Ghent, R.R., et al., Icarus, 217, 169, 2012; 22) Wilson, L. and J. W. Head, Rev. Geoph., 32, 221, 1994; 23) Tanaka, K.L., JGR, 102, 4131, 1997; 24) Skinner, J.A. and A. Mazzini, MPAG 26, 1866, 2009; 25) Parker, T.J. et al., Icarus, 82, 111, 1989; 26) Parker, T.J. et al., JGR, 98, 11061, 1993; 27) Carr, M. H., and J. W. Head, JGR, 108, 2003; 28) Kreslavsky, M.A. and J.W. Head, JGR, 107, 2002.

THE MARTIAN PLANETARY BOUNDARY LAYER

Luis Vázquez,
Departamento de Matemática AplicadaFacultad de Informática, Universidad Complutense de Madrid / 28040-Madrid (Spain), lvazquez@fdi.ucm.es, www.fdi.ucm.es/profesor/lvazquez, www.meiga-metnet.org

We present a thermodynamic characterization of the Martian Planetary Boundary Layer (PBL) for specific selected Sols of Pathfinder and Viking missions. The PBL can be defined as that part of the atmosphere that is directly influenced by the presence of the planet surface, and responds to surface forcing with a time scale of 1 hr or less. Belonging to the PBL, the Surface Layer (SL) is the region at the bottom of the PBL where the sharpest variations in meteorological magnitudes take place. Consequently, so do the most significant exchanges of momentum, heat, and mass with the regolith. On the other hand, the Convective Mixed Layer (CML) is one of the three layers into which the convective PBL can be divided, with the SL and the Entrainment Zone lying respectively beneath and above it. It is characterized by an intense vertical mixing that tends to maintain variables such as potential temperature and humidity nearly constant with height.

STUDY OF MARTIAN ATMOSPHERE IN THE SPICAM IR EXPERIMENT ON MARS-EXPRESS

A. Fedorova[1,2], O. Korablev[1,2], A.Trokhimovsky[1,2], L.Maltagliati[3,4], S.Guslyakova[1,2], F. Montmessin[3], J.L. Bertaux[3], A.Reberac[3] and the SPICAM team, *[1]Space Research Institute, Moscow, Russia; [2]Moscow Institute of Physics and Technology (MIPT), 9 Institutsky dr., 141700 Dolgoprudny, Moscow Region, Russia; [3]LATMOS, Verrières-le-Buisson, France; LESIA, OBSPM, Meudon, France. Contact: fedorova@iki.rssi.ru*

Introduction:

SPICAM a light-weight 4.8 kg UV-IR dual spectrometer on board Mars Express orbiter is dedicated primarily to the study of the atmosphere and ionosphere of Mars. The IR channel of SPICAM is a separate AOTF spectrometer integrated in the optical block of SPICAM along with the UV spectrometer. In this spectrometer for the first time in planetary research the technology of an acousto-optic tuneable filter (AOTF) has been applied that allowed unprecedented mass reduction for such an instrument: 0.7 kg. The spectral range of SPICAM IR varies from 1 to 1.7 μm with the spectral resolution of ~3.5 cm^{-1} (0.45-0.85 nm) that corresponds to spectral power ~2200 near 1.35 μm. The SPICAM IR has been operated from January 2004 on orbit of Mars and a wide flexibility of the spectrometer allows to study the vertical structure and integrated abundance of atmospheric components.

In addition to CO_2 cycle the water and dust cycles are key cycles in the determination of current Martian climate. Using the 1.38 μm H_2O absorption band SPICAM studies the interannual variability and vertical distribution of water during the four Martian Years, including the detection of water supersaturation in the middle atmopshere and understanding of the chemical coupling H_2O-O_3 with simultaneous observations of ozone. The emission of O2 (a^1D_g) at 1.27 mm, produced in the process of photodissociation of ozone is readily detected by the SPICAM IR, allowing to measure Mars ozone in addition to UV measurements. The comparison of the O_2 dayglow observations with photochemical modeling allows to constrain chemical constants. The recent observations of the oxygen nightglow in the same band by SPICAM give an access to poorly understood atmospheric circulation in the polar region. Strongly radiatively active and highly variable Martian dust is a meteorologically important component of atmosphere. SPICAM allows to study the vertical distribution of aerosol optical properties over the several years, in particular bimodal distribution has been detected recently.

We present the overview of the scientific results obtained by SPICAM IR from January 2004 Ls 330 (MY26) to May 2012 Ls 275 (MY31) covering the almost four Martian years.

References

[1] Bertaux et al. (2006) JGR, 111, E10S90, doi:10.1029/2006JE002690, 2006.
[2] Korablev et al. (2006) JGR, 111, E09S03, doi:10.1029/2006JE002696, 2006.

ORDERING AND TRANSPORT PHENOMENA IN SYSTEMS OF CHARGED DUST: FROM GROUND TO MICROGRAVITY EXPERIMENTS.

O. F. Petrov[1], O. S. Vaulina[1] and V. E. Fortov[1],
[1]Joint Institute for High
Temperatures RAS, Izhorskaya 13 bld.2, Moscow, 125412, Russia.
Contact: ofpetrov@ihed.ras.ru

Transport phenomena in dissipative systems of interacting particles are of significant interest in various fields of science and technology (plasma physics, medical industry, physics of polymers, etc.). In particular, viscosity is a fundamental parameter that reflects the nature of the inter-particle potentials and the phase state of the system.

Experimental study of the kinematic viscosity has been carried out for dust particles of different sizes in weakly ionized plasma. Results of measurements of viscosity for weakly correlated dusty-plasma systems in a wide range of coupling parameters are presented. Comparison of the measured viscosity constants with the theoretical estimations and the numerical data are presented.

Dust structures are studied experimentally in DC glow discharge plasmas in mixtures of “light” and “heavy” gases (helium and krypton). Characteristic feature of the dusty plasma structures observed was the formation of linear, chain-like dust structures with strong grain–grain interaction in the ion drift direction. The results of simulations performed for a mixture containing a “heavy”, easily ionized gas suggest a strong effect of gas composition on dust structure formation in discharge plasmas.

For confinement and investigation of strongly coupled charged dust particles, we propose to use a trap based on the known possibility of the levitation of diamagnetic bodies in a nonuniform steady-state magnetic field. The structures formation from large number (~104) of charged diamagnetic dust particles in a cusp magnetic trap under microgravity conditions has been experimentally studied. Using the data of the videorecording of the positions of the particles in the magnetic trap, the magnetic susceptibility and charge of the particles have been estimated and the period of the oscillations of the cloud of the particles, as well as the damping rate of oscillations, has been determined.

An original method for the simultaneous recovery of the interparticle interaction potential and the electrostatic confining potential in plasma-dust systems has been developed. An experimental study of dust particle’s dynamics was carried out for cluster systems, relaxing to their equilibrium state after an external influence on the system. An influence of the external perturbations on the interaction potential profile between dust particles in plasma was analyzed. It was found that the pair potential profile, restored for the perturbed and equilibrium systems, has a different spatial asymptotics.

This work was supported by the Research Program of the Presidium of the Russian Academy of Sciences “Matter under High Energy Densities” and by the Russian Foundation for Basic Research, Project No. 10-02-01428.

THE LUNAR SURFACE: A DUSTY PLASMA LABORATORY

M. Horanyi,
Colorado Center for Lunar Dust and Atmospheric Studies, Laboratory for Atmospheric and Space Physics, and Department of Physics, University of Colorado, Boulder, CO 80309, Contact: horanyi@colorado.edu

Introduction: The Colorado Center for Lunar Dust and Atmospheric Studies (CCLDAS) is one of the seven US teams of NASA's Lunar Science Institute. CCLDAS is focused on experimental investigations of the lunar surface, including dusty plasma and impact processes, the origins of the lunar atmosphere, and the development of new instrument concepts with a complementary program of education and community development. This presentation will show our most recent results: a) the completion of a 3 MV dust accelerator; b) the status of the Lunar Dust Experiment (LDEX) instrument development for the LADEE mission; c) small-scale supporting laboratory experiments; and d) the development of new instrument concepts for surface exploration of airless bodies.

The dust accelerator facility: A 3 MV Pelletron has been installed that contains a dust source, feeding positively charged particles into the large accelerator. The facility is used for impact experiments to study the production of secondary particles, plasma and neutrals, crater formation, and for the testing and calibration of dedicated dust instruments, for example.

The Lunar Dust Experiment (LDEX): is a dust detector instrument designed and built for the Lunar Atmosphere and Dust Environment Explorer (LADEE) mission. LDEX will measure the density and mass of dust particles. It is sensitive to individual impacts by particles > 0.25 micron in radius. Smaller particles can be detected in a cumulative mode, if present in sufficient quantities. LDEX is the first dust detector instrument optimized for operation while exposed to the UV environment above the sunlit lunar surface.

Small-scale laboratory experiments: These experiments are dedicated to the investigations of charging and mobilization of dust on surfaces. The effects of UV radiation, and the solar wind plasma flow. The most recent results address the effects of surface magnetic fields on the generation of intense, localized electric fields that are likely to play an important role in dust transport. The Moon does not have a global magnetic field, unlike the Earth, rather it has strong crustal magnetic anomalies. Data from Lunar Prospector (LP) and SELENE (Kaguya) observed strong interactions be-tween the solar wind and these localized magnetic fields. We use a horseshoe permanent magnet as an analogue to create a magnetic dipole field above an insulating surface in plasma.

New instrument concepts: The flux, direction and size-distribution of interstellar dust can be used to test our models about the large-scale structure of the heliospheric magnetic field, and its temporal variability with solar cycle. The measurements of the speed, composition and size distribution of the recently discovered, solar wind-entrained nanodust particles hold the key to understand their effects on the dynamics and composition of the solar wind plasma. The recently developed Dust Telescope (DT) instrument will be discussed, including its capabilities to measure the mass, charge, velocity vector, chemical and isotopic composition of the impacting dust particles, enabling the unambiguous identification of interstellar and interplanetary particles of various origin. As part of a landing package DT could be used as a modern version of the Lunar Ejecta and Meteorite experiment (LEAM) of Apollo 17. DT could be used to detect the putative population of the slow-moving highly charged lunar dust particles, in addition to the flux and composition of interplanetary and interstellar dust bombarding the lunar surface.

References: http://lasp.colorado.edu/ccldas

DUST IN PLASMA, DUSTY PLASMA AND PLASMA IN LUNAR ENVIRONMENT.

B. Atamaniuk[1], A.S. Volokitin[2],
[1]Space Research Centre of the Polish Academy of Sciences, Bartycka 18A,00-716 Warsaw, Poland; [2] Space Research Institute RAS, 84/32 Profsoyuznaya Str, Moscow, Russia, Contact: batama@cbk.waw.pl

Investigation of electromagnetic and plasma environment around the lunar surface and the near-moon space is of great importance from the viewpoints of science, technology, and manned explorations in the near future.

One of the remarkable features of the lunar environment is charging up of the surface of the moon. However, accurate estimation of the lunar surface potential has been difficult.

Plasma, photons, micrometeorites and energetic particles constantly bombard the lunar surface, producing a tenuous exosphere and a dynamic wake region, and charging the surface to electrostatic potentials reaching kilovolts, producing surface electric fields large enough to affect lunar ions and dust. Meanwhile, plasma interacts directly with crustal magnetic fields, producing perhaps the smallest magnetospheres in the solar system.

Lunar dust can exhibit unusual behavior due to electron photoemission via solar-UV radiation the lunar surface represents complex plasma (“dusty plasma”). The dust grains and lunar surface are electrostatically charged by the Moon’s interaction with the local plasma environment and the photoemission of electrons due to solar UV and X-rays. This effect causes the like-charged surface and dust particles to repel each other, and creates a near-surface electric field. Lunar dust must be treated as dusty plasma.

Using analytic (kinetic (Vlasov) and magnetohydrodynamic theory) and numerical modeling we show physical processes related to levitation and transport dusty plasma on the Moon. These dust grains could affect the lunar environment for radio wave and plasma diagnostics and interfere with exploration activities.

This research is supported by grant O N517 418440

POSSIBLE ORIGIN OF THE FINE DUST IN LUNAR EXOSPHERE.

V.V. Shevchenko,
Sternberg Astronomical Institute, Moscow State University, Universitetskij pr., 13, Moscow, 19991 Russia. Contact: vladislav_shevch@mail.ru

Introduction:

Images taken by Surveyors 5, 6, & 7 have indicated the presence of lofted dust clouds along with estimate for their spatial extent and density [1]. According to model constructed by Kuntz et al. [2] shadowed regions on the lunar surface acquire a negative potential. In particular, shadowed craters can have a negative potential with respect to the surrounding lunar regolith in sunlight, especially near the terminator regions. Here authors analyze the motion of a positively charged lunar dust grain in the presence of a shadowed crater at a negative potential in vacuum. Previous models describing the transport of charged lunar dust close to the surface have typically been limited to one-dimensional motion in the vertical direction, e.g. electrostatic levitation; however, the electric fields in the vicinity of shadowed craters will also have significant components in the horizontal directions. Authors propose a model that includes both the horizontal and vertical motion of charged dust grains near shadowed craters. They show that the dust grains execute oscillatory trajectories and present an expression for the period of oscillation drawing an analogy to the motion of a pendulum. One of the unresolved enigmas from the Apollo era is the existence and characteristics of highly electrically charged dust floating above the lunar surface. Potential evidence for this hypothesized phenomenon came from the Lunar Ejecta and Meteorites (LEAM) experiment on Apollo 17. This instrument reported up to hundreds of impact events per day around local sunrise and sunset whereas the expected impact rate of interplanetary dust particles was only a few impact detections per day. Recently, new arguments were raised that the signals recorded by LEAM may be caused by interferences from heater current switching which occurred most frequently near sunrise and sunset [3].

Surveyor 6 Images of Horizon Glow: Surveyors 5, 6, and 7 captured the first evidence of dust transport on airless bodies with their television cameras [1]. In November 1967 the Surveyor 6 probe soft-landed in Sinus Medii (0.49 deg in latitude and 1.40 deg w longitude) and studied the soil, took pictures and obtained other important data characterizing the lunar environment in advance of the manned Apollo missions. Among its data booty was a curious photograph of a glowing western horizon at sunset. Further study revealed that the pictures captured the glow of electrostatically-levitating moon dust. The glow was seen by additional Surveyor landers. Fig. 1 shows an image was taken by the Surveyor 6 on November 24, 1967, one hour after sunset.

fig. 1

This was interpreted to be forward scattered light from a cloud of dust particles with radii about 5 μm, vertical dimension ~3 - 30 cm, horizontal dimension ~14 m, and about 50 grains on cm^{-2} [1, 4]. The very small size of particles is an important condition of existence of a horizontal levitation of a lunar dust. The term lunar soil is often used interchangeably with lunar regolith but typically refers to only the finer fraction of regolith, that which is composed of grains one cm in diameter or less. Lunar regolith is composed in part of rock and mineral fragments that were broken apart from underlying bedrock by the impact of meteorites. A rock composed of bits and pieces of older rocks is called a breccia. Other lunar dust particles are agglutinates. Agglutinates are small glassy breccias formed when a micrometeorite strikes the lunar regolith. Micro meteorites are a millimeter or less in size. When a micrometeorite strikes the lunar surface, some of the impacted regolith melts and some doesn't, so the product is a glass with mineral and rock fragments entrained. The glass often shows flow features. Agglutinates are typically tens of micrometers to a few millimeters in size. Lunar dust generally connotes even finer materials than lunar soil. There is no official definition of what size fraction constitutes “dust”, some place the cutoff at less than 50 - 70 micrometres in diameter. So, it’s needed to find the origin of very fine dust particles in lunar environment.

Possible Source of Regolith Fine Fraction: Surveyor 6 spacecraft landed about 50 km to the west-southwest of crater Bruce which has diameter 6.7 km and depth about 1.3 km. Fig. 2 shows existence of avalanching and of other downslope movement of material is clearly visible on the inner walls of the crater. According to spectral analysis the iron content in the material of fresh outcrops is an essential characteristic of lunar material of the type. The spectral analysis made on the basis Clementine image (LPI Clementine Mapping Project).

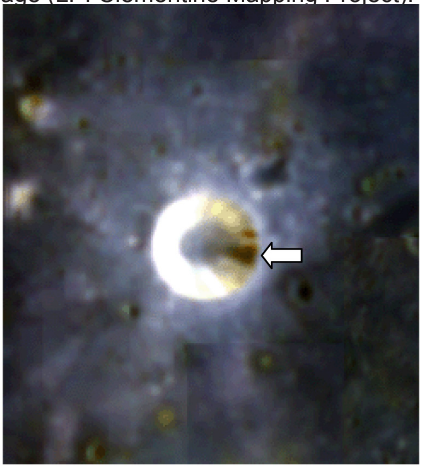

fig. 2

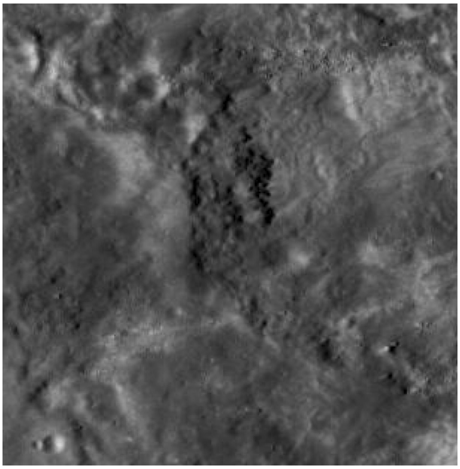

fig. 3

Further study is required for issues such as the very appearance of fine soil in the deep subsurface layers, and the mechanism of formation of the fine fraction, not on the surface as a result of space weathering, but at a depth of several hundred meters. Fig. 3 represents the same slope surface with resolution about 0.5 m per pixel (LRO/LROC image, Courtesy NASA). Wilcox et al. [5] studied the simulated dependence of the structural features of the soil on iron abundance. This study revealed that the iron abundance and particle size of the fine fraction correlate with each other. According to the results presented, several formations are characterized with iron enriched deposits, with the FeO abundance in the range of 17 % to 21 %. The average simulated value of particle size in this case is 6–8 μm. Application of these data to the abnormalities of lunar iron enriched material could explain high fluidity of the slope material, demonstrated in Fig. 3 [6].

Conclusions: Avalanching appears to be a major means of the current erosion on steep lunar slopes. Many features of the surface structures occur where the wall is bowed outward and probably represent slump deposits where portions of the crater wall have collapsed into the crater. Soil inner friction angle is not more than 20^o for upper layer matter. Bulk density of the surface soil is about 1.5 g/cm^3 in the case. The age of the observed lunar slope degradation is very young. It’s possible the process is present. So, subsurface fine dust may be served as permanent source of dust cloud created horizon glow.

Acknowledgements:
This research is supported by joint RFBR grant 11-02-90440-Ukr_f_a.

References:

[1] Rennilson, J. J., Criswell, D. R., 1974. Surveyor observations of lunar horizon-glow. The Moon 10(2), 121-142, doi:10.1007/BF00655715. [2] Kuntz, K. D.; Collier, M. R.; Stubbs, T. J.; Farrell, W. M. The Lunar Dust Pendulum. American Geophysical Union, Fall Meeting 2011, abstract #P13D-1710. [3] O’Brien, B., 2011, Planet. Space Sci., doi:10.1016/j.pss.2011.04.016. [4] Nitter, T., et al., IEEE Trans. Plasma Sci., **22,** 1994. [5] Wilcox, B.B., Lucey, P.G., and Gillis, J.J., Mapping Iron in the Lunar Mare: An Improved Approach, J. Geophys. Res., 2005, vol. 110, pp. 1–10. [6] Gol’dshtein, M.N., Mekhanicheskie svoistva gruntov (Mechanical Properties of Soils), Moscow: Stroiizdat, 1973.

FINE DUST IN THE LUNAR ENVIRONMENT

V.V. Shevchenko, A.A. Berezhnoy, E.A. Kozlova,
Sternberg Astronomical Institute, Moscow State University, Universitetskij pr., 13, Moscow, 19991 Russia. Contact: vladislav_shevch@mail.ru

Introduction:

The question on presence on the atmosphere Moon is rather important. Supervision over coverings of stars the Moon, conducted regularly in many observatories in past, and also other researches with obviousness understood that on the Moon aren't present some appreciable atmosphere. However on the base of the polarimetric analysis of the lunar horns the Soviet astronomer Yu.N. Lipsky considered that on the Moon there is the gas atmosphere which weight on area unit makes 1/10 000 those which is available on the Earth. E. Opik (Ireland), proceeding from other reasons, finds, that the weight of lunar atmosphere over area unit corresponds 1/230 000 terrestrial. If to accept this value it will appear that pressure and density at the Moon surface at least in 1 300000 times is less than gas, than on the Earth.

As the French scientist A. Dolfus if, the density of gases on a lunar surface equals even 1/1000000 terrestrial brightness of a diffused light on horns of a lunar sickle would be so big that lengthening of horns that actually isn't present would be observed has shown. From these reasons follows that density of lunar atmosphere must be less then 10^{-8} of density of terrestrial atmosphere. Still smaller values of density of atmosphere on a lunar surface have been received by means of very sensitive polarimetr of B.Lio (France), shown that it at least in 10^9 times is less, than at. the Earth's surface. Hence, it is possible to consider that gas atmosphere on the Moon practically doesn't exist.

Together the lunar environment is a complex and dynamic system. Without an appreciable atmosphere or large-scale magnetic field, with the exception of regions with strong magnetic anomalies, the solar wind freely reaches the lunar surfaces. Combined with photoemission from the lunar surface due to direct exposure to solar UV radiation, this can lead to surface charging, near-surface electric fields, and the mobilization and transport of the lunar soil [1]. Images taken by Surveyors 5, 6, & 7 in the first time have indicated the presence of lofted dust clouds along with estimates for their spatial extent and density [2].

Surveyor's Images of Horizon Glow: Surveyors 5, 6, and 7 captured the first evidence of dust transport on airless bodies with their television cameras (shown below) [2,3]. Just after sunset, a horizon glow was observed above the western horizon. This was interpreted to be forward scattered light from a cloud of dust particles with radii ~5 μm, vertical dimension ~3-30 cm, and horizontal dimension ~14 m [4]. Recently the modeling dust clouds on the Moon was constructed [5]. Surveyor 5, 6, and 7 had a magnet attached to one of the spacecraft footpads to determine magnetic properties and composition of the soil. Surveyor 7 had additional magnets on a second footpad and the surface sampler. Photographs showing the amount of dust adhering to magnets indicated the amount of magnetic particles in the soil and allowed estimates of the lunar soil compositions when compared with permission experiment photographs of magnets in terrestrial soils of various compositions.

According Rennilson et al. [2] each of the Surveyor 7, 6, and 5 spacecraft observed a line of light along its western lunar horizon following local sunset. It has been suggested that this horizon-glow is sunlight, which is forward-scattered by dust grains (~ 10μ in diameter, about 50 grains on cm^{-2}) present in a tenuous cloud formed temporarily (lap 3 h duration) just above sharp sunlight/shadow boundaries in the terminator zone. Electrically charged grains could be levitated into the cloud by intense electrostatic fields (> 500 V cm^{-1}) extending across the sunlight/shadow boundaries. Detailed analysis of the horizon-glow absolute luminance, temporal decay, and morphology confirm the cloud model. The levitation mechanism must eject 10^7 more particles per unit time into the cloud than could micro meteorites. Electrostatic transport is probably the dominant local transport mechanism of lunar surface fine particles. Surveyor 7 was the first probe to detect the faint glow on the lunar horizon after dark that is now thought to be light reflected from electrostatically levitated lunar dust.

According to Kuntz et al. [6] shadowed regions on the lunar surface acquire a negative potential. In particular, shadowed craters can have a negative potential with respect to the surrounding lunar regolith in sunlight, especially near the terminator regions. Here authors analyze the motion of a positively charged lunar dust grain in the presence of a shadowed crater at a negative potential in vacuum. Previous models describing the transport of charged lunar dust close to the surface have typically been limited to one-dimensional motion in the vertical direction, e.g. electrostatic levitation; however, the electric fields in the vicinity of shadowed craters will also have significant components in the horizontal directions. Authors propose a model that includes both the horizontal and vertical motion of charged dust grains near shadowed craters. They show that the dust grains execute oscillatory trajectories and present an expression for the period of oscillation drawing an analogy to the motion of a pendulum.

The calculations made by Sternovsky et al. [7] show that solar activity can significantly change the conditions for lunar dust transport. The presented model is simplified as it neglects variations with solar elevation angle and additional surface charging processes. It is further expected, that dust mobilization will be the strongest across sunlit-shadow boundary regions caused by local topography. In this picture, positively and negatively charged surfaces are adjacent to each other allowing a much stronger electric field to appear and are the likely places to mobilize dust. The calculations show that dust activity increases faster than linearly with photoelectric emission. This is because both the charge on the dust and the electric field increase with increasing photoemission. The highest dust activity is expected during solar flares.

Fig. 1 shows illumination along western horizon in Surveyor landing site approximately 15 minutes after local sunset (Courtesy NASA/JPL).

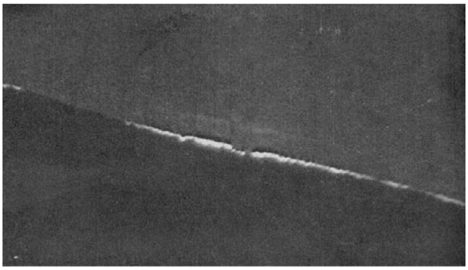

fig. 1

Fig. 2 shows illumination along western horizon in the same site approximately 90 minutes after local sunset (Courtesy NASA/JPL). The illumination disappeared approximately 90 minutes after local sunset completely.

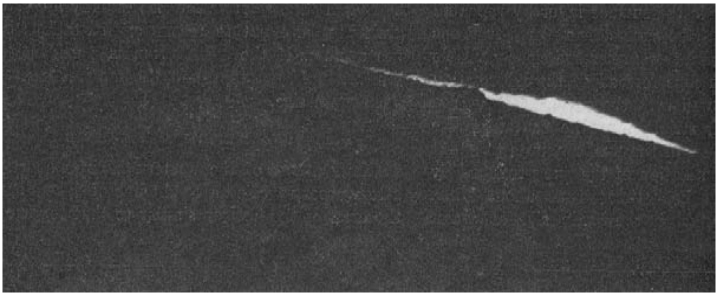

fig. 2

Summary and Conclusions:

The levitation mechanism must eject 10^7 more particles per unit time into the cloud than could micro meteorites. Electrostatic transport is probably the dominant local transport mechanism of lunar surface fines. The event was supported by observation of lunar horizon glow from forward scattering of sunlight by exospheric dust of the Clementine Star Tracker Cameras. According to the data received by means of device LEAM - Lunar Ejecta and Meteorites that has been delivered to the Moon in 1972 within the limits of flight «Apollo 17» and intended for monitoring of a dust, dust storms on the Moon are marked along all lunar terminator and move together with it.

Acknowledgements:
This research is supported by joint RFBR grant 11-02-90440-Ukr_f_a.

References:

[1] Horanyi, M., Charged Dust Dynamics. Annu. Rev. Astron. Astrophys., 34 (1996) 383IMO (2009). http://www.imo.net/live/perseids2009. [2] Rennilson, J. J., Criswell, D. R., 1974. Surveyor observations of lunar horizon-glow. The Moon 10(2), 121-142,doi:10.1007/BF00655715. [4] Nitter, T., et al., IEEE Trans. Plasma Sci., 22, 1994. [5] Szalay J., Horanyi M. Modeling Dust Clouds on the Moon. Lunar and Planet. Sci. 43. 2012. # 1796. [6] Kuntz, K. D.; Collier, M. R.; Stubbs, T. J.; Farrell, W. M. The Lunar Dust Pendulum. American Geophysical Union, Fall Meeting 2011, abstract #P13D-1710. [7] Sternovsky Z., Chamberlin P., Horanyi M., . Robertson S., Wang X. Variability of the lunar photoelectron sheath and dust mobility due to solar activity. J. Geophys. Res., Vol. 113, A10104, doi: 10.1029/2008JA013487, 2008. [8] Zook H. A. and McCoy J. E. (1991) GRL, 18, 2117–2120.

MICROMED: A COMPACT DUST DETECTOR FOR MARTIAN AIRBORNE DUST INVESTIGATION.

F. Esposito[1], C. Molfese[1], F. Cortecchia[1], F. Cozzolino[1], S. Ventura[2], F. D'Amato[3], L. Gambicorti[3],
[1]INAF – Osservatorio Astronomico di Capodimonte, Salita Moiariello 16, 80131 Napoli, Italy; [2] ESA - ESTEC, Product Assurance & Safety Department, Keplerlaan 1, P.O. Box 299 - 2200 AG Noordwijk ZH, The Netherlands; [3]CNR – Istituto Nazionale di Ottica, Largo Fermi 6, 50125 Firenze, Italy.
Contact: francesca.esposito@na.astro.it

Dust is permanently present in the atmosphere of Mars. Its amount varies with seasons and with the presence of local and global dust storms. Airborne dust contributes to determine the dynamic and thermodynamic evolution of the atmosphere, including large scale circulation processes, on diurnal, seasonal and annual time-scales. It plays a key role in determining the current climate of Mars and influenced the past climatic conditions and surface evolution. Dust grains absorb and scatter thermal and solar radiation and act as condensation nuclei for H_2O and CO_2, so influencing the atmospheric thermal structure, balance and circulation. Main parameters influencing the atmospheric heating are size distribution, albedo, single scattering phase function and imaginary part of the refractive index. Moreover, wind and windblown dust represent nowadays the most active processes having long term effects on Martian geology and morphological evolution. Aeolian erosion, dust redistribution on surface and weathering are mechanisms coupling surface and atmospheric evolution and are driven by wind intensity and grain properties. Wind mobilized particles on Mars range in size from less than 1 μm, for suspended dust, to perhaps as large as 1 cm in diameter. The mechanisms for dust entrainment in the atmosphere are not completely understood as the data available so far do not allow us to identify the efficiency of proposed processes. Also the transport of dust can be quantitatively understood only through direct study from the Martian surface of dust grain properties. Beside its scientific interest, the study of atmospheric Martian dust is relevant in the context of analyzing hazard connected to the contamination/failure of payloads in space missions (e.g., solar panels, mechanisms, optical systems) and to the environmental risks for human exploration, due to dust deposition and impacts. The measurement in situ of the amount and mass/size distribution as a function of time, is a fundamental step. It may shade light on climatic processes, and in particular on the airborne dust evolution, and will help to prepare for future missions to Mars.

The MicroMED instrument is the optimized and miniaturized version of the MEDUSA instrument, developed for the Humboldt payload on ExoMars mission. It has been optimized in terms of size and required resources (mass and power). It is able to measure the size of single dust grains in the atmosphere, and so the dust size distribution and number density.

It is based on the optical particle counter (OPC) working principle, analyzing the light scattered from single dust particles. A pump is used to sample the Martian atmosphere, generating a flux of gas and dust across the instrument through the inlet (see Figure 1). When the dust grains reach the Optical Sensor (OS), they cross a collimated IR laser beam emitted by a laser diode. The light scattered by the grains is detected by photodiodes (see Figure 1b), which are amplified by the Proximity Electronics (PE). The intensity of scattered light is a function of the grain size, which is so measured.

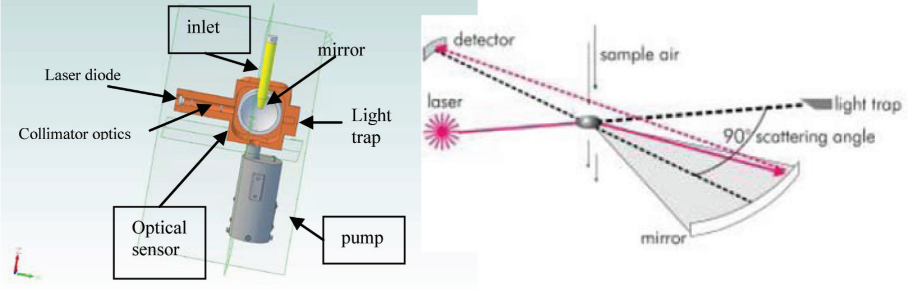

fig. 1. (**a**) MicroMED subsystems. (**b**) OS optical layout.

LUNAR DUSTY PLASMA ENVIRONMENT

S.I. Popel[1], A.P. Golub'[1], G.G. Dolnikov[2], Yu.N. Izvekova[1], S.I. Kopnin[1], A.V. Zakharov[2], L.M. Zelenyi[2],
[1]Institute for Dynamics of Geospheres RAS, Leninsky pr. 38, bldg. 1, 119334 Moscow, Russia; [2] Space Research Institute RAS, Profsoyuznaya 84/32, 117997 Moscow, Russia. Contact: s_i_popel@mtu-net.ru

The surface of the Moon is charged under the action of the electromagnetic radiation of the Sun, solar-wind plasma, and plasma of the Earth's magnetotail. The surface of the Moon and dusts levitating over the lunar surface interact with solar radiation. They emit electrons owing to the photoelectric effect, which leads to the formation of the photoelectron layer over the surface. Dusts located on or near the surface of the Moon absorb photoelectrons, photons of solar radiation, electrons and ions of the solar wind, and, if the Moon is in the Earth's magnetotail, electrons and ions of the magnetospheric plasma. All these processes lead to the charging of dust particles, their interaction with the charged surface of the Moon, and rise and motion of dust. Thus, dust over the Moon is a component of the dusty plasma system; investigations of this system are of significant interest, including technological interest, for instruments mounted on lunar stations, choice of a Moon landing site, etc.

In this work we study the dusty plasma system in the surface layer of the Moon. The situations where dust particles are formed over lunar regolith regions and hydrogen-enriched regions of the surface of the Moon are analyzed. The dust and electron number densities, dust particle charges, and some other dusty plasma characteristics over the surface of the Moon are calculated. We use a modified model [1] in which the charging of dust particles over the surface of the Moon is calculated taking into account the effect of photoelectrons, electrons and ions of the solar wind, and solar radiation. The modification of the model [1] is that here we take into account the photoelectrons from both the lunar surface and the surfaces of dust particles, while in [1] only the photoelectrons from the lunar surface are taken into account. The consideration of the photoelectrons from the dust particle surfaces modifies the model strongly and requires a self-consistent investigation because the photoelectrons influence dust particle distributions while the dust particle distributions determine the number of the photoelectrons. We present the photoelectron and dust distributions obtained as a result of our calculations. We show that the photoelectron density as a function of the height h within the range of the subsolar angles θ from 0° to 89° is described with a good accuracy by the formula

$$n_{e,ph} \approx N_0 \frac{\cos\theta}{\left[1+\sqrt{\cos\theta/2}\,(h/\lambda_D)\right]^2} + N_e (h/h_1)^{\alpha} ,$$

where $N_0 \approx 2\times10^5$ cm^{-3} for regolith regions and $N_0 \approx 2\times10^8$ cm^{-3} for hydrogen-enriched regions, λ_D is the Debye length for photoelectrons with the temperature $T_e \approx 0.1$ eV and the number density N_0, h_1=1 cm, the constants α and N_e are given in Fig. 1 for regolith and hydrogen-enriched regions of the surface of the Moon.

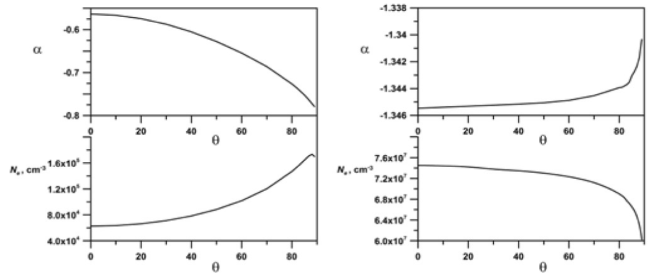

fig. 1. The constants α and N_e vs θ for regolith regions (left panel) and hydrogen-enriched regions (right panel) of the surface of the Moon.

We demonstrate that for hydrogen-enriched lunar regions the height distributions of electrons and dusts are qualitatively the same as in the case of regolith surface. But the characteristics of dust rising over the lunar regolith and hydrogen-enriched regions of the lunar surface are different. The difference is that the dust levitating over the hydrogen-enriched regions has larger sizes (up to ≈ 250 nm), larger charges, rises to larger heights, etc. than in the case when the dust levitates over the lunar regolith region.

This work was supported by the Presidium of the Russian Academy of Sciences (basic research program no. 22 "Fundamental Problems of Research and Exploration of the Solar System") and by the Russian Foundation for Basic Research (project no. 12-02-00270-a).

[1] *A.P. Golub', G.G. Dol'nikov, A.V. Zakharov, L.M. Zelenyi, Yu.N. Izvekova, S.I. Kopnin, S.I. Popel*, JETP Lett. **95**, 182 (2012).

CHARGING AND MOTION OF DUST GRAINS NEAR THE MOON AND ASTEROIDS

N.D. Borisov,
IZMIRAN, 142190 Troitsk, Moscow region, Russia. Contact: borisov@lpi.ru

The exploration of lunar dust started more than 40 years ago. Important results concerning chemical composition, sizes of dust grains, and their motion were obtained by Apollo and Luna missions. The motion of dust grains was registered on the surface of the Moon not only near terminator but also (with less intensity) even far enough in the shadow [1]. From the very beginning it was argued that dust levitation is caused by electric charging and motion in electric fields near the surface. But the charges on dust grains, their masses and velocities still are not measured. Two mechanisms responsible for dust motion were discussed theoretically. The first one is connected with the action of the solar UV radiation [2]. The second mechanism is based on the idea that strong local electric fields are formed on a rough surface even without solar UV radiation [3, 4]. The suggested in [4] model can explain qualitatively the motion of micron size grains and less close to the surface in the shadow.

To understand dust grain charging more in detail different laboratory experiments were carried out to model physical processes near the Moon. But only direct measurements of the electric fields, masses of dust grains, their velocities and electric charges in the vicinity of the Moon can provide us with the information required for construction of a reliable model of dust motion near the Moon. Such investigations are planned on forthcoming missions. The LADEE mission will carry sensitive LDEX instrument to measure charged fine dust component on the orbit around the Moon. Luna-Globe and Luna–Resource will investigate charged dust dynamics and electric fields on the surface not far from the poles of the Moon. The vicinity of the south pole with its strong magnetic anomaly is a very interesting object for scientific exploration. Preliminary estimates show that even rather far from the center of the magnetic anomaly strong enough perturbations in the fluxes of ions and electrons hitting the surface should appear which in turn influence the process of charging. Moreover significant perturbations of the electron concentration, magnetic and electric fields are expected not only at the surface but also above the magnetic anomaly [5].

Strong local electric field could exist also at the surface of asteroids. While the gravity on asteroids is more than two - three orders of magnitude less than on the Moon estimates show that without strong enough electric fields it is hardly possible to lift dust grains from the surface. We discuss the motion of charged dust grains in local electric fields at the surface and large-scale electric fields of the double layer in the shadow.

The forthcoming lunar missions will greatly expand our knowledge about solar wind interaction with airless cosmic bodies like Moon, Mercury, and asteroids. Such investigations are important also for practical purposes because dust on the Moon is one of the most serious ecological problems for the future inhabited stations.

This work was supported by the grant of the Russian academy of sciences Presidium Program 22: “Fundamental problems of research and exploration of the Solar system”.

References.

1. O.E. Berg, F.F. Richardson, H. Burton. Lunar ejecta and meteorites experiment, in: APOLLO 17 Preliminary scientific report, NASA SP-330, 16, (1973).
2. J.E. Colwell, S. Batiste, M. Horanyi, and S. Sture. Lunar surface: dust dynamics and regolith mechanics. Reviews of Geophysics, v.45, RG 2006, (2007).
3. N. Borisov and U. Mall. The structure of the double layer behind the Moon. J. Plasma Physics, v. 67, part 4, 277, (2002).
4. N. Borisov, U. Mall. Charging and motion of dust grains near the terminator of the Moon. Planetary and Space Science, v. 54, 572, (2006).
5. N. Borisov, U. Mall. Interaction of the solar wind with a localized magnetic barrier: application to lunar surface magnetic fields. Physics Letters A 309, 277, (2003).

MODELING OF THE LIGHT SCATTERING BY DUST PARTICLE PLASMA NEAR THE MOON SURFACE

G.V.Belokopytov, A.V.Zhuravlev,
Physical Department, M.V.Lomonosov State University, 119992, Moscow, Russia, Contact: gvb@phys.msu.ru

The observation of the light scattering by dust particles may provide valuable information on the composition and properties of the dust plasma near the Moon surface. The planning and conduction of future experiments needs preliminary analysis of the information capability of different scattering characteristics, and at the next stage – the comparison of the experimental results with numerical calculations made in the framework of appropriate model.

The principal part of the model is the Mie theory based [1] program for computing of the scattering spectra for different parameters, integral (extinction, scattering, absorption cross sections and radiation pressure efficiencies) and differential (scattering diagrams). The computation model for light scattering by lunar dust in its advanced form has to include the database on complex refraction indices of compounds, included in the composition of lunar dust, along with the dimension and height distribution functions of the dust particles in the vicinity of the Moon surface.

These mentioned data are known for today with different measure of completeness. The dimension distribution were studied in [2 -4]. The model of height distribution is now available in [2]. However, the chemical composition and the state of the dust particles in the form of chemical compound, statistical mixture, or matrix system may vary strongly. So the analysis of the dust particles composition must be added to interpret adequately the results of the optical scattering spectra. It should be stressed that the data on the complex refraction coefficient in the visible and near infrared regions are not available for many of constituents of lunar regolite. For correct calculation these data must be determined in special laboratory experiment.

To obtain some qualitative orientation and estimations the Mie theory calculations were made for spherical particles of iron, silicon and magnesium, being between the major components of lunar dust. The amounts of complex refraction index were extracted from [5, 6]. Calculated size dependencies possess a number of common features. The scattering by small particles with dimensions less than the wavelength λ has the dipolar angular distribution and obeys Rayleigh law. The amount of extinction efficiency Q, along with the scattering and absorption one, reaches maximum in condition $D\approx\lambda/2\pi$, D being the particle diameter. However, Si particles have additional resonance maxima at the $Q(D)$ dependencies, which are absent in conducting particles.

Nethertheless, the comparison of optical scattering experiment with model calculations permits some useful conclusions made even in the conditions of essential incompleteness. Consider, for example, the influence of the dimensions distribution of dust plasma particles on the results of optical scattering. Suppose, after [3], that probability density of dimension distribution of the lunar dust particles obeys Kolmogorov law:

$$f(D)=\frac{1}{\sqrt{2\pi}\sigma D}\exp\left\{\frac{\left[\ln(D)-\ln(D_0)\right]^2}{2\sigma^2}\right\}, \quad (1)$$

It is easy to obtain the probability of particle diameter being more than some given amount D by integration the probability density function (1):

$$F_{cum}(D)=\int_D^{+\infty} f(x)\,dx=\frac{1}{2}\operatorname{erfc}\left(\frac{\ln(D)-\ln(D_0)}{\sqrt{2}\sigma}\right) \quad (2)$$

In the case when the some mass of the sample was used for the extraction of the distribution function, the variable to consider is the total amount N_{cum} of the particles with the diameter more than some given amount. To take this case into account, it is enough to modify with normalizing coefficient:

$$N_{cum}(D)=A\cdot F_{cum}(D) \quad (3)$$

Here we conducted the approximation of the experimental cumulative function $N_{cum}(D)$ of the [3] by the analytical expressions (2), (3). As it shown at the fig.1,a, Kolmogorov distribution provides the agreement with experiment [3] with high precision. By means of least mean squares fitting it was found such set of parameters: $A = 6.09\cdot10^9$, $D_0 = 246\cdot10^{-9}$м, $\sigma = 0.887$. The probability density function $f(D)$, with this set of parameters is depicted at the fig.1.b (curve 1).

For the particles of lunar dust plasma it has been taken into account that their dimension probability density function differs from analogous function of lunar regolite. The analysis [2] shows, that for the particles of lunar dust plasma formed by solar irradia tion the probability distribution function differs from Kolmogorov distribution:

$$f_{atm}(D) = \frac{B}{D^3} f(D) \qquad (4)$$

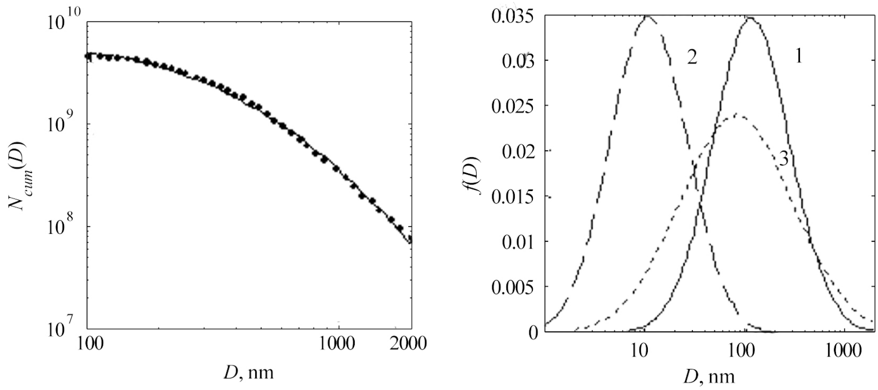

a b

figure 1. The dimension probability functions for lunar dust particles: **a**) $N_{cum}(D)$ – cumulative number, dots – digitalization of experimental data graph [6], continuous curve – fitting by ; **b**) dimension probability densities functions: 1 – $f(D)$, 2 - $f_{atm}(D)$, both D_0 = 246nm, σ - 0.887, 3 – $f_{atm}(D)$ with parameters D_0 = 62um, σ = 1.29.

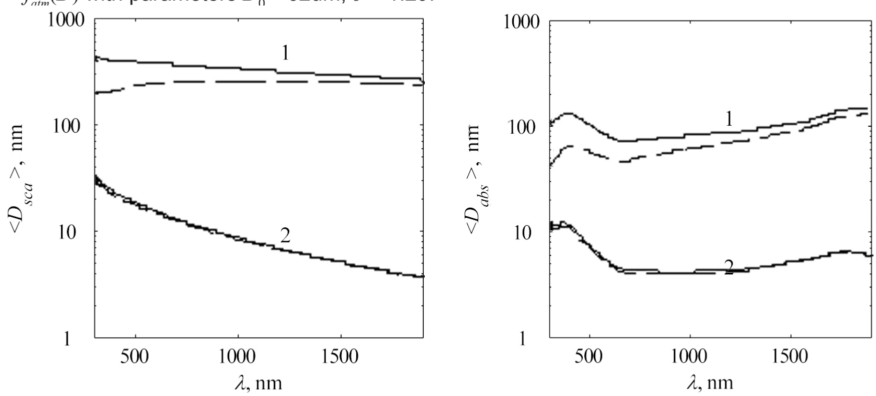

a b

figure 2. Mean effective diameters of scattering (**a**) and absorption (**b**) cross sections. Numeration of curves – see **fig.1.** Continuous curves – calculation with account of all Mie modes. Dashed curves – only dipolar contribution.

Calculated dust particle dimension distribution functions with parameters $D_0 = 246 \cdot 10^{-9}$m, σ = 0.887 are represented at fig.1,b. While the mean diameter of particles on the Moon surface is 246 nm, the median value for particles of lunar dust plasma is much smaller, only 11 nm. Note, that authors of [2] have used for the calculations of the cumulative function the results of [6], which give another set of parameters $D_0 = 62 \cdot 10^{-6}$ м, σ = 1.29. The corresponding function is represented in fig.1,b (curve 3). The amount of median diameter seems overestimated.

We have calculated the scattering and absorption cross sections functions C_{sca} and C_{abs} for iron spherical particles. With use of these results and weight functions $f(D)$ and $f_{atm}(D)$ we have determined mean scattering and absorption cross sections diameters: $\left\langle D_{sca(abs)} \right\rangle = 2\sqrt{\left\langle C_{sca(abs)} \right\rangle / \pi}$, The results obtained are shown in fig.2. The analysis of numerical results demonstrate, in particular, that for the particle ensemble with the distribution function $f(D)$(1 and similarly 3, fig.1,b) the scattering has multimode response with strong multipolar contribution. In contrast, for the case of distribution function $f_{atm}(D)$ (2, fig.1,b) – the dipolar scattering is dominating, which may be easily observed in experiment.

References:

[1] C.F. Bohren, D.R. Huffman, Absorption and Scattering of Light by Small Particles (Wiley, 1998)
[2] A. P. Golub', G. G. Dol'nikov, A. V. Zakharov, et al. // JETP Lett., 2012, V. 95, N. 4, P. 182
[3] Y. Liu, J. Park, D. Schnare, et al. // J. Aerosp. Eng., 2008, V. 21 N. 4, P. 272
[4] J.E.Cowell, S.Batiste, M.Horanyi et al.//Rev. Geophys. V.45, RG2006 (2007)
[5] P.B. Johnson, R.W. Christy // Phys. Rev. B 1974, V.9, N.12 P. 5056
[6] T. Gold, M.J. Campbell, B.T. O'Leary // Proceedings of the Apollo 11 Lunar Science Conference, 1970, V. 3, P. 2149

NUMERICAL SIMULATION OF DUST RING FORMATION AROUND MARS

V. Sizenkov[1], V. Lupovka[1], V. Dmitriev[1], H. Hussmann[3], J. Oberst[1,2,3];
[1]State University of Geodesy and Cartography (MIIGAiK), Gorokhovskiy per., 4, 105064, Moscow, Russia (v_sizenkov@mexlab.ru, v.lupovka@miigaik.ru); [2]Technical University of Berlin, Berlin, Germany; [3]German Aerospace Center (DLR), Berlin, Germany.

Introduction:

Particles ejected from Phobos by meteoroid impacts can be one of the sources of material for dust rings for-mation around Mars. Orbital evolution of the ejected particles is performed by numerical integration method. Mars gravity field, third body attraction and solar radiation pressure are taken into account.

The formation of dust rings:

Overview. It is known, giant planets have the ring structure, consisting of particles of dust, ice and ice blocks. However, it is conceivable that such dust complexes can be formed around earth-type planets. It is assumed that the source material for such ring can be particles ejected from natural planetary satellites by meteoroid impacts [1].

Theoretical studies of this issue have already been performed. Such studies are usually described by the construction of analytical models of circumplanetary rings [2]. We study the possible existence of a ring along the Phobos orbit with using of numerical methods.

Experiment description. Meteoroid ejected particles start moving from almost the same position (in this case, Phobos), but with different velocities and angles of ejecta. We consider the evolution of the orbits of a set of particles with initial velocity vector, modeled stochastically.

Investigation of evolution particle orbits was performed by numerical integration with using the Adams-Bashforth method [4] at the interval of 1000 years. The integration was made in Cartesian coordinates.

Perturbations invoked by the Mars gravity field for up to 30x30, third body attraction (Sun, 7 planets and Moon) and solar radiation pressure were taken into account. SPICE kernels and appropriate SPICE functions were used for obtaining Sun and planets ephemeris and coordinate transformations [3].

In our case, a parent body was Phobos. Its position on January 1, 2000 is used for the initial coordinates of all particles. Physical properties of particles are selected on the basis of the Phobos parameters. Soil density: 1.872 ± 0.076 g/cm^3 and a geometric albedo 0.071 ± 0.012 [4]. Particles that have velocity relative to Phobos more than the 0.34 km/s escape from the Phobos orbit and did not form a ring. Rest particles have relative speed to Phobos varied in the range from -0.26 km/s to 0.13 km/s.

Results: As a result of integration we have that after 100 years all particles are distributed along the orbit of Phobos. Then they gradually form a ring-like structure. In the final position of the particles through the 1000 years after the ejecta the particles are evenly distributed along the orbit of Phobos, and we can say that they form a ring.

Summary: Simulations of orbital evolution of ejecta from Phobos shows that for some initial conditions ejected particles can form ring-like structures. According to our investigation this ring appears to have stability for a minimum of one thousand years. It is too early to make conclusions because of a small number of considered particles. Therefore, the investigation will be continued to a larger number of particles, mass range, and longtime interval.

Acknowledgements
This work has been supported by a grant from the Ministry of Education and Science of the Russian Federation (Agreement № 11.G34.31.0021 dd. 30/11/2010).
The authors are grateful to Charles Acton and his colleagues at NASA's Jet Propulsion Laboratory for kindly providing us with SPICE kernels for 6000 years coverage.

References

[1] Joseph A. Burns, Douglas P. Hamilton, Mark R. Showalter: Dusty rings and circumplanetary dust: observations and simple physics. In Interplanetary Dust (E. Grün, B. A. S. Gustafson, S. F. Dermott and H. Fechtig, Eds.), Springer, Berlin, pp. 641–725, 2001.
[2] Douglas P. Hamilton, Alexander V. Krivov: Circumplanetary Dust Dynamics: Effects of Solar Gravity, Radiation Pressure, Planetary Oblateness, and Electromagnetism , Icarus 123, 503-523 (1996).
[3] Acton, C.H.: Ancillary Data Services of NASA's Navigation and Ancillary Information Facility; Planetary and Space Science, Vol. 44, No. 1, pp. 65-70, 1996.
[4] JPL's HORIZONS System http://ssd.jpl.nasa.gov/?horizons.
[5] Hussmann H.et al., Planet. Space Science, in press, 2012.

EVOLUTION OF UNDERSTANDING OF SOLAR WIND-GASEOUS OBSTACLE INTERACTION

O.Vaisberg,
Space Research Institute, Moscow, Russia

Pioneering work of Alfven, 1971, laid the foundation for solar wind-comet interaction investigation. It was found that Mars and Venus do not have global magnetic field, and both planets may be considered as small comets. However, for some time it was assumed that the main role in creating the obstacle to the solar wind flow in these cases belonged to ionosphere. The currents induced in the ionosphere by motional electric field of magnetized solar wind considered responsible for creation of induced magnetospheres of Mars and Venus.

Measurements on Mars and Venus orbiters in 1970th showed that the main role that controls formation of Martian and Venusian magnetospheres belongs to mass loading of the solar wind flow by exospheric ions ionized by solar UV radiation. It was shown in (Zelenyi and Vaisberg, 1984) that mass loading processes explain important properties of magnetospheres of Venus and Mars, and determines that size of these magnetospheres. Mars orbiters data also showed importance of solar wind induced planetary ions losses for evolution of Martian magnetosphere. Magnetospheres of Mars and Venus are accretion magnetospheres rather than induced magnetospheres.

Experiments on Pioneer-Venus Orbiter provided very detailed description of solar wind influence on Venus upper atmosphere and ionosphere, magnetization of dayside ionosphere at high solar wind ram pressure. Important results also included discovery of magnetic barrier and better understanding of magnetic tail.

Comparison of magnetospheres of Mars, Venus and comets showed that their dimensions can be scaled by gaseous outputs of atmospheric obstacles. Another property of accretion magnetospheres is rather sharp boundary of tails at which solar wind ions are replaced by planetary/cometary ions. Origin of this thin boundary was not explained so far.

Observation on MEX and VEX spacecraft provided additional data on various loss mechanisms and their variability. However, more observations are needed before loss magnitude and the role of transient effects will be sufficiently understood.

This work was supported by the grant of the Russian academy of sciences Presidium Program 22: “Fundamental problems of research and exploration of the Solar system”.

STRUCTURE AND DYNAMICS OF INDUCED PLASMA TAILS.

C. Bertucci,
Institute for Astronomy and Space Physics (IAFE), Buenos Aires, Argentina. Contact: cbertucci@iafe.uba.ar

Introduction:

The pileup and draping of the magnetic field and the acceleration of planetary charged particles are the net result of the electromagnetic coupling between the atmosphere of a weakly magnetized object and an external plasma wind. Plasma observations by several spacecraft around unmagnetized objects throughout the solar system are increasing our understanding about the structure and dynamics of their induced magnetotails. Observations at Mars and Venus have revealed that the spatial distributions of the particle energies within their magnetotails are not uniform, with distinct populations occupying the plasma sheet and the lobes. At Titan, on the other hand, Cassini's survey of the particle density distribution including low energies suggests a plasma wake structure which is different from the one initially expected. This leads to outstanding questions about the estimate of the atmospheric escape in a highly variable plasma environment. In this work, we revisit these and other results from observations as well as simulations and discuss possible particle acceleration processes and the role of the upstream conditions in determining the structure of induced magnetotails.

SOLAR WIND INDUCED ESCAPE ON MARS AND VENUS. MUTUAL LESSONS FROM DIFFERENT SPACE MISSIONS.

E. Dubinin[1],
[1]Max-Planck-Institute for Solar System Research, Max-Planck-str. 2, 37191 Katlenburg-Lindau Germany. Contact: dubinin@mps.mpg.de

The recent measurements performed by the Mars Global Surveyor (MGS), Mars Express (MEX) and Venus Express (VEX) spacecraft provided us with a lot of new information about solar wind interaction with nonmagnetic Mars and Venus. On the other hand the absence of a magnetometer on MEX, a plasma package on MGS and a detector of cold plasma on MGS and VEX impose serious constraints on our vision of the physical processes in plasma environments of these planets. Therefore the mutual lessons from the observations made on both planets by different spacecraft might be very useful and bring us some missing important information. We will discuss in this context structure and dynamics of the solar wind interaction with the planetary ionospheres, processes of ion energization driven by direct solar wind forcing, morphology and effectiveness of different channels and routes through which the ionized planetary matter escapes the planets, their variability with solar wind parameters.

SUPRATHERMAL HYDROGEN AND OXYGEN ATOMS IN THE UPPER ATMOSPHERE OF MARS.

V. I. Shematovich,
Institute of Astronomy of the Russian Academy of Sciences, 48 Pyatnitskaya str., Moscow, Russian Federation. Contact: shematov@inasan.ru

Introduction:

Solar forcing on the upper atmospheres of the terrestrial planets via both UV absorption and atmospheric sputtering results in the formation of the extended neutral coronae populated by the suprathermal (hot) H, C, N, and O atoms (see, e.g., Johnson et al., 2008). The hot corona, in turn, is altered by an inflow of the solar wind and/or magnetospheric plasma and local pick-up ions onto the planetary exosphere. Such inflow results in the formation of the superthermal atoms (energetic neutral atoms-ENAs) due to the charge exchange with the high-energy precipitating ions and can affect the long-term evolution of the atmosphere due to the atmospheric escape.

Model:

The origin, kinetics and transport of the suprathermal H, and O atoms in the transition region (from thermosphere to exosphere) of the upper atmosphere of Mars are discussed. Reactions of dissociative recombination of the ionospheric ions CO_2^+, CO^+, and O_2^+ with thermal electrons are the main photochemical sources of hot oxygen atoms. The dissociation of atmospheric molecules by the solar UV radiation and accompanying photoelectron fluxes and the induced exothermic photochemistry are also the important sources of the suprathermal hydrogen and oxygen atoms. Kinetic energy distribution functions of:

- suprathermal atoms were calculated using the stochastic model of the hot planetary corona (Shematovich, 2004);

- superthermal (ENA) atoms were calculated using the Monte Carlo model (Shematovich et al., 2011) of the high-energy proton and hydrogen atom precipitation into the atmosphere.

Applications:

These functions allowed us to obtain and compare the space distribution of suprathermals in the transition region of Mars. Recent observations of the hydrogen Ly-α emission by the SPICAM instrument onboard Mars Express spacecraft showed the presence of hot and thermal fractions of atomic hydrogen in the extended corona at Mars (Chaufray et al., 2008). Recently, the suprathermal fraction of atomic oxygen in the extended corona at Mars was studied by the far-ultraviolet imaging spectrograph Alice on board Rosetta during the spacecraft swing-by of Mars on 25 February 2007 (Feldman et al., 2011). Collisional coupling between light hydrogen and hot heavy oxygen atoms is considered in calculations as an important additional source of the suprathermal hydrogen atoms in the corona. Results of calculations were also compared with the observations of the UV emissions by the UV spectrometer of SPICAM instrument and ENA spectra measurements made by ASPERA-3 instrument onboard of the ESA Mars Express spacecraft.

This work was supported by the Russian Foundation for Basic Research (Project no. 11-02-00479a), Program 22 of the Russian Academy of Sciences «Fundamental problems of the research and exploration of the Solar System», and the Federal Target Program “Academic and Teaching Staff of Innovative Russia for 2009–2013.”

Chaufray J.E., et al., *Icarus, 195*, 598, 2008.
Feldman P.D., et al., Icarus, 214, 394, 2011.
Johnson R.E., et al., Sp. Sci.Rev., 139, 355, 2008.
Shematovich V. I., Sol. Sys. Res., 38, 28, 2004.
Shematovich V. I., et al, J. Geophys. Res., 116, 2011, doi:10.1029/2011JA017007.

PRECIPITATION OF HIGH-ENERGY ELECTRONS, PROTONS, AND HYDROGEN ATOMS INTO THE UPPER ATMOSPHERES OF MARS AND VENUS.

V. I. Shematovich[1], D. V. Bisikalo[1], S. Barabash[2], *Institute of Astronomy of the Russian Academy of Sciences, 48 Pyatnitskaya str., Moscow, Russian Federation; [2]Swedish Institute of Space Physics, Kiruna, Sweden. Contact: shematov@inasan.ru*

Introduction: Mars is immersed in the magnetized, supersonic solar wind flow and as a response induced currents are set up in the Martian ionosphere. Currents result in magnetic fields deviating the solar wind. A void in the solar wind is created, the induced magnetosphere. The interplanetary magnetic field lines pile up and drape around this obstacle. A bow shock is also formed, which enable the solar wind flow to slow down from supersonic to subsonic velocities. The boundary between the (shocked) solar wind and the induced magnetosphere, often referred to as the induced magnetosphere boundary (IMB), is, however, not completely closed. The gyro-radii of the solar wind particles are large enough, compared to the size of the IMB, to enable the particles to gyrate through the piled up magnetic field and directly interact with the Martian upper atmosphere. This unique property of the small Martian induced magnetosphere allowing solar wind protons and alfa-particles assimilation in the Martian atmosphere represents an important source of some atmospheric species.

Models: A complex of the Monte Carlo models to investigate the kinetics and transport of the high-energy electrons, protons and hydrogen atoms in the upper atmospheres of the Mars and Venus was developed (Shematovich et al., 2008; Shematovich et al., 2011). These models are based on the stochastic interpretation of the collisions of the high-energy particles and the ambient atmospheric gas with taking into account the measured scattering angle distributions. In these models a Direct Simulation Monte Carlo method is used to solve the kinetic equations for the electron, and H/H^+ transport in the upper atmospheres of Mars and Venus including CO_2, N_2 and O.

Applications: The applications of the developed models will be illustrated on the following problems:

- A Monte Carlo model of the electron transport has been developed to calculate the collision-induced component of the Mars dayglow emissions (Shematovich et al., 2008). The model predictions had been compared with SPICAM observations of CO and CO_2^+ FUV emissions. It was found that model reproduces well the observations with the adopted values of collision and excitation cross sections. The peak altitudes are approximately the same for both CO Cameron bands and the $CO_2^+(B^2\Sigma^+ - X^2\Pi)$ doublet. The differences between the calculated for a mean value of SZA=48º and observed emission rates for the CO Cameron bands and $CO_2^+(B^2\Sigma^+ - X^2\Pi)$ doublet are less than 30% and 10% in the peak region, respectively. Calculations suggest the presence of seasonal variations of the altitude of the peak emissions of the CO Cameron bands and CO_2^+ $(B^2\Sigma^+ - X^2\Pi)$ bands.

- A Monte Carlo model was developed to solve the kinetic equation for the H/H^+ transport in the upper Martian atmosphere with taking into account the induced magnetic field (Shematovich et al., 2011). The upward H and H^+ fluxes were calculated, values that can be measured. An energy spectrum of the down moving protons at 500 km adopted from the Mars Express ASPERA-3 measurements in the range 700 eV – 20 keV was used as an input parameter. The particle and energy fluxes of the downward moving protons were equal to 3.0×10^6 cm^{-2} s^{-1} and 1.4×10^{-2} erg cm^{-2} s^{-1}. It was found, that 12% of particle flux and 9% of the energy flux of the precipitating protons is backscattered by the Martian upper atmosphere, if no induced magnetic field is taken into account in the simulations. If a 20 nT horizontal magnetic field, a typical field measured by Mars Global Surveyor (MGS) in the altitude range of 85 km–500 km, was included in the model, it was found that up to the 40% - 50% of the energy flux of the precipitating protons is backscattered depending on the velocity distribution of the precipitating protons. It was concluded that the induced magnetic field plays the crucial role in the transport of charged particles in the upper atmosphere of Mars and, therefore, that it determines the energy deposition of the solar wind.

This work was supported by the Russian Foundation for Basic Research (Project no. 11-02-00479a), Program 22 of the Russian Academy of Sciences «Fundamental problems of the research and exploration of the Solar System», and the Federal Target Program "Academic and Teaching Staff of Innovative Russia for 2009–2013."

Shematovich V. I., D. V. Bisikalo, J.-C. Gérard, C. Cox, S.W. Bougher, and F. Leblanc, Monte Carlo model of the electron transport for the calculations of Mars dayglow emissions. *J. Geophys. Res.*, *113*, 2008, doi:10.1029/2007JE002938.
Shematovich V. I., D. V. Bisikalo, C. Diéval, S. Barabash, G. Stenberg, H. Nilsson,Y. Futaana, M. Holmstrom, and J.-C. Gérard, Proton and hydrogen atom transport in the Martian upper atmosphere with an induced magnetic field, *J. Geophys. Res.*, *116*, 2011, doi:10.1029/2011JA017007.

MARS EXPRESS AERONOMY AND SOLAR WIND OBSERVATION CAMPAIGNS: OVERVIEW AND SELECTION OF RESULTS

O. Witasse[1], H.J. Opgenoorth[2], D. Andrews[2], M. Lester[3], M. Fraenz[4], D. Morgan[5], P. Withers[6], R. Frahm[7], F. Leblanc[8], S. Barabash[9], J.J Plaut[10], R. Orosei[11], F. Montmessin[8], M. Paetzold[12], A. Cardesin-Moinelo[13], H.A. Elliott[7], T. Howard[14]

[1]Research and Scientific Support Department of ESA, ESTEC, PO Box 299, 2200 AG Noordwijk, the Netherlands; [2]Swedish Institute of Space Physics, Uppsala, Sweden. ; [3]Radio and Space Plasma Physics Group, Department of Physics and Astronomy, University of Leicester, Leicester, United Kingdom ; [4]Max-Planck-Institut für Sonnensystemforschung, Max-Planck-Str. 2, 37191 Katlenburg-Lindau, Germany; [5]Department of Physics and Astronomy, University of Iowa, Van Allen Hall 614, Iowa City, IA 52242, USA; [6]Astronomy Department, Boston University, 725 Commonwealth Avenue, Boston MA 02215, USA; [7]Southwest Research Institute, 6220 Culebra Road, P.O. Drawer 28510, San Antonio TX 78228, USA; [8]Latmos, Guyancourt, France; [9]Swedish Institute of Space Physics, Kiruna, Sweden, [10]Jet Propulsion Laboratory, 4800 Oak Grove Drive, Pasadena, CA 91109, USA; [11]Istituto di Astrofisica e Planetologia Spaziali, Istituto Nazionale di Astrofisica, Via del Fosso del Cavaliere, 100, 00133 Roma, Italy;[12]Rheinisches Institut für Umweltforschung, Abt. Planetenforschung, Cologne, Germany; 13 European Space Agency, European Space Astronomy Center, Villafranca del Castillo, PO box - Apt. postal 78, Villanueva de la Cañada, E-28691, Madrid, Spain;[14]Southwest Research Institute, Boulder, USA; Contact: Olivier.Witasse@esa.int

The behavior of planetary upper atmospheres is strongly influenced by the variations in solar activity. At Mars, which does not possess any internal magnetic field, the coupling between the thermosphere, the ionosphere, the induced magnetosphere, and the solar wind is complex; and in a way, the influence is much more direct than at the Earth. The ESA Mars Express spacecraft performs daily measurements of the Mars' upper atmosphere and has acquired a unique data set over a significant portion of the solar cycle, since January 2004. Recently, special coordinated campaigns with four Mars Express instruments have been organised in order to study the effects of solar wind drivers at Mars. Such campaigns took place in March-April 2010 and January-April 2012, when planetary alignments between Earth and Mars (with Mercury and Venus also in 2012) give good opportunities for such studies (see Figure below), where data from solar and solar wind monitoring spacecraft near Earth provided measurements from which to correlate and define the Sun-Mars interaction. We will present an overview of these campaigns and show a selection of results.

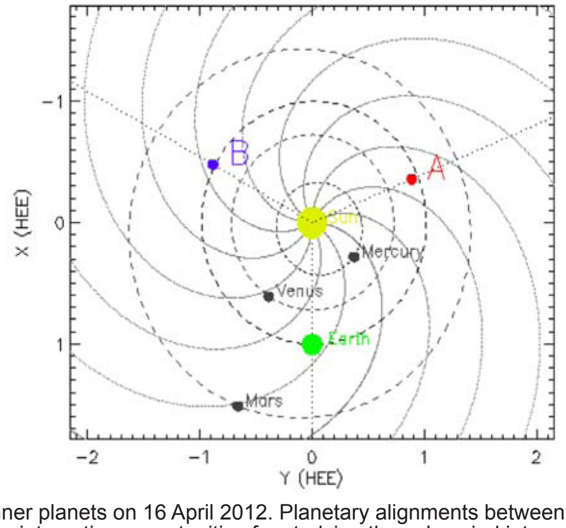

Positions of the inner planets on 16 April 2012. Planetary alignments between Mercury, Earth and Mars give very interesting opportunities for studying the solar wind interaction with planets.

INTERACTION BETWEEN THE SOLAR WIND AND THE MOON OBSERVED BY MAP-PACE ON KAGUYA

Y. Saito[1], S. Yokota[1], M. N. Nishino[1], K. Uemura[1], T. YamamotoO[1], H. Tsunakawa[2], and KAGUYA MAP-PACE TEAM,
[1]Institute of Space and Astronautical Science / Japan Aerospace Exploration Agency, 3-1-1 Yoshinodai, Chuo, Sagamihara, Kanagawa 252-5210, Japan; [2] Tokyo Institute of Technology, 2-12-1 Ookayama, Meguro-ku, Tokyo, 152-8551, JAPAN.
Contact: saito@stp.isas.jaxa.jp

Introduction:

Interaction between the solar wind and a solar system object varies largely according to the object's properties, such as the existence of a global intrinsic magnetic field and/or thick atmosphere. It is well known that the Moon has neither global intrinsic magnetic field nor thick atmosphere. Different from the Earth's case where the intrinsic global magnetic field prevents the solar wind from penetrating into the magnetosphere, solar wind directly impacts the lunar surface. MAP-PACE on Kaguya made observations of low energy charged particles around the Moon at a circular lunar polar orbit of 100km altitude for about 1 year, at ~50km-altitude for about 2months, and some orbits had further lower perilune altitude of ~10km during the last 4 months.

Instrumentation:

MAP-PACE consisted of four sensors: ESA (Electron Spectrum Analyzer)-S1, ESA-S2, IMA (Ion Mass Analyzer), and IEA (Ion Energy Analyzer) [Saito et al., 2008; Saito et al., 2010]. Since each sensor had a hemispherical field of view, two electron sensors and two ion sensors that were installed on the spacecraft panels opposite each other could cover the full 3-dimensional phase space of low energy electrons and ions. One of the ion sensors, IMA, was an energy mass spectrometer that measured mass identified ion energy spectra [Yokota et al., 2009; Tanaka et al., 2009]. The Lunar MAGnetometer (MAP-LMAG) was another component that constituted MAP. MAP-LMAG was a triaxial flux gate magnetometer that was equipped at the top plate of a 12 m long mast to reduce an offset of the interference magnetic field caused by the spacecraft [Tsunakawa et al., 2010; Matsushima et al., 2010; Takahashi et al., 2009; Shimizu et al., 2008]. LMAG measured the vector magnetic field with a sampling frequency of 32 Hz and a resolution of 0.1 nT.

Ion Population on the Dayside of the Moon:

Besides the solar wind, MAP-PACE-IMA (Moon looking ion analyzer) found four clearly distinguishable ion populations on the dayside of the Moon. 1) Solar wind protons reflected/backscattered at the lunar surface, 2) solar wind protons reflected by magnetic anomalies on the lunar surface, 3) reflected/backscattered protons picked-up by the solar wind, and 4) ions originating from the lunar surface/lunar exosphere [Saito et al., 2010].

Solar wind protons reflected/backscattered at the lunar surface. Saito et al. [2008] found that about 0.1% to 1% of the incident solar wind ions were backscattered instead of being perfectly absorbed by the lunar surface. The backscattered ions had lower energy than the incident solar wind ions since part of the energy was lost when solar wind ions collided with the Moon. Although the solar wind consists of alpha particles as a second major component, the backscattered ions consisted of almost no alpha particles. Recently, in order to understand the reflection/scattering characteristics at the lunar surface, the relation between the incidence angle of the solar wind and the output angle of the scattered protons were investigated in detail. It was found that the protons were mostly scattered back inside a scattering cone with ± 40deg. whose center axis was opposite to the incidence vector of the solar wind. It was also found that the energy decrease of the scattered solar wind was most significant along the axis of the scattering cone. Simultaneously with the backscattered protons, there also existed specularly reflected protons when the incident angle was nearly tangential to the lunar surface.

Solar wind protons reflected by magnetic anomalies. Concerning the solar wind protons reflected by magnetic anomalies on the lunar surface, MAP-PACE revealed the plasma structure over lunar magnetic anomalies on the dayside of the Moon using the low altitude data. At ~25km altitude over magnetic anomalies on the Moon, deceleration of the solar wind ions, acceleration of the solar wind electrons parallel to the magnetic field, and heating of the ions reflected by magnetic anomalies were simultaneously observed. The acceleration energy of the electrons was almost the same as the deceleration energy of the ions. It indicates the existence of anti-moonward electric field over the magnetic anomaly above the altitude of Kaguya. The reflected ions had higher temperature and lower bulk velocity than the incident solar wind ions. It suggests the existence of a non-adiabatic dissipative interaction between solar wind ions and lunar magnetic anomalies below Kaguya [Saito et al., 2012].

Reflected/backscattered protons picked-up by the solar wind. The reflected/scattered ions were picked up by the solar wind convection electric field and they were accelerated viewed from the Moon reference frame. Since there existed a solar wind convection electric field seen from the rest frame of the Moon, the backscattered and magnetically reflected solar wind ions were accelerated by the electric field. Saito et al. [2008] showed the acceleration of backscattered solar wind protons for the first time and they named the acceleration as "self-pickup acceleration". This acceleration process should be common to backscattered solar wind ions and magnetically reflected solar wind ions. Since the backscattered/magnetically reflected solar wind ions had initial velocities that were lower than or equal to the incident solar wind ions, the maximum possible acceleration was three times the solar wind velocity, which is different from the pickup acceleration of the ionized neutral particles that have been observed around comets where the maximum acceleration is twice the solar wind velocity.

Ions originating from the lunar surface/lunar exosphere. Yokota et al. [2009] reported the first in situ detection of alkali ions originating from the Moon surface/exosphere. The ions generated on the lunar surface by solar wind sputtering, solar photon stimulated desorption, or micro-meteorite vaporization are accelerated by the solar wind convection electric field and detected by IMA. These ions had the characteristic that the energy is lowest in polar regions (high latitude region) and their energy gradually increased as the spacecraft moved from the polar region to equator region. The ions were observed in only one of the hemispheres. The mass spectra of these ions included C^+, O^+, Na^+, K^+ and Ar^+.

Ions on the Nightside of the Moon:

In the lunar wake region, MAP-PACE found two different types of ion entry into the lunar wake [Nishino et al., 2009; Nishino et al., 2010]. As for the Type-1 entry, solar wind protons entered into the lunar wake in the direction perpendicular to the magnetic field. They gained kinetic energy in one hemisphere while lose in the other hemisphere. As for the Type 2 entry, solar wind protons reflected/backscattered on the dayside of the Moon were picked-up by the solar wind and entered into the deepest lunar wake.

Conclusion:

One of the scientific instruments on Kaguya, MAP-PACE, completed its ~1.5 years of observation of low energy charged particles around the Moon. The newly observed data showed characteristic ion populations on the dayside of the Moon. The MAP-PACE sensors also found new low energy ion/electron populations in the lunar wake region. The newly obtained knowledge about the solar wind – Moon interaction by Kaguya must contribute to the understanding of the plasma environment around non-magnetized solar system objects.

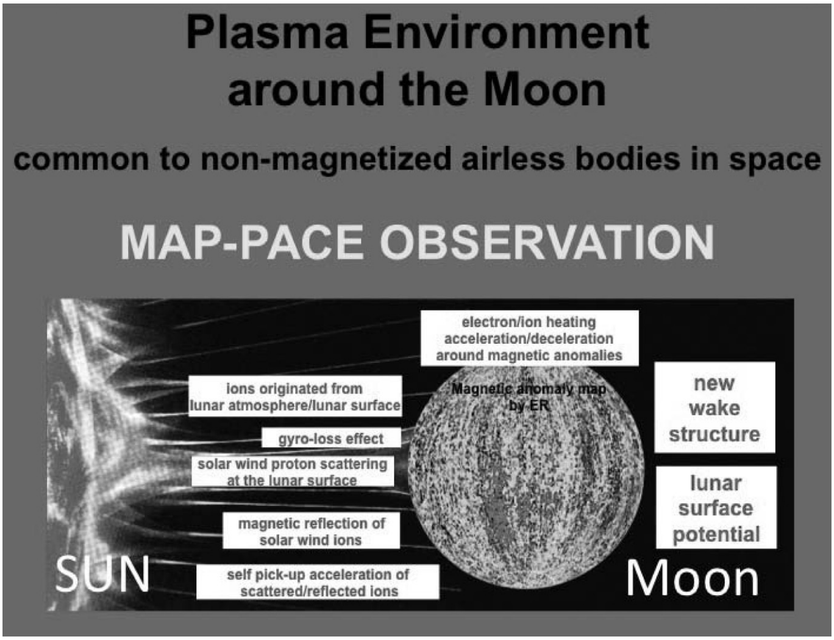

fig. 1. Interaction between the solar wind and the Moon newly found by MAP-PACE on Kaguya

PARABOLOID MODEL OF THE MERCURY MAGNETOSPHERE AS IT LOOKS FROM THE MESSENGER ORBITAL PHASE.

I. I. Alexeev[1], E. S. Belenkaya[1], J. A. Slavin[2],
[1]Skobeltsyn Institute of Nuclear Physics, Lomonosov Moscow State University, Moscow, 119991, Russia; [2]Department of Atmospheric, Oceanic and Space Sciences, University of Michigan, Ann Arbor, Michigan 48109, USA.
Contact: alexeev@dec1.sinp.msu.ru

We discuss a time-averaged model for Mercury's magnetosphere, using MESSENGER magnetometer data from the first three Mercury years when MESSENGER orbiting around Mercury. Based on a paraboloid of revolution approximation to the magnetospheric shape, the paraboloid magnetospheric model has been tested by fitting of the magnetometer data. The magnetospheric field is the sum of contributions from the planetary dipole field, the magnetopause shielding field, and the field due to the tail current sheet. The model magnetospheric magnetic field is specified by a nine parameters:

1) six dipole field parameters:

- the offset of the dipole from the planetary center along the MSO axes: *dx, dy, dz*,
- the dipole tilt, *psi*, and azimuth, *phi*, and
- the equatorial dipole field strength, B_d.

2) three magnetospheric current system parameters:

- the sub-solar magnetopause distance, R_{ss},
- the inner edge (closest approach to the planet) of the current sheet, R_2,
- the tail field, B_T.

The paraboloid magnetospheric Mercury model provides an excellent first order fit to the MESSENGER observations, with a root-mean-square misfit of less than 20 nT globally. For some specific orbits the discrepancy between model forecast magnetic field vector and vector magnetic field measurements is less than 10 nT for each component. Residual field strengths are typically less than 50 nT compared with maximum field strengths in the observations of up to 500 nT.

The significant (up to 480 km) northward dipole offset previously mentioned by *Alexeev et al.,* 2010 have been supported by orbital phase MESSEBGER observations. The tail current sheet crossing by MESSENGER that could be identified as magnetic field depression region well organized by the plane which also shifted to northward direction relative MSO equatorial plane on the dipole offset, *dz*.

THE SOLAR WIND INTERACTION WITH THE LOCAL INTERSTELLAR MEDIUM – RECENT DISCOVERIES MADE BY VOYAGERS AND BY INTERSTELLAR BOUNDARY EXPLORER (IBEX).

V. V. Izmodenov[1,2,3],
[1]Lomonosov Moscow State University, Moscow, Russia; [2] Space Research Institute (IKI) Russian Academy of Sciences; [3]Institute for Problems in Mechanics Russian Academy of Sciences. Contact: vlad.izmodenov@gmail.com

Since 2008 three spacecraft – Voyager 1, Voyager 2 and Interstellar Boundary Explorer (IBEX) - are exploring the outer frontier of the heliosphere, where the solar wind interacts with the local interstellar medium. While both Voyagers provide in-situ data along their trajectories, IBEX is orbiting around the Sun and explores the heliospheric boundaries remotely by measuring global maps of energetic neutral atoms (ENAs) from the outer heliosphere.

This presentation will review current status of the observations and discuss the latest data in contest of modern theoretical concepts of the solar wind – interstellar medium interaction. Current unresolved problems and questions will be underlined.

This work was supported by the grant of the Russian academy of sciences Presidium Program 22: “Fundamental problems of research and exploration of the Solar system”.

ON THE MODELING AGGREGATION OF DUST FRACTAL CLUSTERS IN THE PROTOPLANETARY LAMINAR DISC

A.V. Kolesnichenko*, M.Ya. Marov,**
** M.V. Keldysh Institute of Applied Mathematics, RAS, Moscow, ** V.I. Vernadsky Institute of Geochemistry and Analytical Chemistry, RAS, Moscow*

Evolutionary hydrodynamic model of the formation and growth of fluffy dust aggregates (clusters) in disperse medium of the protoplanetary laminar disc is developed. Basically, the model proceeds from the idea of fractal structure of the primary dust clusters composed originally of the gas and submicron dust particles, which eventually results in planetesimals set up. The disc medium is considered as thermodynamic heterogeneous complex consisted of two interacting subsystems: gas phase of the solar composition (gas continuum) and polydisperse fractal dust phase, the latter consisting of fractions of fractal aggregates and primary condensed monomers. These subsystems are assumed to fill up simultaneously every volume of the Euclid phase space. An original approach to the modeling of hydrodynamic and coagulation processes in such a complex is suggested. It is shown that the process of cluster-cluster coagulation and their partial integration gives rise to the progressive aggregates growing. The point specifically emphasized is that disperse (fluffy) structure of clusters significantly facilitates probability of integration in the collisional processes because of larger geometrical cross section and patterns of motion in the gas medium in terms of friction force change dependence. Dust aggregates of different scales and their internal structure influencing the follow on formation of the intermediate fluffy proto-planetesimals are specially addressed, the latter appearing as the result of the combined physical-chemical and hydrodynamic processes similar to the processes of fractal clusters grow. In contrast to the classic models of protoplanetary cloud based on the continuous mechanics approach when fractions of dusty medium and its fractal nature were not distinguished, our model deals with the set of fluffy dust aggregates as a specific kind of fractal continuous medium where there are hollow regions not fulfilled with particles. Hydrodynamic modeling of such a medium having non-integer mass dimension can be performed in the framework of differential mode of the fractional-integral model with the use of fractional integrals of the order corresponding to fractal dimension of the disc medium.

This work was supported by the grant of the Russian academy of sciences Presidium Program 22: “Fundamental problems of research and exploration of the Solar system”.

MODELING FORMATION OF SELF-GRAVITATING DUST CONDENSATIONS IN A PROTOPLANETARY DISK

A. B. Makalkin, I.N. Ziglina,
Schmidt Institute of Earth Physics, B.Gruzinskaya, 10, Moscow, 123995, Russia.
Contact: makalkin@ifz.ru

Introduction:

Formation of self-gravitating km-sized planetesimals from the 1–10-cm-sized dust aggregates is still a key problem of planet formation theory. In the size range from decimeter-meter to kilometer chemical and van der Waals forces do not work, because the bodies are too large, and gravitation is not effective for growth, because the bodies are too small [1]. Experiments show that collisions of particle aggregates beyond the dm-sizes result in bouncing or fragmentation instead of sticking [2]. Bodies of decimeter to meter in size in the solar nebula (or another protoplanetary disk) quickly migrated to the sun (for ~ 10^3 years from 1 AU) and /or were destroyed in collisions with other particles. This forms so called "m-size barrier" for planetesimal accretion. Therefore a mechanism of gravitational instability (GI) of the dust layer is invoked to form dense dust clumps (condensations) through concentration of particles due to their self-gravity [3]. The condensations subsequently compacted, turning into planetesimals. In the last decade an alternative mechanism of concentration of particles into dense clumps – by turbulence in a protoplanetary disk – is suggested by some authors (e.g., [4]). However turbulence has also a negative effect on the development of GI of dust layer by increasing the relative velocities of particles. The role of turbulence in the formation of planetesimals in protoplanetary disks is not sufficiently studied as yet. Observations of protoplanetary disks around young solar-type stars confirm existence of turbulence in many disks at the T Tauri stage of star evolution, but some basic features of the turbulence, such as lifetime, distribution, structure and possible intermittency, are still unclear. However, it is generally accepted, that GI of the dust layer and formation of condensations is much easier to reach in a quiet time and/or quiet place where turbulent velocities are low enough. In terms of global turbulence driven by magnetorotational instability (MRI) in the disk, such places are called "dead zones". Even in the absence of the global turbulence in the disk, dust particles could not settle to the disk midplane because of counteraction from local turbulence triggered by shear stresses at the boundaries between the dust layer (in Keplerian rotation) and the gas above and below, which rotates slower owing to radial pressure gradient [5]. The shear turbulence prevents the thinning dust layer from reaching the critical density necessary for GI: $\rho_c \approx 0.5 M_*/r^3$, where M_* is the stellar (solar) mass and r is the distance from the star (sun). The problem to reach ρ_{cr} could be solved by reduction the gas/dust mass ratio of one order of magnitude by means of gas removal from the disk through photoevaporation by UV radiation of the young sun. Such a possibility is noticed by a number of authors. However, another problem arises. Some iron-meteorite parent bodies formed within first ~1 Myr (after CAI formation) [6]. From the data on composition of Jovian atmosphere and models of Jupiter's interiors it follows the giant planet is 3-4-fold enriched in solids (or equally depleted in gas). Since Jupiter's formation proceeded for at least 2.2 Myr [7], the planet has formed in more gas-depleted solar nebula than planetesimals, formed in first ~1 Myr. Therefore a significant loss of gas from the disk (3-fold or higher) during formation of first planetesimals seems unlikely.

The only other way for increasing density of the dust layer is redistribution of particles. Since the necessary compaction of the layer in the vertical direction is impossible because of induced shear turbulence, the radial redistribution is invoked. In the protoplanetary disk with global turbulence the redistribution could happen locally, in turbulent vortexes [5]. If disk turbulence is induced by formation of dust layer in the region of disk midplane, the turbulence is rather week and limited to the layer. In this case the redistribution of particles in the dust layer occurs through radial drift of particles (dust aggregates) in the layer towards the sun. The drift is due to the loss of angular momentum by particles which experience a gas drag. Under certain conditions, particles from distant areas drift faster than particles which are closer to the sun, leading to compaction of the layer [8–11]. The study of compaction of dust layer, induction of GI and formation of dust condensations is far from complete, because many physical factors are yet to be taken into account. Here we consider main features of our present modeling and preliminary results.

Main features of modeling:

We consider the global redistribution of mass of the dust layer (also called subdisk) which in fact is the dust-gas layer in the gas-dust protoplanetary disk, including settling of particles (dust aggregates) towards the midplane and particle migration towards the sun. Evaporation of water ice at the "snowline" is taken into account. We calculate time variation of volume (spatial) density and surface (column) density of dust (particle) component of the dust layer (these densities present the total mass of particles in the unit volume and that per unit area respectively). We also compute the radial mass flux of particles in the layer. In the modeling we assume no global turbulence ($\alpha \rightarrow 0$), but account for the induced shear turbulence through calculation of shear stress acting on the layer and rms turbulent random velocities of particles (with suggestion of vanishing average turbulent velocities). When computing particle movement we consider gas drag on the individual particles and also account for the “collective” drag on the layer which is the shear stress. Both drag mechanisms lead to loss of angular momentum. The total particle velocity in the inertial frame is the sum of two parts: the center-of-mass velocity of the narrow annular fragment of the layer and the particle velocity relative the center of mass of this annulus. The total velocity is substituted into the mass conservation (continuity) equation for the column density of dust component. Dividing column density of the layer by layer thickness yields the mean volume density to be compared with the critical one for the onset of GI. The estimated parameters are used in the derivation of dispersion equation, estimating the increment of perturbations and the initial features of dust condensations. We also consider interaction of the condensations with surrounding dust particles to trace the mass increase and compaction of condensations till their turning into planetesimals.

Results and discussion: Sufficient compaction of the dust layer for attainment of GI is found to be possible not for all radial distributions of surface density and temperature of the gas in the protoplanetary disk. The slope of the power distributions $\Sigma_g=\Sigma_1(r/1\text{AU})^{-p}$ and $T=T_1(r/1\text{AU})^{-q}$ should be rather low to satisfy the inequality $p + 1.5q < 2$, e.g. we obtained the effective compaction for the case p=1 and q=1/2 shown in the Figure 1, but not for the cases of p=3/2 and q=1. The exponent p=1 is confirmed by observations of circumstellar disks, and $q \leq 0.5$ is characteristic for thin passive disks. As seen from Figure 1, the GI first occurred in the outer part of the disk (at 50-70 AU for the 100-AU disk) in 5×10^3 yr from the beginning of the layer formation, if particles in the layer reach decimeter size, and GI in 5×10^4 yr if particles are cm-sized. (For simplicity we assume all particles to be of the same size at any given distance at any time). GI covers the formation zone of giant planets in 5×10^4 yr (at any particle size), and at the same time GI reaches the region near 1 AU, but comes to this region from the inner (not outer) zone, close to the metal-silicate evaporation boundary of the layer. (In the inner zone GI happens in 2×10^4 yr.) Finally, in 1×10^5 yr GI occurs in the region about 3–4 AU. Modeling dust evolution in the disk with radius 50 AU shows similar times of GI, but at lower distances. First GI occurs in 5×10^3 yr at ~40 AU. Almost simultaneously it happens at 1 AU and 8 AU. But in the 50-AU disk GI does not occur at 3–4 AU, because the outer boundary of the dust layer passes through this region before the dust layer undergoes sufficient compaction for GI. The modeling shows that during radial contraction and compaction of the dust layer particles pile up and the dust surface density σ_d rises drastically. At 1 AU we obtained increase of σ_d from 11 g cm^{-2} (at the onset of dust layer formation) to 150 g cm^{-2} (at GI). At giant planet distances enrichment in solid material is not so high, but also significant. It follows from this result that most of dust particles would never take part in subsequent processes of planetesimal formation and planet accretion. The particles probably were evaporated at the inner disk boundary and were consequently accreted by the sun.

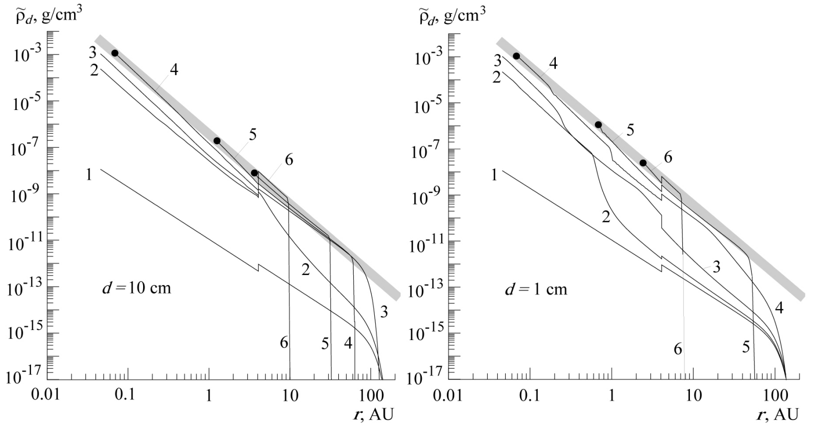

fig. 1. Time variation of mean density distribution in the dust layer of the protoplanetary disk with initial radius r_d=100 AU. (The density is averaged over the thickness of the layer.) Curves 1, 2, …6 correspond to the following time instants from the onset of layer formation (in years): 0, 1×10^3, 5×10^3, 2×10^4, 5×10^4 and 1×10^5. The diagonal band (in gray) shows the critical density for the onset of GI. The band width indicates the uncertainty in the determination of critical density. The bold dots mark the intersections of curves with the middle of the band. The adopted resultant particle size (diameter) in the inner, ice-free region of the layer is 10 cm (*left*) and 1 cm (*right*).

In addition to density, another barrier for GI is particle random velocity which should be rather low to prevent dispersion of newly formed condensations. With an adopted model of induced shear-driven turbulence we modeled GI, derived dispersion relation and estimated perturbation increment. We found that the turbulent random velocities of particles are equal to about a half of the critical velocity for GI. With account for parameter uncertainties (e.g., in critical Reynolds number) this result suggests a rather low probability of formation of dust condensation from the environment which is very abundant in dust. Thus we get one more argument for the low probability of formation of dust condensation in addition to high dust surface density obtained by the modeling.

On the other hand, we found that formation of dust condensations after the GI in the dust layer is very rapid process requiring no more than 100 yr. Subsequent evolution of condensations is determined by their interaction with surrounding dust particles. Our calculation showed that initial masses of condensations in the region near 1 AU are ~ 10^{20}–10^{21} g. After the 10^3–10^4 years of absorption of dust particles and aggregates the condensations compact to densities of solids, tripling their masses and turning into bodies of asteroid mass and size of the order of 10^{21} g and 50 km respectively. The subsequent growth of these bodies to sizes of a few hundred km requires no more than 10^5 yr. Therefore the whole period of formation of 100-km-sized bodies from dust aggregates would not be longer than ~ 10^5 yr. However, the onset of planetesimal formation could be delayed for ~10^6 yr (after CAI). The latter time interval may correspond to the duration of the active turbulent phase of the solar nebula. This interval is consistent with observations of disks around young stars and with ^{182}Hf–^{182}W systematics of some magmatic iron meteorites, which provide data on timing of accretion and differentiation of parent bodies of these meteorites in the solar nebula (~1 Myr after CAI formation) [6].

More calculations and improvements of the model are needed. In particular, we work to improve modeling of the particle growth at collisions and their fragmentation at ice sublimation in order to account for specific features of evolution of the dust layer near the snow line.

This work was supported in part by RAS Presidium Program No. 22 and RFBR, project 11-05-01137.

References: [1] Chiang E., & Youdin A. 2010, Annu. Rev. Earth Planet. Sci., 38, 493. [2] Weidling R., Güttler C., & Blum J. 2012, Icarus, 218, 688. [3] Safronov V.S. 1969. Evolution of the Protoplanetary Cloud and Formation of the Earth and Planets. Nauka Press, Moscow. English Translation: NASA TTF-677. [4] Cuzzi J.N., Hogan R.C., & Shariff K. 2008, Astophys. J. 687, 1432. [5] Weidenschilling S.J. 1980, Icarus, 44, 172. [6] Kleine, T. et al. 2009, Geochim. Cosmochim. Acta, 73, 5150. [7] Hubickyj, O., Bodenheimer, P., & Lissauer, J. 2005, Icarus, 179, 415. [8] Makalkin A.B. 1994, Lunar Planet. Sci. 25, 827. [9] Makalkin A.B., & Ziglina I.N. 2004, Solar System Research, 38, 288. [10] Youdin A.N., & Chiang E.I. 2004, Astophys. J. 601, 1109. [11] Marov M.Ya., Kolesnichenko A.V., Makalkin A.B., Dorofeeva V.A., Ziglina I.N., & Chernov A.V., 2008, in “Problems of Origin and Evolution of Biosphere” LIBROKOM, URSS Press, Moscow.

PLANETS AND THEIR DYNAMICS IN DOUBLE STELLAR SYSTEMS.

I.I. Shevchenko, *Pulkovo Observatory of the Russian Academy of Sciences, Pulkovskoje ave. 65, St. Petersburg 196140, Russia. Contact: iss@gao.spb.ru*

At present time, planets are known to exist in 57 stellar multiple systems (47 double and 10 triple; while 477 exoplanetary systems are identified in total), thus the multiplicity rate of host stars of exoplanetary systems is about 12% (Roell et al., 2012). The majority of planets found in double systems are in S-type orbits (around one component of a binary), and others are in P-type orbits (around both components). The S-type orbits are also called inner orbits, and the P-type orbits are also called outer or circumbinary orbits. Planet formation scenarios and the observed planetary dynamics (often "at the edge of stability") in binaries pose a number of theoretical challenges, especially in what concerns circumbinary planets. In particular, modern models of planet formation in circumbinary planetary systems imply substantial migration of planetary cores to the current locations of planets, whereas dynamical studies point to the plausibility of in situ formation. In this report, the stability of planetary orbits in binary stellar systems is considered with respect to possible formation scenarios, in application to both hypothetical and actual planetary systems in binaries.

The stability diagrams in the "pericentric distance — eccentricity" plane of initial data are considered, and the domains of stable and unstable (regular and chaotic) behaviour are identified for a number of binary systems, including *α* Centauri A–B and *Kepler*-16, 34 and 35. (Hypothetical planets are implied in the first case.) To construct the diagrams, a statistical method based on an analysis of results of massive computations of Lyapunov exponents is used, as proposed and described in Melnikov and Shevchenko (1998). The computations are performed in the framework of the planar restricted and full three-body problems. The Lyapunov exponent criterion, applied for the construction of the stability diagrams, provides much better resolution of the chaos-order borders in the stability diagrams in comparison with a straightforward "escape-collision criterion".

The chaos-order borders possess fractal structure due to orbital resonances; the chaotic domains substantially widen with the eccentricity of the initial orbit of the planet (Popova and Shevchenko, 2012*a*). Besides, the orbit size threshold for the stability of the planetary motion is a function of the binary's mass ratio and eccentricity.

The recently discovered planet *Kepler*-16b follows a circumbinary orbit around a system of two main-sequence stars (Doyle et al., 2011). The stability diagrams in the "pericentric distance — eccentricity" plane show that *Kepler*-16b is in a hazardous vicinity to the chaos domain — just between the instability "teeth" in the space of orbital parameters. *Kepler*-16b survives, because it is close to the half-integer 11/2 orbital resonance with the central binary (Popova and Shevchenko, 2012*b*). (In the Solar system, its survival is analogous to the survival of Pluto and plutinos, which are in the 3/2 orbital resonance with Neptune. The order of the "occupied" half-integer resonance grows with the mass parameter μ of the perturbing binary, because increasing μ shifts the stability border outwards; in the case of the Solar system the relevant "binary" is the Sun and Neptune.) The neighbouring resonance cells are vacant, because they are "purged" by *Kepler*-16b, due to overlap of first-order resonances with the planet.

Stability diagrams in the "pericentric distance — eccentricity" plane constructed for the recently discovered (Welsh et al., 2012) planets *Kepler*-34b and 35b, following circumbinary orbits in double systems of main-sequence stars, show that the planets are at the fractal border of chaos in the phase space of motion; however, they are safe in resonance cells centered, respectively, on 21/2 and 13/2 orbital resonances with the central binaries. Thus the dynamical behavior of planets in the *Kepler*-34 and 35 systems is qualitatively similar to that in the *Kepler*-16 system.

No radial migration was possible in the *Kepler*-16b evolution since its formation, because otherwise it would cross the instability "teeth" and thus would be removed. A similar conclusion is valid in the case of *Kepler*-34b. Note however that in situ formation of *Kepler*-16b is a theoretical challenge, because planetesimal accumulation at the planet present location, according to modern theoretical models, is hard to be accomplished (Meschiari, 2012; Paardekooper et al., 2012). The current resonant (quasiresonant) status of *Kepler*-16b should be taken into account when developing formation scenarios for circumbinary planets.

This work was supported by the grant of the Russian academy of sciences Presidium Program 22: "Fundamental problems of research and exploration of the Solar system".

References: Doyle, L., et al., 2011, Science, 333, 1602; Melnikov, A.V., Shevchenko, I.I., 1998, Astron. Vestnik, 32, 548 [Sol. Sys. Res., 32, 480]; Meschiari, S., 2012, Astrophys. J., 752, 71; Paardekooper, S.-J., Leinhardt, Z.M., Thébault, T., Baruteau, C., 2012, arXiv: 1206.3484 [astro-ph.EP] http://arxiv.org/abs/1206.3484; Popova, E.A., Shevchenko, I.I., 2012a, Pis'ma v Astron. Zhurn., 38, 652 [Astron. Lett., 38, 581]; Popova, E.A., Shevchenko, I.I., 2012b, arXiv: 1207.0101 [astro-ph.EP] http://arxiv.org/abs/1207.0101; Roell, T., et al., 2012, Astron. Astrophys. 542, A92Welsh, W.F., et al., 2012, Nature, 481, 475

MICROMETEORITES OF THE NOVAYA ZEMLYA ARCHIPELAGO.

D. D. Badjukov[1], K. M. Ryasantsev.[1],
[1]V. I. Vernadsky Institute of geochemistry and analytical chemistry, 19, Kosygin str., 199991, Moscow, Russia.. Contact: badyukov@geokhi.ru

Introduction:

The flux of extraterrestrial material to the Earth is around 30,000 t/a [1, 2]. The accreted material consists mostly of interplanetary dust particles that interact with the atmosphere and reach the Earth's surface as micrometeorites (MMs). The MM accretion rate has been estimated to lie in a range from 2,700 to 14,000 t/a [3; 4] and it overwhelms the meteorite flux which is approximately ~50 t/a [5]. The dust accretion rates of the Earth as estimated from MMs in Antarctic ice are fairly compatible with those measured outside the Earth's atmosphere, because uncertainties in the estimations are as high as 50 % if evaporation and disruption of interplanetary dust particles during their atmospheric entry are taken into the account. Asteroids have been considered as the main source of MMs [6]. On the other hand, it has been proposed that MMs might originate from comets [7]. Anyway, some MMs might be related to extraterrestrial rocks, which appear not to be represented in our meteorite collections. Micrometeorites can be found where convenient conditions result in their accumulation and preservation. Initially deep-sea deposits (red clay) were the main source for cosmic spherules (8). Antarctic and Arctic glacier surfaces are good collectors of terrestrial and extraterrestrial dust [7] and now micrometeorites are collected mainly from the Antarctic ice sheet [7; 9; 10]. Polar ice caps can provide specific areas for micrometeorite sampling, too. One such ice cap is located in the Northern Island of the Novaya Zemlya archipelago, Russia.

The Novaya Zemlya glacier sheet:

The glacier sheet of the Northern Island of the Novaya Zemlya archipelago covers approximately 55% of the island's territory. The island is 430 km long, 40 to 45 km wide and 0.9 km high. The maximal age of the glacier ice is estimated to be less than 1 ky [11] and this is also the maximum age of the oldest solid fraction present in the ice. The northeastern part of the sheet is characterized by passive margins where glacier ice contains solid components including accumulated MMs. The glacier seems to have negative annual mass balances [11]. This makes the marginal glacier areas with solid component concentrations to be very suitable places to find fine-grained samples that may contain MMs.

The edges of the glacier margins have a smooth surface with an outward slope of a few degrees. The border zone between glacier and the country rock has an edge moraine that consists of unsorted bedrock debris that covered blue ice. The local folded Silurian sedimentary bedrocks consist of black and gray siltstone, shale, and fine-grained sandstone. Patches of clayish appearing matter are located on the ice surface close to the moraine-glacier border, which consists of accumulated beads of possibly cryoconite. Previous works have been demonstrated that the cryoconite contained cosmic spherules and scoriaceous and unmelted micrometeorites. The maximum MM concentration was ~150 particles per gram in clayish-free fractions studied.

The 2012 field season:

To collect large samples of cryoconite, the margin of the Northern Ice Cap near the Ivanov bay, 1 km to SE from the head of the Snezhnaya river, 76˚54'N, 67˚35'E , was visited during the August 2012 field season. The "Mikhail Somov" ship belonging to the Northern department of hydrological and meteorological service (Arkhangelsk, Russia) was used for delivery of the expedition crew to the base of national park "Russian Arctic" located on the Zhelaniya cap at a former polar station. The expedition started its work on 11 August and finished on 25 August when the crew was evacuated on the ship back. Margins of the glacier at the work area near Snezhnaya are characterized by a 200-m width zone with a high concentration of so-called cryoconite holes with diameters ranging from a few mm to tens of cm and depths of 5 – 30 cm. The holes are filled by water and their bottoms are covered by cryoconite deposits formed a few mm thick layers. During the field work we collected approximately 30 kg of the cryoconite deposits. This amount may contain 10 000 – 100 000 MMs. Preliminary preparation of a small sample in our field camp demonstrated a rather low content of a "sandy" fraction that was rich in different types of MMs, so we were able to recognize cosmic spherules right in the field. Scoriaceous and unmelted MMs have been found in the sample later in the laboratory using stereomicroscope.

This work was supported by the grant of the Russian academy of sciences Presidium Program 22: "Fundamental problems of research and exploration of the Solar system".

References: [1]. Love S.G. and Brownlee D.E. 1993. *Science* **262**: 550-553; [2]. Peucker-Ehrenbrink B. and Ravizza G. 2000.*GC.* **64:** 1965-1970. [4] Taylor S. et al., 1998.. *Nature* 392: 899–903; [4]. Yada et al. 2004. *Earth Planets Space* **56**:67–79. [5]. Halliday et al. 1989. *Meteoritics* 24:173-178; [6] Brownlee et al. 1997. *Meteoritics & Planetary Science* **32:** 157-175; [7] Maurette M., *Micrometeorites and the Mysteries of Our Origin,* Springer, 2006; [8] Brownlee D.E. 1985. *Annual Review of Earth and Planetary Sciences.* **13:** 147-173; [9] Taylor S. et al., 2000. *Meteoritics & Planetary Science* **35:** 651-666; [10] Duprat J. et al., *Advances in Space Research* 39:605-611; [11] Koryakin V.S. 1990. *Arctic glaciers.* Moscow: Nauka press. 158 p. (in Russian).

WATER-ICE CONTENT IN TITAN AND CALLISTO.

A. N. Dunaeva, V. Kronrod, O. Kuskov
Vernadsky Institute of Geochemistry and Analytical Chemistry, Russian Academy of Sciences, Moscow, Russia, Contact: dunaeva@kmail.ru

Introduction:

The total content of H_2O in the cosmic objects and their water/rock ratio are the important criteria for understanding the conditions of origin and evolution of the water-containing cosmic bodies.

In this paper an estimation of the H_2O content in Callisto and Titan, the large icy satellites of Jupiter and Saturn, formed in the outer zone of the relative central planet were performed.

For this purpose, on basis of the approach accepted in the [1, 2], any possible models of the internal structure of the satellites were considered; in this case it was assume that these satellites are composed of three main structural elements: the outer water-ice shell, rock-ice mantle and rock-iron core. The boundaries between the areas, the densities of their constituent materials and the total concentration of H_2O in the satellites were measured by the calculations performed on basis of the equations for a hydrostatic equilibrium, moment of inertia and mass of satellites, the equations for a state of high-pressure water ices [3] and the equation for calculating the ice component concentration in the rock-ice area of satellite.

In all calculations, the density of the internal rocky core of the satellites was assumed to be equal to 3.62 g/cm^3, and the density of the rock-iron (*Fe-Si*) component in the rock-ice area was chosen in the typical range for the chondritic material, taking into account a probable hydration of silicates – from 3.15 to 3.62 g/cm^3 [1].

Computer simulation and results:

The simulation results have shown that Titan and Callisto are partially differentiated satellites in which the substance complete separation in both ice and rock components didn't occurred.

The outer water-ice shell of the satellites with maximum capacity of 330 km for Callisto and 520 km for Titan is composed of the ice I*h* and its high-pressure species (ices III, V, VI), and an internal ocean of liquid water between the Ih-ice and other ice-modifications may probably exist.

The size of the outer water-ice shell is an important parameter that determines the structure and capacity of all underlying satellites layers. Thus, in event of the maximum capacity of the icy crust, no rocky core is being formed in the satellites, and the whole interior of Titan and Callisto looks like undifferentiated rock-ice mixture with an average density of 2.6 g/cm^3 and 2.3 g/cm^3 respectively. On the contrary, when there is no any water-ice crust (or its size is minimum), the inner core of Titan and Callisto has a maximum size up to 1490 km and 1280 km respectively and it's covered by the outer rock-ice mantle with thickness of about 1080 km and 1100 km and with the average density of the matter 1.4 g / cm^3 and 1.6 g/cm^3 respectively.

The total water content in the satellites depends directly on density of the *Fe-Si* component in the rock-ice mantle, and in a less degree this content is determined by size of the outer water-ice shell. At high densities of the *Fe-Si* component, the total water content is not practically changing while the water-ice crust thickness is changing on. In case of low densities of the *Fe-Si* component, there is evidenced an obvious inverse relationship: as the outer ice shell is increasing, the total content of H_2O in the satellites is decreasing (Fig.1).

In general, the performed calculations have revealed that the total content of H_2O in Titan and Callisto, defined as the summary concentration of water in the outer ice shell and inner rock-ice mantle, lies within a fairly narrow range of values of 45 – 52 wt.% and 48 – 54 wt.% respectively. At the same time, a substantial area of the diagrams overlap in the Figure 1 (shown by specks) testifies that the total content of H_2O in Titan and Callisto can be quite the same under the certain admissible parameters of the internal structure and composition of the satellites, notably:

The same low-density of the *Fe-Si* component: in the range of 3.15 to 3.36 g/cm^3,

And simultaneously the external water-ice shell thickness not less than 200 km of Callisto and not more than 330 km of Titan.

The results of the previous studies [4] have shown that the water content in the other large moons of the Solar System, such as Europe and Ganymede, is 7 – 8 wt.% and 46 – 48 wt.% respectively, and the Io moon, the closest to Jupiter, is essentially waterless. The total concentration values of H_2O in the icy moons of Jupiter and Saturn in comparison with their average densities values are shown in Fig. 2.

Figure 2 shows that as the distance from the relative central planet is increasing, the H_2O content in the satellites is increasing as well, but their density is regularly decreasing. In this case all external ice satellites (Ganymede, Callisto and Titan) differs just a little from each other in density and in total water content which in average is about 50 wt.%. This indicates that despite of the fundamental difference in the internal structure (Ganymede, unlike Callisto and Titan, is fully differentiated on the metallic core, the *Fe-Si* mantle and the water-ice shell [4]), all external satellites have almost the same water/rock ratios being close to 1.

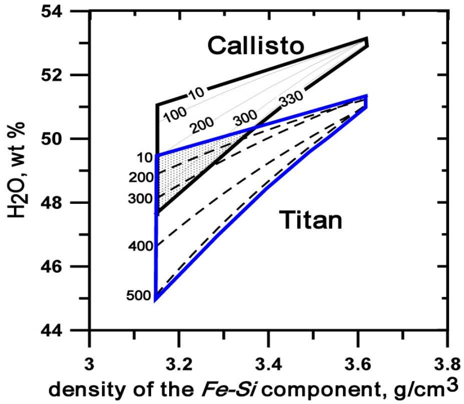

fig. 1: The total water content in Callisto and Titan, depending on the density of the *Fe-Si* mantle component. The blue outline is the model of Titan and the black outline is the model of Callisto. The specks show the range of parameters in which the same content of H_2O in satellites is possible. The solid and dotted lines within the contours are the lines of the satellites water-ice crust equal thickness (indicated by numbers, in km).

The relatively high (and close in the value) water content and the same density of the satellites' rock material in the range of 3.15 - 3.36 g/cm^3 allow to have assumption that Ganymede, Callisto and Titan have the same composition of the *Fe-Si* component, which is characteristic for the hydrated L / LL chondrites [1-2, 4]. This may testify that the rock-ice planetesimals similar in their composition were involved in processes of Ganymede, Callisto and Titan formation, and they appeared as an additional source to bring H_2O and rocky components into the satellites' formation zone. At the same time, depending on temperature and thermal conditions, the redistribution of the material in the satellites (that determines their internal structure) can vary significantly. Thus, Titan and Callisto located in different planetary systems and occupying the most remote (low temperature) position relative to their central planets, are the most similar in their physical characteristics and they have the same internal

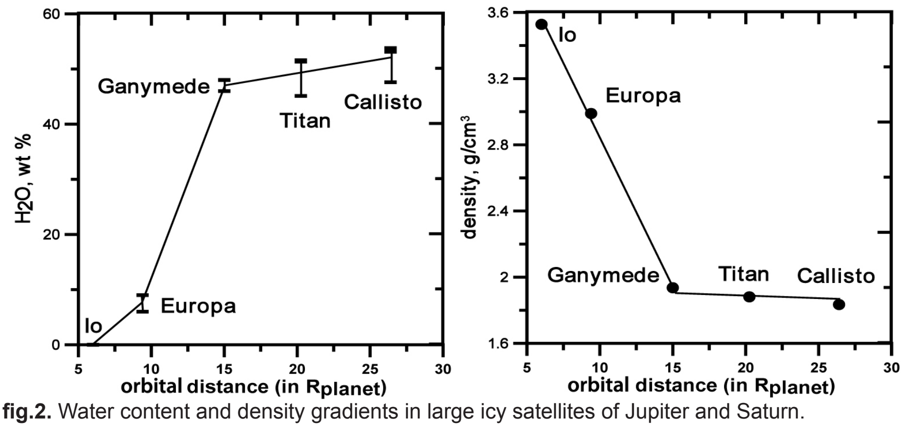

fig.2. Water content and density gradients in large icy satellites of Jupiter and Saturn.

structure being essentially different from the structure of Ganymede which is the nearest to the central planet. Therefore, the structural difference of the outer satellites of Jupiter and Saturn may reflect the influence of different temperature regimes on the processes occurring within the protoplanetary and protosatellite accretion disks.

Acknowledgements:
This work was supported by RFBR grants 05-00178 and 12-05-00033 and by the grant of the Russian academy of sciences Presidium Program 22: “Fundamental problems of research and exploration of the Solar system”.

References:

[1] Kronrod, V.A., Kuskov, O.L.: Chemical differentiation of the Galilean satellites of Jupiter: 1. An internal structure of Callisto's water-ice shell, Geokhimiya, № 9, pp. 968-983, 2003.
[2] Kuskov, O.L., Kronrod, V.A.: Internal structure of Europa and Callisto, Icarus, V. 177, pp. 550–569, 2005.
[3] Dunaeva, A.N., et al.: Phase diagram of H_2O: Thermodynamic functions of the phase transitions of high-pressure ices, Solar System Research, Vol. 44, № 3, pp. 202-222, 2010.
[4] Kuskov, O.L., Kronrod, V.A.: Core sizes and internal structure of the Earth's and Jupiter's satellites, Icarus. Vol. 151, pp. 204–227, 2001.

ICES OF THE SATURN SYSTEM.

V.A. Dorofeeva,
Vernadsky Institute of Geochemistry and Analytical Chemistry RAS, Russia

Introduction. The Saturn system is very complex. It contains a massive ring, as well as many satellites being regular (24) and trapped (38). They all differ in the structure, physical properties and chemical composition. But at the same time, all of these objects have one common property: they all contain ice H_2O. This fact is extremely important because it allows to consider some important problems of cosmogony, in particular, to analyze the conditions of the formation and evolution of the Saturn system objects.

Water ice in the interstellar molecular clouds is known to be in the amorphous state and has a high D/H, may be ~ 7×10^{-5}, as in LL3 chondrites, or even higher [Robert, 2006]. So it has had to remain in the outer regions of the solar gas-dust disk (r > 30 AU). If amorphous ice evaporates when the nebula was heated, its D/H decrease as a result of the isotope exchange reaction HDO + H_2 = DHO + HD up to D/H ~ 1.6 (WSMOW, OH-group of carbonaceous chondrites [Robert, 2006], the comet 103P/Hartley 2 Jupiter-family [Hartogh et al., 2012]). During the subsequent nebula cooling crystalline ice was formed. Crystalline ice of various modifications was also formed in the large (R > 30 km), rock-ice bodies in the process of their differentiation as a result of the internal heating.

The rings of Saturn. According to the «Cassini» research, the most massive of A and B, with a mass of $(0.5\text{-}0.7)\times10^{22}$ and $(4\text{-}7)\times10^{22}$ g respectively [Robbins et al., 2010] consist of a set of particles of nearly pure (95-98 %) of crystalline water ice ranging in size from 10 cm to 10 m [Nicholson et al., 2008]. Such particles could not have been formed by condensation or accumulation. The icy mantle of the differentiated rock-ice body with R ~ 600 km and a mass of 10^{23} - 10^{24} g, which was destroyed by the tidal influence of Saturn could be assumed as its original source. The body was formed in the first 1-2 million years of evolution of the Solar system and has passed the stage of melting ice water due to radioactive heat ^{26}Al and differentiated to form the icy crust [Roussol et al., 2011]. There could be several bodies, but their mass should be sufficient to keep the water in the liquid state during the time, which is necessary for the complete differentiation.

The satellites of Saturn. After the «Cassini» experiments were considerably refined the values of the specific density (ρ) of many moons of Saturn. First of all ρ values characterize the ice/rock in these bodies. Let us compare those with the values of ρ obtained for condensed phases in the condition of equilibrium of the solar cooling system.

In the gas phase of the gas-dust solar disk (nebula) the carbon existed in a form of CH_4, CO, CO_2. The ratio of the oxidized and reduced forms of carbon - $(CO+CO_2)/CH_4$ or CO/$\sum$C controlled the amounts of water vapor and, therefore, the ratio of ice/rock in the condensed phase, that is its density. According to the results of equilibrium calculations in a system of solar composition at low T and P (T <600K, P <10^{-7} bar, Fig. 1), C is found in a form of CH_4, and all oxygen not being included in the rock compounds – in a form of H_2O. In this case, the rock/ice mass ratio will be as ≈ 1:1, and the resulting density of the body as ≈ 1.42 kg/m³ (Fig. 2). But, as it was shown by experimental data, the gas-phase reaction of CO + $3H_2$ = CH_4 + H_2O is kinetically inhibited at T ~ 700 K. In addition, in interstellar clouds not only CO is observed, but the refractory organic compounds (mainly CHON), which may include up to 50% $\sum$C (total mass of C) [Pollack et al., 1994]. In addition, the results of the calculation depend on the remaining uncertainty of our knowledge of the relative contents of volatile elements in a solar composition gas. Comparison tables of relative solar abundances shows that the value of C/O varies from 0.42 (Anders, Grevesse, 1989) to 0.62 (Anders, Ebihara, 1982). In the calculation of the possible range of density rock-ice condensates in the region of the Saturn formation, we used a solar abundances by (Lodders, 2010) with the C/O = 0.46 and for comparison the table of (Lodders, 2003) with the C/O = 0.50. In our calculations we used the following parameters: ρ_{ice} = 0.944, ρ_{org} = 1.7, $\rho_{silicates}$ = 3.36, $\rho_{FeS+FeO}$ = 4.88 kg/m³ (Jonson, Lunine, 2005).

The results (Fig. 2, thick solid and dashed lines) show the variation of the parameters in the assumed range (CO/$\sum$C from 0 to 0.4 and $C_{орг.тв}$/$\sum$C from 0 to 0.5) gives the change in specific density condensate (at zero porosity) from 1.42 up to 1.54 kg/m³ (selected rectangle) with the uncertainties of the bulk composition up to 1.62 kg/m³. This interval includes ρ Dione values, but the density of Rhea and Tethys being two other major regular satellites of Saturn is found to be well below this value. Since these satellites are sufficiently large (D = 1000-1500 km) in diameter, and having hypothetically the zero porosity as well as they are located relatively close to each other (within 5-9 R_{Sat}), the accuracy of calculated Rhea and Tethys ρ value needs clarification.

The corroborated «Cassini» Enceladus ρ value (1.61 g/cm³) may indicate that some of the H_2O was lost during the eruption of water plume.

As for the Titan, it is clear from Fig. 2, that within the entire range of CO/ΣC and $C_{орг.тв}$/ΣC values of solar composition it is impossible to obtain the ρ rock-ice condensate value being 1.88 g/cm3. It can be assumed that some of H_2O was used up in the reaction of serpentinization, and the subsequent formation of the CH_4 Titan's atmosphere by the reduction of CO_2. But it could not so radically increase the density value. It is more likely, the embryo (s) of the Titan began to form at $T > 150$ K, when the H_2O was in a form of gas phase. In the process of nebula cooling the embryos of the Titan firstly included H_2O ice and then other volatiles in a form of CO_2 (ice), crystalline (NH_4OH) and clathrate hydrates of several gases.

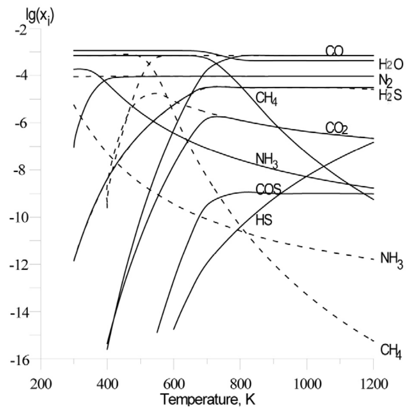

fig. 1. The equilibrium gas phase composition of the protoplanetary gas-dust disk at different temperatures (the formation of condensed phases are taken into account in the calculation) and for two values of the total pressure P = 10.3 bar - solid lines and P = 7.10 bar - dotted line.

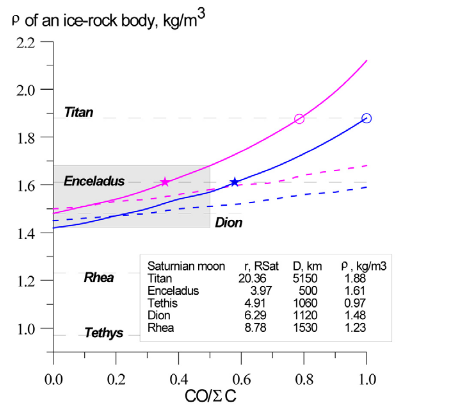

fig. 2. Dependence of the specific density of the condensate on the ratio of CO/ΣC. Solid lines without CHON formation, dotted line - $C_{орг.тв}$/ΣC = 0.5. The thick lines correspond to the results of calculation for total composition system (Lodders, 2010, C/O = 0.46), thin - on (Lodders, 2003, C/O = 0.50).

Volatiles on Titan and Enceladus. The massive Titan's atmosphere which creates the surface $P = 1.5$ bar consists of about 95 mol% of a N_2 and ~ 5 mol% CH_4. It is known that the accumulation of volatiles (N_2, NH_3, CH_4, CO, Ar, Kr, Xe) in the solar nebula was possible in terms of their sorption by the amorphous H_2O ice, or by the formation of solid crystalline and clathrate hydrates. The sorption mechanism is possible at very low temperatures ($T < 35$ K) and most likely implemented in the trans-Neptunian region ($r > 30$ AU) in the formation of long-period comets and Kuiper belt objects. Therefore, it is generally assumed that the composition of Titan's volatiles existed in the form of solid crystalline and clathrate hydrates. Its formation could be realized only in the case that in the region of Saturn H_2O ice was present in the crystalline form. It means that the primary amorphous ice was vaporized. The vaporization requires the pressure values of $10^{-6} – 10^{-8}$ bar at $T > 140$K. The analysis of boundary conditions for thermal model of the solar accretion gas-dust disk indicates that at the stage of disk growth the matter of the inner zones was included in the Saturn region at the conditions of $T > T_{\mathrm{cond.\ ice}\ H2O}$ at the distance of $r \sim 10$ A.U. and saved in the region during the first 1.5-2 million years. This hypothesis is indirectly supported by the experimental D/H values of the isotopic $CH_4 = 1.58\times10^{-5}$ measurements in Titan's atmosphere. If we assume that CH_4 was formed by the CO_2 reduction mechanism in the depths of the ocean under the ice water the (D/H_{CH4}) value should be equivalent to D/H_{H2O}. The value $D/H_{CH4} = 1.58\times10^{-5}$ is surprisingly similar to the value known for the inner regions the solar system.

High value of D/H_{H2O} (2.9×10^{-5}) as well as other gaseous ratios in the Enceladus water plumes supports the hypothesis that the chemical composition of the primary Enceladus was near to cometary and was formed at the large radial distance.

The study was supported in part by RAS Presidium Program №22 and RFBR project 11-05-01137 .

References:

Castillo-Rogez J.C. et al. 2012, Icarus 219, 86–109. Jonson T.V., Lunine J.I. 2005, Nature, 435, 69-71. Lodders K. 2003, Astrophys. J., 591,1220-1247. Lodders K. 2010. Solar System Abundances of the Elements. Principles and Perspectives in Cosmochemistry, Astrophysics and Space Science Proceedings, Volume . ISBN 978-3-642-10351-3. Springer-Verlag Berlin Heidelberg, 2010, p. 379. Pollack J.B. et al. 1994. Astrophys. J., 421, 615-639. Robbins S.J. et al. 2010, Icarus, 206, 2, 431-445. Nicholson P.D. et al. 2008, Icarus, 193, 182-212. Robert F. Solar System Deuterium/Hydrogen Ratio. In : Meteorites and the Early Solar System II Univ. Arizona Press. 2006. 942 pp. p. 341-351. Roussol A.V., Dorofeeeva V.A., Ruskol E.L. Bulletin of the Department of Earth RAS, 2011, 1

AGE AND EVOLUTION OF SATURN'S RINGS

L. W. ESPOSITO, B. K. Meinke, N. Albers, and M. Sremcevic,
LASP, University of Colorado, Boulder, USA;
Contact: larry.esposito@lasp.colorado.edu

Cassini experiments have watched Saturn's ring system evolve before our eyes. Images and occultations show changes and transient events. The rings are a dynamic and complex geophysical system, incompletely modeled as a single-phase fluid.

Key Cassini observations: High resolution images show straw, propellers, embedded moonlets, and F ring objects. Multiple UVIS, RSS and VIMS occutlations indicate multimodal ringlet and edge structure, including free and forced modes along with stochastic perturbations that are most likely caused by nearby mass concentrations. Vertical excursions are evident at ring edges and in other perturbed regions. The rings are occasionally hit by meteorites that leave a signature that may last centuries; meteoritic dust pollutes the rings. Temperature, reflectance and transmission spectra are influenced by the dynamical state of the ring particles.

Saturn's Equinox 2009: Oblique lighting exposed vertical structure and embedded objects. The rings were the coldest ever. Images inspired new occultation and spectral analysis that show abundant structure in the perturbed regions. The rings are more variable and complex than we had expected prior to this seasonal viewing geometry.

Sub-kilometer structure in power spectral analysis: Wavelet analysis shows features in the strongest density waves and at the shepherded outer edge of the B ring. Edges are variable as shown by multiple occultations and occultations of double stars.

F ring kittens: 25 features seen in the first 102 occultations show a weak correlation with Prometheus location. We interpret these features as temporary aggregations. Simulation results indicate that accretion must be enhanced to match the kittens' size distribution. Images show that Prometheus triggers the formation of transient objects.

Propellers and ghosts: Occulations and images provide evidence for small moonlets in the A, B and C rings. These indicate accretion occurs inside the classical Roche limit. Implications: Self gravity causes wakes, viscosity, overstability and local aggregate growth. Nearby moons and resonant forcing drive the ring system away from equilibrium through streamline crowding, which allows enhanced accretional growth. Structures form and disappear at length scales from meters to kilometers, on time scales of hours to months. This cyclic behavior resembles an ecological predator-prey system or a boom-and-bust economic cycle. In such an agitated stochastic system, solid bodies may represent the absorbing states of a Markov chain: rare events can produce a distibution with many transient but a few long-lasting bodies. **Age and evolution**: These bodies would preferentially form at shepherded ring edges near the Roche limit, as hypothesized by Charnoz. These large bodies can sequester material in their interiors, reducing the amount of meteoritic ring pollution and recycling the ring material into new rings. Such processes would allow the rings to be as ancient as the solar system.

TITAN'S PHOTOCHEMICAL MODEL: FURTHER UPDATE, OXYGEN SPECIES, AND COMPARISON WITH TRITON AND PLUTO

Vladimir A. Krasnopolsky[1, 2],
[1]Catholic University of America, Washington, DC 20064, USA; [2] Moscow Institute of Physics and Technology, Doldoprudnyy, Russia.
Contact: vlad.krasn@verizon.net

The photochemical model for Titan's atmosphere and ionosphere is improved using the Troe approximation for termolecular reactions and inclusion of four radiative association reactions. Proper fitting of eddy diffusion results in a reduction of the mean difference between 63 observed mixing ratios and their calculated values from a factor of 5 in our previous Titan's models to a factor of 3 in the current model (Fig. 1). Oxygen chemistry on Titan is initiated by influxes of H_2O from meteorites and O^+ from magnetospheric interactions with the Saturn rings and Enceladus. Two versions of the model were calculated, with and without the O^+ flux. Balances of CO, CO_2, H_2O, and H_2CO are discussed in detail for both versions. The calculated model with the O^+ flux agrees with the observations of CO, CO_2, and H_2O, including recent H_2O CIRS limb observations and measurements by the Herschel Space Observatory.

Major observational data and photochemical models for Triton and Pluto are briefly discussed. While the basic atmospheric species N_2, CH_4, and CO are similar on Triton and Pluto, properties of their atmospheres are very different with dominating atomic species and ions in Triton's upper atmosphere and ionosphere opposed to the molecular composition on Pluto. Calculations favor a transition between two types of photochemistry at the CH_4 mixing ratio of ~5×10^{-4}. Therefore the current Triton's photochemistry is still similar to that at the Voyager flyby despite the observed increase in N_2 and CH_4. The meteorite H_2O results in precipitation of CO on Triton and CO_2 on Pluto near perihelion.

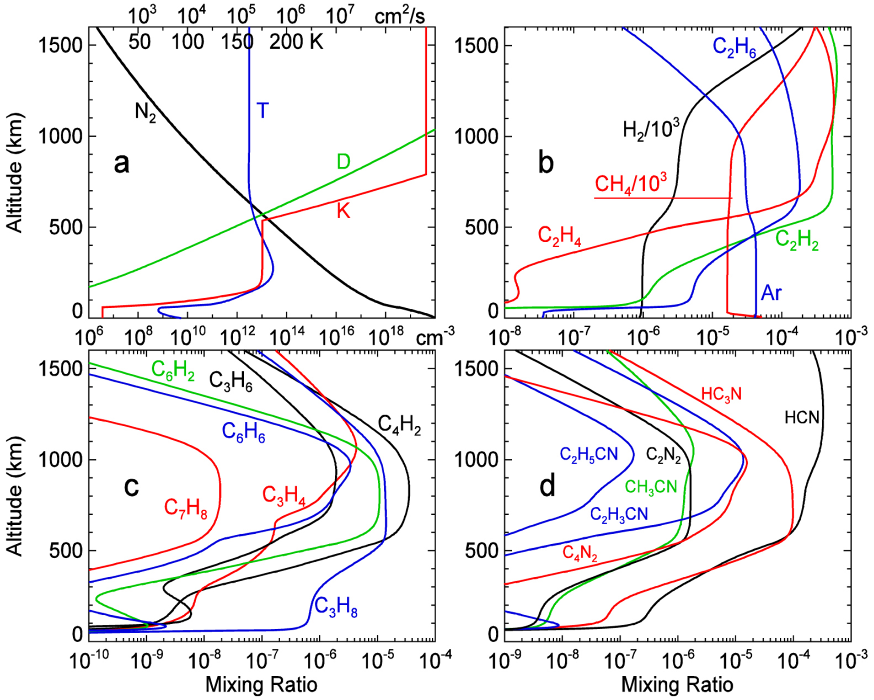

fig. 1. Initial data and calculated vertical profiles of neutral species in the model: (a) profiles of temperature, N_2 density, eddy and molecular (CH_4 in N_2) diffusion; (b) CH_4, H_2, Ar, and C_2H_x hydrocarbon; (c) some other abundant hydrocarbons; (d) the most abundant nitriles..

FURTHER DEVELOPMENT OF THE MODEL OF SPATIAL DISTRIBUTION OF ENERGETIC ELECTRON FLUXES IN VICINITY OF EUROPA

M. V. Podzolko[1], I. V. Getselev[1], Yu. I. Gubar[1], I. S. Veselovsky[1, 2],
[1]Skobeltsyn Institute of Nuclear Physics, Lomonosov Moscow State University, Moscow 119991, Russia; [2] Space Research Institute (IKI), Russian Academy of Sciences, Moscow 117997, Russia. Contact: 404@newmail.ru

At the present time several projects of space research missions to Jupiter's icy moons, including Europa, are being developed. An important factor for these missions will be high radiation risks. In particular Europa's orbit is located inside the region of highly-intensive energetic particle fluxes of Jupiter's radiation belts; the main radiation impact for the spacecraft electronic components behind the shielding of ≥1 g/cm^2 Al will originate from the fluxes of relativistic electrons. Thus the integral flux of electrons with energies ≥5 MeV (a threshold value for the shielding of 2.2 g/cm^2 equivalent to that for Galileo spacecraft) in Europa's orbit is ≈10^7 cm^{-2}·s^{-1}, which is by 4 orders of magnitude higher, then the maximum flux in Earth's radiation belts (maximum energy of electrons in Earth's radiation belts is ≈8 MeV, while for Jupiter it is >100 MeV). Radiation dose in Europa's orbit during 2 months behind 2.2 g/cm^2 will amount to ≈1 Mrad, behind 5 g/cm^2 – to ≈250 krad.

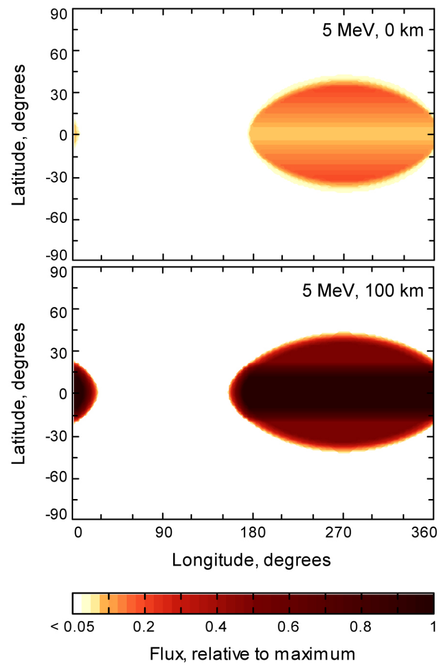

fig. 1. Distribution of differential fluxes of electrons with energy 5 MeV on Europa's surface (upper plot) and at 100 km altitude (lower plot).

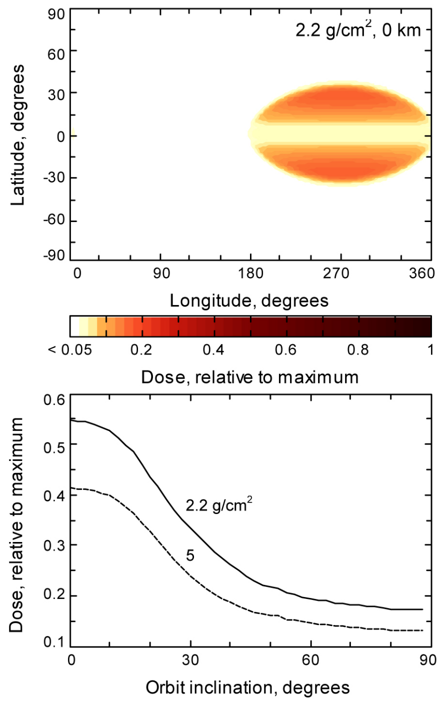

fig. 2. Distribution of radiation doses behind 2.2 g/cm2 on Europa's surface (upper plot); dependency of the radiation doses behind 2.2 and 5 g/cm2 in the orbit around Europa with the altitude of 100 km from its inclination (lower plot).

However, near Europa part of the flux will be shaded by the moon. Moreover, this reduction of the fluxes is sufficiently nonuniform and differs for various particle energies and pitch-angles, and for the surface and the low-altitude orbit. This is caused by several factors: complexity of particle trajectories in Jupiter's magnetosphere relative to Europa, certain disturbance magnetic and electric field in vicinity of Europa, Europa's tenuous atmosphere, and the thickness and configuration of spacecraft's shielding. These factors were taken as the input parameters for the model of spatial distribution of relativistic electron fluxes in vicinity of Europa, which is being developed by the authors.

On the current stage we have performed more accurate computations of spatial distribution of relativistic electrons on Europa's surface and at 100 km altitude, taking into account the relation between the longitudinal drift speed of electrons relative to Europa and their bounce-period, the Larmor motion of the particles near the surface, the difference of Europa's orbital plane from Jupiter's geomagnetic equator plane, and the diffusion of particles.

The results of our modeling can be used for choosing the landing sites and the low-altitude spacecraft's orbits around Europa, less hazardous with regard to radiation influence. The most hazardous on Europa's surface is the trailing side of the moon along its orbital motion. But the radiation dose there behind 2.2 g/cm^2 is ≈4 times lower, than the maximum values without taking into account the influence of Europa, and further decreases from middle latitudes to equator. The safer regions are the leading side of the moon and the high-latitude regions, where the dose is by ≈10 times lower, than maximum value. The orbiter will encounter higher radiation impact. Yet by choosing orbit with the high inclination i > 50°, radiation dose can be lowered to ≈20% of the maximum value without Europa.

References:
Paranicas C., Mauk B. H., Khurana K., Jun I., Garrett H. B., Krupp N., Roussos E., Europa's near-surface radiation environment, Geophys Res Lett, 34, L15103, 5 p., 2007.
Podzolko M. V., Getselev I. V., Gubar Yu. I., Veselovsky I. S., Radiation conditions of a mission to Jupiter and Europa, Solar System Res, 43(2), p. 116–120, 2009.
Podzolko M. V., Getselev I. V., Gubar Yu. I., Veselovsky I. S., Charged particles on the Earth–Jupiter–Europa spacecraft trajectory, Adv Space Res, 48(4), p. 651–660, 2011.

A METHOD OF ORBITS DESIGNING USING GRAVITY ASSIST MANEUVERS TO THE LANDING ON THE JUPITER'S MOON GANIMEDE.

Golubev Y.F.[1] , Grushevskii A.V. [1] , Koryanov V.V. [1] , Tuchin A.G.[1] ,
[1] *Keldysh Institute of Applied Mathematic, Moscow, Russia. Contact: office@keldysh.ru*

Introduction: For the design of the spacecraft flight in the Jovian sphere of influence with multiple flybys of it's natural satellites a quasi-singular semi-analytic construction of the trajectories [1] conducted. Each gravity assist in the satellite's sphere of influence calculated according to pre-counted "indicatrix". As result the possibility of the just-in-time ballistic analysis of landing on the Jovian moon Ganymede opened. A specific variants series of the project of such flight is given.

References: [1] Golubev, U.F., Grushevskii, A.V. and Higrullin, R.Z., 1996. To the Attainability Region Structure for the Earth Atmosphere Descent Problems., In: Cosmic. Res., 1996, № 2, p. 180-189

QUASI-SATELLITE ORBITS IN THE CONTEXT OF COORBITAL DYNAMICS

V.V. Sidorenko[1], A.I. Neishtadt[2,3], A.V. Artemyev[2], L.M. Zelenyi[2],
[1]Keldysh Institute of Applied Mathematics, Miusskaya Sq. 4, Moscow, Russia; [2]Space Research Institute, Profsoyuznaya Str. 84/32, Moscow, Russia; [3]Loughborough University, Loughborough LE11 3TU, UK. Contact: vvsidorenko@list.ru

Studies of long-term evolution of asteroid orbits are crucial for understanding the route passed by the Solar system towards its present configuration. The so-called coorbiting asteroids (those sharing their orbits with major planets) attract special attention in this context: are they the primordial remnants of the building blocks of the corresponding major planet or "emigrants" from other parts of the Solar system?

Best known examples of co-orbits in natural objects are provided by Trojan groups of asteroids and by asteroids moving in horseshoe orbits [1]. These asteroids are precluded from having relatively close encounters with their host planets. However, there exists another class of coorbiting objects in which the opposite is true: they remain very close to the host planet eternally or, at least, for long enough time. Since typically they never enter the planet's Hill sphere, they cannot be considered as satellites in the usual sense of the word. In order to emphasize this specifics they are called quasi-satellites (QS) [2,3].

We explore the properties of QS-orbits under the scope of the restricted spatial circular three-body problem. Via double numerical averaging, we construct evolutionary equations describing the long-term behaviour of the orbital elements of an asteroid. Special attention is paid to possible transitions between motion in a QS-orbit and that in another type of orbit available in the 1:1 mean motion resonance. Rough classification of the corresponding evolutionary paths is given for the asteroid's motion with a sufficiently small eccentricity and inclination.

To illustrate typical rates of the orbital elements's secular evolution, the dynamics of the near-Earth asteroid 2004GU9 was studied. This asteroid will keep describing a QS-orbit for the next several hundred years.

This work was supported by the grant of the Russian academy of sciences Presidium Program 22: "Fundamental problems of research and exploration of the Solar system".

C.D.Murray, S.F.Dermott, Solar System Dynamics, Cambridge University Press (1999)
M.Connors, C.Veillet, R.Brasser, P.Wiegert, P.Chodas, S.Mikkola, K.Innanen, Discovery of Earth's quasi-satellite, Meteorit. Planet. Sci., 39 (2004), 1251-1255.
F.Namouni, Secular interactions of coorbiting objects, Icarus, 137 (1999), 293-314.

COHERENT BACKSCATTERING AND OPPOSITION PHENOMENA EXHIBITED BY SOME ATMOSPHERELESS SOLAR SYSTEM BODIES

J. M. Dlugach[1], M. I. Mishchenko[2],
[1]Main Astronomical Observatory of the National Academy of Sciences of Ukraine, 27 Zabolotny Str., 03680, Kyiv, Ukraine; [2] NASA Goddard Institute for Space Studies, 2880 Broadway, New York, NY 10025, USA . Contact: dl@mao.kiev.ua

Two spectacular optical phenomena observed simultaneously for a class of high-albedo solar system objects are the brightness and polarization opposition effects [1 – 2]. The former is a spike-like intensity peak centered at exactly the backscattering direction. The latter is a sharp asymmetric negative-polarization feature with a minimum at a phase angle compared to the angular semi-width of the brightness opposition effect. As an example, the figure shows the results of observations of these opposition effects obtained for the Galilean satellite Europa and Saturn's rings [3 – 7].

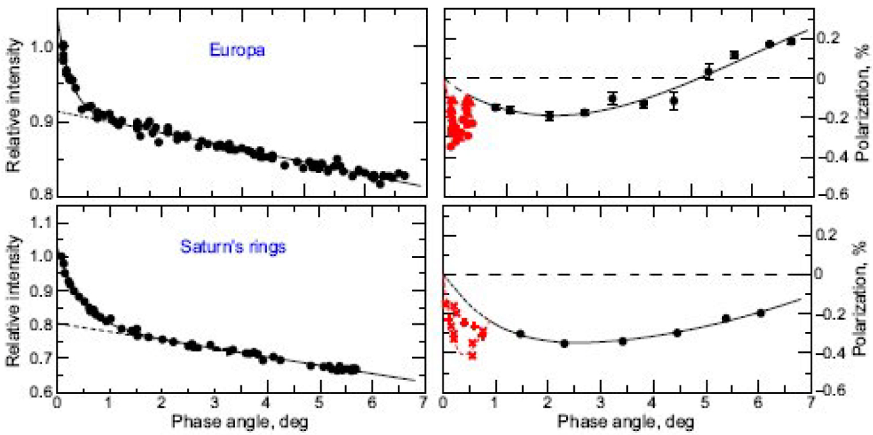

fig. Brightness and polarization opposition effects for Europa and Saturn's rings.

It has been suggested that both effects are caused by the effect of coherent backscattering of electromagnetic waves in particulate media [8 – 10]. This interpretation, if correct, could provide specific physical information about the distant objects that would otherwise be difficult to obtain. However, the interference concept of the effect of coherent backscattering explicitly relies on the notion of phase of an electromagnetic wave. As such, it is strictly applicable only when particles forming the scattering medium are widely separated rather than being in direct contact. Therefore, one needs an unequivocal demonstration of the interference nature of specific backscattering effects observed for planetary regolith surfaces and a definitive proof that coherent backscattering prevails even when the scattering medium is densely packed.

Now such demonstration can only be provided by numerically exact computations of electromagnetic scattering by media consisting of large numbers of randomly positioned particles. Indeed, only by directly solving the Maxwell equations can one (1) eliminate any uncertainty associated with the use of an approximate theoretical approach; (2) control precisely all physical parameters of the scattering medium and vary them one at a time; and (3) compute all relevant optical observables at once. As a consequence, one can study the onset, evolution, and potential decay of all manifestations of coherent backscattering as the particle packing density gradually increases from zero to values typical of actual particulate surfaces. Such results can provide a definitive answer to the physical origin of the brightness and polarization opposition effects.

In our works [11 – 13], we used numerically exact computer solution of the Maxwell equations to simulate the scattering of visible light by realistic models consisting of large number of randomly positioned, densely packed particles. By increasing the particle packing density from 0 up to ~ 45%, we tracked the onset and evolution of the full suite of backscattering optical effects predicted by the low-density theory of coherent backscattering, including the brightness and polarization opposition effects. The results of our computations do demonstrate that the classical low-density predictions can survive (at least in a semiquantitative sense) volume packing density typical of particulate surfaces encountered in natural conditions. So, our numerical data coupled with the results of observations at near-backscattering geometries demonstrate that the brightness and polarization opposition effects detected simultaneously for some high-albedo atmosphereless solar system objects are really caused by the effect of coherent backscattering.

References

Muinonen K., Piironen J., Shkuratov Yu.G. et al. 2002 in Asteroids III, ed. Bottke W.F.Jr et al. (Tucson, AZ: Univ. Arizona Press), 123.
Mishchenko M.I., Rosenbush V.K., Kiselev N.N. 2006, Appl. Opt., **45**, 4459.
Thompson D.T., Lockwood G.W. 1992, J. Geophys. Res., **97**, 14761.
Rosenbush V.K., Kiselev N.N. 2005, Icarus, **179**, 490.
Franklin F.A., Cook A.F. 1965, Astron. J., **70**, 704.
Johnson P.E., Kemp J.C., King R. et al. 1980, Nature, **283**, 146.
Dolfus A. 1996, Icarus, **124**, 237.
Shkuratov Yu.G. 1989, Astron. Vestnik, **23**, 176 (in Russian).
Muinonen K. 1990, “Light scattering by inhomogeneous media: backward enhancement and reversal of linear polarization”, Ph. D. dissertation (University of Helsinki).
Mishchenko M.I. 1993, Astroph. J., **411**, 351.
Mishchenko M.I., Dlugach J.M., Liu L. et al. 2009, Astroph. J., **705**, L118.
Mishchenko M.I., Dlugach J.M., Liu L. 2009, Phys. Rev., **80**, 053824 - 1.
Dlugach J.M., Mishchenko M.I., Liu L., Mackovski D.W. 2011, J. Quant. Spectrosc. Radiat. Transfer, **112**, 2068.

THE RUSSIAN LUNAR PROGRAM: GOALS AND MISSIONS

Lev Zenenyi, Igor Mitrofanov and Anatoly Petrukovich

The new program will be described of future Russian lunar missions. The main scientific goal of the program is studying of lunar poles: volatiles in the regolith and polar exosphere. The main engineering goal is to recover old and to create new space technology for lunar orbiting, landing and surface operations.

The first lunar landing is scheduled on 2015, as the first part of the Luna-Glob project. The limited set of scientific instruments will be delivered to the Moon by this mission, which the primer goal is the testing of landing technology and surface operations. The next mission of 2016 is the lunar orbiter, as the second part of the Luna Glob project. Luna-Resource spacecraft will land on the Moon in 2017 with much larger payload. This mission will perform studies of lunar polar volatiles from the shallow subsurface. The fourth mission of this sequence is the Lunar Polar Sample Return (LPSR), which will return samples of polar regolith to the Earth.

THE EXOMARS PROGRAMME

O. Witasse, J.L. Vago,
Research and Scientific Support Department of ESA, ESTEC, PO Box 299, 2200 AG Noordwijk, the Netherlands; contact: Olivier.Witasse@esa.int

The ExoMars Programme is an ESA-ROSCOSMOS cooperation with some NASA contribution. ExoMars includes two missions, one in 2016 and one in 2018. Exomars is a preparatory step for the future realisation of a Mars Sample Return (MSR) during the second half of the next decade. The 2016 mission includes two elements: an orbiting satellite devoted to the study of atmospheric trace gases, with the goal to acquire information on possible on-going geological or biological processes; and a European Entry, Descent, and landing Demonstrator Module (EDM) to achieve a successful soft landing on Mars. The orbiter will also provide data communication services for all surface missions landing on Mars until end 2022. The mission will be launched in January 2016, using a Proton rocket, and will arrive to Mars in October 2016. The 2018 mission will deliver a 300-kg-class rover and a landed platform to the surface of Mars using a landing system developed by Roscosmos. The mission will pursue one of the outstanding questions of our time by attempting to establish whether life ever existed, or is still present on Mars today. The rover will explore the landing site's geological environment and conduct a search for signs of past and present life, collecting and analysing samples with the Pasteur payload suite from within rocky outcrops and from the subsurface, down to a depth of 2m, using a drill. The platform will carry scientific measurements at the landing site. This presentation will describe the present status of the ExoMars project, the missions' profile, and the various elements' payload.

RUSSIAN CONTRIBUTION TO THE EXOMARS PROJECT

L. Zelenyi[1], V. Khartov[2], A. Lukyanchikov[2], O. Korabev[1], I. Mitrofanov[1]
[1]Space Research Institute (IKI) Profsoyuznaya 84/32, Moscow, Russia. [2]Lavockin Association Leningradskaya 24, Khimki, Moscow reg., Russia Contact: korab@iki.rssi.ru

The ExoMars ESA-led mission is dedicated to study of Mars and in particular its habitability. It consists of two launches, one planned in 2016 to deliver to Mars a telecommunication and science orbiter Trace Gas Orbiter (TGO) and a demonstrator of entry into the atmosphere and landing on the Mars surface, Entry, Descent and Landing Demonstrator Module (EDM). In 2018 a rover with drilling capability will be delivered to the surface of Mars. This mission, previously planned in cooperation with NASA is now being shaped in cooperation with Roscosmos. Both launches are planned with Proton-Breeze. In 2016 Russia contributes a significant part of the TGO science payload. In 2018 the landing will be provided by a joint effort capitalizing on the EDM technology. Russia contributes few science instruments for the rover, and leads the development of a long-living geophysical platform on the surface of Mars.

Russian science instruments for TGO are the Atmospheric Chemistry Suite (ACS) and the Fine Resolution Epithermal Neutrons Detector (FREND). The ACS package (33.5 kg) is dedicated to studies of the composition of the Martian atmosphere and the Martian climate. ACS consists of three spectrometers: NIR channel covers the spectral range of 0.7 – 1.7 μm with resolving power of 20000, aimed to measure H_2O, CO_2, and O_2 emission in nadir, on the limb and in solar occultations. MIR channel is a high-resolution echelle instrument dedicated to solar occultations in the rage of 2.3 – 5.2 μm targeting the resolving power of 50000-80000. MIR is primarily dedicated to sensitive measurements of trace gases, approaching MATMOS detection thresholds for methane, etc. species. TIRVIM channel is a 2-inch double pendulum Fourier-transform spectrometer for the spectral range of 2 – 25 μm (2 – 16 μm with cryocooled detector), and apodized resolution varying from 0.2 to 1.6 cm^{-1}. It is primarily dedicated to monitoring of atmospheric temperature and aerosol state in nadir, and will contribute in solar occultation to detection/reducing of upper limits of some species, complementing MIR and NOMAD. FREND (36 kg) is a neutron detector with a collimation module that significantly narrows the field of view of the instrument, allowing to create higher resolution maps of hydrogen-abundant regions on Mars. The spatial resolution of FREND will be ~40 km from 400 km orbit that is 10 times better than HEND on Mars-Odyssey. The energy ranges are 0.4 eV – 500 keV for epithermal neutron detectors, and 0.5 – 10 MeV for fast neutron detector. Additionally, a dosimeter module for monitoring of radiation levels is included in FREND. Russian instruments for TGO constituent a half of its scientific payload, European instrument being NOMAD for mapping and detection of trace species, and CASSIS camera for high-resolution mapping of target areas.

In the 2018 mission, Russia takes the major responsibility of the descent module. An aerodynamic shield and a parachute system assure the entry phase. At present the descent scenario with integrated retro-propulsion engines and landing on feet is being developed. Subsystems of the descend module will be supplied by both sides.

On the rover, Russia contributes two science instruments. ADRON-RM (1.7 kg) is a neutron detector to assess water contents along the rover track. ISEM (1.7 kg) is a pencil-beam infrared spectrometer mounted at the mast of the rover and is primarily dedicated for the measurements of soil hydration at 3 μm, and the assessment of mineralogical composition. Both instruments will assist with planning rover traverse, rover targeting operations, and sample selection.

A major effort of the Russian science is concentrated on the 2018 landing platform. This is the part of the descent module remaining immobile after the rover egress. The platform, or the long-living geophysical station shall have guaranteed lifetime of one Martian year, and will be able to accommodate up to 50 kg of science payload. The final list of science investigations is yet to be finalized, however it will definitely include the meteorological station, and the geophysical package with a sensitive seismometer. Other investigations will provide analyses of the surface/shallow subsurface material complimentary to these on the rover, a means to analyse atmospheric composition, and other experiments, if resources permit.

JUPITER ICY MOONS EXPLORER: AN ESA MISSION TO THE JOVIAN SYSTEM.

D.V. Titov[1], M.K. Dougherty[2], O. Grasset[3], Ch. Erd[1], E. Bunce[4], A. Coustenis[5], M. Blanc[6], A. Coates[7], P. Drossart[5], L. Fletcher[8], T. van Hoolst[9], H. Hussmann[10], R. Jaumann[10], N. Krupp[11], O. Prieto-Ballesteros[12], P. Tortora[13], F. Tosi[14], A. Wielders[1],
[1]ESA/ESTEC, The Netherlands; [2]Imperial College, UK; [3]Nantes University, Nantes, France; [4]Leicester University, Leicester, UK; [5]Paris Observatory, Meudon, France; [6]IRAP, Toulouse, France; [7]University College London, UK; [8]Oxford University, UK; [9]Royal Observatory of Belgium, Belgium; [10]DLR Institute of Planetary Research, Berlin, Germany; [11]Max Planck Institute for Solar System Research, Katlenburg-Lindau, Germany; [12]INTA-CSIC, Spain; [13]University of Bologna, Italy; [14]Institute for Space Astrophysics and Planetology, Italy. Contact: Dmitri.Titov@esa.int.

JUICE (JUpiter ICy moons Explorer) is the first L-class mission selected for the ESA's Cosmic Vision programme 2015-2025 which has just entered the definition phase. JUICE will perform detailed investigations of Jupiter and its system in all their interrelations and complexity with particular emphasis on Ganymede as a planetary body and potential habitat. Investigations of Europa and Callisto will complete a comparative picture of the Galilean moons. By performing detailed investigations of Jupiter's system, JUICE will address in depth two key questions of the ESA's Cosmic Vision programme: *(1) What are the conditions for planet formation and the emergence of life?* and *(2) How does the Solar System work?*

The overarching theme for JUICE has been formulated as: *The emergence of habitable worlds around gas giants*. At Ganymede the mission will characterize in detail the ocean layers; provide topographical, geological and compositional mapping of the surface; study the physical properties of the icy crusts; characterize the internal mass distribution, investigate the exosphere; study Ganymede's intrinsic magnetic field and its interactions with the Jovian magnetosphere. For Europa, the focus will be on the non-ice chemistry, understanding the formation of surface features and subsurface sounding of the icy crust over recently active regions. Callisto will be explored as a witness of the early solar system.

JUICE will perform a comprehensive multidisciplinary investigation of the Jupiter system as an archetype for gas giants including exoplanets. The circulation, meteorology, chemistry and structure of the Jovian atmosphere will be studied from the cloud tops to the thermosphere. The focus in Jupiter's magnetosphere will include an investigation of the three dimensional properties of the magnetodisc and in-depth study of the coupling processes within the magnetosphere, ionosphere and thermosphere. Aurora and radio emissions and their response to the solar wind will be elucidated. Within Jupiter's satellite system, JUICE will study the moons' interactions with the magnetosphere, gravitational coupling and long-term tidal evolution of the Galilean satellites.

The JUICE spacecraft is scheduled for launch in June 2022. After the orbit insertion in January 2030 the spacecraft will perform a 2.5 year tour in the Jovian system focusing on observations of Jupiter's atmosphere and magnetosphere. During the tour, gravity assists at Callisto will shape the trajectory to perform two targeted Europa flybys and raise the orbit inclination up to 30 degrees. 13 Callisto flybys will enable unique remote observations of the moon and *in situ* measurements in its vicinity. The mission will culminate in a dedicated 8 months orbital tour around Ganymede.

JUICE will be a three-axis stabilised spacecraft with dry mass of about 1800 kg at launch, chemical propulsion system and 60-75 m^2 solar arrays. The high-gain antenna of about 3 m in diameter will provide a downlink capability of not less than 1.4 Gb/day. Special measures will be used to protect the spacecraft and payload from the harsh radiation environment at Jupiter. The spacecraft will carry a highly capable state-of-the-art scientific payload. The model payload consists of 11 instruments with total mass of ~104 kg. The model remote sensing package includes spectro-imaging capabilities from the ultraviolet to the near-infrared, wide angle and narrow angle cameras and a submillimetre wave instrument. The model geophysical suite consists of a laser altimeter and a radar sounder, complemented by a radio science experiment. The model *in situ* package comprises a magnetometer, radio and plasma wave instrument, including electric fields sensors and a Langmuir probe, and a powerful particle package. Actual instruments for the mission will be selected by ESA in the framework of an open Announcement of Opportunity.

VENUS INVESTIGATION AFTER ESA VENUS EXPRESS: RUSSIAN MISSION VENERA-D

Zasova L.V.[1,2], Zelenyi L.M.[1], Korablev O.I.[1,2], Vorontsov V.A.[3], Marov M.Ya.[4], Basilevsky A.T.[4], Gavrik A.L.[5], Ekonomov A.P., Gerasimov M.V.[1], Gotlib V.M.[1], Grigoriev A.V.[1], Gromov V.[1], Ignatiev N.I.[1,2], Khavroshkin O.B.[6], Klimov S.I.[1], Ksanfomaliti L.V.[1], Lipatov A.N.[1], Mitrofanov I.G.[1], Moshkin B.E.[1], Petrukovich A.A.[1], Rodin A.V.[1,2], Sanko N.F.[1], Skalsky A.A.[1], Vaisberg. O.L.[1], Zastenker G.N.[1]
[1]IKI RAS, [2]MIPT, [3]NPOL, [4]GEOKHI RAS, [5]IRE RAS, [6]IFZ RAS, Contact: zasova@iki.rssi.ru

Venus was actively studied by Soviet and US missions in 60-90-th years of the last century. The investigations carried out both from the orbit and in situ were highly successful. After a 15-years break in space research of Venus, the ESA Venus Express mission, launched in 2005, successfully continues its work on orbit around Venus, obtaining the spectacular results. However, many questions concerning the structure and evolutions of the planet Venus, which are the key questions of comparative planetology and very essential for understanding the possible evolution of the terrestrial climate, cannot be solved by observations only from an orbit. Russian mission Venera-D is aimed for both in situ and remote investigations of Venus. Venera-D includes: Lander, Orbiter and Sub-satellite. Two orbiters will work around Venus for the first time. One of the most important element of the mission is the Lander. The assembling of the scientific payloads on Lander was done by specialists of NPOL (on the level of drawings). It should land at the surface of Venus after more than 30 years gap (the last landing on the surface of Venus - VEGA1-2 – took place in 1985). The complex of experiments on Lander is aimed to measure the light and noble gases and its isotopes abundance, composition, chemistry and microphysics of clouds, PTW, chemical, elemental, mineralogical composition of the surface material, natural radioactive elements, and oxide state of the surface, etc. It is planned to use as the Lander of Venera-D a type of Soviet Veneras Lander, which many times successfully worked on the surface of Venus. Scientific payloads on the Orbiter include new instrument and also modernized those working successfully on VEX and old missions. The long living station on the surface (up to 24 hours) was studied: using materials, available now, this station may be done within 100 kg weight.

The authors acknowledge Roscosmos, RAS and TSNIIMASH for support of Venera-D project development.

SAGE MISSION TO VENUS

L. W. ESPOSITO,
LASP, University of Colorado, Boulder, USA;
Contact: larry.esposito@lasp.colorado.edu

SAGE, the Venus Surface and Atmosphere Geochemical Explorer, is a future NASA New Frontiers mission concept, proposed to launch to Venus and land on the flanks of a Venus volcano, where it survives the hellish Venus environment for 3 hours or more. The SAGE lander will photograph the surface during descent and after landing, excavate the surface and irradiate it with lasers and neutrons to measure the composition and surface texture. The minerals that make up Venus upper crust are still unknown. This new information will allow the scientific team to compare Venus to other terrestrial planets (including the Earth), and planets circling other stars. This will clarify the history of Venus surface, atmosphere and climate. We plan to model the history of Venus and predict its future, comparing Venus to Earth and to extra-solar planets. Other partners are the Jet Propulsion Laboratory which provides the SAGE project management, Lockheed Martin of Denver which builds the carrier spacecraft, and the NASA Ames, Goddard and Langley Research centers. Scientific instruments are contributed by Russia's Institute for Space Research (IKI) with contributions from the Swiss University of Bern, and the French National Center for Space Research (CNES). The lander's robotic arm is contributed by the Canadian Space Agency.

SEISMIC RECONNAISSANCE OF MARS WITH A VBB SEISMOMETER.

P. Lognonné[0], T.Gudkova[1], W.B. Banerdt[2], S. Deraucourt[1], D. Mimoun[3], R. Garcia[4], A. Mocquet[5], M. Panning[6], E. Beucler[5], D. Giardini[5],
U. Christensen[6] and the VBB-SEIS team (0) IPGP-Sorbonne Paris Cité, Univ Paris, France Diderot, lognonne@ipgp.fr, (1) Earth Physics Institut, Moscow, Russia, (2) JPL, USA (3) ISAE, France (4) IRAP, France, (5) LPGN, France (6) University of Florida (7) ETHZ, Switzerland (8) MPS, Germany

Introduction: A very-broad-band (VBB) seismometer is the principal instrument of the InSight Mission, one of three NASA down-selected projects in competition for the 2010 Discovery AO. Such an instrument might also be considered on the Russian lander of the EXOMARS lander-rover mission. The goal of SEIS is to determine the interior structure and seismic activity of the planet. We summarize the requirements flow, from instrument performance to expected science performance in terms of interior structure and activity detection.

SEIS noise requirement: Performance and installation quality of VBB seismometer are the most critical parameters to ensure success in terms of seismic signal detection, as negatively demonstrated by the Viking Lander seismometer which was dominated by wind during the day and was weakly sensitive to ground motion during the night (due to emplacement on the lander deck). The InSight seismometer will be robotically installed of the instrument on the ground and include a Wind/Thermal Shield. The improvement of the InSight-VBB requirement over the Viking capability is 1000× for body waves (1 sec) and 65000× for surface waves (20 sec), equivalent to 2 and 3.2 body wave (m_b) and surface wave (m_s) magnitudes respectively.

Seismic and impact signal amplitude estimation: Theoretical estimates from thermoelastic cooling and calculation of the seismic moment release from observed surface faults predict a level of activity ~100× greater than observed shallow moonquake activity. This level would provide ~50 quakes of seismic moment ≥10^{15} Nm (roughly equivalent to terrestrial magnitude m_b=4) per (Earth) year, and ~5× more quakes for each unit decrease in moment magnitude. About 20 impacts can also be detected per Martian year (Figure 1). A few large quakes with moment in the range 10^{17}– 10^{18} Nm might also be expected during the full Mars year nominal mission duration, enabling the detection of free oscillations on the vertical component (Figure 2).

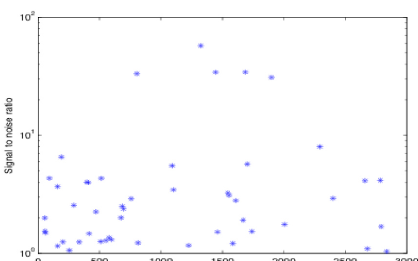

fig. 1. Modeling results of impact SNR with a Monte-Carlo simulation of impactors and seismic amplitude impulse/distance estimates calibrated on the Moon and corrected with the a priori attenuation differences between Mars and the Moon. Large events correspond to impacts of about 1 ton.

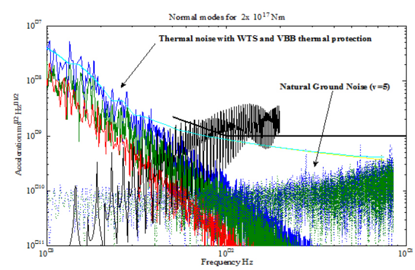

fig. 2. Amplitude of a 3x1017 Nm marsquake free oscillation signal compared to instrument noise (black curve is SEIS requirement, cyan is expected capability) and environment noise (left, temperature, right, pressure, for day, sol,night in blue, green, red respectively). One or two such quakes are expected to occur every 2 years.

Mantle and crust seismic inversion: As only one seismic station is available, structure inversion will be performed using: (i) Secondary seismic data which do not depend on the event location: e.g., free oscillation frequencies for the largest quakes constraining the interior down to 200 km and receiver functions constraining the crust-mantle discontinuity below the landing site; (ii) Seismic impact data from impacts post-located by a Mars orbiter; (iii) Seismic data associated with events with more than 3 different wave arrival time determinations (for V_s inversion with constant V_p/V_s) or more than 4 (for full V_p, V_s inversions).

Seismic activity levels and wave amplitudes have been used to estimate the number of events with multiple arrivals. We estimate that about 35 events will be detected with both P and S waves, and about 10 with P, S and R1 surface waves and core phases (e.g., PcP, ScP). For about half of the events, the R2 surface wave will be also be detected, enabling an epicentral distance determination contaminated only by lateral variability, which can be corrected with 3D modeling. These events and associated seismic data set will allow the determination of seismic velocities down to 600 km to within ±0.25 km/sec, enabling the first seismic model of another planet than Earth and exciting constrains in term of planetary formation and evolution.

ON SCIENTIFIC GOALS OF THE SEISMIC EXPERIMENT "MISS"

T. Gudkova[1], P. Lognonné [2], V.N. Zharkov[1], S. Raevskiy[1], V. Soloviev[1] and "MISS" team**.** *[1]Schmidt Institute of Physics of the Earth, B.Gruzinskaya 10, Moscow 123995, Russia; [2]Institut de Physique du Globe de Paris, 4 av. De Neptune 94100 Saint-Maur des Fossés, France. Contact: gudkova@ifz.ru*

Introduction: Interior structure models of Mars are based on geochemical knowledge, experimental data on the behavior of material at high pressure and high temperature, and information on gravitational field of the planet: the moment of inertia and the Love number k_2. But there are not yet enough data to constrain the velocity and density distributions well. Seismology is the best tool for probing planetary interiors. Most knowledge on the Earth`deep layers came from the seismology: body waves; surface waves and free oscillations. The cost of landing multiple long-lived seismic stations on Mars is high enough. In the seismic experiment "MISS" we will perform analysis based on measurements from a single station. How a single seismometer can be useful to get information on subsurface structure and average global structure of the planet? Nontraditional ways to probe the interiors should be used: data processing of meteoroids' impacts, seismic hum from meteorological forcing, as well as the development of new methods, that can derive interior information from a single seismometer. Many such methods already exist, including source location through P-S and back-azimuth, receiver functions, identification of later phases (PcP, PKP, etc), surface wave dispersion, and normal mode analysis (from single large events, stacked events, or background noise).

What can be determined:

The first goal of the experiment is determining Mars' seismicity level.

The level of tectonic and geological activity on Mars suggests that it should be seismically more active than the Moon but less active than the Earth. Most theoretical models of the seismic activity on Mars, which are based on the thermoelastic cooling of the lithosphere [1, 2], predict a total of 10-100 quakes per year with seismic moments larger than 10^{22} dyne cm. The quakes are related to the cooling of the planet, which accumulates stresses that are then released by quakes. This type of activity is the minimum expected activity on Mars. Taking into account the fact that one can see giant faults on the surface of Mars (within Tharsis region, Tempe Terra, Valles Marineris, Olimpus region), it is not possible apriori to rule out large seismic events.

An additional and very important seismic sources for a planet with a weak atmosphere as Mars are meteoroid impacts, which strike the surface of Mars at a relatively high rate. The number of impacts are expected to be 2-4 times larger then for the Moon [3,4]. Their impact time and location can be known with orbital imaging (high-resolution cameras is on orbiting Mars spacecraft). The main characteristics of the seismic source generated by an impact are its amplitude and cutoff frequency. These parameters allow us to constrain the mass and velocity of the impactor [5].

2) As soon as impacts are located by these non-seimic methods, impacts become the seismic sources that can be used by a single seismic station on a planet for inverting the interior structure. Both P and S arrival time can be used on a seismometer. If the time is not known, the P-S differential travel-times can be used. Natural impacts on Mars are indeed important seismic sources for constraining the crustal and upper mantle structure.

3) Free oscillations, if they are excited, is the most effective tool for sounding of deep interiors. Interpretation of data on free oscillations does not require knowledge of the time or location of the source; thus, data from a single station are sufficient. For torsional oscillations modes with $l \geq 3$ (if a marsquake with $M_0=10^{25}$ dyne cm occurs), with $l \geq 6$ ($M_0=10^{24}$), and with $l \geq 12$ ($M_0=10^{23}$) could be detected. The torsional modes with $l \geq 3$, 6 and 12 can sound the Martian interiors down to 1600, 1100 and 700 km, respectively. The spheroidal modes with only $l \geq 17$ ($M_0=10^{25}$) could sound the outer layers of Mars down to 700-800 km. For a marsquake with a higher seismic moment (10^{26}) the spheroidal modes with $l \geq 6$ could be detected (sounding the outer layers down to 2000 km). Stacking multiple quakes with an equivalent cumulative moment could be apllied.

4) The dispersion curves of surface waves can be used to solve problem of determining the structure of the crust and the upper mantle. The depth to which surface waves are sensitive depends on frequency, with low frequency waves feeling to greater depth and therfore propagating with higher speeds. Low frequency waves are arriving earlier than higher frequencies. They are extremely sensitive to subsurface structure (to the crustal thickness). The data on Rayleigh waves enable one to distinguish between not only the crusts with different composition (MK2M and MK1M, Figure 1), but also between the models based on different temperature distribution in the crust (MK2M,

MK2H and MK2L, Figure 1). The velocity can be calculated from arrival time and estimate of distance from the source, which can be obtained from R1-R2 difference,where R1 is the direct Rayleigh wave arrival, R2 is the arrival of the wave propagating around the planet in the opposite direction.

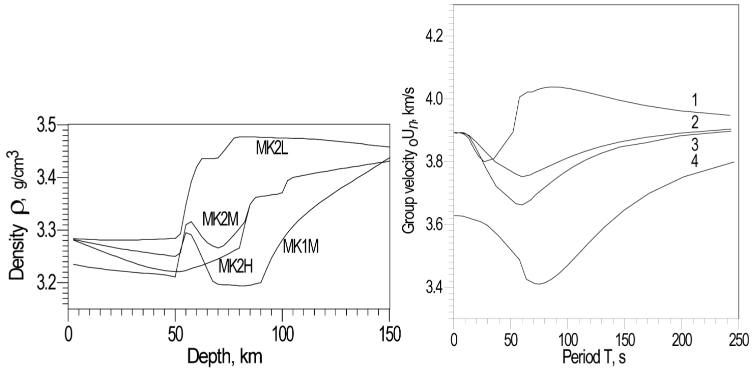

fig. 1. Profiles of density in the different models of the Martian crust (MK1M, MK2M, MK2H and MK2L) are on the left (the data are from [6]) and group velocities $_oU_n$ for a fundamental mode of Rayleigh waves as function of the period of oscillation for these models: 1, MK2L; 2, MK2M; 2, MK2H; 4, MK1M.

5) Estimates of crustal thickness by receiver function method. This method is a powerful tool for studying the depth to the crust-mantle boundary or to other layering within the crust. It was applyied to get shear velocity with depth for the lunar crust [7].

6) Differential measurements of arrival times of later-arriving phases (PcP, PcS, ScS) in comparison to P could put some restrictions on the seismic velocities in the deep mantle [8]. Synthetic seismogram analysis for interoir structure models can lead to identification of these phases. Figure 2 shows the difference in travel-time curves for P, PKP, PcP, S, SKS, ScS waves as function of epicentral distance between a trial model M7_3 [9] and the model A of [10]. We see that the difference is up to 40 s for P and PcP, and up to 100 s for S and ScS arrivels. PcP and ScS, phases reflected from the core, could provide a strong constraint on the core's radius. For diagnostic purposes, the core phases PKP and SKS are the most promising phases in Martian seismology. The difference between models are about 300-350 s.

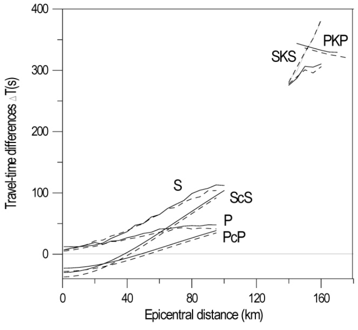

fig. 2. Travel times P, PKP, PcP, S, SKS, ScS waves difference between a trial model M7_3 (R_c=1766 km; the density of 50-km thick crust is 3000 kg/m³) [9] and the model A (R_c=1468 km; the density of 110-km thick crust is 2810 kg/m³) of [10] for the source on the surface (solid line) and at the depth of 300 km (dashed line).

Conclusion. Here we have showed the mission possibility to get seismic information on Martian interiors from only one seismic instrument using non-traditional sources of seismic waves and new seismic techniques.

Very Broad Band seismometer will record the full range of seismic signals, from the expected quakes induced by the thermoelastic cooling of the lithosphere, to the possible permanent excitation of the normal modes. All these seismic signals will be able to constrain the structure of Mars' interiors.

Acknowledgements: This work was supported by Programme National de Planetologie from INSU, the French Space Agency CNES (R&T Program) and Grant No. 12-02-00378 from the Russian Fund for Fundamental Research.

References: [1] Golombek M.P. et al. Science, 258, 979-981, 2002. [2] Knapmeyer M. et al. JGR, 111, E11006, 2006. [3] Lognonné, Ph. and Johnson C.L. in Treatise on Geophysics, 10, 69-122, 2007. [4] Lognonné, Ph. et al. JGR, 114, E12003, 2009. [5] T.V.Gudkova et al., Icarus, 211, 1049-1065, 2011. [6] Babeiko A. et al., Solar System Res.,27,149-165, 1993. [7] Vinnik L.P. et al., GRL, 28, 3031-3034, 2001. [8] Dehant V. et al., PSS, doi :10.1016/j.pss.2011.10.016, 2012. [9] Zharkov,V.N. et al. PEPI, 172, 324-334, 2008. [10] Sohl, F., Spohn.T. JGR,102, 1613-1635, 1997.

BELGIUM-GEODESY EXPERIMENT USING DIRECT-TO-EARTH RADIO-LINK: APPLICATION TO MARS AND PHOBOS.

P. Rosenblatt[1], S. Le Maistre[1], M. Mitrovic[1], V. Dehant[1]
[1]Royal Observatory of Belgium, Avenue Circulaire 3, B-1180 Uccle, Belgium. Contact: Pascal.Rosenblatt@oma.be

Introduction:

The deep interior of terrestrial planets is difficult to investigate without measurements acquired *in situ* (Mocquet et al., 2011). For example, the primary information for Earth's deep interior comes from the seismic data and to some extent from the measurements of the nutations of the planet (i.e. oscillations of the orientation of its rotation axis). These latter measurements have not been yet performed for terrestrial planets (neither for their moons) but instrumentation has already been developed and is ready to be placed at the Martian surface on dedicated missions including geodesy experiment.

The Royal Observatory of Belgium with the Belgian Federal Science Policy Office has developed a radio-science instrument (called LaRa for Lander Radioscience), which has been designed for such geodesy experiment. LaRa allows precise measurement of the Doppler shift of the carrier frequency of the radio-link established between the Lander and Earth-based stations of the NASA Deep Space Network (DSN) or ESA's ESTRACK network (ESA TRACKing). In turn, it allows for monitoring the motion in space of the celestial body on which is landed LaRa. From the precise reconstruction of this motion key information about the interior of those bodies can be derived.

This paper presents this instrument, its performances and some results that can be obtained on the deep interior of Mars and on the internal structure of its major moon, Phobos, in the context of dedicated geodesy experiment. Both celestial bodies are, indeed, the targets of currently planned or foreseen deep space missions, like for example the ExoMars mission to Mars, which relies in a strong collaboration between the European (ESA) and Russian (Roscosmos) space agencies.

The LaRa X-band radio-science instrument:

Initially, conceived as a radio-science instrument for the ExoMars lander tracking experiment, LaRa comprises an analog X-band coherent transponder and two circular polarized patch antennas allowing to measure with a high accuracy the range rate (Doppler frequency shift) between a station on the Earth and a distant lander located at the surface of a planet . The LaRa instrument allows establishing a coherent radio link using a radio signal sent from the Earth ground-stations to the targeted lander and from the lander back to Earth. The measurements performed at the tracking station on Earth provide the relative velocity between the target and the Earth, providing essential information about the rotation and orientation of a planet or moon of the solar system, and therewith about its interior.

The total mass of the instrument is 850 grams including electronics box, antennas, harness and connectors. The physical envelope size is 143.5 mm x 122 mm x 51.5 mm. Its power consumption is of 20 W (peak emission) with a 3 W of power transferred to the radio-wave re-emitted to the Earth. Two patch antennas (one for reception and one for emission) are used, and consist of two disks of 99 mm x 10 mm diameter. The round-trip links budget allows for precision of about 0.1 mm/s (at 60 seconds integration time) on the 2-way Doppler measurements for typical Earth-Mars distances. Both small mass and size of LaRa makes it easy to be implemented onboard a Lander to be placed at the surface of Mars or Phobos.

Scientific objectives:

In this section the scientific objectives for the Martian system that can be achieved by a geodesy experiment, using a LaRa-type instrument, are summarized hereafter.

Mars' deep interior. Relevant data for Mars' interior are currently those of the static gravity field and topography, the tidal effect on an orbiter, and the precession of the spin axis derived from radio-tracking data of orbiting and landed spacecraft (e.g. Dehant et al., 2009). Model of internal structure of Mars have been constructed and constrained by these data (see Rivoldini et al., 2011). In particular, the measurement of the tidal Love number k_2 (expressing Mars' gravitational potential changes in response to the tidal deformation), has allowed to infer a fully liquid core inside Mars with a size of 1794 km +/- 65 km (Rivoldini et al., 2011). However, the k_2 Love number solution can be biased by much than its precision (see Konopliv et al., 2006 and Marty et al., 2009), thus implying a larger error of about 250-300 km on the size of the core (Mocquet et al., 2011). Therefore, an independent measurement of the core state and size is needed. In addition, the current observations cannot precisely determine the temperature profile within the mantle as well as to better constrain its mineralogy.

The precise measurements of the nutations of the spin axis of Mars can provide such independent measurements. Indeed, when the core is liquid, the free core nutation (FCN) induces an amplification of the nutation amplitudes w.r.t. to their values for a solid planet, at the percent level in the large semi-annual prograde nutation amplitude and even more (up to tens of percent) in the ter-annual retrograde nutation (Dehant et al., 2009). As the nutation of a whole rigid Mars can be precisely computed, because of the sufficient knowledge of the solar system body positions, the precise measurements of the nutation can provide measurements of the FCN frequency, therewith of physical parameters of the core (moment of inertia, dynamical flattening, e.g. Dehant et al., 2011). However, the nutation amplitudes have to be measured with enough precision (i.e. at the milli-arcseconds level or the centimeter level at the surface of Mars).

The 2-way Doppler measurements between one Lander on Mars and Earth-based stations can monitor the proper motion of Mars, thus can measure the nutation of its spin axis. Studies have been performed to assess if the mas (or cm) level can be reached, given realistic operational constraints on the Doppler data noise level, Doppler tracking coverage, the mission duration, the landing site location, etc … (e.g. Le Maistre et al., 2012a). It has been shown that the amplitudes of nutation can be measured with a precision of about12 mas after one Martian year of operation, allowing for the confirmation of the presence of a liquid core inside Mars. Moreover, a precision of 30% and 5% are inferred on the determination of the core moment of inertia (related to core size) and the dynamical flattening, respectively (Le Maistre et al., 2012a).

Therefore, the LaRa instrument onboard a dedicated package on a platform to be put on Mars' surface with the ExoMars mission can provide precise measurements of Mars' nutation and in turn valuable information on the deep interior of the planet. Moreover, the geodetic data, in association with seismic, electromagnetic, and heat flow data, can provide significant improvement of our knowledge of Mars' core and mantle physical properties, thereby better constraining Mars' evolution models.

Phobos'internal structure. The origin of the Martian moons, Phobos and Deimos, is still an open issue (captured asteroid or formed in Mars' orbit, e.g. Rosenblatt, 2011). Key constraints on the physical properties prevailing at the origin of small celestial bodies come from a good knowledge of their bulk property and internal structure. As for Mars, the LaRa instrument can be used to perform a geodetic experiment dedicated to the knowledge of the internal structure of Phobos (Rosenblatt et al., 2011).

The aim of a Phobos Geodetic Experiment is to precisely measure the librations (i.e. oscillations of the spin rate and of the orientation of the rotation axis of Phobos) and the second-order coefficients (C_{20} and C_{22}) of the gravity field of Phobos. Since these parameters are related to the internal mass distribution through the principal moments of inertia, they can be used to constrain models of Phobos' interior, i.e. rock, water ice, porosity content, and monolithic vs rubble pile structure, which are key constraints on the origin of the body, Rosenblatt, 2011). However, a precision of about 1% on libration and gravity field solutions is required to be useful to constrain the interior structure of Phobos (Rosenblatt et al., 2011).

As in the case of Mars, the precision that can be reached on the libration measurements using the LaRa instrument has been assessed (Le Maistre et al., 2012b) on the basis of a complete model of Phobos' rotational motion (including short and long periodic libration, Rambaux et al., 2012). A precision of 10^{-5} degrees (or about 2 cm at Phobos' surface) on the determination of the amplitudes of the short periodic libration (orbital or sub-orbital periods) is reached after only a few weeks of operation with about one hour of tracking per day. The LaRa instrument can also be used to track a spacecraft orbiting Mars closely to Phobos (about 50 km, as it was planned for the Phobos-Soil spacecraft before its Landing on Phobos). The LaRa tracking data will allow for determining Phobos' gravity field at the percent level, from the precise reconstruction of the spacecraft orbit. The radio-signal sent back to Earth by the LaRa transponder could be used by the PRIDE experiment (Gurvits et al., 2010) in order to improve the gravity field solution.

However, the 1% or better precision on Phobos' libration and gravity field solutions needs that Phobos' ephemeris be known with much better precision than the current 1 km precision. The laRa Doppler measurements are also well suited for improving the determination of Phobos' orbital motion (Lainey et al., 2011), and in turn, in a global inversion scheme, for determining the proper motion (i.e. libration amplitudes) and the gravity field of Phobos within the percent precision level. This inversion scheme will follow the one using the natural satellite astrometry data together with the spacecraft tracking data proposed in the context of the European project ESPaCE (Thuillot et al., 2011). Note also that star-tracker measurements on the Lander (Andreev et al., 2010) will help this global inversion since they only sense the proper motion of Phobos.

Summary: The LaRa instrument is a well suited candidate for the payload of any

Lander (spacecraft) future missions to the Martian system in order to perform geodetic experiment for providing valuable information on the internal structure of Mars and its moons. The ExoMars mission offers an opportunity for such geodetic mission on Mars and future missions involving network of Landers (like INSPIRE, currently under study at ESA) could extend this concept of geodesy experiment. Moreover, future missions to Phobos, like MMSR (Michel et al., 2011) also under study at ESA, or like GETEMME proposed to ESA (Oberst et al., 2012) could bring the LaRa instrument on Phobos' surface.

References: Andreev et al., 2010, *Sol. Syst. Res., 44,* 438-443; Dehant et al. 2009, *Planet. Space Sci. 57*, 1050-1067; Dehant et al. 2011, *Planet. Space Sci. 59*, 1069-1081; Gurvits et al., 2010, *1st Moscow Sol. Syst. Symp.*, 73; Konopliv et al. 2006, *Icarus 182*, 23-50; Lainey et al., 2011, *EPSC-DPS2011-952*; Le Maistre et al. 2012a, *Planet. Space Sci. 68*, 105-122; Le Maistre et al., 2012b *submitted to Planet. Space Sci.*; Marty et al. 2009, *Planet. Space Sci. 57*, 350-363; Michel et al. 2011, *EPSC-DPS2011-849*; Mocquet et al. 2011, *Planet. Space Sci. 59*, 1048-1061; Oberst et al. 2012, *accepted in Experimental Astron.*; Rambaux et al., 2012, *submitted to Astrophys. & Astron.*; Rivoldini et al. 2011, *Icarus 213*, 451-472; Rosenblatt et al. 2011, *2nd Moscow Sol. Syst. Symp.*; Rosenblatt 2011, *astron. & Astrophys. Rev. 19,* 19-44; Thuillot et al., 2011, *EPSC-DPS2011-1833*.

METNET - NEW KIND OF IN SITU OBSERVATIONS NETWORK FOR MARS

Harri, A.-M.[1], Pichkadtze, K.[2], Korablev, O.[3], Schmidt, W.[1], Guerrero, H.[4], Uspensky, M.[1], Alexashkin, S.[2], Linkin, V.[3], Savijarvi, H.[5], Vazquez, L.[6], Genzer, M.[1], Heilimo, J.[1], Haukka, H.[1]
[1]Finnish Meteorological Institute, Space Research Division, Helsinki, Finland (Ari-Matti.Harri@fmi.fi, +358 9 1929-4603), [2]LA - Lavochkin Association, Moscow, Russia, [3]IKI - Russian Space Research Institute, Moscow, Russia, [4]INTA - Instituto Nacional de Técnica Aeroespacial, Madrid, Spain, [5]HU – Helsinki University, Helsinki, Finland, [6]UCM - Universidad Complutense de Madrid, Spain,

We have developed a new kind of planetary exploration mission for Mars – MetNet in situ observation network based on a new semi-hard landing vehicle called the Met-Net Lander (MNL). The first MetNet vehicle, MetNet Precursor, is planned to be launched in the 2018/2020 launch windows. The eventual scope of the MetNet Mission is to deploy some 20 MNLs on the Martian surface using inflatable descent system structures, which will be supported by observations from the orbit around Mars. Currently we are working on the MetNet Mars Precursor Mission (MMPM) to deploy one MetNet Lander to Mars in the 2018/2020 launch window as a technology and science demonstration mission.

The MNL is carrying a versatile science payload focused on the atmospheric science of Mars. Time resolved in situ Martian meteorological measurements acquired by the Viking, Mars Path finder and Phoenix landers and remote sensing observations by the Mariner 9, Viking, Mars Global Surveyor, Mars Odyssey and the Mars Express orbiters have provided the basis for our current understanding of the behavior of weather and climate on Mars. However, the available amount of data is still scarce and a wealth of additional in situ observations are needed on varying types of Martian orography, terrain and altitude spanning all latitudes and longitudes to address microscale and mesoscale atmospheric phenomena. Detailed characterization of the Martian atmospheric circulation patterns and climatological cycles requires simultaneous in situ atmospheric observations. The scientific payload of the MetNet Mission encompasses separate instrument packages for the atmospheric entry and descent phase and for the surface operation phase.

Total mass of the prototype design is approxximately 24 kg, hence providing about 4 kg of mass for the payload. The modest (in absolute terms) available payload mass is especially well suited for meteorological and atmospheric observations, but also for other environmental investigations — which both can also often be implemented with constrained energy and data storage & transmission resources. Due to the small size of a single lander, MNLs are highly suitable for piggy-backing on larger spacecraft. The small size and low cost make MNLs attractive for missions such as surface networks, landings to risky terrains and pathfinders for high-value landed missions.

The MetNet mission concept and key probe technologies have been developed and the critical subsystems have been qualified to meet the Martian environmental and functional conditions. The flight unit of the landing vehicle has been manufactured and tested. This development effort has been fulfilled in collaboration between the Finnish Meteorological Institute (FMI), the Russian Lavoschkin Association (LA) and the Russian Space Research Institute (IKI) since August 2001. INTA (Instituto Nacional de Técnica Aeroespacial) from Spain joined the MetNet Mission team in 2008, and is participating significantly in the MetNet payload development.

INTA SPACE INSTRUMENTATION AND CAPABILITIES FOR PLANETARY EXPLORATION.

I. Arruego[1],
[1]National Institute for Aerospace Technique - INTA, ctra. Ajalvir, km 4 Torrejón de Ardoz,Madrid, SPAIN; Contact: arruegori@inta.es

Introduction:

INTA, the Spanish National Institute for Aerospace Technique, started one decade ago a program for the development of small Space Platforms. Two of them, weighted ~20kg each, were launched in 2004 and 2009 (Nanosat-01 and 1B). Another one (OPTOS, 3kg) is ready to be launched along first half of 2013. A bigger microsatellite (more than 150kg) is currently under development.

At the same time, different developments in the field of Space Instrumentation have been carried out, many of them tested in-orbit on-board those satellites. Planetary exploration generally requires low-power, low-mass, smart instrumentation, often capable of surviving to extremely harsh environmental conditions. INTA develops smart instruments based on an intensive use of high-performance COTS (*Commercial Of The Shelf* components) that we previously screen and qualify through different tests, and then test in orbit in our platforms.

This trend towards miniaturization was demonstrated with the development of different instruments in the frame of the Mars MetNet Lander Precursor Mission. At present, we are manufacturing different mixed-signal ASICs for Space applications, together with the Microelectronics Institute from Seville, also in Spain.

In this presentation, our capabilities in the development of Space H/W, as well as for complete qualification of Space products, will be presented.

Working from the components to achieve low-mass, low-power:

Since year 2000, first in the frame of an initiative for the development of optical wireless communications inside spacecrafts, and then in different sensors and instruments, we have worked in the qualification of a good number of COTS. From dozens of optical emitters and detectors, to small digital signal controllers, going through operational and instrumentation amplifiers, ADCs and DACs, voltage references, multiplexers, etc., we have characterized them under both radiation and extreme low-temperature environments, to be able to use them on Mars exploration.

Development and qualification of smart Space Instrumentation:

In the last 2 years, we developed a compact magnetometer (72 g, double 3-axis sensor plus 3 axis accelerometer) and a solar irradiance spectrometer (105 g, 11 channels from UV to NIR for in both diffuse and direct sunlight) that were fully qualified to be launch on the first Mars MetNet penetrator.

These developments take profit of the previous efforts in qualifying selected COTS. Besides, Radiation Hardness Assurance (RHA) is achieved not only at component level, but at architectural/instrument level by making a good selection of the necessary RadHard products in the core of our instruments, and introducing additional H/W and S/W protection strategies.

Finally, we have set-up a consortium with the Spanish Institute for Microelectronics, that has allowed us to develop our own mixed-signal ASICs. Last year we manufactured our first version of a complete optical wireless communication transceiver. At present, the layout of a magnetometer conditioning and acquisition ASIC is being finished.

INTA also has all the necessary facilities to fully qualify Space Hardware. This allows us to develop the whole product, from the concept to the launch.

In-orbit qualification on-board our own Small Platforms:

On our Nanosats we have qualified several magnetic and solar sensor technologies, as well as the optical wireless data links (OWLS) technology. A novel radiation monitor is flying on board Nanosat-1B since 2009 with excellent results. Two small wireless microcomputers were put on-board FOTON-M3 capsule in 2007.

The results that we obtain in-orbit in our Small Platforms, used as a test-bed for new technologies or developments, provide a necessary feed-back for future works. For example, at present we are finishing a medium-size radiation monitor with huge measurement capabilities, as an evolution to the one on board Nanosat-1B, that will fly on-board the Spanish Earth Observation Satellite (SEOSAT/INGENIO).

In this way we “close the circle” of the whole development process, from TRL1 to 9.
Given this experience , INTA can be a good partner in the development of scientific instrumentation for planetary exploration.

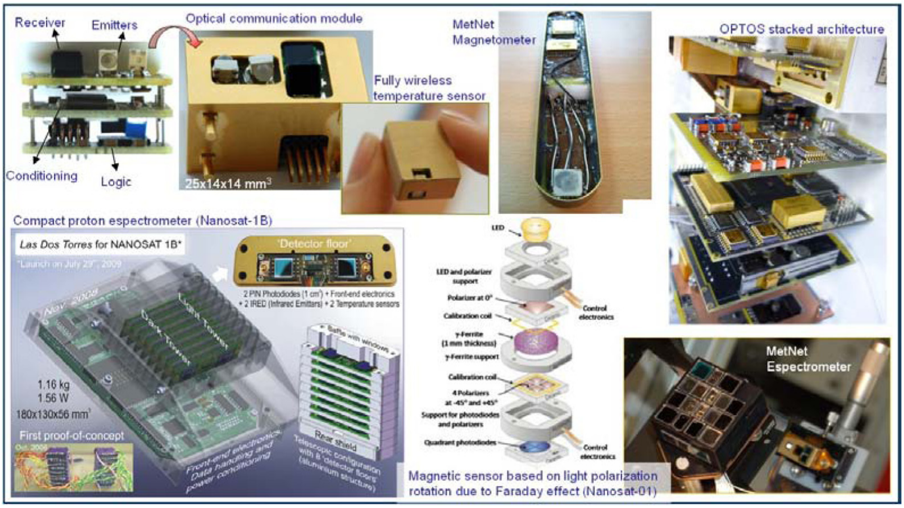

fig. 1: Different smart and compact units/instruments developed in the past

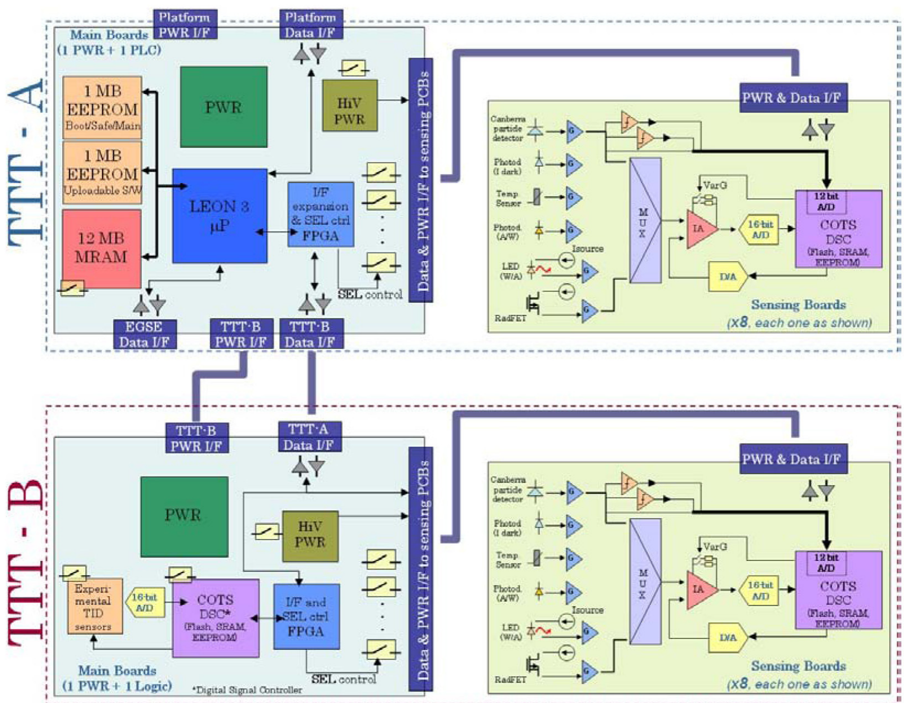

fig. 2: Architecture of "The Two Towers" radiation monitor currently under development for SEOSAT/INGENIO

COMPACT MINIATURIZED SENSORS FOR MAGNETIC MINERALOGY ON MARS

Marina Díaz Michelena,
National Institute for Aerospace Technology (INTA), Spain. Contact: diazma@inta.es

Mars, our nearest neighbour planet is still a mistery for us in many aspects. Amongst them unknown but key topics for the human exploration of the planet, are the ones more appealing not only for the scientific community but for the general public: whether we will be able to breathe and feed ourselves or not, how to stand the low pressure and gravity, the available mineral resources, etc. The shield of our global magnetic field is one of the things which permits the life on the Earth but it is known by the Mars Global Surveyor that there is not such an inner field on Mars. In contrast, Martian crust is partially magnetized (remanent magnetization). From this it is deduced that there could be local magnetospheres which could shield life from cosmic radiation.

Paleomagnetic minerals responsible for these anomalies need to have high values of magnetization and a strong pinning. Though the determination of the materials which stand for the strong and huge (in extension) magnetic anomalies is still an open question, oxides of titanium and iron are likely candidates for their relatively strong magnetizations (magnetite) and exchange (ferri and antiferromangetism in titanomagnetites).

In Earth, magnetic anomalies investigations are performed by means of aeromagnetic surveys (at heights of hundreds of m) and geological surveys with susceptometers, magnetometers and ulterior sampling analysis. Since opportunities to travel to Mars are so limited, the investigation of terrestrial analogous minerals is of great importance for further comparison. At this point the selection of Mars-like scenarios on Earth is one of the most difficult tasks and also a very challenging one for the extreme conditions of our neighbour planet.

For the in situ measurements, balloons, rovers, and landers are the platforms that could allow a magnetometer achieve similar information on Mars together with the sample-return missions From the point of view of magnetic surveys it is desirable to sweep Martian areas of interest with magnetic instruments. In static landers, interesting information can be extracted from the measurement of the thermomagnetic curves of magnetic minerals. No matter the kind of vehicle, the development of compact magnetometers has the critical point of the magnetic cleanliness.

To summarize, we will discuss the question of the Martian magnetic anomalies from the point of view of the minerals composition, the concerns of manufacturing a compact miniaturized magnetometer for a Mars lander and the scientific objectives pursued with such a payload.

RAMAN SPECTROSCOPY FOR THE DETECTION OF BIOLOGICAL MATTER IN MARS ANALOGUE MATERIAL

U. Böttger[1], J.-P. de Vera[1], J. Fritz[2], I. Weber[3], J. Schirmack[4], J. Meessen[5], D. Wagner[4], H.-W. Hübers[1,6];
[1]Institute of Planetary Research/DLR, Rutherfordstr. 2, Berlin Germany; [2] Museum für Naturkunde, Berlin. Germany; [3] Institut für Planetologie, WWU Münster, Germany; [4]Helmholtz Centre Potsdam, GFZ German Research Centre for Geosciences, Germany; [5]Institute of Botany, Heinrich-Heine-University Düsseldorf, Germany; [6]Technische Universität Berlin, Institut für Optik und Atomare Physik, Berlin. Contact: ute.boettger@dlr.de

Introduction Raman spectra will be measured with the Raman Laser Spectrometer (RLS) onboard ExoMars in 2018 to identify organic compounds and mineral products as an indication of former or recent biological activity. Investigation with the same specifications as those onboard the ExoMars mission is conducted to test the potential of identifying biological material on martian analogue material with Raman spectroscopy. Appropriate parameters concerning integration time and number of repititions for the detection of biological matter as well as for the determination of the mineral composition will be derived. In addition, problems are reported on using Raman spectroscopy to discriminate the microorganisms from the mineral background.

Biological sample Cyanobacteria and methane producing archaea are chosen to represent potential life on Mars. Prokaryotes like archaea and bacteria appeared on early Earth at least 3.8 to 3.5 billion years ago (Gya). Life might have developed under similar conditions on Mars as on Earth or might have been transferred from Earth (or vice versa). At that time on Mars the climate was more temperate and wet compared to the present day as inferred from geological evidence for liquid water on the ancient martian surface. Methane is known to be present on Mars. A source is still unknown. Methane might originate from geothermal or biological activities nearby the surface of the red planet. Cyanobacteria and prokaryotes using photosystem I use pigments such as scytonemin and beta-carotene as UV protection. Especially beta - carotene emits a strong Raman signal at the applied laser excitation wavelength. Raman measurements are used for detection of coccid, chain, and biofilm forming cyanobacteria Nostoc commune strain 231-06 (Fraunhofer IMBT CCCryo) on the below described Mars analogue mineral mixtures. Nostoc commune is known to be resistant to desiccation, UV B radiation and low temperatures, and thus suitable as a candidate for a potential life form on Mars. Furthermore, the Raman technique is applied on samples of the methane producing archaea candidatus *Methanosarcina gelisolum* (strain SMA 21) isolated from Siberian permafrost affected soils and on these archaea embedded in the martian analogue material.

Martian analogue material In this investigation two different Mars analogue materials prepared from mineral and rock mixtures are used. The (1) Phyllosilicatic Mars Regolith Simulant (P-MRS) and (2) Sulfatic Mars Regolith Simulant (S-MRS) reflect the current understanding regarding environmental changes on Mars. Weathering or hydrothermal alteration of crustal rocks and of secondary mineralization during part of the Noachian and Hesperian epoch followed by the prevailing cold and dry oxidising condition with formation of anhydrous iron oxides. The use of two different mixtures accounts for the observations that phyllosilicatic deposits do not occur together with sulphatic deposits. P-MRS and S-MRS serve as the analogue geomaterials in which the cells of cyanobacteria and of methanogenes are embedded.

Results Varying periods of measurement time and number of repetitions are used to get optimal Raman spectra for cyanobacteria and methanogenes. If cyanobacteria are present, beta-carotene is the dominant feature in the spectrum. Measurement times need to be adjusted to obtain optimal spectra of the P-MRS and S-MRS with cyanobacteria. Measurements performed with various values of measurement time and number of measurements show clearly the improvement achieved by increasing the time per spectrum from 1s to 20s. But it is desirable to find a set of small values of measurement time and number of repetitions in order to optimize the detection of minerals and biological markers and to reduce the disturbing effect of cosmic rays.

A measurement regime is proposed for mineral mixtures with cyanobacteria on the basis of the RLS instrument characteristics: A procedure on ExoMars should start with a measurement time of only a few seconds to identify both biomarkers and minerals. If no biomarkers can be identified the time and number of measurements need to be increased until spectra of minerals are obtained. The measurement time should be selected between 1s (for b-carotene) and 20s (for minerals) for a laser power of

1mW (spot diameter < 2 µm). Future investigations of Raman measurement parameters should consider the different environmental parameters on Mars like atmospheric pressure, composition and temperature. For methanogens a different measurement regime needs to be developed.

Raman analytics are capable to identify biosignatures like beta – carotene on a multi-mineral mixture similar to those expected to be encountered during the ExoMars mission.

POSSIBLE LOCATION AND METHODOLOGY FOR TRACES OF ORGANIC COMPOUNDS REVEALING IN THE MARTIAN REGOLITH

Managadze G.G[1]., Luchnikov K.A.[1], Moiseenko D.A.[1], Vorob'eva E. A.[1], Kuznetsov A.I.[5], Chumikov A.E.[6], Ziganshin R. Kh.[2], Wurz P.[3], Saralidze G.Z.[1], Managadze N.G.[1], Bondarenko A.L.[1],

[1]Space Research Institute of the Russian Academy of Sciences, Profsoyuznaya 84/32, GSP-7, Moscow, 117997, Russian Federation. Contact: managa@bk.ru, moiseenko-da@yandex.ru; [2]M.M. Shemyakin and Yu.A. Ovchinnikov Institute of bioorganic chemistry of the Russian Academy of Sciences, Miklukho-Maklaya, 16/10, GSP-7, Moscow,11799, Russian Federation. Contact: rustam.ziganshin@gmail.com;[3] University of Bern, Hochschulstrasse 4, CH-3012 Bern, Switzerland. Contact: peter.wurz@space.unibe.ch

In this work, Mars is viewed as the most likely planet to host microbial life under its regolith layer.

Our choice is based on the hypothesis that methane found in different areas on the surface of the planet may be linked to bacteria producing this gas during their life cycle. By analogy with the Earth, these communities may reside inside the planet at the depths of ~10 km, where the concentration of methanogenic bacteria may be quite appreciable. Microorganisms can also be present in the subsurface layer below 30-50 cm.

The results of a numerical simulation of the formation of an impact crater are analyzed, implying that unmelted rock layers from large depths may be ejected, together with microorganisms, to the subsurface layer of the planet.

It is shown that given the characteristic size of the ejection zone for a meteorite with a diameter of several kilometers a lander can be delivered to this area. Another important condition is that the crater chosen for the landing site should be located in a methane efflux area.

Regolith is to be analyzed using an onboard mass spectrometer made at the Space Research Institute of the Russian Academy of Sciences, which is capable of performing high-precision measurements of:

- the elemental and isotopic composition of the regolith using the technique of laser ablation and ionization of the sample;

- molecular ions and elements of the dust components of the subsurface layer of the sample while using soft ionization technique;

It is shown that, if necessary, a simple preparation of the sample may allow regolith to be separated from organic compounds. An analysis of the resulting mass spectra of the elemental composition of these compounds will make it possible to discover signatures of microbial life and identify the biomass. The same sample can also be used for direct measurements of organic molecules performed by subjecting them to laser radiation.

Mass spectra are presented that confirm the efficiency of the instrument including its operation in the MALDI mode. Problems are addressed that limit the implementation of the new methodology and recommendations are given how to circumvent these restrictions.

This work was supported by the grant of the Russian academy of sciences Presidium Program 22: “Fundamental problems of research and exploration of the Solar system”.

MONITORING OF SOLAR SYSTEM PLANETS AND DETECTION OF EXOPLANETS BY SPACE TELESCOPES PLANETARY MONITORING AND STELLAR PATROL.

A. Tavrov[1], A. Kiselev[1], I. Vinogrdov[1], V. Ananjeva[1] , V. Gnedykh[1], N. Sanko, L. Ksanfomaliti[1], O. Koravlev[1],
[1] Space Research Institute, Profsoyznaya str. 84/32, Moscow , Russian Federation; Contact: tavrov@iki.rssi.ru

The Space Research Institute of Russian Academy of Science (IKI RAS) currently develops two middle class space telescopes projects aimed to observe Solar system planets by a long term spectroscopy polarimetry monitoring and aimed to extra solar planets (exoplanets) engineering and scientific goals.

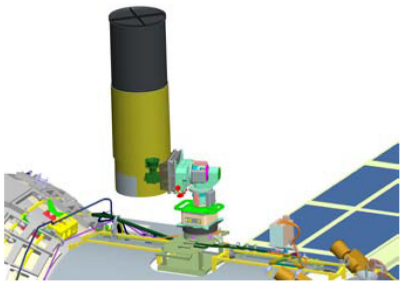
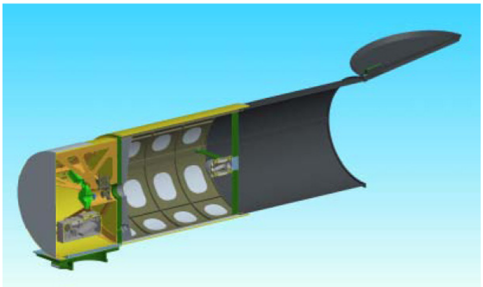

fig.1. “Planetary monitoring” telescope on RS ISS (left), telescope cross-sectional view (top).

“Planetary monitoring” telescope has a 0.6 meter primary mirror diameter and it is planned on board of Russian Segment of ISS It is scheduled to be launched in 2015..2016. It includes 5 science instruments:

1. IR: 1000..4000 nm high-resolution spectrometer R>10000;
2. Visible Field camera with filters wheel;
3. UV-VIS Fourier spectrometer;
4. UV-VIS spectropolarimeter;
5. Stellar coronagraph linked with spectrometer.

The “Planetary monitoring” telescope scientific goals devoted to explore not jet well studied questions on Mars (methane, ozone, dust and clouds, isotope ratio of HDO/H_2O), on Venus (UV absorber, night glow, atmosphere dynamics), icy and gaseous Solar system planets, Jovian moons, Lunar exosphere, comets, meteorites.

This telescope aims also for engineering development of exoplanet study by stellar coronagraphy linked with a low resolution spectrometry.

The “Plnetary monitoring” telescope will have its larger version with up to 1.5 .. 2 meter primary mirror diameter. That mission called “Zvezdnyi (engl. stellar) patrol” and is tentatively scheduled for the launch in 2018 to L2 point on a Navigator automate platform.

“Zvezdnyi patrol” has the main goal to atmospheric characterization of cold exoplanets with spectral near IR instruments. Another goal is to measure more precisely the Solar system planets atmosphere components.

High-contrast imaging is currently the only available technique for the study of the thermodynamical and compositional properties of exoplanets in long-period orbits, comparable to the range from Venus to Jupiter. This project is a coronagraphic space telescope dedicated to the spectropolarimetric analysis of gaseous and icy giant planets as well as super-Earths at visible and near IR wavelengths. So far, studies for high-contrast imaging instruments have mainly focused on technical feasibility because of the challenging planet/star flux ratio of 10^{-8}–10^{-10} required at short separations (200 mas or so) to image cold exoplanets. However, the main interest of “Zvezdnyi patrol” instruments, namely the analysis of planet atmospheric/surface properties, has remained largely unexplored.

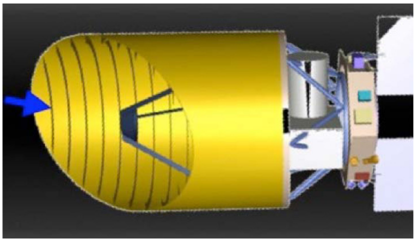

fig.2. “Zvezdnyi (engl. stellar) patrol” telescope to study exoplanets and to precise the spectroscopy of Solar system objects.

TECHNICAL DEVELOPMENT OF A SMALL DIGITAL TELESCOPE FOR IN-SITU LUNAR ORIENTATION MEASUREMENTS (ILOM)

H. Hanada[1], S. Tsuruta[1], H. Araki[1], S. Kashima[1], K. Asari[1], S. Tazawa[1], H. Noda[1], K. Matsumoto[1], S. Sasaki[1], K. Funazaki[2], A. Satoh[2], H. Taniguchi[2], H. Kato[2], M. Kikuchi[2], Y. Itou[2], K. Chiba[2], K. Inaba[2], N. Gouda[3], T. Yano[3], Y. Yamada[4], Y. Niwa[3], H. Kunimori[5], N. Petrova[6], A. Gusev[6], J. Ping[7], T. Iwata[8] S. Utsunomiya[8], T. Kamiya[8] & K. Heki[9],
[1]National Astronomical Oservatory, Oshu, Iwate 023-0861, Japan; [2]Iwate University, Morioka, Iwate, Japan; [3]National Astronomical Oservatory, Mitaka, Tokyo, Japan; [4]Kyoto University, Kyoto, Kyoto, Japan; [5]National Institute of Information and Communications Technology, Koganei, Tokyo, Japan; [6]Kazan Federal University, Kazan, Russia; [7]National Astronomical Observatories of CAS, Beijing, China; [8]Institute of Space and Astronautical Science, JAXA, Sagamihara, Kanagawa, Japan; Hokkaido University, Sapporo, Hokkaido, Japan;
Contact: hanada@miz.nao.ac.jp

Introduction: Observations of the lunar rotation are one of the essential and basic geodetic observations for investigating the interior of the Moon as well as those of lunar gravity fields. Optical astrometric observations as well as the advanced LLR with a new reflector and a new network, and the advanced Very Long Baseline Interferometer (VLBI) are proposed for observations of the lunar rotation in a future lunar mission. We are developing a small telescope for observations of the lunar rotation with target accuracy of 1 mas. Present status of the developments is presented in this paper.

ILOM Project: In ILOM (In-situ Lunar Orientation Measurements) Project, a small telescope like PZT set near the lunar pole determines the orientation of the axis of rotation of the Moon by positioning several tens of stars in the field of view at every moment for longer than one year (see Fig. 1) [1]. Main targets are direct observations of the lunar physical librations and the free librations [4]. The digital PZT will also be a powerful tool to monitor the solid moon tide. An accuracy better than 1 mas is necessary in order to put a strong constraint upon the structure and property of the lunar deep interior, since libration parameters related to property of the lunar core have an amplitude of at most a few mas [2,3].

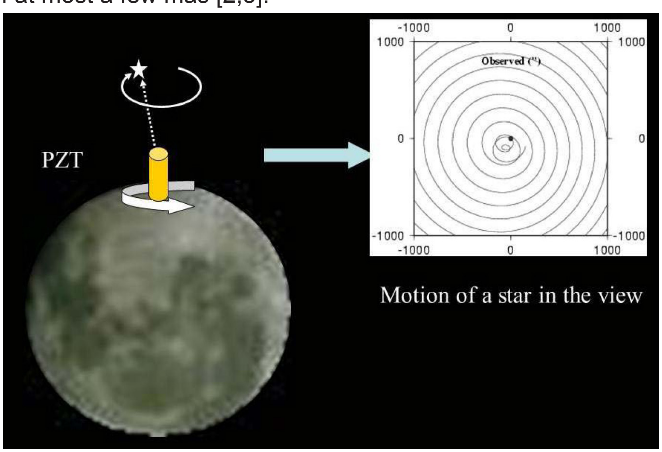

fig.1. Observation of lunar rotation by a telescope on the Moon.

Technical Issues: We have developed a BBM (Bread Board Model) of a digital telescope for ILOM (In-situ Lunar Orientation Measurement) (see Fig.2) and made some experiments in order to know the performance of the optical system and the driving mechanism under the lunar environment. It is a special small digital telescope like PZT (Photographic Zenith Tube) for study of lunar rotational dynamics with the target accuracy of 1 milli-arc-seconds (1 mas).

Effect of large temperature change is one of the most serious problem for such a precise observation. We propose two methods for reducing the effects of such a large temperature variation. One is to use a diffractive lens, and another is to correct the effects by making use of the characteristic patterns in the shifts of star images. Ray tracing simulations show that the tolerance for the temperature change becomes wider by about one order of magnitude by introducing the diffractive lens, and it suggests that the temperature change of up to 5 degrees is allowed for the observation change of 1 mas, which is more than one order of magnitude larger than that for conventional lenses. Regarding the latter method, we succeeded in approximating the effects of uniform temperature change with better than 0.03nm on the CCD array or 10 μas (micro-second of arc) by using a linear function of temperature [1].

We also investigated possible optical effects upon the central position of star images such as the ghost, off focus, stray rays, scattered rays, diffractive rays of unnecessary degrees by using ray tracing simulations and experiments. The effects were proved to be far below the 1 mas level.

The attitude control system, on the other hand, can make the tube vertical within an error of 0.006 degrees (or about 20 arc-seconds), which is within the tolerance for the measurement of 1 milli-arc-second accuracy by using PZT. Performance of the mechanical system on the Moon is evaluated by thermal vacuum test, and there is no serious problem hitherto.

The mercury pool, which is put at the middle point of the focal length of the objective, is used as both a reference level surface and a reflected surface in the optical system. The surface, therefore, should be flat and stable. We evaluated the mercury pool by measuring the roughness of the mercury surface in slightly tilted and vibrational states as well as in a stationary state. The mercury pool made of cupper with the depth of 0.5mm and the diameter of 84mm is the mostly stable, and is a candidate used for preliminary observations on the Earth.

This work was supported by Grant-in-Aid for Scientific Research (B) (Grant No. 22340128) from Japan Society for the Promotion of Science and the Joint Research Projects between Japan and Russia (grant No. 11037711-000282).

fig.1. BBM of the telescope (Iwate Univ.).

References

1. Hanada, H. Araki, H., Tazawa, S. et al, 2012. Development of a digital zenith telescope for advanced astrometry. Sci China-Phys Mech Astron, 55, 723-732.
2. Williams J G, Boggs D H, Yoder C F, et al., 2001, Lunar rotational dissipation in solid body and molten core. J Geophys Res, 106, 27933–27968.
3. Rambaux N., Williams J.G., 2011. The Moon's physical librations and determinaton of their free modes.
Celest Mech. & Dyn Astr, v.109, p. 85-100
4. Gusev A., Petrova N., 2012. Rotation, physical librations and interior of the multi-layer Moon. The second
edition of the book, processed and added, Kazan, Kazan University Press, 220pp. (Russian, in press)

IMPLEMENTATION OF A SELF-CONSISTENT STEREO PROCESSING CHAIN FOR 3D STEREO RECONSTRUCTION OF THE LUNAR SURFACE

E. Tasdelen[1], H. Unbekannt[1], M. Yildirim[1], K. Willner[1] and J. Oberst[1,2],
[1]Technische Universität Berlin, Institute for Geodesy and Geoinformation Science, Planetary Geodesy, Straße des 17. Juni 13510623 Berlin, Germany; [2]German Aerospace Center (DLR), Berlin-Adlershof, Germany.
Contact: e.tasdelen@mailbox.tu-berlin.de

Introduction:

The department for Planetary Geodesy at TU Berlin is developing routines for photogrammetric processing of planetary image data to derive 3D representations of planetary surfaces. The ISIS software, developed by USGS, Flagstaff, is readily available, open source, and very well documented. Hence, ISIS [1] was chosen as a prime processing platform and tool kit. However, ISIS does not provide a full photogrammetric stereo processing chain. Several components like image matching, bundle block adjustment (until recently), digital terrain model (DTM) interpolation from 3D object points or an efficient tool to visualize the resulting 3D models are missing. Our group aims to complete this photogrammetric stereo processing capability by implementing the missing components, taking advantage of already existing ISIS classes and functionality. We report on the development of a new image matching module that is optimized for orbital planetary images and compatible with ISIS formats, an interpolation tool that is developed to compute DTMs from large 3-D point clouds, and a tool to visualize the resulting DTMs in a manner that is suitable for large data sets. The latter includes a module to analyze landing sites on planets and satellites from a geodetic point of view.

Matching Software:

The matching software supports multithreading in order to increase the performance and to handle large images, such as Lunar Reconnaissance Orbiter Camera (LROC) data, efficiently. Currently supported image formats are Vicar, TIFF and ISIS CUBE. The Matcher integrates different area-based matching algorithms like normalized cross-correlation (NCC) and least-squares matching (LSM). NCC delivers an approximate value of disparity. LSM is applied in order to refine the result to sub-pixel accuracy. Within the software, several different matching approaches are available to improve the results for different types of images (smooth and rough surfaces). The definition of the search space, which is the maximum expected image coordinate difference (disparity) in overlapping stereo images, is the main difference between the approaches.

Interpolation Tool:

Large clouds of 3D object point coordinates are used as input data for the DTM interpolation. As a first step, these coordinates are map-projected into a pre-defined cube file, which serves as a target container. The input data can be provided in non-sequential order and there are no specific requirements in terms of spatial distribution or homogeneity of the distribution of the points. The point clouds may also have gaps. On the other hand, it is possible that several object points define only one pixel of the target projection. In our first preliminary implementation of the tool, this is accounted for by applying distance-based weighting to determine exactly one value for the resulting pixel. The implementation of further interpolation methods is in progress. Envisaged methods are nearest-neighbor interpolation and Kriging. Furthermore a triangulated irregular network based (TIN-based) interpolation approach has been implemented, which provides an area-weighted summation of multiple triangles for each raster cell.

Visualization Tool:

The final element in the chain is the visualization of the resulting DTMs. To perform this task, a planetary rendering application was developed. The software is able to visualize large data sets of digital elevation models derived from planetary missions from global to local levels. Accordingly, the software includes some of the most effective algorithms for 3D visualization in order to accomplish the task. In particular, the chunked level of detail algorithm is implemented [3]. The tool supports file formats used in planetary exploration studies and supports state-of-the-art memory management techniques, called out-of-core algorithms. The software is designed to be flexible, open for modifications, and ready to work on all common operating systems.

The rendering engine contains a special module to aid in the selection of landing sites on extraterrestrial bodies. In particular, one can analyze landing sites with respect to Sun visibility and Earth-communication opportunities. This capability can be used to determine the suitability of the site for landing and surface operations.

Results:

With this processing components we have the ability to compute 3D visualization scenes from space mission data. Ultimately this allows us to characterize proposed future landing sites from a geodetic point of view. All the components of the stereo processing chain were tested to achieve an acceptable performance and results.

The matcher was tested with narrow-angle LRO orbital images (Fig.1a). The results of the matcher presented here were carefully compared to the results of another image matching software, e.g. software used at DLR (German Aerospace Center), with respect to number of matches found, completeness and quality of the visual 3D representation. The tests showed that in terms of coverage and completeness, TU matcher delivers high quality results. However, it suffers from large number of outliers. Thus, a post-processing step was applied and misidentified corresponding points were subsequently removed by applying different filter techniques. The resulting disparity map (Fig.1b) and visual control of the final DTM (Fig.1c) show very good agreement with the 3D reconstructions from different software solutions [2].

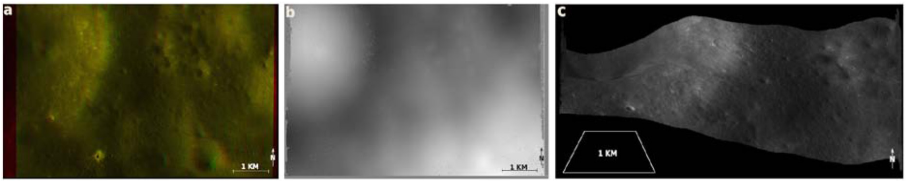

Fig. 1. (**a**) LRO stereo image pair, (**b**) Resulting disparity map, (**c**) Perspective view of DTM from resulting 3D reconstruction

The interpolation tool was tested with 3D points derived from stereo image matching of Lunar Reconnaissance Orbiter's Narrow Angle Camera (NAC) images and Mars Express' High Resolution Stereo Camera of the Martian Moon Phobos. A preliminary result which covers North Massif adjacent to the Apollo 17 landing site, is shown in Figure 2a. DTMs generated from the previous steps are finally used as an input for the visualization application. Figure 2b shows screenshots taken from the vicinity of Apollo 17 landing site.

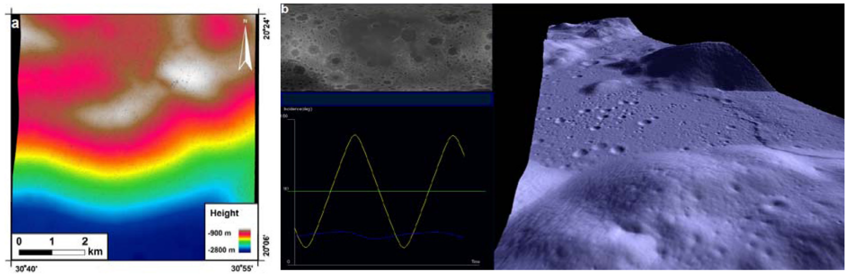

Fig. 2. (**a**) Subset of a preliminary DTM (1.5 meter/pixel) derived by our interpolation tool. Gaps within the terrain model, 1-2 pixels in size, are visible and were caused by inhomogeneous point distribution. (Area: North Massif adjacent to the Apollo 17 landing site.), (**b**) A screenshot from the visualization application, in which the visibility analysis module is integrated. Right side of the window includes 3D visualization from the Apollo 17 landing site; whereas on the left hand side there is a plot showing the sun and earth elevation angles (yellow and blue lines, respectively) over time at the point of interest.

Future Works:

More matching tests and comparisons based on different data sets will be performed in order to judge the capabilities of the software, especially, in terms of accuracy and completeness. The interpolation tool will be further assessed, by comparison of results with equivalent datasets from different software packages, when all interpolation methods are implemented. Moreover, it is envisaged to include other data sets like gravity or dynamic height models in the visualization to provide a more comprehensive analysis of potential landing sites. Results of the evaluation will be reported during the conference.

References:

[1] Anderson, J.A., et al., (2004) Modernization of the Integrated Software for Imagers and Spectrometers (abs. 2039), LPSC XXXV.
[2] I. Haase et al., "Mapping the Apollo 17 landing site area based on Lunar Reconnaissance Orbiter Camera images and Apollo surface photography", J. Geophys. Res., doi:10.1029/2011JE003908, in press, 2012.
[3] T Ulrich. Rendering massive terrains using chunked level of detail control. SIGGRAPH Course Notes, 3(5), 2002.

ABSTRACTS SUBMITED TO SECTION 1. MOON

SEARCHING FOR WATER ICE PERMAFROST ON LUNAR POLES: LEND RESULTS FOR ABOUT THREE YEARS OF OBSERVATIONS.

A. B. Sanin[1], I. G. Mitrofanov[1], M. L. Litvak[1], A. Malakhov[1], D. V. Golovin[1], M. I. Mokrousov[1], R. Z. Sagdeev[4], G. Milikh[4], W. V. Boynton[2], G. Chin[3], G. Droege[2], L. G. Evans[5], J. Garvin[3], K. Harshman[2], T. P. McClanahan[1], R. D. Starr[6],

[1]Institute for Space Research (IKI), Moscow, 117997, Russia; [2]Lunar and Planetary Laboratory, University of Arizona, Tucson AZ, USA, [3]NASA Goddard Space Flight Center, Greenbelt MD, 20771, USA, [4]Space Physics Department, University Maryland, College Park, MD, USA, [5]Computer Sciences Corporation, Lanham MD 20706, USA, [6]Catholic University of America, Washington DC, USA.

Contact: sanin@mx.iki.rssi.ru

Introduction:

More than 50 years ago, it was suggested that some areas near the lunar poles are sufficiently cold to trap and preserve for a very long time (~Gy) hydrogen bearing volatiles, either primordial or produced at the Moon via solar wind interactions or brought to the Moon as water ice by comets and meteoroids [1,2]. The results of observations made by radar onboard the Clementine spacecraft and by neutron (LPNS) and gamma-ray (LPGRS) spectrometers onboard the Lunar Prospector mission have been interpreted as an enhancement of hydrogen abundance in permanently shadowed regions (PSRs) [3]. Unfortunately, the spatial resolution of the LPNS was much broader than the size of any largest PSRs [4] requiring model dependent data deconvolution to resolve signal from PSRs itself.

Data Analysis:

We would like to present updated results of analysis of Lunar Exploration Neutron Detector (LEND) data for about three years of lunar mapping. Data measured by collimated LEND detectors allows one to look at neutron flux distribution at Moon poles with much better spatial resolution then was achieved at previous space missions.

Using the LEND data we had tested the hypothesis that all PSRs are contain a large amount of water ice permafrost and test for hydrogen presents in regolith of regions outside of PSRs.

Discussion:

Both analyses of individual PSRs and studies of groups of PSRs have shown that these spots of extreme cold at lunar poles are not associated with a strong effect of epithermal neutron flux suppression [5]. We found only three large PSRs, Shoemaker and Cabeus in the South and Rozhdestvensky U in the North, which manifest significant neutron suppression, from -5.5% to -14.9%. All other PSRs have much smaller suppression, no more than few percentages, if at all. Some PSRs even display excess of neutron emission in respect to sunlit vicinity around them. Testing PSRs collectively, we have not found any average suppression for them. Only group of 18 large PSRs, with area >200 km^2, show a marginal effect of small average suppression, ~2%, with low statistical confidence. A ~2% suppression corresponds to ~125 ppm of hydrogen taking into account the global neutron suppression near the lunar poles and assuming a homogeneous Hydrogen distribution in depth in the regolith [6].

Testing for hydrogen presents in regolith of regions outside of PSRs has been done by detection of local spots of suppression and excess of epithermal neutron emission at the lunar poles. Found areas there named as Neutron Suppression Regions (NSRs) and Neutron Excess Regions (NERs). These NSRs may be identified with spots of water-ice rich permafrost on the Moon. It is shown that detected NSRs are include in both permanently shadowed and illuminated areas, and they are not coincident with Permanently Shadowed Regions (PSRs) at the bottom of polar craters, as has been commonly expected before LEND presented neutron data with high spatial resolution [7]

References:

[1] Arnold, J. R. (1979) JGR, 84, 5659–5668. [2] Watson, K., Murray B. C. and Brown H. (1961) JGR, 66, 3033–3045. [3] Feldman W. C. et al. (2001) JGR, 106, 23231-23252. [4] Maurice S. et al. (2004) JGR, 109, E07S04, 40 PP. [5] Mitrofanov I. G. et al. (2010) Science, 330, 483. [6] Sanin A.B. et al. (2012) JGR, 117, E00H26. [7] Mitrofanov I. G. et al. (2012) JGR, 117, E00H27.

NEAR INFRARED DIODE LASER SPECTROSCOPY OF C_2H_2, H_2O, CO_2 AND THEIR ISOTOPOLOGUES AND THE APPLICATION TO A TUNABLE DIODE LASER SPECTROMETER (TDLAS) FOR THE MARTIAN PHOBOS-GRUNT AND LUNAR LUNA-RESOURCE AND LUNA-GLOB SPACE MISSIONS.

I. Vinogradov[1], G. Durry[2], A. Titov[1], L. Joly[2], C. Stoeffler[2], J. Cousin[2], T. Decarpenterie[2], N. Amarouche[3], O. Korablev[1], M. Gerasimov[1], O. Roste[1],
[1]Space Research Institute (IKI), 117997, 84/32 Profsoyuznaya Str., Moscow, Russia; [2]GSMA, UMR CNRS 7331, Université de Reims, BP 1039, 51687 Reims, Cedex 2, France; [3]Division Technique de l'Institut National des Sciences de l'Univers, CNRS, 92195 Meudon Cédex, France; Contact: imant@iki.rssi.ru

Abstract:

A near-infrared tunable diode laser spectrometer called TDLAS has been developed that combines telecommunication-type as well as new-generation antimonide laser diodes to measure C_2H_2, H_2O, CO_2 and their isotopologues in the near infrared. This sensor was devoted to the in situ analysis of the soil volatiles of the Martian satellite PHOBOS, within the framework of the Russian space mission PHOBOS-GRUNT. We report accurate spectroscopic measurements of C_2H_2 and $^{13}C^{12}CH_2$ near 1.533 μm, of H_2O and CO_2 at 2.682 μm and of the isotopologues $^{13}C^{16}O_2$ and $^{16}O^{12}C^{18}O$ near 2.041 μm and $H_2{}^{17}O$, $H_2{}^{18}O$ and HDO near 2.642 μm. The design of the TDLAS space spectrometer is also described.

The TDLAS spectrometer was integrated into the Gas Analytic Package (GAP) in conjunction with a Gas Chromatograph – Mass Spectrometer (GC-MS) suite. It was implemented in the PHOBOS-GRUNT spacecraft and launched unsuccessfully in November 2011. The GAP apparatus aimed at analyzing the gases evolving from the pyrolysis of a tiny soil sample, taken from the Phobos surface at the Lander location with a robotic arm. The extremely low expected quantity of evolved gas molecules, the limited space, mass and resources available onboard made it a challenge to realize TDLAS and to yield efficient measurements.

The TDLAS/GAP design is currently being reconfigured for the incoming Russian missions to the Moon polar regions, LUNA-GLOB and LUNA-RESOURCE, as well as for a potential second mission to the Phobos Martian satellite (PHOBOS-GRUNT-II). In this presentation, we will discuss the improvement made to the TDLAS laser sensor, including the spectroscopy, to prepare for these new space missions.

Keywords:

Tunable diode laser spectroscopy, planetary soil sampling and pyrolysis, evolved gas composition and isotopic ratios.

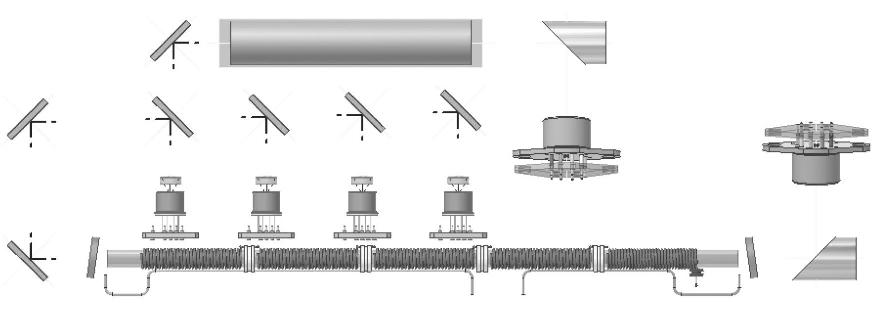

Fig. 1. 3D-CAD view of the novel TDLAS model for the Moon polar landing missions. Up to 4 DFB-laser slots are available for realization of measurements. Ge-etalon at the reference channel provides for additional spectral labels, enhancing accuracy of measurements. Design details are discussed at the presentation.

This work was supported by the grant of the Russian academy of sciences Presidium Program 22: "Fundamental problems of research and exploration of the Solar system".

SURFACE STRUCTURE AND MINERALOGICAL COMPOSITION FROM LUNAR MULTICHANNEL SPECTROMETER.

V. Linkin, A. Lipatov, V. Makarov, G. Zakharkin, S. Antonenko, A.Ekonomov,
IKI RAN, Profsoiuznaia 84/32,Moscow, RF, alekonomo@yandex.ru.

Introduction:

- The mineralogical composition of the polar regions has not been investigated on lunar landers .
- Panoramic image enables us to view a significant portion of the surface (hundreds of meters around the lander).
- Use the zoom will explore the different parts of the surrounding landscape, including the separate rocks. And the fields in the vicinity (1-2 m) can be studied with very high resolution.
- Luminescent analysis has several features that distinguish it from all other types of analysis. Fluorescent analysis of an unusually sensitive. It can be used to detect the presence of a substance in a sample with a concentration of ~ 10E-10 - 10E-11 g / g
- An important advantage of the method are its simplicity and speed
- The use of two methods of expanding possibilities of the instrument as a whole

General characteristics of the TV camera

The angular resolution	3 arcmin
Field of view	5x6-50x60 degrees.
Supply voltage	27.0 V + \ -20%.
Power consumption	2.0 W, the peak current - up to 1.3 A.
Operating temperature	from -90 ° C to +50 ° C,
The data transfer speed	4.8 kbps - 2Mbod
Interface	RS-422
The number of spectral bands	at least 9
Mass	no more than 0.65 kg.
Dimensions of the unit	no more than 126 * 175 * 95 mm.
Informativeness	no more than 100 Mbyte per day.

1) To identify the surface regolith concentrations of rock-forming minerals such as ilmenite (FeTiOz), olivine, low-potassium and high potassium feldspars and pyroxenes, the following filters:
Channel 1 is 278-326 nm;
Channel 2 342-358 nm;
Channel 3 393-436 nm;
Channel 4 is 545-561 nm;
Channel 5 596-610 nm;
Channel 6 635-648 nm;
Channel 7 678-693 nm;
Channel 8 900-930 nm;
Channel 9 970-1020 nm;
or a spectrum ranging from 278 to 1020 nm with a resolution of 12 nm.
2) regolith mapping sites with different concentrations of titanium (Ti), and other mafic minerals, respectively, the following interrelation can be used for individual channels: Channel 4 and Channel 3/channel 8/channel 4.
3) To obtain color images of the lunar surface around the lander imaging must be conducted in the following three filters:
Blue (460-590 nm)
Green (570-665 nm)
Red (660-780 nm)

Photometric mode

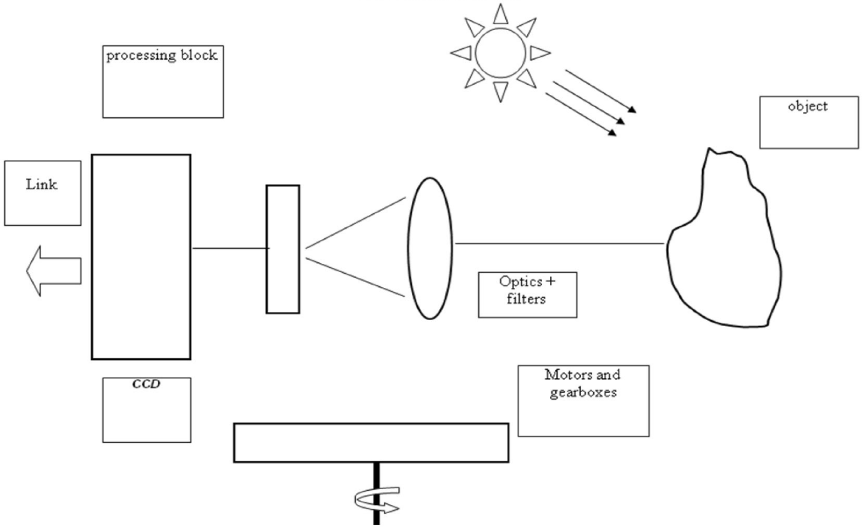

Fluorescent mode

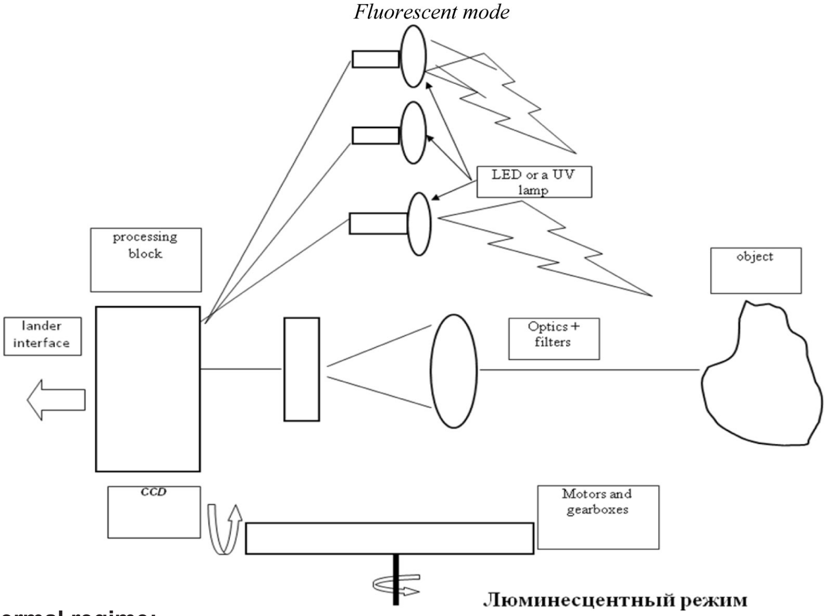

Thermal regime:

Critical thermal regime of the instrument is determined by cooling at night. Hold a minimum temperature within acceptable limits can be achieved by decreasing the heat radiation using a coatings with a minimum emissivity, such as gold. In order to maintain normal thermal regime of the contact thermal resistance should be controlled and quite low.

SIMULATION OF THE LUNAR PHYSICAL LIBRATION OBSERVATIONS USING THE LUNAR POLAR TELESCOPE.

N.K. Petrova[1,2], T.R. Abdulmynov[2], H. Hanada[3],
[1]Kazan Federal University, Kazan, Kremlevskaja, 18, Rusia, [2]Kazan State Power Engineering University, Russia [3] National Astronomical Observatory, Japan. Contact: nk_petrova@mail.ru

Introduction:

Analysis of simulated stellar tracks observable from the lunar surface is a kind of a key to the internal structure of a celestial body. In this connection, the lunar experiments aimed at the study of the Lunar Physical Libration (LPhL) are of great interest. One of the necessary stages of preparation for the upcoming experiments, such as space mission SELENE-2 [1] the project ILOM (In-situ Lunar Orientation Measurement) is the theoretical simulation of the future observations. In this report we present several results of the simulation of polar stars observation by the imitation of the work of the polar telescope, which is planned to be placed on the Lunar pole in the frame of ILOM-project.

The system of selenographic coordinates

In the framework of the current study we simulate the observation with an "ideal telescope" [2]: the telescope will be posed exactly at the lunar dynamical pole (the axis of its tube coincides with the principal inertia axis C of the Moon) and the axes of the CCD-array situated in the lens of the telescope will be ideally directed along the other two principal axes of inertia A and B. The motion of stars will be displayed relatively to the axes of inertia, which are rigidly connected with the lunar body. Reduction of rectangular ecliptical coordinates $\vec{E}$ of any star to the selenographycal coordinates $\vec{S}(t)=\left(x_s,y_s,z_s\right)^T$ may be done with the lunar libration angles $\tau(t),\rho(t),\sigma(t)$ on the basis of equation system, whose common expression can be written in the following form [2]:

$$\vec{S}(t)=\Pi\left(\tau(t),\rho(t),\sigma(t)\right)\vec{E} \qquad (1)$$

Here Π – is a function formed by production of rotation matrixes, used for the transition from the ecliptic coordinate system to selenographic system.

Formulation of the inverse problem

Under the *inverse problem* of LPhL we understand finding the values of libration angles $\tau^o(t)$, $\rho^o(t)$, $\sigma^o(t)$ by using "observed" selenographic coordinates of stars x_s^o,y_s^o,z_s^o measured during the imitation observations. In the inverse problem the angles of libration are considered as unknown variables described by the vector

$$\vec{X}(t)=\left(\tau(t),\rho(t),\sigma(t)\right)^T=\left(x_1(t),x_2(t),x_3(t)\right)^T.$$

Then the system of equation (1) can be rewritten:

$$\mathrm{F}(\vec{X})=\prod\nolimits_z\left(F+x_1-x_3+180^o\right)\times\prod\nolimits_{\bar{X}}\left(-(I+x_2)\right)\times\prod\nolimits_{\bar{Z}}(\Omega+x_3)\times\vec{E}-\vec{S}=0 \qquad (2)$$

F is the distance of the mean longitude of the Moon from the mean longitude of its ascending (northward-bound) node ☊. The constant *I* ~ 1°32.5' is mean inclination of lunar pole to ecliptic pole.

Jacobian of the system (2) turned out to be close to zero. The systems with the Jacobian close to zero can be solved using the *gradient method* [3]. It provides a good convergence for our type of functions $\mathrm{F}(\vec{X})$ within the given accuracy.

Estimation of influence of an inaccuracy in measuring the coordinates on the accuracy of libration angles allows us to do following conclusions:

1) If the inaccuracy in the determination of coordinates e = 1 mas is achieved technologically, then the inaccuracy in the determination of LPhL angles will be $|\Delta\rho|\le\sqrt{2}\varepsilon$ and $|\Delta I\sigma|\le\sqrt{2}\varepsilon$. 2) At the same time, the value of $\tau(t)$ is independent on variation in x, y and, consequently, cannot be determined from the polar stars. This phenomenon is explained by geometry of physical libration: longitudinal librations depend on selenographic latitude d proportionally to cosd, which for the polar zone is close to zero.

Manifestations of the deformability of the lunar body in polar libration

The expansion of Petrova's analytical theory [4, 5] in the case of a deformable Moon was made on the basis of complements, calculated by Chapront et al. [6] to the Moons' libration theory concerning tidal effects. We have carried out the comparison of data (coordinates $\vec{S}(t)$ of the fictitious pole and libration angles $\vec{X}$) obtained in the framework of LPhL theory for the rigid Moon and for the deformable Moon respectively

(k_2 = 0.02992). At the stage of direct problem we calculated coordinates and libration angles for both models. At the next stage (inverse problem) we substituted the coordinates $\vec{S}^d$ obtained within the deformable Moon model into Eq. (2) considering them as observable data and solved this equation for unknown libration angles $\vec{X}$, the initial values for them $\vec{X}$ being taken from the rigid Moon model $\vec{X}^{rigid}$. The residuals $\vec{X}^d - \vec{X}^{rigid}$ $\vec{X}^d - \vec{X}^{rigid}$ shown on Fig. 1 point to well-marked both periodical variations and constant shift ($\Delta\tau$ is insensitive to the changing of model).

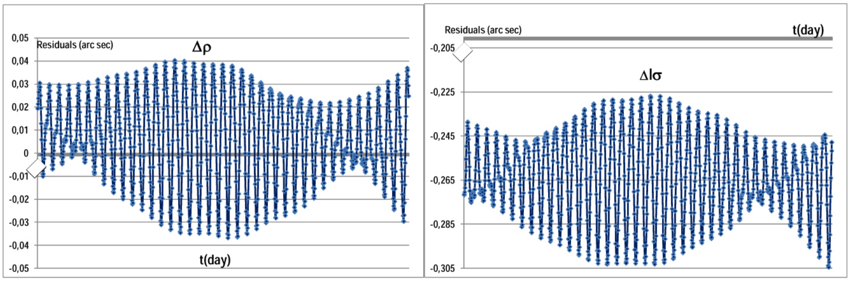

fig. 1. Residuals in libration angles $\Delta\rho = \rho^d - \rho^r$, $\Delta I\sigma = I(\sigma^d - \sigma^r)$ during 39 sidereal months.

We carry out the Fast Fourier Transform on the residuals. Frequency spectra for both angles are similar, only insignificant differences in amplitudes are observed. As an example the spectrum for residuals in ρ is shown on Fig. 2. Numerical values of frequencies, respective periods and amplitudes are given in Table. In order to identify the obtained frequencies with the origin frequencies of libration theory, we calculate $\Delta\rho$ and $\Delta I\sigma$ in analytical form using the software Poisson Series Processor. Comparison with analytical expansion of the residuals allows us to do the following results.

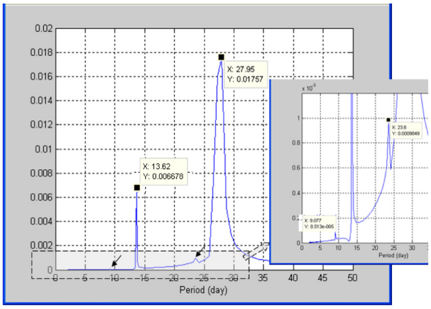

Fig. 2 Spectrum of residuals of $\Delta\rho(t)$ and $\Delta I\sigma(t)$. The unity of ordinate is arc sec.

frequency (revolution per day)	period T (day)	$\Delta\rho$ (arc sec)	$\Delta I\sigma$ (arc sec)
0.11020	9.08	0.0001	0.0002
0.07345	13.62	0.0067	0.0065
0.04237	23.6	0.0009	0.0010
0.03578	27.95	0.0176	0.0174

Most of harmonics in residuals of libration angles are caused by elastic part of P_1 and P_2. These signatures cause corrections in star positions and in the derived libration angles and show sensitivity to the Love number k_2. The anelastic terms will look like phase shifts of the rigid body terms: the cosine terms of P_1 and $I\sigma$ and the sine terms of P_2 and ρ. The largest terms in P_1 and P_2 with amplitudes of ~0.27", come from the anelasticity. They are responsible for appearance of constant shift in $I\sigma$ (-0.2619”) and additional inclination (0.0051″) in ρ, a large constant 0.0066” in ρ comes from elastic model. Coefficients of the cosines in $I\Delta\sigma$ coincide up to 0.001 “ with the data of Williams et al. [7] for the value $k_2/Q_F = 0.001137$. We dare to suggest that the component with the period of 27.95 days is a result of blend of the harmonics, whose periods are close to the lunar rotation period ~27.3 days: *l*, *F*, *l*-2*F*, *l*-2*D*. Analysis of blends is a complicated problem of spectral analysis, nevertheless the improvement of k_2 will cause the total decrease of residuals in this region. Strong harmonic 2*F* with the period of 13.62 days is very useful for the analysis: there are no other harmonics in its vicinity. Weak components with the period of 23.6 days and 9.08 days corresponds to the (*l*+2*F*-2*D*)-term and (*l*+2*F*)-term, respectively. They may be also interesting for analysis, although its amplitude is on the verge of accuracy; however, our simulation reveals this component.

References

[1] Hanada H. et al. (2011), Science China Phys. Mech. Astron. 55 691(4), 723–732, 2012.
[2] Petrova, N., Hanada, H. PSS,.68 (2012), pp. 86-93, doi:10.1016/j.pss.2011.10.002
[3] Demidovich B., Maron I. (2006). Basis of numerical mathematics (Book in Russian), 672p.
[4] Petrova N. (1996) Earth, Moon and Planets, 73, 1, p. 71.
[5] Petrova N., Gusev A. (2008) Rotation, physical libration and interior of the Moon. (Book in Rusian).
[6] Chapront J. et al. (1999) CMDA, 73, 317.
[7] Williams J G, Boggs D H, Yoder C F, et al.,2001, J Geophys Res, 106, 27933–27968.

PHOTOGEOLOGIC ANALYSIS OF THE NORTH POLAR LUNA-GLOB CANDIDATE LANDING REGION.

A. M. Abdrakhimov[1], A. T. Basilevsky [1], J. W. Head [2], L. Dickson [2],
[1]Vernadsky Institute, RAS, Moscow, 119991, Russia, atbas@geokhi.ru;
[2]Brown University; USA.

Introduction:

The main scientific goal of the Luna-Glob mission [1] is to study volatiles [2-4] in the regolith of lunar polar region (70-85°N, 30°W-60°E). We studied the regional geology, which is largely determined by ancient highlands associations, including large basin ejecta [5]. The new regional detailed geologic map was made using recent LRO data [7,8]: WAC mosaic (100 mpp), LOLA, LRO Mini-RF data. The absolute ages of geological units were estimated, defined by the crater size-frequency distribution (D>1.5 км).

Photogeologic analysis:

Three groups of geological units have been identified and mapped (Fig. 1):

Large impact craters. (Cc, Ec, Ic, Nc, pNc), including ejecta, crater floor (Ccf, Ecf, Icf, Ncf) and central peak facies (Ccp, Ecp, Ncp), which were divided based on different preservation states and maturity characteristics, and unit-to-unit stratigraphic relationships. The youngest rayed craters (Cc) are characterized by sharp relief features, high albedo, well preserved rims, central peaks, and high rock fragment abundance. Older (Ec) craters lose rays and have fewer rock fragments. Next older Ic are partly embayed by plains materials, and the oldest (Nc, pNc) are characterized by partly or fully degraded smoothed rim crests and are embayed by plains and basin materials.

The ejecta deposits of impact basins (If, Nbl) sculptured older undivided underlain crater and terrain complexes (IpNcl, IpNl). Mainly the W and S parts of the study region are covered by a blanket of basin ejecta (If), which is radial to the Imbrium basin in the S and morphologically resembles the Fra Mauro Formation [5]. The hummocky If surface is made of sinuous, and straight wide ridges draping over the underlying landscape. The SE parts are covered by an older deposit of irregular hilly material (Nbl), with broadly undulating ridges and troughs and radial to the Humboldtanium basin.

Material of mare (Im)*, plains-forming* (Ip_2, Ip_1) *and older terrain units* (INtp, Ntp, IpNt) fill intercrater space and crater floors. The dark and relatively smooth basaltic mare material Im is observed in the SE part as two small patches of several tens of km across, embaying Ip. The surface of the older plains-forming material (Ip) is represented by brighter and more heavily cratered smooth level plains of two generations with sharp boundaries. These plains materials cover >34% of the mapped area, filling the old crater floors and intercrater lowlands and resembling material of the Cayley Formation, considered to be Imbrium basin ejecta fluidized during emplacement [5]. In the intercrater highland areas we defined three terrain complexes INtp, Ntp, IpNt, mainly in the NE old highland part. Light, fairly smooth and leveled hummocky material INtp filling intercrater lowlands, and old Nc and pNc craters. It is similar to plainsforming Ip, but formed during earlier large impacts. A hummocky terra unit (Ntp) fills craters and mantles highlands. Ntp appears as blocks rising among planar complexes. Ntp is superposed by INtp and younger units, and filled old craters Nc, pNc. The oldest terra material IpNt, mantled intercrater highlands, and has a rough surface. IpNt probably represents remnants of degraded ancient craters and oldest overlapping ejecta blankets, formed during Pre-Nectarian to Imbrium times.

The results and conclusions: Unit relationships, their localities, and age estimations are summarized in Fig.1. They generally confirm the earlier global Lunar Orbiter mapping results [9]. The most probable unit which could be sampled by the lander is a smooth feldspathic Imbrian highland plains-forming material Ip, resembling the Cayley Formation.

References: [1] Mitrofanov I. G. et al. (2011) LPS XLII, Abstract #1798. [2] Feldman W. C. et al. (1998) Science, 281, 1496. [3] Mitrofanov I. G. et al. (2010) Science, 330, 483. [4] Colaprete A. et al. (2010) Science, 330, 463-468. [5] Wilhelms G. H. et al. (1987) USGS Prof. Paper, 1348. [6] Cheek L. C. et al. (2011) JGR, 116, E00G02. [7] Smith D. E. et al. (2010) GRL, 37, L18204. [8] Bussey L. C. et al. (2010) AGU, Abstract # P34A-07. [9] Lucchitta B. K. et al. (1978) USGS Prof. Paper, I-1062. [10] Michael G. G. and Neukum G. (2010) EPSL, 294, 223-229.

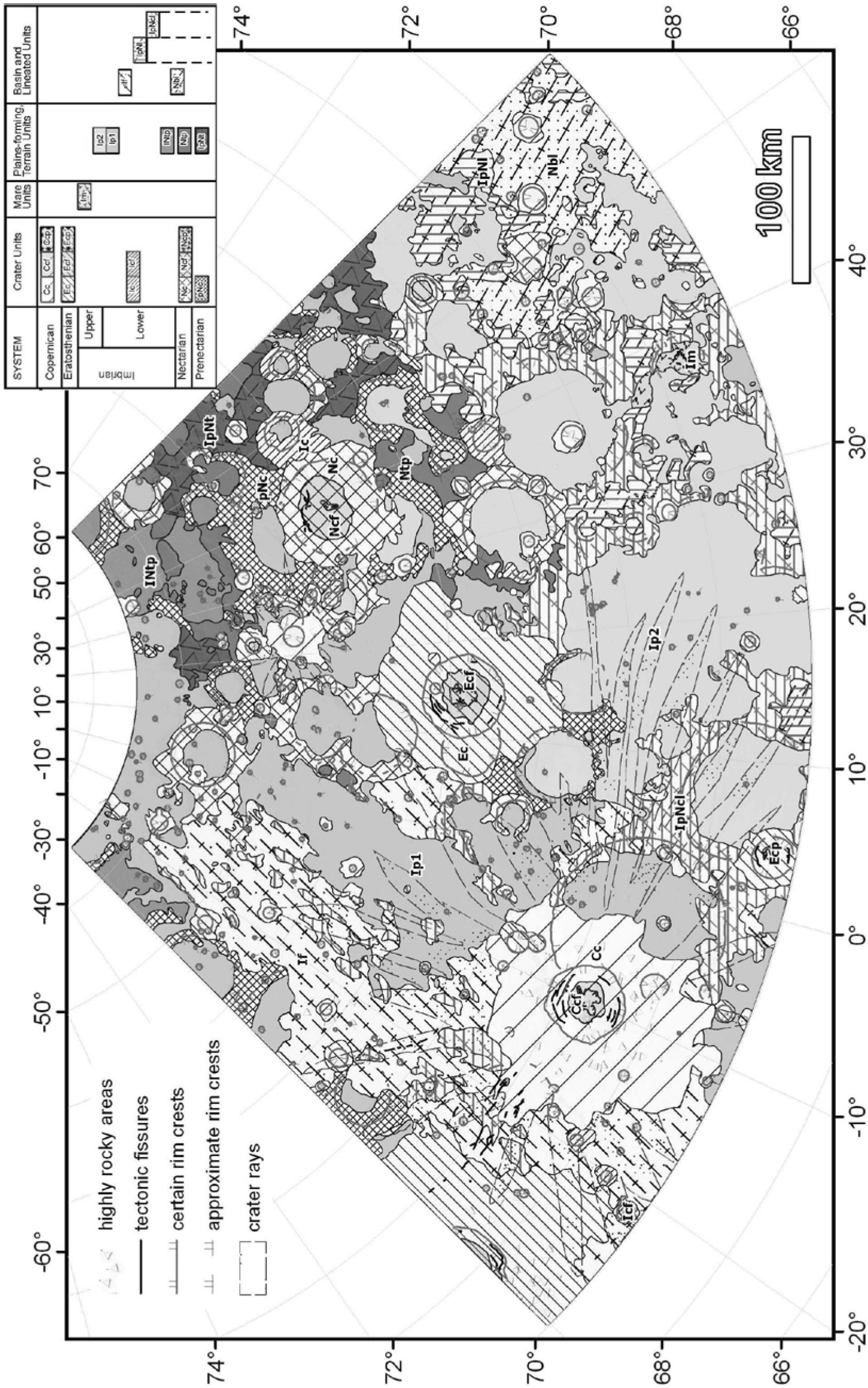

Fig. 1. Geologic map of Luna-Glob polar landing area (277785 sq. km) and stratigraphical scheme. Unit abbreviations see the text. Total area –, units area: crater units: Cc,Ccf,Ccp - 8%; Ec,Ecf,Ecp - 10%; Ic, Icf - 1%; Nc ,Ncf, Ncp - 6%; pNc - 5%; basin units: If - 11%; Nbl - 4%;IpNcl - 10%;IpNl - 4%; mare units: Im - 0.3%; plains-forming units: Ip1 - 16%; Ip2 - 18% (Ip_{total} – 34%); old terra and plains units: INtp - 2%; Ntp - 2%; IpNt - 2%. The crater statistics age estimation by the method [10]: Im - $3.74^{+0.04}_{-0.06}$; Ip_2 - $3.93^{+0.00}_{-0.00}$; Ip_1 - $3.98^{+0.00}_{-0.00}$; INtp, Ntp -$4.05^{+0.02}_{-0.02}$; IpNt- $4.07^{+0.02}_{-0.02}$; If - $4.01^{+0.01}_{-0.01}$; Nbl - $4.05^{+0.02}_{-0.02}$ Ga.

BIG SIZE HOLLOW CCR OF LLR AND LUNAR PHYSICAL LIBRATIONS FOR SELENE–2, CHANG'E–4,5,6 AND LUNA–RESOURCE PROJECTS

A. Gusev[1], H. Noda[2], H. Araki[2], H. Hanada[2], J. Ping[3], F. Kikuchi[2], J. Li[4] , K. Matsumoto[2], S. Sasaki[2], V. Tretyakov[5],
[1]Kazan Federal University, Kazan, Russia; [2]National Astronomical Observatory of Japan; [3]National Astronomical Observatories of CAS, China; [4]Shanghai Astronomical Observatory CAS, China; [5]Space Research Institute, Moscow, Russia. Contact: Alexander.Gusev@mail.ru

The force and free physical librations of the Moon is very sensitive to its interior structure [1]. Numerical models of the Lunar physical libration (LPhL), satisfying the modern Lunar laser data (LLR), necessarily include complex internal stratigraphy of the elastic-viscosity mantle and two-layer lunar core, including an inner rigid core and outer liquid core [1,5].

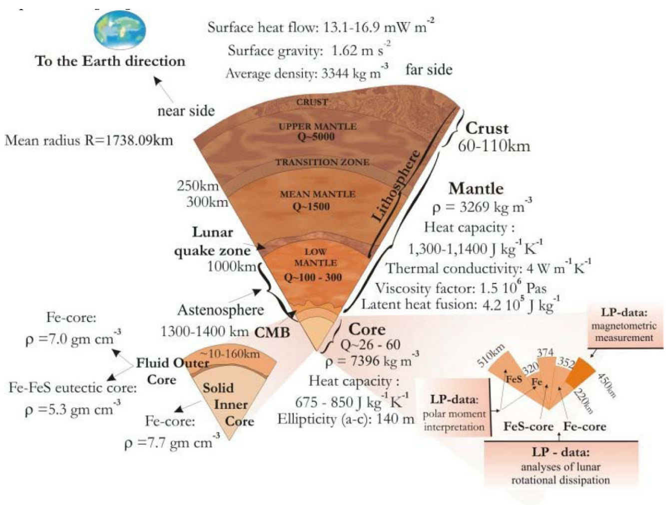

Precision data of a laser location of the Moon give a good basis for determination of amplitudes and phases of the free libration of various types: Chandler Wobble, Free Core Nutation, Inner Chandler Wobble, Free Inner Core Nutation [1] . The lot of periods of free libration and of their interaction with forced terms may be obtained using the analytical approach [2].

free librations of the multi - layer Moon – 2012 yr [1,2]	
"Chandler Wobble amplitude period PCW	8.183»´3.306»(69 ´ 28 m) 27257.27 days = 74.626 yr
precession mode amplitude period	0.032" 8822.88 days = 24.156 yr
longitude mode amplitude period	1.296" 1056.13 days = 2.893 yr
free core nutation period PFCN = 27.312 days in ILRF	0. 016» 144 – 186 yr in ICRF
Free inner core nutation period PFICN = 27.241 days in ILRF	~0.001» 516 - 635 yr in ICRF
Inner Chandler Wobble period PICW	~0.003» 101 - 108 yr

Big size hollow CCR for new generation of the Lunar Laser Ranging

This figure (left slide) shows the candidate of landing sites of Japanese lunar landing mission SELENE-2 [3]. Polar regions are not included as candidate sites due to engineering point of view. Retroreflectors (right slide) with large aperture are needed to improve the range accuracy. Corner Cube Prism is relatively easy to produce, but because of the homogeneity of the material, the aperture is limited up to 10 cm [4]. If one wishes to build a retroreflector with larger aperture than 10 cm, a hollow-type is preferable [3].

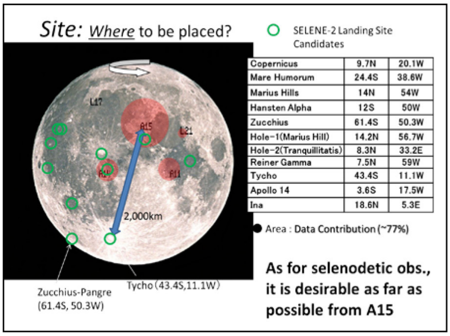

Copernicus	9.7N	20.1W
Mare Humorum	24.4S	38.6W
Marius Hills	14N	54W
Hansten Alpha	12S	50W
Zucchius	61.4S	50.3W
Hole-1(Marius Hill)	14.2N	56.7W
Hole-2(Tranquillitatis)	8.3N	33.2E
Reiner Gamma	7.5N	59W
Tycho	43.4S	11.1W
Apollo 14	3.6S	17.5W
Ina	18.6N	5.3E

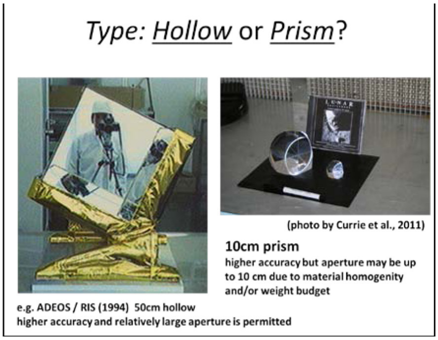

The optical cross section (left slide) is expressed as the formula. According to this formula, the equivalent diameters of CCR to those of Apollo 11 and Apollo 14 are 17.6 cm and 25.4 cm, respectively. There are several candidate materials (right slide) to produce corner cube mirror. Mass, stiffness, thermal properties are important points of view for comparison. A glass ceramic called Clear Ceram-Z (CCZ) has appropriate property for the lunar surface condition.

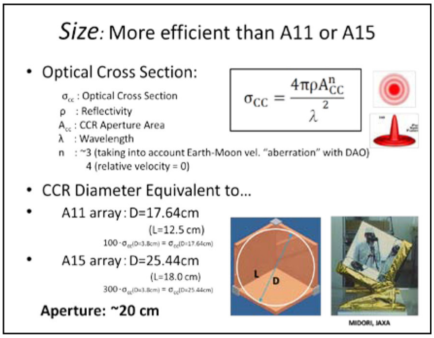

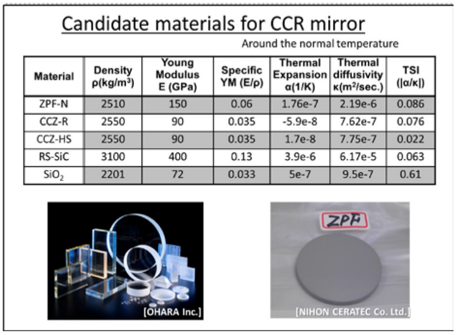

Material	Density ρ(kg/m³)	Young Modulus E (GPa)	Specific YM (E/ρ)	Thermal Expansion α(1/K)	Thermal diffusivity κ(m²/sec.)	TSI (|α/κ|)
ZPF-N	2510	150	0.06	1.76e-7	2.19e-6	0.086
CCZ-R	2550	90	0.035	-5.9e-8	7.62e-7	0.076
CCZ-HS	2550	90	0.035	1.7e-8	7.75e-7	0.022
RS-SiC	3100	400	0.13	3.9e-6	6.17e-5	0.063
SiO_2	2201	72	0.033	5e-7	9.5e-7	0.61

Left slide is a conceptual drawing of the gimbal and the mirror holder. Right slide is a summary sheet of the concept of the retroreflector proposed to Japanese SELENE-2 and may be to Chinese CHANG'E–4,5,6 and may be to Russian LUNA–RESOURCE projects .

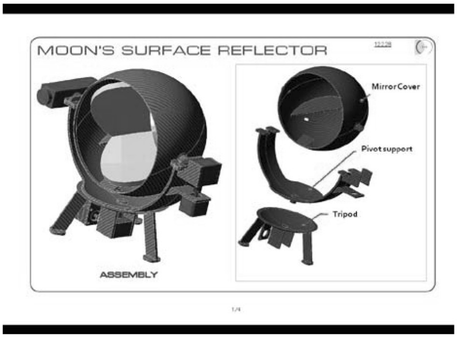

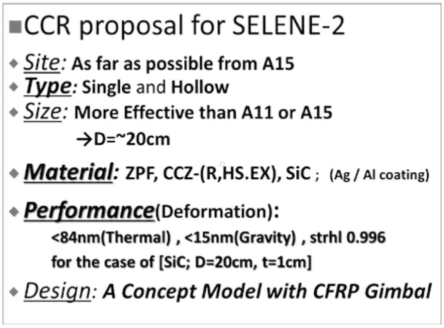

The research was partially supported by the Russian-Japanese grant RFBR-JSPS 11-02-92113-ЯФ_a and

the Russian-Chinese grant RFBR-GFEN 11-02-91160 ГФЕН_a

References

Gusev A., Petrova N., (2012) Rotation, physical librations and interior of the multi-layer Moon. The second edition of the book, processed and added, Kazan, Kazan University Press, 220pp. (Russian, in press)
Rambaux N., Williams J.G., (2011) The Moon's physical librations and determinaton of their free modes. CMDA, v.109, p. 85-100
Noda H. et al. (2012) LPSC XLIII abstract #1855.
Currie D. et al. (2011), A Lunar Laser Ranging Retroreflector Array for the 21st century, Acta Astronautica, 68, 667-680.
Ping J., Hanada H., Gusev A., et al., (2012) May small digital PZT and radiobeacons improve the LPhL for future lunar missions? Abstract of the 25th GA IAU, Beijing, China, 20-31 August, #3.7

IRON ABUNDANCES IN SLOPE AVALANCHES OF LUNAR CRATERS.

Yangxiaoyi LU[1],
[1]National Astronomical Observatories,Chinese Academy of Sciences; Contact:lyxy@bao.ac.cn

Introduction:

Detailed studies of slope avalanches in lunar craters, which can be considered as recent processes observed on the Moon, were begun by the authors in 2 previous works (Shevchenko et al., 2007; 2011; Lu 2 et al., 2011; Shevchenko et al., 2012). In the studies of features of these formations, it has been established that in some cases there occurs outcropping of structures or subsurface layers of lunar regolith with different iron abundances.

It is known that in lunar rocks the abundance of iron, as the main chromophore component, has a significant influence on reflectivity. In the work of Shkuratov et al. (1999a), a close correlation between iron abundance and the optical characteristics of surface materials has been studied in detail over the visible hemisphere. The authors used the landing sites of space probes and manned spacecraft as test areas. These results have been further developed and confirmed by Pieters et al. (2002), and it has been demonstrated with high accuracy that ironenriched pyroxenes are the most optically active components of lunar soil. According to the results of this work, it has been conclusively established that the spectral band of pyroxene absorption of about 1 μm is a reliable parameter for identification of the chemical composition of lunar surface material by remote spectral measurements.

Abnormal slope formations in craters burg and mauri A

Crater burg (copernicus age) is the youngest of the objects considered. it varies with noticeable abnormalities of physical characteristics of surface formations generated by slope movements of material. figure 9 depicts an image acquired from the chang'e 2 spacecraft with the resolution of the original image of about 7 m/pixel.

in southwestern part of crater wall, there is an observed albedo abnormality which corresponds to the formation generated by the slope movement of dark material. The crosssection of the supposed avalanche in its widest part is slightly greater than 1 km, and its length along the slope is greater than 3 km. Movement of loose surface soil occurred with an average incline angle of about 15°. The flow origin is located about 400 m below the wall edge.

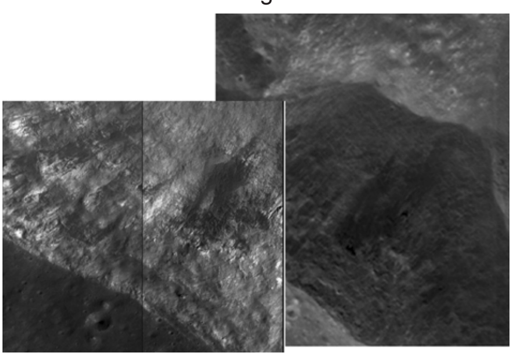

fig. 1. Left, a fragment of images M113778346L and M113778346R, acquired by the narrow angle camera from the LRO spacecraft. Source: http://wms.lroc.asu.edu/lroc. Right, a fragment of image, acquired from the Chang'e 2 spacecraft. Source: http://moon.bao.ac.cn.

Figure 1 shows a fragment of images M113778346L and M113778346R, acquired with the narrow angle camera from the LRO spacecraft with a resolution of 0.48 m/pixel, and a fragment of an image illustrated in Fig. 9, in order to compare the images of the albedo abnormality. The image fragments are brought to approximately one and the same scale. It should be noted that the images were acquired under different conditions of illumination. The local phase angle for the section of the abnormality in the image acquired from the LRO spacecraft is about 40°. In the image from the Chang'e 2 spacecraft, the local phase angle is higher (about 60°), which, however, does not interfere with the detailed comparison of both images.

The procedure by Lucey et al. (2000a; 2000b), described above, using Eqs. (1) and (2), was applied for comparative analysis of the abnormality and slope formations in the northern part of the crater wall.

FeO(wt. %) = –17.43× arctan{(R950/R750 – 1.19)/(R750 – 0.08) – 7.56, (1)

OMAT = [(R750 – 0.08)2 + (R950/R750 – 1.19)2]1/2, (2)

Figure 2 depicts the spectral image of the crater acquired from the Clementine spacecraft using 415 nm (R415), 750 nm (R750) and 950 nm (R950) filters. The images are obtained using automated software developed and implemented in the Lunar and

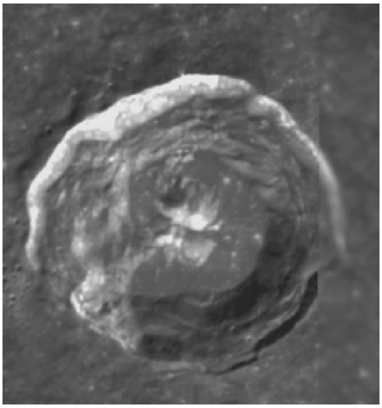

fig. 2. Spectral image of crater Burg, based on images acquired from the Clementine spacecraft in the regions of 415 nm, 750 nm and 950 nm. Resolution of the original images is about 100 m/pixel (LPI Clementine..., 2011).

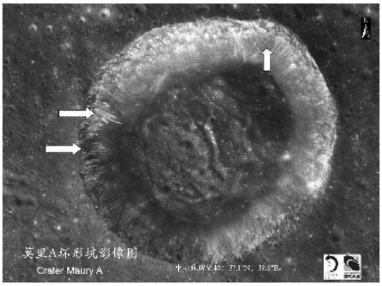

fig. 3. Image of crater Mauri A, acquired from the Chang'e 2 spacecraft on October 23, 2010, from a height of 100 km. Resolution of the original image is about 7 m/pixel. Source: http://moon.bao.ac.cn.

Planetary Institute, USA, LPI Clementine..., 2011. The compared objects are avalanches of light (1) and dark (2) material. The aforementioned abnormality is marked as (3).

A similar procedure was applied for the comparative analysis of slope formations observed in crater Mauri A. Figure 3 depicts an image from a series acquired by the Chang'e 2 spacecraft illustrating crater Mauri A. Area 1 is an avalanche characterized by high albedo and coinciding in shape with typical flows of fine material detected previously in other craters. Areas 2 and 3 are selected by low albedo, which in the first approximation can indicate an increased iron abundance in the surface soil layer. This selection was arrived at after detailed studies based on spectral images.

Results and discussion:

A peculiar feature of slope formations can be related to the same degree of maturity of surface material of the surrounding terrain and light flows of slope material, such as area 1 in crater Burg, area 1 in crater Mauri A and area 2 in crater Daniel. Probably, these flows are formed by surface materials, equally exposed to space weathering. Of greatest interest, of course, is the assessment of the absolute age of the freshest structures. According to the diagram shown, the most immature substance is located in area 3 on the wall of crater Burg (Figs. 1, 2).

Similar slope flows have been studied recently using phase ratios (Shkuratov et al. (2011)), where it has been demonstrated that the surfaces of these formations on the slopes of crater Kepler are rougher than those of the surrounding terrain. This peculiarity of the surface layer of slope formations confirms a high degree of immaturity of the soil of the slope flows and, at the same time, does not contradict the existence of a fine fraction.

If correlation between the optical maturity index, spectropolarimetric maturity index of surface material 2 and exposure age, described by Shevchenko et al. (2012), then the age, corresponding to OMAT ~0.7-0.8, can amount formally to no more than several years. Taking into consideration that the efficiency of the spectral method has not been validated under extreme conditions, these values can contain significant errors. Possibly, at present, the conditions for the generation of subsurface layers, from which the observed flowsoccur, are not fully considered.At the same time, the avalanche surface in area 3 ofcrater Burg, as in other similar cases, contains absolutely no shock craters which can be distinguished at this resolution. Therefore, the general conclusion that the observed slope movements of material can be related to contemporary processes cannot be excluded completely.

Conclusions:

This work discusses the analysis of abnormal structures on the internal walls of craters of various ages.

The craters considered are related to various ages of lunar history covering a significant time interval of formation of the lunar surface. In relation to this, the characteristics of avalanche formations are of great interest, which in terms of morphological properties are very close to each other. In all cases, the abnormal formations are characterized by increases FeO abundance in comparison with the values typical for the forms of landscape, and by the fact that ironenriched layers are located hundreds of meters below the surface layer. These data present a somewhat vertical profile of variations in the chemical composition of the rocks.

Shevchenko et al. (2012) pointed out that one of the unsolved problems of avalanche movements of material is the reason for the existence of regolith fine fraction at a depth of hundreds of meters, which, probably, plays a major role in the generation of highly fluid avalanche flows. This peculiarity is confirmed by new data, and referring to Wilcox et al. (2006) mentioned above, it is possible to assume that the fine substance consists of particles with sizes of about 10 μm. However, in order to explain completely the existence of this particle size fraction in regolith at such depth, further research is required. Herewith, an important circumstance is the correlation between minor particle sizes and iron abundance in soil.

The most significant, and principally new, result of this research is the determination of the age of occurrence of slope movements of material enriched with iron. With all possible errors, the assessments of the age of these formations amount to several tens of years or even less, which agrees with complete absence of shock craters on the surface of the formations. In any case, the exposure age of the surface material of slope flows is far lower than the assumed age of formation of the craters where slope phenomena are observed.

Acknowledgments:
The research was supported by the NSFC No. 10973031 of joint research of Russian-Chinese grant from Russian side RFBI-GFEN 11-02-91160 ГФЕН_а and from Chinese side.

References:
Gol'dshtein, M.N., Mekhanicheskie svoistva gruntov (Mechanical Properties of Soils), Moscow: Stroiizdat, 1973.
Grolier, M.J., Geological Map of the Geminus Quadrangle of the Moon, U.S. Geol. Survey Misc. Geol. Inv. Map I841, Scale 1:1,000,000, 1974.
Lawrence, D.J., Feldman, W.C., and Barraclough, B.L., Global Elemental Maps of the Moon: The Lunar Prospector Gamma Ray Spectrometer, Science, 1998, vol. 281, no. 5382, pp. 1484–1489.
Le Mouelic, S., Langevin, Y., Erard, S., et al., Discrimination between Maturity and Composition of Lunar Soils from Integrated Clementine UV–Visible/Near–Infrared Data: Application to the Aristarchus Plateau, J. Geophys. Res., 2000, vol. 105, no. E4, pp. 9445–9455.
LPI
Clementine Mapping, Project. http://www. lpi.usra.edu/lunar/tools/clementine/2011
Lu, Y. and Shevchenko, V.V., Dry Debris Flow on the 2 Moon: Cgang'å–2 Data, Proc. 42nd Lunar and Planetary Science Conf., Woodlands, 2011, p. 1254.
Lucey, P.G., Blewett, D.T., and Jolliff, B.L., Lunar Iron and Titanium Abundance Algorithms Based on Final Progcessing of Clementine Ultraviolet–Visible Images, J. Geophys. Res., 2000a, vol. 105, no. E8, pp. 20297– 20 305.
Lucey, P.G., Blewett, D.T., Taylor, G.J., and Hawke, B.R., Imaging of Lunar Surface Maturity, J. Geophys. Res., 2000b, vol. 105, pp. 20.377–20.386.
Pieters, C.M., Stankevich, D.G., Shkuratov, Yu.G., and Taylor, L.A., Statistical Analysis of the Links between Lunar Mare Soil Mineralogy, Chemistry and Reflectance Spectra, Icarus, 2002, vol. 155, pp. 285–298.
Shevchenko, V.V., Pinet, P.C., Chevrel, S., et al., The Avalanche Deposits in Lunar Crater Reiner, Proc. LPS–38, League City, 2007, p. 1066.
Shevchenko, V.V., Pinet, P.C., Chevrel, S., et al., The Current Avalanche Deposits in Lunar Crater Reiner . LRO Data, Proc. LPS–38, League City, 2011, p. 1161.
Shevchenko, V.V., Pinet, P.C., Chevrel, S., et al., Modern Slope Processes on the Moon, Sol. Syst. Res., 2012, vol. 46, no. 1, pp. 1–17.
Shkuratov Yu.G., Kaydash V.G., and Opanasenko, N.V., Iron and Titanium Abundance and Maturity Degree Distribution on Lunar Nearside, Icarus, 1999a, vol.137, no. 2, pp. 222–234.
Shkuratov, Yu.G., Kreslavsky, M.A., Ovcharenko, A.A., et al., Opposition Effect from Clementine Data and Mechanisms of Backscatter, Icarus, 1999b, vol. 141, pp. 132–155.
Shkuratov, Yu.G., Stankevich, D.G., Kaydash, V.G., et al., Composition the Lunar Surface as Will Be Seen from SMART–1: Simulation Using Clementine Data, J. Geophys. Res. Planets, 2003, vol. 108, no. E4, pp. 1–12.

GIS MAPPING OF THE TERRITORY OF THE SOVIET LUNAR MISSIONS.

M. A. Baskakova, I. P. Karachevtseva, K. B. Shingareva, E. N. Gusakova, *Moscow state University of Geodesy and Cartography (MIIGAiK)MIIGAiK Extraterrestrial laboratory (MExLAb) Gorokhovskiy per., 4, 105064, Moscow, Russia; Contact: m_baskakova@mexlab.ru, i_karachevtseva@mexlab.ru, tel: +7-499-2673513*

Introduction: With new high resolution images from Lunar Reconnaissance Orbiter the interest to past missions has increased. We have used the newest data for detail mapping and research the landing sites of the Soviet spacecraft.

Sources: The Lunar Reconnaissance Orbiter (LRO) was launched in 2009 [4]. It is a NASA robotic spacecraft currently orbiting the Moon. The main instrument consists of two parts. There is one wide-angle (LRO WAC) camera of resolution 100 m/pixel and two narrow angle (LRO NAC) cameras of resolution 0.5 m/pixel. We have used WAC orthomosaic, which was created from WAC GLD100 [3] and LRO NAC images [6]. Also on LRO there is a laser altimeter LOLA, which makes it possible to create a DEM. In our work we have created a map from LDEM of resolution 30 m/pixel, LDEM1024 [7]. In 2007 Japanese robotic spacecraft Kaguya was launched, which provided images and a DEM of resolution 7-10 m/pixel [8]. DEM from both sources were used for 3D-modeling of the lunar surface.

Mapping results:

The objects of mapping in our work are the landing sites of spacecrafts “Luna-16”, “Luna-17”, “Luna-18”, “Luna-20”, “Luna- 23”, “Luna-24”. Coordinates of these landing sites on MOON ME Coordinate System were taken from [2]. In the first step of work we orthorectified a set of LRO NAC images (about 25 images for all studied sites). With ISIS [9] functions rectification of LRO NAC images was done using the LOLA DEM (LDEM1024) to MOON ME Coordinate System. Using this data we have created some maps (Fig. 1) of landing sites areas of the Soviet lunar missions at high level of details where landing modules is well visible (Fig. 2). These maps created in equidistant cylindrical projection on a scale of 1: 5 000. On the landing sites of “Luna-23” and “Luna-24” we have chose areas measuring 5x5 km and have digitized craters with diameter more than 10 meters. Also we have created the maps of spatial density of craters [1]. Thus, the results of the mapping work will be formed Catalogue of small lunar craters in different parts of the lunar surface. These data can be used for more detail geomorphology analysis based on high resolution DEM.

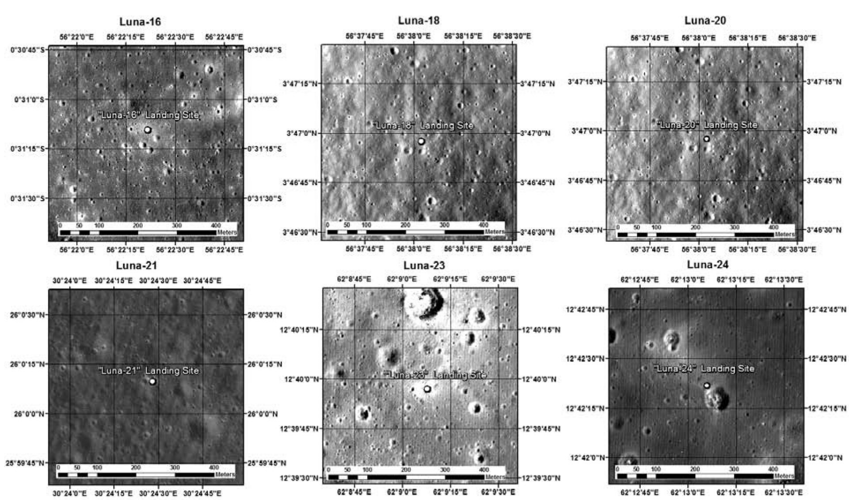

fig. 1. The maps of the landing sites of “Luna 16”, “Luna-18”, “Luna-20”, “Luna-21”, “Luna-23”, “Luna-24”

3D-modeling:

By means LDEM1024 3D-model which covers the landing sites of the “Luna-16”, “Luna-18”, “Luna-20”, “Luna-23”, “Luna-24” was created. The high resolution 3D-model correspond to the area of the landing sites of “Luna-16”, “Luna-17”, “Luna-18”, “Luna-20”, “Luna-23”, “Luna-24” was created based on Kaguya DEM (Fig.3).

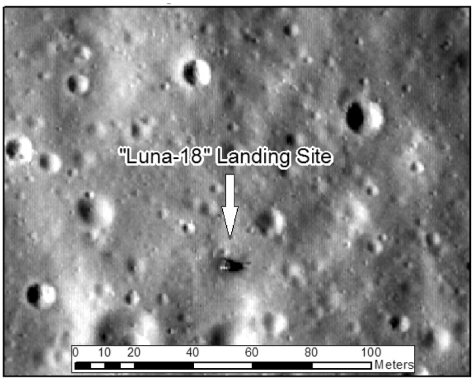

fig. 2. The visible “Luna-18” landing site on the M119482862RE LRO NAC Image

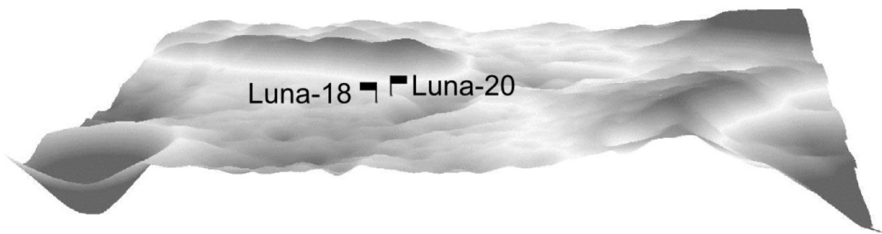

fig. 3. 3D-model of the landing sites of the “Luna-18” and “Luna-20” (Kaguya DEM)

Automatization of mapping process:

Using DEM we have calculated topography parameters of the Lunokhod-1 area, for example, for the surface roughness [1]. We used 5 different techniques for the roughness calculation and to automate the process we applied the ArcGIS Model Builder. Using our model we can run a few processes together and save time for creating maps.

Conclusions:

Creating the maps and 3D-modeling using new recently data allowed us to research the landing sites of the Soviet lunar missions in detail. Now we are collecting the database of small craters for all landing sites of Soviet lunar missions and planning to use new LRO NAC DEM based on Photomod software using methods as describe at [5] for calculating depth of craters, slopes and other parameters.

Acknowledgements:
This work has been supported by a grant from the Ministry of Education and Science of the Russian Federation (Agreement № 11.G34.31.0021 dd. 30/11/2010)

References:

[1] Gusakova E. et al. (2012) Mapping and GIS-Analyses of the Lunokhod-1 Landing Site. Abstract of 43-th LPSC Lunar Planetary Science Conference
[2] Nadezhdina I, et. al. (2011) Comparison of the coordinate data of Soviet space artifacts on the lunar surface. Geodesy and Cartography, № 6. - C. 23-26
[3] Scholten F. et al., (2012) GLD100, J. Geophys. Res., in press.
[4] Robinson M. et al., (2010) Lunar Reconnaissance Orbiter Camera (LROC) Instrument Overview. Space Science Reviews, Volume 150, Issue 1-4, pp. 81-124
[5] Zubarev A. E. et. al. (2012), Features of creating DTM for Luna-Glob landing sites, this issiues
[6] http://wms.lroc.asu.edu/lroc/rdr_product_select
[7] http://ode.rsl.wustl.edu/moon/indextools.aspx
[8] http://www.jspec.jaxa.jp/e/hottopics/20110908.html
[9] http://isis.astrogeology.usgs.gov/

GIS-ANALYSIS OF MOON SURFACE FOR THE LUNA-GLOB AND LUNA-RESOURCE LANDING SITES

A. A. Kokhanov[1], I. P. Karachevtseva[1], A. E. Zubarev[1], J. Oberst [1, 2, 3], M. S. Robinson,

[1]Moscow State University of Geodesy and Cartography (MIIGAiK), MIIGAiK Extra-terrestrial Laboratory (MExLab), Gorokhovskiy per., 4, 105064, Moscow, Russia; [2] German Aerospace Center (DLR);[3]Technical University of Berlin, Germany, [4]Arizona State University, Arizona, USA..

Contact: i_karachevtseva@mexlab.ru, tel: +7-499-2673513

Introduction:

The goal of this work is to provide cartographical support for characterization of potential landing sites of Russian space missions Luna Glob and Luna Resource. Here we present results of the analysis carried out for the sub-polar surface. It allows detect different hazards for the landing modules of spacecrafts.

Resources and products:

For mapping we used various DTMs and images with different resolutions. GLD-100 [5] was used for characterization surface in global scale DTM; LOLA DEM [6] was used for images orthorectification. For orthorectification of LRO NAC images [7] we used functions of the ISIS – USGS software for planetary image processing [1]. Using ISIS we rectificated a big count of the images automatically, and about 100 orthoimages were created from LRO NAC images for the Luna-Glob mission landing sites. The same work was done for the Luna-Recourse target ellipses (Fig. 1) and after that it was used for digitizing craters and boulders on the potential landing sites areas. For founding of boulder groups we also used data from LRO Mini-RF [8]. All craters were included in electronic catalogue that created as geodatabase and contains coordinates and other parameters of craters. Using data from this catalogue could be prepared map of spatial density of craters (Fig. 3) Based on height values from LOLA DTM were created derivative products such as map of slopes (Fig. 2) and map of roughness [2, 3].

All of data and mapping products are loaded in the GIS-project, which allows operatively get the spatial information about surface objects and characteristics for the whole sub-polar area, including the candidates landing sites on the various scales. The new high-resolution DEM from LRO NAC stereo-images is currently being created [9]. Using new DEM we will calculate depth of craters and other topography parameters of lunar surface. The new results of surface analysis and mapping will be presented at the conference.

Acknowledgments:

This work has been supported by a grant from the Ministry of Education and Science of the Russian Federation (Agreement № 11.G34.31.0021 dd. 30/11/2010)

References:

[1] Integrated Software for Imagers and Spectrometers *(http://isis.astrogeology.usgs.gov)*

[2] Karachevtseva I.P. (2012),The Journey of Lunokhod-1 – A Highlight in Early Lunar Exploration. // ESA/ESTEC Conference "Scientific Preparations for Lunar Exploration".

[3] Kokhanov et al. (2012), Cartography Support and Assessment of Candidate Landing Sites for the LUNA-GLOB Mission. //Abstracts of 43Lunar and Planetary Science Conference, № 1756

[4] Robinson, M.S., et al, 2010, Lunar Reconnaissance Orbiter Camera (LROC) Instrument Overview

[5] Scholten et al. (2011) GLD100 – the global lunar 100 meter raster DTM from LROC WAC stereo models, //Abstracts of 42Lunar and Planetary Science Conference, № 2046

[6] Smith et al. (2010), The Lunar Orbiter Laser Altimeter Investigation on the Lunar Reconnaissance Orbiter Mission Space Science Reviews, Volume 150, Issue 1-4, pp. 209-241

[7] Lunar Orbiter Data Explorer *(http://ode.rsl.wustl.edu/moon/indexProductSearch.aspx)*

[8] LOLA Gridded *(http://pds-geosciences.wustl.edu/lro/lro-l-lola-3-rdr-v1/lrolol_1xxx/data/lola_gdr/)*

LRO MRF Dataset *(http://ode.rsl.wustl.edu/moon/DataSetExplorer.aspx?target=mars&instrumenthost=LRO&instrumentid=MRFLRO)*

[9] Zubarev A. E. et. al. (2012), Features of creating DTM for Luna-Glob landing sites, these issues.

NEW NAMES OF LUNAR OBJECTS FOR SOVIET LUNAR MISSIONS

M. A. Baskakova, **I. P. Karachevtseva, K. B. Shingareva, E. N. Gusakova,**
Moscow state University of Geodesy and Cartography (MIIGAiK)MIIGAiK Extraterrestrial laboratory (MExLAb) Gorokhovskiy per., 4, 105064, Moscow, Russia;
Contact: m_baskakova@mexlab.ru, i_karachevtseva@mexlab.ru, tel: +7-499-2673513

Introduction:

New LRO data provide high resolution images that we used for detail research of the “Luna-17” landing site [1]. For this purposes we created geodatabase [3] which includes description of craters and traverse of the Lunokhod-1, measurement of the diameter and depth of craters, the definition of morphological types of craters [2]. We have used our results of GIS mapping and analysis of the Lunokhod-1 area [5] for choose and adapting new names of objects of the lunar surface [4].

Mapping results:

New names on the lunar surface are given to craters along the track of the Lunokhod-1 rover. We selected craters with diameter more than 100 meters, and small very important craters where soil samples were carried out. The selection of the craters along the path of Lunokhod-1 carried out in accordance with the topographical map drawn up in 1971-78 after the mission Lunokhod-1 published the book “Peredvijnaya laboratoriya na Lune Lunokhod-1, Vol. 2 [1]. Also we have used information from the book of the driver operation of the Lunokhod-1 Dougan “Domestic Odyssey Moon, Part 2” [6], where the path of Lunokhod-1 is well described. We have collected information on the coordinates, diameters, depth of the craters and options names of the craters.

As the titles of the craters were selected Russian names (Fig.1). The choice of names for craters was carried out in collaboration with V.G. Dovgan and A.T. Basilevsky – participants of the Lunokhod-1 and the Lunokhod-2 programs. June 14, 2012, new names were adopted by the International Astronomical Union and are included in the Gazetteer of Lunar Names [7].

Conclusions:

In 2011, celebrated 40 years as a program of Lunokhod-1 was completed. Due to this work, the new names of lunar objects by soviet lunar missions finally appeared on the Moon [8]. In future we are planning to research the area of the Lunokhod-2 in detail and give new names to craters along the route of the Lunokhod-2.

Acknowledgements:

The authors consider it duty to express their deep appreciation for the valuable information about the details of the Soviet lunar program Vyacheslav Georgievich Dovgan, the driver of the second crew Lunokhod, and Alexander Tikhonovich Bazilevsky, a member of the research group Lunokhod program, which actively participated in the preparation of proposals for naming objects in the landing area “Luna-17”.

This work has been supported by a grant from the Ministry of Education and Science of the Russian Federation (Agreement № 11.G34.31.0021 dd. 30/11/2010)

References

[1] Barsukov V.L. et. al. (1978) Peredvijnaya laboratoriya na Lune Lunokhod-1, Vol. 2. Nauka (in Russian).
[2] Basilevsky A.T. et. al. (2012) Identification and measurements of small impact craters in the Lunokhod 1 study area, Mare Imbrium. Abstract of 43-th LPSC Lunar Planetary Science Conference
[3] Gusakova E.N et al. (2012) Mapping and GIS-Analyses of the Lunokhod-1 Landing Site. Abstract of 43-th LPSC Lunar Planetary Science Conference
[4] Karachevtseva et al. (2012) New Nomenclature for the Russian Lunar Program including Lunokhods Landing Sites. Abstracts of IAU GA, China, Beijing, 20-31 August, 2012
[5] Karachevtseva I.P. et al. (2012) Atlas of the Lunokhod-1: GIS-mapping of the “Luna-17” landing site area using Lunar Reconnaissance Orbiter data // Actual Problems in Remote Sending of the Earth from Space 2012 (submitted November 2012)
[6] http://kik-sssr.narod.ru/Dovgan--Odisseia-2.htm
[7] http://planetarynames.wr.usgs.gov/Page/MOON/target
[8] http://lpod.wikispaces.com/June+16%2C+2012

GIS-CARTOGRAPHY OF THE LUNOKHOD-2 LANDING SITE

E. Gusakova[1], I. Karachevtseva[1], K. Shingareva[1], N. Kozlova[1], I. Nadezhdina[1], A. Zubarev[1] and J. Oberst[1, 2, 3],
[1]Moscow State University of Geodesy and Cartography (MIIGAiK), MIIGAiK Extraterrestrial Laboratory (MExLab), Gorokhovskiy per., 4, 105064, Moscow, Russia; [2] German Aerospace Center (DLR); [3]Technical University of Berlin, Germany. Contact: e_gusakova@mexlab.ru, i_karachevtseva@mexlab.ru, tel: +7-499-2673513

Introduction:

The Soviet spacecraft Luna 21 launched on the surface of the Moon in January 1973 and deployed the second lunar rover Lunokhod-2. The main goals of the missions were to study the transition zone from sea to mountain formations of continental structures that determined the choice of the landing point and the direction of the route study. These data are of interest in the study of the geological processes that transform the surface of the moon. Until June 1973, Lunokhod-2 acquired about 80,000 TV pictures and 86 stereo images along its traverse and wandered approximately 37 km. The history of the Soviet Lunokhods missions came back into focus recently, when the Lunar Reconnaissance Orbiter obtained high resolutions images (0.3-1 m/pixel). Using these data we mapped the landing site of Luna-21 and traverse of Lunokhod-2 based on GIS-tools.

Sources:

For our work we used Digital Elevation Models (LDEM1024, 30 m/pixel [8]; Kaguya DEM, 7.5 m/pixel [10]), orthorectified Lunar Reconnaissance Orbiter Camera (LROC) Wide Angle Camera (WAC) mosaics (100 m / pixel) and high resolution LROC Narrow Angle Camera (LRO NAC) images (0.3-1 m/pixel) [11].

Mapping and analyses of the Lunokhod-2 area:

The mapped area is about 171 sq. km, that's why for complete coverage of satellite images of the study area used a few image. In the first step of work we orthorectified a set of LRO NAC images (see list of images, Table 1) that covered the all landing site area. With ISIS [9] functions rectification was done using the LOLA DEM (LDEM1024) to MOON ME Coordinate System. Further analysis revealed that these orthoimages have shifted spatial reference. Therefore, after orthorectification, we have to manually adjust the referencing with the help of ArcGIS software, picking up the characteristic points (the centers of big craters or small craters). As a basis for the referencing we used LROC WAC orthomosaic [6, 7].

year	name	incidence, degree	resolution, m/pixel
2009	M101971016R/L	83.2/83.0	1.50/1.49
2009	M106669064R/L	37.8/37.5	1.59/1.61
2009	M109039075R/L	27.4/27.4	0.52/0.53
2010	M122007650R/L	36.6/36.5	0.50/0.50
2010	M146783727R/L	75.5/75.5	0.65/0.65
2011	M165645602R/L	70.2/70.1	0.47/0.47
2011	M168000478R/L	47.6/47.6	0.41/0.42

table 1 – List of LRO NAC into the territory of Luna-21 landing site (Lunokhod-2 area)

Following methods developed earlier on the Lunokhod-1 landing site [2, 5] Lunokhod-2 wheel tracks were mapped in the orthoimages. The full traverse was determined to be about 42 km long, in agreement with previous post-mission published data. Using Kaguya DEM we calculate various morphometric parameters of the Lunokhod-2 area, including topographic roughness and slopes (Fig. 1). Also, we digitized craters with diameters of more than 10 m in the Lunokhod-2 traverse area (Fig. 2) using CraterTools for ArcGIS [3] and created a geodatabase, which consists at this moment of about 17.000 craters including their diameters and depths obtained from the Kaguya DEM (for craters with diameters of more than 50 meters). The crater data allow us to calculate different statistical parameter of surface: crater spatial (Fig. 3) and cumulative densities. The calculation results are preliminary, because our study has only just begun. New results will be present at the conference.

New Terrain model:

We expect to derive a high resolution DEM from LRO NAC stereo image pair finding at the Lunokhod-2 area. Stereo image processing will be done based on Photomod software using methods as describe at [4]. It will allow us to carry out more detailed geomorphological analyses of craters [1], including measurements of relative depth (ratio D/H). However, quality of imaging geometry and illumination for stereo processing remains to be seen.

Conclusions:

The LRO NAC provide an important information for research in morphologies of small craters, which could be compare with results of geologic mapping that had been carried out during the Lunokhod-2 mission. We show that data from both Lunokhod`s missions and new LRO information [2] can be used for mapping with high level of details and surface studies of landing sites for future lunar missions, for example LUNA-GLOB and LUNA-RESOURCE.

Acknowledgements:
This work has been supported by a grant from the Ministry of Education and Science of the Russian Federation (Agreement № 11.G34.31.0021 dd. 30/11/2010).

References:

[1] Basilevsky A. et al. (2012) Identification and measurements of small impact craters in the Lunokhod 1 study area, Mare Imbrium. Abstract of 43-th LPSC Lunar Planetary Science Conference
[2] Gusakova E. et al. (2012) Mapping and GIS-Analyses of the Lunokhod-1 Landing Site. Abstract of 43-th LPSC Lunar Planetary Science Conference
[3] Kneissl T. et al. (2011) Planet. Space Sci., 59, 1243-1254
[4] Zubarev A. E. et. al. (2012), Features of creating DTM for Luna-Glob landing sites, this issiues.
[5] Karachevtseva I. et. al., (2012), Cartography of the Lunokhod-1 Landing Site and Traverse from LRO Image and Stereo Topographic Data, PSS (submitted 29 June 2012).
[6] Robinson M. S et al., (2010) Lunar Reconnaissance Orbiter Camera (LROC) Instrument Overview. Space Science Reviews, Volume 150, Issue 1-4, pp. 81-124
[7] Scholten et al., (2011) GLD100 – the global lunar 100 meter raster DTM from LROC WAC stereo models. Abstract of 42-th LPSC Lunar Planetary Science Conference
[8] http://imbrium.mit.edu/DATA/LOLA_GDR/CYLINDRICAL/JP2/
[9] http://isis.astrogeology.usgs.gov/
[10] http://l2db.selene.darts.isas.jaxa.jp/cgi-bin/search.cgi
[11] http://www.lroc.asu.edu/

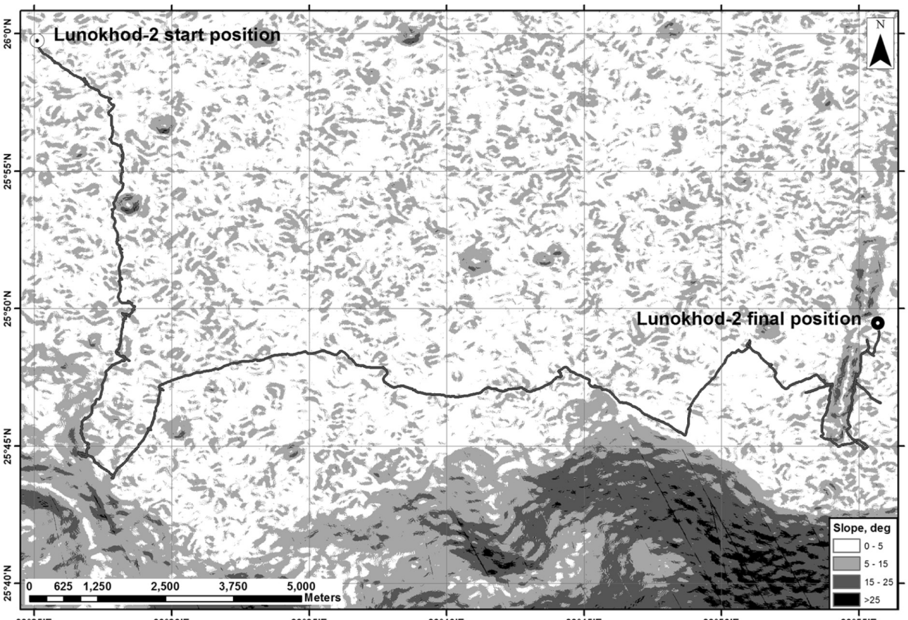

fig. 1. Map of slopes in the Lunokhod-2 area (base line - 7.5 m, Kaguya DEM)

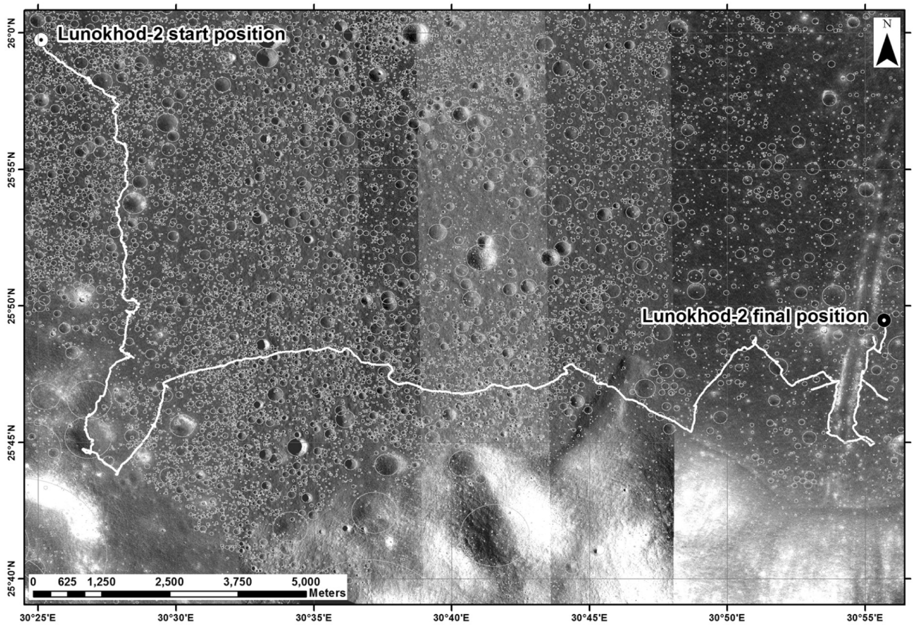

fig. 2. Result of the work: new orthomosaic derived from LRO NAC for the Lunokhod-2 area

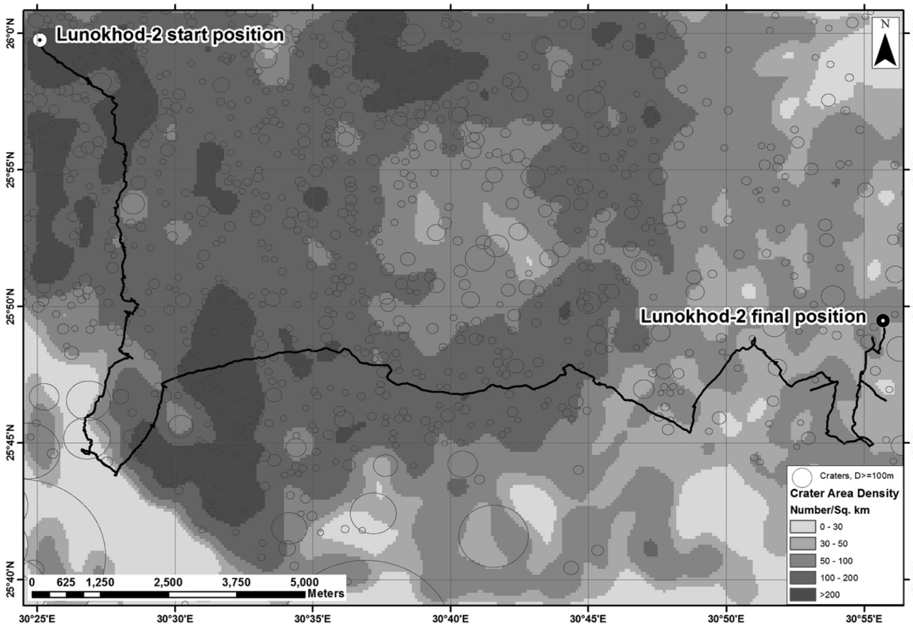

fig. 3. Map of spatial density of craters of Lunokhod-2 area (D> 10 m, search radius 500 m)

RADIO-BEACONS ON THE MOON AND LUNAR PHYSICAL LIBRATION FOR SELENE–2, CHANG'E–3/4, LUNA–GLOB AND LUNA–RESOURCE PROJECTS

A. Gusev[1], H. Hanada[2], J. Ping[3], F. Kikuchi[2], A. Kosov[3], J. Li[4] , K. Matsumoto[2], S. Sasaki[2], V. Tretyakov[5]
[1]Kazan Federal University, Kazan, Russia, [2]National Astronomical Observatory of Japan, [3]National Astronomical Observatories of CAS, China, [4]Shanghai Astronomical Observatory CAS, China, [5]Space Research Institute, Moscow, Russia. Contact: Alexander.Gusev@mail.ru

Introduction: The Lunar rotation is ***sensitive*** to its interior structure. Numerical models of the Lunar physical libration (LPhL), satisfying the modern Lunar laser data (LLR), necessarily ***include complex internal startigraphy*** of the Lunar body. To do this in the framework of an analytical theory is much more difficult. But the ***lot of periods of free libration*** and of their interaction with forced terms may be obtained using the analytical approach [6]. Precision data of a laser location of the Moon give a good basis for determination of ***amplitudes and phases*** of the free libration. Yet the opportunity to study the rotation of a celestial body ***from planetary surface*** in the framework of the planned experiment ILOM [1,5] opens even greater prospects in this direction.

Many space agencies plan a lunar missions, including observations in the near lunar space and/or on the surface of the Moon [1-5]. One of these experiments [2, 4] propose to place two landers with radio beacons on the Lunar near side and to launch one or more Orbiters on the Lunar orbit. The difference of the distances between two radio beacons and Earth will be assumed to be measured by the methods of Inverse VLBI: radio-signal from the various radio beacons will be sent to Earth antenna systems using the Orbiter. The estimation of the physical libration angle accuracy is made for various location and configuration of the radio beacons, which are in polar or equatorial zones of the Moon.

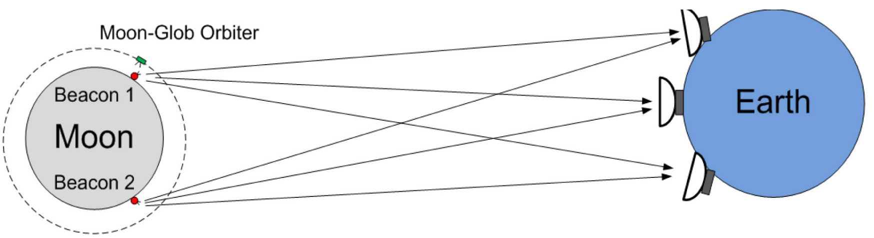

fig.1. Radioscience Experiments with "Moon-Glob" Orbiter Receiver and Beacons on Moon's landers.

Inverse VLBI experiment for the Moon. The Inverse VLBI experiment for the Moon was described at Proceeding of Kazan conference (October, 3-4, 2008, Kazan, Russia) by Dr. Kikuchi et al.. Scheme of the Inverse VLBI is presented on the Fig. 2

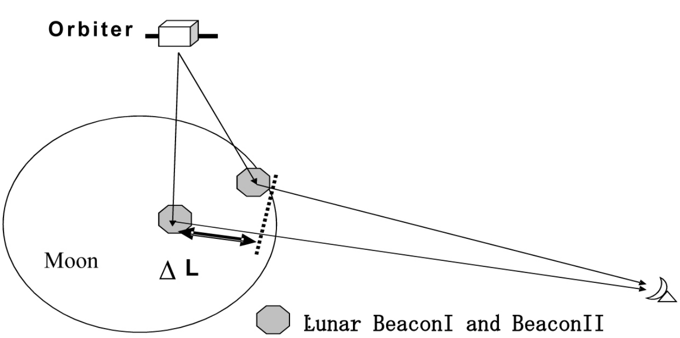

fig. 2. Proposed location of the radio-beacons on the Lunar surface.

The difference of the distances Radio Beacon I - Earth and Radio Beacon II - Earth will be assumed to be measured by the methods of Inverse VLBI: radio-signal from the Radio Beacon I and Radio Beacon II will be sent to Earth antenna using the Orbiter. Difference of the distances ΔL from two Radio Beacons to the ground antenna will be accurately measured. Desired accuracy of ΔL is about 1 to 3 mm depending on frequency of radio signal. On the basis of the given configuration and accuracy it is nec-essary to estimate accuracy of the Lunar physical librations amplitudes on longitude and latitude in the experiment.

Preliminary model of the radio beacon experiment. 1. We consider the system coordinate (Fig.3), whose axis X is directed along the maximal axis of inertia which coincides with the mean direction to the Earth - EM, the axis Z is directed along the mean rotation axis, the Y creates the right system of coordinate - this is the Cassini system. Real rotation of the Moon is deviated from the uniform Cassini rotation. This deviation may be described by two angles: ρ and τ, which represent libration angles, that is deviation from Cassini law. Numerical values of these angles may be estimated, for example, by the theory [6].

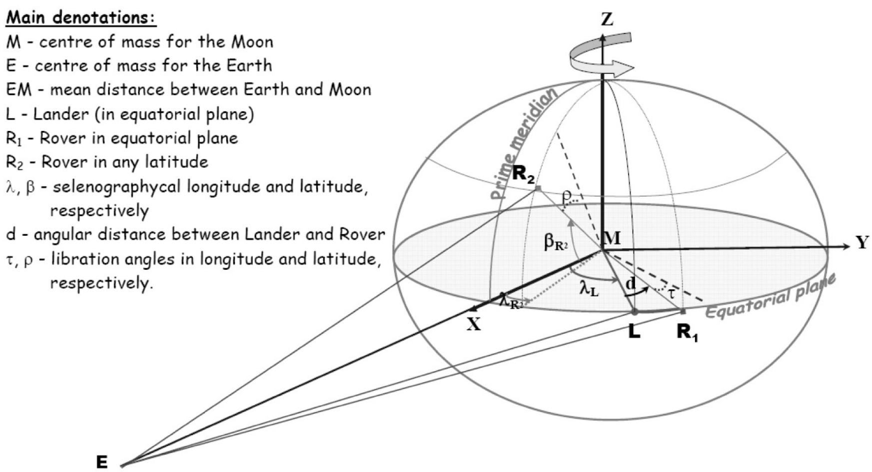

fig. 3. The angles of the physical libration in latitude and longitude.

2. At this stage of approximation we did not consider the diurnal parallax and rotation of the Earth: the receiving antenna is assumed to be rigidly connected with the line EM.

3. We neglect the Lunar ellipticity and set that ML = MR = R = R_{Moon} = 1738 km.

4. Geometrically, the pictures for the longitude's and latitude's libration will be similar, because of this we considered only the libration in longitude. All estimation of longitude's libration should be multiplied by cos(β), where β is the selenography latitude of a beacon. Fig 3 represents the projection onto equatorial plane, where all angles are denoted.

5. We assume that angle τ is also small, because maximal amplitude of the angle is 125 seconds of arc, which is approximately equal to 6 · 10^{-4}. The ratio $\overline{\rho}=\frac{R}{a}\approx 5\cdot 10^{-3}$ is small too.

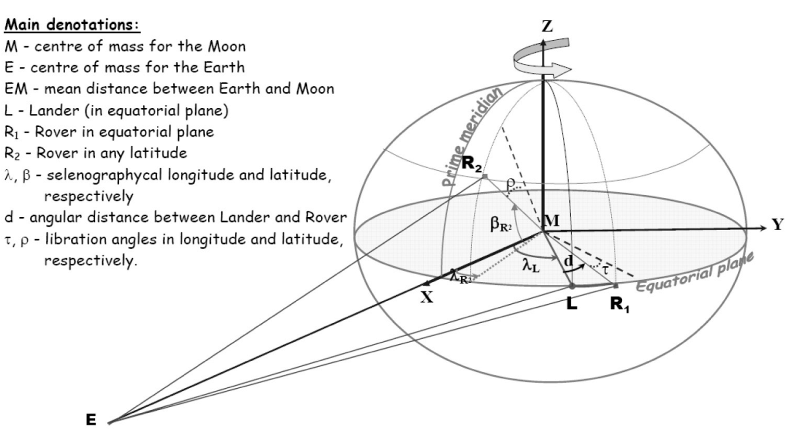

fig.4 Configuration of the Beacon I and Beacon II location in the lunar equatorial plane

Fig. 4 shows four triangles: ΔMLE, ΔMRE, ΔML′E, ΔMR′E. The system of Radio Beacon I and Radio Beacon II (L′, R′) is displaced due to physical libration on the angle τ relatively to an initial position L and R. Difference of distance was obtained the following considerations: $\Delta L' = y' - x'$.

We have: $y'^2 - x'^2 = (y'-x')(y'+x') = \Delta L' \cdot$ ùùxù $+ a \cdot \rho \cdot \quad d \cdot \quad \lambda$,

then we obtained

$$\Delta L' = \Delta L = \frac{y'^2 - x'^2}{(2x' + a\cdot\rho\cdot\sin d\cdot\sin\lambda)} = \sin d\cdot R\left[\sin\lambda + \tfrac{1}{2}\rho\sin 2\lambda + \rho^2\left(\tfrac{1}{2}\sin^2\lambda - \cos^2\lambda\right) + \right.$$

$$\left. + \tfrac{1}{2}\sin d\cos\lambda + \sin d\cdot\rho\left(\tfrac{1}{2}\cos^2\lambda - \sin^2\lambda\right) + \tau\left(\cos\lambda + \rho\cos 2\lambda\right)\right] .$$

As a result, expression ΔL can be written in the form:

$$\Delta L = \sin d\cdot R\left[A(\lambda) + B(\lambda,d) + \tau\left(\cos\lambda + \rho\cos 2\lambda\right)\right]$$

where: $A(\lambda) = \sin\lambda + \tfrac{1}{2}\rho\sin 2\lambda + \rho^2\left(\tfrac{1}{2}\sin^2\lambda - \cos^2\lambda\right)$,

$B(\lambda,d) = \tfrac{1}{2}\sin d\cos\lambda + \sin d\cdot\rho\left(\tfrac{1}{2}\cos^2\lambda - \sin^2\lambda\right)$.

Dependence τ on ΔL has the following expression: $\tau = \dfrac{\left[\dfrac{\Delta L}{\sin d\cdot R} - A(\lambda) - B(\lambda,d)\right]}{\cos\lambda + \rho\cos 2\lambda}$.

Inaccuracy $\delta\tau$ may be determined by the variation method. We assumed, that a longitude λ will be exactly known, that is $\delta\lambda = 0$. This assumption is very rough, but to deduce the dependence of $\delta\tau$ on $\delta\lambda$ analytically is too cumbersome task. As a result we have obtained:

$$\delta\tau(\delta\Delta L, \delta d, \lambda) = \frac{1}{\cos\lambda + \rho\cos 2\lambda}\left[\frac{\delta\Delta L}{\sin d\cdot R} - \frac{\Delta L}{(\sin d)^2\cdot R}\cos d\,\delta d - \tfrac{1}{2}\cos\lambda\left(1 - \rho\cos\lambda\right)\cos d\,\delta d\right].$$

The analysis of this key formula allows estimating inaccuracy in τ in dependence on errors $\delta\Delta L$ and Δd, arising in a course of measuring of ΔL and of d. It's obviously, that $\delta\tau$ decreases in a case when line base d is increased.

Results: 1) The planned accuracy of difference distance determination for radio beacons at 60- 100 mm and the length of base line of 1700-3400 km in the Inverse VLBI experiment will be sufficient to improve accuracy of lunar physical libration, better than 10-30 msec.

2) Analogous estimation of latitude libration has shown the same results: location of the Radio Beacon I and Radio Beacon II in the vicinity of the Lunar limb equator and the prime meridian will give the best estimations for the physical libration angeles.

Conclusion: The best accuracy of longitudinal and latitudinal librations (10 - 30 msec of arc) will be achieved in the equatorial limb and polar zones of the Moon.

The research was partially supported by the Russian-Japanese grant RFBR-JSPS 11-02-92113-ЯФ_a and the Russian-Chinese grant RFBR-GFEN 11-02-91160 ГФЕН_a

References

Hanada et al., 2009, Different kinds of observation of Lunar Rotation and Gravity for SELENE-2. Proc. of Int. Congress “ASTROKAZAN-2009”, Kazan, p. 172 -175

Kikuchi F., T. Iwata, N. Kawano, S. Sasaki, and Q. Liu (2009) Applications of VLBI technique for lunar and Mars exploration. Abstracts of the General Assembly EGU2009, Vienna, Austria, 19-24 April, 2009. EGU2009-4930

Gusev A., Petrova N., (2009) Estimation of the Lunar physical libration accuracy in the Japanese Lunar Space project based on Inverse VLBI. Abstracts of the General Assembly EGU2009, Vienna, Austria, 19-24 April, 2009. EGU2009-1161

Kosov A. et al., (2011) Radioscience Experiments with “Moon-Glob” Orbiter Receiver and Beacons on Moon’s landers. Abstract of the Second Moscow Solar System Symposium (2M - S[3]), Moscow, IKI, 10-15 Oct., 2011

Ping J., Hanada H., Gusev A., et al., (2012) May small digital PZT and radiobeacons improve the LPhL for future lunar missions? Abstract of the 25th GA IAU, Beijing, China, 20-31 August, #3.7

Rambaux N., Williams J.G., (2011) The Moon’s physical librations and determinaton of their free modes. CMDA, v.109, p. 85-100

HIGH-RESOLUTION TERRAIN MODELS FROM LRO STEREO IMAGES FOR LUNA-GLOB LANDING SITE SELECTION

A. Zubarev[1], I. Nadezhdina[1], N. Kozlova[1], I. Karachevtseva[1], J. Oberst[1,2], M. Robinson[3]

[1]Moscow State University of Geodesy and Cartography, Russia, [2]German Aerospace Centre (DLR), Germany.[3]Arizona State University, Tempe, AZ, USA; Contact: lorencs@mail.ru

Introduction:

Lunar exploration is central to the Russian space program. Luna-Glob and Luna-Resource are scheduled for launch in 2015, with the two spacecraft to explore the North and South polar regions, respectively. Luna-Glob will carry drilling equipment for retrieving samples from the subsurface for onboard chemical analysis. To assure a successful mission, it is necessary to have accurate descriptions for the landing site candidates to warrant that the landing sites are safe and scientifically interesting. In support of the Luna-Glob mission, we have created high-resolution Digital Terrain Models (DTMs) for lunar subpolar regions using LROC NAC stereo images.

LRO Images:

The NASA spacecraft Lunar Reconnaissance Orbiter (LRO) was launched on the 19 of June in 2009. While the spacecraft initially operated from a circular orbit (altitude about 50 km) LRO is currently moving in a slightly elliptical near-polar orbit, from where surface ranges for our areas of interest are typically larger (up to 200 km). The orbiter carries the Lunar Reconnaissance Orbiter Camera (LROC) consisting of three cameras: the low-resolution Wide Angle Camera (WAC) and two high-resolution Narrow Angle Cameras (NAC). The NAC cameras obtain images of the lunar surface with resolution up to 0.5 m/pxl from the nominal orbit of 50 km.

Several candidate landing sites for Luna Glob are currently being discussed by the mission engineering and science teams (landing ellipses given in Figure 1). While there was no stereo coverage by LRO for the candidate landing sites until the end of 2011, the sites were specifically targeted by the spacecraft early in 2012. During this study 212 “new” images of the subpolar area were downloaded and analyzed (Figure 2). Images ephemerides, and relevant housekeeping information are available from NASA data libraries http://pds-imaging.jpl.nasa.gov/search/search.html#QuickSearch and http://naif.jpl.nasa.gov/naif/. Also, a convenient browser for searching and downloading images is available from the LROC Science Operations Center, http://wms.lroc.asu.edu/lroc/search.

Results:

The DTMs are produced from stereo images using photogrammetric techniques by means of the PHOTOMOD software. While the majority of the images have resolution of 1.8 m/pxl DTMs with resolution of 25 m/pxl for two landing sites were created to date (Figure 3). However, we expect that improvements in resolution (~5 m/pxl) are possible. DTM production of the third site is pending (hatching rectangle, Figure 2). Updated DTM-products will be presented at the conference.

We have developed program LightsComputations for illumination calculating of target body’s surface (Moon) during the determined periods subject to skyline based on DTM. Illumination computation for Luna-Glob landing sites using the created DTM will be presented.

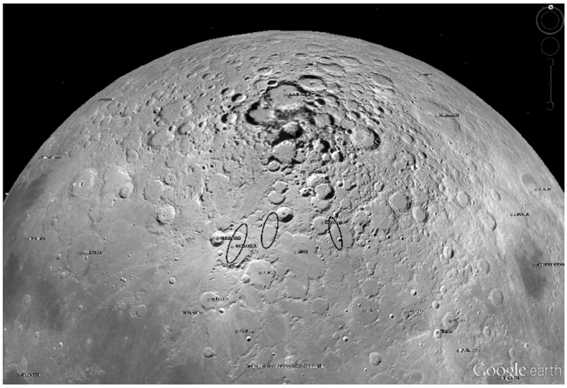

fig.1. Candidate landing ellipses for the Luna-Glob mission (lat: 75.6 long: 8.4; lat: 73.8 long: 357.2; lat: 74.1 long: 34.3).

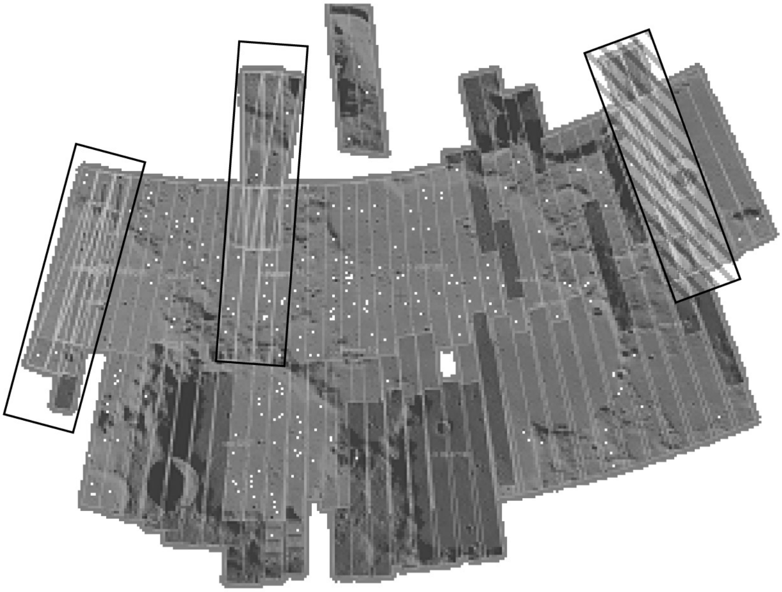

fig. 2. New images (2012) of the Luna-Glob candidate landing sites. Two candidate landing sites for which DTMs were created are marked with rectangles. The hatched rectangle marks the third candidate landing site for which a DTM has yet to be obtained.

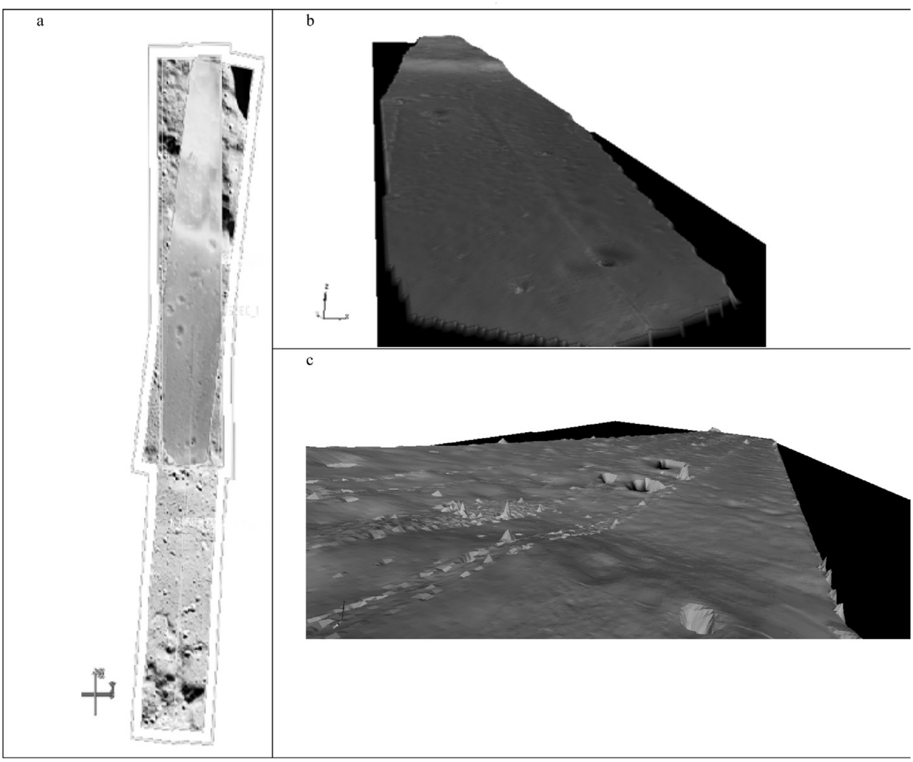

Fig. 3. DEM on the first and the second candidate landing sites of Luna Glob with resolution 25 m/pxl. **a**) DEM referenced to Mercator projection of the first landing site, coordinates lat: 75.6 long: 8.4; **b**) The same DEM, shown as oblique view; **c**) DEM referenced to Mercator projection on the second landing site, coordinates lat: 73.8 long: 357.2, oblique view.

NONLINEARITY OF EARTH`S AND LUNAR OSCILLATIONS.

O.B. Khavroshkin, Alexeii Khrustalev, Vladislav V. Tsyplakov

About free oscillation. Q of the free oscillations of the Earth (FOE), the possibility of energy coupling between the modes, the cases of anomalous splitting of spectrum lines of FOE and the selection combination mods period led to search for features of the oscillations recorded modulation method especially in the case of FOE monitoring mode was observed as a single-mode [1-4]. The latter allowed to research of FOE amplitude $A_{E.O.}$ and the period $T_{E.O.}$ of each cycle of of of FOE oscillation of the Earth: the amplitude of the vibrations directly through the increase in tensile strain determines seismic emission level rise along the length of the entire site, and the period determinate as the distance between the fronts of adjacent areas. Then the excess of $A_{E.S.} \sim A_{FOE}$ of the entire site section of microseismic noise $A_{m.n.}$ in the vicinity of the site, taken from the records in mm, taken as the $A_{E.O.}$, and the distance between the fronts of parts as the period of this oscillation $T_{E.O.}$ measured in sec. Respectively,there were constructed graphs of the functions $T_{E.O.}=T_{E.O.}(\tau)$, $A_{E.O.}= A_{E.O}(\tau)$, where τ - the current time. Unit of τ is the period of FOE during which the parameters of the system (process) is almost unchanged (Fig. 1).

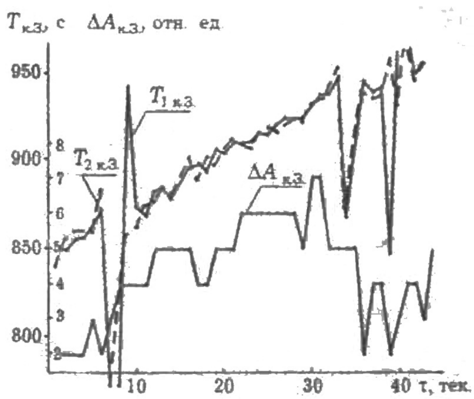

fig.1. The drift of the period of natural oscillations of the Earth $T_{E.O.}$ and synchronous changes in the oscillation amplitudes $A_{E.O.}$. $A_{E.O.} = \Delta A_{E.O}(\tau)$. $T_{E.O.}=T_{E.O.}(\tau)$, in 17-18.VII.1975y.

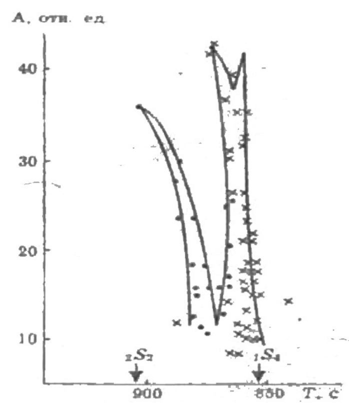

Fig. 2. The manifestation of the “soft” restoring force for the region of the spectrum of oscillations of the Earth: the amplitude-frequency characteristic of the $A_{E.O.}$. $A_{E.O.} = A_{E.O}(\tau)$ for 24 - 25.VII.1976y.

Given the rising trend in the period of time, we can consider the function $A_{E.O.} = A_{E.O.}$ as the amplitude-frequency characteristic (AFC) process, agrees well in shape with a frequency response graph for the case of passage through resonance of a nonlinear oscillatory system with a soft restoring force (Fig. 2).

Moon as a nonlinear oscillator (Fig.3-5).

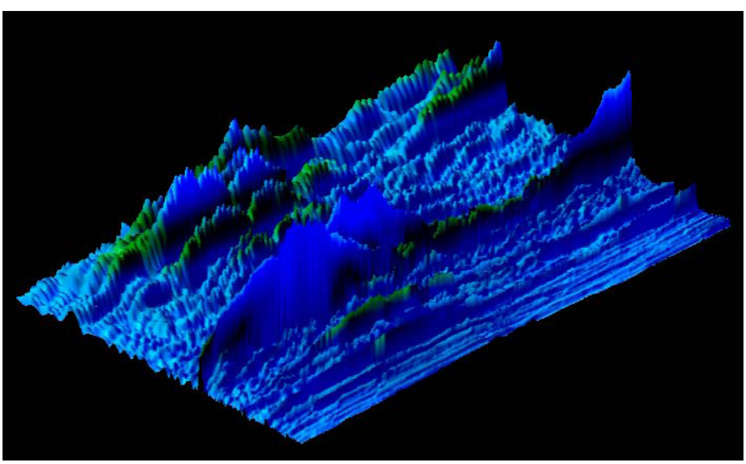

fig.3. Amplitude spectrum frigiency temporal diagram for the observation time in tidal periods.

The Bogolyubov effect in the study of the natural oscillations of the Moon

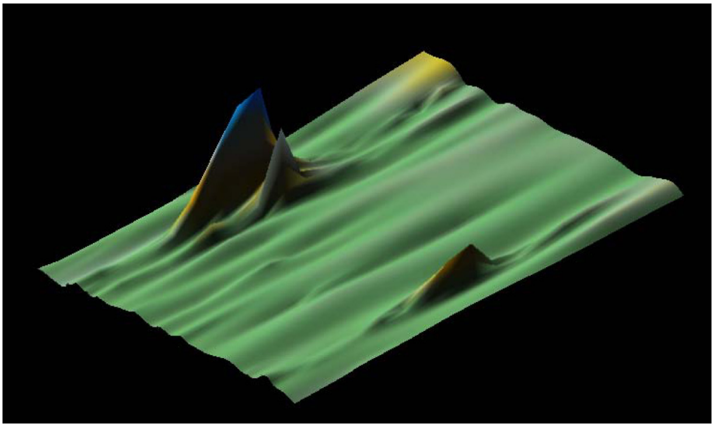

fig.4. Peculiarity of maximum amplitude of the resonance for a minute periods in the range of tidal interactions.

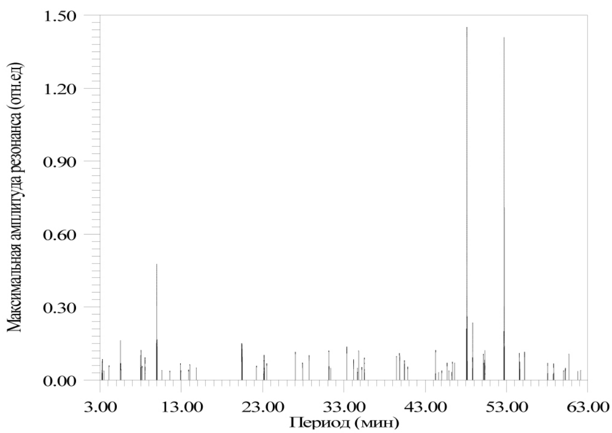

fig.5. The splitting of spectral lines to accordance the Bogolyubov theory in the minute range of periods.

References

1.Karryev B.S., Nikolaev A.V., Khavroshkin O.B., V.V. Tsyplakov. Features of long-wave processes in the seismically active geologic structures. IPhE AN SSSR, VINITI. Dep. M., 1984. № 4991-84. 22p.
2. Rykunov L.N., Khavroshkin OB, V.V. Tsyplakov. Analysis of the spectrum of high-frequency seismic noise envelope after the Alaska and Mexico earthquakes in March 1979 // Dokl. USSR Academy of Sciences, 1980. V.252, № 4. pp.836-838.
3. Nikolaev A.V., Rykunov L.N., Starovoit O.E., O.B. Khavroshkin, Tsyplakov V. V. The nonlinearity of the free oscillations of the Earth // Seismicity and seismic construction in the Far East. DVNTs USSR, MSSSS, Vladivostok. 1982. pp.160-162.
4. Khavroshkin O.B. Some problems of nonlinear seismology. M. UIPE Academy of Sciences, Russia. 1999. 301 p.

APPLYING THE 1-WAY AND/OR 3-WAY RADIO PHASE COUNTING FOR PRECISE LUNAR RANGING

J. Ping[1,2,3], M. Wang[1], N. Jian[2], G. Tang[3], Q. Meng[4], J. Gusev[5], H. Hanada[6], J. Liu[3], J. Li[2] , Y. Lu[1], [1]*National Astronomical Observatories of CAS,Beijing, China;* [2]*Shanghai Astronomical Observatory of CAS, Shanghai, China;* [3] *National Defense Key Laboratory of Science and Technology of BACC, Beijing, China;*[4]*Northeast University, Nanjing, China;* [5]*Kazan Federal University, Kazan, Russia;* [6]*National Astronomical Observatory of Japan, Iwate, Japan; Contact: jsping@bao.ac.cn*

Introduction: Signals of radio beacons and/or of the radio carriers created from the stable frequency standards (like ultra stable oscillator, USO or hydrogen maser) can play an important role when measuring the distance between an Earth tracking site and a Lunar surface lander or a Lunar orbiter, with a relative length resolution of several tenths of millimeter of high sampling rate (1 point per second or higher). The beacons and/or the carriers can either work as 1-way mode or as 3-way mode. The ranging observable can benefit the S/C precise orbit determination process for cruise in the interplanetary space, and for a big elliptical orbit surrounding a target body (moon or mars). If the beacons or carrier transponders are installed on the lunar surface landing missions, like the Luna-Glob, Luna-Resources, Chang'E-3/4 and SELENE-2 missions, ranging observables can be used to improve the lunar rotation (lunar physical libration, LPhL) model. By means of free of weather and lunar phase, the radio method may success the lunar laser ranging (LLR) method.

Development of RSR: Open-loop phase observables have been obtained in global positioning system (GPS/GNSS) radio data at L band. Both of the open loop and of the close loop data have been obtained in planetary radio science experiments at S and X bands. We merged this idea into the development of radio science receiver, RSR, in the 1st China Martian mission Yinghuo-1 project. The new-developed 4-channel digital recording system can retrieve Doppler and phase of 4 carriers in a band-width of 100MHz, which means totally 4 landers and/or orbiters in the same beam of antenna can be tracked simultaneously. If the RSR is set at ground tracking station with uplink carrier transmitted, it can work as close loop model to remove the frequency instability of on-board oscillator, and remove the frequency difference between transmitter and receiver. The RSR can also work as raw data recording only mode, where 4-channel of each with the maximum bandwidth up to 16MHz can be recorded for post-data procession, as well as for VLBI processing mode. Using the post-data procession mode, more than 4 beacons or carriers can be observed.

Test of RSR: The test observations of RSR were carried out at Shanghai and Urumqi stations during the VLBI observation sessions of Chang'E-2, MEX and VEX orbiters. At X-band, the Doppler resolution of 1 pps is better than 5 mHz, 0.2mm/s for 1-way and 3-way tracking, or 0.1mm/s for 2-way close loop tracking. The corresponding relative ranging resolution is 0.1mm. The new developed RSR can be used in both of S/C precise tracking and in lunar/planetary geodetic and geo-physical observations. Currently, 4 RSR have been developed in YH-1 mission. Although the mission failed, the RSR have been installed at Shanghai, Kunming and Urumqi. We planned to use them in up-coming Chang'E-3/4 mission and other near future lunar landing missions.

Comparing to the LLR: radio phase method has some advantages: the observation is free from earth weather; also free from the lunar phase; the observation can be easily obtained by dozen(s) ground stations like VLBI stations, which may remove the biases in LLR due of only a couple sites working; if small antenna applied (6~12meter in diameter), multi-landers can be observed; additionally, the continuous observations will benefit the study of the LPhL and tides of periods of semi-month, month, semi-annual and annual. Gusev gives a brief description of LPhL theory by radio method. We are considering of install an RSR at a planning VLBI station at Kazan University for future observatory under a collaboration frame between CAS and Kazan University.

Acknowledgments:
The research was supported by the NSFC No. 10973031 of joint research of Russian-Chinese grant from Russian side RFBI-GFEN 11-02-91160 ГФЕН_а and from Chinese side

References: Hanada H,. et al., Technical Development of A Small Digital Telescope for In-situ Lunar Orientation Measurements ILOM, in this sysmposium.
Gusev A., et al., Radio-beacons on the moon and LPhL for SELENE-2, Chang'E-3.4, Luna-Glob & Luna-Resource Projects, in this symposium.
Kosov A. et al., (2011) Radioscience Experiments with "Moon-Glob" Orbiter Receiver and Beacons on Moon's landers. Abstract of 2M - S^3, Moscow, IKI, 10-15 Oct., 2011
Ping J. et al., (2010) Brief Introduction of Yhinghuo-1 Mars Orbiter and Open-Loop Tracking Techniuqes, in Gravitation And Astrophysics: pp. 225-232, in Proceedings of the Ninth Asia-Pacific International Conference, Wuhan, China, 29 June – 2 July 2009.

THE LUNAR EXOSPHERE DURING PERSEID 2009 METEOR SHOWER.

A. A. Berezhnoy[1], O. R. Baransky[2], K. I. Churyumov[2], T. K. Churyumova[2], V. V. Kleshchenok[2], E. A. Kozlova[1], V. Mangano[3], A. M. Mozgova[2], V. O. Ponomarenko[2], Yu. V. Pakhomov[4], V. V. Shevchenko[1], Yu. I. Velikodsky[5]
[1]Sternberg Astronomical Institute, Moscow State University, Universitetskij pr., 13, Moscow, 19991 Russia; [2]Astronomical Observatory, Shevchenko National University, Observatorna Street 3, Kiev, 04053 Ukraine; [3]INAF-IAPS, Institute of Astrophysics and Planetology from Space, via del Fosso del Cavaliere 100, 00133 Rome, Italy; [4] Institute of Astronomy, Russian Academy of Sciences, Pyatnitskaya Street 48, Moscow, 119017 Russia; [5] Institute of Astronomy, Kharkiv National University, 35 Sumskaya Street, Kharkiv, Ukraine. Contact: ber@sai.msu.ru

Introduction:

Quick increase of brightness of Na D1 and D2 lines during maximum of Perseid 2009 meteor shower is detected and explained by impacts of Perseid meteoroids on August 13, 2009, 0-1 UT. Mass of impacted Perseid meteoroids is estimated about 15 kg. Non-detection of Ca, Al, and Si impact-produced lines is explained by formation of metal oxides and condensation of dust particles.

Observations and Data Analysis:

The spectroscopic observations of NaI D1 (5896 Å) and D2 (5890 Å) resonance lines in the lunar exosphere were performed on August 12-13, 2009 and August 13-14, 2009 during maximum of Perseid meteor shower with echelle spectrograph MMCS (Multi Mode Cassegrain Spectrometer) at the 2-m Zeiss telescope (Terskol branch of Institute of Astronomy of Russian Academy of Sciences, Kabardino-Balkaria, Russia). The slit of the spectrograph has height of 10˝ and width of 2˝. We used the CCD with size of 1245x1152, where 31 spectral orders in the range from 3720 to 7526 Å were registered. The spectrograph resolution was R = 13 500; the signal to noise ratio in the spectra was about 50 at the position of NaI D1 line. Six echelle spectra were obtained at the distances of 50˝, 150˝, and 250˝ (90, 270, and 455 km, respectively) from the lunar limb above the north pole which was bombarded by Perseid's meteoroids. The exposure time of each spectrum was equal to 1 800 s. The echelle package of the MIDAS software system was used for the spectroscopic data reduction: removing the cosmic ray traces, definition and extraction of echelle orders, the wavelength calibration using the spectrum of a Fe-Ar lamp, the flux calibration using standard star HD214923. As the result of reduction we have the spectrum in absolute fluxes. This spectrum is a superposition of spectrum of lunar exosphere and solar spectrum reflected from the Moon surface and scattered in the Earth atmosphere. For extraction the spectra of lunar exosphere we use the solar spectrum taken as spectrum of daytime scattered light. Spectral transparency of Earth's atmosphere at 600 nm was taken as 88 % at 45 degrees in accordance with [3]. Accuracy of measurements of Na line areas is about 2.5 %.

Results of observations:

Brightness of Na lines at 270 and 455 km from the limb is 109 % and 93 % in comparison with that at 90 km on August 12/13, 2009. Brightness of Na lines at 270 and 455 km from the limb is 89 % and 58 % in comparison with that at 90 km on August 13/14, 2009. Height scale and temperature of Na atoms are estimated as 700±100 km and 3000±500 K on August 13/14, 2009 (see Figure 1).

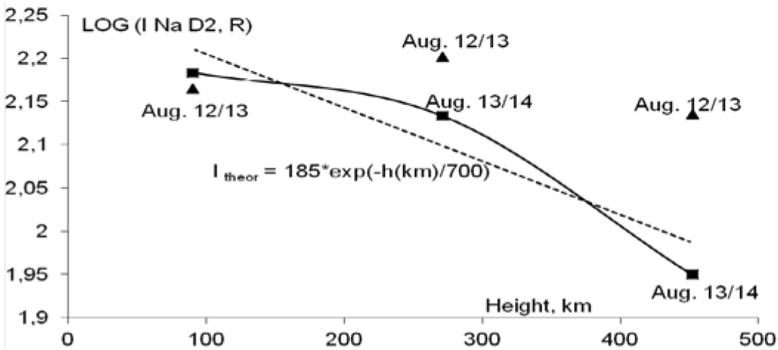

fig. 1. Brightness of Na D2 line versus height above the lunar surface on August 12/13 and 13/14, 2009.

Temperature of Na atoms on August 12/13 cannot be estimated because the column density of Na atoms changes significantly during observations due to meteoroid's impacts. Intensity of the solar wind on August 12/13 and 13/14 was comparable [4], and solar flares cannot explain significant difference between two sets of observations. Obtained results can be explained as evidence of quick increase of brightness of Na lines during maximum of Perseid meteor shower which is responsible for additional column density of impact-produced Na atoms of about 5×10^8 cm^{-2} on August 13, 2009 at 0-1 UT.

Taking properties of Perseid's impacts from [5] our results can be explained by single impact of Perseid meteoroid with mass of about 15 kg or additional mass flux of small meteoroids of about 10^{-16} g cm^{-2} s^{-1}. Upper limits of intensity of lines of other elements Fe (3859 Å), Si (3906 Å), Al (3962 Å), Mn (4033 Å), Ca (4227 Å), Ti (5036 Å), Ba (5536 Å), and Li (6708 Å) are estimated as 14, 16, 12, 18, 11, 13, 14, 17 R, respectively, at 3 σ level.

Condensation and formation of molecules during Perseid's impacts:

Elemental composition of impact-produced cloud is calculated as a mixture of CI chondrite and ferroan anorthosite with mass ratio of 1:50 [5]. At assumed temperature of impact-produced atoms of 3000 K, assuming that loss times from the exosphere $\tau_{loss}(X)$ are equal to ionization time of studied atoms $\tau_{ion}(X)$ which are much longer than the duration of observations $\tau_{obs}(X)$, about 10^3 s, and taking g-factors from [6] theoretical intensities of lines of impact-produced atoms are calculated without taking into account effects of condensation and formation of molecules as 0.8, 380, 70, 0.0015, 1500, 1.5, 0.15, and 5 R for Fe, Si, Al, Mn, Ca, Ti, Ba, and Li lines, respectively. Thus, intensities of Si, Al, and Ca lines are at least in 24, 6, and 140 times less than expected based on stoichiometric model. For the case of $\tau_{loss}(X) = \tau_{bal}(X)$ and $\tau_{loss}(Na) = \tau_{ion}(Na) >> \tau_{obs}(Na)$ depletion factors are equal to 5.5, 4.5, and 30 for Si, Al, and Ca, respectively.

Main Si, Al, and Ca-containing species in the impact-produced cloud are SiO_2, AlO, $Ca(OH)_2$, respectively, [5] for the case of the initial temperature $T_0 = 10^4$ K and the initial pressure $P_0 = 10^4$ bar, $\gamma = 1.2$ in the impact-produced cloud. For the cases of $T_0 = 10^4$ K, $P_0 = 10^2$ bar, $\gamma = 1.2$ and $T_0 = 10^4$ K, $P_0 = 10^6$ bar, $\gamma = 1.2$ main Si, Al, and Ca-containing species are SiO, SiO_2, AlO, Al, Ca, CaO and SiO_2, $Al(OH)_3$, $Ca(OH)_2$, respectively. Based on approach [5] and corrected molecular constants photolysis lifetimes of SiO, SiO_2, AlO, $Al(OH)_3$, CaO, and $Ca(OH)_2$ at 298 K were estimated as 3×10^5, 2×10^5, 6, 2×10^6, 10, 9×10^4 s, respectively. Typical ballistic flight time is about 10^3 s. Thus, slowly-photolyzed molecules such as SiO, SiO_2, $Al(OH)_3$, $Ca(OH)_2$ are not photolyzed during first ballistic flight. Assuming that these molecules are captured by the lunar surface after first ballistic flight we can explain depletion of Si, Al, Ca atoms in the lunar exosphere. Additional depletion occurs due to formation of solid-phase dust particles containing these elements.

Summary and Conclusions:

Based on spectral observations of Na lines in the lunar exosphere maximum of activity of Perseid meteor shower on the Moon is observed on August 13, 2009 at 0-1 UT. These observations show that the intensities of Ca, Al, and Si resonance lines are much weaker than that if we assume that these elements as well as Na are presented in the impact-produced cloud only in the form of atoms. Observed depletion of Ca, Al, and Si atoms in the lunar exosphere are explained by formation of slowly-photolyzed molecules and dust particles. To distinguish between the two models, of unique impact of big meteoroid and numerous impacts of small meteoroids, one should increase the time resolution and provide spectral observations at different position angles that are possible using big 6-8-m telescopes.

Acknowledgements:
This research is supported by joint RFBR grant 11-02-90440-Ukr_f_a and DFFD grant F40 2087. Authors would like to thank staff of Terskol Observatory.

References:

[1] IMO (2009). http://www.imo.net/live/perseids2009
[2] Hamry, M., Suntzeff, N.B., Heathcote, S.R. et al. Southern spectrophotometric standards, 2, Publ. Astron. Soc. Pac., Vol. 106, pp. 566-589, 1994.
[3] Tug, H. Vertical Extinction on La Silla, ESO Messenger, Vol. 11, pp. 7-8, 1977.
[4] http://www.solarmonitor.org
[5] Berezhnoy, A.A. Meteoroid bombardment as a source of the lunar exosphere, Advances in Space Research, Vol. 45, pp. 70-76, 2010.
[6] Sarantos, M., Killen, R.M., Glenar D.A. et al. Metallic species, oxygen and silicon in the lunar exosphere: Upper limits and prospects for LADEE measurements, J. Geophys. Res., Vol. 117, A03103, doi: 10.1029/2011JA017044, 2012.

FULL TOPOGRAPHIC CORRECTION OF M³ REFLECTANCE DATA FOR LUNAR ELEMENTAL ABUNDANCE ESTIMATION

A. Grumpe[1], C. Wöhler[1], A. Berezhnoy[2],
[1]Image Analysis Group, TU Dortmund University, Otto-Hahn-Str. 4, 44227 Dortmund, Germany; [2]Sternberg Astronomical Institute, Moscow State University, Universitetskij pr. 13, Moscow, Russia. Contact: {arne.grumpe | christian.woehler}@tu-dortmund.de, ber@sai.msu.ru

Introduction: In lunar remote sensing, the composition of the surface is commonly derived from the observed reflectance spectra. The normalisation of the surface reflectance to a reference illumination and viewing geometry (commonly: 30° incidence angle, 0° emission angle, 30° phase angle [1]) requires knowledge of the small-scale topography, since without topographic correction significant residual distortions of the spectra tend to occur [2]. Accordingly, insufficient topographic correction leads to topography-related artifacts in metal oxide abundance maps inferred from multispectral imagery [3]. However, the best currently available global lunar digital elevation models (DEMs), the LOLA DEM [4] and the GLD100 [5], have a much lower effective lateral resolution than the M³ image data, the currently best-resolved lunar hyperspectral data set (140 m/pixel in global mode [6]). In this study we therefore describe a framework for the correction of M³ reflectance data with respect to topography on both large and small spatial scales and the estimation of elemental abundances.

Image registration and DEM construction: We apply the photometric stereo based method proposed in [7] to M³ radiance data and a reference DEM (here: the GLD100) of lower lateral resolution than the images. Our method relies on an estimation of the surface gradients by simultaneously minimising the mean squared deviation between the observed reflectances and those expected from the constructed DEM, and the mean squared deviation of the large-scale gradients of the constructed DEM from those of the reference DEM. For DEM construction, only M³ channels with centre wavelengths below 2000 nm are used in order to avoid the thermal emission component. The Hapke model [8] is used as the reflectance function, where the single-particle scattering function is chosen according to the double-lobed form proposed in [9] which is governed by a single asymmetry parameter. Along with the DEM, our approach performs a pixel-wise estimation of the single-scattering albedo and (if two or more images acquired under sufficiently different phase angles are available) the asymmetry parameter. The remaining Hapke parameters describing the opposition effect (which is negligible for the regarded range of phase angles) and the macroscopic surface roughness are chosen according to [10].

Our photometric stereo method is applicable using a single image, but it yields a higher accuracy when several pixel-synchronous images acquired under different illumination conditions are available. The M³ images, however, show misregistrations of up to several kilometers, which might be due to failure of the navigational instruments of Chandrayaan-1 and the resulting problems of M³ selenelocation [11]. Image registration is further complicated by strongly varying illumination conditions during different orbits. Because of the changing illumination and the resulting intensity changes, similarity measures like cross-correlation fail on the M³ images. In contrast, the photometrically reconstructed surface gradients are an illumination-independent representation of the images. Thus, by matching control points (e.g. corner points) of the surface gradient images using cross-correlation, illumination independence is achieved [7].

Spectral parameters, elemental abundances: The thermal emission component is subtracted from the M³ radiance spectra [2]. For each M³ channel, a pixel-wise estimation of the single-scattering albedo and the asymmetry parameter is performed based on the Hapke model [8], relying on the available M³ images and the constructed DEM. The Hapke model [8] is then used to determine the surface reflectance for the (30°, 0°, 30°) reference geometry. Normalised reflectance data of our test region (the crater Aristillus) downloaded from [11] and obtained using our method, respectively, are shown in Fig. 1. Due to the high lateral resolution of our DEM, all topography-related artifacts have been removed from the normalised reflectances. Our DEM of Aristillus is shown in Fig. 2. For each pixel, the continuum of the reflectance spectrum is then removed based on the convex hull [12], which also yields the continuum slopes for the absorption troughs around 1000 nm and 2000 nm. The absorption wavelength, depth, and width of both absorption troughs are determined based on the continuum-removed spectra [2] (cf. Fig. 3). We used global maps of these parameters at a resolution of 0.2 pixels per degree to determine a linear regression model based on the Lunar Prospector elemental abundance maps of the elements Ca, Al, Fe, Mg, Ti, and O [13] (cf. Fig. 4). This regression model allows to construct high-resolution elemental abundance maps along with a petrographic map in terms of the three-endmember model [14] using the spectral parameter maps obtained at full M^3 resolution (cf. Fig. 5).

Summary and conclusion: We have described the determination of reflectance data normalised to a reference geometry based on lunar DEMs of high lateral resolution constructed using a photometric stereo based method. The normalised reflectances as well as the inferred spectral parameters are free of topography-related artifacts. The obtained spectral parameter maps have been used for the estimation of elemental abundances.

References: [1] Pieters, C. M. (1999) Workshop New Views of the Moon 2, 47. [2] Wöhler, C. and Grumpe, A. (2012) In: Innovations for Shape Analysis: Models and Algorithms. Rev. contrib. to Dagstuhl Seminar, Springer, to appear. [3] Jolliff, B. L. (1999). JGR 104(E6), 14123–14148. [4] Li, R. et al. (2011) LPSC XXXXII, abstract #2010. [5] Scholten, F., et al. (2011) LPSC XXXXII, abstract #2046. [6] Pieters, C. M., et al. (2009) Current Science 96(4), 500–505. [7] Grumpe, A. and Wöhler, C. (2011) Proc. 7th IEEE Int. Symp. Image and Signal Proc. and Anal., 609–614. [8] Hapke, B. W. (2002) Icarus 157, 523–534. [9] Cornette, W. M. and Shanks, J. G. (1992) Appl. Optics 31(16), 3152–3160. [10] Warell, J. (2004) Icarus 167, 271–286. [11] Boardman, J. W., et al. (2011) JGR 116, E00G14. [12] Fu, Z., et al. (2007) IEEE Trans. Geoscience and Remote Sensing 45(11), 3827–3844. [13] Wöhler, C., et al. (2011) PSS 59, 92–110. [14] Berezhnoy, A. A., et al. (2005) PSS 53, 1097–1108. [15] http://pds-imaging.jpl.nasa.gov/volumes/m3.html. [16] Wiseman, S. M., et al. (2012) Proc. 2nd Conf. Lunar Highlands Crust, abstract #9025. [17] http://www.mapaplanet.org/explorer/moon.html.

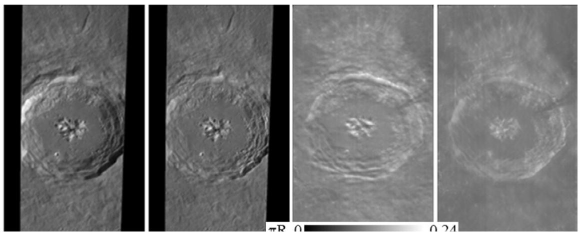

Fig. 1. (**a**) M^3 1579 nm radiance image of Aristillus at 57.9° phase angle. (**b**) and (**c**) M^3 1579 nm reflectance normalised to (30°, 0°, 30°) standard geometry, inferred from images acquired at phase angles of 57.9° and 38.8°, with topographic correction based on the LOLA DEM (from [15]). (**d**) M^3 1579 nm reflectance normalised to (30°, 0°, 30°) with full topographic correction. Images (**b**), (**c**), and (**d**) are scaled to the same reflectance range.

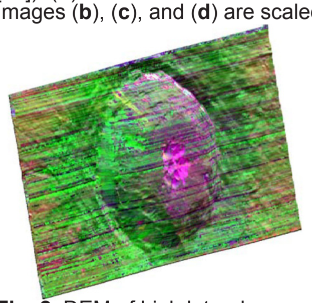

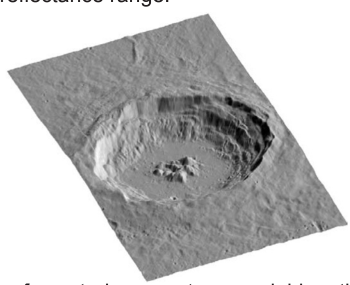

Fig. 2. DEM of high lateral resolution (~140 m), constructed using GLD100 data and M^3 radiance data. View from southwestern direction. The vertical axis is three times exaggerated.

Fig. 3. Map of spectral parameters overlaid on the DEM (R channel: absorption depth of the ~1000 nm trough; G channel: absorption wavelength of the ~1000 nm trough; B channel: absorption depth of the ~2000 nm trough). The presumably noritic central peaks (low absorption wavelength) appear in purple, the olivine streaks on the northeastern crater wall (cf. [16]) (high absorption wavelength, nearly absent absorption at ~2000 nm) in yellow colour.

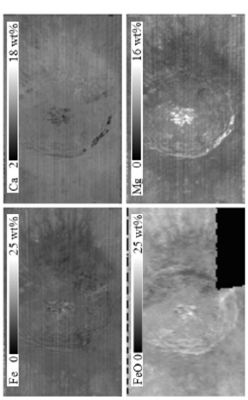

Fig. 4. Abundances of Ca (upper left), Mg (upper right), and Fe (lower left). For comparison, the Clementine FeO abundance map obtained from [17] is shown on the lower right, where the influence of topography is clearly apparent.

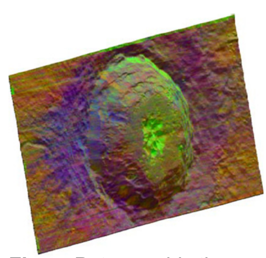

Fig. 5. Petrographic three-endmember map overlaid on the DEM. R channel: mare basalt; G channel: Mg-rich rock; B channel: ferroan anorthosite. The central peaks consist of Mg-rich rock (presumably norite), and a large ferroan anorthosite deposit is apparent at the northern crater wall and rim.

THE MOON: GRAVITY SURVEYS REVEAL ITS REAL WAVE WOVEN TECTONICS

G.G. Kochemasov,
IGEM RAS, 35 Staromonetny, 119017 Moscow, Russia. Contact: kochem.36@mail.ru

The NASA's GRAIL mission will produce an unprecedented detail gravity map of the lunar subsurface as measurements will include some depths of the satellite. One could say that this map will principally repeat the gravity pattern acquired earlier (Fig. 1, 3; [1]), which shows the surface densely "peppered" by even-sized "craters" about 100 km in diameter. The wave planetology admits that some of them are of an impact origin but a bulk is due to an intersection of standing waves produced by an elliptical orbit of the body (Fig. 4).

The lunar community should realize that one of bases of the Moon's geology – crater size – frequency curve is of a complex nature. Impacts surely contribute to this curve but a significant part of it is due to ring structures of non-impact origin. Ring structures can be produced by an interference of standing inertia-gravity waves of 4 directions warping any rotating celestial body moving in an elliptical orbit [2, 3, 4]. Many ring structures observed on solid and gaseous planetary spheres are of such profound nature. They form regular grids of shoulder-to-shoulder even ring structures (Fig. 1, 2) (The best example from the past – Triton's cantaloup surface, from the present- outgassing crater's chains at the Hartley comet core). Their sizes depend on orbiting frequencies: the higher frequency- the smaller "rings", and vice versa. Satellites having two orbiting frequencies in the Solar system are particularly "peppered" with rings as a low frequency modulates a high one producing along with the main ring populations the side populations [4]. The Moon reveals such populations: frequency peaks at 80-140 (an average 100 km), and more than 600 km in diameter (main rings), 10-30 and 300-400 km in diameter (side rings)[4]. Expressed by the lunar radius they are: $\pi R/60$, $\pi R/4$, $\pi R/240$, $\pi R/15$ (Fig. 5)

An important examination of the proposed explanation of the mostly 100-km crater size "peppering" the lunar surface is a comparison it with the well-known supergranulation of the solar photosphere (30 to 40 thousand km granule diameter, $\pi R/48$-60). Both objects orbit (rotate) with the monthly period, thus their wave granulations have to be comparable (Fig. 3). Another striking comparison is in Fig. 1-2: Moon & Mercury having different orbiting periods (29.5 & 88 days) show proportionally different tectonic granules sizes, ~100 & ~ 500 km ($\pi R/60$ & $\pi R/16$).

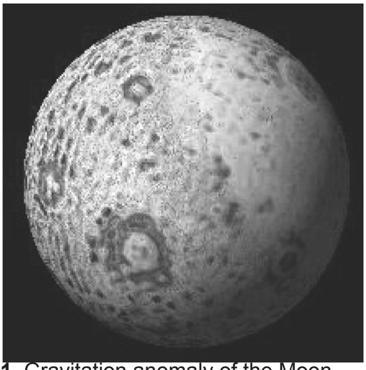

Fig. 1. Gravitation anomaly of the Moon measured by by Kaguya mission. Credit: forum.worldwindcentral.com

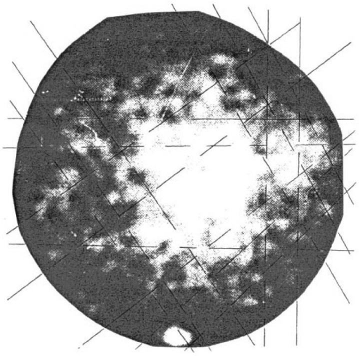

Fig. 2. Mercury is covered by dark or bright circles of similar sizes evenly distributed through its surface [5]. It seems that the circles are disposed along not random lines (aligned). This regularity is rather caused by a more regular process than random impacts.

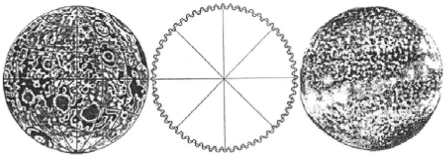

Fig. 3. Comparison of lunar [1] and solar photosphere wave tectonic granulations ($\pi R/48$-60)

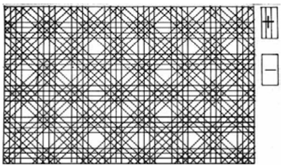

Fig. 4. Graphic representation of crossing waves (+ up, - down) producing chains and grids of round forms (craters) (better seen from some distance).

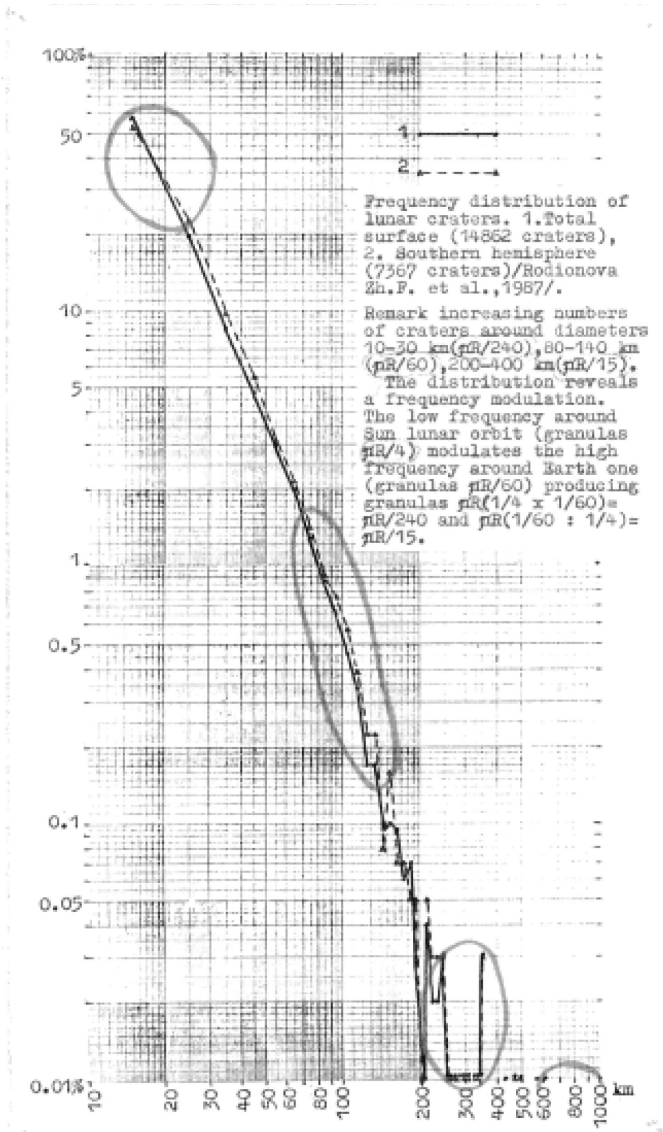

Fig. 5. Frequency distribution of lunar craters with "anomalous" regions (encircled) marking departure from the classical impacts related curve.

References: [1] Konopliv, A.S. et al. (1998) Clementine: gravity survey of the Moon // Science, v. 281, # 5382, 1476-1480. and Konopliv A. S. et al. (2001) Icarus, v. 150, 1-18; [2] Kochemasov G.G. Theorems of wave planetary tectonics (1999) JRA, v.1, #3, 700; [3] Kochemasov G.G. (1992) Concerted wave supergranulation of the solar system bodies // 16th Russian-American microsymposium on planetology, Abstracts, Moscow, Vernadsky Inst. (GEOKHI), 36-37; [4] Kochemasov G.G. (2001) On one condition of further progress in lunar studies // First Convention of Lunar Explorers, 8th to 10th March, 2001, Palais de la Découverte, Paris, France; Programme and Contributed Abstracts; ESTEC, eds: D. Heather and B. Foing, 58 pp (p.26).
[5] Slade, M.A. et al. (1992) Mercury: the radar experiment from Earth // Science, v.258, 635-640.

INFLUENCING TOPOGRAPHY ON FORMATION OF REFLECTED SIGNAL OF LUNAR RADAR.

V. M. Smirnov[1], O. V. Yushkova[1], I. P. Karachevtseva[2], I. E. Nadezhdina[2],
[1]Kotel'nikov Institute of Radio Engineering and Electronics of RAS, Fryazino Branch, Russia; [2]Moscow State University of Geodesy and Cartography (MIIGAiK), MIIGAiK Extraterrestrial Laboratory (MExLab), Moscow, Russia. Contact: vsmirnov@ire.rssi.ru

Introduction: Moon and circumlunar space have recently had an important place in space research of many countries. Earth satellite is an object having the interest both for science and practice. The priority of the investigation is to found ice deposits in the Moon subsurface layer. Subsurface radiolocation is one of the few distant methods for the investigation of internal structure of the space object ground.

Radar complex RLK-L in mission "Luna-Glob": Radar sounding from a spacecraft allows to carry out probing of the lunar subsurface layer on depths from several meters to several kilometers. Such experiments are planned in the mission "Luna-Glob" by a radar complex RLC-L. Its goal is to investigate dielectric properties of the lunar surface and subsurface structure of the soil layer along the flight path of the spacecraft.

Discussions: In subsurface sounding parameters of reflected signal depend on the relief, the dielectric parameters of soil and their depth distribution. It is relief which is important factor influencing on the reflected signal formation. The reflection of impulses from the crests and troughs of large-scale heterogeneities causes the expansion of their front. The scattering signal of a surface roughness leads to the fact that the radar antenna accepts both vertically reflected pulse and the pulses reflected from the side reflectors. As a result, a cumulative pulse with a stretched trailing part is obtained. Questions arise: how strong are these distortions and how to take them into account in processing the received signals and data interpretation? What regions are suitable for radar measurements?

For answering on these questions, modeling of reflecting RLC-L signal by testing region of lunar surface was carried out in the approximation of geometric optics. Real digital elevation model (DEM) of North Polar area of crater Anaxagoras region (Fig. 1-A) was used for the calculations. This DEM has been created during cartography works for support safety landing site of target ellipses (Fig. 1-B) for "Luna-Glob" mission [1]. The reflected signal was considered as a superposition of the signals reflected from each node of the grid of DEM, taking into account the slope of terrain and travel time.

The simulation results show the type of relief of experiment region can be determined using spectrum of the reflected signal. Fig.2-A shows the spectrum of A-signal low-frequency mode RLC-L (The chirp with center frequency of 20 MHz, 5 MHz deviation, the duration of 250 μs), reflected from the area of the mountain ridge (Fig. 2-B). Module of spectrum of the analogical signal is given on fig. 3-A. The one reflected from the surface with coomb (Fig. 3-B). Topographic objects with comparable linear dimensions and a similar orientation were selected for modeling.

DEM has been formed using LRO LOLA data which received during the NASA mission – Lunar Reconnaissance Orbiter (LRO) by laser altimeter Lunar Orbiter Laser Altimeter. The DEM resolution is about 30 m/pixel (along parallel) and 130 m/pixel (along meridian). The data presented in the coordinate system MOON ME (Mean Earth). Z-axis is directed to the center position of the Moon North Pole, the X-axis is directed at the initial meridian passing through the mean position of the Earth. The height of the spacecraft is equal 100 km. The spectrum is calculated for the normed to unity signal. The spectrum of the signal reflected from only one surface point (without the lateral reflections) is shown on Fig. 2-A and Fig. 3-A in gray.

Conclusions:

Now we are testing DEM with resolution 2m/pixel derived from LRO arrow angle (LRO NAC) photogrammetry stereo-image processing for testing region. We expect to derive a high resolution DEM based on methods as describe at [2] which will allow us to carry out analyses the area of "Luna-Glob" target ellipses which are more closely to region of interest of mission than testing region. Preliminary results have shown that data of radar precisely image an investigated surface. These results will be present at the conference.

Acknowledgements: The work has been supported by the Program № 22 "Fundamental problems of research and development of the Solar System" of the RAS Presidium. Also mapping work has been partly supported by a grant from the Ministry of Education and Science of the Russian Federation (Agreement № 11.G34.31.0021 dd. 30/11/2010).

References:

[1] Kokhanov A., I. Karachevtseva, J. Oberst, Ph. Gläser, M. Wählisch, and M. S. Robinson. Cartography Support and Assessment of Candidate Landing Sites for the LUNA-GLOB Mission

Abstracts of 43 LPSC, // Proceedings of 43 Lunar and Planetary Science Conference, # 1750.
[2] Zubarev A. E. et. al. (2012), Lunokhod-1 Panoramic Images and Stereo Topography, these issues.

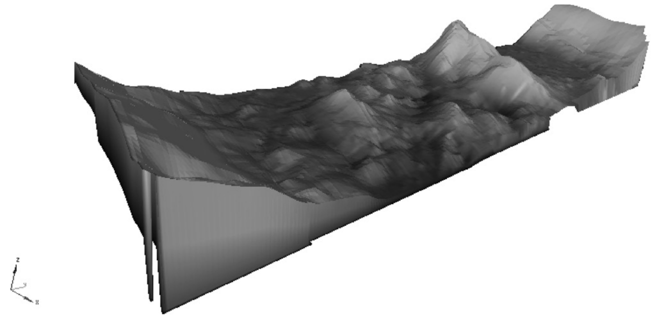

fig. 1-A. 3D-model of DEM for testing area of North Polar region (crater Anaxagoras)

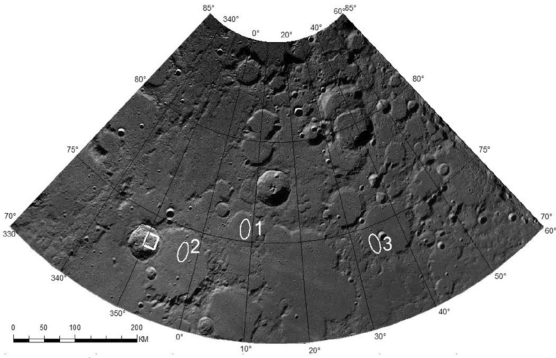

Fig. 1-B. North Polar area of the Moon: the rectangle indicates testing area (crater Anaxagoras region); numbers indicate the target ellipses of "Luna-Glob" mission candidates landing sites.

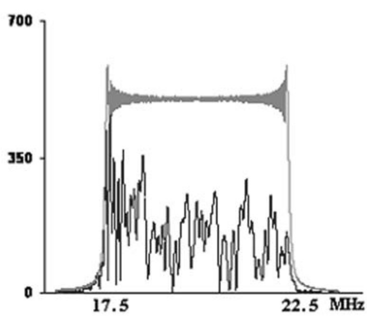

fig. 2-A

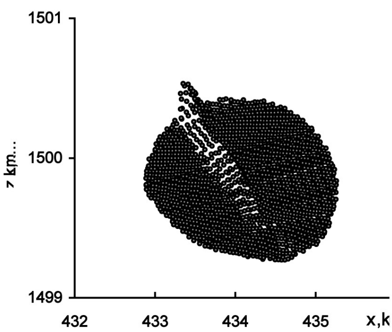

Fig. 2-B

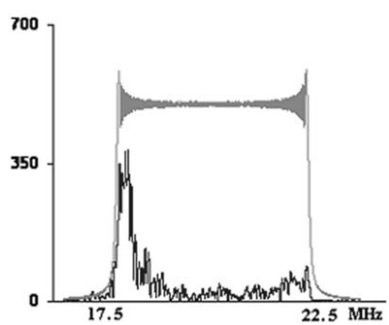

fig. 3-A

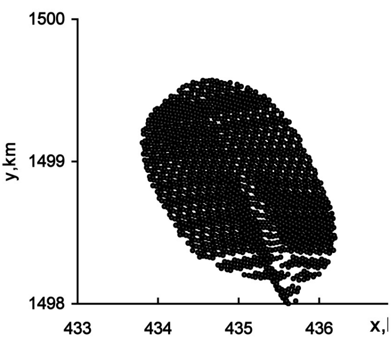

fig. 3-B

SMALL COMETS AS A POSSIBLE SOURCE OF WATER DEPOSITS ON THE MOON

M. P. Sinitsyn,
Sternberg Astronomical Institute, Moscow State University,
13, Universitetsky prosp., Moscow, Russia. Contact: msinitsyn.sai@gmail.com

Introduction:

The actual existence of small comets (microcomets) actively discussed for about 10 years ago in connection the publications of Dr. L.A. Frank from University of Iowa. At present, the recent space exploration reminiscent of the possible existence these cosmic objects. According to the results of spectral measurements of spacecraft Cassini (VIMS), Chandrayaan-1 (Moon Mineralogy Mapper) and Deep Impact [1,2,3] water and hydroxyl are ubiquitous on the lunar surface, including the equatorial regions. In addition, quadrupole mass spectrometer CHACE Chandrayaan-1 showed the presence of water in the exosphere of the Moon [4]. This is a direct proof of the existence of migration of volatiles [5]. These facts mean that surface processes of water and hydroxyl replenishment (especially in equatorial regions) occur at present time. As a source of permanent formation of OH/H_2O currently considered to be interaction of solar wind' protons with the lunar surface [6]. However, as shown by laboratory experiments with irradiation of the samples (similar to the lunar rocks), by protons of the solar wind energy the amount of water formed as a result is negligible or non-existent [7]. Thus, to explain the continued presence of water in the exosphere of the Moon may be offered another source. Such a source is small comets [9].

Small comets (microcomets):

The assumption about the existence of small comets was made by Dr. Frank in the 80s of last century, after the analysis some holes in the earth's atmosphere in ultraviolet light. The diameter of these holes was about 50 km. They are interpreted as a result of microcomets' destruction [8]. By the nature of these atmospheric holes were made some assumption about the small comets (**d**~10m, $\rho \sim 0.01 \div 0.1$g). It should be noted that Frank was also carried out visual observations of small comets that have been published. Frank and Sigwarth believe that the flow of microcomets on the lunar surface is **F**~$1.2 \cdot 10^{-19} cm^{-2} s^{-1}$, that corresponds of fall rate about 0.7 $\min^{-1}$ or 370 000 impacts per year. Such a huge number of small comets incident on the moon is obviously not true. First, the observed of polar water ice deposits have to be so much more with so huge number of comets. Second, the number of events marked by Apollo seismometers is about 1,000 per year. Therefore, we can assume a more realistic value of the flux of small comets **n** ~100 per year. This is lower limit of the possible number of small comets, which does not contradict indications of seismometers.

New data indicating the existence of small comets:

The data some space missions and laboratory experiments indicate the need to search additional sources of water on the Moon.

Spectral observations of surface.

Just three of the infrared spectrometers installed at the three spacecraft yielded similar results [1,2,3]. It is important to note that the spectral lines of water were observed not only in the polar regions, but also in the equatorial. It is especially well seen in the results of the VIMS spectrometer of Cassini (fig.1).

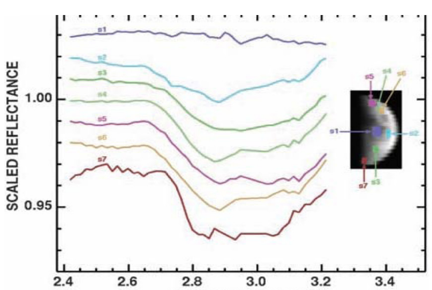

fig.1. The infrared spectra of the illuminated surface of the Moon, (Cassini, VIMS)[1].

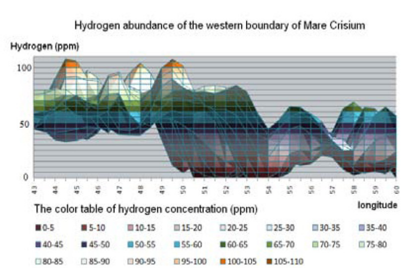

fig. 2 The distribution of hydrogen on the western boundary of mare Crisium

There is well visible absorption lines if figure within the range of 2.8-3 microns. These lines correspond to water and hydroxyl. It is clearly seen as spectra of s2 and s3 correspond to the equatorial region. Jointly with this result, it is important to note that the mass spectrometer CHACE Chandrayaan-1 has found the real presence of water molecules in the exosphere of the Moon [4]. This is a very important result indicates that the migration process of volatile elements is taking place now [5, 6]. Considering these two results together can be concluded that the formation of water and hydroxyl on the Moon occurs continuously. Obviously, the main source, capable of bringing water to the moon is considered to be the solar wind protons. An example of the reaction of protons with the surface is the following [6]:

$$2H^{+}+FeO=Fe^{0}+H_{2}O \qquad (1)$$

This reaction should take place in the interaction of protons with the surface the seas, as there contains iron oxide in abundance. However, the fig.1 shows the spectrum of s1 corresponding to the location of the Mare Cognitium. It is clear seen that this spectrum has not absorption lines on the range 2.8-3 microns, corresponding OH/H_2O.It should be noted that the infrared spectrometer gives information only with the upper few millimeters of the surface. As for a depth up to 2 meters, the distribution of hydrogen obtained by Lunar Prospector Neutron Spectrometer (LPNS) (Fig. 2).The right side of the graph corresponds to the western part of the Mare Crisium. Here also seen a significant drop of hydrogen on the sea area (0-50 ppm) compared to the highlands (50-100 ppm). Thus, possible to assume that reaction (1) with the protons of the solar wind does not provide a significant amount of water neither on the surface nor on the depth.

Laboratory experiments.

To experimentally verify the results of the interaction of solar wind protons with the surface of the Moon were conducted some laboratory tests [7, 8]. Dr. Burke conducted experiments on irradiation of rocks similar to the lunar by protons with energies of the solar wind (1-2 keV). In the experiments, was measured the initial and final content of water and hydroxyl. As a result, it was found that during irradiation the formed OH/H_2O is negligible or absent. In some experiments, the water content is even slightly decreased compared with baseline.

These results cast doubt on the very process of formation of water under the influence of solar wind protons. It is possible that this source of water does not act or acts in a much lesser extent.

Estimated calculations:

Estimate the time required to accumulate all known ice deposits by only small comets. Putting ice deposits about $m_{ice}=2\ 10^{15}$g [10]. Then, the time required for the formation these stocks:

$$t_{trap}=m_{ice}/m_{w} \qquad (2),$$

where m_w - mass of water remaining on the surface after impacts of small comets per year. This mass can be calculated using the equation:

$$m_w=n\ m_k c_{H2O} c_{mat}(1-c_{ph})\sim 1.6\ 10^6 \text{ g/y} \qquad (3),$$

where $m_k\sim 2\ 10^7$ -mass of small comet [9]; $c_{H2O}\sim 0.2$- the concentration of water in one [11]; $c_{mat}\sim 0.1$ - the mass fraction of the comet material remaining in the gravity of the Moon [12]; c_{ph} =0.96 –the part of the water which has undergone photodissociation [5]. Thus, the falling n ~ 100 comets per year corresponds to increasing of ice deposit at the both poles by 1.6 tons. As a result the time from equation (2): $t_{trap}\sim 1{,}25$ billion years. This is a very big, but still realistic period of time. Mainly as an extended period of time due to the destruction of the water in consequence of the photodissociation and a small part of the comets that remain in the gravitational field of the Moon as a consequence of impact process. **For** comparison, the accumulation of ice time, resulting Crider and Vondrak [5] of assumptions about the formation of water from the solar wind and the calculation of the migration is about 83 million years.

References:

[1] Clark, R.N., *Science, 326,562(2009);*
[2] Pieters, C.M. et al. *Science, 326,568(2009);*
[3] Sunshine, J.M. et al. *Science,326,565(2009);*
[4] Sridharan, R. et al. *Planetary and Space Science 58,6,947(2010);*
[5] Crider, D.H., Vondrac, R.R*., JGR 105,E11,26773-26782(2000);*
[6] Crieder, D.H., Vondrak, R.R. *Lunar and Planetary Science Conference (2001),1922;*
[7] Burke, D. et al. *41st Lunar and Planetary Science Conference (2010), 2567;*
[8] Burke, D. et al. *Icarus,211,1082-1088(2011)*
[9] Frank, L.A. and Sigwarth, J.B., *Reviews of Geophysics (ISSN 8755-1209),31,1,1-28(1993);*
[10] Feldman, W.C. et al. *JGR 105(E2), 4175–4195(2000);*
[11] Berezhnoy, A.A., *Advances in Space Research 45, 70–76(2010);*
[12] Ong, L. et al. *Icarus, 207,2,578-589(2010)*

THERMODYNAMIC MODELING THE ANALYSIS OF LUNAR SEISMIC AND TEMPERATURE PROFILES

E. V. Kronrod, O. L. Kuskov, V. A. Kronrod,
Vernadsky Institute of Geochemistry and Analytical Chemistry, Russian Academy of Sciences, Moscow, Russia, Contact:kendr_ka@bk.ru

Introduction:

Until recently most of published seismic models of the Moon were represented as a vertical profile divided into several zones with medium value of P- and S- velocities [1,2]. In the recent work [3] the distribution of seismic velocities is more complicated that gives new possibilities for lunar thermal state and chemical composition researching. The main problem of this work is estimating of seismic models confidence and determination of lunar models constraints by using methods of physic-chemical modeling.

Computer simulation and results:

The approach consists of calculating the seismic velocities from temperature distribution and geochemical data (forward modeling) and retrieving the chemical composition and temperature from the geophysical constraints including the seismic data, the moment of inertia and mass of the Moon (inverse modeling) [4-8]. The forward and inverse problems are solved by the minimization of the Gibbs free energy incorporating equations of state of minerals, phase transformations, anharmonicity (thermal expansion and compressibility), and attenuation effects (anelasticity of mantle material at high temperatures), which should be taken into account due to nonlinear variations in thermodynamic and seismic properties with rising temperature and pressure [4,6]. There is rich variety of bulk composition models proposed for the Moon: from models enriched in Ca and A1 to Earth-like compositions in which Ca and AI content is lower [6].

Different petrological models of the Moon were considered. Three basic petrological models [6]: olivinic pyroxenite (Ol-Px), pyrolite, Ca, Al-fertile composition (olivine-clinopyroxene-garnet – Ol-Cpx-Gar).

Calculation models: Khan model [5] (the values of concentrations were taken from the histogram), constant-depth composition that satisfies geophysical constraints and Mis – composition, that optimally satisfies geochemical and geophysical constraints [7].

I. The analysis of temperature profiles calculated from seismic data and composition.

Calculated from inverse modeling of seismic velocities [3] temperature profiles contain negative trend. Negative trend of temperature profiles calculated for constant composition disagrees with physical constraints. Also calculated from P- and S-velocities temperature profiles have essential distinctions. Hence it appears that in model [3] P- and S-velocities are discordant.

II. The analysis of seismic profiles calculated from temperature and composition.

To estimate seismic profile accuracy we have calculated computational thermodynamic seismic profile. Using input data of chemical composition solving the direct problem of thermodynamic modeling seismic velocities can be calculated. It is necessary to estimate optimal temperature profile for calculating thermodynamic profile.

Constrains on the temperature profile. We determine the probable temperature profile T_{pm} from several criterions: solution of the full inverse problem [9], determined from seismic velocities inversion temperature profile [6], temperature melting of the upper zone of the core [10], absence of melting geological material on the depth upper 1000 km, positive or zero vertical density gradient. Determined temperature should be close to the one-dimensional thermal conduction model. Further constraints of the lunar mantle temperature profile will be considered detailed.

The minimal temperature in the upper mantle. The range of probable temperature variations in the mantle was obtained in the works [6, 8]. We have found the minimal temperature in the upper mantle. The temperature of 500^{o}C at the depth of 150 km satisfy limitations of mass, inertia moment and seismic velocities [2]. For less temperature there is no task solution.

The gradient dT/dH in the mantle. Absence of density inversion is a natural requirement for the hydrostatic equilibrium satellite. Dimensionless moment of inertia of the Moon is similar with the moment of inertia of homogeneous body. Computational modeling confirms the hypothesis of the density homogeneous mantle. From numerical modeling temperature profile with gradient ***dT/dH =1,05-0,0006*H, (H – km)***, was selected. This profile satisfy zero gradient with acceptable accuracy.

The probable temperature profile. We have found acceptable agreement calculated from absolutely different models - the constant density model and uniformly distributed radiation sources model. The mantle temperature is described by equation: ***$T= 1.05\ H-0.0003H^2 +C$*** . Constant C evaluates from known temperature in any point in the mantle. Temperature gradient at the depth of 150-1000 km accurate within 1°C, ***$\delta T_{1000-150} = T_{1000} - T_{150} = 600^oC$.***

The probable temperature at the depth of 500 and 1000 km.

Weber at all [10] gives estimation T=1650° K (1380 C) at the radius R=480км (H=1730-480=1250 км).

We have found dT/dH= 0.375-0.45 degrees per kilometer and the temperature at the depth of 1000 km ***T_{1000}=1200-1250° C.*** It is necessary to set the temperature in some point of the mantle, than calculate constant C. If the minimal temperature is T_{150}=500°C, then the temperature at the depth of 1000 km T_{1000}=1100C. For the temperature T_{1000}= 1200C is needed T_{150}=600C. Probable temperatures T_{150} from different models will be discussed. The temperature T_{150}=570-630C was found from inverse problem with a constraints of moment of inertia, mass and seismic velocities [6, 9]. In the recent paper [9] on the seismic data was obtained ***T_{150}=570+- 100° C***. Summarized these data and constraints ***T_{1000}= 1200- 1250°C*** we have initialized ***T_{150}=600°C***. Correlating all of this data gives probable temperature profile of the lunar mantle at the depth less than 1000 km: **T_{pm}°C =449+1,05*H-0,0003H², H** – depth in kilometers.

We have calculated probable temperature profile for lunar mantle on basis of numerical experiment. Using input data of chemical composition and method of forward modeling, on the base of temperature pprofile seismic velocities can be calculated. Thus we have estimated probable distribution of seismic velocities for the whole range of chemical composition. Veloicity gradient in the article [3] varies greatly from calculated models. Due to our analysis there are no constant composition models with similar velocities.

Following conclusions can be done:

1. Probable temperature profile of the lunar mantle had being estimated:

T_{pm}°C =449+1,05*H-0,0003H², H – depth in kilometers

2. Calculated from seismic velocities [3] and constant composition doesn't satisfy physical limits.

3. Velocities Vp and Vs in model [3] are not consistent.

4. Seismic velocities gradients for model Garcia et al. [3] can't be calculated for constant composition.

Acknowledgements

This research was supported by Russian Academy of Sciences under Programs 22, and by RFBR grant 05-00178 and 12-05-00033.

References

[1] Lognonné P. Planetary seismology // Annu. Rev. Earth Planet. Sci. 2005. V. 33. P. 571–604.

[2] Gagnepain-Beyneix, J., Lognonné, P., Chenet, H. et al. : A seismic model of the lunar mantle and constraints on temperature and mineralogy, Phys. Earth Planet. Inter., Vol. 159, pp. 140-166, 2006.

[3] Garcia, R., Gagnepain-Beyneix, J., Chevrot, S. et al. : Very preliminary reference Moon model, Phys. Earth Planet. Inter., Vol. 188, pp. 96-113, 2011.

[4] Kuskov, O.L., Kronrod, V.A. : Core sizes and internal structure of the Earth's and Jupiter's satellites, Icarus, Vol. 151, pp. 204-227, 2001.

[5] Khan, A., Connolly, J.A.D., Maclennan, J., Mosegaard, K. : Joint inversion of seismic and gravity data for lunar composition and thermal state, Geophys. J. Int. Vol. 168, pp. 243–258, 2007.

[6] Kuskov, O.L., Kronrod, V.A.: Geochemical constraints on the model of the composition and thermal conditions of the Moon according to seismic data, Izv. Phys. Solid Earth., Vol 45, pp. 753–768, 2009.

[7] Kronrod, V.A., Kuskov, O.L.: Inversion of Seismic and Gravity Data for the Composition and Core Sizes of the Moon, Izv. Phys. Solid Earth., Vol 47, pp. 711-730, 2011.

[8] Kronrod, E.V., Kuskov, O.L., Kronrod V.A. : Geochemical and geophysical constraints for thermal field of the Moon, EPSC Abstracts, Vol. 6, EPSC-DPS2011-16.

[9] Kuskov, O.L., Kronrod, V.A., 1998. Constitution of the Moon: 5. Constraints on composition, density, temperature, and radius of a core. Phys. Earth Planet. Interiors 107, 285- 306.

[10] Weber, R., Pei-Ying Lin, Garnero, E. et al.: Seismic Detection of the Lunar Core, www.sciencexpress.org, 2011

ON THE PERSPECTIVES OF RADON MONITORING ON THE MOON

Rudakov V.P.
Shmidt institute of physics of the Earth , RAS B.Gruzinskaja 10, 123995 Moscow, Д 242, Russia, E-mail: rudak45@mail.ru

Among the numerous questions discussed on the European lunar symposium of 2012 in Berlin, two themes connected to a problem of water on Selena [1] and measurements of radon on her surface as applied, besides, to a problem of water in rocks [2] pay to themselves attention.

Experience of long-term monitoring of geodeformation processes of the earth's crust of seismoactive and platform regions of the Earth with use of emanation (radon) method [3] allows designate prospects of its use at studying selenodynamic processes and, first of all, connected with processes of fluidtransportation in the rocks massifs.

One of the basic advantages of radon monitoring is passive, practically continuous process of reception of the information on the variations of measured parameter displaying processes of fluidtransportation in the shallow and deep layers of the rocks massifs.

Not less significant advantage is the opportunity of realization highly effective hindrance defended measurements with the help of the simple device made on the basis of traditional technologies of the field radiometry.

On the basis of the shown preconditions creation of the apparatus - methodical complex of monitoring of the selenodynamic processes, technologically compatible to the channel of the seismic noise measurements and to the other measurements on a surface of the Moon is planned.

This work was supported by the grant of the Russian academy of sciences Presidium Program 22: "Fundamental problems of research and exploration of the Solar system".

1. Colin A, Davies G.R. et.al. Exploring the fiasibility at determining lunar soil water contents with a combined ramal/libs instrument. Proceedings of European Lunar Simposium. Berlin. April 19/20 2012, p.22.
2. Meslin P.Y., Sabroux J.C. et. al. The dorn experiment: an alpha spectrometer dedicated to the characterization of the transport of lunar volatiles. The same collection. P.73
3. Emanation monitoring of geoenvironments and processes. 2009. M. The scientific world. 176 p.

LUNAR SEISMICITY, SOLAR WIND, SOLAR OSCILLATION.

Khavroshkin O.B., Tsyplakov V.V.

Total primary energy impact of solar flares on the moon has several components and can be compared with the kinetic energy of a large meteorite. Because the meteorite impacks is an important part of the seismicity of the total lunar, the search of solar lunar seismicity is equally important scientific interest, especially as previously noted the connection between the Sun and the solar activity and lunar seismicity [1…3]. The most targeted results are presented in [3]. Further research should be expanded to more widespread use of Nakamura's Catalogue (CN) and the parameters of the new features of the Sun and the solar wind [4]. Therefore, in addition to searching seismograms, the consequences of exposure to the lunar surface of interplanetary shock waves (MSY) flare origin, should be analyzed and the characteristics of the wave field (the duration of the seismograms) and assess the prospects of using the Moon as a detector of external influences. The end result of the proposed study was the discovery of seismograms with durations that coincide with periods of the oscillations of the Sun's own, their connection with solar activity (flares), and the prospect of using the Moon as a detector of solar activity.

Reference

1. Khavroshkin O.B., Tsyplakov V.V. Meteoroid stream impacts on the Moon: information of duration of seismograms // Proc. Conf. Meteoroids 2001 (ESA SP-495). Noordwijk, The Netherlands: ESA Publ. Division., 2001.
2. Khavroshkin O.B., Tsyplakov V.V. Temporal structure of meteoroid stream and lunar seismicity according to Nakamura's catalogue // Proc. Conf. Meteoroids 2001 (ESA SP-495). Noordwijk, The Netherlands: ESA Publ. Division., 2001.
3. Khavroshkin O.B., Tsyplakov V.V., Sobko A. A. Solar activity and lunar seismicity//Ingineering physic. 2011. №3.
4. Christensen-Dalsgaard, J. Dirty Solar Models Astron. Astrophys. 1979. 73.

ABSTRACTS SUBMITED TO SECTION 2. MERCURY

MODELS FOR THE ASCENT AND ERUPTION OF MAGMA ON MERCURY: GUIDELINES FROM THE LUNAR PYROCLASTIC VENTS AND MERCURY PIT-FLOOR CRATERS.

L. M. Jozwiak[1], J. W. Head[1], L. Wilson[2],
[1]Department of Geological Sciences, Brown University, Providence, RI 02912, USA;
[2] Lancaster Environment Center, Lancaster University, Lancaster LA1 4YQ, UK. Contact: lauren_jozwiak@brown.edu

Introduction: High-resolution images obtained during the first MESSENGER flyby of Mercury revealed the presence of irregularly-shaped pit craters, rimless steep-sided depressions that are inferred to have formed by non-impact processes [1]. These features range in maximum horizontal dimension from 20 to almost 40 km, and often occur on the floors of impact craters (varying in size from 55 to 120 km in diameter), leading to the designation of these craters as pit-floor craters, although images gathered by the MESSENGER Mercury Dual Imaging System (MDIS) reveal up to 9 pit craters outside impact craters [2]. The pit craters were interpreted to be of volcanic origin [1] on the basis of several lines of evidence: lack of evident rims typical of impact craters; no observable ejecta; irregular shape compared with most impact craters, with the long axis of the pit crater often forming an arc concentric to the rim of the host impact crater. No signs of associated extrusive flows were reported [1]. Pit craters were thus concluded to represent evidence for modification of the surface due to intrusive activity at depth [1] (Figure 1), specifically collapse into an underlying drained magma chamber forming a caldera, and thus representing evidence for near-surface magmatic activity on Mercury [1]. These features were seen to extend the range of evidence for magmatism beyond such surface expressions as smooth plains [3] and pyroclastic deposits [4,5,6]. We use additional observations reported in the literature for Mercury, planetary analogs, and theory of magma ascent and eruption to assess this hypothesis.

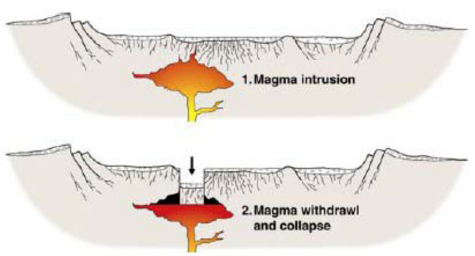

fig. 1. Schematic representation of magmatic intrusion, retreat, and floor collapse hypothesis of pit-floor crater formation (See Gillis-Davis et. al. [1]).

Ascent and Eruption of Magma: The Moon: The frequency and manifestations of magmatic intrusions in the crust of a terrestrial planetary body provide important insights into the dynamics of magma ascent and eruption, for the influence of crustal composition, and the role of shallow crustal structure in emplacement mechanics. For example, conditions of ascent and eruption of magma on the Moon [7,8] favor the propagation of magma through dikes to the surface to often produce high-volume, high-flux eruptions. Evidence exists, however for a range of features associated with shallow intrusion, as dikes propagate to the near surface and stall. Among the most prominent examples of such features are floor-fractured craters (FFC) [9], interpreted to represent magmatic dike intrusions into low-density crater floor breccias, and lateral spreading into a sill-like or laccolith-like body, lifting the floor of the crater in a piston-like manner in the process. This process tends to shallow and fracture the crater floor. Such a shallow intrusion process would seem to be an excellent candidate to produce the pit-floor craters recently documented on Mercury [1]. In order to assess the collapse-caldera hypothesis for their origin, we first review the nature of the FFC population on the Moon, assess similar examples on Mercury [1], and finally, assess the origin of the pit craters as collapse calderas above magmatic intrusions.

Recently [10] we categorized and mapped the distribution of the lunar floor-fractured crater population, and this work also supports the formation of floor-fractured craters by shallow magmatic intrusion. The floor profiles, generated with LOLA topography, show 1) flat fractured floors for the largest craters, and those closest to the mare and

2) smaller craters, and ones farther from the mare have more convex floors and concentric fracture patterns. The first type appears to be a manifestation of an underlying intrusion with greater driving pressures, and/or intrusion thickness combined with a thinner overlying crust, allowing for piston-like floor uplift. The second type of craters appears to be manifestations of smaller intrusions and lower driving pressures, also governed by the thicker highland crust. Since FFCs seem to be an excellent indication of shallow intrusions on the Moon, what types of similar features are seen on Mercury?

Floor Fractured Craters on Mercury: MESSENGER's first Mercury flyby revealed only a single example of a lunar-like floor-fractured crater (Fig. 2); however for MESSENGER, as with Mariner 10, the illumination geometry was less than favorable for the detection of floor-fractured craters over much of the rest of the area imaged. Noted by Head et.al. [3], a 35-km-diameter candidate floor-fractured crater, is located near the margins of extensive deposits of smooth and intercrater plains that have been interpreted to be of volcanic origin by Robinson et al. [11] and Head et al.[12]. In contrast to fresh impact craters [13], the interior of this crater (Fig. 2B, C) appears highly modified, with the south–southeastern wall slumped inward, wall terraces indistinct and obscured, and the floor of the crater generally appearing shallower than for the fresh example.

The most distinctive parts of the crater interior are two dome-like located on the eastern and western parts of the crater floor. These dome-like features are unlike central peaks in their morphology and position; additionally the crater is too small for the domes to represent peak rings [13,14]. Although it appears to lack floor fractures, and its apparent moat ridge does not have a greater elevation than its rim, this floor-fractured crater appears to be most similar to lunar Class IVB [9,10] craters, as exemplified by the lunar crater Gaudibert (33-km diameter). In addition to morphologic similarities, Gaudibert and this Mercury crater, also occur in close proximity to volcanic plains, supporting the interpretation that floor fractured craters are formed by shallow magmatic intrusions whose laccolith-like structure causes bending and uplift in the overlying crater floor [9,10].

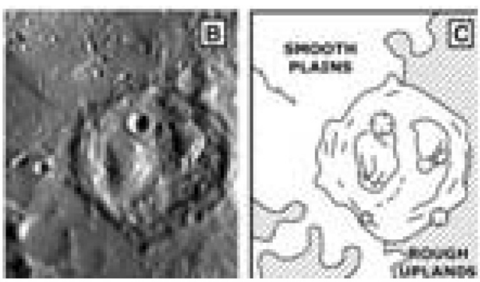

fig 2. (B) Floor-fractured ~ 35-km-diameter crater on Mercury (7.5°N, 104.3°E) (see Head et al. [3]). MDIS NAC image EN0108826977M. (C) Sketch map of major features in (B) showing domes and fractures and proximity to smooth plains. From Head et.al. 2009 [12].

Assessment of Pit-Floor Craters as Shallow Magma Reservoirs: With this interpretation of floor fractured crater formation, the Moon emerges with evidence for at least a few hundred instances of shallow magmatic intrusion where the intrusions lie under crater floors. The question then arises, does Mercury, another heavily cratered terrestrial body, also display evidence for shallow magmatic intrusion? Despite a large crater population [15], and previous assessment of the likely presence of several floor-fractured craters from Mariner 10 data [16], to date only one possible floor fractured crater on Mercury has been reported in MESSENGER data [3].

We have studied the feasibility of this model of magmatic intrusion through dike emplacement as a result of ascending magma overpressurization, and found that subsurface magmatic intrusion forming a magma reservoir is unlikely to be the sole underlying mechanism of crater pit formation. We used order-of-magnitude approximations for compositional parameters [17], the intrusion dimensions modeled from the crater pit dimensions [1], and values comparable to those of other silicate bodies for the material constants, in order to obtain workable guidelines for the initial investigation of this mechanism [18]. Using this model, the theoretical magma over-pressure associated with these crater pits is typically less than that needed to permit common dike propagation into the shallow crust [19]. This result is consistent with the recent work of Wilson and Head [20], who postulated that the mantle and crustal structure of Mercury do not favor small-scale magmatic events, but instead generally favor a smaller number of large-scale massive flooding events from large dikes. This result is supported by the lack of features associated with shallow magmatic intrusion, most notably floor fractured craters, and also small shields and other similar features [11, 12, 21].

This model does not preclude shallow magmatic intrusion on Mercury, but it does suggest that shallow stalling of dikes may arise in more select circumstances, such as in the interiors of impact craters [8]. For example, impact craters can thin the crust and lithosphere and influence the regional stress field, all factors that influence the ascent, stalling and eruption of magma [8]. Furthermore, shallow intrusion and degassing of large dikes can lead to pyroclastic eruptions and volatile venting that might not require the presence of a large shallow magma reservoir [22]. In this scenario, some crater pits could represent pyroclastic events with either explosive or passive degassing of the intruded magma, with the overlying floor subsequently subsiding and forming the observed pits. Head et.al. [22] describe a similar scenario on the Moon in Orientale, wherein a single explosive pyroclasitc event produced an elongated pit, 7.5 km wide by 16 km long. As there is already observed evidence for pyroclastic events on Mercury [4], associated with impact crater floors [4,5,6] the provenance of crater floor pits as subsidence features following a dike emplacement event, volatile exsolution and buildup, but lacking large-scale intrusive magma reservoir should be investigated.

References: [1] J. Gillis-Davis et.al. (2009) *EPSL. 285*. 243-250. [2] J. Gillis-Davis et. al. (2012) *LPSC XLIII*, Abstract #2288.[3] J. W. Head et al. (2008) EPSL [4] L. Kerber et al. (2009) *EPSL, 285*, 263-271. [5] L. Kerber et al. (2009) *Icarus, 206*. 669-684. [6] Gouge et. al. (2012) *LPSC XLIII*, Abstract #1325. [7] L. Wilson and J. W. Head (1981) *JGR, 86*.2971-3001. [8] J.W. Head and L. Wilson (1992) *Geochim.et. Cosmochim. Acta*., *56*. 2155-2175. [9] P. Schultz (1976) *The Moon.15*. 241-273. [10] L. Jozwiak and J.W. Head (2012) *JGR (in revision)* [11] M. S. Robinson et.al. (2008) *Science, 321*. 66-69. [12] J. W. Head et al. (2009) *EPSL, 285.* 227-242. [13] R.J. Pike et.al. (1988) *Mercury, U. of Arizona Press*. 165-273.[14] D. Baker (2012) *LPSC XLIII*, Abstract #1238. [15] Fassett et. al. (2011) *GRL, 38*, L10202. [16] P. Schultz (1988) *Mercury, U. of Arizona Press.* 274-335. [17] L. Wilson and J.W. Head (2008) *GRL, 35*. L23205. [18] A.M. Johnson and D.P. Pollard (1973). *Tectonophysics 18*, 261-309. [19] L. Jozwiak and J. Head (2012) *LPSC XLIII,* Abstract # 2424.[20] L. Wilson and J.W. Head (2012) *LPSC XLIII,* Abstract # 1451. [21] Head et. al. (2011) *Science, 333*, 1853-1856. [22] J.W. Head, L. Wilson, and C.M. Weitz (2001) *JGR, 107*. E1.

MERCURY AS A MEMBER OF THE TERRESTRIAL PLANETS CHAIN WITH REGULARLY CHANGING STRUCTURAL AND COMPOSITIONAL CHARACTERISTICS

G.G. Kochemasov,
IGEM RAS, 35 Staromonetny, 119017 Moscow, Russia. Contact: kochem.36@mail.ru

I. Kepler has shown that all heavenly bodies move in elliptical orbits. After about 100 years I. Newton has shown that the bodies are not simple mathematical points but have certain masses influencing orbits. After about 300 years one now may say that the bodies are not simple structureless masses but have vertical and horizontal structural and compositional characteristics tied to their orbits. The comparative wave planetology [6, 7, 9, 10] deals with these characteristics in relation to orbital characteristics of planetary bodies. Waves warping bodies appear due to keplerian orbits with periodically changing bodies accelerations. Regularly changing bodies characteristics are shown in Fig. 1 & 6, where Mercury's data were predicted before the MESSENGER era [10].

Vesta's convexo-concave shape (Fig. 1, 2) is also a feature (consequence) of the warping fundamental wave present in all bodies, e.g., in Ceres, Earth, Mars.

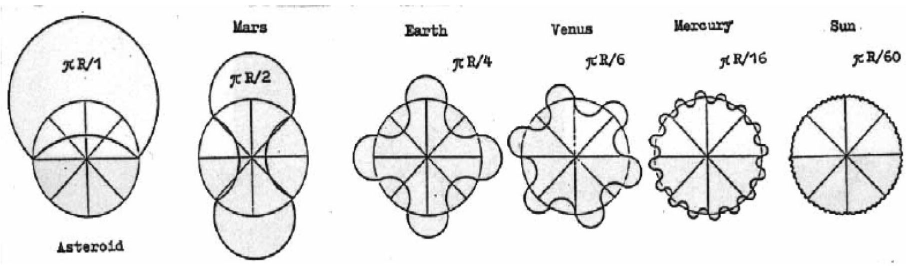

fig. 1. Geometric model of the terrestrial planets (and sun's photosphere) tectonic granulation related to their solar distances

fig. 2. Vesta, south pole, PIA14315

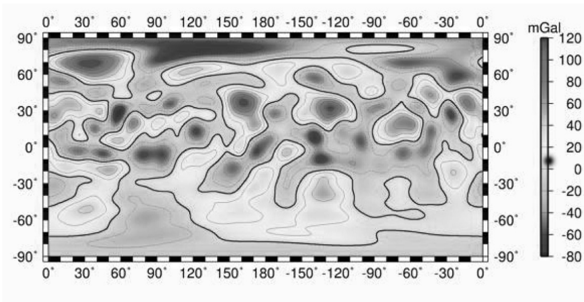

fig. 3. Mercury's gravity [3]. Granules ~500 km across (πR/16)

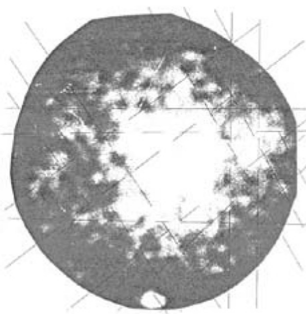

fig. 4. Mercury is covered by dark or bright circles of similar sizes evenly distributed through its surface [1]. It seems that the circles are disposed along not random lines (aligned). This regularity is rather caused by a more regular process than random impacts.

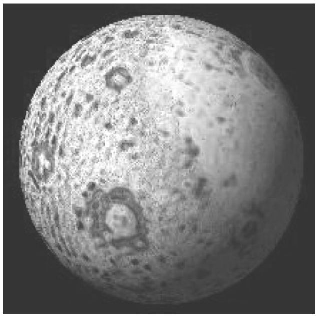

fig. 5. Gravitation anomaly of the Moon measured by by Kaguya mission. Credit: forum. worldwindcentral.com

In 1995 based on available at that time data for terrestrial planets a chart was built (Fig. 6; [10]) connecting them in respect of their chemistry, relief, and tectonic pattern. Mercury before the MESSENGER era has supplied very limited data on these characteristics. Thus, the chart was based mainly on understood regularities of changing cosmic parameters and Mercury as the nearest to Sun planet was assigned in advance as a dull low albedo variations, low relief, tectonically fine grained and with high Mg/Fe in the crust. To justify and explain by a wave interference action its fine tectonic granulation (πR/16) a radar image of its silhouette was used (Fig. 4; [1]). The MESSENGER data later confirm this conclusion providing preliminary results of magnetic, gravity and morphology surveys [2, 3, 8] (Fig. 3). The radar experiment shown very low altitude variations (1-5 km), very smooth surface [4]. X-ray measurements shown very high Mg and low Fe abundances in the crust [5, 15] that was quite a surprise to many planetary scientists but not for us, adherents of the wave planetology. Surprisingly high sulfur content in X-ray measurements of Mercury [5, 11] should be considered as "tails" of intensive degassing [11- 13] (more intensive than in other terrestrial bodies with lesser orbiting frequencies) left on the surface as fumarolic deposits (sulfur rich compounds). An interesting comparison of Mercury with Moon is in Fig.4 & 5: Moon & Mercury having different orbiting periods (29.5 & 88 days) show proportionally different tectonic granules sizes, ~100 & ~ 500 km (πR/60 & πR/16).

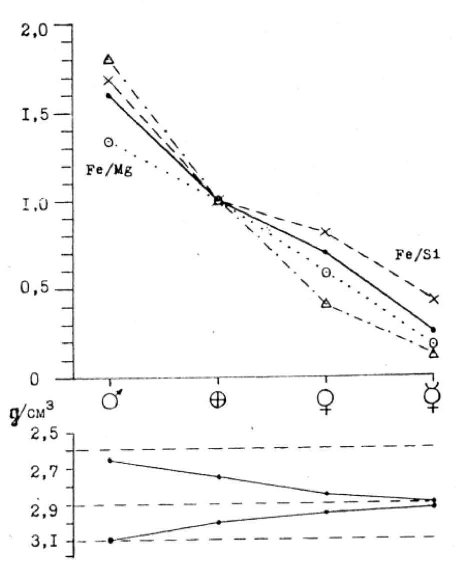

fig. 6. Ratios of some planetary crust parameters compared to the terrestrial ones taken as 1:solid line – relief, dashed line – Fe/Si, dots – Fe/Mg in basalts of lowlands, dot-dashed line – highland/lowland density contrast. Below: increasing highland/lowland density contrast with increasing solar distance [10].

References: [1] Slade, M.A. et al. (1992) Mercury: the radar experiment from Earth // Science, v.258, 635-640.
[2] Johnson C.L., Purucker M.E., Anderson B.J. et al. (2012) MESSENGER observations of Mercury's magnetic field structure // 43rd LPSC, 1355.pdf.
[3] Mazarico E. et al. (2012) The gravity field of Mercury from MESSENGER // 43rd LPSC, 2189 pdf.
[4] Zuber M.T. et al. (2011) Orbital observations of Mercury with the Mercury laser altimeter // EPSC-DPS Joint Meeting 2011, EPSC Abstracts, vol. 6, EPSC-DPS2011-278.
[5] Nittler L.R. et al. (2011) The major-element composition of Mercury's surface from MESSENGER X-ray spectrometry // Science, 333, 1847-1850;
[6] Kochemasov, G. G. (1998) Tectonic dichotomy, sectoring and granulation of Earth and other celestial bodies // "Proceedings of international symposium on new concepts in global tectonics ('98 TSUKUBA)", Tsukuba, Japan, Nov. 1998, p.144-147;
[7] Kochemasov G.G. (1999) Theorems of wave planetary tectonics // Geophys. Res. Abstr., v.1, #3, 700.
[8] Solomon S.C., Klimczak Ch., Byrne P.K. et al. (2012) Long-wavelength topographic change on Mercury: evidence and mechanisms // 43rd LPSC, 1578.pdf.
[9] Kochemasov G.G. (2009) A regular row of planetary relief ranges connected with tectonic granulations of celestial bodies // New Concepts in Global Tectonics Newsletter, # 51, 58-61.
[10] Kochemasov G.G. (1995) Possibility of highly contrasting rock types at martian highland/lowland contact // In: Golombek M.P., Edgett K.S., and Rice J.W.Jr., eds. Mars Pathfinder Landing Site Workshop II: Characteristics of the Ares Vallis Region and Field Trips to the Channeled Scabland, Washigton. LPI Tech.Rpt. 95-01, Pt. 1, Lunar and Planetary Inst., Houston, 63 pp.
[11] McCubbin F.M., Riner M.A., Vander Kauden K.E. et al. Is Mercury volatile enriched or volatile depleted? New insights from combining MESSENGER X-ray , neutron, and gamma-ray spectrometer data //43rd LPSC, 1270.pdf.
[12] Pollack J.B. and Black D.C. (1979) Implications of the gas compositional measurements of Pioneer Venus for the origin of planetary atmospheres // Science, v. 205, #4401, 56-59.
[13] Blewett D.T., Chabot N.L., Denevi B.W. et al. (2012) Spectral and morphological studies of Mercury's hollows // 43rd LPSC, 1329.pdf.
[14] Kochemasov G.G. (2009) On universal tectonic trends of rotating celestial bodies (supertectonics) // New Concepts in Global Tectonics Newsletter, # 50, March 2009, p. 23-34.
[15] Weider Sh.Z., Nittler L.R., Starr R.D. et al. Compositional heterogeneity on Mercury's surface revealed by MESSENGER's X-ray spectrometer // 43rd LPSC, 1472.pdf.

ROLE OF BX IMF COMPONENT FOR THE STRUCTURE OF MERCURY MAGNETOSPHERE

E. S. Belenkaya[1], I. I. Alexeev[1], J. A. Slavin[2],
[1]Institute of Nuclear Physics, Moscow State University, Leninskie Gory, 119992 Moscow, Russia; [2]Department of Atmospheric, Oceanic and Space Sciences, University of Michigan, Ann Arbor, Michigan 48109, USA.
Contact: elena@dec1.sinp.msu.ru

Using a paraboloidal model of Mercury's magnetosphere, we study the magnetospheric magnetic field topology for different orientations of IMF. Special attention is paid to the case of radial IMF. Mercury is the smallest planet in the solar system and it does not have a substantial atmosphere or ionosphere. Mercury is the closest planet to the Sun, and it possesses a week intrinsic magnetic field. Due to these circumstances, IMF plays a major role in the hermean magnetospheric dynamics. Comparison with the better investigated Earth's magnetosphere is fulfilled for clarifying the physical processes (mainly reconnection) existent in the hermean magnetosphere. Except the case of strongly southward IMF, the radial IMF, character to the Mercury environment, also could be connected with the appearance of FTEs. In the last case the quasi-neutral line connected with the FTE generation, is placed in one of the cusps (depending on the sign of BIMFx).

PHOTOMETRIC RELIEF OF THE UNSEEN SIDE MERCURY.

S. G. Pugacheva, V. V. Shevchenko,
Sternberg Astronomical Institute, Moscow State University, Universitetsky 13, Moscow 119992, Russia, sve-pugacheva@yandex.ru

Introduction:

This work presents the results of the researches of the Mercury's surface by photometric method. The basic material for investigations is the cosmic images of the Mercurian surface obtained during the Messenger flyby. According to the data analysis, four main types of relief were distinguished corresponding to different morphological types of the Mercurian surface formations. The purpose of researches is the estimation of the structure of the surface layer of the Mercurian regolith. The Messenger spacecraft launching was held on August 3, 2004. During 6.5 years the craft has overcome more than 7.8 billion km, made 15 revolutions around the Sun, two revolutions around Venus and performed three approaches to Mercury. The orbit of the Messenger spacecraft is highly - elliptical; the height of the spacecraft above the surface at the lowest point is 200 km and more than 15.193 km at its highest point. At the outset of the orbital phase of the mission, the plane of the spacecraft's orbit is inclined 82.5° to Mercury's equator, and the lowest point in the orbit is reached at the latitude of 60° North. The results of the first spacecraft's approach to Mercury on January 14, 2008 were of a great success; sizes of Mercury's visible surface were much more than the ones of the territory, taken by the Mariner - 10 spacecraft (1974-1975) and observed from the Earth. In the second approach on October 6, 2008 pictures of the surface of Mercury's invisible hemisphere were transmitted. Out of 90% of the taken territory, 24% were pictures of the invisible hemisphere. The Messenger spacecraft under other lighting environments and in color considered the planet's surface, previously taken by the Mariner 10. In March 2011, the Messenger spacecraft shot additionally 6% of Mercury's territory and finished survey of the equatorial region of the planet. Mercury's surface area, shot by the Mariner 10 spacecraft and the Messenger spacecraft, is 98% of Mercury's territory.

The data, obtained by the Messenger spacecraft, allowed building a global map of Mercury's geometry, covering more than 90% of the territory, and receive a stereographic image of more than 80% of the territory. Global color map of Mercury has a spatial resolution of 2 km / pixel, and the elevation accuracy of the geometry heights of the northern hemisphere is at average 1.5 m [1].

Photometric relief of different morphological structures:

To study the photometric relief variations of the relief of the Mercury's hemisphere, images of the visible disk of the Mercury were used. Their image was obtained in the recession path section from distances of 27635 km from the center of Mercury (Fig.1).

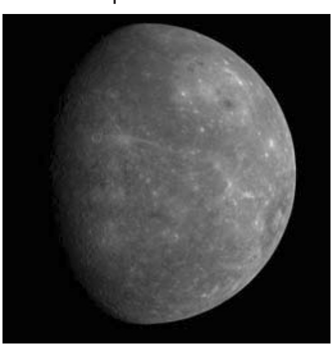

fig. 1. The photo of Mercury's unseen side was taken by Messenger fly 1 departure [1].

The position of the spacecraft in the planetocentric coordinate system was the same: 3.0N and 224.9W. At the time of imaging, the coordinates of the subsolar point were 1.0S, 170W. The image was obtained in a filter with an effective wavelength of 486 nm. The image was digitized and calibrated by means use of the graphic calibration curves.

The histograms of the distribution to the photometric density of the image were calculated. We study morphological relief of the 13 separate areas of the Mercury's surface. The analysis of the present data shows that at least four main types of photometric relief can be distinguished (Fig. 2).

The morphological structures may be represented next types by the heavily cratered terrain (1), the smooth plans (2), and the ejecta terrains of the craters (3), the bright craters and rays (4).

The model of the average integrated lunar indicatrix was used for calibration of the photometric density and calculation of the surface photometric brightness [2, 5, 6].

$$\boldsymbol{\rho} = (\sin \varepsilon \sin A)\, \mathbf{i} + (\sin \varepsilon \cos A)\, \mathbf{j} + \cos \varepsilon\, \boldsymbol{\kappa},$$

The spatial angular function (ρ) is represented by surface described by the current vector in the range of positive values of the angular parameters the angle of incidence of solar rays *i*, the selenocentric value of the reflection angle ε and the azimuthally angle

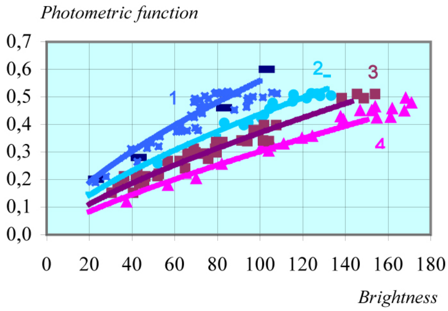

fig. 2. The photometric function of the brightness calculated for difference the morphological structures [2, 3, 4].

A between the planes of incidence and reflection of rays.

The surface structure was obtained from the averaged three-dimensional scattering-phase function correspond to the photometric angular parameters for every type of formation.

The model of Hapke of the bi-directional reflectance was applied to disk-integrated observations of Mercury. The model enables to be determined the structure parameters of the relief from experimental results [7]. The Hapke's theoretical integral phase function involves six parameters: w, B_o, h, θ, and two parameters to describe P(g): b, c. The parameter h characterizes compaction of the regolith and size of the particle. The parameter B_o defines amplitude of the opposition effect. The function P (g) includes two parameters b and c, which determines the phase function form and the nature of scattering (c<0.5 corresponds to forward scattering and c>0.5 to backward scattering). The equation S (θ) allows to calculate the effects of macroscopic roughness on light scattered by a surface having an arbitrary diffuse-reflectance function. The parameter θ is a mean topographic slope angle of the surface. The parameters to Hapke's model were calculated for 4 morphological formations of the Mercury (Table 1). The correlation coefficient varies from 0.944 to 0.972, which indicates a good agreement between of the surface structure and the specified type of photometric relief.

types of the relief.	w	h	B_o	b	c	θ
disk-integrated	0.23	0.09	2.5	0.18	0.15	20°
smooth plans	0.08-0.12	0.070	2.8	0.25	0.18	10°
flat-floored craters	0.10-0.13	0.068	2.6	0.26	0.20	11°
heavily cratered terrain	0.11-0.19	0.062	2.6	0.31	0.25	16°
bright craters and rays	0.19 -0.25	0.057	2.4	0.34	0.29	19°

table 1. Mercury. The photometric parameters of the Hapke's model.

Conclusion:

The analysis of the various data of the integral photometric shows that Mercury's photometric characteristics are indeed very similar to those of the Moon. However studying of the photometric characteristics of Mercury is an actual problem because Mercury has unique physical characteristics. An enormous iron core takes up at least 60% of the planet's total mass - twice as large a fraction as Earth's. Mercury experiences the Solar System's largest swing in surface temperatures, from highs above 700 Kelvin to lows near 90 Kelvin. Mercury's extremely thin atmosphere contains hydrogen, helium, oxygen, sodium, potassium, calcium, and magnesium. Mercury's surface is a combination of craters, smooth, plains, and long, winding cliffs. The darkest plains on Mercury are brighter than their lunar counterparts. The highland/mare albedo ratio is almost a factor of 2 on the Moon; it is only about 1.4 on Mercury. Heavily cratered terrain has approximately the same average albedo as the lunar highlands, and the smooth plains of the Mercury are significantly darker. But Mercury's appearance is blander than that of the Moon. The information about structure and composition of the ejecta can be useful to scientific planning and realization of the future space projects.

References:

[1] NASA's Mission to Mercury http://messenger.jhuapl.edu
[2] Shevchenko V.V. (2004) Astron. Vestn., v.38, n.6, 504-512.
[3] Pugacheva S.G., Shevchenko V.V. (2011) Internation Astronomical Congress "AstroKazan – 2011", 49-52.
[4] Pugacheva S.G., Shevchenko, V.V., (2001) Astron. Vestn., v.35, n. 3, 181-189.
[5] Pugacheva S.G., Shevchenko V.V. (2007) LPS XXXVIII, Abstract #1050.
[6] Pugacheva S.G. (2006) Vernadsky-Brown XXXXIV, Abstract m44-70.
[7] Hapke, Bruce. Space weathering from Mercury to the asteroid belt. // Journal of Geophysical Research. - 2001. -Volume 106.- Issue E5.- P. 10039-10074.

MERCURY STUDIED BY GROUND-BASED ASTRONOMICAL FACILITIES

L. V. Ksanfomality
Space Research Institute of the Russian Academy of Sciences, Moscow, Russia

By space missions as background, a question may arise if there is any sense in continuing Earth-based studies of Mercury and creating images of its surface, when more sophisticated satellite imagery from the Messenger spacecraft is achievable? The most important reason is that Mercury has a strong phase effects (probably stronger than one of the Moon). Because of that, the view of the surface changes completely with the phase of the planet. For example, on space images at the phase of 40--50°, the relief seems to completely “disappear”, and the relief is only visible on the terminator. The main task of Mercury observations in 2006 was to obtain a complete view of the Skinakas Basin [1], which was done on the basis of observations from November 21, 2006 [2]. This day was the most comfortable both in regard to the basin position relative to the terrestrial observer and because of the low position of the Sun above the horizon of the basin.

The views of Mercury in the longitude range 220--355°W, in the phase of 98° (November 21, 2006) have been obtained in advanced processing of electronic images of Mercury. The processing of the first level included stacking of 64 selected original images. The second level processing included stacking of 8 groups of the first level results. In the full processing, about 7800 original electronic images were used.

The images show a position of the planet relative to the Earth, and its surface in the longitude range 220--355°W. The meridian is about 270°W. The periphery of the Skinakas basin is formed by the boundary of the inner rim, which has a relatively regular form. Its width in the meridional direction is 850 km. An annular depression of 1450 km in diameter covers the inner rim. The depth of the depression reaches 2 km.

Literature

1. Ksanfomality, L. The Surface of Mercury in the 210--350°W Longitude Range. Icarus, 2009, V. 200, pp. 367--373.
2. Ksanfomality, L. Study of the Unknown Hemisphere of Mercury by Ground-Based Astronomical Facilities. Solar System Research, 2011, V. 45, pp. 282--297.

ABSTRACTS SUBMITED TO SECTION 3. VENUS

ISKRA-V — A MULTI-CHANNEL DIODE LASER SPECTROMETER EXPERIMENT FOR MEASUREMENT OF SULPHUROUS COMPONENTS IN THE VENUSIAN ATMOSPHERE FROM THE LEVEL OF CLOUDS DOWN TO THE SURFACE DURING DESCENT.

O. Korablev[1], I. Vinogradov[1], M. Gerasimov[1], N. Ignatiev[1], A. Rodin[1], A. Stepanov[1], V. Barke[1], A. Venkstern[1], A. Sapgir[1], M. Zaitsev[1], A. Titov[2], A. Kalyuzhnyy[2], O. Grigoryan[2], G. Durry[3], L. Joly[3], J. Cousin[3], N. Amarouche[4], A. Nadezhdinskii[5], Ya. Ponurovskiy[5], A. Klimchuk[5], *[1]Space Research Institute (IKI), 117997, 84/32 Profsoyuznaya Str., Moscow, Russia; [2]Special Design Bureau of Space Device Engineering of the Space Research Institute, 249100, Tarusa, Kaluga Region, Russia; [3]GSMA, UMR CNRS 7331, Université de Reims, BP 1039, 51687 Reims, Cedex 2, France; [4]Division Technique de l'Institut National des Sciences de l'Univers, CNRS, 92195 Meudon Cédex, France; [5]Prokhorov General Physics Institute, 119991, Vavilov Str., 38, Moscow, Russia. Contact: imant@iki.rssi.ru*

A multi-channel tunable diode laser spectrometer called ISKRA-V (Investigation of Sulphurous Komponents of Rarefied Atmosphere of Venus) has been proposed for retrieving of vertical profile of the Venusian atmosphere composition by realizing measurements on-board the VENERA-D lander at its descent trajectory.

Main work phase of the ISKRA-V experiment will be started at the moment of removing of the lander heat-protection semi-sphere at the altitude of nearly 65 km and will be continued down to the surface touching. Duration of measurements will be defined by the cyclogram of the lander descent, and vertical resolution is expected to be nearly 2 km for 1..2 min duration for one cycle of a full spectra measurement.

A special system of atmosphere sampling will serve for the Gas Chromatogragh – Mass Spectrometer suite and for the ISKRA-V apparatus. For the last case of ISKRA-V, atmospheric portion should be purged from any dust and ice particles, liquid droplets etc. Atmospheric gas sample will be rarefied down to the work pressure of 50 mbar inside the optical cell and pumped out of the cell volume at the end of a measurement cycle. Rarefying ratio will be carefully stored as an important parameter for true retrieving of the out-board atmosphere composition.

For optional measurement sessions of the ISKRA-V apparatus on the surface of Venus, full cycle of spectra measurement will take longer time for better quality of gas sampling, and continuous measurement mode will provide for retrieving of short-time and long-time variations of atmospheric gases contents.

Absorption measurement sensitivity of the ISKRA-V apparatus, featured by a ratio of 10^{-5}, will provide for dynamic range of several orders of magnitude for expected absorption values of a few per cent. Selection of optical path length, providing for output absorption signal level, is possible within 0.3..30 m for each measurement physical channel, individually and once only, during the multi-pass optical system alignment and fixation. High intrinsic spectral resolution $\lambda/\Delta\lambda \sim 10^7$ of diode laser spectroscopy will provide for detailed profiling of molecular absorption lines shape.

Preliminary selection of target molecules of the Venusian atmosphere and of appropriate spectral ranges is the following:

Sulfur dioxide SO_2 — Molecular absorption lines detection is possible near 1380 cm^{-1} with the help of a QCL-laser, emitting at the 7.2 microns range. 30 m of optical path will provide for 90% of absorption at the line maximum at 50 mbar and 300 K. Expected abundance of SO_2 for altitudes of 0..65 km changes from small parts of ppm to more than 100 ppm and is extremely variable at the clouds level.

Carbon monoxide CO, carbon dioxide CO_2, carbonyl sulphide OCS and isotope ratios $^{13}C/^{12}C$ in CO and CO_2, $^{34}S/^{33}S/^{32}S$ in OCS — Molecular absorption lines detection is possible near 2073-2074 cm^{-1} with the help of a QCL-laser, emitting at the 4.82 microns range. Up to 17 m optical path is needed.

Isotopologues of CO_2 and H_2O — There are lot of molecular absorption lines near 2.78 microns, providing for retrieving of ratios $^{13}C/^{12}C$ and $^{16}O/^{17}O/^{18}O$ for CO_2 at 2785 nm, as well as D/H and $^{16}O/^{17}O/^{18}O$ for H_2O at 2783 nm. Same DFB-laser will be used for measurements, being switched between the ranges by its temperature work point change.

CO_2 and H_2O main molecules — There are lot of strong absorption lines near 2.68 microns, and switching between them will be done by the DFB-laser temperature work point change. Some additional strong lines of CO_2 and H_2O may be also used for measurements near 2783 nm (see above).

A monolithic design of the ISKRA-V apparatus might consist of from 2 to 6 DFB-lasers and QCL-lasers, a compact multi-pass Herriott optical cell and a set of individual optical detectors together with drive electronics and necessary peripherals. Atmospheric gas sampling system might be connected with the main measurement unit by appropriate gas, electronics and other needed interfaces.

Earlier spectroscopic simulation studies and development of the inversion program to process the future space data is necessary for effective realization of the ISKRA-V experiment for the VENERA-D mission.

Keywords:

Tunable diode laser spectroscopy, Venusian atmosphere composition vertical profiling, sulphurous components, isotopic ratios.

WATER VAPOUR, CLOUDS, AND THE UV ABSORBER NEAR THE CLOUD TOPS OF VENUS FROM VENUS EXPRESS DATA.

N. I. Ignatiev[1,2], G. Piccioni[3], P. Grossart[4], V. Cottini[5], W. J. Markiewicz[6], *[1]Space Research Institute of Russian Academy of Sciences, Moscow, Russia; [2]Moscow Institute of Physics and Technology, Dolgoprudny, Russia;*
[3]IAPS-INAF, Rome, Italy, [4] LESIA, Observatoire de Paris, Meudon, France; [5]NASA/GSFC, Greenbelt, MD 20771, USA; [6]Max Planck Institute for Solar System Research, Katlenburg-Lindau, Germany. Contact: ignatiev@iki.rssi.ru

Introduction:

Observations of the dayside of Venus with VIRTIS [1] and VMC [2] instruments on board Venus Express have been used to measure the cloud top altitude and water vapour abundance near this level and search for their possible correlation with the UV absorption. An extended analysis of these measurements by Cottini et al. [3] was limited by a northern hemisphere due to geometry of observations on first 1000 orbits of the mission. Further measurements significantly improve the latitudinal coverage and demonstrated symmetric behaviour of clouds and water vapour in both hemispheres. The significant part played by water vapor in the cloud formation, thermal balance and chemistry of Venus atmosphere makes it one of the most important objects for remote sensing studies. Numerous observations have demonstrated high variability of water vapor, which have been attributed to real variability, model errors, and different effective altitude ranges of sounding (see, e.g., a brief review and references in [3]). Recent ground based spectroscopic measurements [4] and those by Venus Express [3, 5] demonstrate a good agreement with, however, some differences, which deserve to be understood better: in particular, temporal variability and absolute values of H_2O abundance measured from different spectral ranges.

Observations:

VIRTIS, the Visible and Infrared Thermal Imaging Spectrometer, is a mapping spectrometer with spectral range from UV to thermal IR: 0.3-5 μm. Its high-resolution subsystem (-H), used in this study, is an echelle grating spectrometer with eight diffraction orders focused on a 270x438 pixel array detector. A complete spectrum, which covers a spectral range from 2 to 5 μm, is thus composed of eight partially overlapped spectra with variable spectral resolution of 1–3 nm. CO_2 and H_2O bands between 2.48 and 2.60 μm in the spectrum of sunlight scattered and reflected by the Venus atmosphere are used to determine the cloud top altitude and water vapour abundance near this level. Background ultraviolet imaging to these measurements is provided by the VIRTIS' moderate resolution mapping subsystem (-M) and VMC, the Venus Monitoring Camera, with the UV channel at 365 nm. A typical track of the VIRTIS-H field of view footprint on the cloud surface during one measurement session (orbit) extends along meridian from one pole to another or covers just a limited latitude range. A detailed description of the measurements, data, model and method of data analysis, and first results are given in [3].

First results:

Results obtained from measurements up to orbit 922 can be summarized as follows [3]. At low latitudes (±40º) mean water vapour abundance is equal to 3±1 ppm and the corresponding cloud top altitude at 2.5 μm is equal to 69.5±2 km. Poleward from middle latitudes the cloud top altitude gradually decreases down to 64 km, while the average H_2O abundance reaches its maximum of 5 ppm at 80º latitude with a large scatter from 1 to 15 ppm. The calculated mass percentage of the sulphuric acid solution in cloud droplets of mode 2 (~1 micron) particles is in the range 75-83%, being in even more narrow interval of 80-83% in low latitudes. No systematic correlation of the dark UV markings with the cloud top altitude or water vapour has been observed.

Recent results:

New measurements (Figs. 1–3) confirmed the first analysis [3] and demonstrated high symmetry with respect to equator in the average cloud top altitudes and water vapour abundances. The amount of water in vapour always exceeds that in cloud particles, indicating that the water vapour abundance near cloud tops is not simply controlled by the equilibrium with the sulfuric acid clouds, but created at this level by other, e.g. dynamical, reasons. The meridional distribution of the water vapour abundance near the cloud tops of Venus is consistent with a combined Hadley and polar cells scheme for the global circulation dynamics.

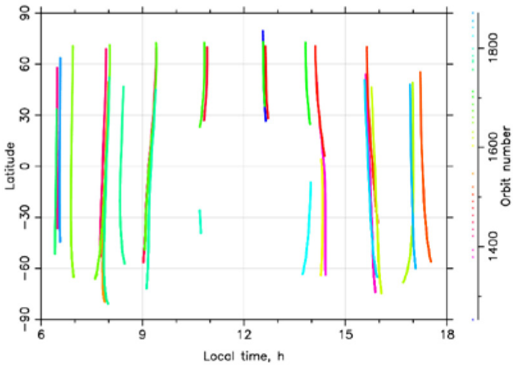

fig. 1. Local time – latitude coverage of VIRTIS-H observations after Venus Express orbit 1000 used in this study. Color coding designates orbit number (right scale).

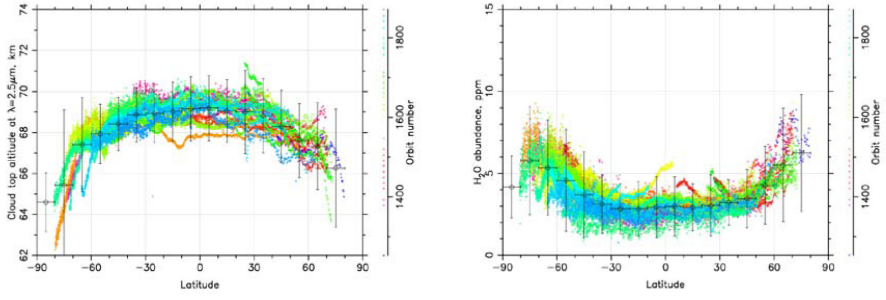

fig. 2. Cloud top altitude (left) and water vapour abundance (right) as a function of latitude for the measurements shown in Fig. 1.

Acknowledgements:
The Venus Express is a mission of the European Space Agency. We thank the Agenzia Spaziale Italiana (ASI) and the Centre National d'Études Spatiales (CNES) for the support and funding of the VIRTIS experiment. We thank all members of the Venus Express project and of the VIRTIS and VMC technical teams. N. I. is supported by the Ministry of Education and Science of Russian Federation grant 11.G34.31.0074, the Russian Foundation of Basic Research grant 12-02-01280, and the Presidium RAS Program 22.

References:

[1] Drossart, P., Piccioni, G., and 29 co-authors: Scientific goals for the observation of Venus by VIRTIS on ESA/Venus Express mission, Planet. Space Sci., Vol. 55, pp. 1653-1672, 2007.
[2] Markiewicz, W. J., Titov, D. V., Ignatiev, N. I., Keller, H. U., and 27 co-authors: Venus Monitoring Camera for Venus Express, Planet. Space Sci., Vol. 55, pp. 1701-1711, 2007.
[3] Cottini, V., Ignatiev, N. I., Piccioni, G., Drossart, P., Grassi, D., and Markiewicz, W. J.: Water vapor near the cloud tops of Venus from Venus Express/VIRTIS dayside data, Icarus, Vol. 217, pp. 561-569, 2012.
[4] Krasnopolsky, V. A.: Spatially-resolved high-resolution spectroscopy of Venus 2. Variations of HDO, OCS, and SO_2 at the cloud tops, Icarus, Vol. 209, pp. 314-322, 2010.
[5] Fedorova, A., Bertaux, J.-L., Marqc, E., Korablev, O., Zykova, A., and Montmessin, F.: Water vapor and the cloud top variations in the Venus' mesosphere from SPICAV observations. EPSC-2012-674.

SULPHUR OXIDES IN VENUS MESOSPHERE DETECTED FROM SPICAV/SOIR VEX SOLAR OCCULTATION

D. Belyaev[1], O. Korablev[1], A. Fedorova[1], F. Montmessin[2], J.-L.Bertaux[2], E. Marcq[2], A. Mahieux[3], X. Zhang[4]
[1]IKI RAS, Moscow, Russia, [2]LATMOS, CNRS/INSU/IPSL, Guyancourt, France, [3]BIRA/IASB, Brussels, Belgium, [4]CalTech, Pasadena, USA;
Contact: dbelyaev@iki.rssi.ru

Sulfur compounds are key components of Venus' atmosphere because this planet is totally covered by H_2SO_4 droplets clouds at altitudes 50-70 km. Any significant change in oxides SO_x above and within the clouds can affect the photochemistry in the mesosphere.

New measurements of sulfur dioxide (SO_2) and monoxide (SO) in the atmosphere of Venus by SPICAV / SOIR instrument onboard Venus Express orbiter provide powerful statistics to study the behavior of gases above Venus' clouds. The instrument (a set of 3 spectrometers) is capable to sound atmospheric structure above the clouds at several regimes of observations (nadir, solar and stellar occultations) either in UV or in near IR spectral ranges. In this paper we present results from solar occultations in the ranges of SO_2 absorption (190-230 nm, 4 μm) and SO (190-230 nm). The dioxide was detected by spectrometer SOIR at altitudes 65-80 km in the IR and by spectrometer SPICAV at 85-105 km in the UV. The monoxide's absorption was measured only by SPICAV UV at 85-105 km. In the lower layer (65-80 km) SO_2 mixing ratio varies around 0.02-0.5 ppmv, and in the upper layer (90-105 km) it increases with altitude from 0.05 to 2 ppmv, while $[SO_2]/[SO]$ ratio is around 1 to 5.

This work was supported by the grant of the Russian academy of sciences Presidium Program 22: "Fundamental problems of research and exploration of the Solar system".

TWENTY FOUR HOURS WATCH ON VENUS SURFACE

A. P. Ekonomov,
IKI RAN, Profsoiusnaia 84/32, Moscow, RF, Contact: alekonomo@yandex.ru

The new concept of thermal insulation:

The appearance of long-lived station (LLS) should be qualitatively different from the landers like Venera 9-14. Venera landers were not designed for the lifetime of more than 2 hours on the surface. Covered with thermal insulation from the outside, they reached the critical temperature after a couple of hours on the surface. Then outer insulation became useless.

There was an idea to develop a thermal insulation for the LLS weighing 100 kg, so that it could survive on the surface of Venus for about 24 hours.

Magnification of a lifetime at surfaces on the order and more demands cardinal change of LLS design.

The necessary changes include the following:
1. spherical pressure vessel will be in direct contact with the atmosphere and must withstand the thermodynamic conditions at the surface (T = 500 ^{0} C, P = 100 bar) for unlimited time,
2. inside the pressure vessel two layers of insulation should be located:
a) a layer of high temperature insulation to protect from thermal radiation adjacent to spherical pressure vessel,
b) a layer of low-temperature thermal insulation to protect from usual thermal conductivity,
3. the heat flux penetrated through insulation must be effectively absorbed with phase change material (PCM) at a temperature of about 50 ^{0}C, which is admissible for electronics.
All of these elements individually known, but their quantitative combinations is other than for the Veneras whose task is to survive on the surface of a couple of hours. For the LLS mass fraction of the thermal protection system is much higher.

LLS computer simulation

LLS was computer-simulated , adopted the following parameters:
- LLS total mass is 100 kg.
- Outer diameter of the titanium spherical pressure vessel is 0.6 meters
- Diameter of a core at the center is about 0.3 m
- The core is protected by a layer 13 cm thermal insulation on the basis of the glass microspheres with conductivity of 0.016 W / m* K.

The core contains 20 kg heat sink of the phase change material, the melting temperature at 50 ° C. The descent scenario in the atmosphere must repeat of Venera series. Equipment heat generation is limited to 3 Watts. Modeling in the Simulink permit performance of such LLS for 27 hours, including 26 hours on the surface.

The design scheme in the Simulink reflects the basic thermal processes during the descent and while on Venus surface.

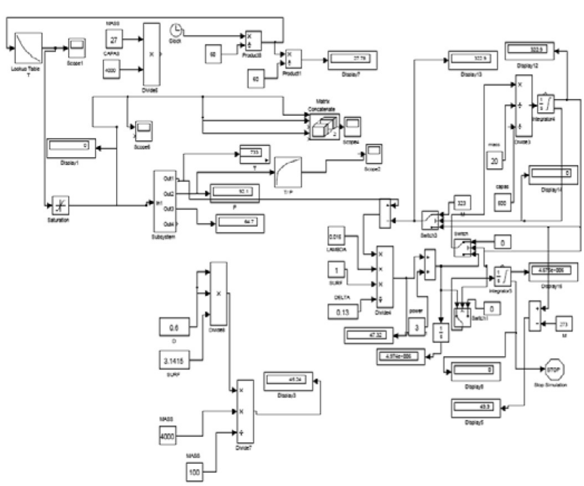

Fig. 1.The design scheme of the thermal regime of long-lived plant on the surface of Venus.

CIRCULATION OF MESOSPHERE OF VENUS AT CLOUD TOP LEVEL ACCORDING TO RESULTS OBTAINED FROM VENUS MONITORING CAMERA (VMC) ONBOARD VENUS EXPRESS.

I.V. Khatuntsev[1,2], M.V. Patsaeva[1,2], D.V. Titov[3], N.I. Ignatiev[1,2]; W.J. Markiewicz[4];
[1]Space Research Institute (IKI), Russian Academy of Sciences, Moscow, Moscow, Russia; [2] Institute of Physics and Technology, Dolgoprudny, Russia; Moscow, Russia; [3]ESA/ESTEC, PB 299, 2200AG Noordwijk, The Netherlands; [4]Max-Planck-Institute for Solar System Research, Max-Planck-Str. 2, 37191 Katlenburg-Lindau, Germany
khatuntsev@gmail.com

6 years of permanent monitoring of the Venus' cloud layer by the ESA spacecraft Venus Express (VEx) provided the opportunity to study dynamics of various mesospheric layers. UV images provided by the VMC allowed studying the circulation at the top cloud layer.

The polar orbit of Venus Express provides optimal conditions for observations of the Southern hemisphere. Observations at ascending arc of the orbit also allow zooming on the planet. Imaging conditions change from global view of the planet with resolution of ~50 km/ px at apocentre to close-up snapshots with resolution of few kilometers.

Total duration of the entire data set of VMC UV images wind-tracked at this moment covers 2232 orbits that correspond to more than 9 Venus years. We analyzed 120 orbits with manual cloud tracking and 555 orbits with digital correlation method. Total number of wind vectors derived in this work is ~40000 for manual tracking and ~385000 for digital method.

Average zonal and meridional wind profiles have been calculated, and vector fields of wind velocities in latitude-time coordinates have been built. In low latitudes the mean retrograde zonal wind at the cloud top (67±2 km) is about 90 m/s with a maximum of ~100 m/s at 40-50ºS. Poleward from 50ºS the zonal wind quickly fades out with latitude. The atmospheric rotation period at the cloud top has a maximum of about 5 days at equator, decreases to ~3 days in the middle latitudes and stays almost constant poleward from 50ºS. The mean poleward meridional wind slowly increases from zero value at equator to about 10 m/s at 50ºS. Poleward from this latitude, the absolute value of the meridional component monotonically decreases reaching zero at the pole. The error of an individual wind measurement is 10-15 m/s. The wind speeds of 70-80 m/s were derived from near-IR images at low latitudes.

During more than 9 years of the Venus Express observations the mean zonal velocity was in the range of 85-100m/s that is in general agreement with the earlier results. The VMC observations indicated a long term trend for the zonal wind speed at low latitudes to increase. VMC UV observations also showed significant short term variations of the mean flow. The velocity difference between consecutive orbits in the jet region could reach about 30 m/s, thus indicating vacillation of the mean flow between jet-like regime and solid body rotation at mid-latitudes.

Fourier analysis revealed periodicities in the zonal circulation at low latitudes. Within the equatorial region, up to 35S, the zonal wind velocity oscillates with a period about 4.83 days which is close to the super-rotation period at the equator. The zonal wind speed oscillates with a period of 4.1-5 days and amplitude of 4-17 m/s.

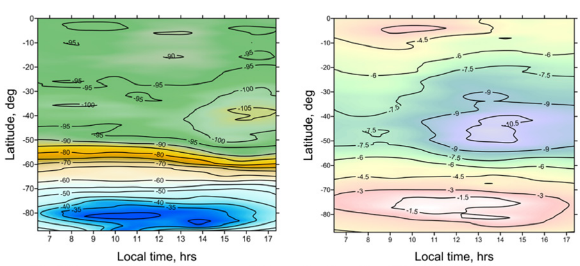

fig. 1. Diurnal variations of the mean zonal (left panel) and meridional (right panel) wind components

The VMC observations showed a clear diurnal pattern of the mean circulation (Fig.1). The zonal wind demonstrated semi-diurnal variations with minimum speed close to noon (11-14 h) and maxima in the morning (8-9 h) and in the evening (16-17 h). The meridional component clearly peaks in the early afternoon (13-15h) at ~50S. The minimum of the meridional wind is located at low latitudes in the morning (8-11h).

OSCILLATION OF RADIO SIGNAL PARAMETERS NEAR THE LOWER BOUNDARY OF THE VENUS IONOSPHERE

A.L. Gavrik, Yu.A. Gavrik, T.F. Kopnina, E.A. Kuleshov.
Kotel'nikov Institute of Radio Engineering and Electronics, Russian Academy of Sciences, Fryazino branch, V. A. Vvedensky sq, 1, Fryazino, Russia. Contact **:** *alg248@ire216.msk.su*

Introduction:

By now more than 900 occultations of the Venus ionosphere and atmosphere have been carried out by the planet orbiters. The altitude profiles of electron concentration and atmospheric density, and laws that determine behavior of the ionosphere and atmosphere under solar radiation have been obtained. However, many questions related to the dynamics of atmosphere-ionosphere system require new information, which can be obtained by a modern analysis technique of occultation data.

The objective of the present study is to obtain new information about the Venus ionosphere using conservation of the adiabatic invariant during occultation experiment analyzing two coherent signals transmitted by the "Venera-15" and "Venera-16" orbiters.

Data and Results:

The diagnostic method of layered structures determines conditions under which the adiabatic invariant is conserved for a wave packet propagating in an inhomogeneous planetary envelope. To test the method, we used recorded digital data of signal field amplitude for radio waves 32 and 8 cm transmitted by the "Venera-15", "Venera-16" orbiters and received by the ground-based station. At this point, precise determination of the intensity and frequency of the coherent signals not only provides verification of the theoretical relationship, but also allows reliable separation of plasma, atmosphere, and noise effects in the radio probing results. The underlying principle of interpretation of radio occultation data allows us to simultaneously analyze transformation of the signal parameters in plasma and in the neutral medium; also, it is well adapted to the problems of detecting stratified oscillations of the refractive index in the atmosphere-ionosphere system and does not involve integral transforms, which restrict the sensitivity of remote methods to small variations in the refractive index of the medium.

The application of the diagnostic method shows that the characteristics of the vertical profile of the refractive index obtained within a short period of time (~1 min), when a radio beam is moving, may be indicative of a wave activity near the lower boundary of the Venus ionosphere. We have found that a wave process of unknown nature caused a perturbation in the atmosphere-ionosphere system and formed a vertical periodic structure consisting of stratified layers of thickness ~6 km at altitudes of 65…115 km. The periodic variations of the refractive index leaded to oscillations of the radio signal intensity and frequency modulation of the probing signals. The periodic oscillation of the radio wave parameters most clearly manifested itself in the lower ionosphere. In the lower region of the ionosphere, about ~30 km, the amplitude of the signal intensity oscillation increased by a factor of about 3 when a radio beam with wavelength of 32 cm was shifted upward. Increase in the amplitude of the periodic oscillations of the signal parameters indicates wave nature of the perturbations of the electron density. The report discusses prospects of applying the method in the project "Venus-D".

Acknowledgements: The work is partially supported by the program No.22 of the RAS Presidium "Fundamental problems of the research and exploration of the Solar system".

REANALYSIS OF THE BISTATIC RADAR DATA OF VENERA-9,10, AND 15,16 SATELLITES.

A.G. Pavelyev[1], S.S. Matyugov[1], A.I. Zaharov[1], O.I. Yakovlev[1],
[1]FIRE RAS, Vvedenskogo sq. 1, Fryazino, 141190 Russia Contact: *alxndr38@mail.ru*

Bistatic radar experiments have been provided during the Venera-9,10 (1975), and Venera 15,16 (1983) satellites missions using circular polarization and downlink radio-communication at wavelength 32 cm. Measurements of the surface micro-relief roughness, bistatic radar reflectivity and dielectric permittivity have been carried out. Investigation of the refractive properties of the Venus atmosphere: the bending angle and refractive attenuation of radio waves at small elevation angle have been fulfilled. Maps of the distribution of bistatic reflectivity were obtained. Five regions disposed in the equatorial area (1975) and two regions are located near the North Pole of Venus (1983). Reanalysis of the bistatic radar data have been provided with aim to compare with the results of Venera-15,16 and Magellan SAR, Magellan and Venus-Express bistatic missions. Polarization measurements made in the mountain regions during the bistatic radar Magellan and Venus - Express missions, possibly, indicated the effect of changes in the surface conductivity of Venus. High-elevation anomalous reflectivity detected during Magellan and Venus Express bistatic radar missions revealed heighten values of the surface conductivity near Cleopatra Patera and broadly over Maxwell Montes at 13 cm wavelength, consistent with a semiconducting surface material. In contrast to Magellan and Venus - Express missions, bistatic Venera-15,16 experiments were carried out in two lowland areas located in the polar region of Venus. The bedrock of these areas may have a common origin with the ground of the nearby Maxwell mountain. The bistatic reflection coefficient changes by 2-4 times relative an expected level in the Northern areas. The origin of these variations may be connected with changes in the surface conductivity. Areas with heighten conductivity correspond to significantly lower values of reflectivity in the bistatic radar measurements at grazing directions of observation with circular polarization. Comparison of the bistatic radar reflectivity maps indicates high level of reflections from the flatland parts of the Venus surface which correspond to dark areas in the monostatic SAR radar images. Regions with extremely low surface roughness have been revealed. RMS of relief elevations in the plain regions varies from 0.4-0.6 degrees to 1.9-2.5 degrees on the horizontal distance of the order of a few hundred meters. There are some features on the reflectivity maps. Some of these features may correspond to a long-scale slopes in the range 2° to 8°. Corresponding values of relief heights are contained 0.5 to 1.5 km. The features are found within the region (in the venerocentric IAU system): -26.5° to -25.0° latitude and 220.0° - 239.2° longitude. One area was revealed with heighten values of permittivity in the range 6.5-7.5, and ground density between 2.7 and 2.9 g/cm^3. The center of this area is located at -23.5° latitude and 230.4° longitude. The extent of this region is 80 km. The results of measurements of the refractive angle and the refractive attenuation of radio waves allow finding the radio physical parameters of the boundary layers of the Venus atmosphere. The refractive angle is changing in the interval 4° to 8°, these magnitudes about 10 times greater than corresponding values in the Earth's atmosphere. The refractive attenuation is about of 10 db (about 6.5 times greater than in the Earth's atmosphere). Comparison of the bistatic data results with results of monostatic and bistatic radio locations provided by use of the Soviet, USA, and Venus Express missions indicates good correspondence. Comparison of the bistatic radar data obtained in the U.S. and in Russia shows promising applications of bistatic method to study the surface conductivity of Venus.

The work was partly supported by Program 22 of Presidium of Russian Academy of Sciences and by grant of Russian Fund of Basic Research No.10-02-01015-a.

SIMULATION OF THE VENUS IONOSPHERIC RADIO OCCULTATION EXPERIMENT WITH THE PARABOLIC DIFFRACTION EQUATION

Ilyushin, Ya.A.[1] **Gavrik, A.L.**[2]
[1]Physical Faculty Moscow State University 119992 GSP-2 Lengory Moscow Russia ilyushin@physics.msu.ru [2]Fryasino branch of the RAS Institute of Radiotechnics and Electronics

Astract: We have used direct simulation of occultation signal using a numerical calculation of the parabolic diffraction equation to analyze variations of signal intensity and phase along the line of trajectory of Venus satellite during an occultation experiment. As a result we have proved the linear relationship between variations of frequency and intensity of the signal deformed by regular spherically symmetric ionosphere. It is shown that correspondence between energy and non-energy parameters of a sounding radio wave proves reliability of the result obtained from inversion of the occultation data.

Introduction: Radio occultation technique is applied for the atmospheric and ionospheric investigations since Mariner-4 interplanetary mission to Mars in 1965 [1]. These experiments drew attention of the radio science community to theoretical research of the radio waves propagation in the planetary gaseous environments. Quite soon the general formulae for the radio occultation data inversion, based on the geometrical optics (GO) approximation and the local spherical symmetry assumption, have been derived [2]. Since that, the radio occultation method proved to be very effective tool for the planetary [3] and terrestrial atmospheric investigations. Simultaneously, these experiments showed a need for more detailed theoretical analysis of the variations of the sounding radio wave field parameters. During further progress in this field, new sophisticated approaches for investigations of the fine atmospheric and ionospheric structure have been proposed. Application of these approaches in practice requires significant improvement of the ratio between the effects under investigation and instrumental errors. These errors, which are largely related to the limited stability of the local oscillator onboard the spacecraft, can be reduced, and the informative variations of the signal phase on the ionospheric path can be increased with the decrease of the sounding signal frequency . However, too large distortion of the lower frequency signal in the inhomogeneous plasma can result in the inapplicability of the geometrical optics approximation, on which the data interpretation techniques [2] are based.

Motivation of this study is the validation of the geometrical optics approximation for the radio occultation data interpretation on the lower frequencies with the direct simulation of the wave field in the Venusian ionosphere by the numerical solution of the parabolic diffraction equation and comparison with the experimental results of the interplanetary space missions Venera-15 and Venera-16.

Approaches and techniques: To increase the radio link potential in the planetary radio occultation experiment, the powerful signal can be transmitted from the Earth and received and analyzed onboard the spacecraft. If a high directive ground-based antenna is used for the transmission, at distances of tens millions kilometer a spot about half a million kilometer in diameter is illuminated with almost homogeneous flat monochromatic decimeter of meter wave. Ionosphere is assumed to be a stationary spherically symmetric refractive medium (plasma) with the smooth vertical density profile The receiver moves across the field of the wave, perturbed by the inhomoheneous ionosphere, and registers the intensity and phase variations of the received signal. The deformation of the field increases with the distance from the ionospheric limb to the spacecraft. At large distances, the effects of diffraction on the small scale ionospheric structures accumulate and the multi-ray field structure can be formed, which complicates the interpretation of the registered wave parameters.

While large scale inhomogeneities of the ionosphere cause significant variations of the amplitude and phase of the monochromatic sounding wave, diffraction on the irregularities of smaller scales can also make important contribution in the wave field. To account for all these effects, direct numerical solution of the parabolic diffraction equation with the finite difference scheme [4] can be used for the wave field simulations.

The complex amplitude of the wave in the 0.25 - 1.5 m wave length range have been calculated on the verticals x=const at the distances 10^3−10^4 km from the limb of the planet. As the model of the refractive medium profile the realistic occultation profile of the Venusian ionosphere from October 14, 1983, has been taken. The 32 cm receiver carried by the spacecraft Venera-15 was at 10^4 km from the ionosphere, the vertical velocity of the ray perigee was 6 km per second. The electron concentration profile N(h) was calculated with the known data inversion technique within the geometrical optics approximation. However, the refraction intensity variation X(h) registered in the experiment indicates the threefold increase of the wave intensity. This means that the receiver was close to the multi-modal propagation region, where the geometrical optics applicability criteria can be violated, so the results of the inversion of the vertical ionospheric profile N(h) can be incorrect.

The correspondence of the immediately registered X(h) with the refractional attenuation X(h) calculated from the observed Doppler frequency shift can be considered as a practical criterion of the validity of the solution technique of the inverse problem for N(h). This conclusion follows from the linear relation between energetic and frequency signal parameters was derived for the spherically-symmetric medium:

$$X(t) = 1 + \lambda L_1 V^{-2}\, df(t)/dt \quad ,$$

where λ is the sounding wave length, L_1 - distance from the spacecraft to the planetary limb, V = dh/dt is the vertical component of spacecraft velocity, f(t) is the deviation of the signal frequency caused by the inhomogeneous ionosphere. This formula establishes the relation between the energetic parameter X(h) and non-energetic parameter f(h). Good agreement between the attenuation $X_f(h)$ calculated from frequency with observed X(h) has been registered in many occultation events. It is worth investigating situations, where the equality $X(h) = X_f(h)$ is violated due to the signal distortions arising from multi-modal propagation and wave diffraction.

Numerical simulations: The results of numerical simulations confirmed linear relation between the measured signal intensity and its frequency deviation in the radio occultation sounding of the spherically symmetric ionosphere by the monochromatic high-frequency wave. Calculations have shown that reliable determination of the function $X_f(h)$ is possible only in absence of the multi-modal propagation and diffraction effects. However, the fluctuations of $X_f(h)$ due to these effects appear before notable distortions of X(h) and f(h). Consequently, correspondence of X(h) and $X_f(h)$ in realistic measurements can be regarded as a practical criterion of the GO applicability. This criterion can be used for data validation in the radio occultation data processing and analysis.

In the focusing regions, there is a fourfold increase of the signal intensity, so there is a doubt in the geometrical optics validity. However, presented results of the analysis of the diffraction effects shows that the correspondence $X_f(h)$ and X(h) is a reliable criterion of the geometrical optics. The discrepancy of the functions X(h) and $X_f(h)$ do not exceed instrumental errors of the measurements. Thus, in these occultation events geometrical optics applicability criteria have been met, and the retrieved vertical profiles N(h) are not corrupted by the diffraction effects.

Conclusions and remarks: Numerical simulations of the radio occultation experiments of the Venusian ionosphere, accounting for the diffraction effects, have been carried out. Validation of the experimental data, previously obtained from the interplanetary space missions Venera-15 and Venera-16, is performed. Applicability of the geometrical optics in the focusing regions with the nearly fourfold increase of the signal intensity, which took place in real experiment, has been shown.

Acknowledgements: The work is partially supported by the program No.22 of the RAS Presidium “Fundamental problems of the research and exploration of the Solar system”.
The authors thank the administration of the Scientific Research Computing Center of the Moscow State University for granting the access to the computational resources of the parallel computing system SKIF-GRID “Tchshebyshev”.

References:

Kliore, A., Cain, D. L., Levy, G. S., Eshleman, V. R., Fjeldbo, G., Drake, F. D., 1965. Occultation experiment: Results of the first direct measurement of mars’s atmosphere and ionosphere. Science 149 (3689), 1243-1248.

Phinney, R. A., Anderson, D. L., Mar. 1968. On the Radio Occultation Method for Studying Planetary Atmospheres. J. Geophys. Res.73, 1819.

Armand, N. A., Gulyaev, Y. V., Gavrik, A. L., Efimov, A. I., Matyugov, S. S., Pavelyev, A. G., Savich, N. A., Samoznaev, L. N., Smirnov, V. M., Yakovlev, O. I., 2010. Results of solar wind and planetary ionosphere research using radiophysical methods. Physics-Uspekhi 53 (5), 517-523.

Ya.A. Ilyushin Fluctuations of the GPS signals on the tangential paths in the lower terrestrial atmosphere: influence of the small-scale structure. Journal of Atmospheric and Solar-Terrestrial Physics 70 (2008) 1863-1869.

THE SEISMIC RESEARCH PROGRAM FOR VENUS LANDING STATION

O.B. Khavroshkin, V.V. Tsyplakov

Classes of Scientific research tasks.

1.Tectonic activity and deformation by solar tides. 2.Venus seismic activity. 3.Internal structure. 4.Volcanic activity. 5.Structure of a micro seismic field and seismic noise. 6. Mechanical and acoustic characteristics of a ground. 7.Other peculiarity of land place.

Methods and Instruments apply for decisions of tasks (1-7).

1. Registration of seismic acoustic emission, micro seismic fields etc.

The equipment: 3-th axial componential seismometer established on Venus surface or surface of landed shock-proof tor balloon. Seismometer can function on temperature condition ~500 C^o. Common weight - (mechanical system + electronics block inside station) - 0,8 kg;
Consume power - 50 mW; Dimensions-10x10x10 sm;Mode of functioning – event recorded, i.e. on excess of a signal on an input in system. The 1-axial high-frequency seismometer established either inside station, or outside of; dump in shockproof variant in separate micropenetrator is possible. Common weight - a seismometer + electronics - 0,250 kg; together with micropenetrator, a radioisotope power source and local telemetry - 3,0 - 3,5 kg; overloads disasseleration - 3.000 g.Consume power ~ 10 mW.
2. Research of properties of a ground. Installation of several send-receive electric and ultrasonic sources in a ground part of a landing ring in weight - 0,05 kg.
3. Research correlation between wind and seismic noise.

About instruments in more detail

1. Creation of 3-D seismometer with next general parameters:
a).Weight – 0.1-0.3kg;
b).Size ~diameter-3-7sm; lengh-3-10sm;
c).Deceleration-<$10^4 g_E$;
d).Temperature of working-700-900K;
e).Sensetivity-10^{-10}sm (in displacement) .
The creation of that seismometer is really in present time.
2. The creation of the high sensitivity seismometer (look below)
3. The creation of the small high velocity penetrator with next general parameters:
a). Velocity of shook on the Venus day surface-500-1500m/s;
b). Range of the deceleration-10^3 -$10^4 g_E$;
c).Weight-1.0-10kg;
d).General sizes: length-0.5-1.5m; diameter-5-10sm;
e).Load: telemetric systems; battery; scientific instruments-seismometer, temperature probe and electric probe.
4. <u>For future.</u> The creation of new electronic systems which possibility works in next surround conditions:
a).Temperature- 700K;
b).Pressure- 100atm (kg/sm^2);
c).Shock resistence-1000 g_E ;
First step is creation of the amplifier.

Seismic features of Venus

Winds. A solar wind. Acoustic radiation.

Besides surface of Venus it was possible to measure speed of winds - about 13 km /h. They are rather weak however they can move small particles of sand or particles similar to them. At the big heights there are stronger winds. At height approximately 50 km from a surface the atmosphere of Venus has four-day the period of rotation. It refers to as superrotation of an atmosphere. At height of 45 km were marked movings winds with speed of 175 km /h and also strong vertical movements of gas were found out. The probes which are carrying out researches of Venus have brought the data which were deciphered as the certificate of presence of lightnings.

All types of winds and streams of an atmosphere are accompanied by vortex formation and radiation of acoustic waves. One of the most powerful generators of waves is a solar wind. American automatic station “pioneer - Venus-1” has found out in the top layers Venus ionospheres (up to 250 km) very fast streams of the ions flying with speed 2−4 km/s. Streams fly from the day time side of Venus to night through terminator which is the line separating the covered side of a planet from dark. Accordingly current have determined as a stream through the terminator. In 1986 Mexican geophysic Actor Peres de Tekhada has shown that the angular moment of this stream is equal to the angular moment, which solar wind loses in vicinities of Venus. So the stream through terminator arises because of viscous friction of a solar wind about an ionosphere of a planet. It is experimentally established that speed of a stream in terminator on a decline on 2 km / with more than on dawn. Both supersonic streams which are bending around a planet through a decline and dawn, meet on the night side thus giving rise to strong turbulence and shock waves. Due to that on the dark side of a planet streams with different speeds, the shock waves extending in a direction of rotation of a planet collide and arises more. Being distributed in depth of an atmosphere the wave disseminates the energy as heat and transfers an atmosphere quite certain angular moment.

On the basis of supervision scientists have established that the capacity lost by a stream of ions is equal $8{,}48*10^{10}$ Wt. Thermal capacity which dissipate because of movement of all atmosphere on the order is less - $1{,}4*10^{9}$ Wt. The same order there can be a capacity lost by a stream on acoustic radiation. Therefore energy hight atmosphere ions quite can not only support rotation of an atmosphere but also create an acoustic field. By other estimations transfer of energy from collision of two ionic streams in an atmosphere is accompanied by the most powerful sound waves with a level 84dB about 0.001Wt/m^2 that for the areas about several square kilometers makes already 10^3 Watt. As density of an atmosphere at a surface and regolith of Venus differ less, than on the order losses of acoustic waves at their transformation in seismic will not exceed tens persents.

Active seismicity on Venus

1. Excitation of seismic waves on Venus is possible pulse source (PS) representing the activator of seismic fluctuations on the basis of electromagnetic machines of shock action created in the West Siberian Branch of the Russian Academy of Science. Processes of interaction PS with a ground are well described in the monography « Research of the Earth by not explosive seismic sources » under Nikolaev A.V. edition (N.A.Britkov's page 228-234 etc.). PS it is submitted on Fig 1. Results of tests PS are submitted on Fig 2.

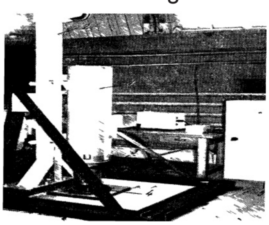

fig. 1. Source of seismic impuls

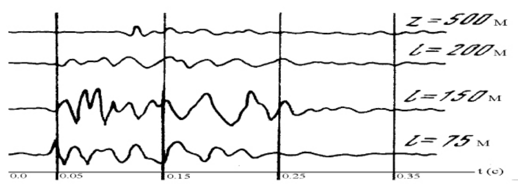

fig.2. Seismogram froms PS

On Venus thus as oscillatory weight the weight of all station (~ 100kg) can be used. During tests PS for the Earth, at injected in 1100J. seismic energy was equal to energy 280J. It is very high efficiency η ~ 0.25. If on Venus to begin to rock 4J. that at preservation of efficiency η ~ 0.25 we shall receive 1J seismic energy which will allow at sensitivity of a seismometer 10-10m in a range of frequencies from units up to tens hertz to receive the information on seismic speeds and existence of borders from kilometer depths of a surface of Venus.

2. Other opportunity of active seismic experiment with Venus is energy of a landing of station of Venus and its transfer to seismicity. Estimating this energy at the rate of Mст ≈ 100kg., speed of landing Vст ≈ 10m/s, η ~ 0.25 under the formula

$$W_c = \frac{MV^2}{2}\eta$$

Substituting we shall receive above mentioned parameters *Wc* = 1200 J. It is rather high energy allowing to receive reflections from Moxo border. Many thanks for discussion to Victor A. Vorontsov (Lavochkin Association).

3. Even for active seismic experiment with Venus it is possible to use siren on droping from a balloon a ballast (an atmospheric cylinder). Doubtless advantage siren is excitation of sound waves in a narrow range of frequencies *Δfs* about 10Hz. Taking into account high density Venus atmospheres the factor of transition of sound energy in seismic should be high enough $K_{s.e.}$ ~ 0.5. Reception of a seismic signal also is carried out in the same narrow range of frequencies. Estimating power opportunities сирены as a ballast in weight of M = 1kg, with flight H = 1000m atmospheres, g = 0.9 m / ß2 we shall receive: E_{imp} = MgH ≈ 900 J. *Wc* ≈ 450J. It also will allow to appear through Venus crust.

IMPACT CRATERS OF THETIS REGIO (V36 QUADRANGLE), VENUS.

E. N. Guseva[1], A. T. Basilevsky[1], J. W. Head[2],
[1]Vernadsky Institute, RAS, Kosygin str., 19, 119991 Moscow, Russia; [2] Department of Geological Science, Brown University, Providence, R.I. 02912, USA. Contact: Guseva-Evgeniya@yandex.ru

Introduction: The V36 quadrangle (Thetis Regio, 25°S-0°N, 120°-150°E) in the equatorial part of Venus is being mapped as a part of the USGS project of 1:5,000,000 geologic mapping of Venus (Basilevsky, Head, 2008; Guseva et al., 2011, 2012). In this mapping effort 13 material and 3 structural units have been identified and their relative age relationship established. In the present study we consider the question of the relations of impact craters of this area with non-crater geologic units. In the study area are observed and mapped materials of 16 impact craters with diameters from 4.25 to 38.1 km: the centers of 15 craters are in the study area and 1 crater is only partly within it. According to the practice of crater-related areal studies we consider only those 15 craters whose centers are in the area. Based on the presence/absence of an associated radar dark halo, a characteristic that is considered an indication of crater age (Arvidson et al., 1992; Izenberg et al., 1994; Basilevsky, Head, 2002a; Basilevsky et al., 2003), craters have been subdivided into two age units: older C1 - with no halo and younger C2 – with a halo (Table). Figures 1-4 show examples of the C1 and C2 craters.

Results: The 15 craters of the V36 quadrangle have been studied in terms of the geologic units on which they are superposed and the structures that deform them. The results of this analysis are presented in the following Table.

	crater name	lat	lon	dia., km	geol.age	superposed on	deformed by
1	Khelifa	-1,52	129,85	10,8	C1	tt(?), ttt	ttt ridges /grooves
2	Whiting	-6,06	127,99	35,7	C1	tt(?), ttt	ttt ridges /grooves
3	unnamed	-1,53	134,45	7,5	C1 (?)	pm	rt single fractures
4	Jutta	0,0	142,66	7,0	C1(?)	psh-pm	rt single fractures
5	Parishan	-0,2	146,50	6,8	C1	psh-pli	pli fractures
6	Gilmore	-6,67	132,75	21,3	C1	tt(?), ttt	ttt ridges /grooves
7	Winnemucca	-15,4	121,06	30,3	C1	ttt-psh	ttt ridges /grooves
8	Jumisat	-15.1	135,62	7,5	C1	rt	rt fractures
9	Larisa	-18,4	131,11	4,25	C2	pli	not observed
10	Mariko	-23,3	132,90	11,5	C2	rt	rt fractures
11	Janina	-2,03	135,67	9,3	C2	pm-rt	rt fractures
12	unnamed	-0,71	138,28	7,5	C2	pm	not observed
13	unnamed	-1,72	138,57	6,5	C2	pm	not observed
14	Badarzewska	-22,6	137,20	29,6	C2	pli	rt fractures
15	Halle	-19,8	145,53	21,5	C2	pwr2	rt single fractures

Basilevsky et al. (2003) studied 853 craters on Venus ≥5 km in diameter (89% of the total crater population of Venus). They found that for craters >16 km in diameter, those with clear parabolic and non-parabolic haloes (corresponding to our unit C2) compose about half of the subpopulation while craters with a faint halo and or having no halo (corresponding to our unit C1) compose the other half. This 50:50 percentage was considered as evidence that craters with clear halos represent the younger 50% of the crater time sequence while craters with a faint or no halo represent the older 50%. The total life time of the observed craters was considered to be roughly equal the mean age of the Venus surface T (that is 0.5 to 1 Ga; McKinnon et al., 1997), so it was concluded that craters with a clear halo have an age <0.5T, while craters with faint or no halo - >0.5T. For craters <16 km in diameter the proportions were found to be different: those with clear halos compose ~1/3 of the subpopulation while craters with faint halos and having no halo compose ~2/3. Correspondingly the first ones are considered to represent the younger 1/3 of the crater time sequence while craters with faint or no halos represent the older 2/3 and the age of the first ones is <1/3T, while the age of the second ones is >1/3T.

As it is seen in the Table, among the 15 craters of the V36 quadrangle, unit C1 is represented by 8 craters and unit C2 - by 7. Of these 15 craters 10 have diameters smaller and 5 craters larger than 16 km. Among those smaller than 16 km, 5 craters represent C1 and 5 – represent C2. Among craters larger than 16 km, 3 craters represent C1 and 2 - C2. Considering the meaning of the interpreted age of the 15 craters we may conclude that 5 of them are younger than 1/3T, 2 – younger than 0.5 T, 5 - older than 1/3 T and 3 – older than 0.5T. So it appears that the 15 craters of the study area form a time line rather similar to that of the total Venus crater population.

Let us consider on which geologic units these craters are superposed. From the earlier analysis by Basilevsky and Head (2002b), generally supported by recent work of Ivanov and Head (2011), it was found that if one were to designate the mean surface age of Venus as T, on the global scale the time duration from the end of formation of tesserae terrain (tt) until the time of wrinkle ridging of regional plains (pwr) was about 0.1-0.2T so their age is from T to ~1.1-1.2T, while the units postdating wrinkle ridging were emplaced within the time period from T until present. Among the V36 geologic units preceding the wrinkle ridging with superposed craters on them there are tessera transitional terrain (ttt), shield plains (psh) and regional plains (pwr). The post-wrinkle ridging units of the area with craters on them are mottled plains (pm), lineated plains (pli) and rifted terrain (rt). On the units of the first group are superposed 5 craters, 4 – C1 and 1 – C2. On the units of the second group are superposed 10 craters, 4 – C1 and 6 – C2. This can be interpreted as an indication that the geologically older units (tt, psh and pwr) compared to the geologically younger ones (pm, pli, and rt) have the noticeably larger absolute age and that among the geologically younger ones dominate those which were emplaced within the last 1/3T of the geologic history of Venus.

Let us consider which structures deform the studied craters. It is seen from the Table that the geologically most ancient structures (ttt ridges and grooves) deform only the C1 crater, 3 craters with diameter >16 km and thus having an age >0.5T, and one crater with diameter <16 km and thus having an age >1/3T. Among other structures deforming the craters, rt-faults dominate and pli-faults are closely similar. These deform both C1 craters (3 cases) and C2 craters (7 cases). The latter observation suggests that the rifting in the study area occurred during the last last 1/3T although the earlier rifting episodes can not be excluded.

Conclusions: The above analysis shows that the relative age sequence of the mapped units established through photogeologic mapping generally agrees with the estimates of absolute ages based on the degree of preservation of the radar-dark haloes of the craters superposed on the units and cut by the different structures. The rifting of the study area was active during the last 1/3T although earlier rifting episodes could also have occurred.

References:

Arvidson R.E., Greeley R., Malin M.C., Saunders R.S., Izenberg N., Plaut J.J., Stofan E.R., and Shepard M.K. (1992), Surface modification of Venus as inferred from Magellan observations of plains, *J. Geophys. Res.,* 97, 13,303-13,317.

Basilevsky A.T., Head J.W. (2002a) Venus: Analysis of the degree of impact crater deposit degradation and assessment of its use for dating geologic units and features. *J. Geophys. Res.*, v. 107, E8, 10.1029/2001JE001584, 5-1 – 5-38.

Basilevsky A.T., Head J.W. (2002b) Venus: Timing and rates of geologic activity. *Geology* 30, No 11, 1015-1018.

Basilevsky A.T., Head J.W. (2008) Geologic mapping of the V-36 Thetis Regio quadrangle: 2008 Progress Report. *Abstracts of the Annual Meeting of Planetary Geologic Mappers*, Flagstaff, AZ, NASA/CP-2008-215469

Basilevsky A.T., Head J.W., Setyaeva I.V. (2003) Venus: Estimation of age of impact craters on the basis of degree of preservation of associated radar-dark deposits. *Geophys. Res. Lett.*, v. 30, 18, 1950 doi:10.1029/2003GL017504.

Guseva E.N., Basilevsky A.T., Head J.W. (2011) Geological mapping of the eastern part of quadrangle V-36: Thetis Regio. Venus. *LPSC-42,* abs. 1350.

Guseva E.N., Basilevsky A.T., Head J.W. (2012) Photogeologic mapping of the Thetis Regio quadrangle (V-36), Venus. *LPSC-43*, abs. 1384.

Ivanov M.A., Head J.W. (2011) Global geological map of Venus. Planet. Space Sci. 59. 1559–1600

Izenberg N. R., Arvidson R. E., Phillips R. J. (1994) Impact crater degradation on Venusian plains, *Geophys. Res. Lett.*, 21, 289– 292.

McKinnon W.B., Zahnle K.J., Ivanov B.A., Melosh, H.J. (1997) Cratering on Venus: Models and observations,
in Bougher, S.W., et al., eds., *Venus II—Geology, Geophysics, Atmosphere, and Solar Wind Environment:* Tucson, University of Arizona Press. 969–1014.

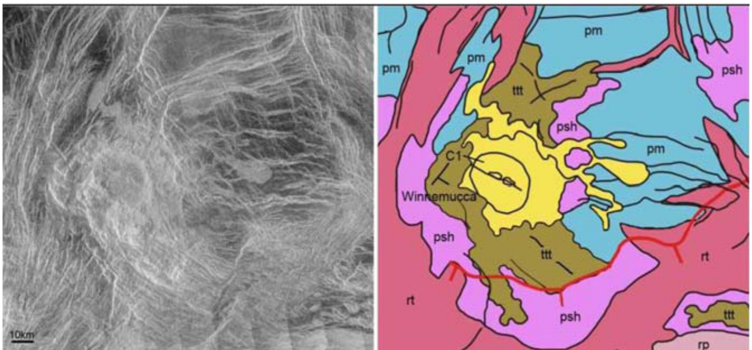

fig. 1. Crater Winnemucca (15.3 S, 121.0 E), D=30.3 km, C1. Left - Magellan SAR image, right - geologic map.

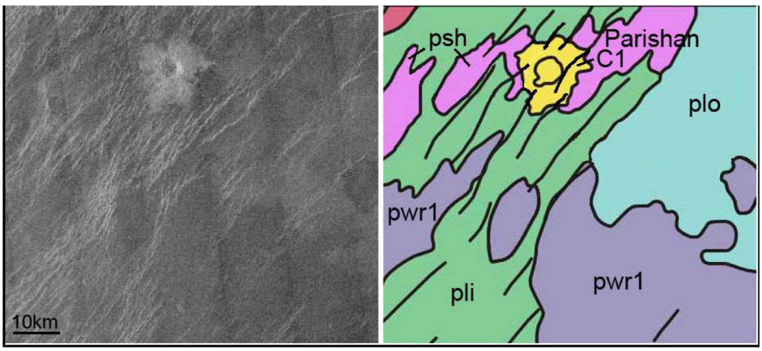

fig. 2. Crater Parishan (0.2 S, 146.5 E), D=6.8 km, C1. Left –Magellan SAR image, right - geologic map.

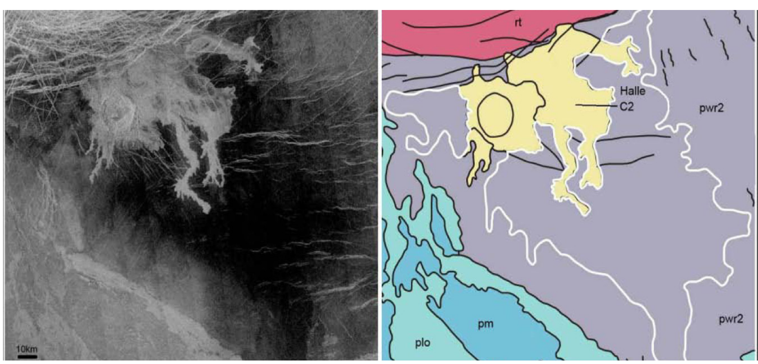

fig. 3. Crater Halle (19.8 S, 145.5 E), D=21.5 km, C2. Left –Magellan SAR image, right - geologic map.

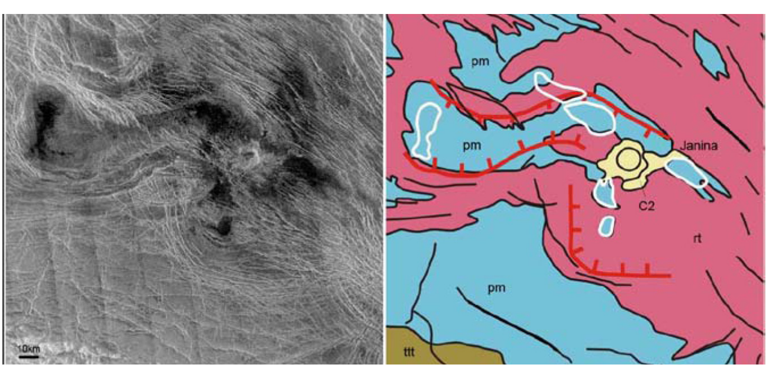

fig. 4. Crater Janina (2.03 S, 135.6 E), D=9.3 km, C2. Left - Magellan SAR image, right - geologic map.

DERIVATION OF ATMOSPHERIC WAVE PARAMETERS FROM INDIVIDUAL MAGELLAN RADIO OCCULTATION RETRIEVALS OF VERTICAL TEMPERATURE PROFILES IN THE VENUS' ATMOSPHERE

V. N. Gubenko, I. A. Kirillovich, A. G. Pavelyev, V. E. Andreev, R. R. Salimzyanov

It is well known that internal gravity waves (IGWs) affect the structure and mean circulation of the Earth' middle and upper atmosphere by transporting energy and horizontal momentum upward from the lower atmosphere. The IGWs modulate the background atmospheric structure, producing a periodic pattern of spatial and temporal variations in the wind velocity, temperature and density. Similar effects are anticipated for the Venus since IGWs are a characteristic of stably stratified atmosphere. For instance, Yakovlev et al. (1991) and Gubenko et al. (2008a) used the radio occultation (RO) data from Venera 15 and 16 missions to investigate the thermal structure and layering of the Venus' middle atmosphere. They noted that a wavelike periodic structure commonly appears in retrieved vertical profiles at altitudes above 60 km in the atmosphere where the static stability is large. Through comparisons between Magellan RO observations in the Venus' atmosphere, Hinson and Jenkins (1995) have demonstrated that small scale variations in retrieved temperature profiles at altitudes from 60 to 90 km are caused by a spectrum of vertical propagating IGWs. There is one general problem inherent to all measurements of IGWs. Observed wavelike variations may alternatively be caused by the IGWs, turbulence or persistent layers in the atmosphere, and it is necessary to have an IGW identification criterion for the correct interpretation of obtained results.

In this context, we have developed an original method for the determination of internal gravity wave parameters from a single vertical temperature profile measurement in a planetary atmosphere (Gubenko et al., 2008b, 2011). This method does not require any additional information not contained in the profile and may be used for the analysis of profiles measured by various techniques. The criterion for the IGW identification has been formulated and argued. In the case when this criterion is satisfied, the analyzed temperature fluctuations can be considered as wave-induced. The method is based on the analysis of relative amplitude thresholds of the wave temperature field and on the linear IGW saturation theory in which amplitude thresholds are restricted by dynamical (shear) instability processes in the atmosphere. When the amplitude of an internal wave reaches the shear instability limit, energy is assumed to be dissipated in such a way that the amplitude is maintained at the instability limit as the wave propagates upwards. An application of the developed method to the RO temperature data has given the possibility to identify the IGWs in the Venus' atmosphere and to determine the magnitudes of key wave parameters such as the intrinsic frequency, amplitudes of vertical and horizontal perturbations of the wind velocity, vertical and horizontal wavelengths, intrinsic vertical and horizontal phase (and group) speeds, kinetic and potential energy, vertical fluxes of the wave energy and horizontal momentum. The obtained results of internal wave studies in the Venus' atmosphere deduced from the Magellan temperature profiles are presented and discussed.

This work was partially supported by the program of the RAS Presidium #22 and the RFBR Grant 10-02-01015-a.

References:

Gubenko, V.N., Andreev, V.E., and Pavelyev, A.G.: Detection of layering in the upper cloud layer of Venus northern polar atmosphere observed from radio occultation data, J. Geophys. Res., 113, E03001, doi:10.1029/2007JE002940, 2008a.

Gubenko, V. N., Pavelyev, A. G., and Andreev, V. E.: Determination of the intrinsic frequency and other wave parameters from a single vertical temperature or density profile measurement, J. Geophys. Res., 113, D08109, doi:10.1029/2007JD008920, 2008b.

Gubenko, V. N., Pavelyev, A. G., Salimzyanov, R. R., and Pavelyev, A. A.: Reconstruction of internal gravity wave parameters from radio occultation retrievals of vertical temperature profiles in the Earth's atmosphere, Atmos. Meas. Tech., 4, 2153-2162, doi:10.5194/amt-4-2153-2011, 2011.

Hinson, D. P., and Jenkins, J. M.: Magellan radio occultation measurements of atmospheric waves on Venus, Icarus, 114, 310– 327, 1995.

Yakovlev, O. I., Matyugov, S. S., and Gubenko, V. N.: Venera-15 and -16 middle atmosphere profiles from radio occultations: Polar and near-polar atmosphere of Venus, Icarus, 94, 493-510, 1991.

BALLISTICS AND NAVIGATION SUPPORT FOR THE VENERA-D MISSION

V. A. Shishov[1], V. A. Stepaniants[1], A. G. Tuchin[1], S. M. Lavrenov[2],
[1]Keldysh Institute of Applied Mathematics, Russian Academy of Sciences, Moscow, Miusskaya Sq.,4, Russia; [2]Moscow State Institute of Electronics and Mathematics (Technical University), Moscow, Bol. Trechsvyatitelskij per., 3, Russia. Contact: {shishov,stepan,tag,sml}@kiam1.rssi.ru

The project Venera-D is supposed to deliver the orbital spacecraft (SC), the descent module (DM) and the subsatellite to Venus. The targeting doctrine for bringing the SC to Venus has to provide with specified angle to enter the SC to the Venus atmosphere. Besides there should be provided with radio vision constraints from on-ground tracking stations and illumination conditions. The first and the second orbital corrections give brining the SC to Venus with prescript accuracy. The second orbital correction is carried out four days prior to the rendezvous with Venus. Then the DM detaches from the base SC and carries on flying autonomously. The base SC after fulfilling the second correction does the withdrawal maneuver to provide the transmission on the outgoing hyperbola with preassigned inclination (90◦) and pericenter height (250 km). With all that the SC should be at the minimum distance from Venus by four hours earlier than the DM would reach its atmosphere. At the DM atmosphere entry moment the base SC should connect with it and retranslate telemetry data to the Earth.

The report presents the count results for window starts on the time span from 2020 to 2026. There are determined power characteristics of flights and selected optimal windows. There are given results of calculations for the DM destination areas on the Venus surface. Various variants of the subsatellite separation from the base SC are considered. These variants are distinguished by orbit periods. And the question of the SC motion determination in the Venus artificial satellite orbit is considered as well.

SO_2 MONITORING ABOVE VENUS' CLOUDS USING VEX/SPICAV-UV NADIR OBSERVATIONS

D. Belyaev[1], E. Marcq[2], F. Montmessin[2], J.L. Bertaux[2], A. Fedorova[1],
[1]Space Research Institute (IKI), Moscow, Russia (dbelyaev@iki.rssi.ru);
[2]LATMOS/UVSQ/CNRS, Guyancourt, France.

SO_2 in the upper atmosphere of Venus is an important tracer of (i) its recent (within 10 million years) geological activity, (ii) the chemistry and photo-chemistry of sulphur-bearing species, including H_2SO_4-H_2O underlying clouds and (iii) general circulation of the atmosphere bringing SO_2-rich air up to levels where photo-chemical destruction occurs. The first monitoring, using Pioneer Venus and ground-based data, showed a two order-of-magnitude decrease from 1980 to 1995 [Esposito et al., 1988]. Latitudinal variations were also constrained in the early 1990s, and exhibited an increasing observable SO_2 column density with increasing latitude [Zasova et al., 1993; Na et al., 1994]. Measurements of SO_2 have resumed since 2006 mainly thanks to SPICAV/SOIR instrument on-board Venus Express, and first studies showed an opposite latitudinal gradient as well as relatively high SO_2 abundance, comparable to the early 1980s [Belyaev et al., 2008; Marcq et al., 2011].

Here we show the results for the 2007-2010 epoch, using an improved version of Marcq et al.'s (2011) model able to cope with non-nadir observations. Strong variability is observed within short (daily) timescales, but there is evidence for two distinct regimes, the most frequent being identical to the situation in 2006 already published (rather high abundances, negative latitudinal gradient), but starting in late 2009, a new regime very similar to the situation during the early 1990s (low abundances, positive latitudinal gradients) has been observed, alternating with the common regime within a few Earth months. Simple modelling suggests that fluctuations in the general circulation and/or sporadic change in SO_2 below 65 km may cause the alternation between both regimes.

This work was supported by the grant of the Russian academy of sciences Presidium Program 22: "Fundamental problems of research and exploration of the Solar system".

References:

Esposito et al., JGR 93 (1988).
Zasova et al., Icarus 105 (1993).
Na et al., Icarus 112 (1994).
Belyaev et al., JGR 113 (2008).
Marcq et al., Icarus 211 (2011).

ABSTRACTS SUBMITED TO SECTION 4. MARS

POLYGONS ON MARS: TOPOGRAPHY DETAILS RECOVERED FROM IMAGES WITH THE IMPROVED PHOTOCLINOMETRY METHOD.

N. V. Bondarenko, I. A. Dulova, Yu. V. Kornienko,
Usikov Institute of Radiophysics and Electronics, National Academy of Science of the Ukraine, 12 Ak. Proskury, Kharkov, 61085, Ukraine Contact: bndr@kharkov.ua

Introduction:

Polygonally patterned ground is widely observed on high latitudes of Mars. Polygons at the Phoenix landing site are ~4 m across, their slopes are gentle (a few degrees), their typical topography amplitude is a few tens of centimeters, and they are superimposed on other geologic landforms, including larger 20–25 m polygons [1]. Morphology and sizes of polygons vary widely over high-latitude terrains on Mars; their morphology has a strong latitudinal zonality, but regional variations are also observed [2, 3]. Formation of the polygonal pattern is usually thought to be initiated by thermal contraction cracking of ice-rich soil, however, the details of the polygon formation and evolution are highly controversial and are a subject of debates [1, 4 and references therein]. Their understanding is a key for deciphering recent climate change on Mars. Detailed morphometry of the polygons can give important constraints on the mechanism of their formation and evolution. The polygons are much smaller than the resolution of laser altimeter MOLA; their topographic amplitude of a few tens of centimeters is at the principal margin of relative vertical accuracy of photogrammetric topography reconstruction with HiRISE stereopairs [5]. The only class of methods useful for quantitative morphometry of small polygons with available remote sensing data is photoclinometry with HiRISE images.

In the present work we show examples of relief reconstruction for the part of polygonally patterned surface in the vicinity of Phoenix landed site based on improved photoclinometry from images taken by HiRISE camera onboard MRO spacecraft.

The method:

The method of improved photoclinometry [6] is based on the accurate mathematical formulation of the problem in the frame of statistical approach. The method allows calculation of the most probable surface height variations based on available images. The height accuracy depends on the noise level of image registration.

The method uses known dependence of the surface facet brightness on its orientation and includes as a first step calculation of topography slope fields from available images. After that [6] the problem solution leads to the Poisson equation with the boundary conditions stated that at the area boundary the normal component of calculated heights gradient should to be equal to the normal component of slopes derived from initial image (Von Neumann condition).

The improved photoclinometry is the most mathematically rigorous. It gives the most probable surface relief in contrast to widely used approach firstly proposed by Van Diggelen [7] (for example, [8]),which in its formulation is a mathematically incorrectly posed problem (as shown in [6]).

Topography reconstruction:

We used small areas (128×128 m) from MRO HiRISE images PSP_008591_2485 and PSP_008855_2485 of Martian surface. Sampling of these images is ~25 cm per pixel, their resolution (the minimal distance between resolvable objects) is about 1 m. Initial images used for relief reconstruction are shown in Fig.1a and Fig. 1b. They have been obtained at the following incidence (illumination azimuth) angles: 48.80° (261.01°) and 51.18° (272.57°), respectively. Directions of surface illumination are shown with arrows in Fig. 1a, b. The difference in illumination azimuth angles is equal to 11.56°. It is rather small (at the best observational conditions for the purposes of relief reconstruction this difference should be > 60° [9]), nevertheless it gives some information about second component of heights gradient.

For calculations of surface heights gradient we adopted Lambert law as an a priori known photometric function of the surface. The surface albedo was considered to be constant over the surface and equal to 0.2. Surface slopes (along the line of illumination) gave variations between -11.45° to 11.37° with slope standard deviation equal to 2.68°.

Results of relief reconstruction using the improved photoclinometry method are presented in Fig. 1c and Fig. 1d as elevation with respect to the mean surface level. Large scale topography of the surface area under study is shown in Fig. 1c. General slope of the surface in the frame of ~1 m is seen. Troughs on the surface marked with purple dash line appear as depressions in Fig. 1c. Here large polygons having sizes in the range of 20 – 60 m can be recognized.

Distribution of small-scale polygons in the area of the study is shown in Fig. 1d as heights deviation from the large-scale surface topography (Fig. 1c). Sizes of these polygons vary between 3 m and 6 m. Trough depths appear to be from ~20 cm to ~40 cm. It is consistent with in situ observations by Phoenix [1].

Conclusions:

The use of the improved photoclinometry method for relief reconstruction from images shows reasonable topographic information. The method allows calculation of the most probable surface topography based on available images, resolution of calculated relief is restricted only by resolution of images used. The method can be recommended for systematic automated morphometric studies of small-scale features on the surface with remote observation data.

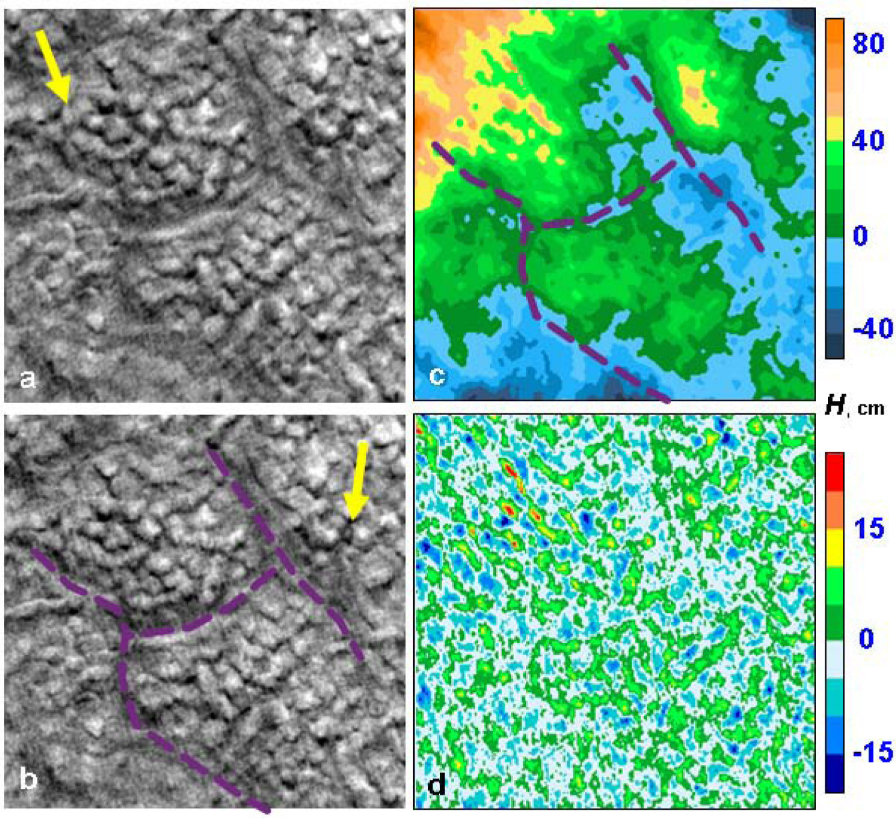

fig. 1.

References:
[1] Mellon, M. T., M. C. Malin, R. E. Arvidson, M. L. Searls, H. G. Sizemore et al. (2009), J. Geophys. Res., 114, E00E06, doi:10.1029/2009JE003418.
[2] Mangold, N. (2005) Icarus 174, 336-359.
[3] Levy, J., J. Head, and D. Marchant (2009) J. of Geophys. Res. 114, E01007.
[4] Levy, J. S., D. R. Marchant, and J. W. Head (2010) Icarus 206, 229-252.
[5] Kirk, R. L., E. Howington-Kraus, M. R. Rosiek, and the HiRISE team (2007), 7th International Conference on Mars, Lunar and Planet. Inst., Pasadena, Calif., 9 – 13 Jul.
[6] Dulova I. A., Yu. V. Kornienko, and S. I. Skuratovskiy (2008) Telecommunications and Radio Engineering, 67 (18), 1605-1620.
[7] Van Diggelen, J. (1951) Netherlands Astron. Inst. Bull., Vol. 11, pp. 283-289.
[8] Lohse V. et al. (2006) Planetary and space science, Vol. 54, pp.661-674.
[9] Skuratovsky, S. I., I. A. Dulova, Yu. V. Kornienko, N. V. Bondarenko (2005) Abstracts of papers 42 Vern.-Br. Microsymp. on Planetology, Moscow, Abstract № m42_61.

THE PROPORTION AND DISTRIBUTION OF MARTIAN IMPACT EJECTA IN THE REGOLITH OF PHOBOS.

K. R. Ramsley[1,2], J. W. Head[2],
[1]School of Engineering, Brown University, Box D, Providence, RI, USA. [2]Department of Geological Sciences, Brown University, Box 1846, Providence, RI, USA. (Kenneth_Ramsley@brown.edu)

Introduction: Samples of the regolith of Phobos are expected to contain fragments of martian crustal material that are launched to Phobos from impact cratering events on Mars [1, 2, 3]. The distribution of martian material in the regolith of Phobos is governed by a process of regolith gardening that is similar to the regolith gardening process on the Earth's Moon. Lunar gravity traps and returns most impact ejecta back to the surface of the Moon, whereas martian gravity traps ejecta from Phobos in martian orbits and returns most of this back to the surface of Phobos [4].

While trapped in orbits of Mars, ejecta fragments from Phobos are size-sorted by orbital perturbation forces. Smaller Mars-orbiting particles among the ejecta from Phobos are more readily influenced by orbital perturbations and tend to seek new orbits that no longer intersect the orbit of Phobos, whereas larger fragments are less readily perturbed and tend to re-collide with Phobos soon after ejection from Phobos. Particles that are smaller than ~300 μm are particularly susceptible to changes in orbital eccentricity and unless they re-accrete immediately onto Phobos they are typically expelled to interplanetary space or de-orbited to the martian atmosphere through a combination of factors that include solar radiation photon pressure and the planetary oblateness of Mars [5, 6]. The lifetimes of Mars-orbiting ejecta from Phobos range from several hours for fragment sizes < ~1 μm, to thousands of years for fragments > ~300 μm [5]. The deposition of a thick regolith on Phobos that buries surface features over geologic time [8, 9] suggests an ejecta re-accretion process where most ejecta from Phobos return to Phobos. Compared to lunar regolith, the orbital size-sorting process is also likely to produce regolith on Phobos that is characterized by proportionately fewer grains with sizes < 300 μm.

The gravitational parameter of Phobos (GM = $0.7127 \pm 0.0021 \times 10^{-3}$ km^3/s^2) [8] results in surface escape velocities from Phobos ranging from ~4 to 10 m/s (depending on the latitude, geographic elevation and local time of the launch site on Phobos) [4, 11] (**Fig.1**). The low gravitation of Phobos immediately retains less than 1% of the material that is produced from initial impacts whereas > 99% exits from Phobos at local escape velocities [12]. Ejecta fragments > ~300 μm that are launched from Phobos at escape velocities that do not escape from the gravity of Mars or collide with the atmosphere of Mars tend to re-accrete onto Phobos during subsequent generations of re-collision impacts [7]. Re-collision velocities from all initial impact sources (martian ejecta and solar system meteoroid projectiles) range from a minimum of ~4 m/s to a velocity that equals the local orbital escape velocity from martian gravitation (~0.7 km/s to ~5 km/s depending on the geographic latitude and local time of the previous impact launch site on Phobos). Due to the mechanics of orbital intersections, the exposure to re-collision impacts is located on the opposite hemisphere of Phobos from the previous impact site. Re-collision impacts produce multiple generations of Mars-orbiting ejecta that launch from Phobos with decreasing distributions of ejection velocities. The Mars-orbiting component of the ejecta re-accretion process concludes once all secondary ejecta from Phobos launch with velocities that are less than the local escape velocity from Phobos.

In addition to ejecta that collide with Phobos from martian impacts, solar system meteoroid (SSM) projectiles deliver a mass flux to Phobos that is ~200X greater than the mass flux of secondary impact ejecta from Mars. SSMs also arrive at Phobos with velocities that are ~10 to 15 km/s [13] compared to typical arrival velocities from martian secondary ejecta that are 2 to 3 km/s [14]. Consequently, SSM projectiles produce a total impact *energy* flux at Phobos that is approximately 1,000X greater than the impact energy flux from martian secondary impact ejecta.

The distribution of fragments of material ejected from Mars that land on Phobos over geologic time will be regionally homogenized and indistinguishable as discrete units on the basis of the following three factors: 1) the entire surface of Phobos is carpeted with high-energy SSM impacts during long periods between martian ejecta events (>10,000 years between Mars-impacting projectiles >100 m [15]), 2) ejecta from Phobos travels in multi-generational martian orbits prior to final re-accretion, and 3) re-colliding ejecta tend to arrive on opposite hemispheres of Phobos from their previous impact ejection sites. We assess these factors in this study.

Method: To compute the proportion of martian material in the regolith of Phobos, we first observe that Mars and Phobos are exposed to the same solar system meteoroid (SSM) impact flux. Mars absorbs SSM projectile energy and re-launches a small portion of this energy in the form of ejecta that intersects with Phobos in orbit. We define the proportion of martian ejecta that is deposited into the regolith of Phobos as the ratio of martian ejecta mass flux that impacts Phobos divided by the SSM mass flux that impacts Phobos. With this proportion constrained, we refer to the observed SSM fragment bulk concentration in lunar regolith data to estimate the specific percentage of martian ejecta fragments in the regolith of Phobos. Where the flux rate of martian ejecta mass that impacts Phobos is ~1/200 of the flux rate of SSM projectile mass, the proportion of ejecta fragments from martian material in the regolith of Phobos should be ~1/200 of the mass of the SSM fragments.

Several key parameters play a role in computing the exposure of Phobos to impact ejecta. Impact cratering events on Mars that are sufficiently large to produce ejecta with martian escape velocities (also crossing the orbit of Phobos) are predicted to equal to 3% of the original SSM projectile mass that collides with Mars [16]. This appears to be a low ejecta production rate; however Mars is a much larger target for SSM flux than Phobos and proportionately there are many more SSM impacts on Mars than on Phobos (3.6×10^7). Our analysis further shows that outbound ejecta plumes rising from Mars take the form of an expanding toroid. Expanding ejecta plumes are regionally localized such that Phobos has a ~7% likelihood of intersecting an outbound ejecta plume immediately after a martian impact event. During a direct intersection with an outbound ejecta plume, the present-day orbit of Phobos sweeps, at most, $\sim 1.7 \times 10^{-5}$ of the total volume of the toroid. An outbound ejecta plume maintains a high-density concentration at the altitude of Phobos for < ~30 minutes whereas Phobos requires more than one hour to pass through the entire volume of an outbound ejecta plume. Consequently, *at most*, Phobos sweeps ~50% of the densest volume of the plume. On average, Phobos encounters a density of outbound ejecta from Mars that is approximately equivalent to a uniformly dense dispersion of fragments that fill the entire volume of the expanding toroid extending from Mars to the altitude of Phobos.

Over the course of several weeks after a martian impact, Phobos is additionally exposed to inbound ejecta particles that arrive from higher-altitude Keplerian trajectories. The flight times of inbound ejecta increase exponentially with higher peak trajectory altitudes and inbound fragments arrive at Phobos in a rapidly thinning flux density that diminishes approximately an order of magnitude per day. The average exposure of Phobos to thinly-distributed inbound ejecta is approximately equal to the average exposure of Phobos to outbound ejecta minus the fragments traveling at escape velocities from Mars that never return at all.

Results: To estimate the proportion of martian fragments in the regolith of Phobos we adopt a lunar regolith value for SSM projectile fragments of 1.5% to 4.5% [17]. Where the impact mass flux from SSMs at Phobos is ~200X greater than the flux from martian ejecta, we predict a concentration for martian ejecta in the regolith of Phobos of ~75 to 225 ppm. When we consider all uncertainties, we set a maximum limit for the global bulk concentration of martian fragments in the regolith of Phobos at 10 to 1,000 ppm.

The orbit of Phobos loses altitude due to secular acceleration from tidal forces [18]. The minimum ejecta velocities from Mars that are required to reach Phobos at higher altitudes that would be typical of Phobos in the geological past are, at most, 5% greater and do not significantly affect the concentration of particles that pass the orbit of Phobos inbound or outbound. However, at greater altitudes the geologically ancient Phobos would have passed through a smaller portion of the higher-density outbound ejecta plume. Consequently we would expect that martian ejecta concen-

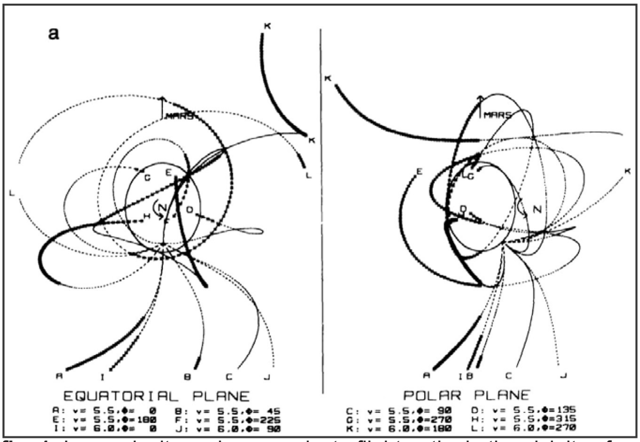

fig. 1: Low-velocity arabesque ejecta flight paths in the vicinity of Phobos [9]. Ejecta that exits Phobos at velocities of ~4 to 10 m/s is influenced by the weak gravity of Phobos, the much stronger gravitation of Mars and the rotation of Phobos during the orbital trajectory.

trations in the regolith of Phobos would trend toward a ~25% reduction at increasing regolith depths.

Scenarios that predict concentrations of martian material on Phobos must account for the greater volume and bombardment intensity from SSM flux, yet there may be scenarios where martian material is concentrated locally or stratigraphically. For example, where Phobos is predicted to be geographically exposed to impacts from martian ejecta [14], fresh secondary craters from Mars may be investigated that preserve martian ejecta fragments. However, craters that result from martian ejecta are produced with velocities that are typically 2 - 3 km/s [14] and are morphologically indistinguishable from SSM impacts. Alternately, globally distributed diffuse layers of martian ejecta might be observed near the base of the regolith of Phobos that represent encounters with ejecta plumes from early basin-forming impacts on Mars.

Spectral reflectance observations [19] support an asteroidal (type) composition. However, it has been proposed that Phobos may have originated from a primordial impact on Mars [20]; thus there is a possibility that a substantial proportion of Mars-like fragments samples may represent material from the original body of Phobos rather than from subsequent secondary impacts.

Conclusions and Implications:

1. The proportion of martian fragments in the regolith of Phobos is likely to be ~75 to 225 ppm.

2. The regional distribution of martian material in the regolith of Phobos is homogenously distributed around the entire geographical body of Phobos including surface regions of Phobos that are not directly exposed to the flight trajectories of impact ejecta from Mars.

3. Geologically ancient orbits of Phobos would have exposed Phobos to as much as ~25% less martian ejecta fragment mass relative to its present-day orbit.

4. Recent secondary impacts on Phobos from martian ejecta may preserve local concentrations of martian ejecta fragments, yet secondary impacts may be difficult to find.

5. Globally distributed diffuse layers of martian material may be observed in the oldest and deepest layers of the Phobos regolith from major basin-forming impacts on Mars.

6. Compared to the lunar regolith, the Phobos regolith is likely to be deficient in grains smaller than ~300 μm.

References: [1] Murray, et al., (1994) *Planet. Space Sci., 42*, 519-526. [2] Lee (2009) *Mars Inst Tech Pub 2009-001,* 6-7. [3] Chappaz, et al. (2012) *AAS/AIAA Space Flight Mechanics Meeting, 12-212,* 1-20. [4] Dobrovolskis and Burns (1980) *Icarus, 42,* 422-441. [5] Hamilton and Krivov (1996) *Icarus, 123,* 503–523. [6] Krivov, et al. (1996) *Celest Mech Dyn Astro, 63,* 313-339. [7] Krivov and Hamilton (1997) *Icarus*, *128,* 335-353. [8] Thomas (1998) *Icarus, 131,* 78–106. [9] Thomas, et al. (2000) *JGR, 105,* 15091-15106. [10] Andert, et al., (2010) *GRL*, 37, L09202, 10.1029/2009GL041829 [11] Banaszkiewicz and Ip (1990) *Icarus, 90,* 237-253. [12] O'Keefe and Ahrens (1985) *Icarus, 62, 328*-338. [13] Juhász, et al., (1993) *JGR, 98,* 1205-12. [14] Ramsley (2012) *Submitted for Publication*, [15] Le Feuvre and Wieczorek (2011) *Icarus, 214,* 3. [16] Melosh (1984) *Icarus, 59,* 234-260. [17] Korotev (1991) *P Lunar Planet Sci, 21,* 229-289. [18] Jacobson (2010) *Astron J, 139,* 668-679. [19] Rosenblatt, et al., (2010) *1st Moscow Solar System Symposium.* [20] Craddock (2010) *Icarus, 211,* 1150-1161.

AGE DISTRIBUTION OF CONCENTRIC CRATER FILL DEPOSITS IN THE SOUTHERN MID-LATITUDES ON MARS.

M. J. Beach[1], J. W. Head[1],
[1]*Department of Geological Sciences, Brown University, Providence, RI 02906, USA*
Contact: michael_beach@brown.edu

Introduction: The only major water ice deposits visible at the surface of Mars currently reside in large ice caps covering the north and south poles of the planet. Obliquity variations during the Amazonian caused a migration of polar ice to the mid-latitudes generating periods of extensive glaciation during that time [1-4]. Deposition of a sublimation lag [1,5,6] on top of the ice generated ideal conditions for long-term preservation of the buried ice. Concentric crater fill (CCF), moraine-like ridges (MLR), lobate debris aprons (LDA), and similar ice-related features and deposits frequently occupy craters in the mid-to-high latitudes of Mars in both the northern and southern hemispheres and were deposited during these periods [7-15].

Extensive catalogs of the global distribution and flow directions of CCF have been compiled and show regular trends in their morphology and locations [13, 15]. Ages calculated for similar ice-rich features such as LDA and pedestal craters give insight to timing of the major glaciations in the mid-latitudes [21, 22]. Here, we analyze the crater size-frequency distribution (CSFD) crater retention ages on the surface of CCF features for 64 southern hemisphere deposits (Figure 1.) to estimate the emplacement age of the sub-surface ice and therefor the timing and destinations of polar ice migration during the Amazonian.

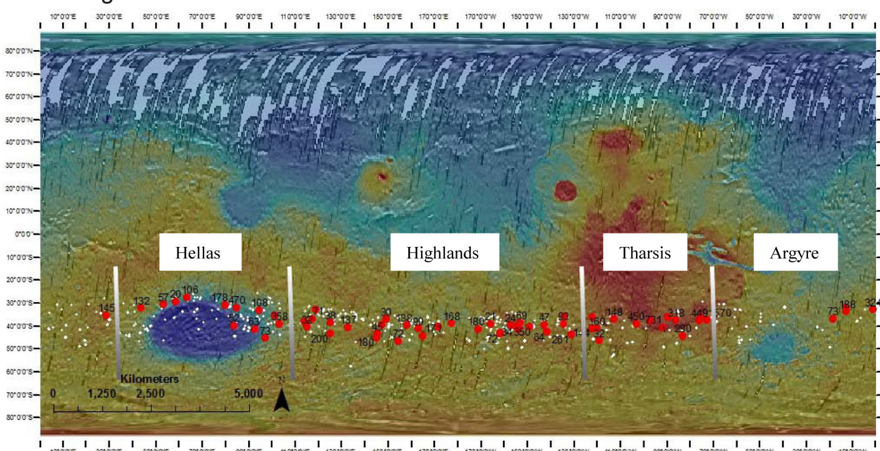

fig. 1. Map of the distribution and ages of CCF deposits in the southern mid-latitudes on Mars. The red circles show the locations and ages of the deposits that have been dated by this study. The white dots show the locations of the CCF deposits from Dickson et al. 2012. Vertical lines show the boundaries of each of the study areas. Background is MOLA color topog-raphy over the visible THEMIS IR daytime global map.

Analysis: In order to identify CCF deposits with ideal morphology for CSFD (high spatial resolution and regional coverage) we used a combination of ~19 m/pixel images from the visible imager portion of the Thermal Emission Imaging System (THEMIS) instrument aboard the Mars Odyssey spacecraft, the CCF flow direction map [15] which shows the locations and flow directions of CCF deposits, and altimetry data from the Mars Orbiter Laser Altimeter (MOLA) aboard the Mars Global Surveyor spacecraft. Deposits were selected based on two main criteria: (1) presence of flow lineations and brain-terrain [7]; and (2) the relative absence of thin mantling material that fills and obscures craters on the CCF surface [16-18]. Crater counts on the CCF deposits were carried out using the ~6 m/pixel images from the Context Camera (CTX) instrument aboard the Mars Reconnaissance Orbiter spacecraft. Crater counting on CCF is complicated by the obscuration and destruction of craters by brain terrain and mantle emplacement, but these textures and deposits have been studied in detail and can be isolated and accounted for [7; 16-18]. The transition from superposed bowl-shaped craters to ring-mold craters (RMC) by penetration to buried ice and viscous relaxation is another uncertainty in counting that needs to be taken into account when interpreting the frequency distribution of craters on debris-covered ice surfaces [19]. Ages were determined using the Neukum [20] production function and produce ages consistent with earlier estimates for related deposits [21].

Results: The age distribution (Figure 2) of the 64 CCF deposits in the southern hemisphere show several features indicative of variable deposition and preservation of ice. The majority of deposits are interpreted to be below 200 Ma with only one deposit older than 500 Ma. Two additional ages over 1 Ga are not included in our counts due to low confidence. This age distribution implies that the majority of CCF deposits were deposited within the last 200 Ma.

What accounts for the spread in ages? Three options are possible: 1) Each age represents the resurfacing age of the individual CCF deposit; 2) the range in ages represents a narrower range of ages modified by degradation and obscuration; and 3) the range represents real variations related to local or regional conditions. We investigate the latter possibility (regional variations) by examining potential regional clustering in ages.

Four main zones (Figures 1,2, and 4) with similar morphology and age of the CCF deposits can be identified from the data as follows; (1) the southern highlands between eastern Hellas basin and the western part of the Tharsis bulge referred to here as the highlands (110°E – 125°W) (Figures 1, 2a, and 4), (2) the southern extent of the Tharsis bulge (125°W – 70°W) (Figures 1, 2b, and 4), (3) North Argyre and the area between eastern Tharsis and western Hellas basin (70°W – 35°E) (Figure 1), and (4) the northern portion of Hellas basin (35°E – 110°E) (Figures 1, 2c, and 4).

The highlands: This area is characterized by an abundance of deposits with minimal modification from mantling material at lower latitudes with some modification at higher latitudes and good preservation for CSFD dating. Deposits in this area range from 14 to 358 Ma with an average age of ~125 Ma for 33 craters in the region. The elevation of the CCF surface in this region ranges from -450 m to 2250 m with an average elevation of 890 m.

Tharsis bulge: Deposits in this area tend to have little mantling material and abundant RMC's on the CCF surface. However, for this region the Neukum plots often do not show a good fit to the frequency distribution. Deposits here range from 32 to 731 Ma with an average of ~273 Ma for 14 craters in the region. The elevation of the CCF surface ranges from 1250 m to 7050 m with an average elevation of 3260 m. Two additional craters were not included from this area due to low confidence.

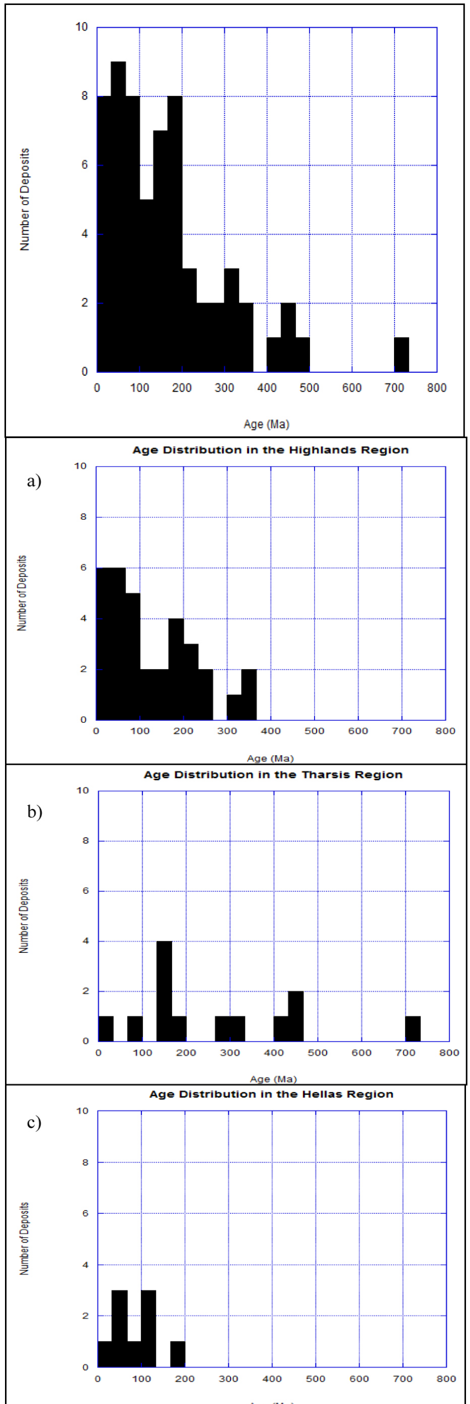

fig. 2. Age distribution histogram for CCF deposits in the southern hemisphere. (**a**) is the age distribution histogram for Highlands region. (**b**) is the age distribu-tion histogram for the Tharsis region. (**c**) is the age distribution histogram for the Hellas region.

Hellas Basin: This area contains ample deposits with good morphology for CSFD dating; however, mantling material is present in many areas despite the lower latitude of deposits in the region. Nine dated examples range from 20 to 178 Ma with an av erage age of ~88 Ma. There are two craters in this region that show anonymously large ages and have not been included in these samples due to low confidence. The elevation of the CCF surface ranges from -6050 m to 1200 m with an average elevation of -2611 m.

Argyre: There are fewer examples of CCF in this region as compared with other areas and, of those, very few have been dated due to a lack of CCF craters to count. For the area on the northern portion of the Argyre basin many surfaces are comprised of mounds or knobs which may be remnants of superposed craters but very few fresh craters or RMC's are present. For the area east of Argyre there are very few CCF deposits, of which only five have been dated. They range from 73 to 324 Ma with an average age of ~183 Ma. The average elevation of the CCF surface for this region is 590 m.

Discussion: From the 64 craters analyzed here, and the 4 distinct regions that have emerged from the dataset based on similar morphology, there are two trends that have appeared. The first is that the maximum ages tend to decrease with higher latitudes. For the highlands region, where the latitude range is the largest, this trend is shown most clearly (Figure 3). This can be explained by the presence and abundance of the latitude dependent mantle. As the quantity of mantling material increases with latitude it tends to fill in small craters and erase them. This effect is most prominent at latitudes higher than ~45°N where mantling material completely covers the CCF surface up to the crater rim-crest reducing the age of the entire surface to the age of the mantling material [23].

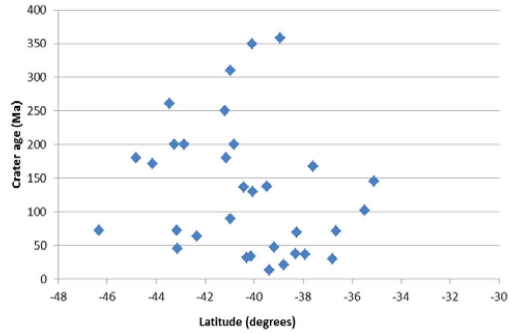

fig. 3. Plot of crater age vs. latitude for deposits in the High-lands.

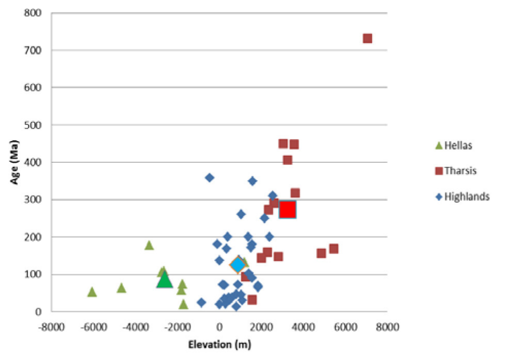

fig. 4. Ages of CCF deposits plotted against elevation by region. The small data points are the individual data points for each occurrence and the large data points are the averages of the regions. Green triangles are for the Hellas region, blue diamonds are for the Highlands region, and red squares are for the Tharsis region.

The second trend is an increase in the age of the CCF surface with increasing elevation. This effect can be seen when comparing the average ages and elevations of three of the four study regions (Figure 4). Due to low confidence and low crater numbers the Argyre region was not considered when comparing elevation and average age. The Hellas Basin region has the lowest average elevation at -2610 m with an average age of ~88 Ma. The highlands region increases in average elevation to 890 m with an average age of ~124 Ma. The highest region, the Tharsis Bulge, has an average elevation of 3260 m and an average age of ~273 Ma. We tentatively interpret this age progression to be related to increased cover of lower elevation CCF deposits with superposed sediment and mantle, thereby decreasing its apparent age.

Conclusions: The Amazonian obliquity history shows low obliquity periods for the last 3–5 Myr, and potentially widely variable obliquity for the last 250 Myr [24]. These variable periods of high obliquity cause migration of polar ice and deposition in the mid-low latitudes and are likely to be responsible for some of the variations in ages within each study area. This study shows that the majority of CCF deposits in the southern hemisphere fall in the 20 – 300 Ma time scale (Figure 2.). This result is consistent with earlier studies for similar ice rich deposits such as LVF and LDA [26], pedestal craters [21], and brain terrain [7] in both the southern and northern hemispheres. Morphologic and crater count evidence support the interpretation that multiple generations of CCF emplacement have taken place which requires episodic emplacement of paleodeposits due to obliquity driven climate variations. The decrease in age with increasing latitude may be influenced by the latitude dependent mantle rather than variations in the emplacement age of the ice [16-18]. The preservation of ice as a function of elevation also alters the calculated age of ice emplacement. The Tharsis study area has very little mantle and shows good preservation of the CCF material. Subsequent periods of mobilization of ice have deposited small amounts of material on the surface (e.g. the latitude dependent mantle), and decreased the calculated ages, rather than adding significant amounts of material to the CCF deposits throughout the southern hemisphere. Future work will examine CCF deposits in the northern hemisphere for comparison of morphology, location, and age trends with the southern hemisphere.

References: [1] Head, J. W. and Marchant, D. R. (2009) LPSC 40, 1356; [2] Mischna, M. A. (2003) JGR http://dx.doi.org/10.1029/2003JE002051.; [3] Levrard, B. et al. (2004) Nature 431, 1072-1075; [4] Forget, F. et al. (2006) Science 311, 368-371; [5] Marchant, D. R. (2002) Geol. Soc. Am. Bull. 114, 718-730; [6] Kowalewski, D. E. (2011) Geomorphology 126, 159-173; [7] Levy, J.S. et al. (2009) Icarus 202, 462; [8] Kress, A.M., and Head, J.W. (2008) GRL 35, L23206; [9] Head, J.W. et al. (2010) EPSL 294, 306; [10] Head, J.W. et al. (2006a) EPSL 241, 663; [11] Baker, D.M.H., et al. (2010) Icarus 207,186; [12] Dickson, J., et al. (2010) EPSL 294, 332; [13] Levy, J.S. et al., (2010) Icarus 209, 390; [14] Dickson, J.L. et al. (2011) LPSC 42, 1324; [15] Dickson, J. et al. (2012) Icarus 219, 723-732; [16] Kreslavsky, M. A. and Head, J. W. (2000) JGR 105, 26695-6712; [17] Mustard, J. F. et al (2001) Nature 412, 411-414; [18] Head, J.W. et al. (2003) Nature 426, 797-802; [19] Kress, A. M. and Head, J. W. (2008) LPSC 39, 1273; [20] Neukum, G, et al. (2001) SSR 96, 55; [21] Kadish, S.J., and Head J.W. (2011) Icarus 215, 34; [22] Mangold, N. (2003) JGR 108, 8021; [23] Head, J. W. et al. (2003) Nature 426, 797-803; [24] Laskar, J. (2004) Icarus 170, 343-364; [25] Kress, A. M., and Head, J. W. (2009) LPSC 40, 1379; [26] Morgan, G. A. et al (2009) Icarus 202, 22-38

PALOS CRATER AND TINTO VALLIS, MARS: ANALYSIS OF PROPOSED FLUVIAL AND VOLCANIC SCENARIOS, AND FURTHER IMPLICATIONS FOR LOCAL GEOLOGY.

A. I. Rauhala[1], V.-P. Kostama[1],
[1]Astronomy Division, Department of Physics, P.O. Box 3000, FI-90014, University of Oulu, Finland. Contact: anssi.rauhala@oulu.fi

Introduction:

The ~53 km Palos crater (2.7ºS, 110.8ºE) located in the northern Tyrrhena Terra is a candidate open-basin paleolake whose rim is breached from the south by a ~180 km long Tinto Vallis. Previous literature has proposed both fluvial [1,2] and volcanic [3,4] origin for Tinto Vallis. Breach on the northern rim of Palos crater on the other hand acts as a source for the ~350 km long Palos outflow channel [4]. The actual origin of Tinto Vallis is crucial when considering the nature of Palos crater floor deposits and possibility of proposed Hesperia–Amenthes fluvial chain [4].

Origin of Tinto Vallis:

The argument for possible volcanic origin is based on comparisons between Tinto Vallis and sinuous rilles. Claimed similarities include the general appearance, lack of abundant tributaries, existence of pit crater chains near source areas (possibly indicative of lava tubes), and morphometric properties such as slopes, sinuosities and width-to-depth ratios [3,4]. However, several arguments can be made against these claims:

Firstly, the downstream development is completely opposite. Tinto Vallis gets progressively wider and deeper downstream, whereas rilles generally get narrower and shallower as expected from thermally eroded lava channels/valleys [5]. On the other hand, experiments indicate that fluvial valleys generally widen downstream due to base level fluctuations, in which case tributaries are not even necessary [6]. Secondly, modeling and observations have indicated that Martian pit crater chains generally relate to tectonic modification, not lava tubes [7]. Thirdly, more profound comparison of the morphometric properties indicates that analogue-wise Martian valleys are much better fit than rilles (as summarized in [8, 9]). Lack of evidence supporting the proposed volcanic origin has led us to conclude that fluvial origin is the most likely option for Tinto Vallis.

Implications for local geology:

General “sapping”-like morphology and chaotic head area of Tinto Vallis have been considered as indicators of intense groundwater activity in the area [3, 4], although funnel-like, possibly fluvial landform on the source area of Tinto Vallis hints that catastrophic flooding might have contributed to the formation in addition to steadier groundwater influenced erosion. Other possible indicators of groundwater activity include several paleolake candidates in the immediate vicinity of Palos crater (see Figure 1), all of which seem to have relatively small drainage areas. Several proximate floor-fractured craters, which are otherwise rare in the area, could also be a manifestation of groundwater activity [10].

Our crater counting measurements, done on both Tinto Vallis and likely fluvial deposits on Palos crater floor, indicate that major fluvial activity and main lake-phase likely ended around 3.6–3.5 Ga ago. This is somewhat younger age than generally associated with Martian valley networks [11], but on the other hand, it would be in agreement with some climatic models which indicate that the study area was among the last few places where precipitation might have fueled aquifer recharge as Mars was drying from Noachian towards the Hesperian period [12]. As Tinto Vallis seems to be slightly older than the Palos outflow (~3.5-3.2 Ga [4]), the two were likely created in separate fluvial episodes. Due to the likely fluvial origin of Tinto Vallis, any subsequent (partial) volcanic resurfacing of the Palos floor [3, 13] would have happened through the northern breach of Palos rim during the plains formation on Amenthes Planum.

Drainage basin analysis indicates that several smaller and degraded valleys south from Tinto Vallis drain into its chaotic head area. These valleys seem to originate close to the edges of Hesperia Planum, although they are partially obscured by subsequent ejecta deposits. It is possible that prior to the formation of ridged plains these valleys extended farther to Hesperia Planum, and Tinto Vallis with Palos crater were part of a longer fluvial chain through which materials were transported from Hesperia to Amenthes Planum.

Conclusions:

Tinto Vallis likely formed around 3.6–3.5 Ga ago as a fluvial valley, possibly affected by both flooding and steadier groundwater influenced fluvial erosion. Palos outflow channel, originating from Palos crater, was likely formed in later episode. Prior to the plains formation in Hesperia and Amenthes Planum, Tinto Vallis and Palos crater may have been part of a longer Hesperia–Amenthes fluvial chain.

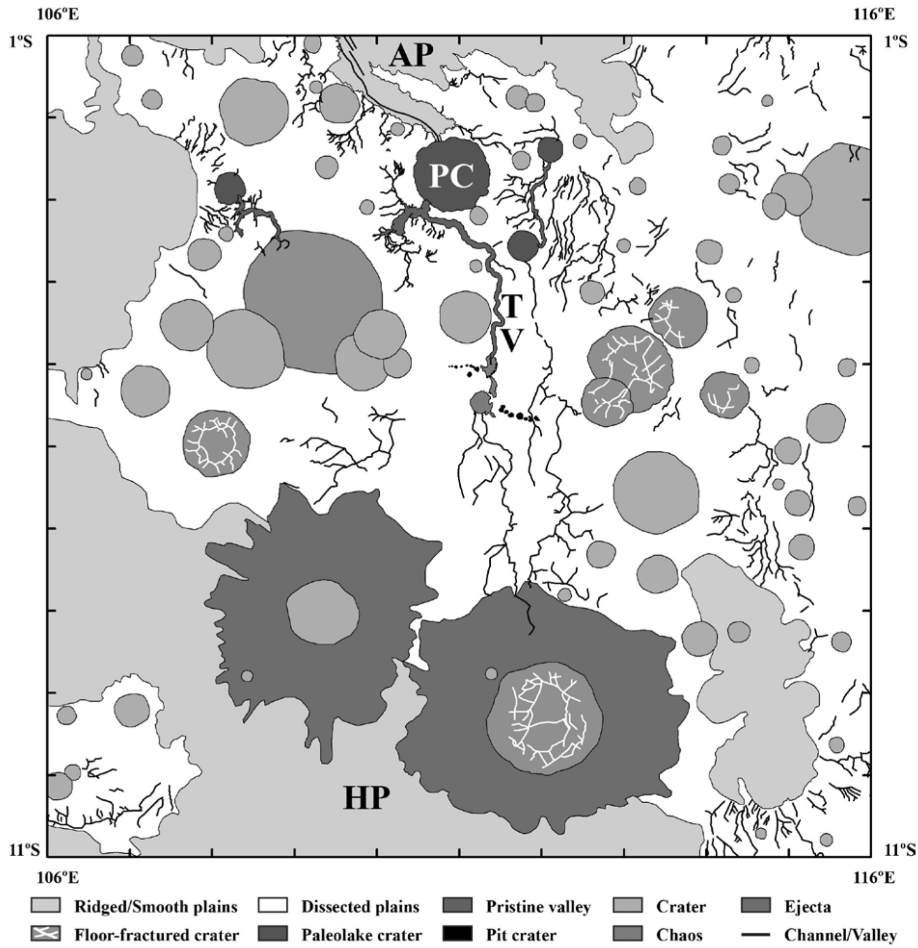

fig. 1. Geomorphological map of the study area. (AP = Amenthes Planum, HP = Hesperia Planum, PC = Palos crater, TV = Tinto Vallis)

References:

[1] Carr, M. H. (1995), J Geophys. Res., 110, 7479–7507.
[2] Carr, M. H. and Malin, M. C. (2000), Icarus, 145, pp. 366–386.
[3] Leverington, D. W. (2006), J. Geophys. Res. 111, E11002.
[4] Erkeling, G. H. et al. (2011), Icarus, 215, 128–152.
[5] Hurwitz, D.M. et al. (2012), J. Geophys. Res., 117, E00H14.
[6] Martin, J. et al. (2011), J. Sediment. Res., 81, pp. 64–79.
[7] Smart, K. J. et al. (2012), J. Geophys. Res., 116, E04005.
[8] Rauhala, A. I. and Kostama, V.-P. (2012), LPSC 43, #2261.
[9] Rauhala, A. I. and Kostama, V.-P. (2012), EPSC2012, #444.
[10] Sato, H. et al. (2010), Icarus, 207, pp. 248–264.
[11] Fassett, C. I and Head, J. W (2008), Icarus, 195, pp. 61–89.
[12] Andrews-Hanna, J. C. et al. (2012), LPSC 43, #2706.
[13] Goudge, T.A. et al. (2012), Icarus, 219, pp. 211–229.

RAMAN SPECTROSCOPY OF MINERALS AT SIMULATED PLANETARY CONDITIONS FOR SPACE EXPLORATION

S. G. Pavlov[1], U. Böttger[1], I. Weber[2], D. Grunow[1], N. Deßmann[3], N. Tarcea[4], J. Popp[4], E. K. Jessberger[2] and H.-W. Hübers[1,3],
[1] Institute of Planetary Research, German Aerospace Center (DLR), Berlin, Germany, [2] Institut für Planetologie, Westfälische Wilhelms-Universität Münster, Germany, [3] Institut für Optik und Atomare Physik, Technische Universität Berlin, Berlin, Germany, [4] Institute of Physical Chemistry, Friedrich-Schiller-Universität, Jena, Germany, Contact: sergeij.pavlov@dlr.de

Introduction:

New exploration tasks for space missions to solar system bodies demand new techniques and instrumentation for remote and *in situ* analysis. Inelastic light scattering (Raman) spectroscopy is considered as a powerful tool for mineralogical and organic matter *in situ* surface investigation for the future missions to Mars and the Moon [1,2]. On the ExoMars mission the Raman Laser Spectrometer (RLS) shall identify minerals produced by water related processes, igneous minerals and their alteration products, as well as organic compounds in the Martian surface rocks and soils. Environmental conditions influence Raman spectra [3-5] and result in spectra different to those in conventional mineral databases measured at laboratory ambient conditions.

The goal of this study is to investigate the influence of planetary conditions on the positions and bandwidths of the characteristic Raman lines prior to the future space missions. We determined the Raman spectra in environmental conditions varying from Earth-like (ambient 1 bar atmosphere, room temperature) through Martian-like (8 mbar CO_2 atmosphere, 220 K) to Moon-like (vacuum below 10^{-4} mbar, mean 130 K on the pole) or asteroid like (vacuum and < 10 K) conditions. The results of a Raman spectroscopic study of different rock forming and water bearing minerals and the minerals found in the Martian meteorite Dar al Gani 670 (DAG670) are presented. The investigated minerals include the sylvite (KCl), anhydrite ($CaSO_4$), gypsum ($CaSO_4 \cdot 2H_2O$), phlogopite ($KMg_3[AlSi_3O_{10}(OH,F)_2]$), tremolite ($Ca_2Mg_5[Si_4O_{11}(OH)]_2$), carnallite ($KMgCl_3 \cdot 6H_20$), five olivine samples (four forsterites (Mg_2SiO_4), including the San Carlos olivine, and one fayalite (Fe_2SiO_4)). The Martian meteorite DAG670 is classified as a shergottite and consists of pyroxene, olivine and a feldspathic glass groundmass with minor inclusions of chromite ($FeCr_2O_4$) and sulphide as well as calcite ($CaCO_3$), a terrestrial weathering product. The minerals chosen for this study are (1) known as weathering or sedimentary products on the Earth and some of them have already been detected on Mars [6-8], (2) easy to prepare for Raman measurements and available in large amounts, and (3) good indicators for spectral line shifts in Raman spectra due to changes of ambient conditions [4,9].

Measurement Details:

Initial images of the minerals have been taken by light optical microscope with transmitted light and a polarization unit. Detailed images and elemental mappings on the coated thin sections of the minerals have been obtained with a scanning electron microscope (SEM) JEOL JSM-6610LV. Quantitative analysis of most of the minerals have been made with an electron probe micro-analyzer (EPMA) JEOL JXA-8900 Superprobe. For the DAG 670 meteorite, eight selected areas were marked by laser ablation for subsequent detailed studies by SEM and Raman spectroscopy on the uncoated sample, and finally, EPMA on the coated section. We performed Raman measurements with a confocal Raman microscope Witec alpha300 R. The laser excitation wavelength is 532 nm; the resolution of the spectrometer is 4-5 cm^{-1}. A Nikon 10x objective was used with a spot size on the sample in focus of about 1.5 µm. To represent the RLS instrument on ExoMars a laser power of 1 mW on the sample was chosen. The samples were fixed to the cold finger in the Oxford cryostat MicrostatH-iResII with their polished side towards incident laser beam. The excitation laser has been focused on the sample surface. The scattered light has been collected through a crystalline quartz glass window in the cryostat.

Results and Discussion:

As a rule, there are no detectable frequency shifts of Stokes lines in the Raman spectra for the investigated minerals due to the presence of a CO_2 atmosphere or due to the pressure variation from ambient down to 10^{-4} mbar at a fixed temperature. However, different temperature related frequency shifts of Raman lines have been observed for different atmospheric conditions, such as vacuum and carbon dioxide. Some of the minerals show Stokes lines that undergo detectable temperature related frequency shifts, but often with no systematic gradients of different sign and strength.

Raman bands for O-H stretching modes (between 3200 and 3600 cm^{-1}) in hydrated minerals (gypsum, carnallite) show no distinct frequency shifts due to change of environment atmosphere but vary in their line intensities. The O-H stretching band in carnallite shows specific line structure becoming resolved with decreasing temperature. This can be explained with a sharpening of the individual OH – stretching lines possibly due to increased ordering of the water molecules in the crystal lattice by its cooling [9,10]. Low-frequency (100-400 cm^{-1}) translational modes exhibit the largest temperature related frequency shifts, up to about 10 cm^{-1} (at 10 K) in comparison with room temperature. Some minerals, such as tremolite, exhibit detectable variations of positions of Raman lines with temperature only below 100 K.

For the olivine mineral group, both the Raman line widths and their frequencies, are affected by temperature. The magnitude of the frequency shifts depends on the olivine type and its orientation relative to the incident light. All four forsterites show only slight temperature dependent shifts of the Stokes lines (up to 3 cm^{-1}), while fayalite is characterized by shifts up to 6 cm^{-1}. The temperature dependence might be an effect of dynamic field splitting. In addition, magnetic interactions can occur in fayalite that may be responsible for more significant temperature dependent Raman shifts [11]. No change in the Raman spectra of the olivines with the atmospheric composition or its pressure has been observed. Although the forsterites have a similar composition, the relative intensity of the main Raman peaks is different. This is attributed to different and accordingly random orientation of the crystals in natural samples. No irreversible changes in the Raman spectra of the olivines were detected.

The Raman measurements on the Martian meteorite DAG670 are sensitive to mineral zonings in pyroxene by Raman shifts in two bands and possible grain orientation effects are visible in the change of the relative peak intensity. The position and bandwidth of the Raman lines are slightly shifting with temperature. The direction of the shift depends on the mineral type. The influence of pressure and kind of atmosphere is negligible. Raman measurements enable high spatial resolution with detection of the particles in micrometer size range. Special attention must be paid to the analysis of FeS in meteorites because a mineral transformation can take place under certain power of exciting laser and under certain specific environmental conditions.

In summary, temperature variations have been found as the only factor that caused significant shifts of the some lines in Raman spectra of minerals in Martian analogs and in the Martian meteorite. Typically observed variations are about few cm^{-1} per 100 K that can be neglected in classification of minerals based on positions of major characteristic bands in Raman spectra, but must be considered for identification of minerals. The chosen experimental conditions will contribute to interpretation of the forthcoming RLS data from the ExoMars space mission. More analyses on minerals relevant for Mars are necessary to evaluate the expected data prior the mission.

Acknowledgements:
The authors thank Prof. Dr. F. Langenhorst from the Institute for Geosciences, University of Jena, for providing two olivine samples. This work was partly supported by a grant 50 QX 0602 from the Deutsches Zentrum für Luft- und Raumfahrt and by the Helmholtz-Alliance “Planetary Evolution and Life”.This work was supported by the grant of the Russian academy of sciences Presidium Program 22: “Fundamental problems of research and exploration of the Solar system”.

References:
[1] The ExoMars Rover Instrument Suite (ESA), web: http://exploration.esa.int/science-e/www/object/index.cfm?fobjectid=45103&fbodylongid=2130;
[2] E. Diaz, C. Pérez, A. Moral, O. Álvarez, C. Tato, H. Thiele, M. Colombo, I. Hutchinson, R. Ingley, J. J. Thocaven, F. Rull, S. Maurice, J. Popp, H. G. M. Edwards, Raman Laser Spectrometer development for lunar applications, in Abstracts of the European Lunar Symposium, 19-20 April, Berlin, pp. 29-30 (2012).
[3] J. T. Kloprogge, and R. L. Frost, Raman microscopy at 77 K of natural gypsum CaSO4 center dot 2H(2)O, J. Mater. Sci. Lett. 19, 229-231 (2000).
[4] Chi Hong Chio, S. K. Sharma, and D. Muenow, Micro-Raman studies of gypsum in the temperature range between 9 K and 373 K, Am. Mineral. 89, 390-395 (2004).
[5] Chi Hong Chio, S. K. Sharma, and D. Muenow, The hydrates and deuterates of ferrous sulfate (FeSO4): a Raman spectroscopic study, J. Raman Spectrosc. 38, 87-99 (2007).
[6] J. L. Gooding, Chemical weathering on Mars thermodynamic stabilities of primary minerals (and their alteration products) from mafic igneous rocks, Icarus 33, 483-513 (1978).
[7] J. L. Bandfield, Global mineral distributions on Mars, J. Geophys. Res. 107, 9–1-9–21 (2002).
[8] V. Chevrier, P. Rochette, P.-E. Mathé and Olivier Grauby, Weathering of iron-rich phases in simulated Martian atmospheres, Geology 32, 1033-1036 (2004).
[9] Chi Hong Chio, S. K. Sharma and D. Muenow, Micro-Raman studies of hydrous ferrous sulfates and jarosites, Spectrochimica Acta 61A, 2428-2433 (2005).
[10] M. Chaplin, Water structure and science, web: http://www.lsbu.ac.uk/water/methods.html.
[11] B. A. Kolesov and C. A. Geiger, A temperature-dependent single-crystal Raman spectroscopic study of fayalite:
evidence for phonon-magnetic excitation coupling, Phys. Chem. Minerals 31, 155-161 (2004).

CRATER COUNTS ON MARTIAN OUTFLOW CHANNELS IN HELLAS REGION BY USING HIGH RESOLUTION IMAGES.

S. Kukkonen, V.-P. Kostama,
Astronomy, Department of Physics, P.O. Box 3000, FI-90014 University of Oulu, Finland. Contact: soile.kukkonen@oulu.fi

Introduction:

The usability of the small (<500 m diameter) impact craters in crater counting has been a subject of ongoing debate. The availability of the new high resolution images obtained by the CTX and HiRISE cameras onboard MRO allows us to extend the crater size-frequency distributions to smaller craters providing new insights into the erosional and depositional histories of the surfaces.

In this work we present our results of age determination from the northeastern Hellas outflow channels based on CTX and HiRISE datasets. We compare the erosional and depositional histories of the surfaces of the channels and reveal information on the benefits and limitations of high resolution imagery used in age determination studies.

Crater counts on the northeastern Hellas outflow channels:

The Hellas impact basin is one of the largest known impact structures on Mars. The northeastern rim region of the basin is characterized by several channel features of which the most prominent are the large outflow systems of Dao, Niger, Harmakhis and Reull Valles [1–3]. Dao, Niger and Harmakhis Valles are located within a large smooth-surfaced depression (Hesperia–Hellas trough, HHT, [4, 5]; SW trough in [6]), which connects Hesperia Planum and the Hellas basin. Reull Vallis does not connect to the basin, but instead it ends abruptly close to the source area of the Harmakhis Vallis. It has been suggested that there may be a subsurface connection between Reull and Harmakhis Valles [7].

The general morphology of the channels' floors indicates that the regional geologic history has been complex. All of the channels are covered by several distinct viscous flow units which clearly postdate the channel formation indicating lateral glacial-like activity in the channels. On such terrain, we can expect that small craters are unaffected by distant secondaries, because they mostly postdate the latest secondary-forming impacts.

We have estimated the cratering model ages for the units on the floor of the channels by using the Mars Reconnaissance Orbiter Context Camera (CTX) and High Resolution Imaging Science Experiment (HiRISE) datasets. Our preliminary results from the Dao, Niger and Harmakhis Valles have been presented in [8, 9] and from the upper part of Reull Vallis (including Hesperia Planum and the Morpheos basin) in [10, 11, 12]. In general, the HiRISE imagery has a better spatial resolution, 0.25–0.5 m/px, which is an important factor on this kind of young surfaces, where there are only few large craters (>1 km diameter). However, the availability of the HiRISE images varies and on the eastern Hellas region, most of them focus on the wall of the channels only. The CTX images cover the entire channel systems and part of the Morpheos basin and Hesperia Planum with the resolution ~5m/px.

Results:

The crater size-frequency distributions based on the CTX and HiRISE images show that the evolution of the channels has been complex. Due to the lateral activity on the floors of the channels, the original formation age of the channels cannot be measured directly, so the stratigraphic correlations are needed. The viscous flow units themselves have been modified by at least two distinct resurfacing events. For example, for the viscous flows on Dao Vallis, the CTX images give an age of 200–900 Ma with the resurfacing events occurring at 40–80 Ma and 15–35 Ma (Figure 1a). Due to the resolution limit of the CTX imagery, no younger ages can be detected. The crater size-frequency distributions based on HiRISE images show the unit of 15–35 Ma and also a younger unit which is only 3–7 Ma old (Figure 1b). The older crater populations, in turn, are missing or they are insufficient for fitting the isochrones, due to the limited area of the images and thus the limited number of the largest craters.

A similar kind of dataset-dependence can be also detected from the other channels. The crater data based on the HiRISE data from the floors of Niger, Harmakhis and Reull Valles show only the youngest surface units (on Niger Vallis we found cratering model ages of ~4 Ma and 12–15 Ma, and on Harmakhis and Reull Valles of ~2–3 Ma) whereas the crater counts from the CTX imagery indicate that the floors of the canyons also consist of older surface (40–80 Ma). However, there seem to be regional differences.

Conclusions:

Crater countings on high resolution and high quality CTX and HiRISE images are a useful way to estimate the resurfacing histories on the young surfaces where the percentage of the secondary craters is small. However, for the detailed surface evolution studies, the crater counts from datasets of only one camera are not always sufficient, but the reference data from the other camera are needed.

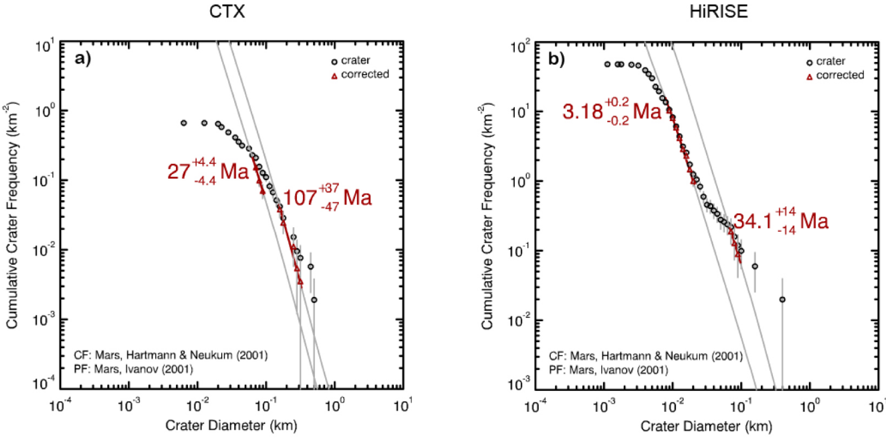

fig. 1. Cumulative crater size-frequency distributions from the viscous flow of Dao Vallis based on the a) CTX data and b) HiRISE images (produced with Craterstats). The crater size-frequency distribution based on the CTX images (the counting area is ~520 km^2) shows that the floor on the Dao Vallis head consists of two units with ages of 107 Ma and 27 Ma. No younger units can be detected due to the resolution limit of the CTX images. The crater size-frequency distribution for the same unit measured from the HiRISE images (the counting area is ~50 km^2) shows the unit of 34.1 Ma, but also the younger unit with an age of 3.18 Ma. The resurfacing correction used here has been developed by [13].

References:

[1] Greeley, R. and Guest, J.: USGS Map I-1802-B, 1987. [2] Carr, M.: Water on Mars, Oxford Univ. Press. 229, 1996. [3] Leonard, G. and Tanaka, K..: USGS Map I-2557, 1998. [4] Kostama, V.-P. et al.: Evidence for multiple ice deposits on the northeastern rim of Hellas basin, Mars EPSL 294, pp. 321-332, 2010. [5] Korteniemi J. et al.: Dike indicators in the Hadriaca Patera-Promethei Terra region, Mars, EPSL 294, pp. 466-478, 2010. [6] Ivanov et al.: Major episodes in the geologic history of western Promethei Terra, Mars, JGR, E110, E12S21, 2005. [7] Mest, S. C. and Crown, D. A.: Geology of the Reull Vallis Region, Mars, Icarus, Vol. 153, Issue 1, pp.89-110, 2001. [8] Korteniemi, J. et al.: Morphology and Ages of Units on the Floor of Dao Vallis Head, Mars: Preliminary Results, LPS XXXXIII, p. 1555, 2012. [9] Kukkonen, S. et al.: Crater Counting Using the High-Resolution Images: Case Study of Martian Outflow Channels in Hellas Region, EPSC, p. 685, 2012. [10] Kostama, V.-P. and Kukkonen, S.: Analysis of the Upper Parts of Reull Vallis and the Morpheos Basin, Mars: Preliminary Results, LPS XXXXII, p. 2408, 2011. [11] Kostama, V.-P. et al.: Dating the resurfacing event of Morpheos basin (upper Reull Vallis), Mars: Implications for the extent of the basin, EPSC-DPS, p. 900, 2011. [12] Kostama, V.-P. and Kukkonen, S.: Hellas outflow channel study: the formation and timing of Waikato and Reull Valles, Mars, EPSC, p. 878, 2012. [13] Michael, G. and Neukum, G.: Planetary surface dating from crater size-frequency distribution measurements: Partial resurfacing events and statistical age uncertainty, EPSL, 294, pp. 223-229, 2010.

3-D MODEL OF THE MARTIAN SURFACE

J. A. Brekhovskikh[1], Zh. F. Rodionova[2],
[1] Space Research Institute, Moscow, Russia; [2] Sternberg State Astronomical Institute Lomonosov Moscow University, Russia. Contact: julia_br@iki.rssi.ru , marss8@mail.ru

Introduction:

The history of creation of martian globes has more then 150 years (1, 2, 3).The new Hypsometric Globe of Mars is based on Lazer Altimeter data of Mars Global Surveyor spacecraft. The diameter of the globe is 24 cm. Coordinates and heights of 64 800 points on the surface of Mars were used for creating a 3-D Model of the surface of Mars.. A digital model of the relief was constructed with ArcGIS software. Contour lines were added together with hill-shading on the globe. The names of the main features – lands, plateaus, mountains, lowlands – plains and also some large craters are labeled. The places of landing sites of spacecraft are shown.

The Hypsometric globe of Mars is based on our Hypsometric maps of Mars, scale 1:26 000 000 (4), compiled at the Sternberg State Astronomical Institute (SAI) in cooperation with the Department of Cartography and Geoinformatics Faculty of Geography Moscow State University. The heights on the map show the results of Mars Global Surveyor altimetry. Elevation is reckoned from a triaxial ellipsoid equipotential surface. The height scale contains 21 step heights. To a height of 8 km the contour interval is 1 km. Up to 12 km the interval is 2 km. Above 12 km the interval is given within 10 km. The technology to create the globe using thermoplastic materials provides for forming the hemispheres of the sheets with the printed image on them and gluing the hemispheres at the equator. The original hemisphere prepared with the image is placed in the plastic molding device, and at high temperature using a metal template the hemispheres are pressed. Western and Eastern hemispheres were recut as the northern and southern hemispheres in the azimuthal projection taking into account the law of deformation occurring during forming of the plane in the hemisphere. Transforming the original cartographic image on the plane into an undistorted image on the field in this way can only be done if the distortion of the lengths of the meridians in the original projections will be constant equal to $m = 2/\pi$, and the distortion of the lengths of the parallels of latitude be a function of the form $n = (\pi\text{-}2\varphi):(\pi\cos\varphi)$ (5). This requirement corresponds to an azimuthal equidistant projection to the plane of section passing through the center of Mars. The projection is an orthogonal grid. The parallels are represented by equally spaced concentric circles, and meridians - the straight lines emanating from the center of the circles. When placing the original map, we took into account the fact that when forming the hemispheres the original image is stretched by more than half. As the tension is not even the names of relief forms were arranged parallel to the equator. To construct the cartographic image software ArcGis10 was used. The final design was carried out in a graphics editor Coral Draw. Based on project data previously made in ArcGis hypsometric maps were made for the southern and northern hemisphere and redesigned in the the azimuthal projection, prepared by the grid. Then the map images Eps format were transferred to Coral Draw, where the labels were made for landforms, map grids and prepared the layout for printing in accordance with the requirements of the publisher.

A preview sample image of the northern and southern hemispheres of Mars for the hypsometric globe is shown on Fig. 1. Most of the northern hemisphere of Mars is occupied by a relatively smooth plains For example, Vastitas Borealis has a depth of -4 - 5 km as Utopia Planitia and Acidalia Planitia. Arcadia, Chryse, and Amazonis Planitiae are higher by 1 km. In the southern hemisphere the plains are relatively few. There are Hellas Planitia, 2300 km in diameter, and a depth of -8 km and 800 km in diameter and Argyre Planitia and with the depth of about 3 km. The average height of the highlands of Mars are 3-4 km. Syria Planum is located on the plateau heights of 5 - 6 km, and Sinai Planum at 3 to 5 km, Solis Planum is at 3 to 4 km, Hesperia Planum and Syrtis Major Planum at 1 to 2 km. At the equator, is the largest mountain – Tharsis Montes with a diameter of about 6000 km and a height of 9 km. Above it tower three extinct volcanoes: Ascraeus, Pavonis and Arsia Mons located on the same line. The volcanoes have height of 14-18 km. The highest volcano on Mars - Olympus Mons. Its height is 21 km. In the equatorial zone of Mars is a giant system of faults with steep slopes - Valles Marineris. It has a maximum depth of 6 km and the width at the widest part is about 700 km.

Names of parts of the relief on the globe are given in the Latin version published by the International Astronomical Union [http://planetarynames.wr.usgs.gov].

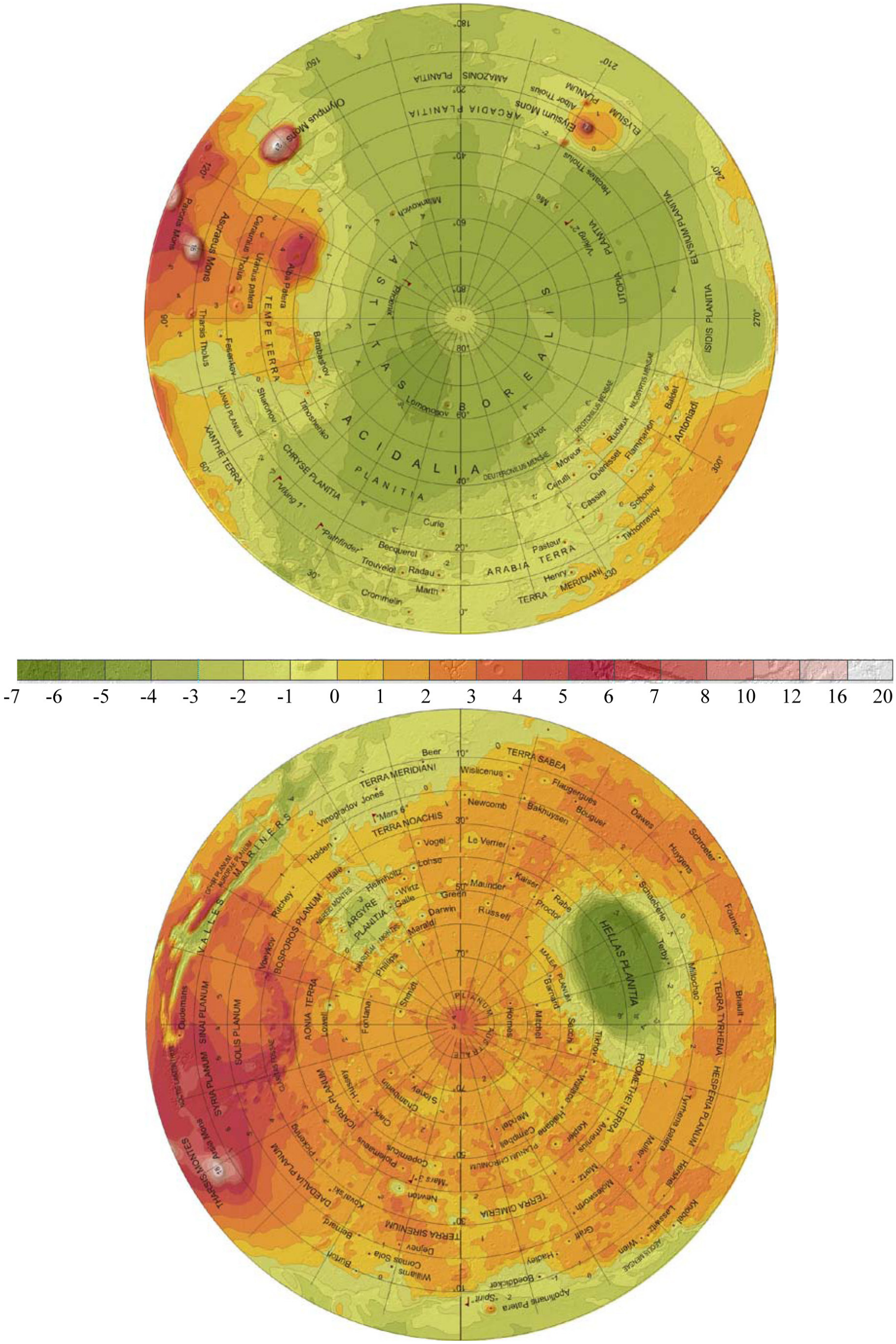

fig. 1. The Maps of the Northern and Southern Hemispheres of Mars.

References:

1. Blunck J., Jons H.P.Der Rote Planet Im Karten Bild. Staatsbibliothek zu Berlin. 1993, 132 p.

2. Mokre Jan. The Globe Museum of the Austrian National Library. Bibliophile Edition. Vienna, 2005, 72 p.

3. Rodionova Zh.F. Space achievements and maps and globes of planets//Geodesy and Cartography, Moscow,
1991, N 7, p. 15-22. 4. Ilukhina J.A., Rodionova Zh.F. Gipsometricheskaya karta Marsa. Moscow, 2004.

5. Boginsky V. M., Rodionova Zh. F., Myshetskaya E. N. Opyt sozdaniya globusa Luny na termoplastichnom materiale//Geodezy and Cartography. 1990, № 6, p. 28-34.

SURFACE GRAVITY AND DYNAMICAL ENVIRONMENT OF PHOBOS.

X. Shi[1], K. Willner[2], J. Oberst[1, 2]
[1]German Aerospace Center (DLR), Rutherfordstraße 2, 12489 Berlin, Germany; [2]Technical University Berlin, Straße des 17. Juni 135, 10623 Berlin, Germany. Contact: xian.shi@dlr.de

Introduction:

Different scenarios have been proposed to explain the formation and evolution of the widely-spread groove structures on the Martian moon Phobos [Thomas, et al., 1979; Davis, et al., 1980; Murray, et al., 1994; Wilson, et al., 2005; Duxbury, et al., 2010, Murray & Iliffe, 2011]. Some suggest that slopes are key factors affecting the groove formation and regolith processes. However, slope directions on Phobos' surface are not easily determined, as its dynamical environment is affected by self-gravitation, as well as considerable centrifugal and tidal forces. In this work, a constant-density gravity model of Phobos was developed, using the latest Digital Terrain Model (DTM). Tidal and centrifugal effects were added to evaluate the dynamical environment, which is represented through dynamic heights and surface slopes. Models were also computed with centrifugal and tidal effects turned off, simulating Phobos' greater distance from Mars early in its history.

Data and Methods:

The recently developed DTM of Phobos, with a resolution of ~100m [Willner, et al., 2012], was used to form a triangulated shape model. The surface gravity field of this polyhedron was then developed by assuming a uniform density of 1.876g/cm^3 [Andert, et al., 2010]. Following the definition by Thomas [1993], we calculated dynamic height maps for Phobos. A reference potential of 67.5663m^2/s^2, and a reference gravity of -0.0084m/s^2 were used. To complete our model, an averaged tidal effect with mean orbit distance to Mars was considered, together with a centrifugal effect caused by the synchronous rotation. Surface slopes were calculated as the angle between vectors of surface acceleration and surface normal.

Results and Discussions:

The resulting dynamic height has a range of roughly -1000m to +800m (Figure 1), with the highest point at (85º.17E,17º.55N) and lowest point at (179º.63E,8º.26S). The pattern of dynamic heights reveals the importance of tidal forces due to Phobos' proximity to Mars.

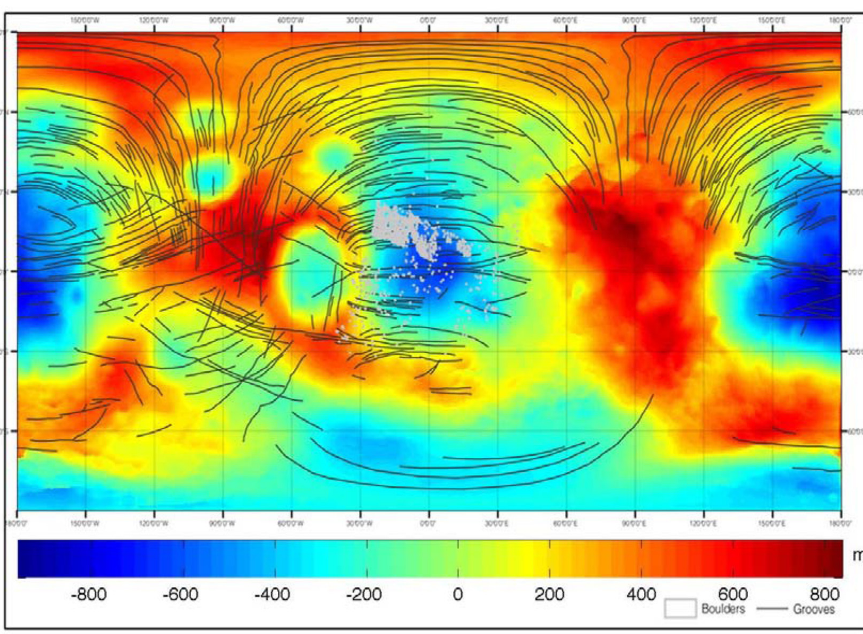

fig. 1. Color-coded dynamic heights of Phobos with mapped grooves and surface boulders, which may have been transported downslope. An equidistant cylindrical projection was used.

Preliminary analyses show no global correlation between the downslope directions and the pattern of grooves in most areas. Instead, groove orientations were more often observed to be perpendicular to slopes. However, the subset of grooves in the sub-Mars region, believed to be related to crater Stickney [Murchie, 1991], does show an alignment with the downslope directions. These suggest transport of material downslope along the grooves, which is supported by accumulations of surface boulders found at the end of the slopes (figure 1).

We demonstrate that orientations and magnitudes of surface slope are affected by increasing tidal effects (due to Phobos approaching Mars in the course of its history). As shown in figure 2, increasing tidal forces have diminished the steep slope on the east rim of Stickney, making the west rim relatively steeper, which is consistent with the downslope transport of regolith seen in Mars Orbiter Camera images of the Stickney area [Thomas, et al., 2000].

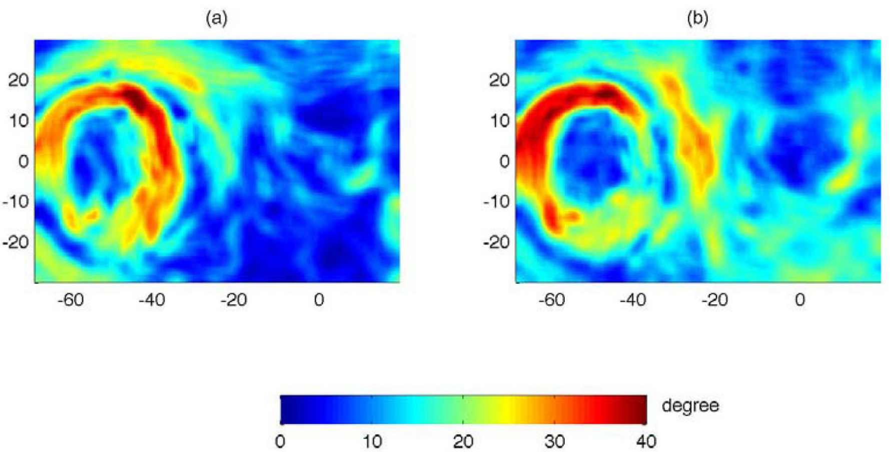

fig. 2. Slopes in the region of crater Stickney based on (a) self-gravitational force only (simulating Phobos' greater distance from Mars early in its history); (b) self-gravitational force, centrifugal force and tidal force.

Outlook:

In the following work, comparison of geometric and dynamic topography will be carried out locally, especially along some of the prominent grooves. The movement of particles according to the dynamical environment will be simulated to test possible formation scenarios of the grooves.

Acknowledgement: The authors would like to thank Przemyslaw Bielecki for his work on the groove and boulder map of Phobos. This study is supported by the DLR-DAAD joint scholarship.

Andert, T., Rosenblatt, P.; Pätzold, M., Häusler, B., Dehant, V., Tyler, G., and Marty, J., 2010, Precise mass determination and the nature of Phobos, *Journal of Geophysical Research,* 37:9202.
Davis, D., Weidenschilling, S., Chapman, C., and Greenberg, R., 1980, Dynamical studies of Phobos and Deimos: groove origin and ejecta dynamics, Reports of Planetary Geology Program, 14-16.
Duxbury, T., Robinson, M., van der Bogert, C., Thomas, P., Neukum, G., and Hiesinger, H., 2010, Phobos grooves, a lunar analogy, *38th COSPAR Scientific Assembly,* 38, 641.
Murchie, S., Britt, D., Head, J., Pratt, S., Fisher, P., Zhukov, B., Kuzmin, A., Ksanfomality, L., Zharkov, A., Nikitin, G., Fanale, F., Blaney, D., Bell, J., and Robinson, M., 1991, Color heterogeneity of the surface of PHOBOS - Relationships to geologic features and comparison to meteorite analogs, *Journal of Geophysical Research, 96:*5925-5945.
Murray, J., Rothery, D., Thornhill, G., Muller, J., Iliffe, J., Day, T., and Cook, A., 1994, The origin of Phobos' grooves and crater chains, *planet. Space Sci.,* 42(6):519-526.
Murray, J. and Iliffe, J. 2011, Morphological and geographical evidence for the origin of Phobos' grooves from HRSC Mars Express images *Geological Society of London Special Publications, 356:*21-41.
Thomas, P., Veverka, J., Bloom, A., and Duxbury, T., 1979, Grooves on Phobos - Their distribution, morphology and possible origin, *Journal of Geophysical Research,* 84(B14):8457-8477.
Thomas, P., 1993, Gravity, tides, and topography on small satellites and asteroids - Application to surface features of the Martian satellites, Icarus, 105:326-344.
Thomas, P., Veverka, J., Sullivan, R., Simonelli, D., Malin, M., Caplinger, M., Hartmann, W., and James, P., 2000, Phobos: Regolith and ejecta blocks investigated with Mars Orbiter Camera images, *Journal of Geophysical Research,* 105:15091-15106.
Willner, K., Shi, X., Oberst, J., Karachevceva, I., Roatsch, T., and Hoffmann, H., 2012, Improved Phobos shape and gravity working models, The XXII Congress of the International Society for Photogrammetry and Remote Sensing, Melbourne.
Wilson, L. and Head, J., 2005, Dynamics of Groove Formation on Phobos by Ejecta from Stickney Crater: Predictions and Tests, *36th Annual Lunar and Planetary Science Conference,* 36, 1186.

ANALYSIS OF SPECTRAL IMAGES OF PHOBOS

V. S. Patsyn[1], V. A. Malinnikov[1], A. V. Grechishchev[1], J. Oberst[1,2], *[1]Moscow State University of Geodesy and Cartography (MIIGAiK), Moscow, RUSSIA; [2] German Aerospace Centre (DLR), Institute of Planetary Research, Berlin, Germany.*
Contact: v_patsyn@mexlab.ru

Introduction:

We have investigated the spectral reflectance of the surface of Phobos, using remote sensing data obtained by the HRSC (High Resolution Stereo Camera) of the European Mars Express mission. Color ratios reveal that the Phobos' surface is heterogeneous, in agreement with the previous studies based on the Phobos-2 and Mars Reconnaissance Orbiter data.

The object of study: The Martian's satellites are considered "unusual" because of their small size and proximity to Mars. The theory of their origin is the subject of much debate. The surface of Phobos can be represented by an ellipsoid whose dimensions are 13.3 x 11.1 x 9.3 km [1]. The major axis of Phobos is directed to Mars. Phobos has a circular orbit whose radius is 9515 km.

HRSC: characteristics of the camera: HRSC is a high-resolution stereo camera, which allows one to receive both images in different spectral bands (blue, green, red and near infrared) and panchromatic images (channels: stereo 1 and the photometric 1, nadir, photometric 2, stereo 2). To study the spectral characteristics of Phobos' surface we have used 4 spectral bands (IR, Red, Green and Blue) (table 1) from image data obtained by the HRSC on Mars Express [2]. The HRSC data have more spectral bands than previous cameras and images have wider coverage (including parts of the Phobos far side) than the previous data sets.

channel	the angle of deviation,°	spectral range, nm
IR	+15.9	970±45
GREEN	+3.3	530±45
BLUE	-3.3	440±45
RED	-15.9	750±20

table 1: Characteristics of spectral channels

Photometric corrections processing of HRSC data: Photometric processing was carried out according to the Hapke formula:

$$I/F=\omega/4\times\mu 0/(\mu 0+\mu)\times\{[1+B(\infty,h,B0)]\times P(\infty)+[H(\mu 0)\times H(\mu)-1]\}\times S(\infty,\theta) \qquad (1)$$

The Hapke parameter values were adopted from [3].

Geometric transformation: The ISIS (Integrated Software for Imagers and Spectrometers) software was used for the geometric projection of images of Phobos in the object-fixed cartographic coordinate system [4], taking into account the orbit and attitude of the spacecraft, the Phobos' shape and its orientation. For accurate co-registration of projected images, the "pixel by pixel" method implemented in the Scanex Image Processor software was applied [5]

Albedo maps: After combining the spectral images with each other, there was built a mosaic of Phobos' surface for each of the 4 channels individually. Albedo images for each flyby was obtained, using «reflectance scale factor» as a conversion factor of brightness values of pixels in the albedo (Figure 1, 2).

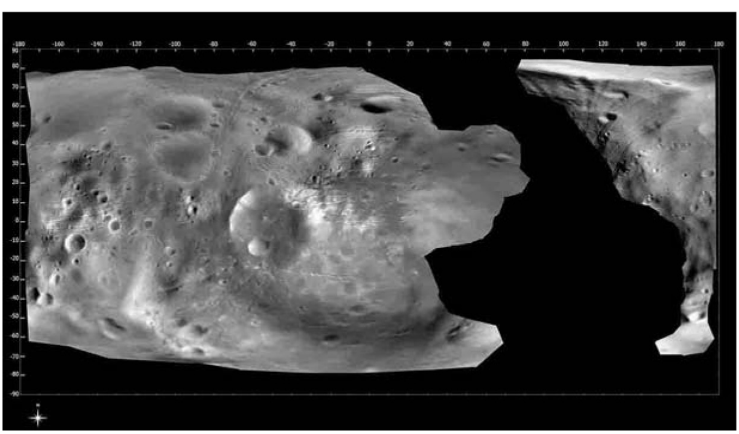

fig. 1. Mosaic image of the Phobos' surface in natural colors (red, green and blue channels)

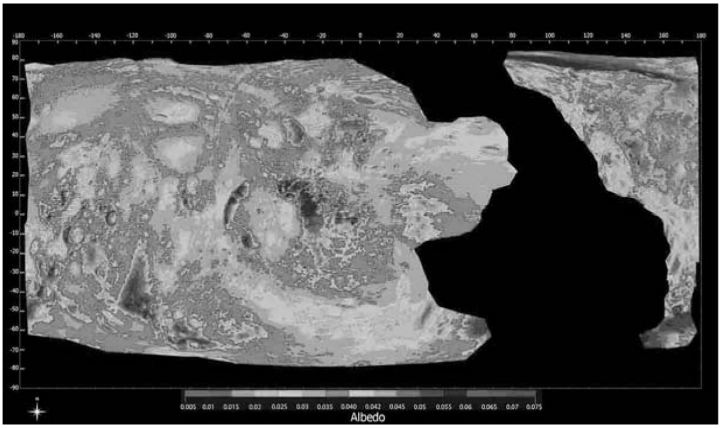

fig. 2. Map of Phobos' surface which shows the distribution of values of the albedo in the GR-channel

Spectral processing of HRSC data: On the basis of accurate combined co-registered images, there were calculated spectral indices i.e. color ratios, in particular, there was computed the "Index" value:

$$Index=V/NIR \qquad (2)$$

where V=(G+B)/2 is the spectral brightness in the visible range (obtained by adding green and blue channels, and divided by 2), and NIR is the spectral brightness in the near- infrared channel (Figure 3). This formula allowed us to compare the results of the Mars Express spacecraft survey with those obtained in the Phobos-2 Soviet mission [6].

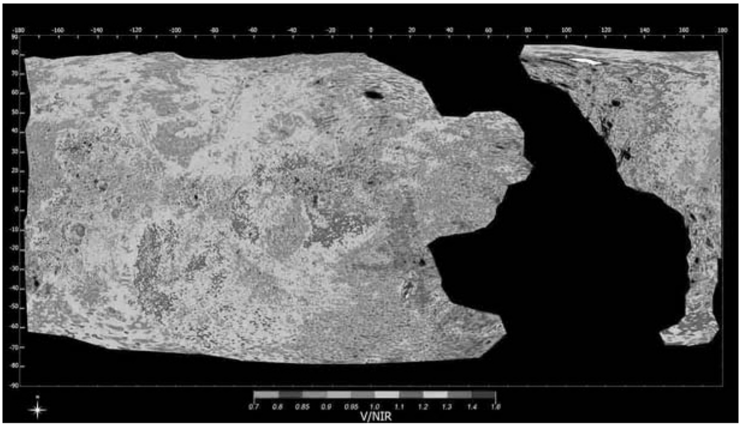

fig. 3. Map of the spectral index V/NIR distribution on Phobos' surface

Acknowledgement: This research was funded by the Russian Government (MEGAGRANT, Project name: "Geodesy, cartography and the study of planets and satellites", contract № 11. G34.31.0021).

References: [1] M. Wählisch et al. (2010) A new topographic image atlas of Phobos. Earth and Planetary Science Letters, 294, 547-553. [2] R. Jaumann et al. (2007) The high-resolution stereo camera (HRSC) experiment on Mars Express: Instrument aspects and experiment conduct from interplanetary cruise through the nominal mission. Planetary and Space Science, 55, 928-952. [3] P. Simonelli et al. (1998) Photometric properties of Phobos' surface materials from Viking images. ICARUS, 131, 52–77. [4] http://isis.astrogeology.usgs.gov/. [5]http://scanex.ru/en/software/default.asp?submenu=imageprocessor&id=index. [6] G.A. Avanesov (1994) Television studies of Phobos, Moscow, Nauka.

DEVELOPMENT GEOPORTAL FOR ACCESS TO PHOBOS DATA AND SCIENTIFIC ANALYSES

E. Matveev [1], I. Karachevtseva [1], J. Oberst [1, 2, 3],
[1]Moscow State University of Geodesy and Cartography (MIIGAiK), MIIGAiK Extraterrestrial Laboratory (MExLab), Gorokhovskiy per., 4, 105064, Moscow, Russia; [2]German Aerospace Center (DLR); [3]Technical University of Berlin, Germany.
Contact: e_matveev@mexlab.ru, i_karachevtseva@mexlab.ru, tel: +7-499-2673513

Introduction:

Conceptual approaches of Planetary Geographic Information Systems for mapping of Solar System bodies have been developed by researchers of the Laboratory for Planetary Cartography at the Moscow State University of Geodesy and Cartography (MIIGAiK), who have been involved in GIS-oriented planetary mapping since 2003 [1]. The works were continued within the MIIGAiK Extraterrestrial Laboratory (MExLab), which was organized in 2010 and funded by the Ministry of Education of the Russian Federation. MExLab scientists work with different planetary data, such as terrestrial planets and their satellites, including small bodies of the Solar system. Phobos was a priority for research deal with the mission Phobos-Grunt. Despite the failure to start the mission, we have many scientific results and it is very important to provide access to all researchers for planning future missions.

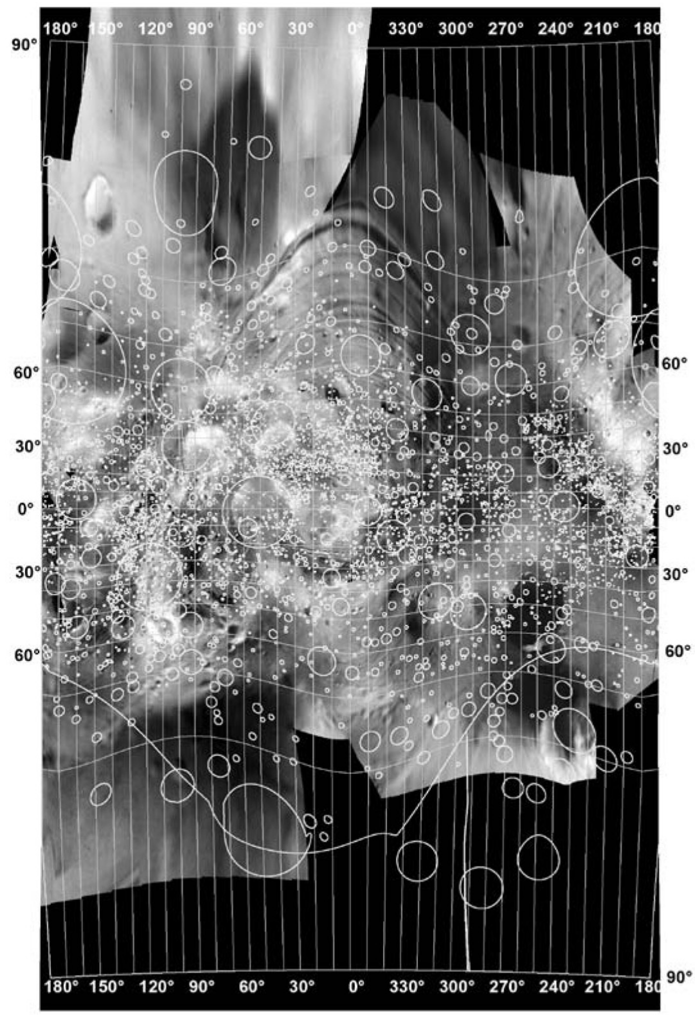

fig. 1. GIS Phobos: New orthomosaic developed in MIIGAiK using projection for 3-axial ellipsoid (Bugaevskiy projection) and based on modern Phobos Control point network [2]

Sources:

The Phobos information system was developed as a personal geodatabase, because the amount of Phobos data is still small. To create the system, the global DTM and mosaic derived from European “Mars Express” images (MEX) were used [3]. Additionally separated MEX and Viking orthoimages were converted and loaded into ArcGIS. Based on these data different derivatives products (slopes, shaded relief, vector Crater and Grooves layers and results of their statistics) were received during geo-analyses in GIS [4]. Also new Phobos control point network [2], newest DEM and orthomosaic developed using SRC Mars Express images (Fig.1), maps of landing sites, results of spectral [5] and crater analyses developed in MIIGAiK were used for creating GIS-oriented information system [6].

Methodology:

The goal of our work is to provide easy integration of Phobos data from many sources including MIIGAIK works, results of former and current missions provided by many organizations such as DLR, NASA, and Russian Academy of Science. For data management will be used ArcGIS Server software and method of access to data via «Phobos» Geoportal. For development “Phobos” Geoportal it is necessary to implement several important stages: to design of data model structure, to create metadata, to load information to database and provide public access to all results. Based at the conceptual data model approach for planetary mapping [7], we are developing logical and physical planetary data model for realization “Phobos” Geoportal. For data modeling we use eXtensible Markup Language (XML) and create XML-schema (Fig. 2), which provides description of the data, their relationships, domain names and topological constraints [8]. For images metadata will be used PDS4 [9] standard and for ArcGIS vector layers metadata we use standard of Federal Geographic Data Committee [10]. For the implementation PDS standard [11] into ArcGIS was developed “Metadata Converter” software.

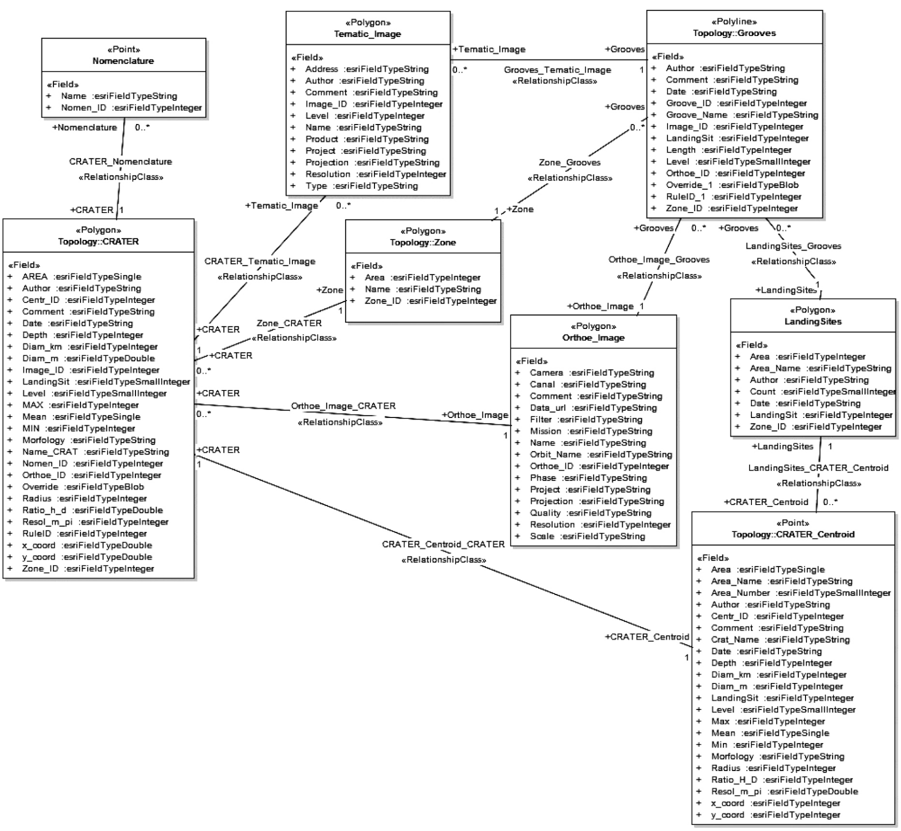

fig. 2. The preliminary structure of “Phobos” data model (XML-schema)

Conclusions:

The main goal of work is universal structure (template) of the planetary geodatabase structure, containing vector and raster layers. Now we are testing our results develop ing “Phobos” Geoportal and loading new data to geodatabase. The new results of this work will be presented at the conference.

Acknowledgements:
This work has been supported by a RFBR grant № 11-05-91323 “Geodesy, cartography and research satellites Phobos and Deimos” (join research with the Fund of Helmholtz), and also partially supported by grant of the government of the Russian Federation (Megagrant) on the topic: “Geodesy, cartography and study of planets and satellites”, agreement №11.G34.31.0021.

References:

[1] Cherepanova E., Karachevtseva I. et al. GIS “The Solar System Planets” Case Study of the ArcGIS Planet Data Model // International Cartographic Conference. 2005
[2] Zubarev A.E., I.E. Nadezhdina, A.A. Konopihin. Problem of processing of the remote sensing data for the shape modeling of the small bodies of the Solar system // Modern problems of remote the earth sensing from space, Space Research Institute RAS, Moscow, 2012 (in press).
[3] Wählisch M., Willner K., Oberst J., Matz K.-D. , Scholten F., Roatsch T., Hoffmann H., Semm S., Neukum G., 2010. A new topographic image atlas of Phobos, Earth and Planetary Science Letters 294, 547–553.
[4] Oberst J., I.P. Karachevtseva, et.al. Development global crater catalog of Phobos and GIS-analysis of the distribution of craters. Moscow, The Second Moscow Solar System Symposium, 10-14 October, 2011.
[5] Patsyn V.S, V.A.Malinnikov, A.V. Grechishchev. Research of spectrometric characteristics of the surface of Phobos on the HRSC data from the Mars Express spacecraft // Modern problems of remote the earth sensing from space, Space Research Institute RAS, Moscow, 2012 (in press).
[6] Karachevtseva I. et.al. Global Phobos Geodatabase and GIS analyses. Abstracts of 43 LPSC, // Proceedings of 43Lunar and Planetary Science Conference, # 1342
[7] Gasselt S. van, A. Nass. Planetary mapping – The datamodel’s perspective and GIS framework // Planetary and Space Science 59 (2011) 1231-1242
[8] ESRI (2008), XML Schema of the Geodatabase http://downloads.esri.com/support/whitepapers/ao_/XML_Schema_of_Geodatabase.pdf
[9] Crichton D. PDS4: Developing the Next Generation Planetary Data System // Planetary Data Workshop, USA, Flagstaff, June, 2012.
[10] Federal Geographic Data Committee http://www.fgdc.gov/index.html .
[11] Planetary Data System http://pds.nasa.gov/

ABOUT SOME INNER STRUCTURES OF THE EARTH, THE MOON AND MARS AS GEODYNAMICAL CONSEQUENCES OF THE ACTION OF MECHANIZM OF THE FORCED RELATIVE OSCILLATIONS OF THEIR CORE AND MANTLE.

Yu. Barkin[1,2,3], H. Hanada[1], S. Sasaki[1], M. Barkin[4],
[1]National Astronomical Observatory of Japan, Mizusawa, Japan; [2]Sternberg Astronomical Institute, Moscow, Russia; [3]Visiting professor at Mizusawa Astronomical Observatory of Japan; [4]Moscow Aviation Institute, Russia. Contact: barkin@inbox.ru

In connection with the planned space missions to the Moon and Mars to study the internal structure of these celestial bodies by seismic methods seem to be very relevant theoretical studies of possible features or internal structures of these celestial bodies. The mechanism of forced oscillations of the core and mantle of the celestial bodies and study of their geodynamic and geophysical consequences gives us opportunity to study some inner structures of the Earth, the Moon and Mars.

Introduction. The mechanism of forced relative oscillations of displacements and rotations under the action of the gravitational attraction of external celestial bodies [1] in the last decade, has attracted wide attention of specialists in various sciences of the earth and planetary science. On the base of this model some were solved fundamental problems of geodynamics and celestial mechanics, geology, geodesy and geophysics have been solved. This paper presents the results of the study of the possible role of forced relative oscillations of the core and mantle of the Earth, the Moon and Mars in the formation of the shell structure of these celestial bodies. First and foremost, the existence and nature of the zones of low seismic velocities (LVZ), as well as the zones of the extreme radial deformation of the spherical layer of the mantle (Fig. 1 (a-d)). As shown, the zones of low seismic velocity correspond to the spherical zones of the mantle for which the displacement of the particles are either small or absent and the change in directions of displacements is observed. The basis of this research is the solution of the problem of elasticity about the deformation of the mantle at the core displacements [2].

About model. As in [2], we consider the two-shell planet, consisting of a core and mantle. The mantle is considered as a visco-elastic body with a free surface and with a fixed base of the mantle. The core is considered as an unchangeable body the center of mass of which makes a small displacements and oscilations relatively to the mantle. These relative displacements can be realized due to the presence of a thin layer of low viscosity between the core and mantle. And these displacements find their confirmation in modern high-precision observations of the Earth's geocenter motion [3]. In a restricted treatment of the problem it is assumed that the core executes a given motion along the polar axis (the secular drift and oscillations of small amplitude). The displacements of the center of mass of the planet, as well as unidirectional displacements of the gravitating nucleus (or rather its excess mass caused by the density contrast of the core and mantle) cause the deformation of all layers of the mantle, for which the analytical description has been done in [2]. In this paper, we focus on the study of the radial deformation of the layers of the mantle and the allocation of special zones, spherical layers experiencing extreme effects of the gravitational nature of the core or do not experience any. It is important to emphasize that the position of these zones does not depend on the style of the displacements of the core, but is determined by the elastic parameters of the mantle and the sizes of the core and the mantle. It allows us to carry out preliminary studies of the location of specific zones in an internal structure of the Moon and Mars for their models as the "core-mantle system." Symptoms of the relative displacements of the core and the mantle of these celestial bodies seen in the secular and cyclical changes and variations of geophysical and geodynamic processes.

The radial deformation of the mantle of the planet (Earth, Moon, Mars). These deformations are discribed by formula: $u_r = \rho K_c\left[B_0 + C_0 + \left(B_2 + C_2\right)\zeta^2 + B_3\zeta^3 + \left(B_5 + C_5\right)\zeta^5\right]\zeta^{-3}\sin\varphi$ [3], where φ is a latitude, $\rho = \rho(t)$ is a changeable in the time distance between the centers of mass of the mantle and the core, which is a given function of time. $K_c = \Delta m_c / (\lambda r_m)$ is a dimensionless coefficient, Δm_c is a superfluous mass of the core, determining the gravitational effect of the deformation of the mantle by moving core, f is a gravitational constant. $\Delta m_c = 4\pi r_c^3\left(\delta_c - \delta_{m,l}\right)/3$, where δ_c is a mean dencity of the core, $\delta_{m,l}$ is a dencity of the mantle at its base. For the adopted the two-shell models of the Earth, of Mars and of the Moon were obtained following values: $K_{c;Earth} = 0.20883$, $K_{c,Mars} = 0.003779$,

$K_{c,Moon} = 0.006520$. Non-dimensional variable $\zeta = r/r_m$, where $r = |\mathbf{r}|$, characterizes the position of any point of the mantle with the radius vector $\mathbf{r}$. Thus, for points on the surface of a spherical core of the Earth $\zeta = \zeta_0 = r_c/r_m$, and at he surface of the planet $\zeta = 1$. Coefficients B_i and C_i are known functions of elastic parameters of the mantle λ, μ and geometric parameter ζ_0 [3]. For these models the core and mantle of the Earth, the Moon and Mars, respectively, we have: $\zeta_0 = 0.5462$, $\zeta_0 = 0.5462$ and $\zeta_0 = 0.5462$.

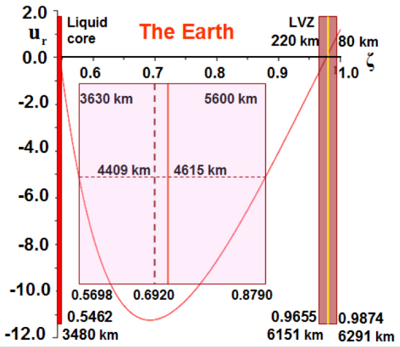

a) The radial deformation of the Earth's mantle.

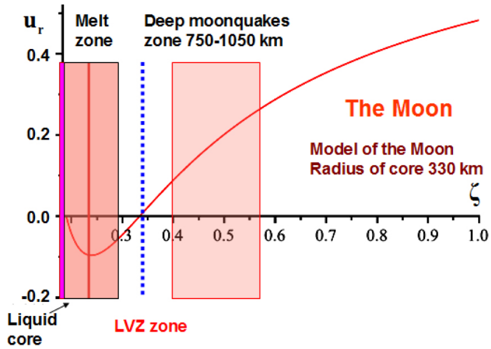

b) The radial deformation of the mantle of the Moon.

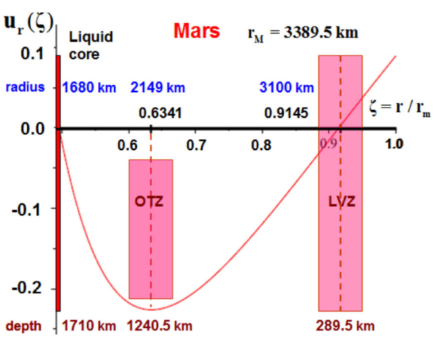

c) The radial deformation of the mantle of Mars.

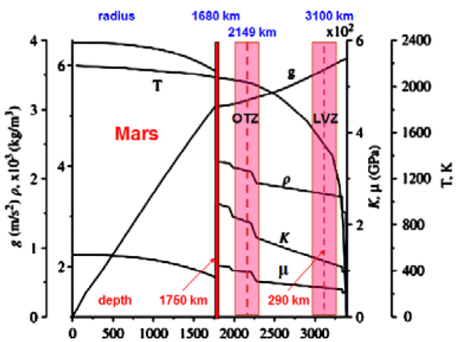

d) Zharkov's model of Mars and predicted zones.

fig. 1. (a-d). The graphs are the radial displacement of particles of the mantle, expressed in arbitrary units $10^{-3}\rho$. On Fig. 1 (d) the location of the identified zones is pointed on the graphs of famous Zhakov's Mars model. On the figures (c, d) OTZ is an olivine transition zone.

Conclusions. For the Earth, the origin of the low-velocity zone and its position is determined by the mechanism of forced displacements of the Earth's core. A similar low-velocity zone at about 300 km depth is predicted for Mars. Partially melt zone of the Moon with an average radius about of 416 km, possibly associated with the gravitational excitation and deformation of the shifting and oscillating core of the Moon. These findings are important for the preparation and conducting of seismic experiments on the Moon and Mars in the planned space missions.

References:

[1] Barkin Yu.V. (2002) Explanation of endogenous activity of planets and satellites and its cyclicity / / Proceedings of the Section of Earth Sciences, Russian Academy of Natural Sciences. Moscow, VINITI. No. 9, C. 45-97. In Russian.
[2] Barkin Yu.V., Shatina A.V. (2005) Deformation of the Earth's mantle due to core displacements // Astronomical and Astrophysical Transactions. V. 24. No. 3. P. 195-213.
[3] Barkin Yu.V., Vilke V.G. (2004) Celestial mechanics of the planet shells // Astronomical and Astrophysical Transactions. V. 23. Issue 6, P. 533-554.

MODELING MARTIAN METEOROID STREAMS GENERATED BY COMETS

V. Dmitriev[1], V. Lupovka[1], V. Sizenkov[1], J. Oberst [1,2,3],
[1]State University of Geodesy and Cartography (MIIGAiK), Gorokhovskiy per., 4, 105064, Moscow, Russia; [2] Technical University of Berlin, Berlin, Germany; [3] German Aerospace Centre (DLR), Berlin, Germany. Contact: v.lupovka@miigaik.ru, v_dmitriev@mexlab.ru

Introduction:

Mars and its natural satellites are bombarded by meteoroids from the asteroid belt, meteoroid streams generated by comets, and sporadic meteoroids. Meteoroid streams are the results of comet degradation which form during comet approaches to the Sun. Modeling of Martian meteoroid streams requires several work steps: identify potential parent bodies of Martian meteoroid streams – comets that have orbits approaching to the Mars orbit; construct models of potential meteoroid streams; determine their radiants and activity time; estimate the probability and velocity of possible meteoroid encounters with Mars and Martian satellites.

Selecting potential parent bodies of Martian meteoroid streams:

A database of 1037 periodical comets [1] was analyzed for selecting potential parent bodies of Martian meteoroid streams. Coordinates and distances of the nearest approaches of comet orbits to Mars orbit were calculated for each comet from the database. We identified 137 comets in orbits that approach Mars orbit within less than 0.15AU. Among them 88 comets approach Mars orbit within less than 0.1AU, and 17 comets of them approach Earth orbit within less than 0.10AU as well. The well-known comet 1P/Halley from this list is the parent body of two meteor showers: the Eta Aquarids in early May, and the Orionids in late October [1, 2].

The Model:

Model of meteoroids distribution in the stream tube was constructed by using parameters of the Eta Aquariids and the Orionids meteoroid streams. For modeling we used meteoroid streams parameters from [1, 2, 3]: time of maximum activity (specifically, the solar longitude when the shower or storm maximum occurs), the maximal cumulative particle flux, the profile description index, and the cumulative mass distribution.

The meteoroid cumulative particle flux of terrestrial meteoroid streams in [1, 2, 3] is presented as function of the solar longitude (i.e. as function of time). For modeling Martian meteoroid streams the cumulative particle flux (ρ) was recalculated as function of distance (r) from the stream axis:

$\rho(r) = ae^{br}$ $\rho(r) = ae^{br}$,

where a - parameter depending on the cumulative mass distribution, b – depends on specific stream structure and describes the profile description index. In this case comet velocity vector in the moment of the nearest approach is considered as a stream axis. Also we supposed that the moment of the nearest approach is the time of maximum activity.

Validation test:

We have checked the validity of our assumptions by applying the same approach for modeling Earth meteoroid environments. We identified 102 comets which come close to the Earth's orbit. These comets are candidates for parent bodies of terrestrial meteor showers. From the working list of 444 terrestrial meteor showers, currently the parent bodies of 94 meteor streams are identified: 45 of them are comets, the rest are asteroids [2]. From 102 near-Earth comets that we selected, 20 comets are parent bodies of terrestrial meteor showers. Others selected comets do not form meteor showers, or these streams do not identified with comets yet.

Stochastic modeling of meteoroid impacts on Phobos:

The stochastic modeling of meteoroid impacts on Phobos was performed by uniform random-event generator on a sphere [4]. Directions and velocities of possible impacts were calculated. Radiant coordinates were determined by comet velocity vectors at the moment of the nearest approach to Mars orbit. The effect of meteoroid screening by Mars and impact velocity dependence on leading or tailing Phobos hemisphere were taken into account. The effect of meteoroid screening by Mars is about 11% of particles that impact on the Phobos hemisphere oriented to Mars or about 5.5% of common impact number. Velocities of particles that impact onto Phobos leading and tailing hemisphere are different for up to ±2 km/s. Also comparison of simulated and observed crater distribution on Phobos is discussed.

Summary:

A database of 1037 periodical comets was analyzed for selecting potential parent bodies of Martian meteoroid streams. As a result, 137 candidates were found for parent bodies of Martian meteor showers. The time of activity of these potential Martian meteoroid streams was obtained. The model of the cumulative particle flux as function of distance from the stream axis was constructed. The model allows estimating probability and velocity of possible meteoroid encounters with Mars and Martian satellites and was used for modelling of Phobos meteoroid bombardment. The results of stochastic modelling of meteoroid impacts on Phobos are presented and compared with observations.

Acknowledgements:
This work has been supported by a grant from the Ministry of Education and Science of the Russian Federation (Agreement № 11.G34.31.0021 dd. 30/11/2010).

References:
[1] JPL's HORIZONS System http://ssd.jpl.nasa.gov/?horizons.
[2]. The IAU Meteor Data Center (MDC), http://www.astro.amu.edu.pl/~jopek/MDC2007/.
[3] Bieler T.: Modeling of impact from meteoroids streams test of ESABASE/DEBRIS final report, Consultancy No. 149/98/BIELER, 29p., 1998.
[4] Press W. H., Teukolsky S. A., Vetterling W. T.: Numerical Recipes. The Art of Scientific Computing. Third Edition, Cambridge University Press, 1237p., 2007.

CORRECTION OF THE IONOSPHERE INFLUENCE IN SUBSURFACE SOUNDING OF MARS GROUND

V.M. Smirnov, O.V. Yushkova,
Kotel'nikov Institute of Radio Engineering and Electronics of RAS, Fryazino Branch, Russia. Contact: vsmirnov@ire.rssi.ru, o.v.y@mail.ru

Introduction:

Interpretation of the data measurements is the important stage for extracting complete scientific information at carrying out of radiophysical probing with using automatic interplanetary stations. The question of the proper interpretation of radar measurements is crucial to the reliability of such data. Parameters of the reflected signal depend on a planet ionosphere, its surface and properties of subsurface layer. It is necessary to notice, that the dominant could be a reflection both the ionosphere and the surface of the planet, according to the frequency range of the signal. The sounding signals can be distorted due to the dispersion in the ionosphere plasma. This distortion depends on two factors. One is the maximum electron concentration. It determines the ionosphere transparency for radio waves. The other is the Total Electron Content which is the main ionosphere characteristic defining the level of distortion and the signal shape after penetration of the ionosphere. Here we will discuss ways to dispose of the ionospheric effect, taking into account that, as a rule, the ionosphere is unknown and changes with time and space. The investigation was motivated by the MARSIS experiment on Mars Express [1-3] and by a similar experiment in future.

The characteristics of the MARSIS pulses

We first briefly characterize the pulses used in the MARSIS system. The multi-frequency radar has four bands with centered frequencies $\bar{f}$ = 1.8, 3.0, 4.0 and 5.0 MHz. An important parameter is the ratio of the signal frequency half bandwidth and the center frequency - $p=\frac{B}{2\bar{f}}=\frac{\Delta\Omega}{2\bar{\omega}}$, $\bar{\omega}=2\pi\bar{f}$, $\Delta\Omega=2\pi B$, where *B* is the spectral band of the signal. The chirp with a frequency band of 1.0 MHz is used by MARSIS for the transmitted signal. Parameter *p* is referred as the broadband coefficient. The main characteristics of the MARSIS signals are collected in Table. From here it is follow that, all bands are broadband with $2p \geq 0.2$.

band number	1	2	3	4
center frequency, MHz	1.8	3.	4.	5.
center wavelength, m	166,67	107,14	78,95	62,5
broadband coefficient	0.28	0.17	0.13	0.10

table. Main characteristics of the MARSIS signals

Modeling results

For numerical modeling distribution of radio waves on a line «spacecraft - an ionosphere - a surface – an ionosphere - spacecraft» has been developed model of high-altitude distribution of dielectric permeability of the Mars ionosphere. A priori information for model is the real profile of electron concentration. The results of numerical modeling based on Fourier decomposition of frequency dependence of a square of the signal spectrum module, reflected from the dielectric-non-uniform environment "ionosphere-ground", have shown, that harmonics with numbers more than 100 describe influence of an ionosphere. Thus, the filtration of harmonics with numbers is more 100 in Fourier transformation of a spectrum of the reflected signals allows to correct distortions, inserting the Mars ionosphere. The specified procedure allows eliminating dispersive influences of ionosphere even in that case when information about ionosphere absence. This same procedure may be used to diagnose the existence of the ionosphere of investigated space object.

Acknowledgements. This work has been supported by the Presidium program of the RAS «Fundamental problems of researches and development of Solar system».
This work was supported by the grant of the Russian academy of sciences Presidium Program 22: "Fundamental problems of research and exploration of the Solar system".

References:

1. Picardi G., et al. Mars Advanced Radar for Subsurface and Ionosphere Sounding (MARSIS). Models and System Analysis/ Technical Report N. MRS-001/005/99.
2. Armand N.A., Smirnov V.M. and T. Hagfors. Distortion of radar pulses by Martian ionosphere. Radio Sci., 38, NO. 5, 1090 (2003).
3. Smirnov V.M., Chernaya L.F., Yushkova O.V., Rykov K.N. Radar sounding of Mars from the orbit of the Mars-Express automatic interplanetary station. Cosmic Research, 2006. T. 44. No 4. P. 317-328.

EXPLANATION OF THE SPECTROPHOTOMETRIC PROPERTIES OF MOON AND MARS BY SHADOW MECHANISM.

A.V. Morozhenko[1], A.P. Vidmachenko[1], N.M. Kostogryz[1],
Main Astronomical Observatory of National Academy of Sciences of Ukraine, Ak. Zabolotny 27, Kyiv 03680, Ukraine. Contact: vida@mao.kiev.ua

Up to now different versions of the shadow mechanism, and sometimes involve a coherent mechanism use for the analysis of data on the phase dependence of brightness atmosphereless celestial bodies. Modification of B. Hapke [4] models are divided into two groups: a) W. Irwine [6] and E. Yanovitskij [10, 11] (unknown parameters are a single scattering albedo ω, particle packing factor g, semi-transparent of particles æ and the scattering function χ(α)) and 2) [1, 2, 5, 8], which introduced an additional 4-6 parameters and coefficients. These modifications achieved a good agreement between observed and calculated opposition effects in several wavelengths, but there are difficulties in analyzing of the color index C(α) dependency and photometric contrast of features with changing of phase angle K(α) and on disk (μ_o=cos í).

We explored the possibility to obtain good agreement of observed and calculated values of C(α), K(α) and K(μ_o) on the Moon and Mars surfaces with a minimum number of unknown parameters using a modification of Yanovitskij [9, 10]. As ω and æ parameters are mutually dependent, we propose empirical relation between them æ=$(1-\omega)^n$. Assuming that [χ(0°)/χ(5°)] = χ(5°/χ(10°], the data on the phase dependence of brightness and of the opposition effect at a single wavelength, we determined the values of ω, χ(α) , g, and the first term of the expansion χ(α) in a series of Legendre polynomials x1, which we use for calculation the correction for multiple scattering. Good agreement between calculated and observed data of C(α)=U(α)-I(α) for dark and bright parts of the lunar surface and the integral disk was reached with n≈0,25, g=0,4 (porosity 0,91), x=-0,93, ω=0,137 at λ=359 nm and 0,394 at λ=1064 nm, and for Mars with a value of n≈0,25, g=0,6 (porosity 0,84), x1≈0, ω=0,210 at λ=359 nm and ω=0,784 at λ=730 nm (see table 1, Fig. 1, 2).

α°	0	1	2	3	4	5	10	20	30	40	50
χ(α), Moon	3,054	3,011	2,969	2,896	2,858	2,841	2,643	2,334	2,019	1,740	1,534
χ(α), Mars	1,533	1,525	1,516	1,508	1,499	1,491	1,450	1,305	1,200	1,148	0,988
α°	60	70	80	90	100	110	120	130	140	150	
χ(α), Moon	1,371	1,208	1,069	0,905	0,761	0,616	0,485	0,417	0,381	0,341	
χ(α), Mars	0,932	0,855	0,819	0,828	0,835	0,862	0,899	0,985	1,010	1,118	

table 1. Scattering function of the Moon and Mars

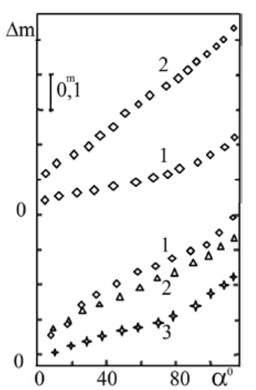

fig. 1. Comparison of the observed [7] and calculated (g = 0,4, n = 0,25) color index Δm=m(359nm)-m(1064 nm) with phase angle for the dark (Centre of Plato, ω(359nm)=0,0955, ω(1064 nm)=0,278) - 2, and light (East of Clavius D, ω(359nm)=0,204, ω(1064 nm)=0,615) moon features - 1, for the average Moon (ω(359nm)=0,137, ω(1064 nm)=0.394) - 3, and as æ=1 - 4.

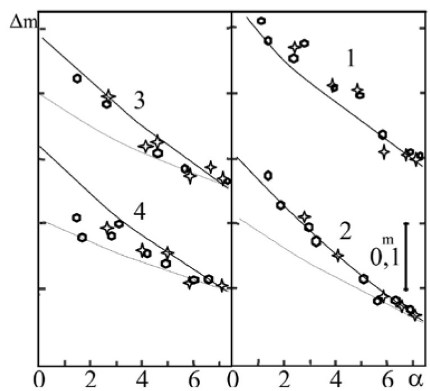

fig. 2. Comparison of observed and calculated opposition effects for the dark (Sirtis Major, open circles) and light (Arabia - ²) features on the disk of Mars [12] at λ=430 nm - 1, 550 nm - 2, 670 nm - 3 nm and 1040 - 4, for which ω=0,310, 0,467, 0,577, 0,613 (Sirtis Major - thick line) and ω=0,355, 0,638, 0,853, 0,939 (Arabia - thin line), respectively, for g=0,6, n=0,25.

Some studies examined the combined effect of shadow and coherent mechanisms. We tried to find observational evidence of the presence of the coherent mechanism. The opposition effect of brightness when $\alpha<1°$ coherent mechanism only enhances the shadow effect, so these mechanisms are difficult to separate. However, polarization measurements of 13 features on the lunar surface at small values of α [3] do not exclude the possibility of a coherent mechanism to manifest the light components at long wavelengths.

For the Moon at α=1,6° the angle of plane of polarization is ψ=92° in the filter U, 112° in the filter G, 102° in the filter I (Copernicus, L=-20° 08', φ=+10° 11') and ψ=87° in the filter U, 88° to the filter G, 89° in the filter I (Platon, L=-10° 32', φ=+51° 25').

1. Bowell E., Hapke B., Domingue D., Lumme K., et al. Applications of photometric models to asteroids // Asteroids II /Eds. Binzel R.P., Gehrels T.. Matthews M.S. // Tucson: Univ. Arizona Press. – 1989. - P. 524-556.
2. Buratti B.J., Hillier J.K., Wang M., The lunar opposition surge: observations by Clementine // Icarus. – 1996. - V. 124, No 2. – P. 490-499.
3. Gehrels T., Coffeen D.L., Owings D. Wavelength dependence of polarization. III. The lunar surface // Astron. J. - 1964. - V. 69, No 10. - P. 826-852.
4. Hapke B. A theoretical function for the lunar surface // J. Geophys. Res. - 1963. - V. 68, No 15. - P. 4571- 4586.
5. Hapke B. An improved the theoretical lunar photometric function // Astron. J. – 1966. - V. 71, No 5. - P. 333-339.
6. Irwine W.M. The shadowing effect in diffuse reflection // J. Geophys. Res. - 1966. - V. 71, No 12. - P. 2931-2937.
7. Lane A.P., Irvine W.M., Monochromatic phase curves and albedos for the lunar disk // Astron. J. - 1973. -V. 78. - No 3. - P. 267-277.
8. Lumme K., Bowel E. Radiative transfer in the surface of atmosphereless bodies. I. Theory // Astron. J. - 1981. - V. 86, No 11. - P. 1694-1704.
9. Morozhenko A.V. Effects of coherent scattering in polarization properties of Galilean satellites of Jupiter? // Kinematic and Physics of Solar system bodies. – 2008. – V. 24, No 2. – P. 155-157.
10. Morozhenko A.V., Yanovitskij E.G. An optical model of the surface of the Moon // Astronomy Reports. - 1971. - V. 48, No 1. - P. 172-183.
11. Morozhenko A.V., Yanovitskij E.G. An optical model of the Martian surface in the visible region of spectrum // Astronomy Reports. – 1971. – V. 48, No 4. – P. 795-809.
12. O'Leary B.T., Jackell L., The 1969 opposition effect of Mars. Full disk, Syrtis Mayor and Arabia // Icarus. - 1979. - V. 13, No 3. - P. 437-448.

SIGNATURES AND CHARACTERISTICS OF INTERNAL GRAVITY WAVES IN THE MARS' ATMOSPHERE AS REVEALED BY THE MGS RADIO OCCULTATION TEMPERATURE DATA ANALYSIS

V. N. Gubenko, I. A. Kirillovich, A. G. Pavelyev, V. E. Andreev, R. R. Salimzyanov and A. A. Pavelyev,
Kotelnikov Institute of Radio Engineering and Electronics of the Russian Academy of Sciences, 141190, Vvedenskogo sq. 1, Fryazino, Moscow region, Russia.
Contact: vngubenko@gmail.com

It is well known that internal gravity waves (IGWs) affect the structure and mean circulation of the Earth' middle and upper atmosphere by transporting energy and horizontal momentum upward from the lower atmosphere. The IGWs modulate the background atmospheric structure, producing a periodic pattern of spatial and temporal variations in the wind velocity, temperature and density. Similar effects are anticipated for the Mars since IGWs are a characteristic of stably stratified atmosphere. Temperature profiles from the Mars Global Surveyor radio occultation (MGS RO) measurements reveal vertical wavelike structures assumed to be atmospheric IGWs in the Mars' lower atmosphere (*Creasey et al*., 2006). The very large IGW amplitudes inferred from MGS RO data imply a very significant role for IGWs in the atmospheric dynamics of Mars. There is one general problem inherent to all measurements of IGWs. Observed wave-like variations may alternatively be caused by the IGWs, turbulence or persistent layers in the atmosphere, and it is necessary to have an IGW identification criterion for the correct interpretation of obtained results.

In this context, a new method for the determination of IGW parameters from a single vertical temperature profile measurement in a planetary atmosphere has been developed (*Gubenko et al*., 2008). This method does not require any additional information not contained in the profile and may be used for the analysis of profiles measured by various techniques. The criterion for the IGW identification has been formulated and argued. In the case when this criterion is satisfied, the analyzed temperature fluctuations can be considered as wave-induced. The method is based on the analysis of relative amplitude thresholds of the wave field and on the linear IGW saturation theory in which these amplitude thresholds are restricted by dynamical (shear) instability processes in the atmosphere. When the amplitude of an internal gravity wave reaches the shear instability limit, energy is assumed to be dissipated in such a way that the IGW amplitude is maintained at the instability limit as the wave propagates upwards. We have extended the analysis technique of *Gubenko et al*. (2008) in order to reconstruct the complete set of IGW characteristics (including such important parameters as the kinetic and potential wave energy and IGW fluxes of the energy and horizontal momentum) from temperature perturbations in a single vertical profile (*Gubenko et al*., 2011). We propose also an alternative analysis method to estimate the relative amplitude threshold (and to extract IGW parameters) from perturbations of the Brunt-Vaisala frequency squared in a single vertical profile (*Gubenko et al*., 2011). An application of the developed method to the RO temperature data has given the possibility to identify the IGWs in the Mars' stratosphere and to determine the magnitudes of key wave parameters such as the intrinsic frequency, amplitudes of vertical and horizontal perturbations of the wind velocity, vertical and horizontal wavelengths, intrinsic vertical and horizontal phase (and group) speeds, kinetic and potential energy, vertical fluxes of the wave energy and horizontal momentum. The obtained results of internal wave studies in the Mars' stratosphere found from the MGS RO temperature profiles are presented and discussed.

This work was supported by the program of the RAS Presidium #22 and the RFBR Grant 10-02-01015-a.

References:

Creasey, J. E., Forbes, J. M., and Hinson, D. P.: Global and seasonal distribution of gravity wave activity in Mars' lower atmosphere derived from MGS radio occultation data, Geophys. Res. Lett., 33, L01803, doi: 10.1029/2005GL024037, 2006.
Gubenko, V. N., Pavelyev, A. G., and Andreev, V. E.: Determination of the intrinsic frequency and other wave parameters from a single vertical temperature or density profile measurement, J. Geophys. Res., 113, D08109, doi:10.1029/2007JD008920, 2008.
Gubenko, V. N., Pavelyev, A. G., Salimzyanov, R. R., and Pavelyev, A. A.: Reconstruction of internal gravity wave parameters from radio occultation retrievals of vertical temperature profiles in the Earth's atmosphere, Atmos. Meas. Tech., 4, 2153-2162, doi:10.5194/amt-4-2153-2011, 2011.

ABSTRACTS SUBMITED TO SECTION 5. DUST AND DUSTY PLASMA IN SPACE

INFLUENCE OF DUST ON RADIANCE SPECTRA OF VARIOUS ASTRONOMICAL OBJECTS

M. I. Błęcka, L. Zasova

The dust is an important constituent of the surfaces and environments of planets (e.g. Mars) and other astronomical objects like comets and asteroids. The measured spectra are strongly affected by the processes taking place in atmospheres and on the surfaces and by the structure, composition and the spatial distribution of dust. The particles of the dust, illuminated by solar light, scatter, absorb and emit radiation. The reflected and emitted radiation are transmitted through the atmospheres before being collected by observing instruments. The reflection, absorption, scattering, and emission processes depend on the object-Sun geometry and on the thermal state of the surfaces.

In the present paper we are mainly concentrated on the influence of optical parameters of dust on spectra. To this purposes the equation of radiative transfer through the assembly of dust grains and various gases is solved. The number density distribution of the dust grains in the atmospheres and their size distribution are drawn from the recent theoretical models. A few phenomenological scattering phase functions are taken into account.

The main purposes of the paper are:

1) discussion of various dust materials, size distributions and optical parameters
2) demonstration of simulated spectra done by means of a radiation transfer models
3) comparison the results of simulated with observed spectra

RADAR IMAGE FORMATION OF NEAR-EARTH ASTEROIDS

Y. A. Gavrik, E. A. Kuleshov, A. L. Gavrik,
Kotel'nikov Institute of Radio Engineering and Electronics of RAS, Fryazino, Russia, alg248@ire216.msk.su

Introduction: It is a vast number of asteroids move around Sun, and knowing their physical properties is essential to understanding the evolution of the solar system. While radar astronomy collects detailed information on the orbits, sizes, shapes, and composition of many asteroids, it also gives an access to information about the hazard potential of individual NEOs that may threaten Earth and the viability of proposed mitigation strategies. To improve the capabilities of asteroid observations with unmodulated radar signals, we have developed reconstruction of radar scattering image which allows one not only to get an equatorial hull of the asteroid but also to estimate some of the scattering properties of its surface using another representation of the spectra intensity of radar echoes. Using our scattering image technique it is possible to retrieve information about scattering law of asteroid surface and indicate local reflection areas on its surface. The image reconstruction process was probed on the asteroid 1998 WT24 during its closest approach to the Earth in 2001 when it was observed by Evpatoria–Medicina bistatic radar system [1]. To construct an image we have chosen 101 spectra with high signal to noise ratio to cover the whole rotation of the asteroid. A time interval between the spectra was about ~1.5 min that corresponds to the rotation angle ~0.04 rad. Constructed image are shown on the figure.

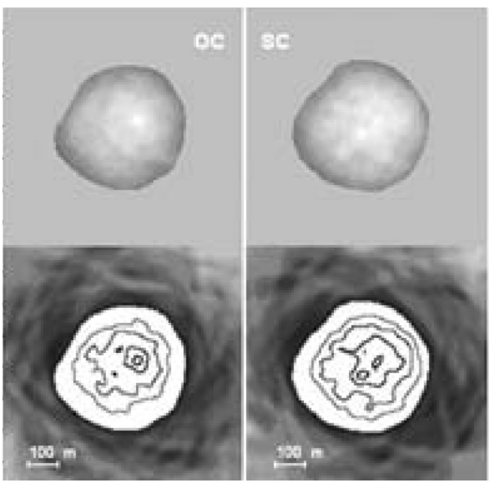

fig. Scattering image of asteroid 1998 WT24 obtained for OC(left) and SC(right) polarizations

On the top images, a dark-gray color we interpret as a concavity while group of radar-bright pixels we interpret as a raised feature with the evidence of high scattering. At the same time, the bottom images provide more convenient information representing the same intensity of pixels in the form of contour lines corresponding to identical brightness of the top image. The contour lines within hull correspond to four values of brightness: 0.97, 0.9, 0.8 and 0.6 of the maximum value of brightness. The brightness outside hull are characterized the accidental nature of a noise.

Results: It is easy to see on the figure that scattering properties of asteroid 1998 WT24 show considerable structures, identical in both OC and SC polarizations. Constructed image also demonstrates that the asteroid hull has asymmetrical shape with maximum dimension of 420 m for OC polarization and 435 m for SC. A minimum one is 380 m for both polarizations. A layout of axes of the minimum and maximum sizes almost the same for both polarizations. However, small differences of the hull between OC and SC might indicate scattering features on the borders of the asteroid. It clearly distinguishes asymmetrical shape of the brightness distribution; the outlines have irregular shapes because of the maximum brightness are observed not in the center of the asteroid. Also there are three regions with high brightness but their positions are different for OC and SC polarizations. Our constructed image demonstrates integral scattering features and main surface particulars correspond to more detailed delay–Doppler images presented by Busch M.W. et al [2].

Thus, presented technique is enhancing radar observation of NEO's by reconstructing scattering images that do not only provide information about an asteroid hull, but also emphasize areas with features on the surface like peaks or edges whose scattering features are unique while small details of the relief are missed.

Acknowledgements: The work is partially supported by the program No.22 of the RAS Presidium "Fundamental problems of the research and exploration of the Solar system".

References: 1. M. di Martino et al. (2004) Results of the first Italian planetary radar experiment. Plan.&Sp. Science, V.52. Is.4.
2. Busch M.W. et al. (2008) Physical properties of near-Earth Asteroid 1998 WT24. Icarus, 195 (2).

LOW FREQUENCY TURBULENCE IN INHOMOGENEOUS DUSTY PLASMAS.

A. Volokitin[1], B. Atamaniuk[2],
[1] Space Research Institute RAS, 84/32 Profsoyuznaya Str, Moscow, Russia; [2] Space Research Centre of the Polish Academy of Sciences, Bartycka 18A,00-716 Warsaw, Poland, Contact: a.volokitin@mail.ru

In space plasma often contains dust particles that become electrically charged. Notable examples are the dusty plasma, the atmosphere of comets, planetary rings, the lower ionosphere. In laboratory research, the most important case is the formation of dusty plasma near the walls of the devices with magnetic confinement of plasmas (tokamaks, etc.). Under these conditions, the plasma temperature is not too high, and collisions of the neutrals, ions, electrons and dust with each other, as well as the presence of plasma inhomogeneity, plays an important role in the development of turbulence in a magnetized plasma. In our report, basing on a linear analysis of the effect of dust particles on the properties of low-frequency waves and the conditions of instability, we consider stabilization of nonlinear instabilities via three-wave interaction. Emphasis is placed on a resistive instability of drift waves, but also the results of studies in other cases, including the instability of current carrying and Farley-Buneman instability. Because this problem requires essentially three-dimensional consideration due to the specifics of the nonlinear interaction of low frequency waves in a magnetized plasma, it is very difficult for fully 3D numerical simulations. However, considering the conditions under which the linear growth rates are lower than the frequency drift waves, we can assume that nonlinear interaction also remains weak. Then, despite the important role of dissipative processes of the original system can reduce the nonlinear equations to a system of ordinary differential equations describing the dynamics of the wave amplitudes in the active medium taking into account the three-wave interaction and use it to explore different regimes of turbulence.

Usually, studies focus on examining the well-developed phase of plasma turbulence when there is a wide spectrum of plasma waves. On the other hand, is well known that even systems with a finite number of interacting waves can be realized in the turbulent state of the active media. At the same time the essential role of dissipation of the waves suggests that, at low threshold of instability, a typical perturbed state of the plasma can be described as a finite set of interacting waves, some of which are unstable and others are strongly damped. In such cases, the number of waves remains finite, but because of competition between the instability and damping of the waves when they interact, the dynamics of the amplitudes of the waves becomes stochastic in nature and the so-called few-mode turbulence. In analyzing the conditions of the various modes of instability of nonlinear low-frequency waves and discussed the transition from quasi-periodic regime to a few-mode turbulence, and then to the fully developed turbulence, depending on the density and composition of the dust component of the plasma.

This research is supported by grant O N517 418440

ABSTRACTS SUBMITED TO SECTION 6. INTERACTION OF SOLAR WIND WITH MARS, VENUS, MERCURY, AND MOON

PRINCIPLE OF LOCALITY AND ANALYSIS OF RADIO OCCULTATION DATA

A. G. Pavelyev[1], K.Zhang[2], A.A. Pavelyev[1], Y.A. Liou[3], C.S. Wang[2], J. Wickert[4], T.Schmidt[4], and Yu. Kuleshov[2];
[1] FIRE RAS, Vvedenskogo sq. 1, Fryazino, 141190 Russia Contact: alxndr38@mail.ru; [2]RMIT University, Melbourne Australia
E-mail: kefei.zhang@rmit.edu.au; [3]CSRSR, NCU, Taiwan. E-mail: yueian@csrsr.ncu.edu.tw; [4]GeoForschungsZentrum Potsdam (GFZ-Potsdam) Telegrafenberg, 14473 Potsdam Germany E-mail: wickert@gfz-potsdam.de

The fundamental principle of local interaction of radio waves with a spherically symmetric medium is formulated and introduced in the radio occultation (RO) method of remote sensing of the ionosphere and atmosphere of the Earth and planets. In accordance with this principle, the main contribution to variations of the amplitude and phase of radio waves propagating through a medium makes a neighborhood of a tangential point where gradient of the refractive index is perpendicular to the radio ray. A necessary and sufficient condition (a criterion) is established to detect from analysis of RO data the displacement of the tangential point from the radio ray perigee. This criterion is applied to the identification and location of layers in the atmosphere and ionosphere by use of GPS RO data. RO data from the CHAllenge Minisatellite Payload (CHAMP) are used to validate the criterion introduced when significant variations of the amplitude and phase of the RO signals are observed at RO ray perigee altitudes below 80 km. The detected criterion opens a new avenue in terms of measuring the altitude and slope of the atmospheric and ionospheric layers. This is very important for the location determination of the wind shear and the direction of internal wave propagation in the lower ionosphere, and possibly in the atmosphere. The new criterion provides an improved estimation of the altitude and location of the ionospheric plasma layers compared with the back-propagation radio-holographic method previously used.

The work was partly supported by Program 22 of Presidium of Russian Academy of Sciences and by grant of Russian Fund of Basic Research No.10-02-01015-a.

MONITORING SOLAR WIND INFLUENCE ON LAYERS IN THE LOWER IONOSPHERE USING EIKONAL ACCELERATION/INTENSITY METHOD FROM ANALYSIS OF GPS OCCULTATION DATA

A.G. Pavelyev[1], J. Wickert[2], T.Schmidt[2], A.A. Pavelyev[1], K.Zhang[3], Y. A. Liou[4], Yu. Kuleshov[3],
[1] FIRE RAS, Vvedenskogo sq. 1, Fryazino, 141190 Russia
Contact: alxndr38@mail.ru; [2]GeoForschungsZentrum Potsdam (GFZ-Potsdam) Telegrafenberg, 14473 Potsdam Germany E-mail: wickert@gfz-potsdam.de web page http://www. gfz-potsdam.de; [3]RMIT University, Melbourne Australia E-mail: kefei.zhang@rmit.edu.au; [4]CSRSR, NCU, Taiwan.
E-mail: yueian@csrsr.ncu.edu.tw

Effects of radio waves propagation in the trans-ionospheric communication link satellite-to-satellite (refraction, diffraction, and scattering) are analysed by use of the high stability signals of GPS navigational system registered during radio occultation (RO) experiments. An analytical model is introduced for description of the radio waves propagation in a stratified medium consisting of sectors having the spherically symmetric distributions of refractivity. Model presents analytical expressions for the phase path and refractive attenuation of radio waves. Model is applied for analysis of the radio waves propagation effects along a prolonged path including the atmosphere and two parts of the ionosphere. Model explains significant amplitude and phase variations at the altitudes 30-90 km of the RO ray perigee as connected with influence of the inclined ionospheric layers. By use of the CHAllenge Minisatellite Payload (CHAMP) radio occultation (RO) data a description of different types of the ionospheric contributions to the RO signals at the altitudes 30-90 km of the RO ray perigee is introduced and compared with results of measurements obtained earlier in the communication link satellite-to-Earth at frequency 1.5415 GHz. A classification of the ionospheric effect is based on comparison of the amplitude variations and second derivative on time of the eikonal scintillations (eikonal acceleration) of RO signal. An innovative eikonal acceleration technique is described and applied for the identification, location, determining the height, slope and displacement from the RO ray perigee of the ionospheric layers. A coherent part of the amplitude and eikonal acceleration variations corresponds to effects of layered structures (refraction and diffraction), an uncorrelated part is relevant to impact of small-scale irregularities (scattering and diffraction). In this contribution it is shown that (1) the S4 index of amplitude variations can be considered as an index of the ionospheric plasma influence on RO signal in the trans-ionospheric satellite-to-satellite links in a like fashion with the S4 index introduced formerly for the trans-ionospheric satellite-to-Earth links (2) the S4 index can be used in the satellite-to-satellite links as a radio-physical index of activity of plasma disturbances in the ionosphere; and (3) the relative number of GPS RO events with high values of the S4 index in the satellite-to-satellite links can be used to establish a connection between the intensity of plasma disturbances and solar activity. The general number of RO events with strong amplitude variations can be used as an indicator of the ionospheric activity. We found that during 2001-2010 the daily averaged S4 index measured during CHAllenging Minisatellite Payload (CHAMP) mission depends essentially on solar activity. The maximum occurred in January 2002, minimum has been observed in summer 2008. Different temporal behavior of S4 index has been detected for polar (with latitude greater than 60º) and low latitude (moderate and equatorial) regions. For polar regions S4 index is slowly decreasing with solar activity. Quasi-periodical oscillations (with time period of about 5-7 month) of the S4 index were detected which may correspond to possible impact of the solar wind and ultraviolet emission.

The work was partly supported by Program 22 of Presidium of Russian Academy of Sciences and by grant of Russian Fund of Basic Research No.10-02-01015-a.

ABSTRACTS SUBMITED TO SECTION 7. PROBLEMS OF COSMOGONY

ISON COOPERATION FOR NEAR-EARTH ASTEROID RESEARCH

Yu. N. Krugly[1], I. E. Molotov[2], N. M. Gaftonyuk[3], R. Ya. Inasaridze[4] , A. V. Sergeev[1], V. G. Shevchenko[1], I. G. Slyusarev[1], I. N. Belskaya[1], V. G. Chiorny[1], V. V. Koupianov[5], V. V. Rumyantsev[3], O. A. Burkhonov[6], S. A. Ehgamberdiev[6], L. V. Elenin[2], V. A. Voropaev[2], A. R. Baransky[7], N. H. Minikulov[8], M. I. Gulyamov[8], S. K. Abdulloev[8], E. Litvinenko[5], A. Aliev[6],
[1]Institute of Astronomy, Karazin Kharkiv National University, Sumska str. 35, Kharkiv 61022, Ukraine; [2]Keldysh Institute of Applied Mathematics, RAS, Moscow, Russia, [3]Crimean Astrophysical Observatory, Crimea, Ukraine, [4]Kharadze Abastumani Astrophysical Observatory, Ilia State University, Tbilisi, Georgia, [5]Pulkovo Observatory, RAS, St. Petersburg, Russia, [6]Ulugh Beg Astronomical Institute, UAS, Tashkent, Uzbekistan, [7]Kiev Shevchenko National University, Kiev, Ukraine, [8]Institute of Astrophysics, TAS, Dushanbe, Tajikistan, Contact: krugly@astron.kharkov.ua

Introduction:

In orbits that cross the Earth's orbit, there are thousand small bodies - Near-Earth Asteroids (NEAs), which constitute a potential threat of collision with the Earth. The study of their physical and dynamical parameters is required to assess the risk of such an impact for our civilization. Currently, the process of NEAs discovery is much faster than getting data on physical parameters of these bodies. Acquisition of such characteristics as sizes, shapes, rotation parameters, surface composition, densities will permit to evaluate the degree of risk and the possibility of preventing potentially *catastrophic* impacts with the Earth.

The International Scientific Optical Network (ISON) [1] has carried out photometric observations of NEAs during last five years in regular mode. The available facilities for asteroid investigations and the main obtained results will be presented.

Observations and results:

The CCD-telescopes with apertures from 40 cm up to 2.6 m are used for carrying out the observations. They are located at different observatories in Middle Asia (Gissar, Kitab, Maidanak), Caucasus (Abastumani, Kislovodsk), Ukraine (Kharkiv, Kiev, Nauchyj, Simeiz), and USA (New Mexico). All these facilities operate under ISON support. The method of observations and data reduction can be found in [2]. The obtained measurements of asteroid's magnitudes have typically accuracy of 0.01-0.03 mag.

Our observations are mainly aimed at getting lightcurves to determine the rotational periods, sizes and shapes of NEAs. We focus our research on the study of binary asteroids, and detection and investigation of the YORP effect. Particular interest is devoted to Potentially Hazardous Asteroids (PHAs) and the newly discovered NEAs accessible for photometry with the ISON telescopes. We also carry out photometric observations of NEAs in support of radar observations.

More than 60 NEAs have been investigated in the frame of project in past three years. We have obtained more than 200 lightcurves which are used to derive rotational properties of the observed asteroids. Absolute magnitudes and BVRI colors were obtained for about 20% of them. 10 asteroids were observed to investigate of the YORP effect, and for 3 asteroids the YORP effect was detected. We discovered 2 new binaries, (8373) Stephengould and (3352) McAuliffe, and other 3 NEAs were suspected as binaries. Rotation periods of 14 NEAs have been obtained for the first time. We found 2 super-fast rotators, 2001 FE90 and (326290) 1998 HE3, and 6 asteroids with the rotation periods longer 16 hours.

Conclusion:

The ISON cooperation has proved its efficiency for study Near-Earth asteroids. Obtained results will be included in international databases and will provide important knowledge needed to develop methods of preventing potentially *catastrophic* impacts to the Earth.

References: [1] Molotov I. et al. 2008. *Advances in Space Research*, 41, 1022-1028. [2] Krugly Yu. N. et al. (2002) *Icarus,* 158, 294-304.

PHASE FUNCTION OF BRIGHTNESS AND CIRCULAR POLARIZATION OF THE HIGH-ALBEDO ASTEROID 44 NYSA.

F. P. Velichko,
Institute of Astronomy of Kharkiv Karazin National University,
35 Sums'ka str., 61022 Kharkiv, Ukraine. Contact: fvelichko@ukr.net

Introduction: 44 Nysa is the largest member of a small taxonomic class of asteroids with a high-albedo of surface. It has diameter about of 71 km, and is classified as an E-type with IRAS albedo of 0.55 [1]. According to the results of previous observations it was found that the asteroid has rotation period of 6.422^h, and lightcurve amplitude ranged of 0.19^m–0.55^m [2]. Nysa characterizes by elongated shape with semiaxis ratios a/b=1.7, b/c=1 and by presence of a significant concavity (close to bifurcation) on the surface [3]. On surface of the asteroid can dominate mixture of a bright, enstatite-like mineral plus a low-iron orthopyroxene [4]. There are the magnitude-phase dependences measured on 1986 and 2005 oppositions at north aspect of the asteroid [2,5], and composite phase dependence of linear polarization points to possible existence of opposition effect of polarization [2].

Observations: New observations of the asteroid 44 Nysa have been obtained at the 0.7-m telescope of Institute of Astronomy of Kharkiv University. Telescope was equipped by CCD camera ML 47-10 with BVRI standard filters and by one-channel photoelectric polarimeter with V filter. Photometry and polarimetry were carried out during asteroid's apparition on 2011 in the range of phase angle 0.6º-26.5º [6], and at the south aspect episodic observed earlier, only.

Results: Photometry of the asteroid shows that amplitude of lightcurve equals to 0.26^m (α=5.5º) in all four BVRI spectral bands. A comparison with lightcurve at larger phase angle shows a significant changes of the amplitude up to 0.38^m at α=21.4º. The observations confirm our previous data on 1987 about anomalous growing of the lightcurve amplitude as ≈0.008 mag/deg under south aspect contrary to slight changes under north one [2]. It was else found that exist changes of the color B-V with amplitude 0.03^m on surface of the asteroid before the secondary lightcurve maximum.

Magnitude phase dependence of brightness of Nysa on 2011 apparition is presented in Fig. 1. As one can see, there isn't difference in opposition surge of brightness between our observations and on 2005 [2]. At the same time the linear part of our dependency (south aspect) lies little lower, got under north aspect of the asteroid view.

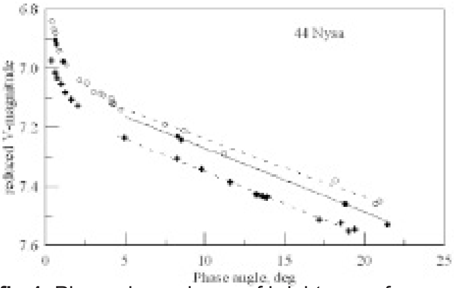

fig.1. Phase dependence of brightness of 44 Nysa. Filled symbols – our measurements, opened and cross symbols – data on 1986 and 2005 from [2,5].

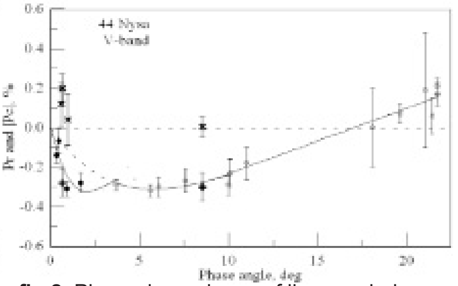

fig.2. Phase dependence of linear polarization Pr of 44 Nysa. Symbols (•,○) – data from [2,7]; (+) – our measurements on 2011. Module of circular polariza tion Pc is shown by (×) symbol.

Polarimetry of the asteroid 44 Nysa was carried out during three dates both in opposition for minimum possible phase angle, and for phase angle near 8º. It was found that in the range of the opposition effect of linear polarization (see Fig.2), and of the opposition brightness surge (see Fig.1) module of the circular polarization in V-band equals to 0.20±0.07% and 0.12±0.11% at phase angle 0.64º and 0.60º, accordingly. Whereas, in the range of regular negative branch of the phase dependency of linear polarization the observations show that circular polarization reaches zero (see Fig. 2). This is one of the first observations of circular polarization of asteroids and the first data for the asteroid 44 Nysa.

Acknowledgements: Author grateful for help at observations to S.Zaitsev and F.Kulish.

References: [1] Tedesco E.F. et al. (2002) Astron. J., 123, 1056-1085. [2] Rosenbush V.K. et al. (2009) Icarus, 201, 655-665. [3] Shepard M.K. et al (2007) Icarus, 195, 220-225. [4] Clark B.E. et al. (2004) J. Geophys. Res., 109, E02001. [5] Harris A.W. et al (1989) Icarus, 81, 365-374. [6] Velichko F.P. (2011) ASYS, 12-14 May, 2011. Chernigiv, Ukraine, 14-15. [7] http://PDS.jpl.nasa.gov.

GAS DUST STREAMS, CRUST SEISMIC NOISE, EXOBIOLOGY

Khavroshkin O.B., Tsyplakov V. V., *khavole@ifz.ru*

As against the majority of researches on a problem the Earth – Space which are considering the rare event impact of a large meteorite the basic threat of a civilization in the present a space dust on the foreground is put forward another as not less dangerous but permanent existing and is more concrete it is seeds of exolife as a part of exobiology. Sources and receivers of a dust, their feature and the characteristic are considered. The extensive experimental material is given according to lunar seismicity and supervision over seismic acoustic fields of various regions of the Earth.

Information content of the lunar seismology. Information content of the Nakamura`s Catalog of moonquakes is very rich: from solar-earth tides to clustering among the meteoroid streams [1, 2]. The histograms from meteoroid impacts seismic data revealed the seismic wave responses of the Moon to solar oscillations and the action on the lunar surface by dust-gas plasma of meteoroid streams [3]. The time series of seismic events were generated as follows: on an axis of ordinates – the peak amplitudes of events in standard units, on an abscissa – seismogram durations of the same moonquakes and subsequent time intervals between them were put aside [4]. Spectrum of the series of meteoroid streams seismicity disclosed time picks on orbital periods some planets and their satellites and solar oscillations [4, 5]. The research of peculiarities of histogram envelopes [3] and comparative common analysis solar bursts data and mass meteoroid distribution are confirmed [3,4] and revealed Forbush`s effect for gas-dust plasma [6]. Hidden astrophysical periodicities of lunar seismicity were obtained early from an analysis of time series [7] which were similarity to series [4]. The path of results of [7] is presented in the Table. First hypothesis for explanation of the Table results is existing gas-dust streams from binary stars near systems solar system and interacting with lunar surface; second is correlation them to the gravitational radiation from the same stars. We suppose that first hypothesis is more real.

Abiologic processing of space organic. The dust too interacts with meteoroid surface and moons very often. The parameters of impacts are similiarity to effects which are existing in case time moment big meteoroid impact [8]. So the chance of new chemical composition appearance is more. Space organic in form of a meteorite or dust can include to geologic matter and in this case the processing realizes by throw mechanism of seismic acoustic emission (crust seismic noise) or by vibrations [8, 9].

Characteristic of binary stars systems and picked out periods of lunar seismicity

№ tabl 1	lunar periods, day	name of sistem	half period/ period day	masses of component solar unit.		distans parsec	gravitation radiation Gd/s
4	6.7	V380 Cyg	6.21	13.3	7.6	4168	10^{21}
		CV Vel	T = 6.89	6.0	6.0	1047	
5	4.8	V356 Sgr	4.45	12.3	4.7	3090	10^{21}
6	3.5	CV Vel	3.44	6.0	6.0	1047	2×10^{21}
		h Agl	3.58			100	
7	2.25	UW Cma	2.20	43.5	32.5	8912	5×10^{24}
8	2.03	AG Per	T = 2.029	4.5	4.5	660	
		α Vir	2.007	10.3	6.4	257	3×10^{22}
9	1.33	V906 Sco	1.393	3.5	2.8	251	
10	0.966	G Aql	0.975	6.8	5.4	549	2×10^{23}
11	0.666	Y Aql	0.651	7.5	6.9	275	5×10^{23}
12	0.543	IM Mon	0.595	8.4	5.6	724	1×10^{24}
14	0.323	VV U.Ma	0.343	2.1	0.5	512	1×10^{22}
		YY Eri	T = 0.321	0.76	0.5	42	1×10^{22}
16	0.265	i Boo	0.268	1.35	0.68	12	1×10^{23}
20	0.160	SW Lac	0.160	0.97	0.82	74	1×10^{23}
21	0.142	j U.Mi	T = 0.143			>100	
28	0.0751	j U.Mi	0.0715				
29	0.0559	WZ Sge	T = 0.0559	0.08	0.6	100	
34	0.0285	WZ Sge	0.0280	0.08	0.6	100	4×10^{22}

table

On the basis of these researches according to the spectral analysis it is identified more than ten sources the gas dust streams playing potentially effective role of carriers seeds of exolife. Astrobiological activity of the Sun, comets and meteorites as objects which carrier's and\or regulators of streams with seeds of exolife is explained. If the solar system is reached by the gas-dust streams from binary stars, then all bodes in space have particles of star dust on their surfaces and/or atmospheres. Solar system has made 8-10 revolutions around galactic center and thus captured dust from many thousands stars. As these stars caught in turn dust particles from other stars too then probably our solar system has mainly dust samples from all objects of our galaxy. The age of galaxy and old stars is approximately more than15 billion years and that of the Earth is only ~ 4, 5 Gyr. Genesis of Life for the Earth has not more than 3 billion years. Thus comparative analysis of simple balance of these times shows that the genesis of Life for Earth is the result of galactic processes/objects and not of the solar system of course.

Peculiarity of Life Genesis. After formation of the solar system all old and new captured dust particles are first accumulated in the Oort cloud and then they are carried by comets to planets. The modern state of the Earth exists for more than 3 billion years, so possibilities for appearing Life were always. These processes had happened a few times during this period of the Earth state. The sizes of the universe and galaxies at τ_0 < 1 billion years could be much less than modern estimates (for example, up to ~15 times in diameter), that implies the existence of a common gas-dust exchange. The density of physical fields and radiations at the moment τ_0 was many orders of magnitude higher than the density existing now. Disintegration of neutron substance and nucleus of heavy unstable elements have caused constantly existing streams of left polarized electrons which have determined

chirality's asymmetry of original organic molecules and thus the chirality of the existing biological world [10]. Some types of radiations functionally could replace enzymes during formation of self-reproducing molecular structures. Man is used only 10 % of the genetic information. It indicates the common total surplus of a genetic material of biosphere of the Earth and other celestrial bodies [11]. Probably, at the moment τ_0 in unique conditions and with sufficient time for creation the universal galactic gene was created which different elements are capable to create biospheres on planets with the widest set of external conditions and for various stages of development of everyone. If the universal uniform galactic genome exists, this universality will appear as redundancy. The universal model of the gene logically contacts the concept of a prediction and designer, hence, the model of occurrence of life and the Creator is logically more proved.

The new astrophysical paradigm of an origin and development of life on the Earth and planets is offered and proved[12].

References

1. Sadeh D. Possible sidereal period for the seismic lunar activity // Nature, 1972. Vol. 240, p.139
2. Oberst J. and Nakamura Y. A Search for Clustering among the Meteoroid Impacts Detected by the Apollo Lunar Seismic Network // ICARUS, Vol. 91, 315-325, 1991; Balazin M. and Zetzsche A. // PHYS.STAT.SOL., Vol.2, ,1962 1670-1674
3. Khavroshkin O.B. and Tsyplakov V.V. Meteoroid stream impacts on the Moon: Information of duration of the seismograms / In: Proceedings of the Conference METEOROID 2001, Swedish Institute of Space Physics, Kiruna, Sweden, 6-10 August 2001
4. Khavroshkin O.B. and Tsyplakov V.V., Temporal Structure of Meteoroid Streams and Lunar Seismicity according to Nakamura's Catalogue / In: Proceedings of the Conference METEOROID 2001, Swedish Institute of Space Physics, Kiruna, Sweden, 6-10 August 2001
5.O.B.Khavroshkin, V.V.Tsyplakov. Moon exogenous seismicity: meteoroid streams, micrometeorites and IDPs, Solar wind // Herald of the DGGGMS RAS: Electr. Sci.-Inf. J., 4(21)'2003 http://www.scgis.ru/russian/cp1251/h_dgggms/1-2003/scpub-3.pdf
6. O.B.Khavroshkin, V.V.Tsyplakov. Peculiarities of envelops of histograms of lunar impact seismogram durations / In: Geophysical research essays. Schmidt United Institute of Physics of the Earth Press, Moscow, 2003. 471 p., (in Russian).
7. O.B.Khavroshkin, V.V.Tsyplakov. Hidden astrophysical periodicities of lunar seismisity // Herald of the DGGGMS RAS: Electr. Sci.-Inf. J., 4(14)` 2000 http://www.scgis.ru/russian/cp1251/h_dgggms/4-2000/scpub-3.pdf
8. Managadze G. G. Plasma meteorit impact and prebiologic evolution.-M.: FIMATLIT, 2009.-352p.
9. Ammosov S. M., G. I.. Voitov, A. O. Grinevskii et all. About peculiarities under soil atmosphere on seismic field of few vibrators. Reports of Academy of science USSR, v.296, №5, 1987y.
10. Gusev G. A., T. Saito, V. A. Tsarev, A. V. Uryson. A Relativistic Neutron Fireball from a Supernova Explosion as a Possible Source of Chiral Influence. Orig. Life Evol. Biosph. (2007) 37:259-266 DOI 10. 1007/s11084-007-9066-5
11. L. Zelenyi, O. Korablev, E. Vorobyova, M. Martynov, E.L. Akim, A. Zakharov. Europa Lander Mission: A Challenge to Find Traces of Alien Life. Galileo's Medicean Moons: their impact on 400 years of discovery. Proceedings IAU Symposium No. 269, 2010 C. Barbieri, S. Chakrabarti, M. Coradini & M. Lazzarin, eds.°c 2010 International Astronomical Union DOI: 00.0000/X000000000000000X
12. O.B.Khavroshkin, V.V.Tsyplakov. Earth`s prcesses and gas dust streams. Herald of Russian Academy of Natural Science, № 3, 2010y., p.p.66-76

NAVIGATION OF THE RADIOASTRON MISSION.

M. V. Zakhvatkin[1], V. A. Stepanyants[1], I. S. Ilyin[1], Yu. N. Ponomarv[2], A. G. Tuchin[1], G. S. Zaslavsky[1]
[1]Keldysh Institute of Applied Mathematics, Moscow, Miusskaya sq. 4, Russian Federation; [2]Astro Space Center of Lebedev Physical Institute, Moscow, Profsoyuznaya st. 84/32. Contact: zakhvatkin@kiam1.rssi.ru

Introduction:

July 18, 2011 the 10 m radio telescope mounted on the “Spectrum-R” spacecraft was successfully launched into Earth’s highly elliptical orbit. In order to increase orbital lifetime, two-impulse orbital correction was performed 7 months after the launch. Height of apogee of the resulting orbit ranges between 273 and 373 thousand km, the period is 8.2-10.3 day, inclination of the orbit varies during the flight from 5 to 85 degrees.

The use of space radio-telescope (SRT) within Radioastron project along with earth-based radio telescopes allows carrying on very long baseline interferometric observation of distant cosmic radio sources. For successful correlation of interferometric data the motion of the SRT should be very well known.

“Spectrum-R” precise orbit determination is a challenging task. Solar radiation pressure acts on different surface elements of the satellite during the flight. Besides direct orbital disturbance, it produces a torque about center of mass. Desirable orientation of the satellite is kept by system of flywheels. Long influence of the same disturbing moments results in permanent increase of flywheels angular speed, which require, at some point, an unloading – quick slowdown and compensation of resulting angular momentum by means of jet engines of stabilization system. Jet engines are organized such way, so unloading creates disturbing momentum of center of mass. Daily increment of speed caused by such procedures is 5 – 10 mm/sec. Corresponding coordinate displacement is about 400 – 800 m, what surpasses accuracy of radio range measurements by several times. Time span, on which orbit is to determined, should not be less than one full turn i.e. 8 – 10 days. During that period unloadings will take place several times, therefore the flight cannot be considered as passive.

Several sources of the Radioastron orbital information are used in navigational process. Control stations in Ussuriysk and Bear Lakes provide range and range rate data. Tracking stations on territory of Russian Federation (Puschino) and other countries provide accurate Doppler data from hydrogen maser installed on the satellite. In addition “Spectrum-R” has corner-cube reflectors, which allow to perform laser ranging.

This presentation describes the experience of navigational support of the Radioastron scientific program. The presentation discusses the satellite motion model, which takes into account disturbing impulses that occur during unloadings, by presenting them as instantaneous velocity increments. This presentation shares the technique of joint determination of orbital parameters, reflectivity coefficients, which determine solar radiation pressure, and unloading impulses by using all accessible orbital information: radio range and range rate measurements, laser tracking data, telemetry information and astrometric measurements.

ABSTRACTS SUBMITED TO SECTION 8. GIANT PLANETS AND SATELLITES

DEVELOPMENT OF THE COORDINATE AND CARTOGRAPHY SUPPORT OF FUTURE INTERNATIONAL MISSION ”LAPLACE_P” TO JUPITER’S MOON GANYMEDE

D. Zhukov, K. Shingareva , A. Zubarev, V. Patraty
Moscow State University of Geodesy and Cartography (MIIGAiK), Extraterrestrial Laboratory (MExLab), Gorokhovskiy per., 4, 105064, Moscow, Russia;
Contact: d_zhukov@mexlab.ru, jukich@yandex.ru, tel: +7-499-2673513

Introduction:

An international mission proposed in collaboration between Russian Space Agency (Roscosmos) and the European Space Agency (ESA). The Jupiter Ganymede Orbiter will execute an exploration of the Jupiter system before settling into orbit above Ganymede. The overarching goal of LAPLACE mission is the study of the emergence of habitable worlds around gas giants. It will look to answer such questions as: What have been the conditions for the formation of the Jupiter system? How does Jupiter work? [1, 2].

A preliminary study of Ganymede`s surface on the basis of remote sensing data, obtained by the various past NASA missions, will help to make a coordinate and cartography support for the further exploration of the Ganymede, and create it`s surface model with the GIS methods.

Sources:

To reach these purposes, a various data from “Voyager-1”, “Voyager-2” [3] and “Galileo” [4] missions, was collected. Recent data about Ganymede was obtained by spacecraft “New Horizons” [5], which investigated the system of Jupiter on the way to Pluto. Currently the main source of data about the celestial bodies is an American information resource Planetary Data System [6]. Besides the raw satellite images and the results of their preprocessing, it also contains metadata that provides various information about the parameters of satellite imagery. For our goals we used more than 100 satellite images, obtained by several spacecrafts, “Voyager-1” (24 img.), “Voyager-2” (87 img.) and Galileo (10 img.).

Mapping:

The first step was the pre-processing of raw satellite images using the Vicar software [8]. Despite the standardized data`s description in PDS, processing of remote sensing data has some difficulties, for example in determining the image`s elements of the external orientation. Parameters which we need to calculate them, are stored in a database NAIF SPICE [7], and to perform these calculations some special software was developed in MIIGAiK.

Main results: Elements of external orientation, remote sensing data and metadata were used for the processing of images of the Ganymede`s surface. There were also performed geometric and radiometric correction of data using Vicar software [8]. Then, all the data were converted from the original formats (*.Img, *.Imq) to the *.Tiff format, and loaded into Photomod software, for the photogrammetric processing (Fig. 1). Currently, there were created more then 700 tie points on the individual images using the characteristic objects on the surface of the body. The main problem in tie points creation, for the formation Ganymede’s control point network, is connected to the difference in resolution between the images, which were also taken from different angles relative to the surface, and the presence of some lacunas in Ganymede`s photomosaic.

Conclusions: Completed data collection and preliminary processing of images of Ganymede`s surface. With the using of Photomod software were created tie points for block adjustment of the images and creating control point network. The obtained results will be used for further processing and analysis of the surface of the body: creating a control point network, defining the shape of the body, as well as the formation of DEM and orthomosaic. These data will be the starting point for studying the surface of the body where the interesting geomorphological phenomena, which were presented in [10, 11, 12, 13]. The results will be used in the future international mission to Ganymede.

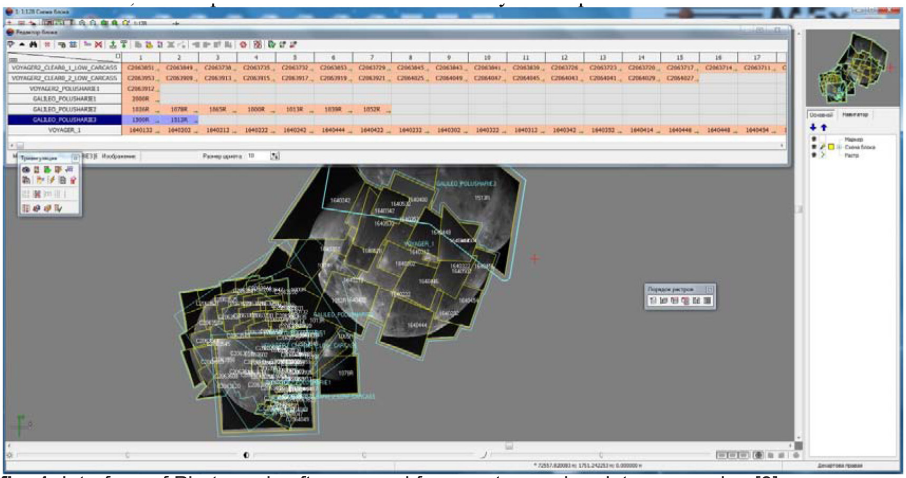

fig. 1. Interface of Photomod software used for remote sensing data processing [9].

References:

[1] http://www.novosti-kosmonavtiki.ru/content/numbers/352/04.shtml
[2] http://sci.esa.int/science-e/www/object/index.cfm?fobjectid=44037
[3] http://solarsystem.nasa.gov/galileo/
[4] http://voyager.jpl.nasa.gov/
[5] http://www.nasa.gov/mission_pages/newhorizons/main/index.html
[6] http://pds.nasa.gov/
[7] http://naif.jpl.nasa.gov/naif/
[8] http://www-mipl.jpl.nasa.gov/vicar.html
[9] http://www.racurs.ru/
[10] Singer, Kelsi N.; Bland, Michael T.; McKinnon, William B.; Schenk, Paul M.: Relaxed impact craters on Ganymede: not all sulci are created equal. Lunar and Planetary Science Conference, 2012.
[11] Freeman, J. (2006). Non-Newtonian stagnant lid convection and the thermal evolution of Ganymede and Callisto. Planetary and Space Science 54 (1): 2-14.
[12] Showman, A. P.; Malhotra, R. (1997-03). Tidal evolution into the Laplace resonance and the resurfacing of Ganymede. Icarus (Elsevier) 127 (1): 93-111.
[13] Barr, A. C.; Canup, R. M. (March 2010). Origin of the Ganymede / Callisto dichotomy by impacts during an outer solar system late heavy bombardment. 41st Lunar and Planetary Science Conference (2010).

THE IMPACT OF THE INTERPLANETARY MEDIUM ON THE GALILEAN SATELLITES OF JUPITER

A. I. Klianchin[1], V.V. Prokofjeva-Mikhailovskaya[2].
[1]Main Astronomical Observatory of the National Academy of Sciences of Ukraine 27 Akademika Zabolotnoho St. 03680 Kyiv, Ukraine; [2]Crimean Astrophysical Observatory Scientific Research institute, 98409, Ukraine, Crimea, Nauchny.
Contact: klyanchin@ukr.net

The photometric properties of the Galilean satellites of Jupiter are determined by scattering properties of surfaces. Avramchuk and Shavlovsky (1998) conclude that the microstructure of the surface of Ganymede and Callisto is similar to the microstructure of the lunar surface. At the same time, the surface of the satellites Europa and Io has significantly different microstructure.

Galilean satellites are located at different distances from Jupiter, and therefore are undergone to different effects of the interplanetary medium. Satellites Io and Europa are close to Jupiter. The radii of their orbits are about 421 thousand and 671 thousand kilometers (about 6 and 9.5 Jupiter radii). The time of their revolution around Jupiter are 1,769 days for Io and 3,551 days for Europe. These satellites are situated in powerful magnetosphere of Jupiter, which makes a complete rotation for ≈ 10 hours. Therefore, the magnetic field lines of Jupiter overtake and leave behind these satellites. At the same time, high-energy ionized particles trapped by the magnetic field, bombard the rear (trailing) hemisphere of satellites. This mechanism makes the leading hemisphere of Io and Europa satellites brighter than the trailing hemisphere. Ganymede is at a distance of about 1 million kilometers of Jupiter, making a complete revolution around Jupiter for 7.15 Earth days. The albedo of the Ganymede surface of 0.43 ± 0.02.

Satellite Callisto is at a distance of about 2 million kilometers (26.6 radii) from Jupiter and makes a complete rotation around of 16.7 days. Callisto is the most cratered body of the solar system. It is subject to bombardment by particles of solar wind and small bodies that are in the interplanetary medium. The albedo of its surface is only 0.17 ± 0.02. It has dark leading hemisphere. It is subject to bombardment by particles of solar wind and small bodies that are in the interplanetary medium. The low albedo of the surface indicates on the presence of dust in the crust. The dark material is a thin “veil.” This material may be debris, formed due to collision of meteoritic material with the surface of the satellite. Bright spots on a dark surface - meteorite craters, in the process of their formation the lighter material was excavated onto the surface of the satellite.

Thus, Io, Europa and Ganymede, located in a magnetic field of Jupiter, have a brighter leading hemisphere and darker rear hemisphere. Callisto is situated far from Jupiter, it has a bright rear hemisphere and a darker leading one. This issue can be concluded from ground light curves obtained in Crimean Astrophysical Observatory in the band V.

SEASONAL CHANGES IN SATURN'S ATMOSPHERE FROM THE MOLECULAR ABSORPTION BANDS CCD-SPECTROPHOTOMETRY IN 1995-2012

V.G Tejfel., A.M.Karimov, G.A.Kharitonova, G.A. Kirienko, V.D.Vdovichenko
Fessenkov Astrophysical Institute, Almaty, Kazakhstan. tejf@hotmail.com

Introduction: The study of the methane absorption bands variations on disks of Jupiter and Saturn has a long history in Fessenkov Astrophysical Institute beginning of 1960-th. From 1995 the CCD-cameras are using for planetary photometry and spectrophotmetry, Most of these observations were directed to the study of the molecular absorption bands (methane and ammonia) behavior on the disks of both planets. These regular observations have permitted to track some seasonal changes in the Saturn's atmosphere during more than half part of its orbital period: from the equinox in 1995 to equinox 2009 and hereinafter to 2012.

The observation and processing technique: The observations in 1995-2003 were carried out with the prism spectrograph and CCD-camera ST-6V and beginning of 2004 the diffraction spectrograph SGS with CCD ST-7XE is used for planetary observations in the 7.5-m Cassegrain focus of 0.6-m Karl Zeiss telescope. In addition to the spectrograms of the Saturn equator and central meridian the scanning of planetary disk was done by consecutive records of zonal spectrograms from S-Pole to N-Pole. at the spectrograph slit oriented in parallel to big axis of the ring There were recorded about ten thousands spectrograms and their processing is continuing for comparative study of the molecular absorption variations and other changes in Saturn's atmosphere and cloud cover. The measurements of CCD-spectra were carried out to derive the profiles of the absorption bands and estimate their central depths and equivalent widths. As a result of the spectrograms processing a number of the atlases of profiles of the methane absorption bands and atlases of latitudinal variations of these bands parameters have been prepared for each observational season.

Latitudinal CH_4 absorption differences at 1995 and 2009 equinoxes In 1995 sharply expressed asymmetry of the methane absorption in southern and northern hemispheres has been noted [1]. For all bands the stronger absorption was observed at the temperate latitudes of Northern hemisphere. Minimum absorption is characteristic for an equatorial belt and it remained during all periods of Saturn's observations. At the temperate latitudes of Southern hemisphere the absorption was much less, than in Northern . It was possible to expect that the opposite picture must take a place at equinox 2009, that is to say the lowered absorption should be in Northern hemisphere and raised in the Southern one. However the observed results were very different from expected (Fig.1,2). Actually in 2009 the equivalent widths and depths of the CH_4 727 nm absorption band have near equal values at temperate latitudes of both hemispheres. The minimum absorption was observed in the equatorial belt. The absorption bands CH_4 619 nm, 702 nm, 675 nm and others are some weaker in Southern hemisphere and show increase in Northern hemisphere as in 1995. Thus, though the overall picture of latitudinal variations of absorption differs from observed in 1995., but there was not opposite character of asymmetry

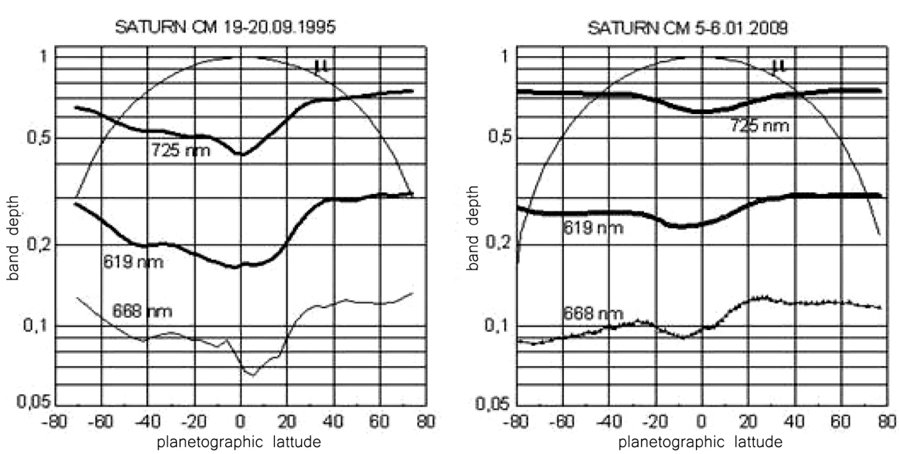

fig.1-2. Latitudinal variations of the methane band depths at the Saturn equinoxes in 1995 and 2009.It is shown also a cosine of emergence angle $\mu=\cos\varepsilon$.

The methane absorption behavior between equinoxes and after 2010. Last period of the maximum ring opening was in 2001-2003. At this time and in 2004 the greatest methane absorption took place at Southern latitudes about -20--30 degrees though the absorption minimum was observed in equatorial belt and at temperate Southern latitudes with small recession towards high latitudes. Near S-Pole some increase of absorption was noticeable.. During the period between 1995 on 2009 the appreciable trend of the absorption in a Southern temperate belt of Saturn was observed. as the growth of the CH_4 725 nm band depth from 0.55 to 0.75.

After 2009 equnox the intensity of this band is nearly equal at the temperate latitudes of both hemispheres. The weaker absorption bands CH_4 619 nm, 702 nm, 675 nm and others show smaller absorption in Southern hemisphere and increase in Northern hemisphere as in 1995 (Fig.3). Most interesting particularity have been noted at the comparison jf the CH_4 725 nm and 619 nm band intensities. The ratio of their equivalent widths W619/W725 is systematically about 20 per cent greater in Northern hemisphere (Fig.4)

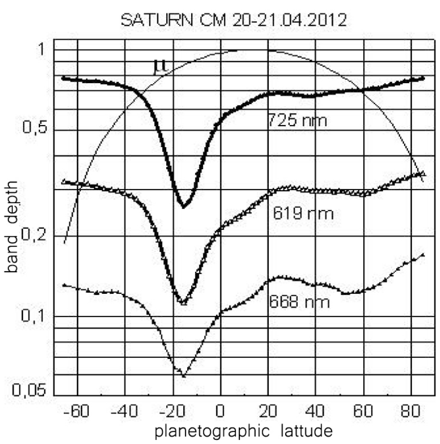

fig.3. Latitudinal variations of the methane band depths in 2012

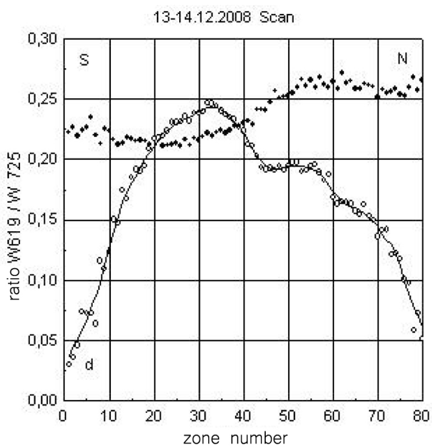

fig.4. Zonal changes of the ratio W619/W725 and the brightness variation from the scan spectra

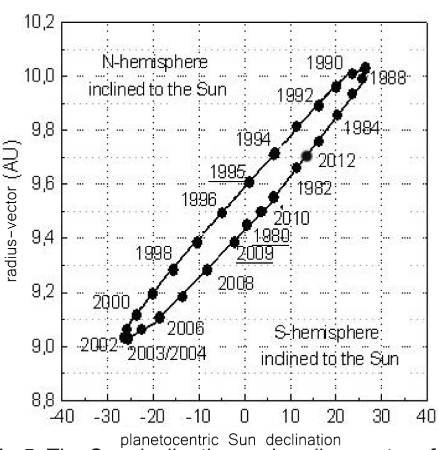

fig.5. The Sun declination and radius-vector of Saturn at full orbital rotation

Discussion: An absence of mirror asymmetry for longitudinal absorption distribution at equinox 2009 in comparison with 1995 is caused most likely by distinctions in the insolation regime of hemispheres of Saturn during the periods of the maximum inclination of equator of a planet to a direction on the Sun and in the years previous to equinoxes. Before 1995 equinox (Fig.5) Saturn was on greatest distances from the Sun and the inflow of solar radiation for Northern hemisphere inclined to the Sun was the least. Before last equinox the distance from the Sun was the least and accordingly raised influx of radiation falled on Southern hemisphere. Convective processes in Southern hemisphere should be thus a little weakened and it was confirmed by Saturn's images from "Cassini" [2]. It should affect in volume density of the cloud layer. Most likely it went down or an optical thickness of the haze above the cloud deck was increased. Accordingly it may cause noticeable strengthening of the absorption bands formed at the multiple scattering process within the clouds and haze. The ammonia absorption is also increased in Northern hemisphere in comparison with Southern as follows from the NH3 645 nm band. measurements, but that is particular problem [3] as well as a comparison with infrared thermal studies of Saturn [4].

References: {1] Tejfel V.G.(1997) *Sol.Syst.Res.,31*,198-206. [2] Baines R.H. et al.(2005) *Earth, Moon &Planets, 96,*119-147. [3] Tejfel V.G., Karimov A.M.(2009) *EPSC*, *4,* 34. .[4] Fletcher N., et al. (2010):, *Icarus, 208,* 337-352

CIRCULAR POLARIZATION OF GALILEAN SATELLITES OF JUPITER.

F. P. Velichko, V. A. Psarev, A. Rikhteghar,
Institute of Astronomy of Kharkiv Karazin National University, 35 Sums'ka str., 61022 Kharkiv, Ukraine. Contact: fvelichko@ukr.net

Introduction: Polarimetric studies of the Galilean satellites have shown that these objects differ in terms of their surface microtexture and albedo [1]. But, this pertains to observations of the linear polarization. Circular polarization was absolutely deprived of observers' attention.

Observations: Our polarimetry was carried out with 70-cm reflector of Institute Astronomy of Kharkiv Karazin National University and 100-cm reflector of Crimean Astrophysical Observatory (Simeiz). Both telescopes were equipped by a single channel photoelectric polarimeter with standard V filter of Johnson-Morgan system. As an analyser the fast rotating quarter wavelength retarded plate and polaroid was used. Measurements of the circular polarization of Io, Europa, Ganymede and Callisto were obtained for April, 2005; June, 2007; July, 2008; June-August, 2009; August-November, 2011 [2] .

Results: Polarimetry of the satellites were performed at phase angle ranging from 0.14º to 11.0º. It has given us possibility to compose phase-angle dependences of circular polarization for Galilean satellites in entire range of phase angles accessible to the ground-based observations. Average accuracy of the measurement of circular polarization equals to ±0.04%. The obtained data were approximated by linear function and presented in Fig.1.

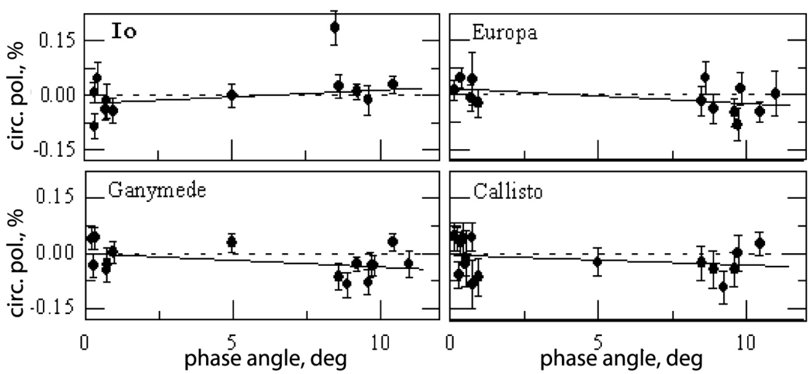

fig.1. Composite phase-angle dependendences of circular polarization in V-band for Io, Europa, Ganymede and Callisto. The solid line is a linear fit to observed data.

The slope parameter ε_v of linear function turned out to be small and for all four satellites are near 0.4 % per 100º of phase angle. In Table are presented values ε_v and σ_ε (accuracy of its determination) both our observations of Galilean satellites and average dependency for comets, theoretical calculation for optical active particles OAP and mixture of needle-like small oriented particles with spherical ones [1]. As one can see the satellites Europa and Ganymede have ε_v which in two times exceed σ_ε, and for Io and Callisto they are comparable with value σ_ε. If for Europa, Ganymede and Callisto the trend of phase-angle dependency are approximately the same, but with available data set for Io the trend are opposite formally. It is interesting to note that the results of the observations of the satellites, comets and theoretical calculations are in good agreement between itself, qualitatively. Moreover, the phase dependencies of the satellites and cometary dust have similar parameters.

object	phase angle range, (deg)	ε_v (10^{-2} per degree)	$\pm\sigma_\varepsilon$
Io	0.32-10.46	+0.4	0.3
Europa	0.14-11.00	-0.4	0.2
Ganymede	0.22-11.00	-0.4	0.2
Callisto	0.14-10.46	-0.3	0.3
Comets	≈24-121	-0.3	0.5
OAP	≈0-125	-0.1	-
mixture	≈0-70	±1.2	-

table. Slope of phase-angle dependence of polarization.

References: [1] Mischenko M. et al. (2010) Polarimetric Remote Sensing of Solar System Objects. AKADEMPERIODYKA, Kyiv, 292 p. [2] Velichko F.P., et al. (2012) Astron. Tsirk. (in press).

ACCESS AND SCIENTIFIC EXPLOITATION OF PLANETARY PLASMA DA-TASETS AT MARS, VENUS, MERCURY AND MOON WITH CDPP/AMDA WEB-BASED FACILITY IN RELATION TO THE EUROPLANET-RI IDIS PLASMA NODE ACTIVITIES.

N. Andre[1,2], B. Renard[1,2], E. Budnik[3], V. Genot[1,2], C. Jacquey[1,2], B. Cecconi[4], A. Fedorov[1,2], R. Hitier[5], N. Bourrel[1,2], M. Gangloff[1,2], E. Pallier[1,2], M. Bouchemit[1,2], B. Besson[6], F. Topf[7], W. Baumjohann[7], M. Khodachenko[7], H. Rucker[7], T. Zhang[7],

[1]IRAP, CNRS, 9 avenue du colonel Roche, 31068 Toulouse, France; [2]Universite Paul Sabatier, IRAP, 9 avenue du colonel Roche, 31068 Toulouse, France; [3]Noveltis, 2 Avenue Europe, 31520 Ramonville Saint Agne, France;[4]LESIA, Observatoire de Paris, Section de Meudon, 92195 Meudon cedex, France; [5]Co-Libri, Cremefer 11300 Pauligne, France; [6]CNES, Centre spatial de Toulouse, 18 avenue Edouard Belin, 31401 Toulouse, France; [7]Space Research Institute, Austrian Academy of Sciences, Graz, Austria. Contact: amda@irap.omp.eu

Introduction:

The field of planetary sciences has greatly expanded in recent years with space missions orbiting around most of the planets of our Solar System. The growing amount and wealth of data available make it difficult for scientists to exploit data coming from many sources that can initially be heterogeneous in their organization, description and format. It is an important objective of the Europlanet-RI and IMPEx projects (supported by EU within FP7) to add value to space missions by significantly contributing to the effective scientific exploitation of collected data; to enable space researchers to take full advantage of the potential value of data sets. To this end and to enhance the science return from space missions, innovative tools have to be developed and offered to the community. AMDA (Automated Multi-Dataset Analysis, http://cdpp-amda.cesr.fr/) is a web-based facility developed at CDPP Toulouse in France (http://cdpp.cesr.fr) for on line analysis of space physics data (heliosphere, magnetospheres, planetary environments) coming from either its local database or distant ones. AMDA has been recently integrated as a service to the scientific community for the Plasma Physics thematic node of the Europlanet-RI IDIS (Integrated and Distributed Information Service, http://www.europlanet-idis.fi/) activities, in close cooperation with IWF Graz (http://europlanet-plasmanode.oeaw.ac.at/index.php?id=9). We will report the status of our current technical and scientific efforts to integrate in the local database of AMDA various planetary plasma datasets (at Mercury, Venus, Mars, Earth and moon) from heterogeneous sources, including NASA/Planetary Data System (http://ppi.pds.nasa.gov/).

ABSTRACTS SUBMITED TO SECTION 9. NEW PROJECTS AND INSTRUMENTS

MExROVER – THE NEW PROJECT OF MIIGAIK IN PLANETARY GEODESY, CARTOGRAPHY, AND PHOTOGRAMMETRY.

M. V. Semenov, N. M. Gavrushin, M. S. Bataev, E. K. Makhina,
MIIGAiK Extraterrestrial Laboratory (MExLab), Moscow, Russia;
Contact: n.gavrushin@gmail.com, semenov1220@gmail.com

Introduction:

The MIIGAiK Extraterrestrial Laboratory (MExLab) is currently developing an automatic mobile platform MExRover, designed for simulating rover activities on the surface of earth-type planets and satellites. In the project, we develop a hardware and software platform for full rover operation and telemetry processing from onboard instrument, as a means of training undergraduate and postgraduate students and young scientists working in the field of planetary exploration.

The project is designated for multipurpose applications. One important focus is on research in photogrammetry, in particular, digital surface model creation for macro- and microrelief surveying in real-time for autonomous navigation. Other special attention is given to development of research programs with participation of students and young scientists of the University, for public awareness and education purposes. MExRover would be a bridge from the old soviet Lunokhod experience to the new research base for the future rover technology development support.

Rover Design:

The design of the rover and its instrument suite allows acquiring images and navigation data satisfying the requirements for photogrammetric processing. The data will allow us to create high-quality color panoramas as well as DTMs (Digital Terrain Models) in the rover vicinity. IMU and GNSS data are used not only for post-mission reconstruction, but also for real-time tracking of the rover traverse. A local operator may control the rover remotely from a distance up to 2 km. The telemetry system allows the operator to continuously monitor all the systems in real-time. A remote command center connects to the operator via satellite data link and controls the mission. The rover has onboard an automatic control system (ACS), which controls all the processes. The system includes a 10 GB storage system and standard interfaces for communicating with devices constituting the payload.

The MExRover has a modular design, which provides maximum flexibility for accomplishing different tasks with different sets of additional equipment weighing up to 15 kg. The framework can be easily disassembled and fit into 3 transport boxes. The weight of the boxes allows transporting them on foot, by car, train or plane.

The imaging system included in the standard design comprises two camera sets: low resolution TVcameras and a high resolution stereo camera. More instruments are planned to be installed later as auxiliary equipment, such as: IR camera, spectrometer, video camera, odometer, solar radiation sensor, temperature sensor, wind sensor, magnetometer, radiation detector, and microphones.

Specification:

dimensions W×L×H	600×1000×250 mm
maximum weight	60 kg
payload weight	20 kg
cruising range	3 km
mean velocity	1 km/h

Acknowledgements:
This work is supported by the Ministry of Education and Science of the Russian Federation (MEGA-GRANT, Project name: “Geodesy, cartography and the study of planets and satellites”, contract № 11.G34.31.0021 dd. 30.11.2010).
This work was supported by the grant of the Russian academy of sciences Presidium Program 22: “Fundamental problems of research and exploration of the Solar system”.

MULTI-CHANNEL GROUND PENETRATING RADAR FOR SPACE APPLICATIONS.

V. N. Marchuk, V. M. Smirnov, O. A. Byshevski-Konopko,
FIRE RAS, Fryazino, Russia. Contact: Marchuk@ms.ire.rssi.ru

Introduction:

The problem and prospects of multi-channel ground penetrating radar for research of surface of space objects from a rover board is discussed.

Modern scientific and technical achievements allow to create a ground penetrating radars (GPRs) of new type: multichannel wideband systems. Productivity of such devices increases in proportion to number of channels. Besides, these devices has a possibility of use of the new algorithms considering distribution of a radio-wave across movement of a radar, at the expense of what it is possible to achieve significant improvement of resolution after additional processing of the received data.

Multi-channel GPRs showed good results when using in archeology [1-3], in construction, in municipal services [4-6], that is where careful research of a deep structure of soil before carrying out excavation and other earthwork is required. It is possible to expect that advantages of such radar in comparison with single-channel GPR will be so obvious at their use for sounding of soil of other planets and their satellites: Moon, Mars, Europe, Calisto etc.

A number of programs and algorithms are developed for processing of radar-tracking multichannel GPR in our Institute. These programs were applied to data processing of a multichannel GPR “DAO3d” developed for the Don archaeological society. The radar consists of two parts: 4-channel and 6-channel antenna systems that in the sum gives 10 channels. The frequency band of radar is from 150 MHz to 450 MHz. The module from 4-channels (length 1.3 m) passed preliminary tests on ranges and archaeological platforms in the Rostov region. Tests of 10-channel system (length 3 m) are planned soon. This radar can be used further as a prototype and the working model for development of multichannel GPR for space applications (MC GPR SA). Frequency band of MC GPR SA can be displaced in area of high frequencies (700 MHz and more) because on space objects there is no moisture and absorption of radio-waves caused by it.

The program for processing 3d-data “GeoRad3d-Pro” is developed on the basis of a complex of programs for a two-channel GPR “Gerad-2” [7]. It was modernized and added with subroutines of display 3-dimensional images of a cube and plane slices (Fig.1- Fig.3). This software package after corresponding to completion can be used for data processing of development of multichannel GPR for space applications.

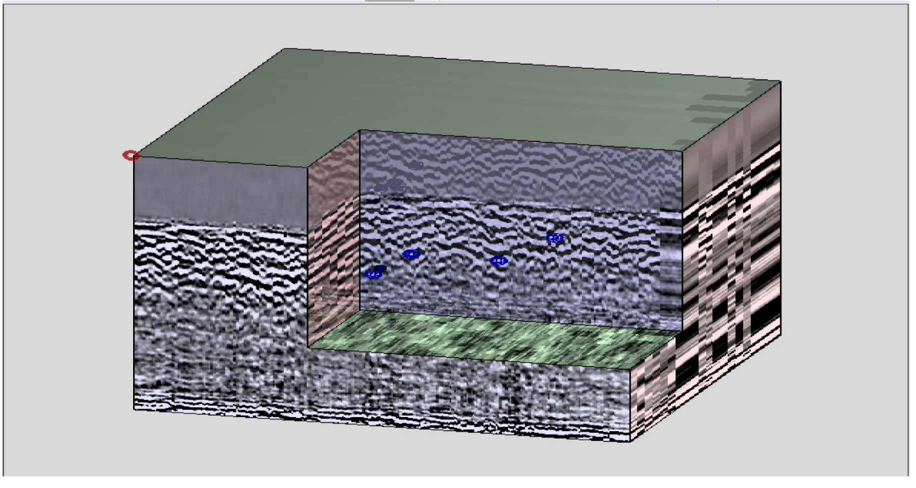

fig.1. The 3d-view results of 3-dimetional data processing. Detected objects are shown as ellipse markers.

The main problems which need to be solved when developing multichannel GPR for space applications:

1) calibration and setup of channels for formation of identical signals in a form, amplitude and a phase;

2) elimination of influence of the next aerials on quality of a radiated signal by selection of their optimum relative positioning and isolation by their absorbing material;

3) theoretical and experimental justification of an optimum gap between antenna system and studied soil;

4) minimization of weight characteristics of the device;

5) increase of accuracy of positioning of antenna system in the course of carrying out experiments.

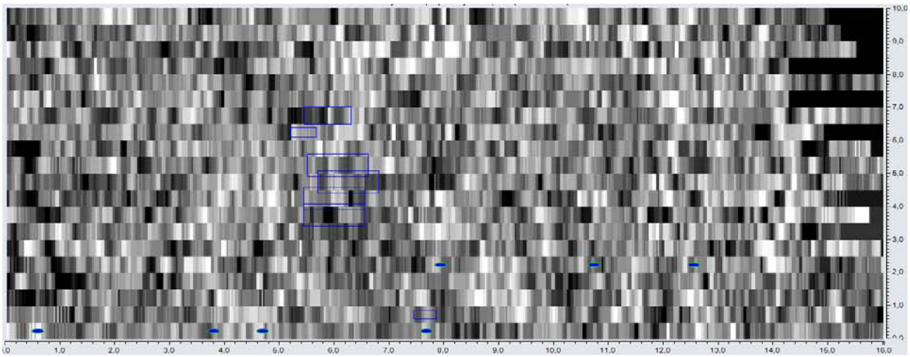

fig.2. The 2d-view slice of 3-dimetional data processing. Research depth is 1.6 m. Detected objects are shown as ellipse markers (small) and as rectangle (large).

References

Linford, N., Linford, P., Martin, L. and Payne, A. Stepped frequency ground-penetrating radar survey with a multi-element array antenna: Results from field application on archaeological sites. Archaeological Prospection, 17: 187–198. doi: 10.1002/arp.382, 2010.
Dean Goodman, Alexandre Novo, Geostudi Astier, Gianfranco Morelli, Geostudi AstierSalvatore Piro, Doria Kutrubes, Henrique Lorenzo. Advances in gpr imaging with multi-channel radar systems from engineering to archaeology // SAGEEP 2011 Charleston, South Carolina USA
Immo Trinks, Jaana Gustafsson, Jesper Emilsson, Christer Gustafsson, Bernth Johansson et Johan Nissen. Efficient, large-scale archaeological prospection using a true 3D GPR array system // ArcheoSciences, suppl. 33, 2009, pp. 367-370
U.Wollschlager, H. Gerhards, Q. Yu, K. Roth. Multi-channel ground-penetrating radar to explore spatial variations in thaw depth and moisture content in the active layer of a permafrost site // The Cryosphere, 4, 269–283, 2010, www.the-cryosphere.net/4/269/2010/
Marshall Bradleya, Thomas Wjttenb, Robert MCCUmmjflSa, Mike Crowea, Scott Stewarta, Mike DUnCana. Mine detection with a multi-channel stepped-frequency ground penetrating radar // Part ofthe SPIE Conference on Detection and Remediation Technolqqies for Mines and Minelike Tarciets IV • Orlando, Florida • April 1999, SPIE, Vol. 371, pp.953-960.
Ralf Birken, Douglas E. Miller, Maclyn Burns, Paul Albats, Robert Casadonte, Ross Deming,Tony Derubeis, Thorkild Hansen and Michael Oristaglio. Efficient large-scale underground utility mapping in new york city using a multi-channel ground-penetrating imaging radar system // Proc. SPIE Vol. 4758, 2002.
Marchuk V.N., Bazhanov A.S., Shtern D.Ya., et.al. The Two-Channel Georadar “Gerad-2” / // 32nd Microsymp. on Comparative Planetology: abst. int. conf. - Moscow, October 9-11, 2000. - p. 171.

BISTATIC RADAR FOR SUBSURFACE SOUNDING OF THE MOON AND PLANETS USING POWERFUL ARTIFICAL AND SPORADIC SPACE RADIO-EMISSION.

A.G. Pavelyev[1], S.S. Matyugov[1], O.I. Yakovlev[1],
[1]FIRE RAS, Vvedenskogo sq. 1, Fryazino, 141190 Russia Contact: *alxndr38@mail.ru*

Studying the subsurface structures of the Moon, planets, and other object in Solar System is an important direction in the space research. To obtain the information on the planetary subsurface structure up to depth 1-10 km it is necessary to use radio waves in the Low Frequency (LF), Medium Frequency (MF), or High Frequency (HF) bands with wavelength from 1m up 3 km. The depth of radio sounding is proportional to the wavelength, the intensity of the radio-emission source, and depends on the conductivity of the ground. The bistatic subsurface remote sensing of the planets with a global coverage can be achieved using the powerful Earth-based transmitters, and/or sporadic space sources including radio emission of the Sun, Earth's or planetary magnetospheres. Previously transmitter devices installed onboard of a satellite located in the planetary orbit have been used for bistatic sounding the surfaces of the Moon, Venus, and Mars. The main part of bistatic data analysis has been provided at the Earth. At the present time it is more effective to illuminate the investigated planetary surfaces in the uplink regime using powerful Earth based transmitters, and/or sporadic radio emission of the Sun, Earth's or planetary magnetospheres because significantly greater value of the signal/noise ratio $r = N_E / N_S$, where P_E, P_S are the powers of the Earth-based and satellite transmitter, N_E, N_S are the signal/noise values, and T_E, T_S are the noise temperatures of the Earth-based and satellite receiver corresponding to the uplink and downlink regimes. An advanced onboard receiver can make preliminary analysis of the bistatic data and then downlink the results to an Earth station. It follows that the energy potential of bistatic radar can increase 100 times or more in the uplink regime, depending on the ratio of powers of the Earth-based and satellite transmitters. For example, when the powers of the Earth-based and satellite transmitter are 100 kW and 10 W, and the noise temperatures of the satellite and ground-based receivers are 600 K and 40 K, respectively, than the energy potential of bistatic radar increases about 660 times, that makes it possible to obtain radio images of the surface in decimeter and centimeter frequency band. The temperature of the receiver noise increases in the low frequency band because influence of the space radio-emission. In this case the noise temperatures T_E, T_S are nearly equal and effectiveness of the bistatic uplink radar is greater significantly by 40-60 db. The same conclusion is valid for the radio occultation experiments which aims are the studying the vertical structures of the atmospheres and ionospheres of the planets and their moons. Another interesting possibility consists in using the sporadic space radio-emission for uplink bistatic radar subsurface sounding of the planetary ground. The main source is the powerful sporadic radio-emission of Earth in the frequency band 100 KHz – 2 MHz. This radio-emission has been firstly detected onboard the satellite «Electron-2» in the Earth's magnetosphere at the altitude ~45 thousand km. The power of the source may be as high as 1 million kilowatts, and the angular size as seen from the Moon is below 1 degree. The source is located in the areas of intensive polar lights in the Northern or Southern polar region. The polarization of emission is circular and depends on the orientation of the Earth magnetic field in the source. The bistatic radar technique consists of obtaining the correlation function of the space radio signal that illuminates the surface and the reflected signal to determine the density and structure of the ground. Preliminary analysis revealed parameters of the satellite receivers as dependent on the type of radio source. Spatial resolution and depth of sounding for Moon, Mars, Venus and other objects in the Solar system are obtained.

This work was supported by the grant of the Russian academy of sciences Presidium Program 22: "Fundamental problems of research and exploration of the Solar system".

SCIENTIFIC – EDUCATION PROJECT "LUNA - 2015+": SPIN-ORBIT EVOLUTION, SELENODESY AND GEOPHYSICS OF THE MOON

A. Gusev,
Kazan Federal University, Kazan, Russia; Contact: Alexander.Gusev@mail.ru

MODERN MAIN PROBLEMS OF THE MOON: selenodesy and selenophysics

1. Serious discrepancy of present eccentricity rate from LLR and theory.
2. Reliable sources of luunar free libration and free nutation.
3. Origin of lunar dissipation and damping time of free nutations and free librations.
4. Rotation momentum of the Moon and momentum of inertia of the lunar mantle and lunar core.
5. Effects of non-hydrostatic core-mantle topography and core dynamics acting on the lunar rotation.
6. Precessing pole offset from lunar core term.
7. Origin of 0.26 arc second offset at lunar rotation.
8. Improvement of analytical physical libration theory.
9. Creation of the lunar astronomical annual almanac.
10. Problem of resonant amplification of free librations and nutations.

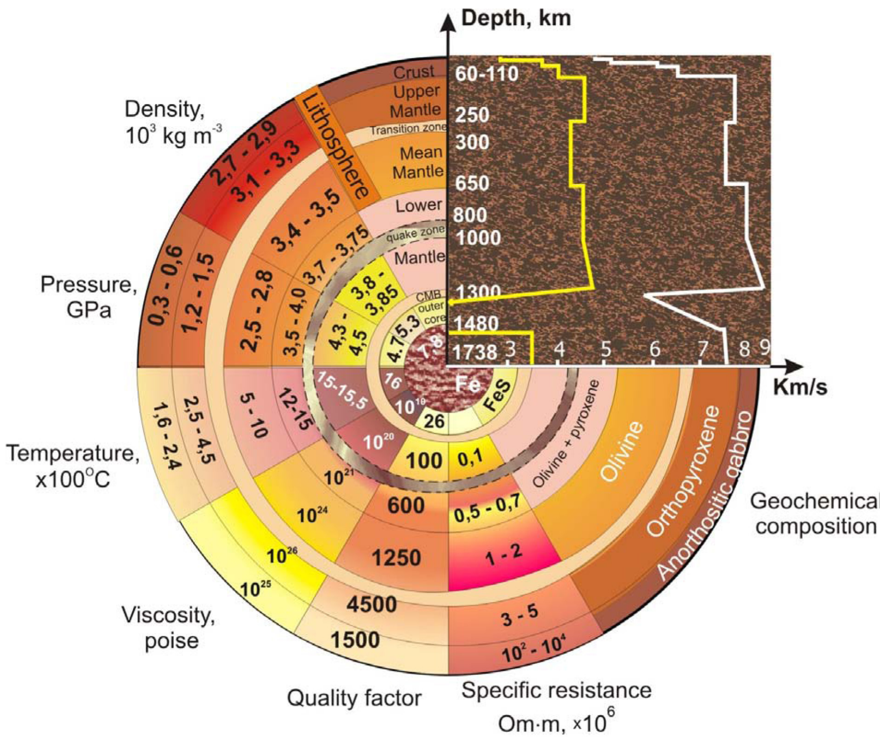

fig.1. Geophysical cross-section of the Moon [1]

The Project of **"The Moon – 2015 +"** is directed on the decision of fundamental problems of celestial

mechanics, selenodesy and geophysics of the Moon connected to carrying out of complex theoretical researches and computer modeling:

a) construction of the analytical theory of rotation of the two / three-layer Moon and reception on its basis of physical libration tables for their application at processing precision obsrvation; construction of a lunar annual almanac.

b) The analysis of spin - orbital evolution of the early Moon, an estimation of internal energy dissipation , modeling of the long-term mechanism of maintenance free librations the Moon;

c) the analysis of differentiation of a lunar core, detailed elaboration of plume-tectonics of a mantle and a core of the early Moon, evolution of a boundary layer a core - mantle, reconstruction of gravitational and viscous - mechanical interaction of a lunar core and a mantle, resonant dissipation of internal energy, calculation free and forced nutations a lunar core, free and force libration of the lunar core – mantle system ;

d) the decision of a inverse problem lunar gravimetry near lunar poles, construction of geodynamic model of a lunar crust, a mantle and a core, Moho boundary, reconstruction of initial mascons on the Moon, creation of precision topographical, gravitational and geophysical models of the Moon on the base of modern observation dates.

fig.2. The interior of the Moon (Weber, 2011, reconstruction of seismic dates from Apollo mission)

COMPLEX OF ACTIONS TO THE PROJECT "THE MOON – 2015+ "

1) Expansion and strengthening of close scientific contacts to the international scientific organizations on lunar subjects: COSPAR, IAF, IAU, CODATA, ESA (EU), NASA, JPL (USA), JAXA (Japan), CNSA (China), ISRO (India); participation in the international conferences and short-term scientific training. The invitation and the organization of the international lunar - planeatry conferences and the congresses: 40th SA COSPAR (2014, Moscow); 30th GA IAU (2018, Kazan);

2) Annual Russian lunar meetings and seminars on the basis of the various scientific organizations with invitation of foreign participants;

3) Creation of a regional centre of science on research of the Moon on base EAO of Kazan University with a powerful scientific infra structure maintenance.

4) Creation of the lunar sub-commission at the President of the Russian Federation, Ministry of Science and Education (MSE) of the Russian Federation (RF), Russian Space Agency (RSA), the Russian Academy of Science (RAS), the Russian Foundation Basic Investigation (RFBI);

5) Reservation and distribution of scientific grants on lunar subjects on a target competitive basis by Administration of the President of the RF, the MSE, the RFBI, RSA: 10 grants on 2 million rubles on 2013 - 2014 yrs; 15 grants - on 3 million rubles on 2015 - 2016 yrs;

6) Creation of uniform accessible bank of the scientific and technical data on the Moon within the framework of the project, creation of a website of the project in Russian and English languages within the framework of the universal standard of databases - " the Virtual Moon - 2015 + ";

7) Expansion of preparation of students, post-graduate students, young candidates of sciences and doctors on specialties: a space geodesy, planetary geophysics - in conducting high schools of the RF: the Moscow University, St. Petersburg University, Kazan University;

8) The Edition of the scientific encyclopedia " the Moon - 2015 + " and a lunar annual almanac (2014 yr.) with the purpose of scientific - methodical maintenance of practical exploration of the Moon;

9) Creation active, scientific - cognitive 3D-planetarium "Development and the Future of the Moon" (Kazan, 2014 yr.).

The International Center of the Science, Education and the Internet Technologies "GeoNa - 2017"

For the further successful development of scientific-educational and innovative-technological activity of the Russian Federation, the Republic Tatarstan, Kazan is offered the national project - the International Center of the Space Science, Cosmic Education and the Newest Space Technologies **"GeoNa"** (**Geometry of Nature** – **"GeoNa"** is developed wisdom, enthusiasm, pride, grandeur), which including: original designs building "GeoNa" - "Lobachevsky's surface", 59 floors, height 215 m (with a spike 302 m), the general area in 148,000 sq. metres, a modern complex of conference halls (up to 4 thousand seats), center the Internet of Technologies, Computer center, 3D Planetarium "Moon", training complex "Physics Land", active museum of space sciences, cognitive system "Knowledge Spheres of the Universe ", oceanarium with a fresh-water segment (5 million liters), botanical and landscape oases, business-hotel, where will be hosted conferences, the congresses, fundamental scientific researches, educational and recreation-tourist actions at a world organizational level.

fig.3. The International Center of the Space Science, Cosmic Education and the Newest Internet Technologies **"GeoNa - 2017"**

The research was partially supported by the Russian-Japanese grant RFBI-JSPS 11-02-92113-ЯФ_а and

the Russian-Chinese grant RFBI-GFEN 11-02-91160 ГФЕН_а

References

Gusev A., Petrova N., (2012) Rotation, physical librations and interior of the multi-layer Moon. The second edition of the book, processed and added, Kazan, Kazan University Press, 220pp. (Russian, in press)

Weber et al.,, (2011) Seismic detection of the Lunar core. Science, v. 331 (6015), p. 309-312.

PLANETARY RADIO INTERFEROMETRY AND DOPPLER EXPERIMENTS (PRIDE) WITH PLANETARY MISSIONS.

D.A. Duev[1,2], T.M. Bocanegra Bahamon[1,3,4], G. Cimò[1], L.I. Gurvits[1,3], G. Molera Calvés[1], S.V. Pogrebenko[1],

[1]Joint Institute for VLBI in Europe, Oude Hoogeveensedijk 4, 7991 PD Dwingeloo, the Netherlands; [2]Faculty of Physics, Lomonosov Moscow State University, GSP-1, Leninskie gory, 119991 Moscow, Russia; [3]Department of Astrodynamics and Space Missions, Delft University of Technology, 2629 HS Delft, The Netherlands; [4]Shanghai Astronomical Observatory, 80 Nandan Road, 200030 Shanghai, PR China; Contact: duev@jive.nl

The Planetary Radio Interferometry and Doppler Experiment (PRIDE) is designed as a multi-purpose, multi-disciplinary enhancement of space missions science return. The essence of PRIDE is in its ability to provide ultra-precise estimates of spacecraft state vectors based on phase-referenced VLBI tracking and radial Doppler measurements. These estimates can be used for a variety of scientific applications (both fundamental and applied) including planetary science (measurements of tidal deformations of planetary moons; atmosphere dynamics and climatology; seismology, tectonics, internal structure and composition of planetary bodies), ultra-precise celestial mechanics of planetary systems, gravimetry, spacecraft orbit determination and fundamental physics.

PRIDE can be conducted with (almost) any radio-emitting spacecraft. Current PRIDE ”customers” include the ESA’s Venus Express mission and the Russian Space Agency’s Space VLBI mission RadioAstron. To be more concrete, PRIDE-observations of RadioAstron as a target can significantly improve the orbit determination of the spacecraft - a factor critically important for the success of the whole mission. In addition to this, a better link between the Terrestrial and Celestial reference frames can be established by means of direct VLBI-tracking of GLONASS satellites using the methods developed within the PRIDE initiative.

PRIDE has been considered in a number of prospective space science and planetary missions, such as Gaia (astrometry), JUICE/Laplace (Jovian system), MarcoPolo-R (asteroid sample return).

In this presentation, we describe the principles of measurements, processing and analysis of PRIDE data developed at the Joint Institute for VLBI in Europe (Dwingeloo, The Netherlands) and present demonstration results of the latest observing campaigns conducted with several operational science missions in 2009–2012.

AEROSOL INVESTIGATIONS IN MARTIAN ATMOSPHERE BASING ON THE WIDE-ANGLE POLARIZATION SKY BACKGROUND MEASUREMENTS (THE ASTRO-DUST PROJECT)

O.S. Ugolnikov, I.A. Maslov,
Space Research Institute, Russian Academy of Sciences

The polarization measurements of the scattered radiation field are the well-known tool of the investigations of the medium microphysical characteristics, including the aerosol particles properties. If the measurements are conducted during the twilight period, the resulting parameters can be obtained as the function of the altitude. The work is successfully continuing on the Earth, the aerosol is being investigated in the troposphere, stratosphere and mesosphere.

The basic problem of such method on the Earth is the difficulty of aerosol scattering separation on the background of Rayleigh and multiple scattering. These components of sky background are the principal on the Earth, but they are both weaker on Mars, where the atmosphere is optically thin and the basic scattering is made by aerosol particles. The exactness of their microphysical investigations is expected to be better than on the Earth.

The polarization sky background (daytime and twilight) are suggested to hold during the ExoMars-2018 mission. The measurement device can have a little weight (0.2 kg) and power requirement (about 0.5 Watt). It can provide the information about different kinds of Martian dust in the atmosphere, including the dust storm periods.

SPICE: AN ARCHITECTURE FOR PROVIDING OBSERVATION GEOMETRY SUPPORTING SOLAR SYSTEM MISSIONS.

C. Acton[1],
[1]Jet Propulsion Laboratory, 4800 Oak Grove, Pasadena, CA, USA. Contact:cacton@jpl.nasa.gov

Introduction:

An important but often overlooked element of planning for and conducting solar system science missions is the infrastructure needed by scientists and engineers to determine and share the various aspects of mission geometry--items such as positions, instrument pointing directions, and target body size, shape and orientation. Making such computations can be time consuming and error prone.

An ancillary information system named "SPICE" has been developed at NASA over the past 20 years to substantially solve this problem. SPICE has been used by NASA scientists since the days of the Galileo mission. It has also been used by scientists associated with solar system missions operated by the Russian Space Agency, the European Space Agency, the Japanese Space Agency and the Indian Space Agency.

The SPICE system is comprised of elemental data files and associated software used to read those files and compute the quantities of interest to scientists such as range, lighting angles and field-of-view projections onto a planetary surface.

SPICE has proven to be very reliable and stable, and is rather easily applied to any kind of solar system or space physics mission.

This paper (or poster) provides a summary of important and unique features of SPICE of likely interest to the international space science community, and it outlines possibilities and programmatic requirements for further use of SPICE during the next decade of solar system exploration.

The research described in this publication was carried out at the Jet Propulsion Laboratory, California Institute of Technology, under a contract with the National Aeronautics and Space Administration.

BALLISTIC SUPPORT OF “SPECTR-RG” SPACECRAFT FLIGHT TO THE L_2 POINT OF SUN-EARTH SYSTEM

I.S. Ilin, G.S. Zaslavskiy, S.M. Lavrenov, V.V. Sazonov, V.A. Stepaniants, A.G. Tuchin, D.A. Tuchin, V.S. Yaroshevskiy,
Keldysh Institute if Applied Mathematics RAS, 117997, 84/32 Profsoyuznaya Str, Moscow, Russia

«Spectr-RG» mission presupposes a flight to the vicinity of the Sun-Earth system L2 point and halo orbit motion in the L2 point vicinity. The following methods and calculation algorithms have been developed:

- an algorithm, building nominal trajectories for one impulse flights to the halo orbit in the vicinity of the Sun-Earth system L_2 point, including a Lunar swingby maneuver or not;
- an algorithm, calculating ballistic parameters, needed for implementation of spacecraft trajectory corrections on its way from Earth to halo orbit and stationkeeping of the spacecraft moving in halo orbit;
- an algorithm, evaluating the accuracy characteristics of orbit determination and forecast based on trajectory measurements, provided by ground tracking stations.

The calculation of trajectories for one impulse flight from Earth to a halo orbit (including a Lunar swingby maneuver or not) uses initial approximations building algorithms. These initial approximations are built by two variables function isolines calculation and analysis. This is the function of the flight orbit pericentre height above the Earth surface. The arguments of the function are special parameters, describing the halo orbit.

For searching the time span, allowing to perform a gravitational maneuver in the vicinity of Moon to enter the halo orbit, there is an angle limit for Earth – Sun and Earth – Moon vectors.

The following halo orbit design requirements, providing required spacecraft solar cell panels illuminance and radio visibility from Russian tracking stations, situated in the northern hemisphere, were taken into account:

- if the spacecraft is near the ecliptic plane, it can enter the penumbra area;
- if the spacecraft gets too far from the ecliptic plane, there are long periods of time with no radio visibility.

The problem of obtaining halo orbits with the given values of parameters, determining orbit geometry in the ecliptic plane and in the plane orthogonal to it has been solved. Characteristic velocity needed for keeping the spacecraft in halo orbit has been evaluated. Primary evaluations of orbit parameters determination and forecast accuracy have been obtained.

Developed methods and algorithms were applied for “Spectr-RG” spacecraft orbit design and can be used for its flight implementation.

MASS-SPECTROMETRIC METHODOLOGY FOR SIGNS OF LIFE SEARCH VIA ANALYSIS OF THE ELEMENT COMPOSITION OF THE SUPPOSED BIOMASS EXTRACTED FROM AN ICY MATRIX

Moisseenko D.A., Managadze G.G., Vorob'eva E.A., Chumikov A.E., Managadze N.G.;
Space Research Institute of the Russian Academy of Sciences, Profsoyuznaya 84/32, GSP-7, Moscow 117997, Russian Federation,
moiseenko-da@yandex.ru, managa@bk.ru, esautin@yandex.ru

A mass-spectrometric methodology for identifying signs of life in a sample extracted from an icy matrix of extraterrestrial objects is presented. The structure and composition of a laboratory prototype of an onboard measurement facility addressing the assigned astrobiological task is analyzed.

The proposed instrument can be used to analyze the element composition of the supposed extraterrestrial biomass and compare it to the element composition of terrestrial microorganisms. Biomass is to be identified by a number of criteria: the presence and abundance ratio of matrix biogenous elements – H, C, N, O; abundance ratios of biogenous macroelements, P/S, K/Ca, the presence of other biologically important elements (e.g., Cl) and microelements, such as Mg, Fe, Cu, Zn, and F.

The results of measurements performed on microorganisms *Bacillus subtilis, Bacillus pumilus, Arthrobacter, Sphingomonas, Acinetobacter* and soil samples *Green River Shale SGR-1b, Dolomitic Limestone, Basalt BHVO-2* confirm the applicability of this methodology methodology. Various methods of extracting the biomass from the icy matrix are discussed.

The element composition of the sample studied is to be performed using the onboard LASMA time-of-flight laser mass-reflectron identical to the instrument developed for the «Phobos-Grunt» mission. The system of sample preparation is based on the separation of the biomass from water by evaporating pre-desalted aqueous solution obtained by melting the icy core.

The methodology can be used to search for and identify biomass in ice samples retrieved from his subsurface layer of Solar-System planets or satellites of the planets, such as Mars, Europa, and Enceladus.

This work was supported by the grant of the Russian academy of sciences Presidium Program 22: "Fundamental problems of research and exploration of the Solar system".

TRANSIT OBSERVATIONS EXOPLANETS IN THE CRIMEAN ASTROPHYSICAL OBSERVATORY

Antoniuk K. A.[1, 2], N., Pit' N.V.[1], Ksanfomality L.V.[2],
[1]Crimean Astrophysical Observatory, Crimea, Ukraine, [2]Space Research Institute of the RAN, Moscow, Russia

Abstract. There are profiles of brightness obtained at nine transits of exoplanets WASP-43b, WASP-16b, HAT-P-36b, WASP - 3b, WASP-24b. Observations were obtained using 1.25-m telescope AZT – 11 of the CrAO Research Institute. They were made using CCD-photometer in R- band photometric system of Cousins. For the WASP-43b object 4 transits were obtained, which show the amplitude of the brightness variations about $0^m.05$ (Fig. 1). A typical error of a single observation is $0^m,003$. A control of the star brightness stability shows no variability with an amplitude exceeding $0^m.01$. The brightness of the star WASP-43b out of transites varies at different nights, which one can treat as a long-term variability of stars itself. From one transites to another the eclipse profile changes. The curve is observed both as a symmetrical or asymmetrical profile. The variability of the profile may be associated with spots on the star disc. The star spectral type is K7V.

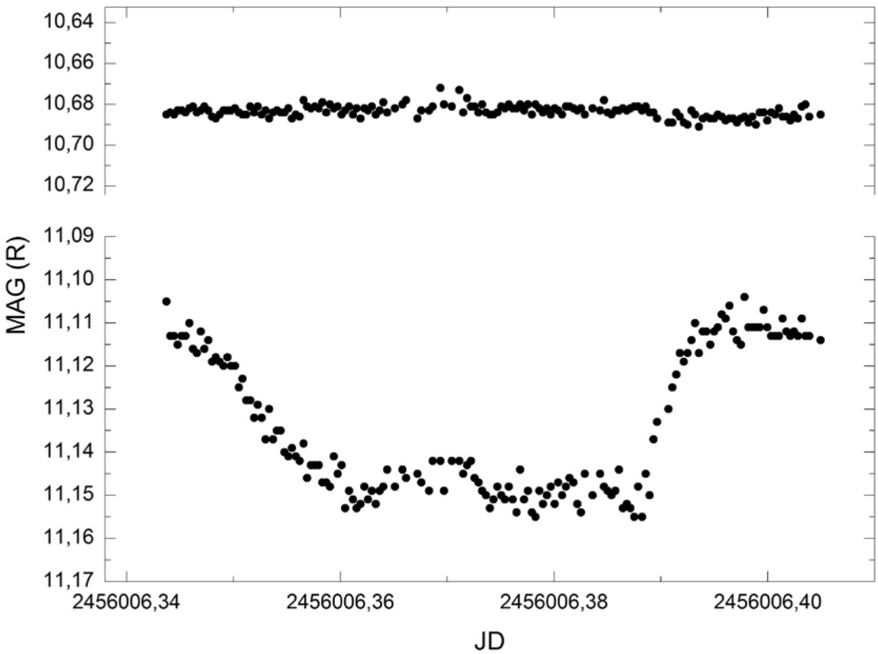

fig. 1. The light curve of the exoplanet WASP - 43b transit across the stellar disk (lower curve) obtained 19.03.2012 by the 1.25-m telescope of the Crimean Astrophysical Observatory. The upper curve – control of the star brightness stability.